Applications for Through-Vial Impedance Spectroscopy (TVIS) in the Development of Pharmaceutical Freeze-Drying Processes

Yowwares Jeeraruangrattana

Leicester School of Pharmacy, De Montfort University

July 2020

PhD Thesis

In partial fulfilment of the requirements for the degree of

Doctor of Philosophy

Submitted to

De Montfort University

Declaration

I, Yowwares Jeeraruangrattana, declare that the content presented within this thesis is original undertaken by myself for the Doctor of Philosophy Degree, at the School of Pharmacy, Faculty of Health and Life Sciences, De Montfort University, Leicester, United Kingdom. I confirm that information derived from other sources has been indicated accordingly in this thesis.

Abstract

In recent years, through-vial impedance spectroscopy (TVIS) has been identified as a process analytical technology for the determination of critical process parameters within individual vials, at user-defined locations across a lab-scale freeze dryer. Much of the work to date, which is collated in Muhammad Sohail Arshad's (2014) PhD thesis, employed a guard electrode assembly attached to a standard 10 mL type-I tubular glass vial and focused on the dielectric loss peak during (1) the freezing steps (demonstrating the impact of the filling volume and the influence of sucrose on the crystallisation of mannitol), (2) the annealing steps (establishing a method for the measurement of the glass transition temperature) and (3) the primary drying steps (determining the primary drying rate and the end point), with some observations on the manifestation of the collapse event. These studies were restricted to the investigation of the dielectric loss peak associated with the relatively low conductivity solutions sucrose, mannitol and maltodextrin whereas the more conductive solutions (i.e. those solutions spiked with electrolytes) were not investigated. Also, no attempt was made to measure product temperature and the determination of drying rate was impossible with this vial design. Therefore, the full potential of TVIS technology was not realised.

In this research programme, the TVIS measurement vial was re-designed in order to further develop and refine applications for TVIS technology across the freezing, annealing and drying stages of the lyophilisation cycle, with new methods being developed for the determination of (1) nucleation onset and ice-growth end point (this could be applied to the more conductive solutions containing high levels of salt), (2) the glass transition temperature, (3) the sublimation rate and (4) the ice temperatures at the sublimation interface and at the base of the vial, from which the heat transfer coefficient, in-vial product collapse event, and the dry layer resistance could be determined. In order to characterise phase transition (1) and (2), it was necessary to look at the characteristics of the real part capacitance (i.e. dielectric storage) in high and low frequency region (relative to the characteristic relaxation frequency of the ice) instead of simply relying on the characteristic of the dielectric loss peak in the imaginary part capacitance.

In chapter 6, the design of the TVIS measurement vial was revisited in order to establish whether it was possible to improve the quality and applicability of the TVIS spectrum by studying the factors that affect measurement response, namely (1) guard vs non-guard electrode designs, (2) electrode dimensions (with the height of the electrode increasing from 5 mm to 15 mm), (3) the position of the electrode above the base of the vial and (4) electrode attachment techniques (i.e. adhesive copper foil, sputter coating, tape wrap and glass surface treatment). A standard vial with 10 mL of nominal capacity and a non-guard-type electrode pair with dimensions of 19 x 10 mm, positioned at a distance of 3 mm from the base of the vial, is the suggested geometry for the measurement vial. This design can then be used as the standard vial for tracking the progression of the product during the various stages of the freeze-drying process – freezing, annealing and primary drying. No additional dielectric processes were observed from the adhesive of the copper foil electrode, and it is acceptable to use this adaptable method for investigating different vial designs in the future.

In chapter 7, a universal method for determining the ice nucleation temperature of conductive solutions was developed. When cooling 5% sucrose solutions with different salt concentrations (0%, 0.26% and 0.55% NaCl), it was clear that the Maxwell-Wagner (MW) relaxation process of the liquid state of these conductive solutions (i.e. the sample containing salt) remained outside of the TVIS measurement window (even at the sub-zero temperatures that the solutions reaches prior to nucleation). It was only after the ice started to form that a relaxation peak emerged within the experimental frequency window (owing to the presence of an ice phase within the vial). Therefore, an approach based on the MW relaxation peak could not be used to determine the liquid to solid phase transition (ice nucleation). Instead, at low frequency (i.e. 10 Hz), the real part capacitance was found to be more useful for indicating the point of nucleation, given the sensitivity of the MW relation peak to the temperature of the solution. Another interesting observation was that at a frequency above ice relaxation (i.e. 0.2 MHz), the real part, which has almost no temperature dependence, could identify the point where the solidification process was completed. Then, the ice growth period could be calculated from the difference in time

between the onset and end point of the ice crystallisation process. Notably, based on this particular study, the ice formation period increases with increased salt concentration.

In chapter 8, different facets of TVIS response were investigated in order to provide an insight into the underpinning of physical mechanisms related to phase change and the structural modification of the product contained in a conventional 10 mL TVIS vial during the freezing and annealing steps. Aqueous solutions of 5% w/v sucrose were treated to three different cooling–heating cycle experiments with annealing/holding temperatures of −35 °C, −32 °C and −10 °C. Each experimental solution was annealed three times and two key observations were made. The first was that the drift in the amplitude of ice relaxation peak (C''_{PEAK}) during the holding period was more pronounced at higher annealing temperatures, especially when the annealing was performed above its glass transition temperature, T'_g (as determined by DSC). This observation was explained by the alteration of the ice crystal structure during the recrystallisation process, which increases the conductivity of mobile charges and results in greater charge accumulation at the glass wall (which is a factor that indirectly impacts the magnitude of the ice relaxation peak). The second observation was that by heating the frozen sucrose solution through its glass transition (to –10 °C), it was possible to demonstrate an inflection in the temperature profile of C'(0.2 MHz), which coincided with the T'_g of the sucrose solution. Unlike the structure alteration, this discontinuity of the real part might be a consequence of the temperature dependence of the unfrozen phase rather than the ice relaxation process, and it was therefore proposed that this transition provides an opportunity to develop a new method for measuring the in-situ glass transition of the freeze-concentrated phase.

In chapter 9, a method was developed for predicting the sublimation rate and ice interface temperature, based on the peak amplitude (C''_{PEAK}) and the peak frequency (F_{PEAK}) of ice relaxation in a frozen aqueous solution of 5% w/w lactose. Dried layer resistance (Rp) could be determined from these critical process parameters. The results showed a relationship between the sublimation rate and the microstructure of the dried matrix, particularly when the ice temperature at the sublimation front reached the critical product temperature. It may therefore

be concluded that this method could be used for the routine determination of in-vial collapse temperature and whether the collapse temperatures determined by the freeze-drying microscope are relevant to the process scale.

In the last chapter, the TVIS measurement vial was once again modified with the development of a dual-pair electrode system for predicting ice temperature at the sublimation front and at the base of the ice cylinder. From these two temperatures and the sublimation rate (as predicted using the method described in chapter 9), it was possible to estimate the single-vial heat transfer coefficient using a method first defined by Pikal and his co-workers (1984). The value of the heat transfer coefficient for this vial type was comparable to that found in published work (Tchessalov, 2017).

In conclusion, this work highlights the prospective applications of broadband (10 Hz to 1 MHz) impedance measurement, known as through-vial impedance spectroscopy, for investigating the in-vial characteristics of a solution within a freeze dryer and during the freezing, re-heating and sublimation phases. A range of physical phenomena was inferred from data extracted from both the real and imaginary parts of the TVIS spectrum and then used to deliver a comprehensive set of process parameters that will be valuable in the development and optimisation of future freeze-drying processes. Further work should consider a wider range of solutions containing small molecule and biological drugs in particular, and the extension of the applications to the secondary drying phase. Then it may be said that the work has come full circle by expanding on the earliest work on TVIS-type methodologies that was undertaken by Phe Suherman and collated in her PhD thesis of 1991.

Table of contents

Declaration I

Abstract II

Table of contents VI

List of figures XII

List of abbreviations (unit) XXXVII

Definition of TVIS terminology XLIV

Acknowledgements XLV

1. Introduction 1
   1.1. The freeze-drying process 1
      1.1.1. Fundamentals of the freeze-drying process: phase diagram 2
   1.2. Stages of freeze-drying 4
      1.2.1. Freezing 4
         Crystallization of ice 7
         Crystallization in aqueous solution 8
      1.2.2. Annealing 10
         Morphological changes of ice crystals during annealing 12
         Phase transition of amorphous phase during annealing 16
      1.2.3. Primary drying 23
         Heat transfer mechanism in freeze drying 25
         Mass transfer mechanism in freeze-drying 28
      1.2.4. Secondary drying 30
   1.3. Available process analytical technology for freeze-drying 31
      1.3.1. Product temperature 33
         Single vial techniques 33
         Batch techniques 35
      1.3.2. Chamber pressure measurement 38

2. Gap in the knowledge 42

3. Aim and objectives 44
3.1. Aim 44
3.2. Objectives 44
Objective 1: 44
Objective 2: 44
Objective 3: 44
Objective 4: 44
Objective 5: 45
Objective 6: 45
4. Rationale for the selection of excipients 46

5. An overview of Through-vial impedance spectroscopy 48
5.1. Objective 48
5.2. Introduction to the electrical properties of material 48
5.2.1. Electrical conductivity 49
5.2.2. Dielectric polarization 49
5.2.3. Dielectric constant or relative permittivity 52
5.2.4. The use of electrical measurement in freeze-drying 54
5.3. Through-vial impedance spectroscopy 55
5.3.1. Impedance spectroscopy measurement 55
5.3.2. Equivalent electrical circuit 58
5.3.3. Description of Through-vial impedance spectroscopy measurement 65
5.3.4. Dielectric mechanisms of aqueous solution and its frozen state 71
Liquids and the Maxwell-Wagner Polarization of the Glass 71
Frozen Water and the Dielectric Relaxation of Ice 75
5.3.5. Equivalent circuit for TVIS vial 79
5.3.6. Applications of Through-vial impedance spectroscopy 83
TVIS parameters 84
The application of TVIS parameters for monitoring freeze-drying process. . 88
5.3.7. Limitations of through-vial impedance spectroscopy 92

6. Electrode optimization for TVIS measurement vial 97
6.1. Objective 97

6.2. Materials and methods 98
Study I 99
Study II 100
Study III 101
Study IV 103
Study V 105
6.3. Results and Discussion 109
Study I 109
Study II 116
Study III 119
Study IV 121
Study V 133
6.4. Summary 135

7. Characterisation of phase transition during freezing step by TVIS 136
7.1. Objective 136
7.2. Materials and Methods 136
7.2.1. Preparations 136
7.2.2. Vial filling and loading the freeze dryer 136
7.2.3. Through-vial impedance spectroscopy 139
7.2.4. Freezing protocol 140
7.2.5. Photographic images 140
7.2.6. Analysis impedance spectrum 141
7.3. Results and Discussion 142
7.3.1. TVIS parameters for characterisation of liquid-solid phase transition 142
Ice nucleation 146
Solidification 152
7.3.2. Determination of ice nucleation temperature 157
7.3.3. Impact of salts on the ice formation period 166
7.4. Summary 169

8. Effect of annealing on the structure of frozen matrices 170
8.1. Objective 170
8.2. Material and Methods 170
8.2.1. Preparations 170

8.2.2. Thermal analysis 170
Conventional differential scanning calorimetry 170
Modulated differential scanning calorimetry 171
8.2.3. Vial filling and loading of the freeze dryer 171
8.2.4. Through-vial impedance spectroscopy 174
8.2.5. Freeze-drying protocol 175
8.2.6. Impedance analysis software 176
8.3. Results and Discussion 177
8.3.1. Determination of glass transition temperature of freeze-concentrated solution by thermal analysis 177
8.3.2. Characterisation of the structural modification of frozen matrices by the through-vial impedance spectroscopy technique 180
TVIS spectrum 180
Impact of annealing temperature and cycles 185
Effect of annealing on the microstructure of the frozen matrix 194
8.3.3. Determination of glass transition temperature of freeze-concentrated solution by through-vial impedance spectroscopy technique 199
8.4. Summary 201

9. TVIS approach to assessment product during primary drying 202
9.1. Objective 202
9.2. Materials and Methods 202
9.2.1. Preparations 202
9.2.2. Differential scanning calorimetry 202
9.2.3. Freeze-drying microscope 203
9.2.4. Vial filling and loading the freeze dryer 203
9.2.5. Through-vial impedance spectroscopy 206
9.2.6. Freeze drying protocol 207
9.2.7. Scanning electron microscope 208
9.3. Results and Discussion 209
9.3.1. Determination of critical temperature by thermal analysis and freeze-drying microscope 209
9.3.2. Process parameters 210
9.3.3. TVIS results 211
9.3.4. Measurement of product temperature 217

Ice temperature calibration 217
Prediction of ice temperature at the TVIS node 218
9.3.5. Estimate of the residual ice mass 220
Compensation of C''_{PEAK} for temperature 221
Conversion of $\hat{C}''_{PEAK}$ to ice mass 226
9.3.6. Primary drying rate determination 228
9.3.7. Estimation of the ice height and the dry layer thickness 229
9.3.8. Ice interface temperature prediction 231
9.3.9. Dry product resistance determination 235
9.3.10. Impact of collapse on sublimation rate 241
9.4. Summary 242

10. An application of dual-electrode TVIS for primary drying process monitoring 243
10.1. Objective 243
10.2. Materials and Methods 243
10.2.1. Measurement principle 243
10.2.2. Vial filling and loading the freeze dryer 247
10.2.3. Freeze-drying protocol 248
10.3. Results and Discussion 250
10.3.1. Ice temperature calibration 250
10.3.2. Temperature compensate for C''_{PEAK} 251
10.3.3. Primary drying rate determination 252
10.3.4. Prediction of ice interface and ice base temperatures 254
10.3.5. Qualification of the ice interface temperature prediction 256
10.3.6. Qualification of primary drying rate estimation 258
10.3.7. K_v determination 259
10.3.8. Limitations of TVIS system 261
10.4. Summary 267

General conclusion and future work 268
General conclusion 268
Future work 269

References 270

Publications 288
Journal articles 288
Poster presentations 288

Appendix I 296
Standard operating procedure for assembling a copper foil electrode and wiring of a TVIS measurement vial 296

Appendix II 316
Fill factor calculation 316

Appendix III 317
Calibration of C''_{PEAK} for liquid height 317

Appendix IV 318
Calibration of C''_{PEAK} for ice height 318

List of figures

Figure 1 The freeze-drying process: (I) freezing; (II) annealing (optional); (III) primary drying; (IV) secondary drying. The solid line represents temperature and the dashed line represents pressure. 2

Figure 2 Phase diagram of water 3

Figure 3 Illustration of the constitutional supercooling region during freezing of solutions. The accumulation of solutes in the liquid near the ice surface produces a concentration gradient that affects the equilibrium freezing temperatures. 10

Figure 4 The growth of ice crystals over time. The sucrose solution (28.6%) was annealed at −8 °C (Hagiwara, Hartel & Matsukawa, 2006). 12

Figure 5 Illustration of the various processes of sintering: surface diffusion; gas phase transport; boundary diffusion; and volume diffusion. The grey dashed line represents the ice boundary and the radius of concave and convex curve are r_1 and r_2, respectively. 14

Figure 6 A schematic state diagram of sucrose solution at constant pressure showing equilibrium melting line for ice (T_m) and glass transition line (T_g). The glass transition line is predicted by using the Gordon-Taylor equation with the following value: (1) a constant value (k_{GT}) = 4.94, (2) T_g water = 136 K, and (3) T_g of sucrose = 343 K (Constantin, Schneider & Corti, 2016). At maximum freeze-concentrated concentration (C_g') of 80%, glass transition temperature (T_g') is −45 °C. The melting temperature of mixture at C_g' is denoted by T_m' (Roos, 2010). 23

Figure 7 Illustration of two mechanisms involving primary drying process. Heat from the heat source (freeze dryer shelf) transfers into the frozen product through the bottom of the glass vial including the gap (due to the curvature of vial's bottom) in order to sublime ice (heat flux) and the ice vapour from sublimation flows through the dried layer (mass flux). 25

Figure 8 Heat transfer mechanisms during primary drying: *direct conduction* from the shelf, *radiation* either from walls of the dryer or/and the lyophilizer door, and *gas conduction* (convection). 26

Figure 9 Process analytical technology (PAT) technology for monitoring primary drying process 32

Figure 10 Temperature measurement sensor (a) vial containing a fine-gauge thermocouple wire along with a device (thermocouple holder from Millrock Technology, USA) for positioning the thermocouple tip at the centre of the vial and touching the bottom, (b) vial containing a Pt100 RTD sensor (Nail et al., 2017), (c) TEMPRIS wireless sensor contained in the vial having the electrode (19 x 10 mm) on the external surface of glass vial (defined as a TVIS vial), and (d) a small RTD developed by Ellab Inc., Denmark (Nail et al., 2017). 34

Figure 11 Manometric temperature measurement (MTM) valve isolates the freeze dryer chamber from the condenser. Open and closed positions of MTM valve are demonstrated. .. 36

Figure 12 Schematic of Tunable diode laser absorption spectroscopy (TDLAS) installed in the connecting duct between freeze dryer chamber and condenser..... 37

Figure 13 Schematic of pressure gauge: (a) thermocouple gauge, (b) Pirani gauge, and (3) capacitance manometer (Kurt J. Lesker Company, 1996). 39

Figure 14 Demonstrating a process monitoring technique "the comparative pressure measurement" for immunoglobulin formulation: capacitance manometer (a solid black line), Pirani gauge (a solid dark grey line). The shelf temperature and product temperature are represented by a dashed black line and a solid light grey line, respectively. The end point of primary drying is marked by the black arrow while the grey arrow indicates a spike due to a desorption process at the early stages of secondary drying. 41

Figure 15 Outline of the objectives demonstrated in the freeze-drying cycle. 45

Figure 16 Dielectric polarization mechanism: (a) electronic polarization; (b) ionic or atomic polarization; (c) orientational polarization; and (d) interfacial polarization 51

Figure 17 Illustration of charge and discharge process of capacitor: (a) neutral capacitor (uncharged); (b) capacitor charges; and (c) capacitor discharges 52

Figure 18 Real (ε_r') and imaginary (ε_r'') parts of the complex relative permittivity ($\boldsymbol{\varepsilon}$) of material corresponding to frequency. Interfacial polarization is prominent at frequencies below MHz range, Orientation polarization occurs at frequencies around 10^9-10^{10} Hz; ionic polarization

influences the permittivity at a frequency range of 10^{12}-10^{13} Hz, and electronic polarization is observed at frequencies around 10^{14}-10^{16} Hz (Nickelson, 2019)..... 53

Figure 19 A sinusoidal waveform of voltage in an AC circuit..... 57

Figure 20 Illustrating a phase difference (φ) when an AC source connects to the test object which consists of resistance (R) and capacitance (C) element (RC circuit). In this RC circuit, the resultant current leads the voltage by 45°, or phase difference is −45°. Note, a negative phase shift means that the voltage lags behind the current. 57

Figure 21 (a) series and (b) parallel combination of the circuit elements..... 59

Figure 22 Impedance response of the single elements: (a) resistance and (b) capacitance. The values for the resistance (R) and the capacitance (C) are 200 MΩ and 0.60 pF, respectively. . 60

Figure 23 Typical impedance responses of a resistance and a capacitance (a) in series and (b) in parallel. The values for the resistance (R) and the capacitance (C) are 200 MΩ and 0.60 pF respectively. 61

Figure 24 (a) Impedance responses of the complex composite object and (b) capacitance spectrum of the same object. The equivalent circuit model used for this object is represented by $C_2 - (R = C_1)$, ''−'' and ''='' mean a series and a parallel arrangement of the circuit element respectively. The values for the resistance (R), the capacitance 1 (C_1) and the capacitance 2 (C_2) are 200 MΩ, 0.04 pF and 0.60 pF respectively. The impedances of individual elements are shown in the top graph of (a), R;C_1; and C_2, and are represented by a grey dotted line, a grey solid line, and a grey dash line, respectively. Real-part capacitance in the limit of low frequency ($C'(0)$) and high frequency ($C'(\infty)$) is demonstrated in the top graph of (b); while the characteristics of dielectric loss peak (imaginary-part capacitance), namely peak frequency (F_{PEAK}) and peak amplitude (C''_{PEAK}) are illustrated in the bottom graph of (b)..... 63

Figure 25 TVIS measurement system comprising the following basic parts: (a) a data acquisition (DAQ) card and the processing software installed in a computer CPU, (b) an impedance analyser, (c) a pass-through, (d) a junction box, a TVIS measurement vial (vial on the left side) and thermocouple (TC) contained vial (vial on the right side) locate in the freeze dryer chamber, (e) a user interface, and (f) data analysis software. The TVIS measurement vial and TC vial is placed on the bottom shelf of the freeze dryer while the five-channel multiplexer (junction box) sits on

the top shelf of the freeze dryer. A thermocouple tip is manually placed at the centre point of the volume of sample bounded by the electrodes (TVIS sensing node) to represent the product temperature of the TVIS measurement vial (Smith et al., 2017). The black solid arrow demonstrates the pathway of the stimulating signal while the grey dotted arrow is the pathway of the sensing signal..... 68

Figure 26 (a) sketch of a standard 10 mL Type I tubular glass vial (supplied by Adelphi-HP as VC010-20C), modified with a pair of 19 x 10 mm electrodes attached to the external surface of the vial at a position of 3 mm from the base (referred to as “single electrode system”); (b) a projected view and cross-sectional three-dimensional drawing of the segment of the TVIS vial containing sample; and (c) dimension of the TVIS vial d_b : The distance of the bottom edge of the electrode from the base of the vial; h_{RE} : height of the sample in the region bounded by the electrode; h_E : height of the electrode; d_m : distance from the base of the vial of the mid-point of the sample contained within the region bounded by the electrodes. The fill factor is defined as a ratio of the height of the sample within the region bounded by the electrode (h_{RE}) to the electrode height (h_E). The calculation is demonstrated in Appendix II. 70

Figure 27 TVIS measurement vials: various designs of containers for freeze-drying that have been modified with copper foil electrodes (10 mm in height and 3 mm from the base for each container). From left to right are: (a) 10-mL Type I tubular glass vial, 20 mm crimp-neck (supplied by Adelphi-HP as VC010-20C); (b) 5-mL Type I tubular glass vial, 20 mm crimp-neck (supplied by Adelphi-HP as Adelphi VC005-20C); (c) 5-mL Type I tubular glass vial, screw-neck (supplied by Adelphi-HP as Adelphi VCD005); and (d) 2.5 mL glass ampoule (provided by the National Institute of Biological Standards and Control, UK)..... 71

Figure 28 (a) real and (b) imaginary capacitance spectrum of (1) double distillation water (the solid lines) and (2) 0.14 mM potassium chloride solution (the dashed line) contained in a TVIS-modified Adelphi VC010-20C glass tubing vial (with electrodes of dimension 19 x 10 mm and positioned 3 mm from the base). The simulation data of both samples at a frequency above TVIS range (1 MHz-1 THz) are illustrated by dotted lines. For water, the measurement at three temperatures of +20 °C, −20 °C and −40 °C are shown. The increments in the real-part capacitance spectrum (a) for water sample are marked with Roman numerals: (I) is the simulated contribution

to the capacitance resulting from orientation polarization of the liquid water at +20 °C, with a dielectric loss peak at frequency of ~ 17 GHz (microwave range); (II) the physical mechanism is contributed by the Maxwell-Wagner polarization of the glass wall of the TVIS vial at ambient temperature (+20 °C), with a loss peak frequency of 18 kHz; (III) and (IV) are the contribution from dielectric relaxation of frozen water at −20 °C and −40 °C respectively, for which the dielectric loss peak frequencies are 2.6 kHz and 537 Hz, respectively. For 0.14 mM KCl, the addition of a small amount of electrolyte (i.e. KCl) in double-distilled water could contribute to the polarization mechanisms of the water by shifting the dielectric loss peak from 18 kHz to the higher frequency at 0.26 MHz. 73

Figure 29 Illustration of a glass segment in contact with an electrode. This schematic shows the physical mechanisms occurring in a TVIS vial filled with a liquid product. The basic component of the product is water (permanent dipole molecule), which has both dielectric properties (dipole polarization or orientation polarization) and conductivity (Grotthus or proton-hopping). The polarization process of the glass wall is contributed by the electronic polarization occurring at microwave frequency. The physical-based equivalent circuit of the product contained in the TVIS vial could be modelled by a parallel RC circuit of the solution (R_sC_s) connected with the capacitance of the glass wall-sample interface (C_G). Note C_G means the sum of the glass wall-sample capacitance (C_g) from two glass segments in contact with electrode ($C_G = C_g^2/2C_g$). 75

Figure 30 Illustration of a glass segment in contact with an electrode. This schematic shows the physical mechanisms occurring in a TVIS vial having a frozen product. The equivalent circuit model describing the physical characteristics of the TVIS vial containing the frozen product is modelled by one of the distributed elements known as the Cole-Cole element, Co, the instantaneous capacitance of ice, $C_s(\infty)$; and the glass wall capacitance, C_G. The Cole-Cole element representing the dielectric relaxation of ice and instantaneous capacitance of ice reflects the physical mechanisms of the frozen sample. The ice-glass wall capacitance, meanwhile, is modelled by C_G, which is the total glass wall capacitance from two glass segments in contact with electrode, $C_G = C_g^2/2C_g$..... 78

Figure 31 Normalised data of the experimental data and fitting data of ice at temperature −20 °C and −40 °C. The experimental data are represented by circle symbol, −20 °C (closed); −40 °C (open), and the fitting data are denoted by line, −20 °C (black); −40 °C (grey). The simplified model for frozen $C_G - (C_s(\infty) = Co)$ is used for fitting. In order to demonstrate more clearly the broadening of the relaxation peak, the imaginary capacitance is plotted on a log scale against normalised $Log\ F_{PEAK}$, which is obtained by normalising each spectrum with its peak frequency. 79

Figure 32 TVIS test object. The TVIS vial is a standard tubular glass vial supplied by Adelphi (VC010-20C), modified by attaching a pair of electrodes (dimensions 10 mm by 19 mm) directly to the external of glass vial at a distance of 3 mm from the vial baseline. Double-distilled water corresponding to a fill factor of 0.8 (~3.3 g) was placed in the the TVIS vial..... 80

Figure 33 Demonstrating the differentiation of low frequency response between the measurement spectrum of 5.75 g ultrapure water corresponding to a fill factor of 1.2 (water is above electrode) and model data is generated from a complex model, $C_2 - C_1 = R$. The values of model parameters are 2.80 pF, 3.69 pF and 1.88 MΩ for C_2, C_1 and R repectively. The arrow indicates the upward trend of water spectrum at frequency below 1 kHz..... 81

Figure 34 Broadband dielectric response of ultrapure water 3.5 g filled in TVIS vial at +20 °C and −20 °C. (a) Ultrapure water contained in a modified TVIS vial by replacing MCX connector (133-3402-101, Johnson-Cinch connectivity, USA) and micro coax cable 36 AWG (9436 WH033, Alpha wire, USA) with banana plug and a metal wire placed on the dielectric sample cell of broadband dielectric spectrometer or BDS (Alpha-A, Novocontrol, Germany) before inserting into cryostat. (b) Real part of the permittivity of water in liquid state (+20 °C) and frozen state (−20 °C) measured by BDS system. (c) Imaginary part of the permittivity of water and ice measured by BDS system. The Maxwell-Wagner (MW) polarization process of glass-sample interface moves to lower frequency outside the TVIS measurement range (10 Hz to 1 MHz)..... 82

Figure 35 The TVIS response of ultrapure water equivalent to fill factor 0.7 (3.4 g) filled in the TVIS measurement vial with 19 x 10 mm electrodes at a distance of 3 mm from the vial's base is fitted to: (a) simplified model, $C_G - (R_s = C_s)$; and (b) enhanced model having CPE element to account for the physical mechanism occurring within a porous borosilicate glass matrix, ($C_G =$

$CPE) - (R_s = C_s)$. By inclusion of CPE element, the fit results match perfectly with the data. 83

Figure 36 Experimental data of resistivity of ultrapure water from 0-100 °C (Bevilacqua, 1998) 85

Figure 37 C''_{PEAK} dependence on the height of sample from the bottom edge of the electrode (a) ultrapure water at temperature ~ 22 °C, and (b) frozen water at −22 °C. *Zone I* is the region above the electrodes where the fringing field contributes to the overall capacitance despite the fact that the sample in this region is above the electrodes; *Zone II* is the non-linear response region when the sample is close to the top edge of the electrodes; *Zone III* is the quasi-linear response region to the sample where the electric field is uniform; *Zone IV* is the non-linear response region to the sample close to the bottom edge of the electrodes where the electric field is not constant. Note the method of C''_{PEAK} calibration for the sample height is illustrated in Appendix III and in Appendix IV for liquid and frozen sample, respectively. 87

Figure 38 Demonstrating temperature dependence of real-part capacitance at 10 Hz (filled circle) and 0.2 MHz (open circle) of (a) pure ice (Smith & Jeeraruangrattana, 2019a), and (b) 5% w/v sucrose in a frozen state (data from Chapter 8). The data are recorded during the re-heating stage from −40 °C to −10 °C with 0.5 °C·min^{-1} for pure ice and from −50 °C to −10 °C with 0.2 °C·min^{-1} for the frozen 5% w/v sucrose, respectively. 88

Figure 39 Basic TVIS responses of the dielectric loss spectrum (imaginary-part capacitance) of a 10 mL standard TVIS vial (electrode dimension of 19 x 10 mm at distance 3 mm from the vial's base) containing 3.5 g double-distilled water during the freeze-drying process: (a) cooling the liquid phase; (b) liquid-solid phase transition (water to ice); (c) re-heating of frozen water; and (d) primary drying. 90

Figure 40 A schematic of the recent applications of different features of TVIS technology for monitoring the freeze-drying process. 91

Figure 41 (a) Real and (b) imaginary-part capacitance of 3.5 g ultrapure water contained in the TVIS vial either with or without a thermocouple (TC). The influence of the thermocouple on the liquid spectra (+20 °C) is evidenced by the distortion of the spectrum of water contained in the

TVIS vial with a thermocouple (filled circle); however, the thermocouple has a lower impact on the spectrum when the sample is in the frozen state at −20 °C (open circle). 93

Figure 42 TVIS responses - (a) real part and (b) imaginary part - of a TVIS containing 3.2 g ultrapure water at 19 °C, showing an identical shape between the TVIS vial without thermocouple (TC) and the same vial with either a fibre-optic or wireless sensor (TEMPRIS®). 94

Figure 43 The temperature calibrations of two cycles of re-heating are plotted using the temperature data from (1) thermocouple (TC) in the vial close to the TVIS vial and (2) a wireless system (TEMPRIS®) within the TVIS vial. There is no significant difference in the calibration coefficient between using the product temperature in the nearest neighbouring vial and the temperature in the TVIS vial (measured by TEMPRIS®)..... 94

Figure 44 The capacitance spectra, (a) real and (b) imaginary part, of ultrapure water (2.5 g) contained in the TVIS vials, (c) a coated vial (TopLyo®), and (d) a standard vial. The meniscus observed in a standard vial (d) introduces additional glass wall impedance at frequencies below 250 Hz. 96

Figure 45 A summary of the experimental studies performed for optimizing TVIS measurement vial. 98

Figure 46 Photographic images of two different types of TVIS measurement vial. (a) TVIS vial with guard vial (G) with guard electrode around the active electrodes, each with dimensions of 18 x 5 mm (w x h). The guard vial with 2 g of double-distilled water placed on the freeze dryer shelf is shown on the left. (b) TVIS vial having only a pair of active electrodes (18 x 5 mm), referred to as the non-guard TVIS vial (NG). The non-guard vial with 2 g of double-distilled water placed on the freeze dryer shelf is demonstrated on the right. 99

Figure 47 Non-guard vials with an electrode height of (a) 5 mm, (b) 10 mm, (c) 12.5 mm and (d) 15 mm. (e) The non-guard TVIS vial with an electrode height of 10 mm (c) was used for demonstrating a liquid level at the fill factor of 1. 100

Figure 48 Various attachment techniques are conducted for making the TVIS measurement vials: (a) adhesive tape; (b) sputtering by sputter coater (Q150RS, Quorum Technologies, Sussex, UK); (c) physical direct contact; and (d) glass surface treatment. 102

Figure 49 (a) Vial arrangement on a single shelf of the freeze dryer. The TVIS modified vial (labelled TVIS, position 75) and two thermocouple containing vials (labelled TC, position 74 & 76) were placed at the centre of the shelf. The water-filled vials are represented by "W" and those left empty are labelled with the number position in the dryer; (b) a Virtis Advantage Plus XL freeze dryer (SP Scientific, USA) equipped with DMU- TVIS system; (c) a junction box placed on the top shelf of the freeze dryer; and (d) a pass-through enabling the signal to be transmitted from the TVIS vial to the impedance spectrometer (DMU-TVIS). 104

Figure 50 The TVIS measurement vial with the electrodes positioned at (a) 1 mm from base (TVIS1); and (b) 3 mm from base (TVIS3). The right image demonstrates the filling volume of double-distilled water corresponding to a fill factor 0.9 for each electrode configuration; (c) electrode trimming machine 106

Figure 51 An arrangement of vials loaded into the freeze dryer. The TVIS vial with a distance from base of 1 mm (labelled as TVIS1, position 85) and 3 mm (labelled as TVIS3, position 75) were filled with water (3.2 g and 3.5 g, respectively). Two thermocouple-containing vials placed close to the TVIS vials are filled with water (3.2 g and 3.5 g) for representing the ice temperature in TVIS1 and TVIS3, respectively. The "W" denotes the other water-filled vials and those left empty are labelled with the position number on the freeze dry shelf. A cluster of nineteen water-filled vials is arranged at the centre of an array of the empty vials. All 160 vials are loaded into a Virtis Advantage Plus XL freeze dryer (SP Scientific, USA)..... 108

Figure 52 (a) Real and (b) imaginary-part capacitance spectra of 2 g liquid water contained in TVIS vial with a guard (open symbol) and without one (closed symbol). Both types of TVIS vials have 5 mm height for the active electrode. The measurement was conducted at ambient temperature..... 110

Figure 53 A schematic illustration showing the influence of the presence of a guard electrode on the electric field at the border of the active electrodes (sensing/driving electrodes). A fringing effect at the edge of the measurement electrodes can be reduced by surrounding these electrodes with a guard ring. 111

Figure 54 Equivalent circuit model for the TVIS vial containing the sample in the liquid state. C_G is a glass wall capacitance, CPE element is a low frequency contribution of glass wall, C_s and R_s are sample capacitance and resistance, respectively. 112

Figure 55 Percentage relative error of measurement data to fitting data from (C_G=CPE)-(R_s=C_s) model. Note Q and α are CPE parameters. 113

Figure 56 (a) Real and (b) imaginary part of the capacitance spectrum of water filled in the guard vial; (c) real and (d) imaginary part of the capacitance spectrum of water filled in the non-guard. The measurement is performed at room temperature. The black dots represent the measured data points whereas the simulation results of three models are represented as follows: the grey solid line is a typical model of liquid contained in the TVIS vial, C_G-(R_s=C_s); the black dot line represents a non-ideal behaviour of the capacitor at low frequency (CPE); and the black solid line is the glass wall-sample contribution element (C_G =CPE). The double-headed arrow (a and c) marks the dielectric relaxation range. The impact of CPE (low) on the peak amplitude and peak frequency is illustrated. 115

Figure 57 A non-guard measurement vial (nominal capacity 10 mL) with the following electrode geometries: 5 mm height (grey square); 10 mm height (black circle); 12.5 mm height (grey circle) and 15 mm height (black square), is used for measuring the capacitance spectra of water at different filling volumes (fill factor between 0.5 and 1.5). Peak amplitude (C''_{PEAK}) derived from data at liquid level below and above the upper edge of electrodes is represented by the closed circle and open circle symbol respectively. 117

Figure 58 (a) Real and (b) imaginary-part capacitance of double-distilled water contained in a 10 mL standard vial attached with electrodes (10 mm height and 19 mm width) at four different fill factors: 0.8 (2.6 mL, grey filled square), 1.0 (3.3 mL, black filled circle), 1.2 (4.0 mL, grey filled circle) and 1.4 (4.7 mL, black open square). These were exemplified to demonstrate a decrease in the peak amplitude when the water level is above the electrode. A frequency range of 1 kHz to 0.5 MHz is selected for fitting to discard the effect of a low-frequency dispersion and high-frequency noise 118

Figure 59 Percentage errors of water spectrum contained in the non-guard vial with the following electrode height: 5, 10, 12.5 and 15 mm. Relative error of water at a fill factor of 0.8 is

calculated based on the basic model comprising constant phase element, $(C_G = CPE)$-$(R_s = C_s)$. The data within a frequency range of 0.5 MHz to 10 Hz have been analyzed. 119

Figure 60 (a) Real and (b) imaginary-part capacitance in a normalised scale of liquid water at ambient temperature (23-24 °C). The measurement results of 5 g water filled in the TVIS vial, attached with a 19 x 10 mm electrode pair at a distance of 3 mm from the vial's base, using various attaching methods: surface treatment (grey closed symbol); physical direct contact (grey opened symbol); glue (black closed symbol); and sputtering (black open symbol). These were compared with each other..... 120

Figure 61 (a) Real and (b) imaginary-part capacitance in normalised scale of two TVIS vials, each containing 5 g of liquid water. Both vials were prepared from 10-mL type I tubular glass vials having hydrophobic coating (TopLyo®) and with an electrode pair (19 x 10 mm) attached using either physical direct contact (grey open symbol), glue (black closed symbol) or sputtering technique (black open symbol). The measurements were performed at ambient temperature (23-24 °C). 121

Figure 62 (a) Temperature and TVIS parameters, (b) F_{PEAK} and (c) C''_{PEAK}, of 2 g double-distilled water contained in a Type I tubular glass vial (nominal capacity 10 mL) with a pair of non-guard electrodes with dimensions of 10 x 19 mm (h x w) attached to the outside of the vial during freezing to −40 °C with 0.67 °C/min rate. The onset of ice nucleation in the TVIS vial (black dashed line A, 1.13 h) and neighbouring vial with a thermocouple (grey line B, 1.10 h) were presented. The nucleation temperature in TC vial is −10.1 °C..... 123

Figure 63 Time profiles of (a) temperature, (b) F_{PEAK} and (c) C''_{PEAK} parameters during annealing of 2 g frozen water contained in 10 mL glass tubing vial attached with a 10 x 19 mm (h x w) non-guard electrode pair. The various stages of annealing are as follows: re-heating (period C); holding (period D); and re-cooling (period E). 125

Figure 64 Temperature dependencies of (a) peak frequency (closed symbol) and (b) peak amplitude (open symbol) of frozen water contained in the non-guard vial attached with a pair of 10 x 19 mm (h x w) electrodes during re-heating (circle symbol) and re-freezing (triangular symbol)..... 126

Figure 65 Temperature calibration of ice in a non-guard TVIS vial, attached with a pair of electrodes (19 x 10 mm), during the annealing process. Data from re-heating and re-freezing are represented by black circle and grey triangle, respectively. 126

Figure 66 (a) Ice temperature and TVIS parameters, (b) F_{PEAK} and (c) C''_{PEAK}, during primary drying step. 2 g of frozen water in NG TVIS vial with 19 x 10 mm electrode pair was sublimed at −20 °C and 400 µbar (set programmed). Given that C''_{PEAK} is a function of ice mass, a gradual decrease in C''_{PEAK} after applying vacuum (F) corresponded to loss of ice mass, which could be classified into two regions according the drying profile (linear region and non-linear). 128

Figure 67 (a) Product temperature estimated by temperature calibration of re-heating step ($T_{F_{PEAK}}$) and measured from the thermocouple (TC) during primary drying. The point of application of vacuum is set as zero hour. (b) Close-up of the first 2 hours. $T_{F_{PEAK}}$ and T_{TC} is in agreement each other for 0.7 h period. 130

Figure 68 Real-part data (black dot) in logarithm scale and fitting results (grey solid line) to the model for dielectric relaxation of ice (i.e. capacitance in parallel with Cole-Cole element, $C{=}Co$ model) from impedance spectrum analysis software (RelaxIS3, rhd instruments, Germany) at a certain point in primary drying: (a) 11 h, (b) 12 h, (c) 13 h, (d) 14 h, (c) 15 h and (f) 16 of primary drying, before the decrease rate of C''_{PEAK} starts to slow down. The distortion was clearly observed after applying a vacuum at 10.8 h for 2 h (i.e. 13 h of primary drying. b). Percentage relative error (RE) of ice relaxation time (τ) was performed over the data between 100-0.2 MHz. Note the equivalent circuit model of frozen ice has been described in Smith and Polygalov (2019)..... 132

Figure 69 Real-part capacitance in logarithm scale of different electrode configurations at the selected time: (a-c) initialisation of primary drying and (d-f) when C''_{PEAK} corresponds to 30% of the initial value. The TVIS vial had different distances from the vial's base: (a and d) 0 mm; (b and e) 1 mm; and (c and f) 3 mm, were determined. The grey solid line was simulated from the fitting model, $C{=}Co$ model (Smith & Polygalov, 2019)..... 134

Figure 70 Schematic vertical cross-section of two vials containing 3.6 g of sucrose-salt solution. **Right:** A modified TVIS vial attached with a pair of copper electrodes (19 x 10 mm), positioned

at 3mm from the vial base (~ 2 mm from the internal base of the vial). **Left:** A standard vial (10 mL nominal capacity) with a type-T thermocouple inserted in the liquid sample. The thermocouple sensor bead was positioned at a height corresponding to that of the TVIS sensing node (6.5 mm): i.e. half the 7mm sample height occupying the electrode region (7/2 = 3.5 mm) was added to the sample height below the lower edge of the electrode (3 mm). The unmodified nearest vial (left) is used to refer to the product temperature in the neighbouring TVIS vial. The fill factor (Ø) shown here is 0.7, which means that the sample height in the electrode region is 7 mm for an electrode height of 10 mm..... 138

Figure 71 (a) An arrangement of vials on a shelf of the Virtis Advantage Plus XL benchtop freeze dryer. Three thermocouple-containing vials (labelled TC1, TC2 and TC3) and the TVIS vials (labelled S-1, S-2 and S-3) were placed in the first row close to the chamber window. The other vials with the numbered position on the shelf were filled with ultrapure water. (b) The Virtis Advantage Plus freeze dryer equipped with a TVIS system, comprises a five-channel TVIS junction box inside freeze dryer and an impedance analyser outside the freeze dryer. The signal from the junction box is sent and received via the pass-through installed on the manifold hose of the Virtis Advantage Plus XL freeze dryer. A digital camera was set to observe the nucleation event of the sample-filled vials. (c) The image demonstrating the position of thermocouple vials and TVIS vials containing each sample solution positioned on the freeze dryer shelf..... 139

Figure 72 Illustration of the region of interest (area within the rectangle) for each sample: (a) 5% w/v sucrose solution (S-1), (b) 5% w/v sucrose with 0.26% w/v NaCl (S-2), (c) 5% w/v sucrose with 0.55% w/v NaCl (S-3). 141

Figure 73 Demonstrating five lines' selection on the image at 4 h of the freezing process: (a) 5% w/v sucrose solution (S-1), (b) 5% w/v sucrose with 0.26% w/v NaCl (S-2), (c) 5% w/v sucrose with 0.55% w/v NaCl (S-3)..... 141

Figure 74 TVIS parameters derived from (a) real part capacitance, i.e. C'(10 Hz) and C'(0.2 MHz); (b) imaginary part capacitance, C''_{PEAK} and F_{PEAK}. This example spectrum was measured from 5% w/v sucrose solution within the TVIS vial at +20 °C before freezing. 142

Figure 75 The TVIS response (real part and imaginary part capacitance) of 5% sucrose with different salt concentrations at +20 °C (liquid state) and −40 °C (frozen state): (a-b) 0% NaCl, (c-d) 0.26% NaCl, (e-f) 0.55% NaCl. 144

Figure 76 Temperature dependencies of (a) peak amplitude (filled triangle) and peak frequency (open triangle); (b) real part capacitance at 10 Hz (filled circle) and 0.2 MHz (open circle) for pure ice (Smith & Jeeraruangrattana, 2019). The measurement data is recorded during the re-heating stage from −40 °C to −10 °C with 0.5 °C·min-1. 145

Figure 77 Experimental results for 5% w/v sucrose demonstrate the onset of nucleation. (a) is the profile of the product and shelf temperature; (b) and (c) are time profiles of the TVIS parameter C''_{PEAK} and F_{PEAK}; (d) and (e) are time profiles of real part capacitance C'(10 Hz) and C'(0.2 MHz); (f) is the images recorded using a digital camera; (g) and (h) are imaginary and real part capacitance spectra before and after nucleation in the TVIS vial. The dashed line demonstrated discontinuity in the profile due to ice nucleation. 147

Figure 78 Experimental results for 5% w/v sucrose with 0.26% w/v NaCl demonstrate the onset of nucleation. (a) is the product profile and shelf temperature; (b) and (c) are the time profiles of the TVIS parameter C''_{PEAK} and F_{PEAK}; (d) and (e) are the time profiles of the real part capacitance C'(10 Hz) and C'(0.2 MHz); (f) is the images recorded using a digital camera; (g) and (h) are imaginary and real part capacitance spectra at the selected time points. The dashed line demonstrates discontinuity in the profile due to ice nucleation. 149

Figure 79 Experimental results for 5% w/v sucrose with 0.55% w/v NaCl demonstrate the onset of nucleation. (a) is the product profile and shelf temperature; (b) and (c) are the time profiles of the TVIS parameter C''_{PEAK} and F_{PEAK}; (d) and (e) are the time profiles of real part capacitance C'(10 Hz) and C'(0.2 MHz); (f) is the images recorded using a digital camera; (g) and (h) are imaginary and real part capacitance spectra at the selected time points. The dashed line demonstrates discontinuity in the profile due to ice nucleation. 151

Figure 80 Experimental results for 5% w/v sucrose demonstrate the solidification endpoint. (a) and (b) are the time profiles of real part capacitance C'(10 Hz) and C'(0.2 MHz). The vertical black dashed lines demonstrate the onset of ice nucleation (1.97 h) and solidification endpoint (2.24 h) determined by TVIS; (c) is the real part capacitance spectra at the selected time points;

(d) is the selected images demonstrating the solidification process. The progression of ice growth is illustrated by the white dashed line; (e) is the intensity profile of the defined area (Figure 72a) of the selected images (d). The defined area of the selected images is analysed using image processing software (ImageJ)..... 153

Figure 81 Experimental results for 5% w/v sucrose with 0.26% w/v NaCl demonstrate the solidification endpoint. (a) and (b) are the time profiles of real part capacitance C'(10 Hz) and C'(0.2 MHz). The vertical black dashed lines demonstrate the onset of ice nucleation (1.73 h) and solidification endpoint (2.17 h) determined by TVIS; (c) is the real part capacitance spectra at the selected time points; (d) is the selected images demonstrating the solidification process. Progression of the ice growth is illustrated by the white dashed line; (e) is the intensity profile of the defined area (Figure 72b) of the selected images (d). The defined area of the selected images is analysed using image processing software (ImageJ). 155

Figure 82 Experimental results for 5% w/v sucrose with 0.55% w/v NaCl demonstrate the solidification endpoint. (a) and (b) are the time profiles of real part capacitance C'(10 Hz) and C'(0.2 MHz). The vertical black dashed lines demonstrate the onset of ice nucleation (1.80 h) and solidification endpoint (2.41 h) determined by TVIS; (c) is the real part capacitance spectra at the selected time points; (d) is the selected images demonstrating the solidification process. The progression of ice growth is illustrated by the white dashed line; (e) is the intensity profile of the defined area (Figure 72c) of the selected images (d). The defined area of the selected images is analysed using image processing software (ImageJ). 156

Figure 83 Temperature dependencies of (a) peak amplitude (closed triangle) and peak frequency (open triangle); and (b) real part capacitance at 10 Hz (closed circle) and 0.2 MHz (open circle) of 5% w/v sucrose solution during the liquid cooling phase. 158

Figure 84 Determination of the ice nucleation temperatures (T_n) of 5%w/v sucrose using the following TVIS parameters: $Log\ F_{PEAK}$, C''_{PEAK}, and C'(10 Hz). (a-c) are the temperature profiles from the thermocouple in the nearest neighbour vial (T_{TC1}) and shelf temperature (T_s); (d-f) are the time profile (from 1.0 h to 3.5h) of the TVIS parameters: (d) $Log\ F_{PEAK}$, (e) C''_{PEAK}, (f) C'(10 Hz); (g-i) are the calibration plots between the thermocouple temperature within the adjacent vial (T_{TC}) and the value of (g) $Log\ F_{PEAK}$, (h) C''_{PEAK} and (i) C'(10 Hz). The grey region

demonstrates the data range used to create the temperature calibration curve. The nucleation temperature measured from the thermocouple (T_n(TC)) is −9.5 °C. At the onset of ice nucleation of 1.90h, the corresponding values of $Log\ F_{PEAK}$, C''_{PEAK}, and C'(10 Hz) are 4.26 pF, 0.543 pF and 2.49 pF, respectively. The nucleation temperatures of −10.6 °C, −11.0 °C and −10.5 °C are predicted from $Log\ F_{PEAK}$, C''_{PEAK}, and C'(10 Hz). Note: the nucleation temperature is extrapolated from the calibration plot of $Log\ F_{PEAK}$, C''_{PEAK}, and C'(10 Hz): denoted as $T_n(F_{PEAK})$, $T_n(C''_{PEAK})$ and $T_n(C'_{10\ Hz})$. 161

Figure 85 Determination of ice nucleation temperatures from C'(10 Hz) — $T_n(C'_{10\ Hz})$— of 5%w/v sucrose with either 0.26% (S-2) or 0.55% NaCl (S-3). (a-b) are the temperature profiles from the thermocouple in the nearest neighbour vial (T_{TC}) and shelf temperature (T_s): (a) S-2 (T_{TC2}) and (b) S-3 (T_{TC3}); (c-d) are the time profiles of the C'(10Hz) value of (c) S-2 and (d) S-3 over a 2.5 h freezing stage (from 1.0 h to 3.5 h); (e-f) are the calibration plots between the thermocouple temperature within the adjacent vial (T_{TC}) and value of C'(10Hz) for (e) S-2 and (f) S-3. The shaded region demonstrates the data range used in creating the temperature calibration of the supercooled solution. The nucleation temperatures measured from the thermocouple (T_n(TC)) are −7.7 °C and −10.6 °C for S-2 and S-3. At the onset of ice nucleation, C'(10 Hz) for S-2 and S-3 are 2.91 pF and 3.06 pF, respectively. The nucleation temperatures predicted from C'(10 Hz) are −11.1 °C and −11.8 °C. 163

Figure 86 Nucleation temperature of 5%w/v sucrose with either 0% NaCl (S-1), 0.26% NaCl (S-2) or 0.55% NaCl (S-3). The value above the white bar and grey bay indicates the nucleation temperature from the thermocouple (T_n(TC)) and TVIS technique ($T_n(C'_{10\ Hz})$), respectively. . 165

Figure 87 Time required for complete ice formation of 5% w/v sucrose solution with either 0% (S-1), 0.26% (S-2) and 0.55% NaCl (S-3). Real part capacitance at 10 Hz and 0.2 MHz is used to determine the beginning and end of the ice formation process. 167

Figure 88 Vertical cross-sections of two vials containing 3.2 g of 5% w/v sucrose solution. **Right:** Modified TVIS vial attached with a pair of copper electrodes (19 x 10 mm) positioned at 2 mm from the internal vial base. **Left:** A standard vial (10 mL nominal capacity) with a type-T thermocouple is inserted in the liquid sample, so that the thermocouple bead is positioned at

the bottom centre of the vial, where it provides a surrogate product temperature for the same position in the nearest TVIS vial. The fill factor (Ø)is 0.7: which means that the sample height in the electrode region is 7 mm for an electrode height of 10 mm. 172

Figure 89 Arrangement of vials on a shelf of the Virtis Advantage Plus XL benchtop freeze dryer. Three thermocouple-containing vials (labelled TC) were placed in a triangle, with the TVIS measuring vial (labelled CH2) at the triangle centre. The TC vials and TVIS vial were located among the sample cluster. The sample-filled vials are represented by '**S**'; the left vials with the numbered position on the shelf were filled with ultrapure water. 173

Figure 90 (a) Photograph from the front of the dryer showing the array of vials placed on the bottom shelf of the dryer and the TVIS junction box on the middle shelf. The fine white cables emerging from the right side of the vial array are connected to one channel of the 5-channel TVIS junction box. (b) Photograph of the left side of the dryer, showing the 5-channel I-to-V convertor of the impedance analyser, which sends and receives the signal to/from the junction box via the pass-through installed on the manifold hose of the Virtis Advantage Plus XL freeze dryer. 174

Figure 91 An illustration of the thermal cycles used in this experiment with annealing hold temperatures of −35 °C (black solid line), −32 °C (black dotted line), and −10 °C (grey solid line). 176

Figure 92 An example of (a) real and (b) imaginary capacitance spectrum of 5% w/v sucrose at −15.2 °C, obtained from the first re-heating stage of the annealing cycle with −10 °C as the hold temperature, demonstrating the determination of the TVIS parameters derived from the LyoView™ software: C'(10 Hz), C'(0.2 MHz), C''_{PEAK}, and F_{PEAK} (shown in bold font). 177

Figure 93 A DSC thermogram of frozen 5% w/v sucrose solution, showing the overlay of heat flow and midpoint T'_g values (in bold) for different scanning rates. Heating rates of 5, 10, and 20 °C·min^1 are represented by light grey, black and dark grey respectively. 178

Figure 94 The glass transition temperature of 5% w/v sucrose solution of −34.9 °C is calculated from the step in the reversing heat flow of mDSC thermogram. 180

Figure 95 (a) Real and (b) imaginary part capacitance spectra of 5% w/v sucrose contained in a 10 mL TVIS vial, demonstrating the temperature dependency of the dielectric relaxation of ice at temperatures between −50 °C and −30 °C. These spectra were obtained during the first re-heating stage, from −50 °C to −10 °C, with a 0.2 °C·min^{-1} rate. The parameters from the dielectric loss peak of ice in the imaginary part (C''_{PEAK} and F_{PEAK}) and real part at the selected frequency (i.e. 10 Hz and 0.2 MHz), were extracted using LyoView™ software. (c) The normalised values of C''_{PEAK} (filled triangle) and $Log\ F_{PEAK}$ (open triangle) are demonstrated. (d) the normalised C'(10 Hz) and the normalised C'(0.2 MHz) are presented by filled and open circle, respectively. The vertical dashed line shown in (c) marks the glass transition temperature (T'_g = −34.3 °C). The transition temperature shown in (d) are −35.2°C for C'(10 Hz) and −34.7 °C for C'(0.2 MHz). 181

Figure 96 Temperature dependencies of real part capacitance at 10 Hz (black dots) and 0.2 MHz (open dots) of (a) pure ice (Smith & Jeeraruangrattana, 2019) and (b) 5% w/v sucrose in the frozen state. The value for real part capacitance was recorded during the re-heating stage from −40 °C to −10 °C with 0.5 °C·min^{-1} and −50 °C to −10 °C with 0.2 °C·min^{-1} for (a) pure ice and (b) the frozen 5% w/v sucrose, respectively. 184

Figure 97 Freeze-thaw profiles of 5% w/v sucrose solution. The sample was initially frozen at −50 °C, and then the shelf temperature increased at the heating rate of 0.2 °C·min^{-1} until the annealing temperature of either (a) −35 °C, (b) −32 °C or (c) −10 °C was reached. 185

Figure 98 Temperature profiles of 5% w/v sucrose during three cycles of freeze-thaw processes: (a) −35 °C, (b) −32 °C and (c) −10 °C. Two thermocouples contained in the same vial at different positions were used to measure product temperature during the freeze-thaw processes. One temperature sensing node (TC1) was placed at the bottom centre of the vial; the other (TC2) was close to the sample level (i.e. just below the sample meniscus). The product temperatures from TC1 and TC2 are represented by a solid line and dotted line, respectively. 187

Figure 99 Temperature dependency of the normalised values of (a) $Log\ F_{PEAK}$ and (b) C''_{PEAK} parameters of the frozen 5% w/v sucrose solution from three re-heating stages of each freeze-thawing process (i.e. −35 °C, −32 °C and −10 °C). TVIS-derived parameters were plotted against

the thermocouple temperature, averaged from three nearest neighbour vials. The double-headed arrow indicates the product temperature as follows: below the T_g' (region I) and above the T_g' (region II). (c)-(e) are the zoom views of (a) while (f)-(h) are the zoom views of (b) for each freeze-thawing process: −35 °C, −32 °C and −10 °C. The open symbols represent the cycle annealed below the T_g' value of −34.3 °C (i.e. −35 °C); whereas data treated at shelf temperatures of −32 °C and −10 °C (above the glass transition temperature) are presented in grey and black closed symbols, respectively. The circles, squares and triangles are the first, second and third re-heating stages, respectively. 188

Figure 100 Effect of annealing temperature on peak frequency (F_{PEAK}) and peak magnitude (C''_{PEAK}). The frozen 5% w/v sucrose solution was annealed for 2 h (holding period) at the following shelf temperatures: −35 °C (open symbols), −32 °C (grey closed symbols), and −10 °C (black closed symbols). The circles, squares and triangles represent the first, second and third annealing cycles, respectively. The vertical dashed lines marked at 0.8 h and 1.35 h of annealing period where temperature change (ΔT) and C''_{PEAK} reach a plateau, respectively. 196

Figure 101 Time profiles of the parameters during the holding of a 5% w/v sucrose solution at −10 °C (a) Normalised C''_{PEAK} and (b) Normalised resistance. The fitting parameter resistance was determined by RelaxIS3 software (rhd instruments, Germany), using the model for a frozen solution ($C_G - C_s = R_s = Co$) (Smith and Polygalov 2019). Data recorded during the temperature constant (0.8 h -2.0 h) are demonstrated. The circles, squares and triangles represent the first, second and third annealing cycles, respectively. 198

Figure 102 Normalised TVIS parameters: $Log\ F_{PEAK}$, C''_{PEAK}, C'(10 Hz), and C'(0.2 MHz), extracted from the capacitance spectrum of 5% w/v sucrose solution recorded during three reheating cycles: (a) first cycle, (b) second cycle and (c) third cycle. This figure demonstrated the normalised TVIS parameters—$Log\ F_{PEAK}$, C''_{PEAK}, C'(10 Hz), and C'(0.2 MHz)—at product temperature range from −45 °C to −25 °C. Note, each reheating step, the frozen sucrose was ramped from −50 °C to −10 °C at 0.2 °C·min^{-1}. 200

Figure 103 Vertical cross-sections of two vials containing 3.1 g of 5% w/v lactose solution. **Right***:* Modified TVIS vial attached with a pair of copper electrodes (19 x 10 mm) positioned 3 mm from

the external vial base (~ 2 mm from the internal base of the vial). **Left***:* Unmodified nearest neighbour vial with two type-T thermocouples. The beads of the thermocouples were placed at the bottom centre of the vial (TC2), at the height corresponding to the middle of the sample within the electrode sensing region (TC1). The fill factor (Ø) shown here is 0.7, which means that the sample height in the electrode region is 7 mm for an electrode height of 10 mm. 204

Figure 104 (a) An arrangement of vials on the shelf of the Virtis Advantage Plus XL freeze dryer. The TVIS modified vial (labelled TVIS) and the thermocouple-containing vial (labelled TC) were placed close to the centre of the shelf. The sample filled vials are represented by "L"; those left empty are labelled with the number position in the dryer. (b) Five-channels TVIS junction box (left photo) placed on freeze dryer shelf, and the pass-through (right photo) for the TVIS cabling, connected to the manifold hose on the outside of the Virtis Advantage Plus XL freeze dryer.206

Figure 105 A mDSC thermogram of 5% w/v lactose solution. The glass transition temperature of the maximally freeze concentrated solution (T_g') of −30.2 °C is demonstrated by a step in the reversing heat flow. The arrows mark the onset of the glass transition temperature (−32.8 °C) and the collapse temperature (−28.2 °C)..... 209

Figure 106 Freeze-drying microscope of 5% w/v lactose solution. (a) Drying at −30 °C, (b) onset of collapse at −28.2 °C, (c) complete collapse at −25 °C..... 210

Figure 107 Freeze drying process profile of 5% w/v lactose solution. 211

Figure 108 (a) Real and (b) imaginary capacitance spectra recorded every 2 min during the freeze-drying of the 5% w/v lactose solution. 212

Figure 109 An example TVIS spectra of 5% w/v lactose solution during (a-b) freezing, (c-d) re-heating from −51 °C to −26 °C, (e-f) primary drying (0-5 h)..... 213

Figure 110 An example dielectric loss spectrum of the 5% w/v lactose solution at −20.3 °C (during re-heating of the frozen solution) to demonstrate the meaning of C''_{PEAK} and F_{PEAK} of the ice relaxation peak, as determined by LyoView™ software..... 214

Figure 111 TVIS method for determining drying rate and ice interface temperature, from which dry layer resistance is estimated. 216

Figure 112 (a) Selected imaginary capacitance spectra of 5% w/v lactose solution in a 10 mL TVIS measurement vial with a pair of 19 x 10 mm electrodes, demonstrating temperature dependency of the dielectric loss peak during the reheating stage (temperature ramp from −51 °C to −30 °C at 0.7 °C·min^{-1}); (b) Temperature calibration used to estimate the ice temperature during primary drying is determined from the plot of the thermocouple temperature located at the TVIS node, i.e. the midpoint of the sample within the electrode region (T_{TC1}) and logarithm of the peak frequency (F_{PEAK}), recorded during the reheating period. 217

Figure 113 Temperature profiles during the primary drying stage, showing the thermocouple temperature (T_{TC}), TVIS predicted temperature ($T_{F_{PEAK}}$), and shelf temperature (T_s). The downward grey arrow points the step in the T_{TC1} profile at 8.1 h; whereas the two upward black arrows point the dips in the $T_{F_{PEAK}}$ profile at 12.3 h and 15.2 h, respectively. The dotted line extrapolated from $T_{F_{PEAK}}$ data (from the 12.3 h time point onwards) is drawn to show the expected response if it were to follow a trajectory similar to that displayed by the thermocouple temperature (T_{TC}). The double-headed arrow marks the time period where $T_{F_{PEAK}}$ and T_{TC} become stable. 219

Figure 114 (a) Temperature coefficient of peak amplitude (C''_{PEAK}) during re-heating from −51 °C to −30 °C at 0.7 °C·min^{-1}. (b) The first derivative of the temperature coefficient of C''_{PEAK}, divided by the value of C''_{PEAK} at the same temperature (expressed as a percentage) is referred to as the percentage uncertainty, which on average is ~ 0.70% per °C for this particular experiment.. 223

Figure 115 Primary drying profiles of peak magnitude before and after temperature correction (C''_{PEAK} and $\hat{C}''_{PEAK}$, respectively). (a) Profile for the first 9 h of primary drying; (b) Close-up of the first 3 h. The various steps of primary drying are: Period I Holding at −40 °C; Period II Ramping temperature from −40 °C to −10 °C at 0.1 °C·min^{-1}; Period III Holding at −10 °C. The standardisation temperature (T_{ref}) used to compensate the temperature dependency of C''_{PEAK} is −44 °C. Five arrows marked A, B, C, D and E run parallel to the data to demonstrate the relative differences in gradient between the uncompensated and compensated values of C''_{PEAK} both before the onset of the temperature ramp (A and B, respectively) and after the temperature ramp (C, D and

E, respectively). Before ramping, the surrogate sublimation rate (from $d\,C''_{PEAK}/dt$) is higher for the uncompensated values before the temperature ramp, but reduces almost to zero immediately after it. The implication might be that the sublimation rate is slowing; whereas the compensated values continue at the same apparent sublimation rate as before the ramp. Then as the temperature continues to ramp, the apparent drying rate for the compensated values begins to increase (arrow E), as we might expect. 225

Figure 116 Illustration of ice mass in different regions at the start of primary drying. An approximate 2.15 g of the initial ice (2.76 g) occupies the electrode region. 228

Figure 117 Ice mass contained in the vial (black solid line) and sublimation rate ($d\,m_{C''_{PEAK}}/dt$) (grey solid line) over 9 h of primary drying process, estimated from the standardised $CPEAK''$ ($\hat{C}''_{PEAK}$). The different stages of primary drying are presented as periods I, II and III for the hold period at −40 °C, the re-heating stage from −40 °C to −10 °C, and the hold period at −10 °C, respectively. 229

Figure 118 TVIS predicted ice height within the electrode boundary ($h_{C''_{PEAK}}$, black solid line) and dry layer thickness (l_d, grey solid line) during the first 9 hours of primary drying of 5% w/v lactose. 231

Figure 119 Illustration of the methodology predicting ice interface temperature a) Two-points extrapolation (method I), b) thermal heat transfer (method II). h_i is the position of the height of ice interface, equivalent to the sum of the ice layer height within the electrode region (h_{RE}) and the layer height below the electrode (h_{BE}); h_n is the height of the TVIS node. 232

Figure 120 Comparison of ice interface temperature predicted by method I (extrapolating from two-points (Smith et al. 2018) and method II (heat transfer equation). 235

Figure 121 Results of 5% w/v lactose during the first 9 h of the primary drying stage. (a) The thermocouple temperature profile (T_{TC1}, grey solid line), TVIS predicted temperature ($T_{F_{PEAK}}$, black solid line) and calculated ice interface temperature from method II T_i, black dashed line); (b) Ice partial pressure at the sublimation front (black solid line) and condenser (black dotted line), and sublimation rate (grey solid line) over the drying period; (c) product resistance (R_p, black solid line). Periods I, II and III denote the first hold period of 1.1 h after applying the

vacuum, the shelf temperature ramp from −40 °C to −10 °C over a period of 5.1 h, and the second hold period of primary drying, respectively. When the ice temperature at the sublimation front reaches −33.3 °C —horizontal black dashed line in (a), dry product resistance starts to decrease: which indicates the beginning of a microcollapse event. 239

Figure 122 Dry product resistance (R_p, black solid line) and TVIS-predicted ice interface temperature T_i(grey solid line) as a function of dry layer thickness for lactose, freeze-dried from a 5% w/v solution (over the first 8.87 h of primary drying). Period I, II and III are holding at −40 °C ($T_{F_{PEAK}}$−44.3 ± 0.31 °C), re-heating from −40 °C to −10 °C (0.1 °C·min^{-1}), and holding at −10 °C, respectively. Product resistance starts to fall continuously after the ice interface temperature (T_i) reaches −33 °C, corresponding to the dry layer thickness of 1.51 mm. 240

Figure 123 Scanning electron photomicrographs of a freeze-dried cake of 5% w/v lactose at the end of the cycle. (a) An overview of a vertical cross section of freeze-dried cake at a magnification of 25x; (b-d) Morphology of the dried layer at a magnification of 500x (b) top, (c) middle and (d) bottom. 241

Figure 124 Method of calibrating temperature response of the TVIS system using a dual pair of electrodes. **Left**: Standard type I glass tubing vial (Adelphi VC010-20C of nominal volume 10 mL) with two type-T thermocouples placed at a height equivalent to the centre-points of the upper and lower electrodes; **Right**: a TVIS modified vial with two pairs of copper foil electrodes (only one electrode from each pair is shown here). 244

Figure 125 Example model spectrum to demonstrate determination of F_{PEAK} and C''_{PEAK} values. 245

Figure 126 Arrangement of vials on the middle shelf of a Virtis Advantage Plus freeze dryer. Positions 75 and 76 are the TVIS modified vial and the thermocouple-containing vial. 248

Figure 127 (a) Selection of imaginary capacitance spectra of ice from the top electrode pair of the TVIS vial, during the reheating ramp from −45 °C to −10 °C; (b) Calibration plots from the re-heating stage for the prediction of ice interface temperatures from estimates of F_{PEAK} measured during the subsequent primary drying stage. 250

Figure 128 (a) Temperature dependency of C''_{PEAK} for the top electrode. The second-order polynomial expression for temperature coefficient of peak amplitude of top electrode is also given; (b) values for C''_{PEAK} during primary drying, before and after correction for temperature. The nomenclature of the corrected value of the peak height is $\hat{C}''_{PEAK}(t)$. 252

Figure 129 The dependency of C''_{PEAK} on the ice cylinder height in the region bounded by the top electrode at −20 °C. The gradient of the linear portion of the graph ($m_{h/C}$) at fill heights from the bottom edge of the top electrode greater than 2 mm is equal to 9.749 mm·pF^{-1} (0.975 cm·pF^{-1}), and provides the calibration factor to convert rates of change in C''_{PEAK} to values of the ice mass during primary drying. 253

Figure 130 Illustration of the calculation of ice height at 2.4 h into the primary drying stage for an Adelphi VC010-20C type I glass tubing vial. 255

Figure 131 A 2 point-temperature determination for extrapolation to the ice interface temperatures of interest (i.e. T_i and T_b). The example shown here is from 2.4 h into primary drying (during the steady state period). 255

Figure 132 (a) Predicted ice interface temperatures at the sublimation front (T_i) and base of the ice (T_b), during the first 5 hours of primary drying (determined by extrapolating the TVIS predicted temperatures at the centre of the top and bottom electrode spaces); (b) A close-up view of the inset in (a). 256

Figure 133 (a) Temperature dependency of partial pressure of ice. The grey arrow demonstrates the corresponding partial pressure of ice at the sublimation interface (~250 µbar) when drying is activated by the condition whereby the anticipated temperature of the ice interface reaches a value of −34 °C while the black arrow indicates the ice interface temperature corresponding to the set chamber pressure of 350 µbar; (b) Predicted ice interface temperature T_i (see Section 10.3.3) as a function of primary drying time. The constant temperature region between 2 and 2.8 h starts once the shelf has reached its set temperature of 0 °C. During this time, the predicted ice interface temperature is almost constant at -33.1 °C; (c) Predicted ice interface temperature T_i at the activation point when the drying rate starts to increase dramatically; (d) Temperature-

standardised values of $\hat{C}''_{PEAK}$ The plot also highlights those values at the beginning and end of the steady state period in which the drying rate is constant. 258

Figure 134 Comparison of the TVIS predicted estimate for the K_v value of a 10 mL glass tubing vial with previously published data for similar type of vials. 261

Figure 135 Two different scenarios for the shape of the sublimation interface at five equally spaced points (t_1 to t_5). (a) is the ideal scenario, whereby the shape of the sublimation interface does not change throughout the primary drying cycle; whereas (b) is the more typical pattern of changes to the sublimation shape. At the beginning of primary drying (t_1 to t_2), the shape of the ice layer does not change in either scenario; therefore, we expect C''_{PEAK} to be directly proportional to the ice mass. However, as drying proceeds (t_2 to t_5), the surface area of the sublimation interface shown in scenario (b) starts to increase and an air gap between the ice and glass wall appears. Under those circumstances, the relationship between C''_{PEAK} and ice mass will deviate from linear. Scenario (b) occurs routinely when drying ice; but the transition point between linear to non-linear will be reached sooner in the edge than the core vial..... 263

Figure 136 The equivalent circuit model for frozen water contained in the vial. The left part of the model represents the impedance of the glass wall with the instantaneous polarization of glass modelled by a capacitor (C_G); and the low frequency dispersive polarization of glass modelled by a constant phase element (CPE). The instantaneous capacitance ($C_s(\infty)$) and dielectric relaxation of ice (Co) are demonstrated on the right side of the model. 264

Figure 137 Equivalent circuit modelling of an example spectrum of ice. The data points are the measured values of the imaginary capacitance spectrum of ice at -20 °C during the re-heating part of the annealing stage. The black solid line in (a) demonstrates the data fitted to the complete model ($C_G = CPE - C_s(\infty) = Co$) as shown in the top right. (b) shows the simulation results (the grey dashed line) when glass wall impedance (C_G and CPE) has been removed from the completed model. RelaxIS3 (rhd instruments, Germany) was performed for modelling.. 265

List of abbreviations (unit)

$-$	Series arrangement in an electrical circuit
$=$	Parallel arrangement in an electrical circuit
a	Experimental constant value in the expression for the ice crystal size
A	Cross-sectional area of material; i.e. electrode (m^2)
A_e	Projected external cross-sectional area of the base of the vial (m^2)
A_i	Internal cross-sectional area of the vial (m^2)
A_s	Interfacial area between the TVIS electrode and the glass wall (m^2)
A_w	Warburg coefficient
$\propto$	Energy accommodation factor
α	Exponent of a constant phase element
β	Experimental constant in the expression for the crystal growth rate
$\boldsymbol{C}$	Complex capacitance (F)
C	Capacitance (F)
$\Delta C'$	Increment in the real-part capacitance (F)
C'	Real-part capacitance (F)
$C'(0)$	Real-part capacitance in the limit of low frequency (F)
$C'(\infty)$	Real-part capacitance in the limit of high frequency (F)
C''	Imaginary-part capacitance (F)
C''_{PEAK}	Peak amplitude of the imaginary-part capacitance (dielectric loss) spectrum (F)
$C''_{PEAK}(t)$	Peak amplitude (F) at any time t
$C''_{PEAK}(T)$	Peak amplitude (F) at any temperature T
$C''_{PEAK}(T_{ref})$	Peak amplitude (F) at the reference temperature T_{ref}
$\hat{C}''_{PEAK}$	Temperature-compensated peak amplitude (F)
$\hat{C}''_{PEAK}(0)$	Temperature-compensated peak amplitude (F) at the time point when the vacuum is applied
$\hat{C}''_{PEAK}(t)$	Temperature-compensated peak amplitude (F) at any time t
C_c	Capacitance of compact layer (F)
C_d	Capacitance of diffusion layer (F)
C_{dl}	Capacitance of double layer (F)
C_g	Capacitance of glass-sample interface (F)

C_G	Total capacitance of glass-sample interface (F)
C_g'	Maximally freeze-concentrated concentration (% w/w)
c_i	Molar concentration
C_s	Sample capacitance (F)
$C_s(\infty)$	Sample capacitance in the limit of high frequency (F)
Co	Cole-Cole element
CPE	Constant phase element
d	Ice layer thickness (m)
D	Diameter of ice crystal size (m)
d_{cap}	Diameter of capillaries in a model structure with the vertical pore (m)
d_s	Average distance between the TVIS electrode pair, including the glass wall thickness (m)
dC''_{PEAK}/dt	Surrogate measurement of the sublimation rate for non-standardized peak amplitude ($F \cdot h^{-1}$)
dm/dt	Sublimation rate ($g \cdot h^{-1}$)
$dm_{\hat{C}''_{PEAK}}/dt$	Sublimation rate derived from TVIS parameters $\hat{C}''_{PEAK}$ ($g \cdot h^{-1}$)
dq/dt	Heat transfer or heat flux (W or $J \cdot s^{-1}$)
DE	Distributed element
e	Elementary charge of an electron (C)
e	Emissivity of material (dimensionless)
E'	Storage modulus (Pa)
E''	Loss modulus (Pa)
e_s	Effective emissivity for freeze dryer shelf radiation (dimensionless)
e_v	Effective emissivity for top radiation, i.e. from shelf above vial (dimensionless)
$\boldsymbol{\varepsilon}$	Complex dielectric permittivity (dimensionless)
ε	Permittivity ($F \cdot m^{-1}$)
ε'	Real-part permittivity or dielectric constant ($F \cdot m^{-1}$)
ε''	Imaginary-part permittivity or dielectric loss ($F \cdot m^{-1}$)
ε_∞	Permittivity in the limit of very high-frequency or instantaneous permittivity ($F \cdot m^{-1}$)
ε_o	Permittivity of free space or vacuum ($F \cdot m^{-1}$)
ε_r	Relative permittivity or dielectric constant (dimensionless)

ε_r'	Real-part relative permittivity or dielectric constant (dimensionless)
ε_r''	Imaginary-part relative permittivity or dielectric loss (dimensionless)
ε_s	Permittivity in the limit of very low-frequency or static permittivity ($F \cdot m^{-1}$)
f	Frequency (Hz)
F_{PEAK}	Peak frequency of the imaginary-part capacitance (dielectric loss) spectrum (Hz)
G	Temperature gradient across the frozen zone ($K \cdot m^{-1}$)
G	Conductance (S)
γ	Surface tension or surface free energy ($N \cdot m^{-1}$)
h_{BE}	Liquid or ice layer height below the electrode-bounded region (m)
$h_{\hat{C}''_{PEAK}}(t)$	Ice layer height within the electrode-bounded region derived from TVIS parameters $\hat{C}''_{PEAK}$ (m) at any time t
h_E	Height of electrode (m)
h_i	Predicted height of the ice interface (m)
$h_i(t)$	Predicted height of the ice interface (m) at any time t
h_n	Predicted height of TVIS node from the internal base of the vial (m)
$h_n(t)$	Predicted height of TVIS node from the internal base of the vial (m) at any time t
h_{RE}	Liquid or ice layer height within the electrode-bounded region (m)
$h_{RE}(0)$	Ice layer height within the electrode-bounded region (m) at the time point when the vacuum is applied
$h_{RE}(t)$	Ice layer height within the electrode-bounded region (m) at any time t
h_t	Height from the internal base of the vial (m)
i	Van't Hoff factor
i	Imaginary number equal to $\sqrt{-1}$
I	Electric current (A)
k	Geometric cell constant (m)
K	Recrystallization rate constant
k_B	Boltzmann constant ($J \cdot K^{-1}$)
K_c	Heat transfer coefficient contributed by conduction ($W \cdot m^{-2} \cdot K^{-1}$)
K_f	Freezing point constant of solvent
k_g	Factor described the scattering of gas molecule
K_g	Heat transfer coefficient contributed by gas conduction or convection ($W \cdot m^{-2} \cdot K^{-1}$)

k_{GT}	Constant in the Gordon-Taylor equation
K_r	Heat transfer coefficient contributed by radiation ($W \cdot m^{-2} \cdot K^{-1}$)
k_s	Geometric cell constant of sample (m)
K_v	Heat transfer coefficient ($W \cdot m^{-2} \cdot K^{-1}$)
κ	Thermal conductivity ($W \cdot m^{-1} \cdot K^{-1}$)
κ_i	Thermal conductivity of ice ($W \cdot m^{-1} \cdot K^{-1}$)
L	Inductance (H)
l_d	Dry layer thickness (m)
$l_d(t)$	Dry layer thickness (m) at any time t
L_D	Debye length (m)
L_f	Latent heat of fusion ($W \cdot s \cdot g^{-1}$)
L_s	Latent heat of ice sublimation ($W \cdot s \cdot g^{-1}$)
l_v	Equivalent gas layer thickness (m)
Λ_0	Free molecular heat conductivity of the gas at 0°C ($J \cdot s^{-1} \cdot m^{-1} \cdot K^{-1}$)
λ_0	Heat conductivity of gas at atmosphere ($W \cdot m^{-1} \cdot K^{-1}$)
λ_1	Experimental constant value in the expression for the ice crystal size
λ_2	Experimental constant value in the expression for the ice crystal size
m	Molality
m_{BE}	Liquid or ice mass below the electrode-bounded region (g)
$m_{\hat{C}''_{PEAK}}(t)$	Ice mass within the electrode-bounded region derived from TVIS parameters $\hat{C}''_{PEAK}$ at any time t (g)
$m_{h/C}$	Gradient of the linear portion of the calibration of C''_{PEAK} for ice layer height
m_{RE}	Liquid or ice mass within the electrode-bounded region (g)
$m_{RE}(0)$	Ice mass within the electrode-bounded region (g) at the time point when the vacuum is applied
$m_{RE}(t)$	Ice mass within the electrode-bounded region (g) at any time t
m_t	Total ice mass contained in the vial (g)
$m_t(t)$	Total ice mass contained in the vial (g) at any time t
μ	Ionic strength (molar)
n	Experimental constant in the expression for the crystal growth rate
N_A	Avogadro's constant (mol^{-1})
ω	Angular frequency ($rad \cdot s^{-1}$)
ΔP	Pressure differential across the dry layer (Pa or bar)

P_c	Ice vapour pressure inside the freeze dryer chamber (Pa or bar)
P_{cd}	Ice vapour pressure at the condenser (Pa or bar)
P_{curve}	Vapour pressure above curvature (Pa or bar)
P_i	Ice vapour pressure at the ice interface (Pa or bar)
P_o	Equilibrium vapour pressure (Pa or bar)
P_v	Ice vapour pressure within the head space of the vial (Pa or bar)
$\emptyset$	Fill factor
ϕ	Compensation factor accounting for the temperature dependency of the peak amplitude
Φ	Porosity
φ	Phase difference between the voltage and current
Q	Electric charge on electrode plate (C)
$\mathcal{Q}$	Admittance value of a constant phase element (F)
r	Radius of the curvature (m)
R	Crystal growth rate
R	Resistance (Ω)
r^*	Critical radius of ice crystal (m)
$\bar{R}$	Mean crystal radius (m)
$\hat{R}_\rho$	Area-normalised dry layer resistance ($Pa \cdot m^2 \cdot s \cdot g^{-1}$)
R_c	Chamber to condenser resistance per vial ($Pa \cdot s \cdot g^{-1}$)
R_g	Gas constant (8.314 $J \cdot K^{-1} mol^{-1}$)
R_p	Product dry layer resistance ($Pa \cdot s \cdot g^{-1}$)
R_s	Solution resistance (Ω)
R_S	Stopper resistance ($Pa \cdot s \cdot g^{-1}$)
R_T	Total resistance to mass flow from the ice vapour interface to the condenser ($Pa \cdot s \cdot g^{-1}$)
ρ	Resistivity (Ω·m)
ρ_i	Density of ice ($kg \cdot m^{-3}$)
ρ_p	Resistivity of the dry layer ($Pa \cdot m^3 \cdot s \cdot g^{-1}$)
σ	Conductivity ($S \cdot m^{-1}$)
t	Time (h)
T	Temperature (°C or K)
T_b	Ice temperature at the internal base of the vial (°C or K)

T_c	Collapse temperature (°C or K)
T_{cd}	Ice temperature at the condenser (°C or K)
T_{eu}	Eutectic temperature (°C or K)
ΔT_f	Depression of freezing point (°C or K)
T_f	Equilibrium freezing temperature (°C or K)
$T_{F_{PEAK}}$	TVIS predicted temperature at the sensing node (°C or K)
$T_{F_{PEAK}(BE)}$	TVIS predicted temperature at the sensing node of the bottom electrode (°C or K)
$T_{F_{PEAK}(TE)}$	TVIS predicted temperature at the sensing node of the top electrode (°C or K)
T_g	Glass transition temperature (°C or K)
T_g'	Glass transition temperature of freeze-concentrated solution (°C or K)
T_i	Ice temperature at the sublimation interface (°C or K)
T_m'	Melting temperature of freeze-concentrated solution (°C or K)
T_n	Nucleation temperature (°C or K)
ΔT_s	Degree of supercooling (°C or K)
T_s	Shelf temperature (°C or K)
T_{sol}	Solution temperature (°C or K)
T_{TC}	Product temperature from the in-vial thermocouple (°C or K)
τ	Tortuosity
τ	Relaxation time or time constant (s)
τ_{ice}	Relaxation time of ice (s)
V	Applied voltage (V)
v	Viscosity (Pa·s)
$\bar{V}$	Specific volume ($m^3 \cdot kg^{-1}$)
w	Mass fraction
W	Warburg element
$\boldsymbol{Y}$	Admittance (S)
Y_{CPE}	Admittance of a constant phase element (S)
$\boldsymbol{Z}$	Complex impedance (Ω)
Z	Impedance (Ω)
Z_C	Impedance of capacitance (Ω)
Z_{CPE}	Impedance of constant phase element (Ω)

z_i	Charge number of ion
Z_L	Impedance of inductance (Ω)
Z_R	Impedance of resistance (Ω)
Z_W	Impedance of Warburg element (Ω)
$\|Z\|$	Impedance magnitude (Ω)
$\|Z\| \sin \varphi$	Imaginary part of the complex impedance or reactance

Definition of TVIS terminology

Electrode-bounded region	Refers to that part of the cylinder that is confined within the perimeter of the electrode pair, which is occupied by a sample (i.e. a liquid sample or a frozen mass). The cylinder can be thought of as comprising concentric cylinders of the sample and the glass wall. This region does not include that part of the cylinder that is confined within the perimeter of the electrode pair, which does not contain the sample (i.e. the air space and the dry layer of the product are not included in this region).
TVIS node	That point at the centre of the volume of the sample (i.e. the liquid sample or the frozen mass) inside the vial, which is bounded by the electrodes on the outside of the vial. Its position, in the vertical direction, is exactly half-way up the sample that occupies the region bounded by the electrodes. In order to estimate its position from the inside base of the vial, then, the distance between the bottom of the electrode and the inside surface at the base of the vial is added to the half-height of the sample.
$Log\ F_{PEAK}$ calibration	A calibration plot of temperature vs $Log\ F_{PEAK}$ that is established during a temperature ramp which is incorporated into the lyophilization cycle after the freezing stage but before the onset of primary drying. The relationship between temperature and $Log\ F_{PEAK}$ over the sub-zero temperature range is modelled by a second-order polynomial and the polynomial coefficients are used to estimate the temperature at the TVIS node from the values of $Log\ F_{PEAK}$ recorded during primary drying.
$T_{F_{PEAK}}$	Ice temperature, at the loci of the TVIS node, during the primary drying stage. These temperatures are predicted from a calibration of temperature against $Log\ F_{PEAK}$. The assumption is that this temperature represents the average temperature of the ice in the region bounded by the electrodes. For the justification of this assumption, see Smith et al. (2017).

Acknowledgements

First of all, I would like to express my sincere appreciation to my supervisors, Prof. Dr Geoff Smith and Dr Irina Ermolina, for their continuous support throughout my PhD programme, and for their patience, and for enlightening my knowledge. I have learned something new and was offered many different perspectives. Their guidance has been very helpful for me during my time in UK. I hope that I can return the favour sometime in the future.

My sincere thanks to Mr Evgeny Polygalov for training me in basic electronic work, and for his support for Through-vial impedance spectroscopy system (TVIS) during my time at De Montfort University, although he has already left the university. I am very grateful for his assistance.

I am deeply indebted to Dr Paul Matejtschuk, Kiran Malik, and Chinwe Duru at The National Institute for Biological Standards and Control (NIBSC) for their guidance, discussion, and support throughout my use of their facilities.

Thanks also to Anton Mangold of IQ Mobil Solutions for the loan of TEMPRIS® sensors.

Many thanks to my colleagues in the TVIS group, particularly Baskar Pandya and Anand Vadesa for sharing knowledge and helping me not only with research but also with my English. I gained a lot of additional insights from their comments, and I am really happy to have worked with them; it was a pleasure having them as friends.

Financial support from the Government Pharmaceutical Organization, Thailand (GPO) for my PhD study is greatly appreciated. I would like to extend special thanks to my colleagues at R&D (GPO) for supporting me across the miles.

I also would like to thank Dr Rachel Armitage for SEM work and sputtering gold. I also kindly acknowledge all staff members at the Faculty of Health and Life Sciences for their support and help in every situation.

Finally, I would like to express my gratitude to my parents and to my lovely sister (Pornthip Jeeraruangrattana) for their love, support, and encouragement throughout my research.

1. Introduction

1.1. The freeze-drying process

Freeze drying, also termed as lyophilization, is a low-temperature desiccation technique commonly used in the food, chemical, biological, and pharmaceutical industries (Costantino & Pikal, 2004; Fetterolf, 2010). In pharmaceuticals, it is generally used to increase product stability and extend shelf-life, particularly with delicate products such as protein molecules (Tang & Pikal, 2004). Additionally, the freeze-dried product is usually in a solid form with a more porous structure; thus, it can be easier to handle during transportation and storage, and may also have a reduced reconstitution time (Pržić, Ružić & Petrović, 2004; Baheti, Kumar & Bansal, 2010).

According to Jennings (2008) lyophilization is defined as a stabilization procedure in which the product is frozen and then the solvent is removed by sublimation (primary drying) and desorption (secondary drying) respectively, until the residual solvent is at a sufficiently low level to inhibit both microbial growth and chemical degradation. A typical freeze-drying process consists of three main steps: (1) freezing; (2) primary drying; and (3) secondary drying. A thermal treatment process also known as annealing is an optional step in which the product is held at the temperature between T_g' and the melting point of ice for a specified time period. This additional step is used to modify the frozen structure and/or crystallize ingredient(s) in the preparation, thereby decreasing primary drying time and improving the homogeneity of the batch (Searles, Carpenter & Randolph, 2001a; Wang & Pikal, 2012). These stages are illustrated in Figure 1.

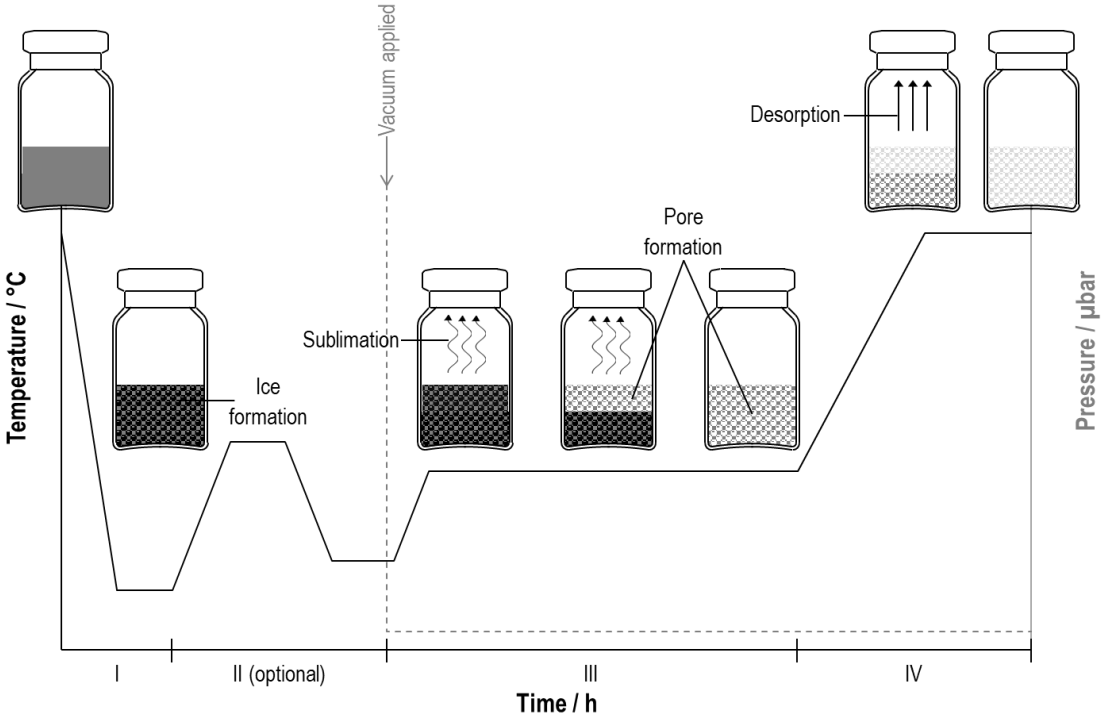

Figure 1 The freeze-drying process: (I) freezing; (II) annealing (optional); (III) primary drying; (IV) secondary drying. The solid line represents temperature and the dashed line represents pressure.

1.1.1. Fundamentals of the freeze-drying process: phase diagram

As mentioned earlier, the freeze-drying process involves the removal of either water and/or solvents through a sublimation process in which ice or frozen solvent (e.g. tert-butanol) is converted into gas without first transforming to the liquid state. The fundamentals of freeze drying can be explained by using a phase diagram. Since most of the products suitable for freeze-drying are aqueous in nature, the phase diagram (pressure–temperature diagram) of water in the schematic of Figure 2 is illustrated. This diagram provides not only the physical state of substance as a function of pressure and temperature, but also phase boundaries that represent the phase coexistence equilibrium.

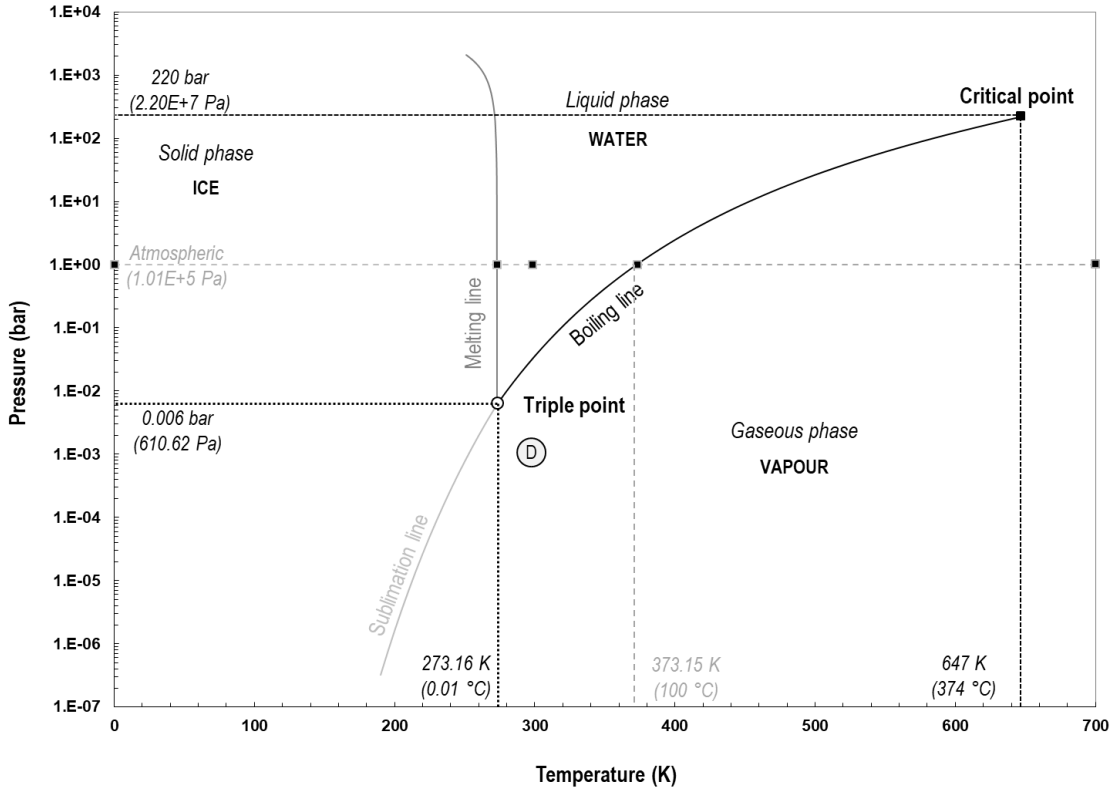

Figure 2 Phase diagram of water

There are three regions in the phase diagram of water: solid state (ice); liquid state (water); and gaseous state (vapour). These regions are divided by the equilibrium line known as phase boundaries (solid line in Figure 2). Any points on this line mark the conditions in which two phases are in equilibrium. For example, at atmospheric pressure (grey horizontal dash line), water and vapour coexist in equilibrium at 100 °C (grey vertical dash line), known as boiling point, and a phase change from liquid state to gaseous state can occur at any conditions on or below this boiling line. At the triple point of water (temperature of 273.16 K and pressure of 0.006 bar), the three phases of water are in thermodynamic equilibrium. The end point on the phase diagram is called the “critical point” (temperature of 647 K and pressure of 220 bar). Above the critical point, water and vapour cannot be distinguished, and are instead referred to as a supercritical fluid.

This phase diagram also provides an understanding of the basic principles of the freeze-drying process. For example, at a sea-level pressure and a room temperature of 25 °C, water is in a liquid state (point A in Figure 2). When water is cooled down below its melting line (point A to B in Figure 2), water will be converted from a liquid state to a solid state or ice (point B in Figure 2). By reducing the pressure below the triple point (point B to C in Figure 2) along with the increasing temperature (point C to D in Figure 2) the ice is forced to sublime directly to the gaseous state (point D in Figure 2). If the temperature is further increased, the bound solvent (especially unfrozen water) is eliminated to obtain the target level of residual solvent.

1.2. Stages of freeze-drying

1.2.1. Freezing

After loading the filled product containers into a freeze dryer, the product is cooled down to form the frozen matrix. In this step, the product temperature is generally controlled by the freeze dryer shelves. First, the shelf temperature is decreased to reduce the product temperature below its equilibrium freezing point. The liquid at this point is known as a "supercooled liquid". The supercooled liquid is cooled further until it reaches nucleation temperature, when the ice nuclei is initiated. These nuclei then grow into ice crystals, the extent of their size (the ice crystal growth or solidification) is the following step. In this phase, ice crystal undergoes growth only, without the formation of new ice crystal. The solidification usually starts directionally from the vial's bottom to the top (Tsotsas & Mujumdar, 2011), and from the outside to the centre (Burns, Stickler & Stewart, 1992). Subsequently, a frozen matrix with a different structure (i.e. crystalline form, amorphous matrix, or a mixture of the two) is obtained (Kasper & Friess, 2011). However, to ensure complete solidification, the frozen product should be held at the set temperature for a period of time (i.e. final freezing temperature practically is below T_g' for amorphous materials or below T_{eu} for crystalline materials). The holding time depends on fill height and should be at least 2 hours for products with a fill height higher than 1 cm (Tang & Pikal, 2004). Apart from shelf temperature and the holding period, the freezing rate is another parameter to be optimized. A fast freezing rate creates small ice crystals, which produce small

pores after sublimation; this then requires increasing primary drying time owing to the slower rates of diffusion through the narrow channels in the solid matrix. Conversely, a slow freezing rate could induce a phase separation of some components in some preparations (Heller, Carpenter & Randolph, 1999). According to Tang and Pikal (2004), a freezing rate of 1 °C·min^{-1} is generally to be recommended.

Freezing is regarded as the first and critical step in the freeze-drying process (Rey, 2010). One of the main factor impacting the overall efficiency of the process and the critical quality attributes of the product (i.e. reconstitution time, appearance and product stability) is the stochastic (random) nature of the ice nucleation process. These uncontrolled variables have an impact on the ice nucleation temperatures and ice growth rates, which then affect dry layer resistance. When coupled with the thermal heterogeneity of the dryer, this then causes variations in drying rates and therefore process end points for individual vials across the dryer, and the potential for non-uniformity in the production batch.

The relationship between the freezing process and the subsequent drying behaviour has been reported in a number of publications (Roy & Pikal, 1989; Kochs et al., 1991; Kochs et al., 1993; Searles, Carpenter & Randolph, 2001b; Tang & Pikal, 2004; Assegehegn et al., 2019). A higher degree of supercooling results in ice forming at a lower temperature and is likely to generate many small ice crystals. In this way, a greater tortuosity of the interconnected pores within the dry layer (left behind once the ice has sublimed) is acquired. A high product resistance (R_p) slows down mass flux during primary drying, and consequently prolongs the sublimation process. A decrease in drying rate with an increase in the degree of supercooling has been reported (Searles, Carpenter & Randolph, 2001). Rambhatla et al. (2004) demonstrated that a more efficient process can be achieved by controlling the nucleation temperature (i.e. the primary drying time can be reduced by ~30 % as nucleation temperature increase by 10 °C). Similar findings have been reported by Nail et al. (2017).

However, the foremost problem is that the ice formation phenomenon is uncontrollable: various factors from either the freeze-drying process or the preparations itself (e.g. impurity

contamination) contributing to this. To overcome these issues, various approaches have been developed through which to control the ice formation process, as summarized by reviews (Geidobler & Winter, 2013; Kasper et al., 2013; Assegehegn et al., 2019). Common methods are: (1) the use of ice nucleant (i.e. Pseudomans Syringe or Snowmax® or Silver Iodide powder); (2) pre-vial treatment (Searles, Carpenter & Randolph, 2001); and (3) gap-freezing (Kuu et al., 2013). However, these approaches could not be applied in the commercial production process due to safety and regulatory concerns. The ice fog technique (FreezeBooster® by Millrock, Veriseq® by Linde, and LyoCoN® by Martin Christ) and the pressurization-depressurization method (ControLyo™ by Praxair) are currently scalable technologies that produce more uniform and larger ice crystals at desired nucleation temperatures over controlled nucleation periods, in commercial batches. Nevertheless, all of these technologies either require a dryer re-engineering (for example, an overpressure resistant chamber is required for pressure-based technology), or may not be applicable to the larger dryers due to poor ice-fog distribution followed by a variation of the sublimation rate.

Even without the availability of controlled nucleation technology, our understanding of frozen structures (such as average ice crystal size, ice distribution) enables us to predict the pore dimension, including tortuosity within the dried matrix after ice has sublimed, and thereby to estimate the dried product resistance that is one of the critical parameters for building the design space for the primary drying process. Although techniques such as microbalance (Pikal, M. J. et al., 1983), MTM (Tang, Nail & Pikal, 2005, Milton et al., 1997, Tang, Nail & Pikal, 2006c), and TDLAS (Kuu et al., 2011) have been used for the estimation of the dried product resistance, the determination of ice morphology and the variation within frozen matrices is an alternative method. Several techniques have been studied for acquiring information on ice structure, including the use of scanning electron microscopes (SEM) with image analysis techniques to determine the porous structure of freeze-dried cake (Arsiccio et al., 2019; Grassini et al., 2016). Surface area analysis (known as Brunauer-Emmett- Teller (BET)) was used for determining the surface area of the cake and then correlated to the pore dimension (Rambhatla et al., 2004). X-ray computed tomography has also been used for studying the microstructure in a product

(Pisano et al., 2017; Nakagawa et al., 2018). However for a real time estimation, in process, a system based on an infra-red thermography has been introduced recently. By determining the rate of crystalline growth (R) and the temperature gradient across the frozen zone (G), the ice crystal size (D) could be predicted based on the mathematic expression below (Colucci, Maniaci & Fissore, 2019; Nakagawa et al., 2007):

$$D = a\mathrm{R}^{-\lambda_1}\mathrm{G}^{-\lambda_2} \qquad \text{Equation 1}$$

where a, λ_1 and λ_2 are constant values and could be obtained from the experimental data

Crystallization of ice

Ice crystallization is described as two successive processes: the ice formation or nucleation, and the subsequent crystal growth or solidification.

Ice Nucleation

In principle, ice and water are in equilibrium at freezing point, for example 0 °C at atmosphere (Figure 2). However, in fact, water remains liquid even when cooled down to 0 °C and needs to reach the temperature below theoretical freezing point before ice formation starts. The water in this stage is referred to as supercooled liquid which is in a thermodynamically unstable phase. During supercooling, water molecules are arranged to form clusters by hydrogen bond, and then immediately disintegrate (Cook & Hartel, 2010; Kasper & Friess, 2011). Once the cluster has a minimum size known as a critical radius (r^*), a stable nucleus is formed and serves as a site for further ice growth. When the first stable nucleus appears (called primary nucleation), the secondary ice nucleation subsequently occurs throughout the entire system.

By assuming that the spherical ice nucleus is formed in a homogeneous system (pure water without any impurities or contaminants), the critical radius could expressed by the Equation 2 (Zaritzky, 2016):

$$r^* = \frac{2\gamma T_f}{L_f \Delta T_s} \qquad \text{Equation 2}$$

Here, γ is the surface tension (free energy per unit area of the interface); ΔT_s is the degree of supercooling calculated from the difference between the equilibrium freezing temperature (T_f) and the ice nucleation temperature (T_n), $\Delta T_s = T_f - T_n$; and L_f is the latent heat of fusion (for water 335 k·J·kg^{-1} at 0 °C). From Equation 2, the critical radius is a function of the degree of supercooling. With a low degree of supercooling a large ice nucleus is formed, leading to a greater number of large ice crystals forming in the system.

Ice growth

When the stable ice nuclei are formed, crystal propagation commences by adding molecules on the solid-liquid interface. The crystal growth is controlled by two mechanisms: the rate of removal of latent heat liberated during the phase transition, and the rate of mass transfer, i.e. the liquid molecules diffuse and add on crystals to grow their size, whereas solid molecules depart from the surface to bulk liquid (Zaritzky, 2016). The crystal growth rate (R) is a function of supercooling according to the expression below (Petzold & Aguilera, 2009) :

$$\mathrm{R} = \beta(\Delta T_s)^n \qquad \text{Equation 3}$$

Here, ΔT_s is the degree of supercooling calculated from the difference between the equilibrium freezing temperature (T_f) and the ice nucleation temperature (T_n) or $\Delta T_s = T_f - T_n$; β and n are experimental constants.

From Equation 3, it follows that the lower the degree of supercooling (higher ice nucleation temperature) the slower the ice growth rate, or the longer the ice solidification time, which in turn results in larger ice crystals (and vice versa).

Crystallization in aqueous solution

Most parenteral preparations are aqueous solutions, and therefore the ice formation in those preparations is heterogeneous (e.g. water containing solutes or particles). According to the colligative property of the solution, the equilibrium freezing point of the solvent can be suppressed by adding any solutes. This property is proportional to the solute concentration, and the depression of the freezing points (ΔT_f) for dilute solution could be estimated by:

$$\Delta T_f = K_f \mathrm{mi} \qquad \text{Equation 4}$$

where K_f is the freezing point depression constant of the solvent (for water is 1.86 kg·°C·mol^{-1}), m is a molality of solute and i is the van't Hoff factor (the number of particles produced in solution per individual molecule of solute, e.g. i = 1 and 2 for sucrose and NaCl respectively).

In the case of heterogenous solutions, when ice nucleus begin to grow, the solute is rejected from the ice phase and then accumulates at the ice-liquid interface, leading to the concentration of the solute in the liquid surrounding the ice front (Figure 3). This is followed by a decrease in the equilibrium freezing temperature (i.e. the higher solute, the lower freezing point temperature) with a gradient that levels off to the freezing point of the bulk solution. The zone ahead of the ice interface where the solution temperature (T_{sol}) is below the freezing temperature (T_f) is defined as the region of constitutional supercooling (Figure 3). The existence of this zone causes an unstable condition for ice growth and therefore the ice front is susceptible to small changes. If an ice crystal protrudes just slightly from the ice plane into the supercooled region, the ice will grow increasingly (crystal growth rate α degree of super cooling, Equation 3) with the segregation of solute. This is one factor responsible for the final frozen structure of the heterogeneous system (Petzold & Aguilera, 2009; Zaritzky, 2016).

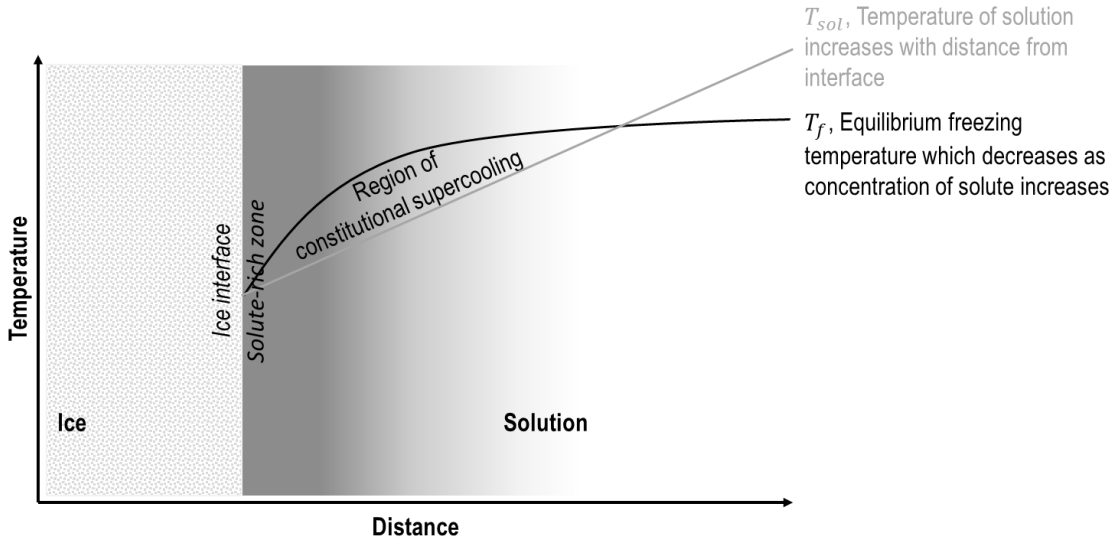

Figure 3 Illustration of the constitutional supercooling region during freezing of solutions. The accumulation of solutes in the liquid near the ice surface produces a concentration gradient that affects the equilibrium freezing temperatures.

1.2.2. Annealing

Annealing is an optional thermal treatment process in which the frozen product is kept at a specified temperature (usually above the glass transition temperature (T_g') of the formulation) for a defined time period. It usually consists of warming, holding, and then often cooling. One purpose of this process is to promote the crystallization of active ingredients (Gatlin & Deluca 1980; Korey & Schwartz, 1989) and excipients such as glycine, mannitol or salts (Carpenter et al., 1997; Milton et al., 2007; Lu & Pikal, 2004) that might partially crystallize during the freezing stage. A crystalline bulking agent could yield a stable matrix that would shorten the primary drying time and provide an acceptable product appearance. It is possible to dry above the collapse temperature (T_c) if the proportion of bulking agent is high enough when compared with the amorphous phase (i.e. 3:1), as suggested by Wang and Pikal (2012). Lack of complete of crystallization could lower the T_g' (Lueckel et al., 1998), give rise to vial breakage during primary drying (Jiang et al., 2007), or affect shelf-life stability during storage (Lueckel et al., 1998). Hirakura (2004) reported the event of ampoule breakage due to the incomplete crystallization of sodium dibasic phosphate in an interleukin formulation. In cases of maximising the

crystallization, Tang and Pikal (2004) suggested annealing the product at temperature 10-20 °C above T_g' but below the T_{eu} of the bulking agent for sufficient time (defined by the quantity of crystalline materials and the filling depth).

Another aim of annealing is to improve the homogeneity of ice crystals by encouraging ice crystal growth (Kasper & Friess, 2011). Restructuring of the annealed product might occur through a thermodynamic driven process (Roos, 2007). The extent of annealing time contributes to the increase in size of the ice crystal (Figure 4). The average ice crystal size of a sucrose solution increased five-fold after annealing at −5 °C for 31 h (Nakagawa et al., 2018). As a result of the annealing, variation of crystal size and small ice crystals are eliminated, resulting in more uniform microstructure, greater crystal size, and less size variation when compared with the non-annealed process.

As a consequence of larger ice crystals, the sublimation process can be expected to be accelerated (reducing primary drying time), because the dried product resistance to vapour flow is reduced (Searles, Carpenter & Randolph, 2001; Tang & Pikal, 2004; Abdelwahed, Degobert & Fessi, 2006). The improvement of batch homogeneity by annealing was also demonstrated by Searles and coworkers (Searles, Carpenter & Randolph, 2001). In contrast to these results, Esfandiary et al. (2016) found that annealing could increase product uniformity in protein-based formulations and could also increase primary drying time by 20% when compared with a non-annealing cycle. This is because of the production of a thick layer of concentrated solute on the surface of the sample after annealing exhibiting a compact skin formation that could decrease the sublimation rate. Similar to Lu and Pikal (2004), they reported delayed primary drying time due to the partial blockage of water vapour flow as a result of the crystallized material obtained from annealing. Furthermore, the annealing process can also decrease the specific surface area of the product and might consequently require a longer secondary drying time (Pikal et al., 1990). Therefore, understanding the impact of annealing on the formulation can assist the design of appropriate lyophilization cycles.

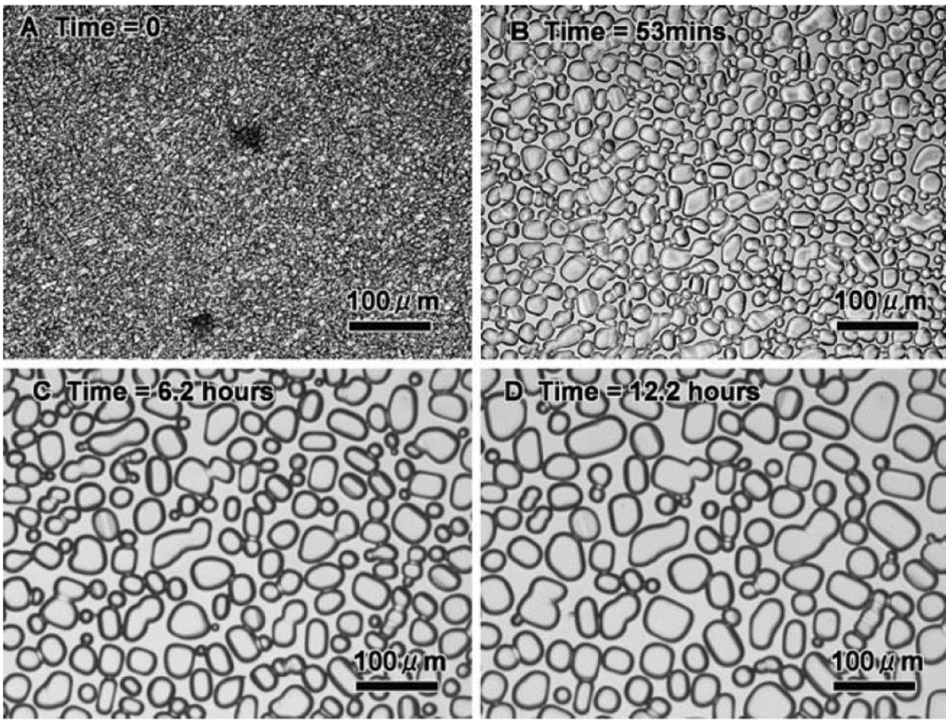

Figure 4 The growth of ice crystals over time. The sucrose solution (28.6%) was annealed at −8 °C (Hagiwara, Hartel & Matsukawa, 2006).

Morphological changes of ice crystals during annealing

Searles (2010) proposed two key mechanisms controlling the change in ice crystals during the thermal treatment process: (1) sintering, and (2) Ostwald ripening.

Sintering

Surface free energy or surface tension (γ), here, is defined as the energy associated with the curvature. This free energy plays a critical role in the kinetic process of the changes of the ice morphology. From a thermodynamic view, an increasing of heat and bulk liquid (i.e. an ice crystal melts) by annealing could increase the mobility of an amorphous system (e.g. the unfrozen fraction acts like a wetting liquid), which is followed by higher surface energy. Therefore, the system tries to lower the system energy by reducing the surface area (i.e. increase particle size). There are two main mechanisms concerning ice restructuring during thermal treatment: surface transport, and bulk transport. First, surface transport, including surface diffusion and gas phase transport (Figure 5): this process is responsible for neck growth by re-arranging molecules (i.e. H_2O) to form bonds. For surface diffusion, the movement of molecules at the curved surface

could be explained using the Young-Laplace equation, which links energy (stress) and curved surfaces. For spheres, this equation is below:

$$Stress = \frac{2\gamma}{r} \qquad \text{Equation 5}$$

where γ is surface tension, and r is the radius of a curved surface. Therefore, the stress at the neck region with a smaller radius (concave) is typically higher than the sphere surface (convex). As a result, the molecules are migrated from the concave to the ice boundary and then this concave region becomes more available, hence the molecules from the convex region (mass source) will flow to fill up the concavity (mass sink) and make it flatten (reduce stress). In other words, the microstructure curvature drives mass flow by removing both convex and concave surfaces and moving towards a flat surface (German, 2010).

Gas phase transport is another process that forms part of surface transport (Figure 5). The vapour pressure increases as temperature increases (e.g. small ice crystals melt). Following the Kelvin equation (Equation 6), which states that the vapour pressure above a curvature is larger than of the same substance above a flat surface, gas diffuses towards the neck area:

$$P_{curve} = P_o e^{(\frac{2\gamma\bar{V}}{R_g T r})} \qquad \text{Equation 6}$$

where P_{curve} is the vapour pressure over the curved surface, P_o is the equilibrium vapour pressure, $\bar{V}$ is the specific volume, R_g is gas constant, r is radius of curvature and T is temperature.

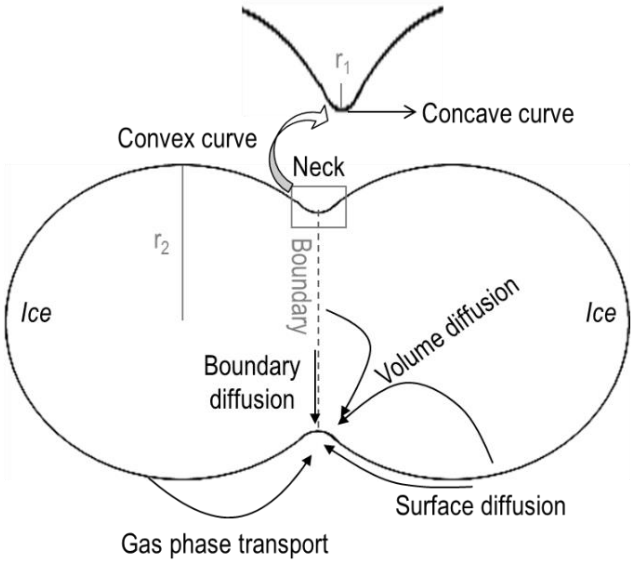

Figure 5 Illustration of the various processes of sintering: surface diffusion; gas phase transport; boundary diffusion; and volume diffusion. The grey dashed line represents the ice boundary and the radius of concave and convex curve are r_1 and r_2, respectively.

Another mechanism thought to contribute to microstructural change is that of bulk transport, or bulk flow. This transport process causes the coalescences of ice crystals. At the ice boundary, the molecules are in disorder and are liquid-like, providing ice molecules to diffuse from boundary to neck (known as boundary diffusion) as shown in Figure 5 (Riley, 1988).

For crystalline particles, the concentration of vacancies (the absence of a molecule or an atom in the crystal lattice) at the surface of a crystalline is surface stress-dependent (German, 2010). For instance, the vacancy concentration of a concave surface is higher than a convex one such that the vacancies distribute through the solid. In effect, the material flows in the opposite direction to diffusion of the vacancies (Djohari, Martínez-Herrera & Derby, 2009). In this case, since the concentration of vacancies at the neck region is higher than that far from the neck, the vacancies leave the neck by diffusion through interior lattice or along particle surfaces (defined as volume diffusion, Figure 5) whereas material flows into the neck according to the aforementioned and finally coalesce.

Ostwald ripening

Ostwald ripening, also known as recrystallization, is a phenomenon describing an increase in size of crystals over time. This is a thermodynamically-driven energetically favourable (spontaneous) process which minimizes the overall surface energy of the system because the larger particles are typically more stable than the smaller ones (i.e. smaller particles have higher surface areas to volume ratios). Given that the molecules on the surfaces are in a higher energy state than the ordered molecules inside the particle, the water molecules at the surface of ice crystals tend to detach from their crystals and diffuse through the unfrozen fraction before depositing on the surface of the larger particle hence lowering the total energy of the system. As a result, the ice crystals with a radius larger than critical size become larger in their size whereas the small ice crystals disappear. The crystal growth rate can be explained by the classical Lifshitz-Slyozov-Wagner (LSW) theory as follows:

$$\bar{R}^3(t) - \bar{R}^3(0) = Kt \qquad \text{Equation 7}$$

where $\bar{R}^3(t)$ and $\bar{R}^3(0)$ are, respectively, the mean crystal radii at time t and at the initial recrystallization time (i.e. $t = 0$), and K is the recrystallization rate constant that is a function of the diffusion coefficient of the dispersed phase (water in this case). The recrystallization rates have a direct relationship with the diffusion coefficient, thus the diffusivity of the water in a freeze-concentrated unfrozen phase could be used for predicting the recrystallization rate of ice crystals. For example, the increase in water mobility could increase the recrystallization of ice. Although the mobility of water could be affected by the solute, for sugar solutions with concentration less than 30%, the recrystallization rate is more dependent on water mobility in the freeze-concentrated solution than the sugar content (Hagiwara, Hartel & Matsukawa, 2006).

The average particle size estimated by the LSW theory is usually narrower than measured results (Baldan, 2002) because this theory is based on the assumption of an infinite dilution system in which the interaction between the particles is negligible, when in fact there is an interaction among particles in the real system. Therefore, many attempts have tried to model this, based on the finite volume fraction of the dispersed phase. Baldan (2002) reviewed these proposed

models and concluded that further work is required to precisely formulate the kinetics of the Ostwald ripening theory.

Phase transition of amorphous phase during annealing

The freezing of a solution during the first stage of a lyophilization cycle separates much of the water into an ice fraction and concentrates the solutes into what is known as the unfrozen fraction. After the ice forms, one or two things may happen to the unfrozen fraction. In one case, which is typical for an excipient like mannitol, the solute may precipitate or crystallize from the solution to form an additional solid phase (Franks & Auffret, 2007). In another case, the solute may remain in the solution state and the unfrozen fraction continues as a liquid-like (rubbery) phase until it transitions to an amorphous glass at a certain temperature, known as the glass transition temperature or T_g' (Pansare & Patel, 2016).

Any excursions above the glass transition will significantly reduce the viscosity of the unfrozen fraction (i.e. increasing the mobility of the amorphous matrix) to an extent that the matrix will collapse (when it is no longer supported by the surrounding ice crystals), leading to dramatic changes in the appearance of the product and even a reduction in shelf-life due to the increased instability of the active pharmaceutical ingredient (Lueckel et al., 1998; Liu, 2006; Passot, 2007). The temperature at which this phenomenon occurs is known as the collapse temperature (T_c), which is typically above the glass transition temperature (Pikal & Shah, 1990). Thus, T_c is literally the critical process parameter.

Ultimately, the glass transition of any maximally freeze-concentrated solution depends on its composition and the glass transition of the individual components or solutes (Carpenter et al., 1997). A mixture of excipients (each with its own function) is used in a lyophilized drug formulation (Bedu-Addo, 2004). Salt (e.g. NaCl) is usually used for adjusting the tonicity of the product to reduce the irritation at the site of the injection. Unfortunately, the presence of excipients in the formulation, especially salts, has a negative impact on the glass transition of the concentrated unfrozen phase (Shalaev & Franks, 2002). For example, a combination comprising 91% sucrose and 9% sodium chloride (NaCl) in a 5% w/v solution has a T_g' which is

~ 7 °C lower than a 5% w/v solution of sucrose alone (Shalaev & Franks, 1996). This means that any product formulation with (in particular) added salt may need to be dried at low temperature (and moderate pressure) compared to the formulation without salt. The same reason explains why some potential excipients are excluded from formulation because the glass transition in their maximally concentrated state is too low and exceeds the capability of some freeze dryers.

It follows that an understanding of the glass transition and the collapse temperature is a prerequisite to the development of an effective freeze-drying cycle, i.e. one that has a primary drying stage of acceptable length and also produces a product that meets the critical quality attributes of appearance, moisture content, and stability.

Glass transition measurement

Glass transition is a second order phase transformation occurring in amorphous materials. This phenomenon is a time-dependent, non-equilibrium process. At temperatures well below the glass transition, the mobility of molecules in an amorphous matrix is limited, resulting in solid-like brittle materials defined as being in a glassy state. Meanwhile, viscous, liquid-like materials (rubbery state) would be obtained if the glassy material were to be heated above the glass transition temperature. Since the glass transition is associated with the change in thermodynamic and physical properties of amorphous materials (e.g. conductivity, viscosity), various techniques have been used for determining glass transition temperatures and sometimes different methods can provide different results (Saldivar-Guerra et al., 2013; Bandeira et al., 2015).

Thermal analysis such as differential scanning calorimetry (DSC) is used extensively for measuring glass transition temperatures. This method defines glass transition by using an endothermic step change in the heat flow of the thermogram. The glass transition temperature can be reported by using the onset, mid-point and offset point of the step transition, but the mid-point is used in practice (Her, Lih-Min & Nail, 1994; Gabbott, 2008). Duru et al. (2015) used the standard DSC to demonstrate the impact of residual moisture content contained in the influenza reference standard on the glass transition temperature. The effect of the protein

concentration on the critical temperature of the freeze-drying formulations was studied using the typical DSC by Depaz et al. (2016). They found that T_g' increased with an increase in the protein concentration. Various types of DSC have been developed to increase the sensitivity and functionality (Balasubramanian et al., 2016). Modulated DSC (mDSC) is one version of DSC that applies a sinusoidal (modulated) heating rate on top of the linear heating rate used in the conventional DSC. This technique is helpful for detecting a weak transition and/or overlapping transition, especially in pharmaceutical preparations that usually present with low concentrations and multiple excipients (Thomas, 2005).

Thermomechanical analysis (TMA) is another technique for defining glass transition. TMA measures a deformation of the sample under applied constant stress (static load). Similarly to TMA, dilatometry also measures changes in dimension as a function of temperature, but no external load is applied in this technique (Koontz, 2019). For highly crystalline material, the sensitivity of TMA is better than DSC (Foreman, Sauerbrunn & Marcozzi, 2013).

The next technique for T_g' determination is dynamic mechanical (thermal) analysis (DMA or DMTA). Unlike TMA, oscillatory stress is applied and measures the change in the mechanical stiffness (stiffness is the property of a material to resist the elastic deformation). As a consequence of glass transition, molecular mobility increases and the elastic properties of the material (the storage modulus, E') decrease rapidly whilst the viscous behaviour (loss modulus, E'') increases. The onset of a dramatic drop in storage modulus marks the point where the strength of material starts to decrease (easy to deform). The energy lost (dissipated) into the molecular friction for flowing the material is represented by the loss modulus, and the loss factor (tan delta) is described by the viscoelastic properties of material and is also used for indicating the transition point of the material (also known as damping) (E''/E'). The greater tan delta means the materials behave more in a more viscous manner (liquid-like state). The glass transition temperature practically reports using the value of tan delta along with the frequency used in the measurement; however, if one would like to compare glass transition from DMA with other techniques, the measurement frequency of 1 Hz is recommended (Foreman,

Sauerbrunn & Marcozzi, 2013; Pansare & Patel, 2016). DMA has a greater sensitivity than DSC (Roos & Yrjö, 2010). Ward and Matejtschuk (2019) demonstrated that DMA could determine T_g' of 5% human serum albumin whereas this could not be resolved by mDSC. Similarly, Abiad et al. (2010) compared the conventional DSC, mDSC and DMA by measuring T_g of hydroxypropyl methylcellulose (HPMC). They found that only standard DSC could not detect the glass transition temperature and the T_g value measured by mDSC was approximately 2 °C lower than DMA. This agrees with work done by Gearing et al. (2010), which found that T_g' from DMA was higher than from the DSC method. In spite of the DMA benefit, the common issue usually found in DMA analysis is the loss of water contained in the sample during heating. Thus, to prevent water loss while performing the DMA measurement, a stainless sheet pocket was used when preparing the sample (Laaksonen & Roos, 2000; Ward & Matejtschuk, 2019).

Since the electrical property relates to the material behaviour, dielectric analysis (DEA) based on the impedance measurement has been introduced to investigate the glass transition. DEA measures the dielectric properties of material, known as permittivity, under applied voltage. The permittivity of material corresponds to how the dipoles and ions existing in material rearrange themselves (polarization) under the electric field. Once the material is beyond glass transition, molecular mobility increases result in a change in relaxation behaviour of the material, as well as permittivity. The use of DEA for determining the critical temperature of lyophilized products was demonstrated by Morris et al. (1994). This technique is less frequently used in the pharmaceutical industrial when compared with thermal analysis techniques; however, the commercial instrument, Lyotherm, (Biopharma Process Systems Ltd.), which integrates the impedance analysis and differential thermal analysis (DTA), has been used in lyophilization research and development. With two different features, Lyotherm allows the operator to gather more information about the material behaviour such as glass transition, softening, crystallization (Ward & Matejtschuk, 2019; Smith & Polygalov, 2019). The use of data obtained from this combination technique for designing the freeze-drying cycle was demonstrated by Bandari and co-workers (2013) using Gemcitabine as a model drug. Beside the above-mentioned, other techniques used for observing the molecular mobility such as nuclear magnetic resonance

(NMR) could be used to determine glass transition temperatures because the molecular mobility is usually associated with temperature and phase transition (Roos & Drusch, 2016a).

In the lyophilization area, the critical temperature known as collapse temperature (T_c) is used practically because it describes the temperature at which the loss of frozen structure occurs. For a number of years now, it has been standard industrial practice to predict the product collapse temperature for a freeze-drying process through an off-line technique known as freeze-drying microscopy (FDM). Typically, the collapse temperatures determined by FDM are 1-3 °C higher than the glass transition temperatures, though in some cases this difference has been shown to be as high as 10 °C (Meister & Gieseler, 2009; Depaz, Pansare & Patel, 2016; Fonseca et al., 2004). The premise for the in-process prediction of collapse is the assumption that the processes leading to collapse within the microscope are the same as those within the product container, i.e. glass vial. However, while FDM provides the conditions corresponding to the basic attributes of the first stages of the freeze-drying process (i.e. freezing followed by drying of the frozen sample at reduced pressure), the measurement is based on a microscale (i.e. 1-2 µL of sample) and therefore FDM results may not represent the bulk sample contained within a vial. This issue was realised when the collapse temperature measured by FDM was found to be ~ 3 °C lower than that measured in-vial by optical coherence tomography-based FDM, OCT-FDM (Mujat et al., 2012; Greco et al., 2013). However, one drawback of the OCT approach is the bulky instrumentation associated with this technique; thus, it could not be integrated within a conventional freeze dryer without alteration to the hexagonal packing of the vials. It is therefore not clear whether the isolated vial presents the same product collapse as a vial within a cluster inside a conventional freeze dryer. More recently, an optical fibre system (OFS) based on fibre Bragg grating (FBG) technology has been introduced for measuring the critical temperature during the freeze-drying cycle (Kasper et al., 2013; Horn & Friess, 2018). However, like all temperature probes, the insertion of the sensor within the product can alter the way in which the ice forms, which might in turn impact the properties of the microstructure and the mechanical strength of the frozen mass of the monitored vial (i.e. the vial containing the sensor). Another recently introduced technology for monitoring both critical temperatures (T_g' and T_c),

through-vial impedance spectroscopy (TVIS) measures the impedance spectrum of the sample filled in the glass vial that has been modified with a pair of copper electrodes, attached to the external surface of the vial (Smith, Polygalov, 2019). It was shown to be sensitive to the glass transition temperature of 10% maltodextrin (Smith, Arshad et al., 2013) and the collapse of a 3% w/v solution of sucrose (Smith, Arshad, Nazari et al., 2014). The available analytical techniques used for determining the critical temperature are summarized in Table 1.

Table 1 Summary of the available analytical methods for determining glass transition temperature (T_g') and collapse temperature (T_c)

Analytical method	Measurement	Mode	T_g' / T_c
Differential scanning calorimetry (DSC)	Heat flow or heat capacity	Off-line	T_g'
Thermomechanical analysis (TMA)	Dimensional deformation	Off-line	T_g'
Dilatometry	Dimensional deformation	Off-line	T_g'
Dynamic mechanical (thermal) analysis (DMA or DMTA)	Viscoelastic properties	Off-line	T_g'
Dielectric analysis (DEA)	Dielectric properties (permittivity)	Off-line	T_g'
Differential thermal analysis (DTA)	Temperature difference between reference and sample	Off-line	T_g'
Nuclear magnetic resonance (NMR)	Molecular mobility	Off-line	T_g'
Positron annihilation lifetime spectroscopy (PALS)	Free volume of material	Off-line	T_g'
Electron spin resonance (ERS)	Molecular mobility	Off-line	T_g'
Freeze-drying microscope (FDM)	Structural change (visual)	Off-line	T_c
Optical coherence tomography based FDM (OCT-FDM)	Structural change (visual)	In-line	T_c
Optical fibre system (OFS)	Refractive index	In-line	T_c
Through-vial impedance spectroscopy (TVIS)	Dielectric properties (permittivity)	In-line	T_g' / T_c

State diagram

It is well-known that water acts as a plasticizer. By increasing water content in material, the mobility of material is enhanced and thereby the glass transition temperature is lowered. Hence,

glass transition temperature depends on the water content presence in the material. The influence of water content on material can be demonstrated by state diagram. In contrast to phase diagrams that show the physical state of pure substance as a function of pressure and temperature, state diagrams presents the state of the mixture at different water content (concentration). A schematic state diagram of sucrose solution is shown in **Figure 6**. The T_g line indicating the glass transition of the mixture is calculated using Gordon-Taylor equation (Gordon, Taylor, 1952) below:

$$T_{g,\,mixture} = \frac{w_1 T_{g,1} + k_{GT} w_2 T_{g,2}}{w_1 + k_{GT} w_2} \qquad \text{Equation 8}$$

where $T_{g,\,mixture}$ and $T_{g,i}$ are the glass transition temperature of the mixture, the component i , w_i is the mass fraction of component i, and k_{GT} is Gordon-Taylor constant from the experiment.

The T_g line shown in the state diagram indicates the state of the mixture at different concentration. During ice formation, freeze-concentration of the solution referred to as unfrozen fraction takes place. At the maximum concentration of freeze-concentrated solution (C_g'), glass transition is defined as T_g' and the melting temperature of ice and unfrozen fraction is T_m'. At the region between T_g' and T_m', the maximum ice formation could be achieved (Roos & Karel, 1991). State diagrams allow us to design the lyo cycle. If the product temperature is above T_m', ice melt associated with a decrease in viscosity resulting from the transformation of glassy (~10^{12} Pa·s) to rubbery state (~10^{7} Pa·s) could increase the chance of collapse product and then be followed by high residual water content. Furthermore, in case that freezing does not attain the perfectly glassy state (i.e. maximum freeze-concentrated solution), the remaining freezable water could depress the glass transition temperature of the frozen product. Annealing at temperatures between T_g' and T_m' might help to maximise the ice formation (Roos & Karel, 1991).

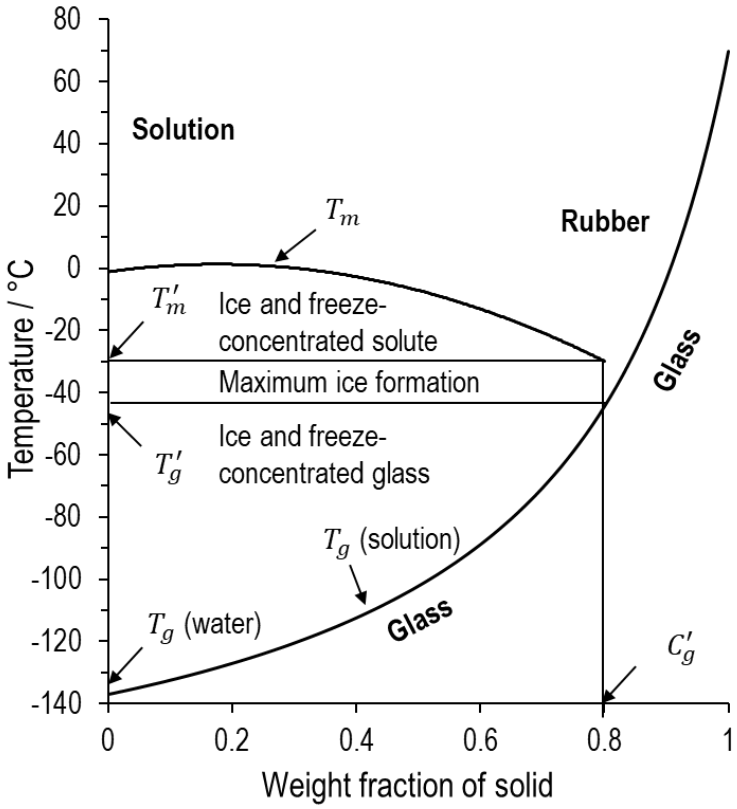

Figure 6 A schematic state diagram of sucrose solution at constant pressure showing equilibrium melting line for ice (T_m) and glass transition line (T_g). The glass transition line is predicted by using the Gordon-Taylor equation with the following value: (1) a constant value (k_{GT}) = 4.94, (2) T_g water = 136 K, and (3) T_g of sucrose = 343 K (Constantin, Schneider & Corti, 2016). At maximum freeze-concentrated concentration (C'_g) of 80%, glass transition temperature (T'_g) is −45 °C. The melting temperature of mixture at C'_g is denoted by T'_m (Roos, 2010).

1.2.3. Primary drying

Of the all freeze-drying stages, the primary drying stage is acknowledged as the longest and most energy-intensive. This step removes unbound water existing as ice (including solvent) by sublimation. Practically, the chamber pressure is reduced to be within the range of 50-150 mTorr and the shelf temperature provides sufficient heat energy to drive the sublimation process of the product (Tang & Pikal, 2004).

To avoid product failure occurrence during primary drying, the main parameters controlling the primary drying process are the operation pressure and the chosen shelf temperature (Oetjen & Haseley, 2018). The ice temperature at sublimation surface (the outcome of a thermodynamic

equilibrium phenomenon for sublimation) can be affected by these variables. For example, the ice temperature at sublimation front decreases from −30 °C to −40 °C when the operation pressure is reduced from 0.4 to 0.1 mbar. Nevertheless, this does not mean that the controlled pressure can reduce the primary drying time, but it is applied for adjusting the temperature of ice at the sublimation front (Oetjen & Haseley, 2018). The rate of drying depends on the heat supplied to the product; therefore, in practice, the freeze-drying cycle often applies the higher pressure and/or operate at the higher shelf temperature to enhance heat transfer.

Primary drying comprises two main mechanisms as illustrated in Figure 7: (1) the sublimation energy transfer to the product in order to change ice to vapour directly without becoming a liquid state (heat transfer), and (2) the migration of water vapour at the sublimation front to condenser or absorber through a closure (mass transfer). Heat and mass transfer occurring in the primary drying step are coupled and can be expressed by Equation 9 (Tchessalov, 2017):

$$\frac{dm}{dt} = \frac{A_e K_v (T_s - T_b)}{L_s} = \frac{(P_i - P_v)}{R_T} = \frac{A_i (P_i - P_v)}{\hat{R}_\rho} \qquad \text{Equation 9}$$

Heat transfer *Mass transfer*

where A_e is the external cross-sectional area of the base of the vial in m^2, K_v is the vial heat transfer coefficient, T_s is the shelf temperature in °C, $T_b$is ice temperature at the internal base of the vial in °C, L_s is the latent heat of sublimation of ice (679.9 $Cal \cdot g^{-1}$ or 2846 .5 $W \cdot s \cdot g^{-1}$ at −30 °C), P_i is the ice interface pressure which is calculated using Clausius-Clapeyron as Equation 10 (Murphy, Koop, 2005) , P_v is the headspace ice vapour pressure, R_T is total resistance to mass flow from sublimation interface to condenser, A_i is internal cross-sectional area of the vial, and $\hat{R}_\rho$ is area-normalised dry layer resistance. Note that R_p is related to the cross-sectional area of the product; therefore, to compare product resistance between formulation, the area-normalised dry layer resistance ($\hat{R}_\rho$) is recommended (Pikal, 1985). These equations are based on the assumptions that (1) all the heat supplied to the vial is used for ice sublimation, (2) ice sublimes in the horizontal plane and (3) radiation is constant over the entire temperature range.

$$P_i = e^{(28.9074-\left(\frac{6143.7}{T_i}\right))} \quad \text{Equation 10}$$

where P_i and T_i are the partial pressures of ice in Pascal (Pa) and ice temperatures in Kelvin (K) at the ice interface, respectively.

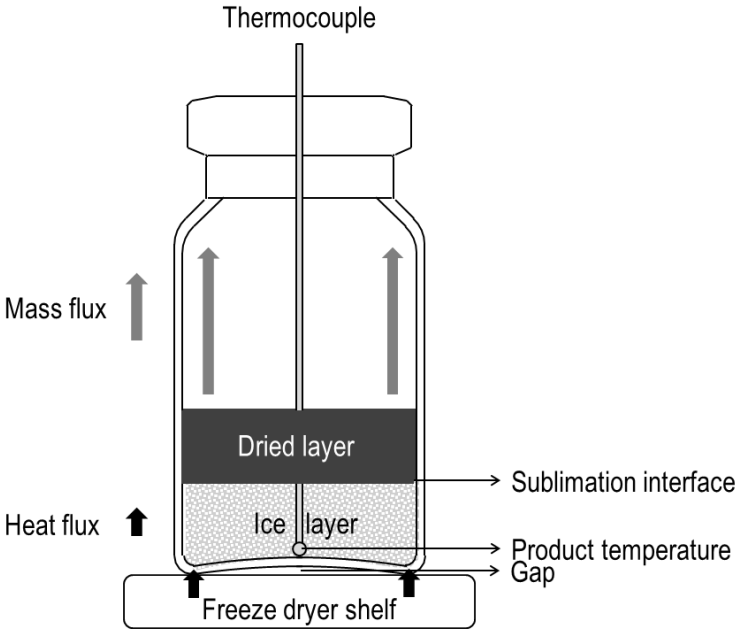

Figure 7 Illustration of two mechanisms involving primary drying process. Heat from the heat source (freeze dryer shelf) transfers into the frozen product through the bottom of the glass vial including the gap (due to the curvature of vial's bottom) in order to sublime ice (heat flux) and the ice vapour from sublimation flows through the dried layer (mass flux).

Heat transfer mechanism in freeze drying

The main mechanism responsible for heat transfer in the primary drying stage is summarized in Figure 8. The vial heat transfer coefficient (K_v) has contribution from three components as expressed below:

$$K_v = K_c + K_r + K_g \quad \text{Equation 11}$$

where K_c describes the heat contributed from direct conduction between shelf and the vial's bottom, while thermal radiation from the surface such as the chamber door and the walls of the freeze dryer is expressed by K_r, and K_g is the thermal coefficient corresponding to the gas conduction and/or convection. From these three terms, only K_g is dependent on the chamber

pressure when the pressure is well below the range where molecular flow occurs (molecules move independently). K_g generally means the conduction of gas at the space between the shelf and the vial's base (Pikal, Roy & Shah, 1984; Hottot, Vessot & Andrieu, 2005; Ganguly, Nail & Alexeenko, 2013) and could be calculated according Equation 12 (Pikal, Roy & Shah, 1984):

$$K_g = \frac{\propto \Lambda_0 P_c}{1 + l_v(\frac{\propto \Lambda_0}{\lambda_0})P_c} \qquad \text{Equation 12}$$

where $\propto$ is the term related to the energy accommodation factor, Λ_0 is free molecular heat conductivity of the gas at 0°C which equal to 2.06 $W \cdot m^{-2} \cdot Pa^{-1} \cdot K^{-1}$ for pure water vapour (Hottot, Vessot & Andrieu, 2005), l_v is the equivalent gas layer thickness between the vial's base and the shelf surface, P_c represents the chamber pressure (Pa), and λ_0 is heat conductivity of gas at atmosphere.

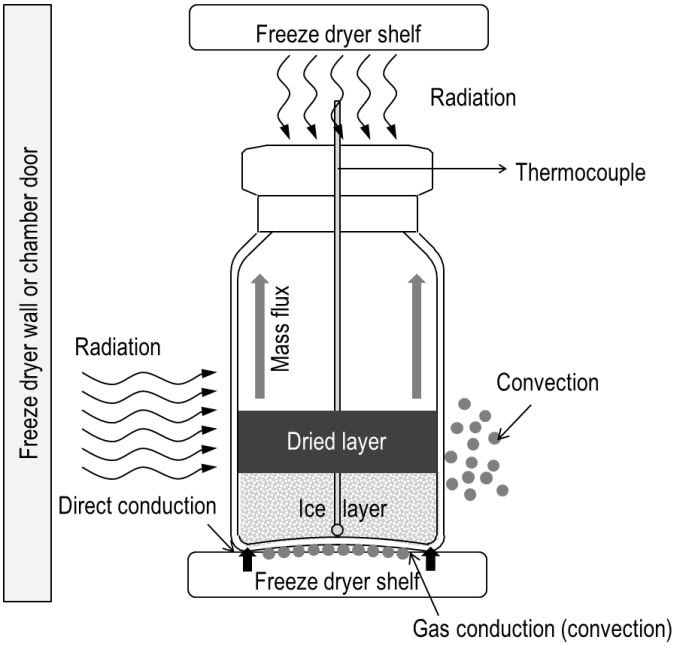

Figure 8 Heat transfer mechanisms during primary drying: *direct conduction* from the shelf, *radiation* either from walls of the dryer or/and the lyophilizer door, and *gas conduction* (convection).

Unlike gas conduction, the radiant heat can transfer to the product by wave without requiring a medium (i.e. it can occur in vacuum conditions). The energy intensity depends on the emissivity

(e) of the surface. The radiative heat transfer coefficient (K_r) could be estimated by the simplified equation below (Pikal, 1985):

$$K_r = 10^{-4}(e_v + e_s) \qquad \text{Equation 13}$$

where e_v and e_s are the effective emissivity for the top radiation (the shelf surface above vial) and shelf, respectively.

Nail (1980) first pointed out that the gas under the concave of the vial's bottom could limit the heat flux. However, the freeze-drying process usually operates at low pressure, and it is generally accepted that the heat transfer contributed by convection is insignificant. This conclusion was evidenced by the experiment in which the vial was suspended at 11 mm above the surface of the freeze-drying shelf to remove the contribution from the heat conduction. Rambhatla and Pikal (2003) found that the heat transfer is independent of the chamber pressure when the chamber pressure ranging from 50 to 250 mTorr and also that the motion of gas molecules (i.e. convection) could not be responsible for the heat transfer. Although recently, some studies have reported that the contribution of the convective heat played a part of heat transfer when operating at chamber pressures greater than 100 mTorr (Scutella et al., 2017; Ganguly, Nail & Alexeenko, 2013).

Factors affecting vial heat transfer apart from chamber pressure are equipment and container. Thermal flow due to radiation depends on both the surface and properties of the radiating material. The reflective material (i.e. shining) has lower emissivity compared to a blackbody. The concept of radiative heating could be used for justifying the drying behaviour of the edge vial (i.e. edge vials dry faster and are warmer than core vials), and this phenomenon is defined as "edge effect". The contribution of radiative heating is much more important when scaled up. A lab-scale freeze dryer normally uses a plexiglass door, which has greater emissivity than stainless steel; thus, the front vials of a lab-scale freeze dryer (close to the chamber door) might dry faster than the scale-up batch (Rambhatla & Pikal, 2003). However, the impact of thermal radiation on the overall heat transfer could be relatively less important when the primary drying is performed

at a much higher chamber pressure than those recommended by Tang and Pikal (2004). For example, in theory, crystalline mannitol (T_{eu} −1.4 °C) can be dried at pressure of 600 mTorr, and hence the convective component becomes a largest source of the heat transfer compared to the radiation.

The vial geometry in terms of (1) the contact area between the shelf surface and the vial's bottom and (2) the curvature of the vial's bottom also participates in the heat transfer (K_v) through contact and gas conduction. The thermal conduction coefficient (K_c) depends on the area at which the shelf surface and the vial bottom are in contact with each other (Kuu, Nail & Sacha, 2009), whereas the concavity of the vial bottom has an impact on heat transfer once the high chamber pressure is performed (Cannon, 2004; Scutella et al., 2017; Brülls & Rasmuson, 2002). The source of K_v variability resulting from the heterogeneity of vial dimension was demonstrated by Scutella et al. (2017). They suggested that the variation of vial geometry has to be taken into consideration during the cycle design.

Mass transfer mechanism in freeze-drying

After heat is supplied to frozen mass for converting ice into water vapour, mass transfer is a subsequent mechanism. Water vapour diffuses from the ice sublimation front through various resistances (e.g. dried product layer) to the condenser. According to Equation 9, resistance is one factor influencing the sublimation rate besides ice vapour pressure that corresponds to the ice temperature (Equation 10). The total resistance to mass flow (R_T) is contributed by three elementary components in series: (1) product resistance (R_p), (2) stopper resistance (R_S), and (3) chamber to condenser resistance (R_c) as given by Pikal et al. (1984):

$$R_T = R_p + R_S + R_c \qquad \text{Equation 14}$$

where R_c is chamber to condenser resistance per vial ("scaled" resistance).

The stopper resistance means the resistance to vapour flow through the stopper opening, which depends on the available area imposed by the position of the stopper at the vial neck and the dimension of the stopper (e.g. number of legs) as well. As well as resistance from the stopper,

there is an additional resistance due to water vapour passing from the chamber to the condenser where vapour has already been trapped and turned into the ice. The diameter of the duct connecting chamber and condenser in most freeze dryers is usually large enough and the condenser could also manage the vapour water generated during the drying process. Therefore, there is no significant resistance arising during routine operations (Costantino & Pikal, 2004). However, in the case that the process is beyond the performance of the condenser (e.g. a high ice thickness), such resistance (R_c) could become a limiting factor for the sublimation rate, particularly in the lab-scale freeze dryer (Rambhatla, Tchessalov & Pikal, 2006).

Both R_s and R_c are directly proportional to the operating pressure because the dimension of either stopper-opening or tube is larger than the mean free path of gas molecules (referred to as viscous flow), while the pore dimension within the dried layer is smaller compared to the mean free path of gas molecules (referred to as molecular flow) so that R_p depends on the difference in partial pressure. In case of free molecular flow, the resistance to water vapour flow (R_p) in dried cake could be expressed according to Equation 15 (Costantino, Pikal, 2004):

$$R_p = l_d \frac{\tau^2}{\Phi} \frac{3}{2} \left(\frac{k_g}{2 - k_g} \right) \frac{1}{d_{cap}} \sqrt{\frac{\pi R_g T}{36}} \qquad \text{Equation 15}$$

where the calculation of R_p is based on a porous cake with thickness l_d; tortuosity τ; porosity Φ, d_{cap} is diameter of capillary tube in the porous structure, k_g is a factor described the scattering of gas molecule, R_g is gas constant, and T is temperature

According to Pikal's works, he and his co-workers concluded that the total resistance was dominated by R_p (~90%), and the combination of R_s and R_c (~10%) could be negligible (Pikal et al., 1983; Pikal, Roy & Shah, 1984). Then, the dried product resistance (R_p) is the most important variable for mass transfer. In 1983, Pikal et al. used the microbalance technique along with a freeze-drying microscope to investigate factors influencing dried product resistance. They explained that the water vapour flux depended on the pore and the channel left behind by the sublimed ice. The larger the ice crystal (i.e. after annealing), the lower the product resistance.

Contrary to heat transfer (which depends on the chamber pressure and the dimensions of the vial), mass transfer is controlled by (1) freezing characteristic (Roy & Pikal, 1989; Kochs et al., 1991; Kochs et al., 1993; Searles, Carpenter & Randolph, 2001; Tang & Pikal, 2004; Lu & Pikal, 2004; Hottot et al., 2004) and (2) formulation (Pikal, 1985). An increase in cake resistance could be observed when transferring technology from laboratory to GMP conditions because the production environment (i.e. clean room area) could increase the degree of supercooling, leading to smaller ice crystals and then followed by high product resistance (Rambhatla, Tchessalov & Pikal, 2006). For the formulation aspect, different materials, as well as different concentrations, could alter the product resistance behaviour (Pikal et al., 1983), thereby changing primary drying time. These results agree with the work done by Schneid and Gieseler (2008b), who also observed the product resistance increase with the filling depth due to a modification in freezing behaviour.

1.2.4. Secondary drying

After primary drying, not all water and/or solvent has been removed, and there is still some moisture and/or solvent (5% to 20% of the 'dry' weight) left in the freeze-dried cake (Tang & Pikal, 2004; Mayeresse et al., 2009); the presence of water can decrease the glass transition temperature (Levine & Slade, 1988b; Roos & Karel, 1991). Consequently, the product can collapse easily as the temperature increases, particularly during secondary drying. Furthermore, the residual moisture content in the lyophilized product generally impacts the product stability. Water existing in the product can enhance mobility of the system resulting in an increased reaction rate and thereby affecting the product stability (Lueckel et al., 1998; Bell, Hageman & Bauer, 1995; Herman et al., 1994). Therefore, the removal of these solvents (including water) is required. This desorption process, called secondary drying, is performed by elevating the temperature to remove the unnecessary solvent from the product until a suitable moisture level in the dried product is achieved. Practically, the residual moisture content of the finished product should be below 1% (Seligmann & Farber, 1971; Pikal & Shah, 1997; Pikal, 1994). However, in some protein formulations, the thermal stress during secondary drying or

excessively dry conditions could damage or alter the activity of either proteins or microorganisms. In this case, an intermediate water content (1%-5%) might be the optimal range for stabilizing such products (Breen et al., 2001) . Hence, there is no doubt that a stability study must be performed to establish the optimum moisture content of every product.

Unlike primary drying, the main process parameter of secondary drying is the product temperature (Pikal et al., 1990). The product temperature should be controlled to be well below the glass transition temperature of the intermediated dried product from primary drying (T_g). If the product temperature exceeds T_g, the dried product will soften (more fluidity) and finally lose the cake structure. The deformation of cake structure ranges from shrink (volume contraction) to partial collapse, collapse and melt-back. It follows that these products would have a lower specific surface area (SSA) (Schersch et al., 2010), and consequently limit the desorption process. As a result, the finished products usually contain high residual solvent and/or moisture content and have a poor reconstitution. In addition, collapsed or melt-back products are not acceptable due to their inelegant appearance and inferior product quality (US Food and Drug Administration, 2014). To avoid these issues, a slow ramp temperature is suggested (Costantino & Pikal, 2004). Given that SSA plays a key role in the secondary drying stage, the higher the SSA, the faster the desorption process. However, one should note that primary drying process could be accelerated by enlarging the pore structure (e.g. annealing), which, in turn, reduces SSA. Therefore, optimizing the process is necessary to increase the efficiency of the lyophilization process in terms of a reduction in process times.

1.3.Available process analytical technology for freeze-drying

According to the FDA Guidance for Industry on Process Analytical Technology (PAT), PAT should be used for designing and controlling a manufacturing processes in order to ensure that quality is built into the product rather than being assessed once the finished product has been manufactured (US Food and Drug Administration, 2004). During the development of freeze-dried products, pre-lyophilization analysis such as DSC and FDM is required to characterise formulation properties, namely the glass transition temperature (T_g'), the eutectic temperature

(T_{eu}), and the collapse temperature (T_c). These critical temperatures are then used for designing the process cycle. The benefit of the pre-lyo study is to minimize cost and streamline the freeze-drying process (Ward & Matejtschuk, 2019). PAT is not only applied to monitor the scale-up to the commercial batch but it is also used at the lab-scale, to provide a comprehensive understanding of product and process (Patel, Lobo & Shah, 2013). However, due to the complicated lyophilization process and lack of efficient PAT tool, the implementation of PAT has proved to be both a challenge and attractive. Various process monitoring devices have been developed throughout the last few decades (Figure 9), but few with potential to be incorporated into the industrial freeze dryer. Additionally, it is well-known that product temperature and pressure are critical process parameters affecting heat and mass transfer process in primary drying, which is recognized as the rate-limiting step in the lyophilization process, as mentioned earlier. For this reason, product temperature and pressure monitoring tools in production freeze dryers will be emphasized in this section.

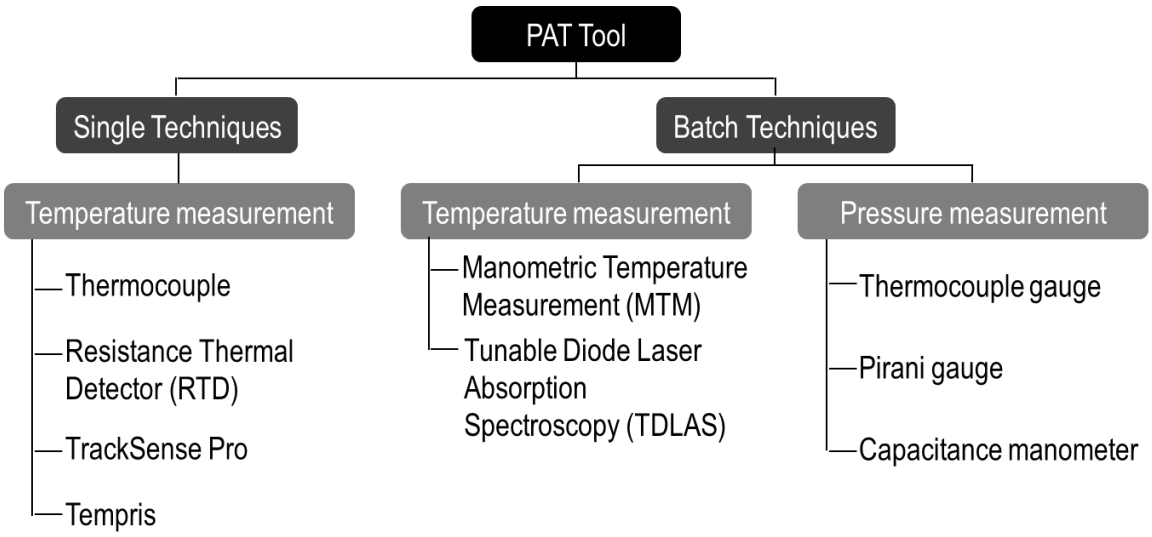

Figure 9 Process analytical technology (PAT) technology for monitoring primary drying process

1.3.1. Product temperature

Single vial techniques

Thermocouples (Type-T, made from copper-constantan, is generally used in lyophilization processes) (Nail et al., 2017) and resistance temperature detectors (abbreviated to RTD) are the traditional temperature sensors used for both laboratory and production scale investigations (**Figure 10**a and **Figure 10**b). The measurement principle of the thermocouple is based on thermoelectric effect describing the electrical voltage differences as a result of temperature differences whereas RTD is using the principle that the electrical resistance of metals is temperature-dependent. A standard RTD commonly uses a platinum element with a resistance 100Ω at 0 °C, known as Pt100 (Murgatroyd, 1997). In general practice, it is recommended that these sensors (i.e. thermocouple, RTD) are positioned inside and at the centre of the base of the vial, where one expects the last vestiges of the ice mass will be removed (Li & Nail, 2006). To achieve this requires a fastening device to avoid the misplacement of the probe (**Figure 10**a). The positioning of the sensor at the base of the vial is an appropriate strategy for witnessing the end-point of primary drying and for determining the vial heat transfer coefficient (K_v) but is less useful when trying to predict the closeness of the sublimation interface temperature (T_i) corresponding to the temperature at which the dry layer will collapse (T_c) from a process efficiencies perspective (using elevated shelf temperatures). For this application, it might be necessary to have two 'point' sensors positioned at two heights within the ice layer, and to predict ice base and ice interface temperatures assuming a linear temperature gradient across the ice layer.

Thermocouples are point measurement devices, owing to the small size of the bead (diameter ~0.25 mm for 30 AWG), whereas RTDs measure the average temperature of 'sensing region' as a consequence of the relatively large size of the sensing element. The latter creates the potential for the RTD to be exposed to both the ice layer and the dry layer, with the inevitable consequences of uncertainty in what is actually being measured. This is also true, but to a lesser extent with a new RTD with smaller sensing probe (diameter ~1.8 mm) which been developed

by Ellab Inc, Denmark (**Figure 10**d). And so it follows that the thermocouple is recommended over the RTD even though the RTD has some benefits over the thermocouple in terms of robustness, accuracy, precision and linearity (Nail et al., 2017).

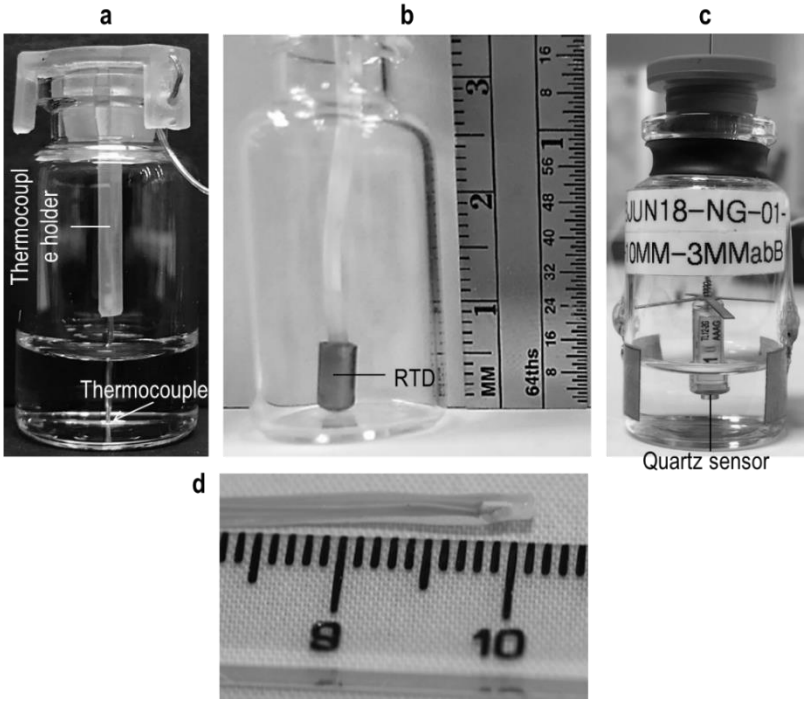

Figure 10 Temperature measurement sensor (a) vial containing a fine-gauge thermocouple wire along with a device (thermocouple holder from Millrock Technology, USA) for positioning the thermocouple tip at the centre of the vial and touching the bottom, (b) vial containing a Pt100 RTD sensor (Nail et al., 2017), (c) TEMPRIS wireless sensor contained in the vial having the electrode (19 x 10 mm) on the external surface of glass vial (defined as a TVIS vial), and (d) a small RTD developed by Ellab Inc., Denmark (Nail et al., 2017).

Recent guidelines recommend that the thermocouple wire should be of 36 AWG; however, slightly larger wires (i.e. 30 AWG) could be used for higher-fill volumes (Nail et al., 2017). These recommendations agree with Schneid et al. (2015). Issues with compatibility with regulatory requirement (i.e. GMP) and the loading systems of commercial dryers have been addressed successfully using wireless remote temperature sensors: (1) TrackSense Pro sensor (Ellab Inc, Denmark), and (2) Temperature Remote Interrogation System (TEMPRIS), introduced by IQ Mobil Solutions, Germany (**Figure 10**c). TrackSense Pro Sensor transmits the data recorded by thermocouple or RTD via the ISM band (Radio frequency band) to the data logger. In contrast,

the TEMPRIS sensor is quartz crystal, and the vibration of the quartz sensor can be converted to the product temperature. An external antenna of TEMPRIS system (transmitter) sends a signal with a specific radio frequency (2.4 GHz) to the quartz sensor, and the sensor that is in contact with the product is then vibrated at the frequency differing from an original signal depending on its temperature. From this, one can calculate the product temperature. Schneid and Gieseler (2008a) compare the temperature profiles of a lyo cycle from TEMPRIS with thermocouple and manometric temperature measurement (MTM); the measurement results of this system were in agreement with other technologies.

Whilst the thermocouple and RTD sensors (in particular those which have been adapted for wireless mode operation) might be applicable to all scales of freeze dryers, their main drawback is that the nucleation temperature of a vial containing an immersed temperature sensor can be as much as 5 °C higher than those vials without the sensor (Nail et al., 2017), with potential consequences for rates of ice crystal growth. In addition, the ice structure that develops from ice growth patterns, developing from nucleation sites on the probe, will be somewhat different from that which develops from nucleation sites on the base of the vial. Furthermore, given the direct relationships between ice crystal structures and the dry layer resistance, there will be an inevitable impact on rates of primary drying such that the sensor-containing vials cannot be considered to be representative of those vials in their local vicinity. To address this quite significant disadvantage, various non-invasive methods have been developed over the last 5-6 years. However, those techniques (such as thin-film thermocouple) are under development and are thus beyond the scope of this review.

Batch techniques

The first batch technique to be developed was the manometric temperature measurement (MTM, **Figure 11**), reported by Milton et al. (1997). This technique is also known as the pressure rise test (PRT) because its concept is based on an increasing pressure in the freeze dryer chamber by closing an isolation valve between chamber and condenser during a defined time period, typically less than 30 seconds (Nail et al., 2017; Tang, Nail & Pikal, 2006a; Gieseler et al., 2007),

as illustrated in **Figure 11**. MTM combines data from the increase in pressure within the freeze-drying chamber (that results from a transient closing of the isolation value between the drying chamber and the condenser) with a mathematical equation to predict the 'batch average' temperatures at both the ice front (T_i) and at the ice base (T_b) within the vial. However, MTM becomes less reliable in scenarios where (1) the primary drying has nearly finished, as a result of the inherently low ice vapour pressure in the chamber as the ice is depleted from the population of vials (Tang, Nail & Pikal, 2005); and/or (2) the formulation contains either a high solid content and/or a high amorphous component (Gieseler, Kramer & Pikal, 2007). This is especially true of high weight fraction protein formulations such as monoclonal antibodies (Schneid et al., 2015).

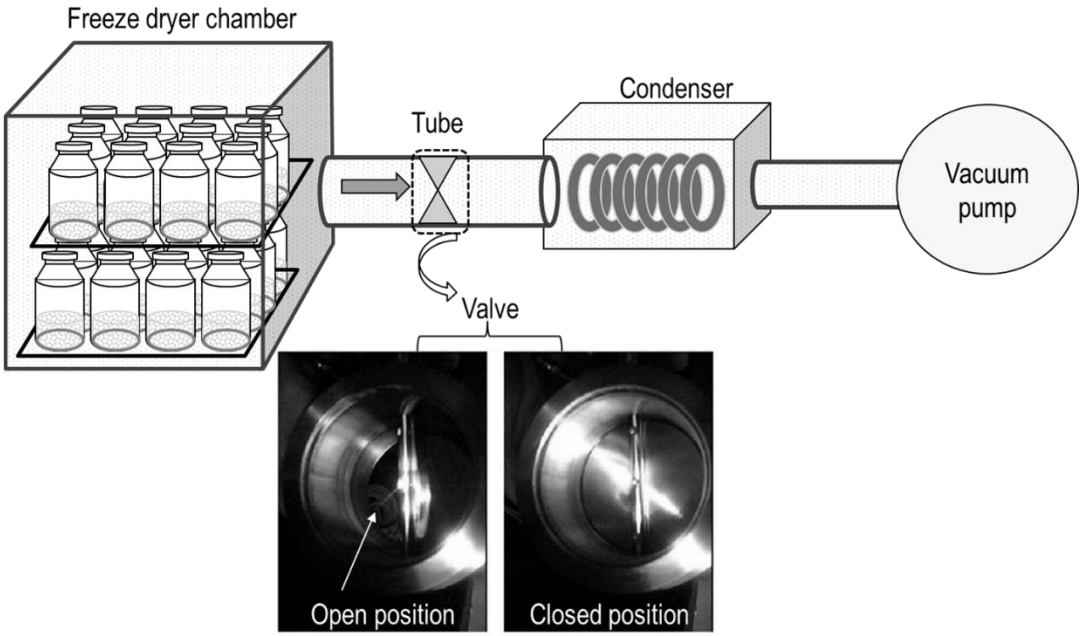

Figure 11 Manometric temperature measurement (MTM) valve isolates the freeze dryer chamber from the condenser. Open and closed positions of MTM valve are demonstrated.

Some years after the introduction of MTM, Gieseler and coworkers (2007) evaluated the potential of Tunable diode laser absorption spectroscopy (TDLAS) for monitoring the sublimation rate during product development and process scale-up. TDLAS uses the concept of laser light adsorption; the amount of light absorbed is proportional to the concentration of gas or water vapour (molecules/cm^3) in a laser assembly tube connecting between chamber and

condenser as shown in Figure 12 (Gieseler et al., 2007). The gas concentration measurement using TDLAS can be calculated from the signal intensity according to the Beer-Lambert equation (Patel & Pikal, 2009). Additionally, the Doppler effect due to the gas flow enables us to calculate the flow velocity of gas and then the sublimation rate (Gieseler et al., 2007). Although TDLAS has been proved to be a potential PAT tool for in-line monitoring of the freeze-drying process during product development and process scale-up, one should note that this system could not be incorporated into all freeze dryers, only those with a specific configuration (i.e. length of connecting duct) (Gieseler et al., 2007).

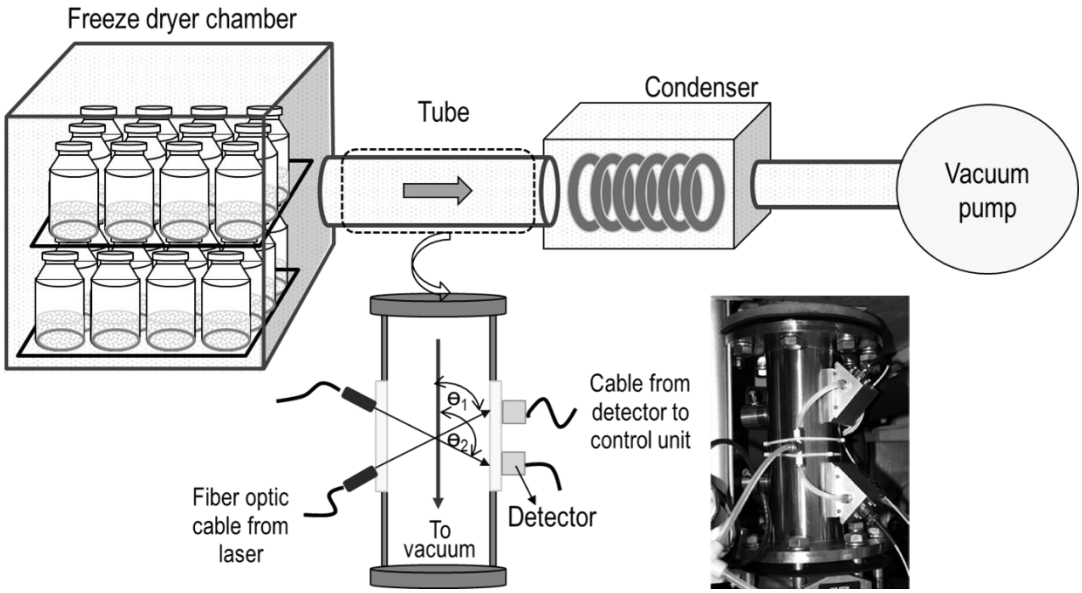

Figure 12 Schematic of Tunable diode laser absorption spectroscopy (TDLAS) installed in the connecting duct between freeze dryer chamber and condenser.

Both MTM and TDLAS provide information on temperatures at the base of the ice and at the sublimation interface, as well as on the drying rates, and so both techniques have been used successfully to characterise critical parameters of the system such as heat transfer coefficients and dry layer resistances (Gieseler, Kramer & Pikal, 2007; Kuu et al., 2011; Kuu, Nail & Sacha, 2009; Kuu, Hardwick & Akers, 2006; Milton et al., 1997; Tang, Nail & Pikal, 2006; Tang, Nail & Pikal, 2006b; Awotwe−Otoo, Agarabi & Khan, 2014). Both methods are also non-invasive and therefore won't alter the 'natural' characteristics and progression of the freeze-drying cycle. However, these techniques are limited in one sense, in that they only provide a collective

'average' measurement of the batch and so if there is any significant heterogeneity in temperature and drying rates across the dryer and between shelves these factors need to be accounted for in order to ensure that the process is modelled effectively. One way to account for this heterogeneity is to make certain assumptions concerning (1) the numbers of vial that can be considered as edge vials in proportion to the overall size of the batch, and (2) the impact of radiant heating, and to introduce factors which model the faster drying rates of these vials (Tchessalov, 2017). An alternative and indeed complementary approach would be to combine a non-invasive batch method such as MTM or TDLAS with a number of single measurements in the edge vial populations. An example of this approach is the "LyoMonitor" which multiplexes data from MTM and thermocouples in order to control the primary drying cycle (Barresi et al., 2009).

1.3.2. Chamber pressure measurement

There are three types of vacuum gauges that measure pressure below atmospheric pressure, and that are usually installed in a lyophilizer: (1) thermocouple vacuum gauge (Figure 13a); (2) Pirani gauge (Figure 13b); and (3) capacitance manometer (Figure 13c). Of these, the first two devices work on the basis of thermoelectric effect. For thermocouple vacuum gauges (Figure 13a), a thermocouple is jointed to a filament. This filament is heated up by a constant current. When gas molecules collide with the heated filament, heat is transferred to them (i.e. heat loss from the heated filament) causing a temperature change that could be translated into voltage and then converted into the pressure. Thermocouple pressure gauges are often installed in the less expensive laboratory freeze dryers (Nail et al., 2017; Murgatroyd, 1997).

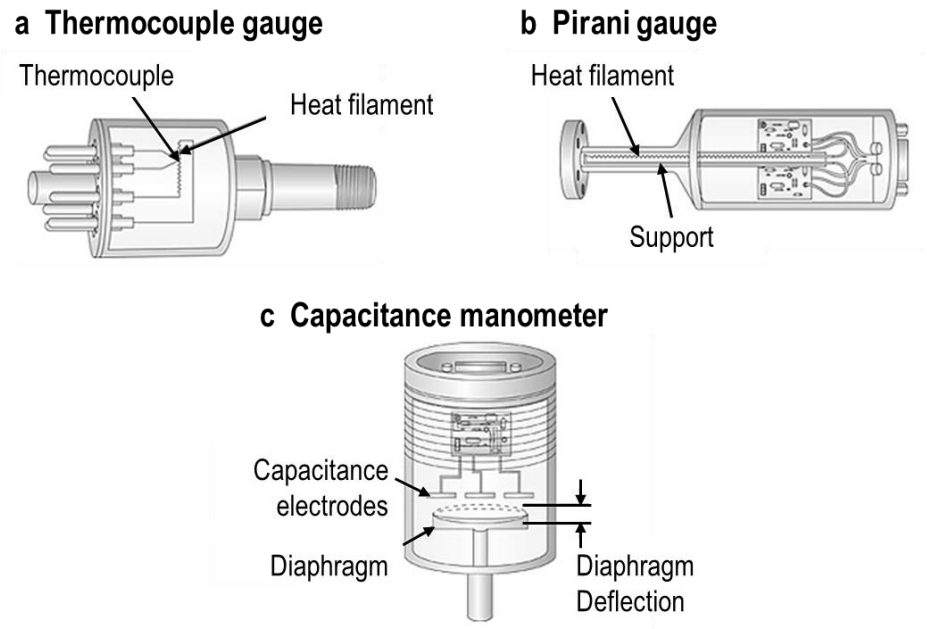

Figure 13 Schematic of pressure gauge: (a) thermocouple gauge, (b) Pirani gauge, and (3) capacitance manometer (Kurt J. Lesker Company, 1996).

Unlike thermocouple gauges in which temperature of the heating filament is measured by thermocoupling wire, Pirani gauges measure the temperature sensed by the change in resistance of the heated wire (i.e. resistance is proportional to temperature). This device consists of two filaments and is used as the two arms of a Wheatstone bridge. One is maintained at a constant gas pressure system (defined as the reference filament), while the other is exposed to the surrounding environment (known as the measurement filament). The temperature change of the measurement filament is detected and compensated by the circuit in order to maintain the filament temperature at a constant value.

Since thermal conductivity-type gauges (i.e. Thermocouple gauge and Pirani gauge) operate using hot wire, one should bear in mind that an explosion might happen when lyophilizing product containing an organic solvent (e.g. tert-butanol). However, this could be prevented by turning off these devices or flushing with nitrogen gas before running the freeze-drying cycle (Nail et al., 2017). Another concern is the GMP aspect because the sterilization method currently used for lyophilizer is steam sterilization (121 °C at 1.5 bar), although hydrogen peroxide sterilization has been introduced recently (García, 2019, US Food and Drug Administration,

2014). Therefore, it is necessary to ensure that pressure gauges perform well. Nail and his co-authors (2017) compared two types of heating filament (platinum/iridium and gold-plated tungsten), and concluded that moist heat sterilization has an impact on the lifetime of filaments, and therefore the shortcoming of the measurement should be taken into account when selecting the filament types.

Next, capacitance manometer (i.e. MKS Baratron®) is an electro-mechanical gauge having a metal diaphragm, typically using Inconel alloy (Nail et al., 2017), for isolating a measurement side (which is exposed to the surrounding gas system), and a vacuum side (sometimes referred to as the reference side). A differential between the sides causes diaphragm deflection, which is then converted to an electrical signal (capacitance) and thereby pressure. Since an output of the capacitance manometer is based on physical change rather than the gas properties, this instrument is virtually independent of the composition of the gas being measured (Patel & Pikal, 2009). If a capacitance manometer operates at high temperatures such as those encountered during steam sterilization, Heated capacitance manometers are an option to prevent condensation within the gauge and thus maintain the accuracy of the device (Osborn & Hansen, 2002).

When comparing all three pressure gauges, the capacitance manometer is the best in terms of accuracy (Osborn & Hansen, 2002; Nail et al., 2017) because the Pirani gauge gives the measurement value 60% higher than Capacitance manometers as a result of the thermal conductivity of water vapour being almost twice as high as nitrogen gas (as shown in **Figure 14**) (Patel, Doen & Pikal, 2010). The guideline suggests using capacitance manometers together with Pirani gauges to monitor the overall chamber pressure and the leak at the condenser (Nail et al., 2017). With the comparative pressure measurement, the end-point of primary drying could be determined by using the point where the pressure measured by the Pirani gauge reaches equilibrium with the capacitance manometer (marked by a black arrow in **Figure 14**). Also, the pressure spike in the Pirani gauge method could be seen at the beginning of secondary drying (marked by a grey arrow in **Figure 14**). This is because the unfreezable solvent is released when

the temperature rises (i.e. a desorption process), and therefore the process end-point could be estimated by the point where the Pirani gauge approaches the capacitance manometer measurement.

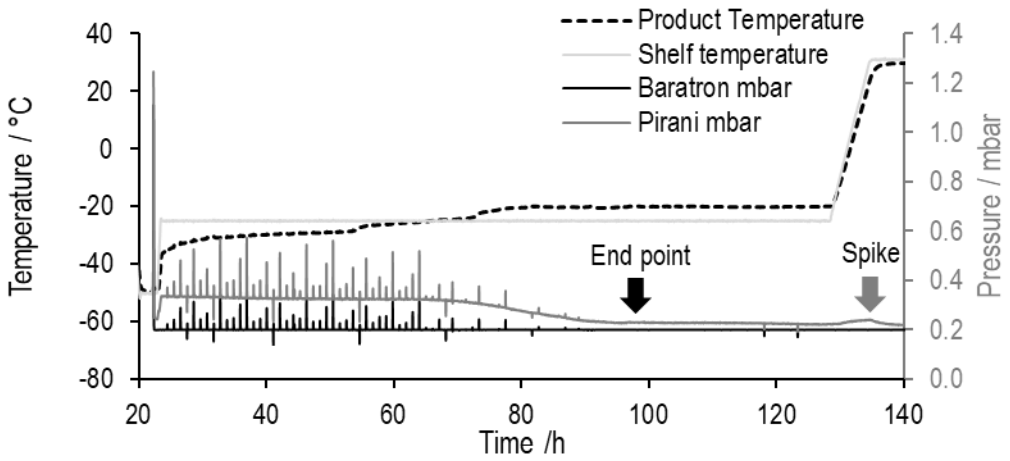

Figure 14 Demonstrating a process monitoring technique "the comparative pressure measurement" for immunoglobulin formulation: capacitance manometer (a solid black line), Pirani gauge (a solid dark grey line). The shelf temperature and product temperature are represented by a dashed black line and a solid light grey line, respectively. The end point of primary drying is marked by the black arrow while the grey arrow indicates a spike due to a desorption process at the early stages of secondary drying.

2. Gap in the knowledge

Although primary drying has been acknowledged as the most challenging step underpinning the efficiency of the freeze-drying process, there are various stages involved in this process. Most available process analytical technologies (PAT) are focused primarily on measuring product temperature and/or sublimation rate during the primary drying step. Some of these offer batch measurement, e.g. manometric temperature measurement (MTM), which provides the average data of the entire batch, but they do not account for the critical area of the dryer, such as edge vials. This issue could be overcome by coupling with a single technique (e.g. thermocouple). However, this measurement system is an invasive technique, which could create a source of uncertainty in the measurement, and consequently the measuring results of the product contained in the vial containing the sensor may not accurately represent the product behaviour in the vial without one. Also, these PATs are not all-in-one techniques that enable monitoring of the several stages of freeze-drying. With the exception of the process aspect, the critical formulation parameters (such as glass transition temperature) are considered equally important. In practice, these formulation variables could be analysed by standard off-line techniques such as differential scanning calorimetry (DSC) or freeze-drying microscopy (FDM) before the lyo cycle is designed. However, existing non-invasive PATs have a limitation in terms of their characterization of in-vial critical formulation parameters. These formulation variables (measured by pre-lyophilized techniques) may not correspond to the actual characteristics of the product contained in the vial due to the difference in various factors such as sample size and heating rate.

Over the past 5 years, a new technique called Through-vial impedance spectroscopy (TVIS) has been implemented as a single-vial, minimally-invasive process analytical tool. This technique measures the dielectric characteristics of the material within the vial at discrete frequencies over the range of 10 Hz to 1 MHz. Two parameters of relaxation characteristics, peak amplitude (C''_{PEAK}) and peak frequency (F_{PEAK}), offer general approaches with which to assess a range of critical process parameters. F_{PEAK} is strongly sensitive to temperature, hence this is used for

determination of the product temperature (including during the crystallization process) whereas C''_{PEAK} can be used to determine the amount of ice remaining during the primary stage, thereby estimating the sublimation rate. Previous work has demonstrated the potential use of TVIS for characterizing a wide range of the processes taking place during lyophilization, such as phase transition behaviour. It can also determine the critical parameters during primary drying, including the end-point (Arshad, 2014). In this work, various features of TVIS responses are explored to investigate the different facets of the freeze-drying cycle and also to establish effective methods for implementing the TVIS data so as to achieve the accurate value of the critical parameters known as K_v and R_p, typically used for generating design space.

3. Aim and objectives

3.1. Aim

The aim of this PhD was to explore and develop application uses of an impedance-based technique known as through-vial impedance spectroscopy (TVIS) for the determination of process variables within the final product container and within the freeze dryer, and to demonstrate how these parameters can be used for process development.

3.2. Objectives

The principal objectives of this research were as follows:

Objective 1: To provide a brief description of the electrical properties of material and an overview of through-vial impedance spectroscopy technology along with its applications and limitations

Objective 2: To research those factors associated with the design of the electrode system that impact the characteristics and the quality of the impedance spectrum generated by through-vial impedance spectrometer. Factors investigated were: (1) electrode design; (2) the electrode height; (3) the method for attaching the electrode to the glass; and (4) the position of electrode from the base of the vial

Objective 3: To investigate the use of through-vial impedance spectroscopy for characterizing the phase behaviour of sugar-salt solutions during the freezing stage. TVIS parameters such as peak amplitude (C''_{PEAK}), peak frequency (F_{PEAK}) and real-part capacitance (C') at fixed frequency were used to characterise the ice formation process in terms of ice nucleation and the solidification.

Objective 4: To explore the use of through-vial impedance spectroscopy for characterizing the behaviour of frozen samples during a thermal treatment processes. The dielectric loss parameters during re-heating and the holding stage from three freeze-thaw cycles were used to

demonstrate a structural modification of frozen matrices (sugar-based preparations). Also, the real-part capacitance at fixed frequency was proposed for measuring the glass transition temperature of the frozen state.

Objective 5: To evaluate the applicability of through-vial impedance system to providing an insight into the structure-sublimation rate relationship of a freeze-dried lactose solution during primary drying. By using the characteristic of the dielectric loss peak, a TVIS approach was developed for (1) predicting ice temperature at the sublimation interface, and (2) estimating the rate of primary drying from which the dried product resistance (R_p) can be obtained.

Objective 6: To establish a new approach to through-vial impedance spectroscopy for monitoring the primary drying process. A measurement vial with an innovative electrode design was used to assess various critical process parameters (product temperature and drying rate) and then to demonstrate how the vial heat transfer coefficient (K_v) can be calculated.

The objectives concerning the application of through vial impedance technology in the characterization of key steps of freeze-drying process are summarized in Figure 15 (objective 2-objective 5).

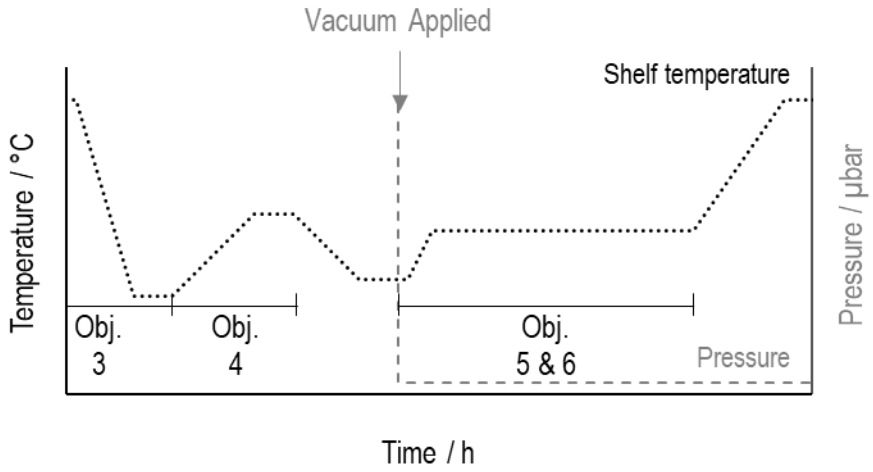

Figure 15 Outline of the objectives demonstrated in the freeze-drying cycle.

4. Rationale for the selection of excipients

In this study, the excipients commonly used in lyophilized formulation were selected. Disaccharide sugar including sucrose and lactose have the same empirical formula ($C_{12}H_{22}O_{11}$) and are usually used as lyoprotectants and/or bulking agents (Wang, 2000). Various publications have demonstrated the effectiveness of disaccharide as a universal stabilizing agent for protein formulations (Carpenter et al., 1997; Arakawa et al., 2001). When comparing sucrose and lactose, sucrose is preferable, although both can prevent protein from stress during the lyophilization process (i.e. freezing and drying) and lactose can provide a higher glass transition temperature for solid state (T_g); this can enhance the storage stability, i.e. ~65 °C for sucrose (Crowe, Reid & Crowe, 1996) and ~100 °C for lactose (Wang, 2000). This is because lactose is a reducing sugar that can then turn to a brown colour via the Maillard reaction (Rossi et al., 1997; Andya et al., 1999; LI et al., 1996). Despite the fact that sodium chloride (NaCl) is commonly used for adjusting the tonicity of parenteral formulations, it is not recommended for lyophilized products because salt can depress the glass transition temperature of the freeze-concentrate (T_g') (Nail & Gatlin, 2016), and consequently the process has to be operated at very low temperatures presenting difficulties in processing. Thus, sucrose was the first choice for the study of freezing and annealing; however, for in the investigation of solidification behaviour, NaCl was added because this excipient can influence the crystallization process of the sugar solution (Mazzobre et al., 2001). Another rationale for the use of sucrose as a model formulation for annealing experiments is that sucrose is an amorphous material (as well as maltodextrin, which was used in the previous study) (Smith et al., 2013). Sucrose, however, exhibits different dielectric behaviour when compared to maltodextrin. Sucrose shows two distinct processes at temperatures above −20 °C whereas only a single process was observed in maltodextrin (Smith et al., 2013). This second process also could not be detected by broadband dielectric spectroscopy (BDS system). For the primary drying experiment, lactose was selected as a bulking agent instead of sucrose; while both excipients have similar critical temperatures at ~−32 °C (Costantino, Pikal, 2004), the drying behaviour is different (Gieseler, Kramer & Pikal, 2007) and

lactose has been evidenced in micro-collapse by Milton et al. (1997). Hence, we selected this excipient for investigation of a microcollapse event. A list of excipients used in this work is summarized in **Table 2**.

Table 2 Summary of the excipients used in the present study

Material	Study	Chapter
Sucrose	Freezing, Annealing	7 and 8
NaCl	Freezing	7
Lactose monohydrate	Collapse	9

5. An overview of Through-vial impedance spectroscopy

5.1. Objective

The objective of this chapter is to provide a fundamental understanding of the electrical properties of material and an overview of through-vial impedance spectroscopy (TVIS) technology. This chapter also describes the TVIS measurement principle, dielectric mechanisms, application of TVIS for monitoring freeze-drying process and the limitation of the technology.

5.2. Introduction to the electrical properties of material

The electrical impedance (Z) of an object describes the total restriction of the object to the charge flow when a voltage (electrical potential difference) is applied to it via electrode in contact with the measured object. In other words, the impedance reflects the way in which the electric current (flow of charge) passes through the object. A high impedance object means that it is difficult for the current to flow (termed “impede”), whereas a low impedance object implies that the object allows the current to flow freely (termed “admit”). Mathematically these properties are related to one another by an inverse relationship according Equation 16, so in effect, they are formally equivalent:

$$Z = \frac{1}{Y} \qquad \text{Equation 16}$$

where Z is an impedance with a unit of Ohm (Ω) and Y is a reciprocal of the impedance defined as admittance whose unit is Siemen (S).

In general, preparations for freeze-drying mainly use water as the vehicle; therefore, two electrical properties relevant to aqueous solutions - electrical conductivity and dielectric polarization - are mentioned.

5.2.1. Electrical conductivity

Electrical conductivity describes the ability of an object to allow charge to flow through it or to transfer electric charge. In aqueous electrolyte solution, for example, the movement of charged species (e.g. ions) in the water is responsible for the conductivity of the solution. The more ions contained in the water the more charges are carried, and the higher the conductivity. In electrical circuit terms, this behaviour can be expressed by conductance (G). The inverse of conductance is defined as resistance (R) according to Equation 17. The unit for conductance and resistance are ohm and siemen, respectively.

$$G = \frac{1}{R} \qquad \text{Equation 17}$$

Both parameters not only depend on the inherent properties of the object but also its physical parameters, such as cross-sectional surface area and length. If the geometry is taken into account then the intrinsic properties of material, conductivity (σ) and resistivity (ρ), could be derived from the given equation:

$$G = \frac{\sigma A}{L} \qquad \text{Equation 18}$$

$$R = \frac{\rho L}{A} \qquad \text{Equation 19}$$

where L is the length of material, A is the cross-sectional area of material, and the quantity of L/A or A/L is called cell constant.

Metals are generally very conductive (i.e. low resistivity), whereas plastics and glasses tend to have very low conductivity (i.e. high resistivity). Both conductivity and resistivity are temperature-dependent.

5.2.2. Dielectric polarization

Some materials are poor electrical conductors; however, these materials can rotate, align or orient under the application of an electric field. These materials are called “dielectric” and the

behaviour of such materials when an external electric field is applied to it is “dielectric polarization”. Pure water is a good example. Pure water is a polar molecule and cannot conduct electricity by itself (only the ions dissolved in water can conduct the electricity); however, water molecules can be polarized or can orientate themselves in the electric field. There are four types of dielectric polarization: (1) electronic polarization; (2) ionic or atomic polarization; (3) orientational polarization; and (4) interfacial polarization (Mitchell, 2004; Raju, 2017). In brief, electronic polarization is found in monoatomic gas such as helium. This molecule, in general, has a nucleus at the centre and electrons distributed around the nucleus like a sphere. The presence of the electric field causes the displacement of the electron cloud as shown in **Figure 16**a. Ionic (atomic) polarization is usually found in ionic crystals (e.g. NaCl). It occurs due to the displacement of cations and anions as shown in **Figure 16**b. Next, orientational polarization arises from the dipole molecule, known as dipole polarization. This dipole polarization is seen in material such as water. A net dipole moment of unpolarized water molecules is zero. When applying the electric field, the molecules begin to rotate and align with the electric field and yield the net dipole moment (**Figure 16**c). Finally, interfacial polarization or space charge polarization refers to the accumulation of charges at the boundaries between two dielectric materials or electrode and a dielectric material, when the electric field is applied (**Figure 16**d). Unlike other types of dielectric polarization, this interfacial polarization causes charge migration through bulk material. For instance, in the case of tap water contained in a glass vial, this phenomenon can be observed at the interface between the glass wall and the water when applying the external field.

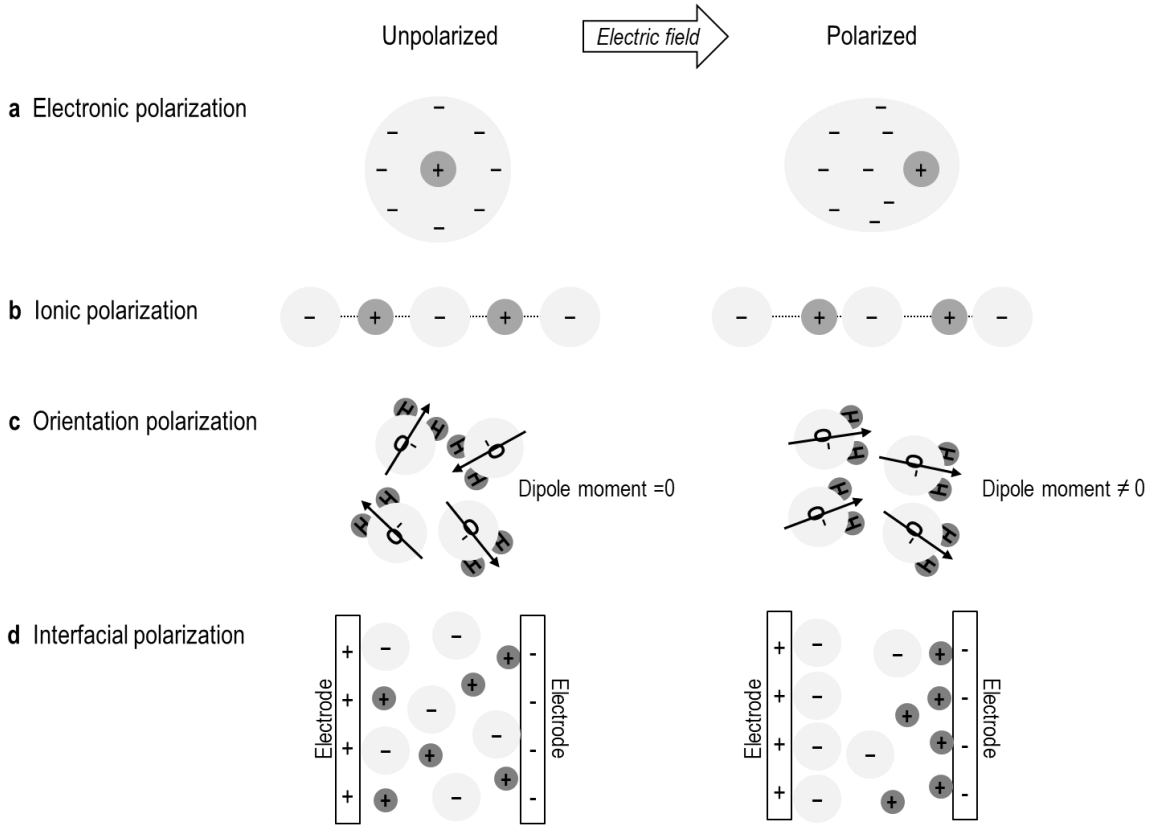

Figure 16 Dielectric polarization mechanism: (a) electronic polarization; (b) ionic or atomic polarization; (c) orientational polarization; and (d) interfacial polarization

A simple example of dielectric polarization can be shown using a capacitor, a dielectric material placed between two conducting electrode plates (**Figure 17**a). When the capacitor is connected to direct current (DC) power supply, the dielectric material will be polarized and will yield the accumulation of charges on the surface of the electrode; this process is called “charge”, **Figure 17**b. Dielectric polarization is reflected in the electrical capacitance (C), which is defined as the ability to store energy in the form of an electrical charge. Alternatively stated, this is the quantity of the accumulated charges (Q) over the applied voltage (V), $C = Q/V$. The unit of capacitance is in Farad (F). The accumulated charge will discharge once the external electric field is removed. It follows that the polarized molecules return to their previously randomized stated (**Figure 17**c).

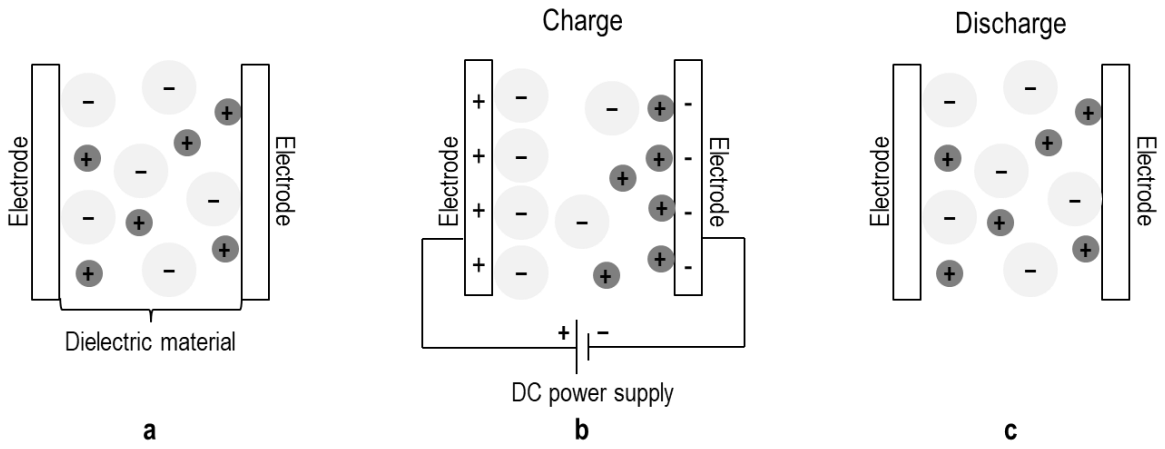

Figure 17 Illustration of charge and discharge process of capacitor: (a) neutral capacitor (uncharged); (b) capacitor charges; and (c) capacitor discharges

5.2.3. Dielectric constant or relative permittivity

When the electrical capacitance of a capacitor containing the dielectric material (C) is compared to that of its counterpart without dielectric material (C_o) (in other words the volume between electrodes is occupied by a vacuum), the dielectric constant (ε_r) is provided as given below (DoITPoMS University of Cambridge, 2004a):

$$\varepsilon_r = \frac{C}{C_o} \qquad \text{Equation 20}$$

The dielectric constant measures the extent of polarization of material under the external field; therefore, the higher the dielectric constant, the greater the polarization. Permittivity is an alternative description of dielectric property of a material. This parameter is used for describing the ability of a material to respond to the electric field, and the ratio between the permittivity of the dielectric (ε) and the permittivity of free space or vacuum (ε_o) is the dielectric constant or relative permittivity (ε_r). The permittivity of free space or vacuum is 8.854 x 10^{-12} F·m^{-1}. Another expression of the dielectric constant is as follows (DoITPoMS University of Cambridge, 2004):

$$\varepsilon_r = \frac{\varepsilon}{\varepsilon_o} \qquad \text{Equation 21}$$

As opposed to DC (as mentioned above), the measurement of dielectric constant under alternating current (AC) is more complicated because the dielectric constant varies with frequency. The responses of dielectric material as a function of frequency are highlighted in **Figure 18**. Therefore, the relative permittivity requires the expression in terms of the complex number, according to Equation 22 (Komarov, Wang & Tang, 2005)

$$\boldsymbol{\varepsilon} = \varepsilon_r' - i\varepsilon_r'' \qquad \text{Equation 22}$$

where $\boldsymbol{\varepsilon}$ is the complex relative permittivity, ε_r' is real part relative permittivity (referred to as dielectric constant), ε_r'' is an imaginary part relative permittivity (referred to as dielectric loss), and i is an imaginary number equal to $\sqrt{-1}$. The dielectric constant represents energy storage capability when the material is exposed to the electric field, whereas dielectric loss represents the energy dissipation through the movement or polarizing of charge that results in dielectric heating (DoITPoMS University of Cambridge, 2004b; Nelson & Trabelsi, 2012).

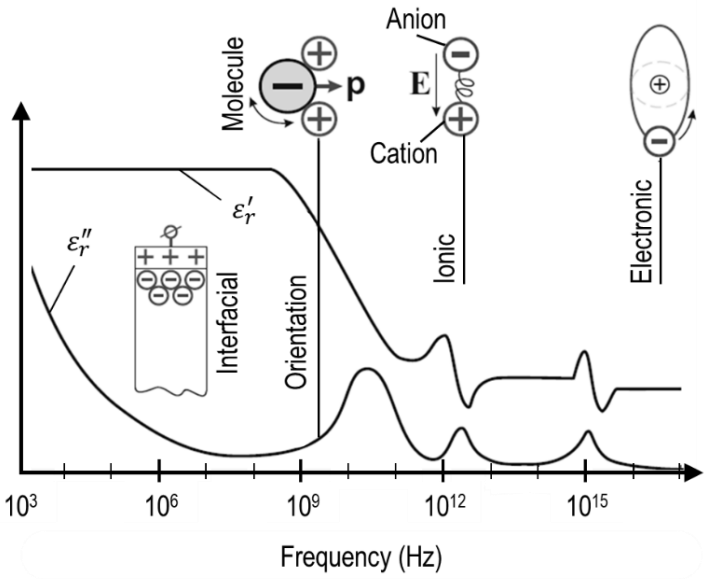

Figure 18 Real (ε_r') and imaginary (ε_r'') parts of the complex relative permittivity ($\boldsymbol{\varepsilon}$) of material corresponding to frequency. Interfacial polarization is prominent at frequencies below MHz range, Orientation polarization occurs at frequencies around 10^9-10^{10} Hz; ionic polarization influences the permittivity at a frequency range of 10^{12}-10^{13} Hz, and electronic polarization is observed at frequencies around 10^{14}-10^{16} Hz (Nickelson, 2019)

5.2.4. The use of electrical measurement in freeze-drying

The application of electrical properties to the investigation of various processes associated with freeze-drying has been used for many years. Since the conductivity of a material suddenly increases when the temperature of that material is above the melting temperature, there are a number of studies determining eutectic temperature through the measurement of changes in the electrical resistance as a function of temperature (Greaves, 1954; Rey, 1960; Rey, 1960; DeLuca & Lachman, 1965; DeLuca, 1977). The resistance thermometry probe was suggested for observing the product temperature during a freeze-drying cycle by Adams (1991). Based on the electrical measurement technique, Martin Christ GmbH (Germany) has launched a process-monitoring tool that measures the electrical resistance of the sample at a fixed frequency of 1 kHz, the LyoRx system. This system can detect the crystallization process and also monitor the product temperature, by which it allows automatic controlling of the energy supply during the main drying step to minimize the risk of batch failure (i.e. product collapse).

However, the use of electrical measurement was restricted to the determination of the crystallization event, and was not used for the glass transition temperature. Some years later, Her et al. (1994) measured the glass transition temperature of freeze-concentrated solution using electrical thermal analysis (ETA), demonstrating the use of electrical thermal analysis (ETA) that combined a temperature sensor with a resistance sensor. A number of reports have since used electrical analysis, particularly dielectric measurement, for studying the mobility and transition temperature of the sample (Morris et al., 1994; Evans et al., 1995; Bhugra et al., 2006; Rey, 2010; Suherman, Taylor & Smith, 2002; Smith et al., 2013). Evan et al. (1995) concluded that the glass transition temperature of mannitol and the eutectic temperature of the salt solution obtained from dielectric analysis (DEA) agree with the thermal analysis technique (i.e. DSC) and literature. Given that dielectric analysis measures the molecular dynamic effect whereas thermal analysis measures the heat effect, the dielectric analysis is a useful complementary technique to thermal analysis for characterization of the material properties. An instrument that has integrated both techniques has been commercially available as the off-

line technique for pre-lyophilization analysis known as Lyotherm (Biopharma Process Systems Ltd., UK). This system comprises dielectric analysis at a single frequency (1 kHz) as a function of impedance ($|Z| \sin \varphi$) to track the change in molecular motion, together with differential thermal analysis (DTA) to provide transition temperature (Ward & Matejtschuk, 2019). This provides helpful information (such as the critical temperature) for developing the freeze-drying process. As mentioned previously, this method applies a fixed frequency while the response of the material is different according to the measured frequency; thus, a range of frequency (broadband) for impedance analysis has been proposed. Alkeev et al. (2015) connected a capacitive sensor with a self-oscillating circuit for monitoring the lyophilization process of biological products whilst Smith's group developed the system that is more suitable for vial freeze-drying by placing the electrodes in contact with the vial container externally, termed a remote electrode system. Suherman et al. (2002) used this system to investigate the influence of water content on molecular relaxation of the lyophilized ovalbumin contained in a glass vial. Contrary to near-infrared spectroscopy (NIR) and Raman spectroscopy, the uses of electric measurement for monitoring residual moisture content of freeze-dried cake is not well-established. Over the years, the remote electrode system developed by Smith and his coworkers has been improved, becoming a non-invasive impedance-based technique for monitoring lyophilization process known as through-vial impedance spectroscopy (TVIS). The potential application of TVIS to monitoring various stages of freeze-drying was described by Smith et al. (2017).

5.3. Through-vial impedance spectroscopy

5.3.1. Impedance spectroscopy measurement

Impedance spectroscopy (IS) is a modern analytical instrument for characterization of the electrical properties of the material (including their interfaces) at a range of discrete frequencies (i.e. frequency domain). The general approach is to observe the response signal (i.e. resultant current or voltage) when applying the stimulating signal (i.e. input current or voltage) to the electrodes with materials in between them (Barsoukov & Macdonald, 2005). The response of

the material to the oscillating electric field occurs at the timescales (so-called relaxation time) of an inverse frequency (f), $f = 1/2\pi\tau$ (University of Washington, 2018). For example, the relaxation time at a relaxation frequency of 100 Hz is 0.0016 seconds. This characteristic is particular to the polarization mechanism; therefore, it could be used to recognize the relaxation processes of the test object, e.g. electrode-material system (Hongbo, 2018). For instance, interfacial polarization usually takes place at sub-MHz frequency as shown in **Figure 18**. Due to the continuous growth of broadband impedance technology, an impedance analyzer with a wide range of frequency options (over 10 decades) is now available for a comprehensive study of the kinetic mechanisms, including both fast and slow processes (Smith et al., 1995).

To provide a better understanding of impedance measurement, the basic concept of impedance is introduced here in brief. Impedance (Z) describes the restriction of an electrical system to the flow of charges and has a unit of Ohm, the same as resistance. This electric component would become a resistance (R) if current (I) and voltage (V) are in-phase with each other (no phase shift between them); in other words, when constant voltage is applied (i.e. direct current, DC). Under this condition, impedance follows the Ohm's Law:

$$Z \text{ or } R = \frac{V}{I} \qquad \text{Equation 23}$$

However, with an alternating current (AC) the oscillating nature of the applied voltage (i.e. a sinusoidal waveform as shown in **Figure 19**) the voltage at any time t, $V(t)$, is given by:

$$V(t) = V_o \sin(\omega t) \qquad \text{Equation 24}$$

where V_o is a magnitude of voltage and ω is an angular frequency. The conversion to angular frequency is:

$$\omega = 2\pi f \qquad \text{Equation 25}$$

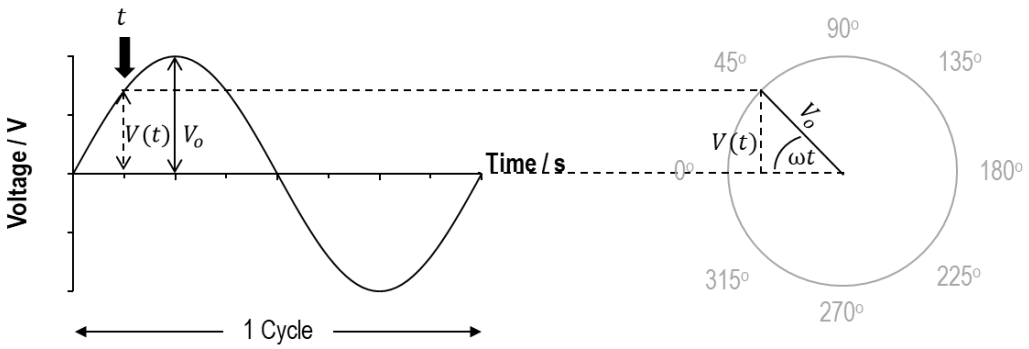

Figure 19 A sinusoidal waveform of voltage in an AC circuit.

When a sinusoidal voltage is applied to the material possessing both resistance and capacitance properties (the so-called RC circuit) the resultant current can have a phase shift (φ) in respect of the voltage. The output current at any time t, $I(t)$, can be expressed as:

$$I(t) = I_o \sin(\omega t + \varphi) \qquad \text{Equation 26}$$

Hence the analogous expression of impedance to Ohm's law is given by substituting voltage (Equation 24) and current (Equation 26) to give:

$$\boldsymbol{Z} = \frac{V(t)}{I(t)} = \frac{V_o \sin(\omega t)}{I_o \sin(\omega t + \varphi)} \qquad \text{Equation 27}$$

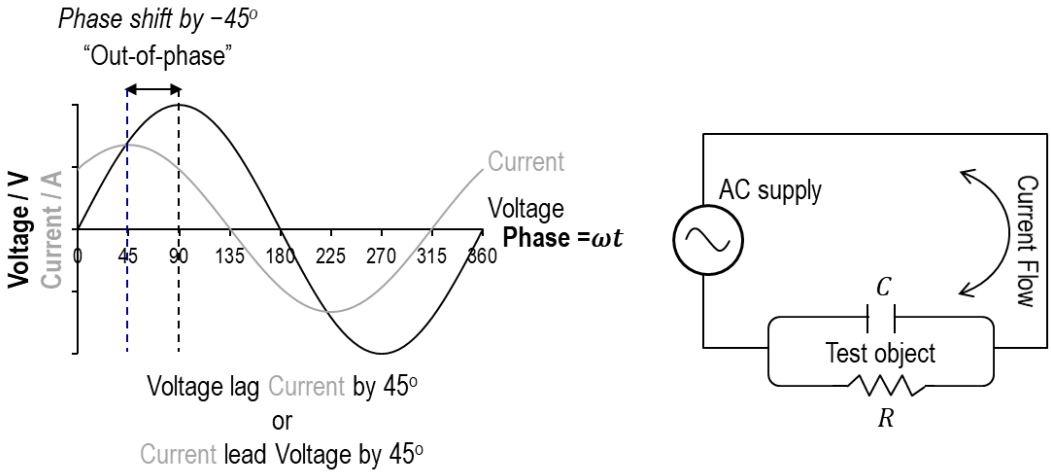

Figure 20 Illustrating a phase difference (φ) when an AC source connects to the test object which consists of resistance (R) and capacitance (C) element (RC circuit). In this RC circuit, the resultant current leads the voltage by 45°, or phase difference is −45°. Note, a negative phase shift means that the voltage lags behind the current.

5.3.2. Equivalent electrical circuit

Impedance spectra reflect the physical processes of the object being tested (e.g. electrolyte resistance, dielectric relaxation, double layer capacitance, etc.). One common method used for interpretation of the measurement data relies on equivalent circuit models. These models are built from passive elements such as resistors, capacitors, and inductors, and the distributed elements such as the Cole-Cole dispersion (Co), and the constant phase element (CPE). In effect, each is describing how the impedance of each element varies with the frequency of the applied field. For example, a test object that behaves like a pure capacitor has an impedance that decreases in proportion to the inverse of the frequency of the applied field. The impedance of some circuit elements used in the models is shown in **Table 3**.

Table 3 Impedance of some circuit elements used in the models (Wallaur, 2013)

Circuit elements	Symbol	Impedance	Parameter
Resistance	R	$Z_R = R$	R: Resistance of the resistor
Capacitance	C	$Z_C = \frac{1}{i\omega C}$	C: Capacitance of capacitor
Inductance	L	$Z_L = i\omega L$	L: Inductance of inductor
Constant phase element	CPE	$Z_{CPE} = \frac{1}{Q(i\omega)^{\alpha}}$	Q: Admittance value α: Exponent factor
Cole-Cole element	Co	$Z_{Co} = \frac{C}{(1+(i\omega\tau)^{\alpha})^{1}}$	C: Capacitance of capacitor τ: Time constant of process α: Exponent factor
Warburg element	W	$Z_w = \frac{A_w}{\omega^{0.5}} - i\frac{A_w}{\omega^{0.5}}$	A_w: Warburg coefficient

The equivalent circuit models usually consist of a number of these elements combined in series or parallel. In the case of an individual circuit element connected in series (**Figure 21**a), the total impedance of the circuit model can be calculated by:

$$Z_{Total} = Z_1 + Z_2 \qquad \text{Equation 28}$$

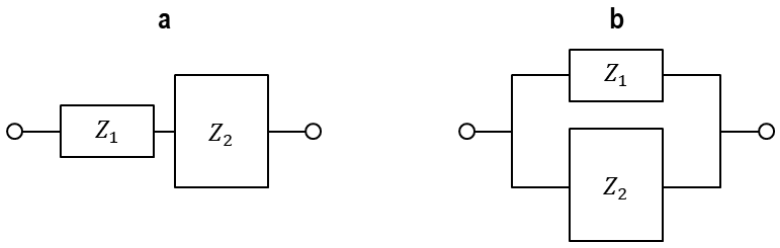

Figure 21 (a) series and (b) parallel combination of the circuit elements

By contrast, if two circuit elements are combined in parallel (**Figure 21**b), then the overall impedance of the composite circuit model can be calculated by:

$$\frac{1}{Z_{Total}} = \frac{1}{Z_1} + \frac{1}{Z_2} \qquad \text{Equation 29}$$

From Equation 28, it is implied that the impedance of a circuit element in series is influenced by the higher impedance element (Z_2 in **Figure 21**a) whereas the element with the lower impedance (Z_1 in **Figure 21**b) dominates the total impedance in the parallel circuit according to Equation 29.

In real systems, the material being measured is a composite of various characteristics, for example, one that has both an electrical resistance and capacitance; here, the impedance spectrum that results will be dominated by one or other element, depending on the frequency of the electric field. In order to understand this, and to see the relevance to the TVIS approach, it is helpful to start with a single element, namely resistance, and capacitance and then a few simple example circuits comprising those elements (i.e. resistance and capacitance) but in two different arrangements. The first arrangement has the two elements linked like two elements of a chain (i.e. in series) and the second arrangement is when they are linked side by side (i.e. in parallel).

Firstly, considering the single component, the impedance of a resistance is independent of frequency (top graph of **Figure 22**a) because there is no phase shift (φ is constant at zero, as shown in the bottom graph of **Figure 22**a). In contrast, it can be seen in the top graph of **Figure**

22b that the impedance spectrum of a capacitance is strongly frequency-dependent, $Z_C = 1/i\omega C$ (**Table 3**), and also exhibits a negative slope on the plot of $Log\ |Z|$ and $Log\ f$.

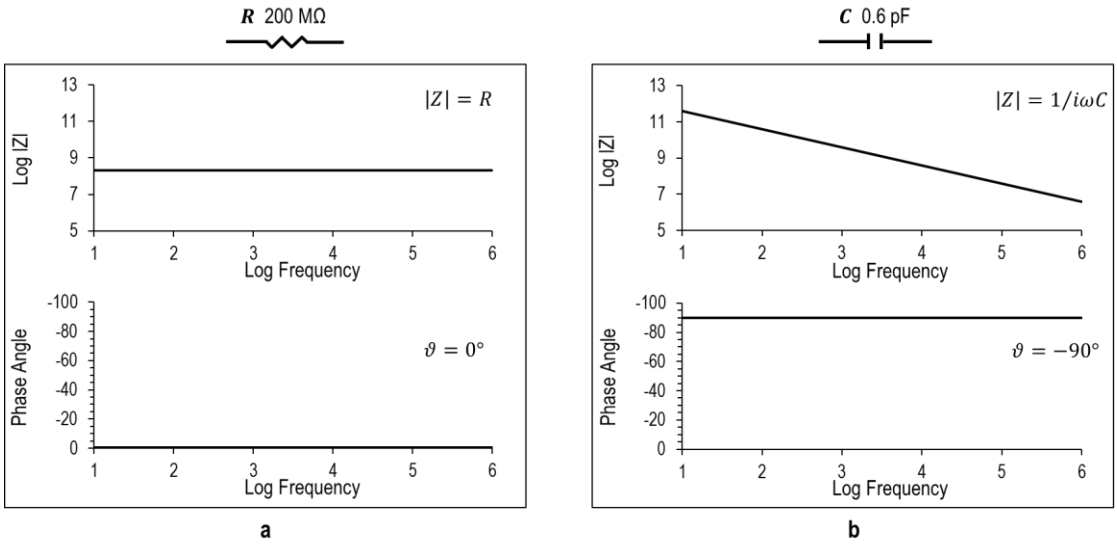

Figure 22 Impedance response of the single elements: (a) resistance and (b) capacitance. The values for the resistance (R) and the capacitance (C) are 200 MΩ and 0.60 pF, respectively.

Given that the impedance of an object is defined by the amount of current that flows for any applied voltage, the element that effectively controls the amount of current that passes through the composite object will define its impedance. And so, the element that dominates in a series circuit is the one with the highest impedance as that provides the greatest restriction to the flow of current, whereas the element which controls in a parallel circuit is the one with the lowest impedance as that element provides the lowest impediment to the passing of current.

It follows that, in a series circuit at low frequency, the capacitance dominates the impedance spectrum (top graph of **Figure 23**a) because the impedance of the capacitance is so high compared to the resistance (**Figure 22**), so that current that flows through the circuit is manipulated by capacitance; whereas at high frequency the impedance of capacitance is lower than the resistance (**Figure 22**) so that the impedance spectrum is dominated by the resistance as shown in the top graph of **Figure 23**a.

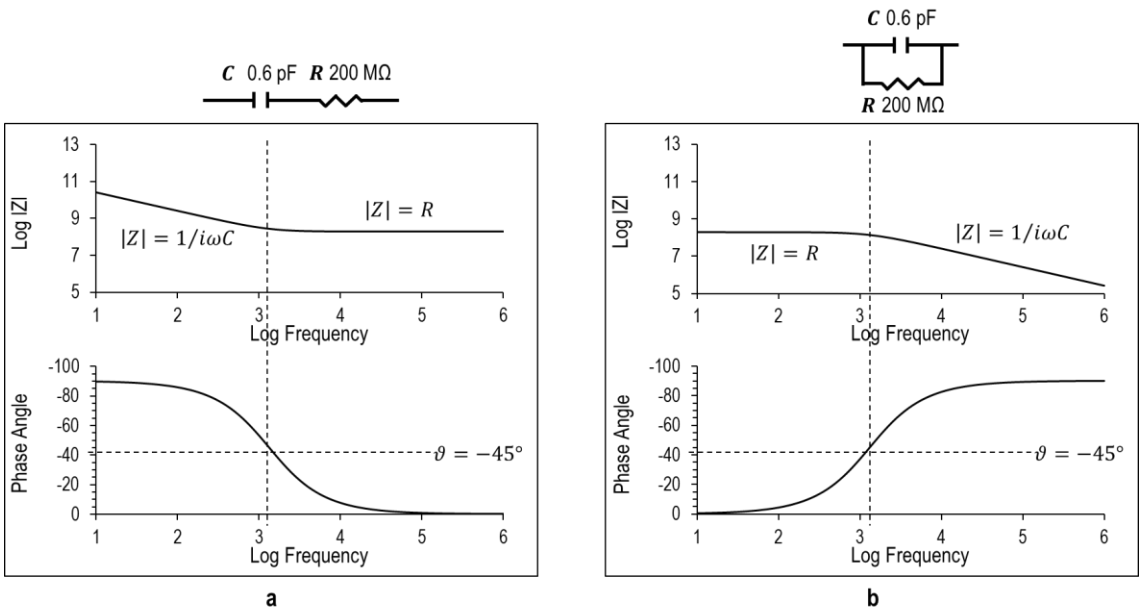

Figure 23 Typical impedance responses of a resistance and a capacitance (a) in series and (b) in parallel. The values for the resistance (R) and the capacitance (C) are 200 MΩ and 0.60 pF respectively.

The opposite proves to be the case for a parallel circuit of a resistance and a capacitance (**Figure 23**b). As mentioned earlier, the impedance of the parallel circuit is governed by the lowest impedance element. Hence, at low frequency, the impedance spectrum is controlled by the resistance instead of the capacitance (top graph of **Figure 23**b) because the impedance of the resistance is lower than that capacitance (**Figure 22**), such that current that passes through the object is manipulated by resistance; conversely, at high frequency the impedance spectrum is dominated by the capacitance (top graph of **Figure 23**b) since the impedance of resistance is higher than that capacitance (**Figure 22**) so that the current flowing through the circuit is dominated by the capacitance.

Now, considering a more complex composite object, a rather simple example of a complex circuit is a combination of a resistance (R) and a capacitance 1 (C_1) in parallel, which is placed in series with another capacitance 2 (C_2) as shown in **Figure 24**. This example model is relevant to the physical characteristics of a liquid sample contained in a TVIS vial. A combination of R and

C_1 in parallel models the solution in the vial whilst another C_2 provides a first approximation for the impedance of the glass wall and its interface with the solution.

At frequency below 1 kHz, the impedance of the resistance R (a grey dotted line in the top graph of **Figure 24**a) is lower than the capacitance C_1 (a grey solid line in the top graph of **Figure 24**a), therefore resistance R dominates the impedance of the $R = C_1$ circuit (Note: '=' means a parallel arrangement in an electrical circuit); but this $R = C_1$ circuit is in series with the capacitance C_2 which has a higher impedance (a grey dashed line in the top graph of **Figure 24**a), thus the current that flows through the entire circuit is manipulated by capacitance C_2. At a frequency range of 1-30 kHz, similar to the low frequency (< 1kHz), the impedance of the $R = C_1$ circuit is dominated by the impedance of the resistance element and the impedance of this resistance R is also higher than the impedance of the capacitance C_2, such that the resistance R dominates the impedance of the complex circuit and therefore the phase angle (φ) increases from -90 to zero, as seen in the bottom graph of **Figure 24**a. At frequencies above 30 kHz, the impedance of capacitance C_1 has fallen below the impedance of the resistance R, so that the capacitance C_1 dominates the impedance spectrum of $R = C_1$ circuit. The circuit now acts like two capacitances combined in series, and therefore the high frequency impedance is dominated by the sum of the impedance of capacitance (Equation 28).

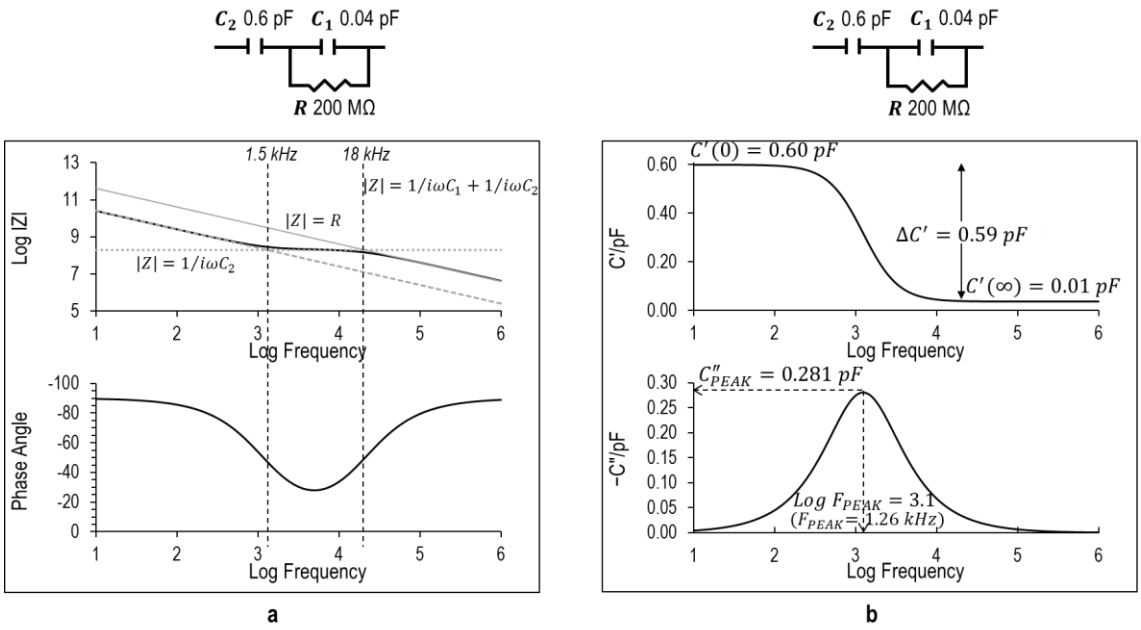

Figure 24 (a) Impedance responses of the complex composite object and (b) capacitance spectrum of the same object. The equivalent circuit model used for this object is represented by $C_2 - (R = C_1)$, ''−'' and ''='' mean a series and a parallel arrangement of the circuit element respectively. The values for the resistance (R), the capacitance 1 (C_1) and the capacitance 2 (C_2) are 200 MΩ, 0.04 pF and 0.60 pF respectively. The impedances of individual elements are shown in the top graph of (a), R; C_1; and C_2, and are represented by a grey dotted line, a grey solid line, and a grey dash line, respectively. Real-part capacitance in the limit of low frequency ($C'(0)$) and high frequency ($C'(\infty)$) is demonstrated in the top graph of (b); while the characteristics of dielectric loss peak (imaginary-part capacitance), namely peak frequency (F_{PEAK}) and peak amplitude (C''_{PEAK}) are illustrated in the bottom graph of (b).

The complex impedance ($\boldsymbol{Z}$) of the complex model in **Figure 24**, could be converted into the form of the complex capacitance ($\boldsymbol{C}$) as the following steps:

$$\boldsymbol{Z} = Z_{C_2} + Z_{R=C_1} \qquad \text{Equation 30}$$

$$\boldsymbol{Z} = Z_{C_2} + \frac{1}{(\frac{1}{Z_R} + \frac{1}{Z_{C_2}})} \qquad \text{Equation 31}$$

$$\boldsymbol{Z} = \frac{1}{i\omega C_2} + \frac{1}{\frac{1}{R} + i\omega C_1} \qquad \text{Equation 32}$$

$$\boldsymbol{Z} = \frac{1 + i\omega R(C_2 + C_1)}{i\omega C_2 - \omega^2 C_2 C_1}$$ Equation 33

Given the complex impedance ($\boldsymbol{Z}$) is an inverse of a complex capacitance ($\boldsymbol{C}$) (Equation 34), by substituting Equation 33 for Equation 35, the terms of complex capacitance ($\boldsymbol{C}$) are obtained (Equation 36).

$$\boldsymbol{Z} = \frac{1}{\boldsymbol{C}}$$ Equation 34

$$\boldsymbol{C} = \frac{1}{\boldsymbol{Z}}$$ Equation 35

$$\boldsymbol{C} = \frac{C_2 + i\omega R C_2 C_1}{1 + i\omega R(C_2 + C_1)}$$ Equation 36

The complex impedance could be written in rectangular form as below:

$$\boldsymbol{C} = C' + iC''$$ Equation 37

where C' is the real-part capacitance (or simply the capacitance) and C'' is the imaginary-part capacitance (otherwise known as the dielectric loss). From the complex capacitance expression (Equation 36), the terms for real (C') and imaginary (C'') part capacitance can be calculated. This is achieved by multiplying the nominator and denominator by the complex conjugate of the denominator (Equation 38), and by grouping, the real (C') part (Equation 40) and imaginary (C'') parts (Equation 41) are obtained.

$$\boldsymbol{C} = \frac{(C_2 + i\omega R C_1 C_2)(1 - i\omega R(C_1 + C_2))}{(1 + i\omega R(C_1 + C_2))(1 - i\omega R(C_1 + C_2))}$$ Equation 38

$$\boldsymbol{C} = \frac{C_2 + \omega^2 R^2 C_2 C_1 (C_1 + C_2) - i\omega R C_2^2}{1 + \left(\omega R((C_1 + C_2)\right)^2}$$ Equation 39

$$C' = \frac{C_2 + \omega^2 R^2 C_2 C_1 (C_1 + C_2)}{1 + \left(\omega R((C_1 + C_2)\right)^2}$$ Equation 40

$$C'' = -\frac{\omega R C_2^2}{1 + (\omega R((C_1 + C_2))^2} \quad \text{Equation 41}$$

Figure 24b shows an example capacitance spectrum of the forms described in Equation 40 (top graph) and Equation 41 (bottom graph). The low frequency real-part capacitance, $C'(0)$, is dominated by C_2 (0.6 pF), whereas at high frequency the real-part capacitance, $C'(\infty)$, is given by the series addition of C_1 and C_2 (0.01 pF) according to Equation 42.

$$C'(\infty) = \frac{C_1 C_2}{(C_1 + C_2)} \quad \text{Equation 42}$$

The increment in the real-part capacitance (i.e. the step of the spectrum), $\Delta C'$, can be calculated from the value of $C'(0)$ and $C'(\infty)$ as follows:

$$\Delta C' = \frac{C'(0)^2}{C'(0) + C'(\infty)} \quad \text{Equation 43}$$

For the imaginary-part capacitance (dielectric loss spectrum) shown in the bottom graph of **Figure 24**b, it can be seen that when the frequency approaches zero, the value of C'' tends to zero, and this value then increases as the frequency increases until it reaches the maximum of C''_{PEAK} (peak magnitude) at a frequency F_{PEAK} (peak frequency). Beyond that point, C'' decreases towards zero as the frequency increases. The main characteristics of the dielectric loss peak, C''_{PEAK} and F_{PEAK}, are given as equations below (Smith & Polygalov, 2019):

$$C''_{PEAK} = \frac{C_2^2}{2(C_1 + C_2)} \quad \text{Equation 44}$$

$$F_{PEAK} = \frac{1}{2\pi R(C_1 + C_2)} \quad \text{Equation 45}$$

5.3.3. Description of Through-vial impedance spectroscopy measurement

Through-vial impedance spectroscopy (TVIS) was first patented by Smith et al. (2011) as a method for monitoring a lyophilization process by continuously measuring an electrical

impedance of the test object (a TVIS vial and its content) undergoing the freeze-drying process. The TVIS measurement system consists of seven main parts (**Figure 25**):

(1) The TVIS measurement vial (**Figure 25**d). This TVIS vial is a glass container for lyophilization (e.g. vial, ampoule) modified by directly attaching one or two pairs of conductive electrodes (e.g. copper, gold) to the external surface of the container. The electrodes' dimension depends on the container size. Practically, the width of electrode is a quarter of the vial's circumference; the height of the electrode varies depending on the container size and filling volume. The position of electrode from the base can be adjusted; however, to avoid the current leak through a stainless-steel shelf, a distance of 3 mm from the vial's base is recommended for a 10 mL vial. The wire of the cable is soldered to the electrode affixed on the container (the procedure is in Appendix I). A drawing showing the dimension of a standard 10 mL TVIS measurement vial (supplied by Adelphi-HP as VC010-20C), attached with a pair of copper electrodes (19 x 10 mm) positioned at 3 mm from the external vial's base (showing the dimension) is illustrated in **Figure 26**. Various designs of the TVIS measurement vial are shown in Figure 27.

(2) A five-channel multiplexer (known as a junction box, **Figure 25**d). This electrical enclosure is usually placed inside the freeze dryer on one of the stainless steel shelves of the dryer. The purpose of this box is to serve as the communal spot for the wire. The stimulating signal from the impedance analyzer is split into 5 ports (called "Drive") and each port has a sensing port (called "Sense") to receive the resultant signal from the test object. This junction box can be made from metal or plastic and connects to the TVIS measurement vial via MCX connector.

(3) A bespoke pass-through for cables (**Figure 25**c). Since the impedance spectroscopy (**Figure 25**b) is located outside the freeze dryer such that pass-though is required to link the signal from the junction box (inside the freeze dryer) to the impedance analyzer (outside the freeze dryer), this pass-through is usually connected to a manifold hose of the freeze dryer (QuickSeal® valves for Virtis Advantage Plus XL freeze dryer) to ensure that the pressure inside chamber (in vacuum range) can be effectively controlled.

(4) A high-precision impedance analyzer with a frequency range of 10 Hz to 1 MHz (for DMU-TVIS, **Figure 25**b) or 10 Hz to 10 MHz (for Sciospec-TVIS). This has been specifically designed for the measurement of the impedance spectrum of the measurement container filled with a product that then undergoes the freeze-drying process. This analyzer converts the sensing current to voltage using a transimpedance amplifier (a current-to-voltage converter).

(5) Data acquisition (DAQ) system and the processing software installs in the computer (**Figure 25**a). This PC-based DAQ is used for converting an analogue signal (i.e. voltage) into a digital format (graphic and text format). The control software allows the operator to define the impedance parameters such as frequency range, stimulating voltage, and scanning interval (the time between the measurement spectrum). Full details are given by Arshad (2014).

(6) User interface (**Figure 25**e). This graphical user interface allows users to interact with the electronic device, including controlling a software displaying the real-time measurement.

(7) Data analysis software (LyoView™) as illustrated in **Figure 25**f. This data representation and analysis software has been designed for three-dimensional (3D) and two-dimensional (2D) visualization and analysis of data generated by the TVIS measurement control software and also Novocontrol BDS data.

Further description of the TVIS measurement system is provided by Smith and Polygalov (2019).

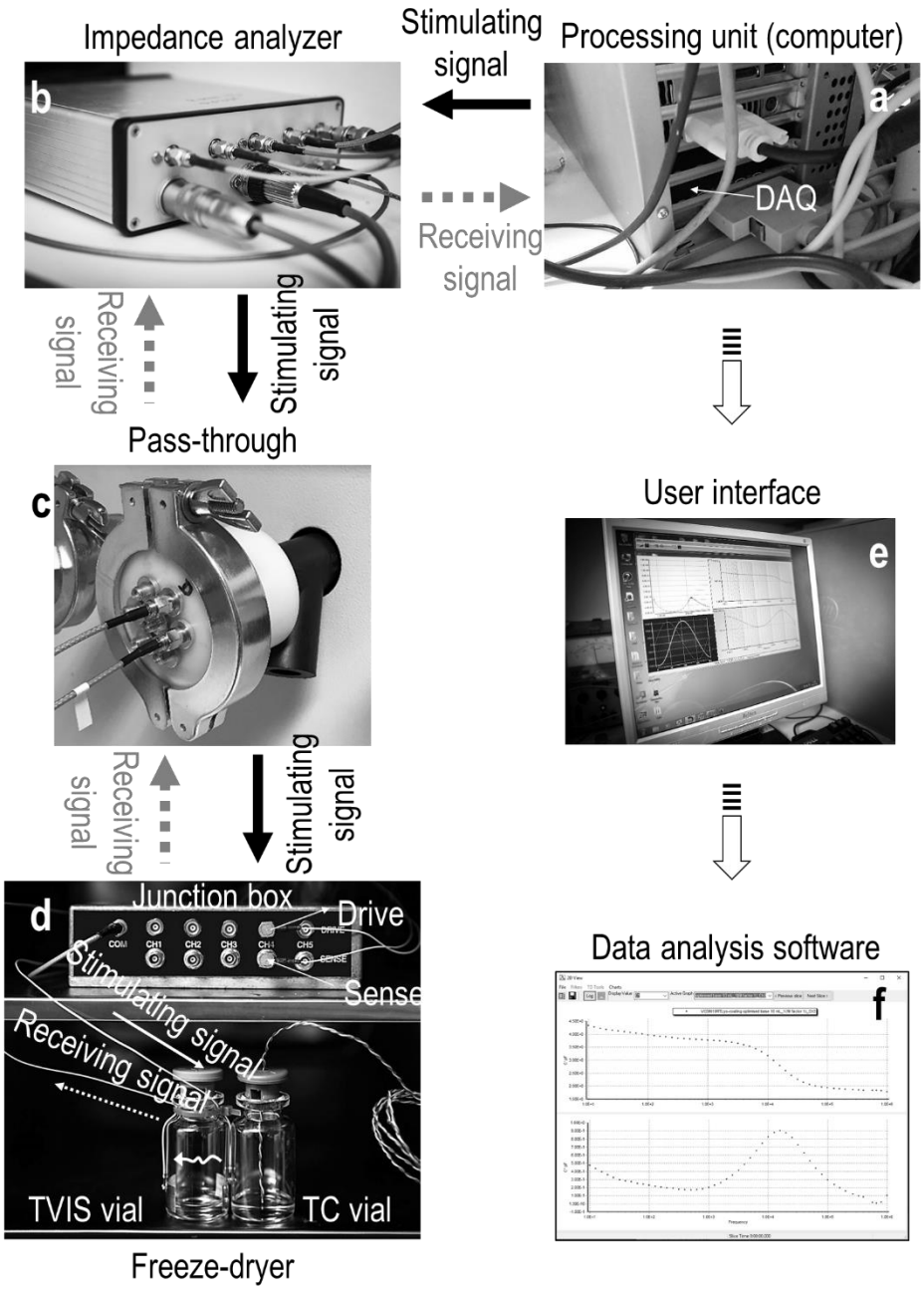

Figure 25 TVIS measurement system comprising the following basic parts: (a) a data acquisition (DAQ) card and the processing software installed in a computer CPU, (b) an impedance analyser, (c) a pass-through, (d) a junction box, a TVIS measurement vial (vial on the left side) and thermocouple (TC) contained vial (vial on the right side) locate in the freeze dryer chamber, (e) a user interface, and (f) data analysis software. The TVIS measurement vial and TC vial is placed on the bottom shelf of the freeze dryer while the five-channel multiplexer (junction box) sits on the top shelf of the freeze dryer. A thermocouple tip is manually placed at the centre point of the volume of sample bounded by the electrodes (TVIS sensing node) to represent the product temperature of the TVIS measurement vial (Smith et al., 2017). The black solid arrow demonstrates the pathway of the stimulating signal while the grey dotted arrow is the pathway of the sensing signal

The principal operation of a TVIS system starts from the DAQ installed in the computer (**Figure 25**a), which sends the excitation signal (i.e. stimulating voltage) into the impedance analyzer (**Figure 25**b) and this stimulating signal is passed to the junction box (**Figure 25**d) via the pass-through (**Figure 25**c) mounted on the available port of a freeze dryer before distributing it to the five drive ports in the multiplexer or junction box (**Figure 25**d). The excitation voltage is then applied to the object under test (TVIS vial with a sample shown in **Figure 25**d) and due to the oscillating nature of the voltage (sinusoidal waveform as demonstrated in **Figure 19**), this test object allows the current to flow through the sample and turn back to the sensing port of the junction box (**Figure 25**d) and then the impedance analyzer (**Figure 25**b) where the current is converted to voltage before returning back to the DAQ in the computer (**Figure 25**a) to process the data. The data will be presented on the computer screen (**Figure 25**e) and saved in a suitable format (i.e. DAT file) in real-time before analysis using the specific software (**Figure 25**f).

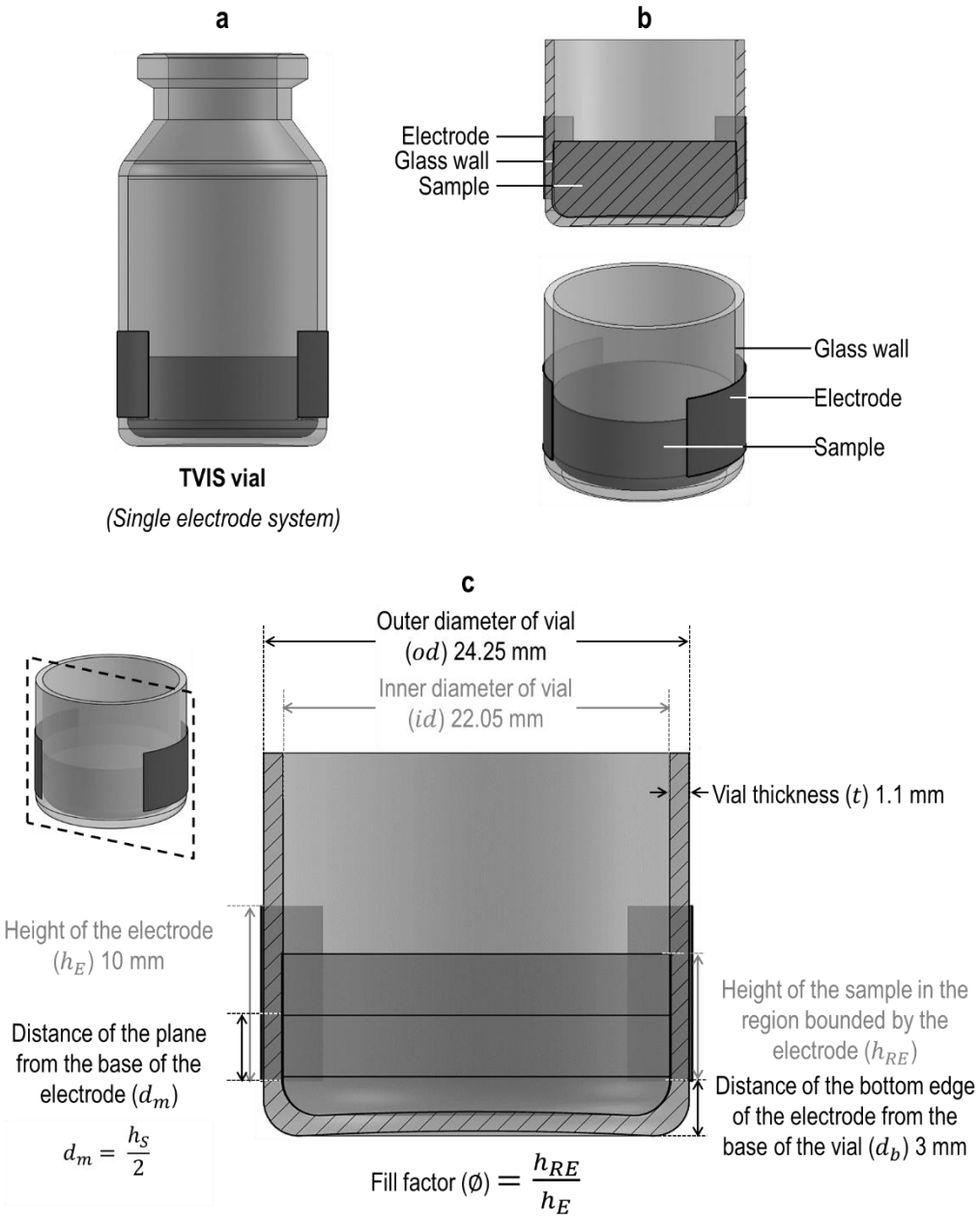

Figure 26 (a) sketch of a standard 10 mL Type I tubular glass vial (supplied by Adelphi-HP as VC010-20C), modified with a pair of 19 x 10 mm electrodes attached to the external surface of the vial at a position of 3 mm from the base (referred to as "single electrode system"); (b) a projected view and cross-sectional three-dimensional drawing of the segment of the TVIS vial containing sample; and (c) dimension of the TVIS vial d_b : The distance of the bottom edge of the electrode from the base of the vial; h_{RE} : height of the sample in the region bounded by the electrode; h_E : height of the electrode; d_m : distance from the base of the vial of the mid-point of the sample contained within the region bounded by the electrodes. The fill factor is defined as a ratio of the height of the sample within the region bounded by the electrode (h_{RE}) to the electrode height (h_E). The calculation is demonstrated in Appendix II.

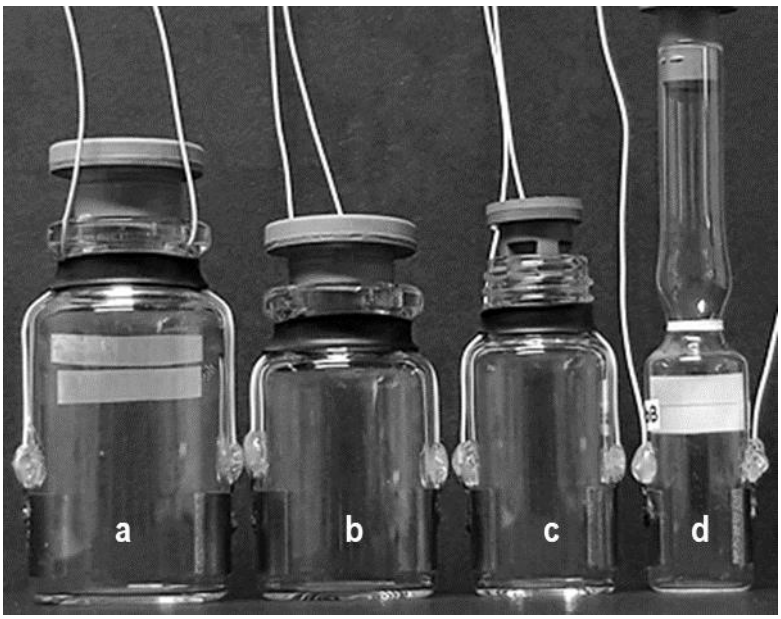

Figure 27 TVIS measurement vials: various designs of containers for freeze-drying that have been modified with copper foil electrodes (10 mm in height and 3 mm from the base for each container). From left to right are: (a) 10-mL Type I tubular glass vial, 20 mm crimp-neck (supplied by Adelphi-HP as VC010-20C); (b) 5-mL Type I tubular glass vial, 20 mm crimp-neck (supplied by Adelphi-HP as Adelphi VC005-20C); (c) 5-mL Type I tubular glass vial, screw-neck (supplied by Adelphi-HP as Adelphi VCD005); and (d) 2.5 mL glass ampoule (provided by the National Institute of Biological Standards and Control, UK)

5.3.4. Dielectric mechanisms of aqueous solution and its frozen state

Liquids and the Maxwell-Wagner Polarization of the Glass

Most of the pharmaceutical formulations for freeze-drying are generally aqueous solutions. At TVIS measurement range (10 Hz-1 MHz), the peak in the imaginary capacitance (i.e. the dielectric loss peak) and the increment in the real part are primarily contributed by an interfacial polarization, known as Maxwell-Wagner polarization (MW), and ionic conduction or DC conductivity (Komarov, Wang & Tang, 2005). One might wonder if the main component is water why the physical processes are not dominated by the orientation (dipole) polarization of water molecule. A possible explanation is that the dipole polarization of water is usually found at the microwave frequency range (10^9-10^{10} Hz), as demonstrated by the black dotted line in **Figure 28**. The presence of MW relaxation process (the black solid line in **Figure 28**) is a result of the charge accumulation at the boundary of multiphase (i.e. interface between a glass wall and a liquid

sample) due to the charge migration through a liquid sample. Therefore, it is important to note that the impedance response of the liquid sample filled in the TVIS vial is from the interfacial layer between glass and the liquid product (the black solid line in **Figure 28**), and the TVIS study of the liquid state is mainly based on the interaction of glass and solvent and is not related to the permittivity of water. For a crystalline structure like a borosilicate glass (e.g. glass vial), the main polarization mechanism is electronic polarization (Callister & Rethwisch, 2013); however, the contribution from the other mechanisms (e.g. space charge polarization) may be found in defective (non-pure) glass.

Here, the MW process at glass-liquid interface is first considered. When a voltage (V) is applied to a test object (i.e. TVIS vial and its content), a glass wall starts to charge, but the charging rate of glass wall capacitance depends on the solution resistance (R_s) which regulates the flow of mobile species (e.g. ion) to the glass wall. The rate of charging is typically defined as a time constant, τ (i.e. the time taken for a capacitor to charge 63.2% of a supply voltage) and could be approximated thus:

$$\tau \approx R_s C_g \qquad \text{Equation 46}$$

where τ is the time constant or relaxation time in second and $C_g$is the capacitance of glass-sample interface.

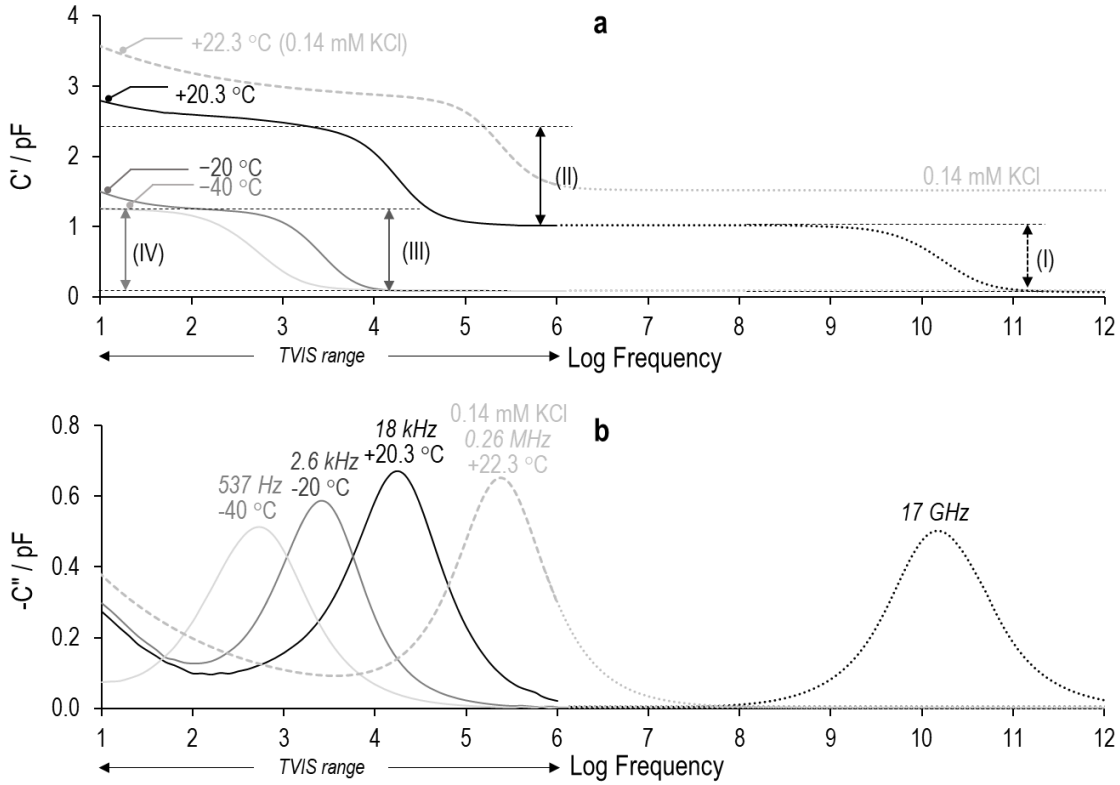

Figure 28 (a) real and (b) imaginary capacitance spectrum of (1) double distillation water (the solid lines) and (2) 0.14 mM potassium chloride solution (the dashed line) contained in a TVIS-modified Adelphi VC010-20C glass tubing vial (with electrodes of dimension 19 x 10 mm and positioned 3 mm from the base). The simulation data of both samples at a frequency above TVIS range (1 MHz-1 THz) are illustrated by dotted lines. For water, the measurement at three temperatures of +20 °C, −20 °C and −40 °C are shown. The increments in the real-part capacitance spectrum (a) for water sample are marked with Roman numerals: (I) is the simulated contribution to the capacitance resulting from orientation polarization of the liquid water at +20 °C, with a dielectric loss peak at frequency of ~ 17 GHz (microwave range); (II) the physical mechanism is contributed by the Maxwell-Wagner polarization of the glass wall of the TVIS vial at ambient temperature (+20 °C), with a loss peak frequency of 18 kHz; (III) and (IV) are the contribution from dielectric relaxation of frozen water at −20 °C and −40 °C respectively, for which the dielectric loss peak frequencies are 2.6 kHz and 537 Hz, respectively. For 0.14 mM KCl, the addition of a small amount of electrolyte (i.e. KCl) in double-distilled water could contribute to the polarization mechanisms of the water by shifting the dielectric loss peak from 18 kHz to the higher frequency at 0.26 MHz.

From Equation 46, it follows that any changes in the resistance and/or the capacitance can influence the charging process and thereby the time constant. For example, by adding a small amount of electrolyte in a double-distilled water (e.g. 0.014 mM KCl), the conductivity of water increases, which in turn decreases the sample resistance, resulting in an acceleration of the

charging process that would be reflected by a small value in the time constant. Referring to the previous section (section 5.3.1), the time constant is a reciprocal of the frequency such that a faster charging process could shift the frequency of the loss peak (relaxation frequency) to the higher frequency compared to the process without salt (i.e. doubled-distilled water), as demonstrated in **Figure 28**.

Given that the major composition of the product in liquid state is water, which exhibits both dielectric properties (Dipole polarization as shown in **Figure 29**) and ion conductivity (Grotthus mechanism or Proton hopping as shown in **Figure 29**), the product solution demonstrates not only electrical resistance but also electrical capacitance. Then, the physical characteristics of the liquid contained in the TVIS vial could be described by a relevant model having the solution resistance (R_s) and the solution capacitance (C_s) in parallel that is then placed in series with the capacitance of the glass-sample interface (C_g) as presented in **Figure 29**, and the time constant should be accounted for in the solution resistance as below:

$$\tau = R_s(C_g + C_s) \qquad \text{Equation 47}$$

where C_s is the approximate value for the electrical capacitance contribution from the volume of the liquid that occupies the electrodes region. For liquid sample, this parameter relates to the height of the sample volume bounded within the electrode region resulting in Equation 48:

$$C_s = \varepsilon_o \varepsilon_s k_s \qquad \text{Equation 48}$$

where ε_o is the permittivity of vacuum (8.854 x 10^{-12} F·m^{-1}), ε_s is a static permittivity which is described the behaviour of material (e.g. water) at low frequency end, and k_s is the geometric cell constant of the sample. In the case of a parallel plate capacitor (two electrode plates are arranged opposite one another), this cell constant is a ratio of the area of an electrode occupied by the sample (A) to the distance between the electrodes or the thickness of dielectric material (d), $k_s = A/d$.

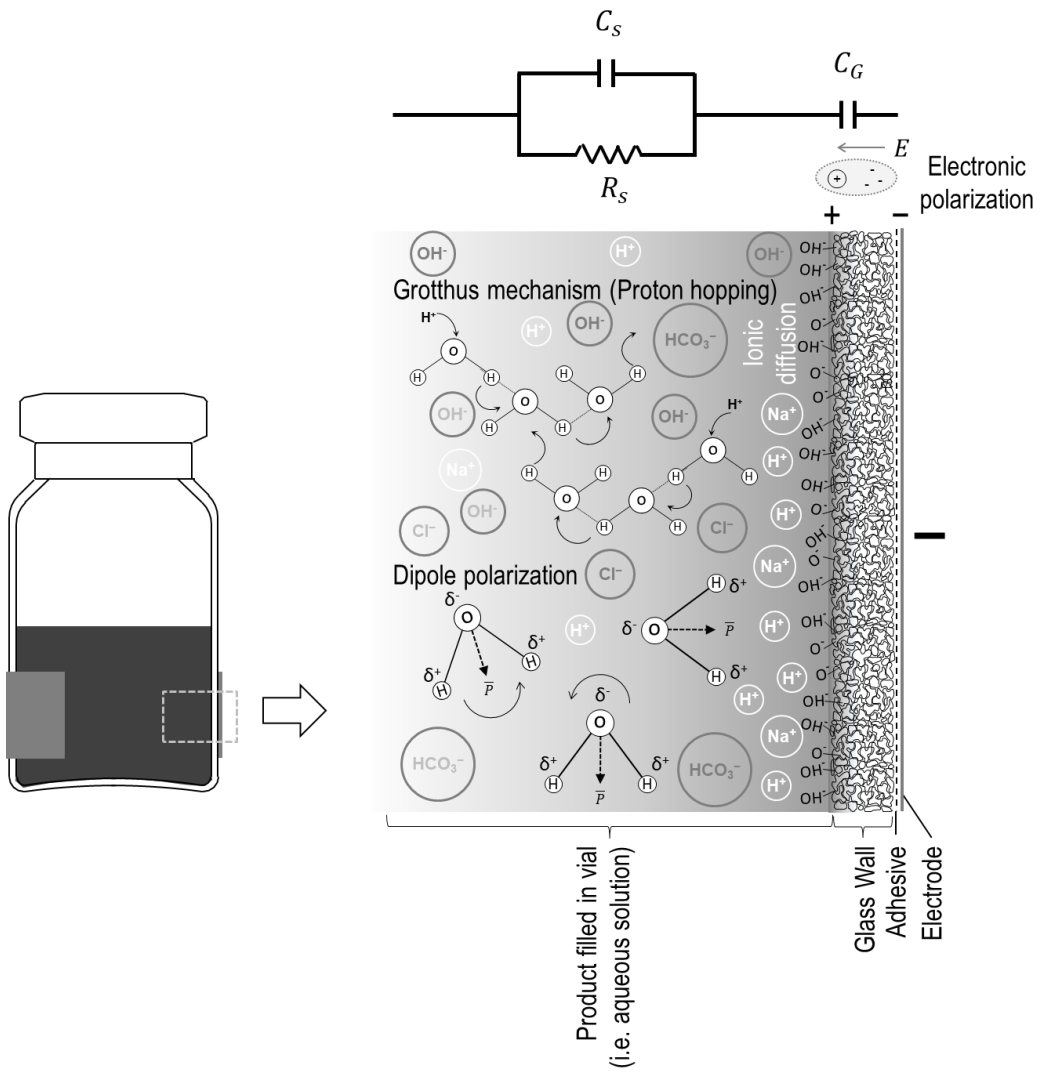

Figure 29 Illustration of a glass segment in contact with an electrode. This schematic shows the physical mechanisms occurring in a TVIS vial filled with a liquid product. The basic component of the product is water (permanent dipole molecule), which has both dielectric properties (dipole polarization or orientation polarization) and conductivity (Grotthus or proton-hopping). The polarization process of the glass wall is contributed by the electronic polarization occurring at microwave frequency. The physical-based equivalent circuit of the product contained in the TVIS vial could be modelled by a parallel RC circuit of the solution (R_sC_s) connected with the capacitance of the glass wall-sample interface (C_G). Note C_G means the sum of the glass wall-sample capacitance (C_g) from two glass segments in contact with electrode ($C_G = C_g^2/2C_g$).

Frozen Water and the Dielectric Relaxation of Ice

The capacitance spectrum of a TVIS vial containing a double-distilled water sample measured at different temperatures of +20, −20 and −40 °C is shown in **Figure 28**. These spectra have been made from experimental data (the solid lines) and simulation response of microwave dielectric

polarization of water (the dotted line). Once the ice formed, it can clearly be seen in **Figure 28** that the dielectric loss peak at ambient temperature moves from ~18 kHz to the lower frequency when the product temperature is sub-zero (−20 and −40 °C). Due to the similar shape of the relaxation peak between ice and liquid water contained in the glass vial (i.e. Maxwell-Wagner polarization), one might suppose that the temperature dependence of the resistance is the cause of the displacement of the relaxation peak through the ionic conductivity mechanism (Komarov, Wang & Tang, 2005). However, in fact, it is not because the electrical resistivity of ice is higher than that water (Artemov, 2014), but instead because the MW polarization process is replaced by a new physical process known as dielectric relaxation of ice, and this is frequency-dependent over the TVIS measurement range (10 Hz to 1 MHz). For example, at −20 °C, the permittivity of pure ice changes from 99.4 at low frequency, known as static permittivity or ε_s (Haynes, Lide & Bruno, 2017), to a typical value of 3.16 at high frequency, so-called instantaneous permittivity or ε_∞ (Petrenko & Whitworth, 2002).

Since the structural features of ice with both dielectric and conductive properties are fascinating, many attempts have been made over the years to study the characteristics of ice, including the dielectric properties of ice or how the protons move (Hobbs, Jhon & Eyring, 1966; Gough, 1972; Johari & Jone, 1976; Johari & Whalley, 1981; MacDowell & Vega, 2010; Artemov & Volkov, 2014; Popov et al., 2015; Sasaki et al., 2016; Popov et al., 2017). Ice Ih, a hexagonal ice crystal achieved from freezing water, is commonly used as a classic material for much ice study. Johari and Whalley (1981) observed the two relaxation transitions of ice Ih; one transition occurred at a temperature above −38 °C (the high temperature cross-over), whereas another one was found in very low temperatures (the low temperature crossover). Recently, the mechanism at high temperature of ice (up to −38 °C) was investigated by Popov et al. (2017). They proposed that the relaxation mechanism of ice crystal involves two mechanisms, one called L-D defect (i.e. orientation fault) and another ionic defect (i.e. proton hopping), as demonstrated in **Figure 30**. Nevertheless, the dominant mechanisms depend on ice temperature. L-D defect is responsible at temperatures below the crossover point of ~−38 °C (235 K), and vice versa (Popov et al., 2015). As a consequence of these two mechanisms, a single relaxation at temperatures below

−38 °C is a symmetrical broadening following Debye law, while the relaxation at a temperature beyond the crossover temperature of −38 °C towards higher temperature is also symmetric but narrower, according the Cole-Cole model (as demonstrated **Figure 31**). The Cole-Cole relaxation equation is given as below:

$$\boldsymbol{\varepsilon} = \frac{(\varepsilon_s - \varepsilon_\infty)}{(1 + (i\omega\tau)^{1-\alpha})} + \varepsilon_\infty \qquad \text{Equation 49}$$

Here, $\boldsymbol{\varepsilon}$ is a complex permittivity as a function of frequency and α is an exponent factor describing the shape of the spectra (broadening factor). When $0 < \alpha < 1$, the relaxation is wider than a Debye relaxation. If the value of α is zero, this expression would reduce to Debye model leading to Equation 50. For example, at ice temperatures of –20 °C and –40 °C, the broadening factor decreases from 1.00 to 0.97 (**Figure 31**)

$$\boldsymbol{\varepsilon} = \frac{(\varepsilon_s - \varepsilon_\infty)}{(1 + i\omega\tau)} + \varepsilon_\infty \qquad \text{Equation 50}$$

Another main feature is that instantaneous permittivity is almost independent of temperature (Petrenko & Whitworth, 2002). Gough (1972) demonstrated that the ε_∞ would continuously decrease from ~3.19 at 0 °C to a value of ~3.09 at absolute temperature. Conversely, the static permittivity tends to increase as temperature decreases according to the Curie–Weiss law, $\varepsilon_s - \varepsilon_\infty = A/(T - T_{cw})$ where T_{CW} approaches to zero (Popov et al., 2017).

On the subject of TVIS, the frozen product (e.g. ice) contained in TVIS measurement vial could be described by the equivalent circuit shown in **Figure 30**. Unlike the model of the liquid-filled in the TVIS vial, the sample capacitance is modelled by the distribution circuit element known as the Cole-Cole element and the instantaneous sample capacitance, $C_s(\infty)$, in parallel. The dispersive relaxation process of ice is represented by the Cole-Cole element whilst the sample capacitance at high-frequency limit describes the physical mechanism related to the charge distortion (electronic polarization). For resistance element in the liquid model, it is not necessary to have this element in the frozen model because the resistivity of the frozen product (particularly pure ice) is very high, and therefore the impedance of the parallel circuit will

dominate by the lower impedance (Section 5.3.2) and could then be removed. Thus far, the acquired knowledge of ice characteristics (including the dynamic transition of ice relaxation) would be useful if we are to develop a better understanding of the behaviour of products under cold processes such as freeze-drying.

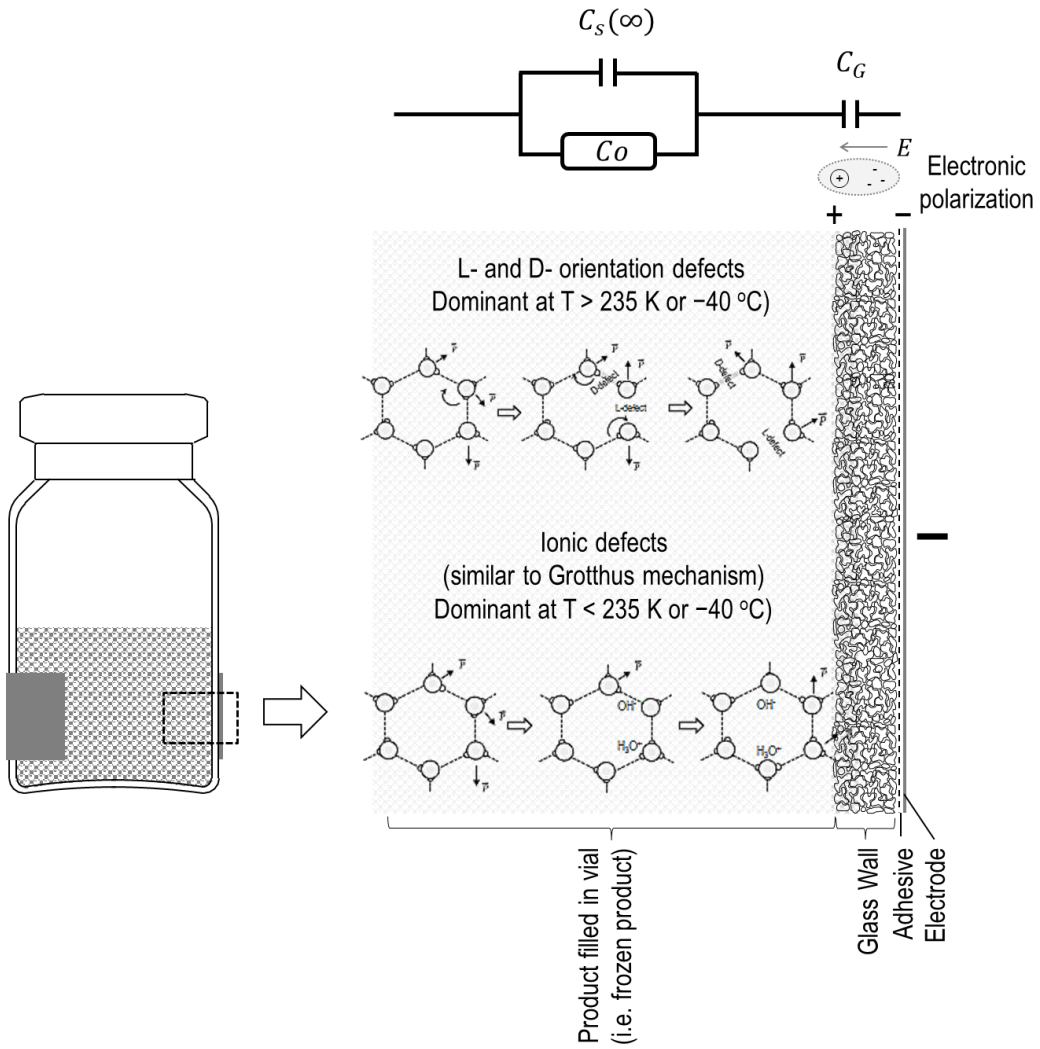

Figure 30 Illustration of a glass segment in contact with an electrode. This schematic shows the physical mechanisms occurring in a TVIS vial having a frozen product. The equivalent circuit model describing the physical characteristics of the TVIS vial containing the frozen product is modelled by one of the distributed elements known as the Cole-Cole element, Co, the instantaneous capacitance of ice, $C_s(\infty)$; and the glass wall capacitance, C_{G}. The Cole-Cole element representing the dielectric relaxation of ice and instantaneous capacitance of ice reflects the physical mechanisms of the frozen sample. The ice-glass wall capacitance, meanwhile, is modelled by C_G, which is the total glass wall capacitance from two glass segments in contact with electrode, $C_G = C_g^2/2C_g$.

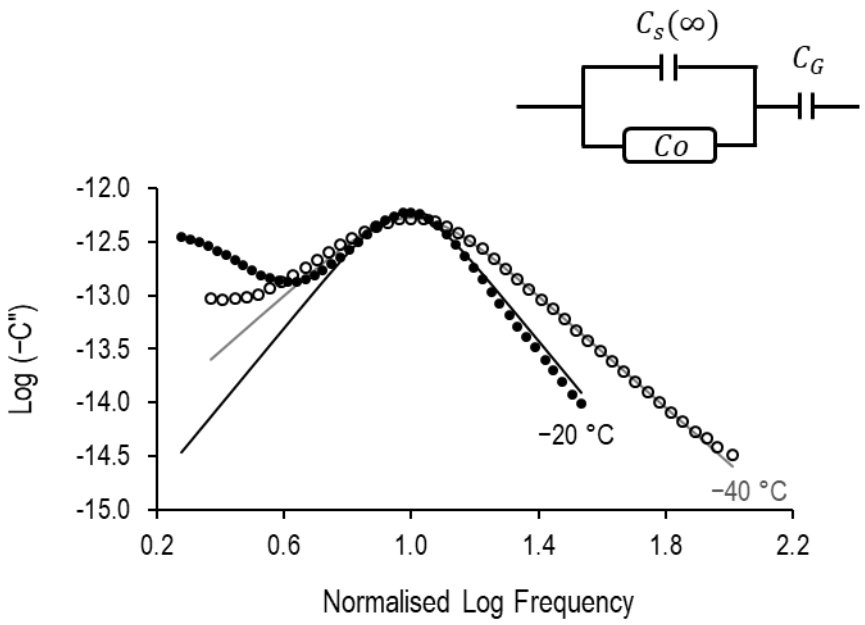

Figure 31 Normalised data of the experimental data and fitting data of ice at temperature −20 °C and −40 °C. The experimental data are represented by circle symbol, −20 °C (closed); −40 °C (open), and the fitting data are denoted by line, −20 °C (black); −40 °C (grey). The simplified model for frozen $C_G - (C_s(\infty) = Co)$ is used for fitting. In order to demonstrate more clearly the broadening of the relaxation peak, the imaginary capacitance is plotted on a log scale against normalised $Log\ F_{PEAK}$, which is obtained by normalising each spectrum with its peak frequency.

5.3.5. Equivalent circuit for TVIS vial

The complex model, $C_2 - (R = C_1)$, shown in **Figure 24** (Section 5.3.2), provides a first approximation for the TVIS test object (**Figure 32**), which is a modified glass vial (with an electrode pair attached directly to the outside of the vial) filled with a solution of interest. However, before addressing the TVIS response for solutions, it is helpful to start with a consideration of the response from water. As can be seen from **Figure 33**, an actual spectrum from the TVIS vial filled with water at +22 °C (black dotted) shows similarities to the model spectrum, $C_2 - (R = C_1)$ (black line). The use of a simple capacitance and a simple resistance to model the solution inside the vial is quite satisfactory because the permitivity and conductivity of aqueous solutions are independent of frequency over the experimental range of the TVIS instrument (10 Hz – 1 MHz). The peak frequency (F_{PEAK}) of the complex model is a function of the all three circuit elements (Equation 45), which means that any changes in temperature or

the ionic content of the solution could shift the spectrum. For example, the peak frequency moves to the higher frequency as a presence of salt (as mentioned in Section 5.3.4)

Figure 32 TVIS test object. The TVIS vial is a standard tubular glass vial supplied by Adelphi (VC010-20C), modified by attaching a pair of electrodes (dimensions 10 mm by 19 mm) directly to the external of glass vial at a distance of 3 mm from the vial baseline. Double-distilled water corresponding to a fill factor of 0.8 (~3.3 g) was placed in the the TVIS vial.

However, in this real system, one can see that the real and imaginary capacitance of the water spectrum (black dotted in **Figure 33**) both increase towards low frequency (black arrow in **Figure 33**), whereas the real-part capacitance of the model system reaches a plateau at low frequencies and the imaginary-part capacitance tends toward zero (black line in **Figure 33**). This indicates that the use of a capacitance to model the glass wall impedance is an over-simplification for the properties of this test object.

The process observed for the water-filled vial is known as a Maxwell-Wagner process, and occurs at the boundary of the conductive dielectric liquid (water) and less conductive glass wall. In effect, the time constant associated with the dielectric loss peak is a measure of the characteristic time for charging the glass wall and sample through the electrical resistance of the solution (Equation 47).

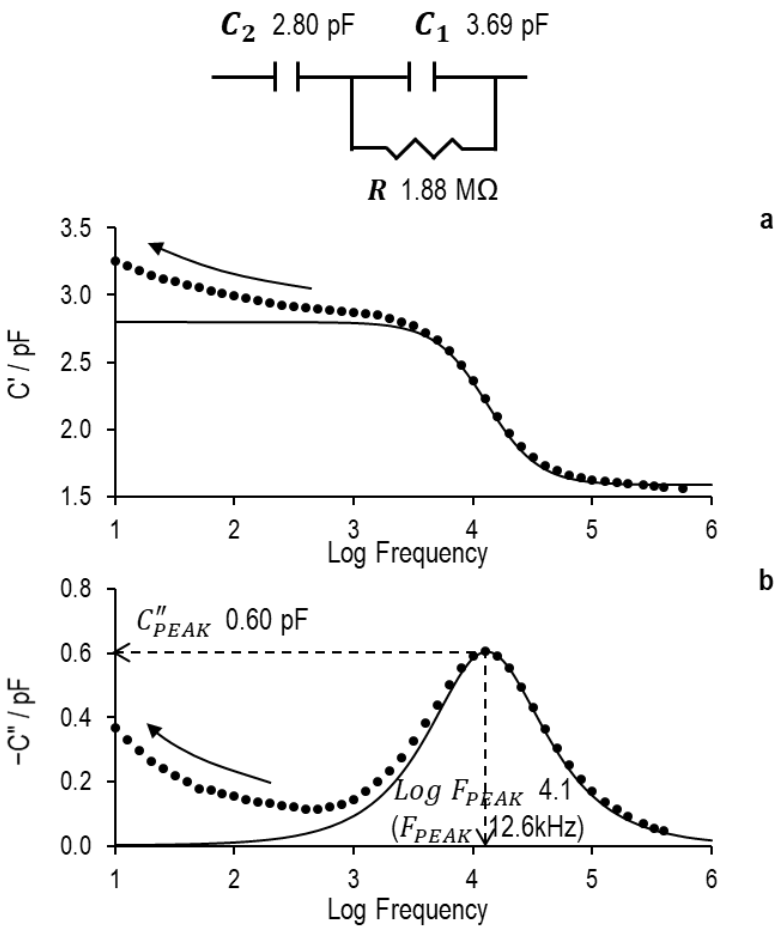

Figure 33 Demonstrating the differentiation of low frequency response between the measurement spectrum of 5.75 g ultrapure water corresponding to a fill factor of 1.2 (water is above electrode) and model data is generated from a complex model, $C_2 - (C_1 = R)$. The values of model parameters are 2.80 pF, 3.69 pF and 1.88 MΩ for C_2, C_1 and R repectively. The arrow indicates the upward trend of water spectrum at frequency below 1 kHz.

For frozen water, the sample capacitance is no longer constant over the TVIS frequency owing to the fact that the dielectric relaxation frequency of ice lies in the sub-kHz frequency range. For instance, based on the experimental data of ice measured by TVIS system at −40 and −20 °C (**Figure 28**), the peak frequencies corresponding to these temperatures are 537 Hz and 2.6 kHz, respectively. Additionally, the electrical resistance of ice is significantly higher than water (Artemov & Volkov, 2014) such that one can neglect the series resistance that would be used to model the resistance of the sample as mentioned previously in Section 5.3.4. This also means that the Maxwell-Wagner charging of the glass and sample capacitances is shifted to very low frequency, as demonstrated in **Figure 34**.

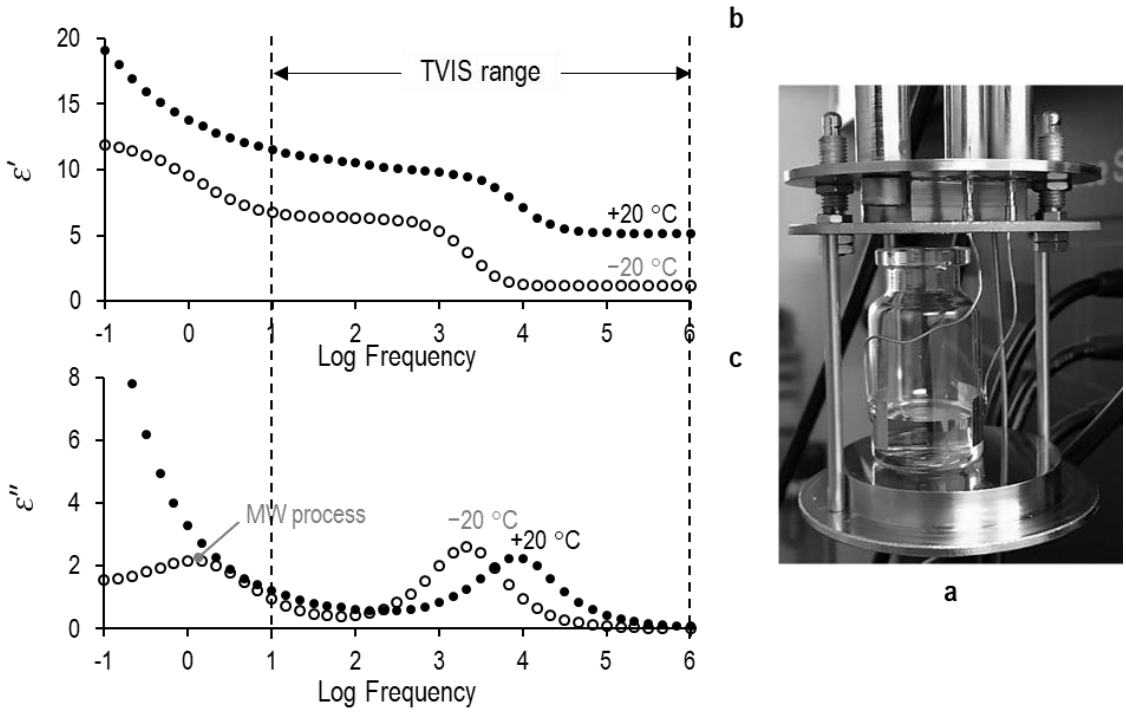

Figure 34 Broadband dielectric response of ultrapure water 3.5 g filled in TVIS vial at +20 °C and −20 °C. (a) Ultrapure water contained in a modified TVIS vial by replacing MCX connector (133-3402-101, Johnson-Cinch connectivity, USA) and micro coax cable 36 AWG (9436 WH033, Alpha wire, USA) with banana plug and a metal wire placed on the dielectric sample cell of broadband dielectric spectrometer or BDS (Alpha-A, Novocontrol, Germany) before inserting into cryostat. (b) Real part of the permittivity of water in liquid state (+20 °C) and frozen state (−20 °C) measured by BDS system. (c) Imaginary part of the permittivity of water and ice measured by BDS system. The Maxwell-Wagner (MW) polarization process of glass-sample interface moves to lower frequency outside the TVIS measurement range (10 Hz to 1 MHz).

Furthermore, there is a contribution to the glass wall capacitance, which is presumably from the diffusion/percolation of charges (protons) through the porous glass matrix because borosilicate glass contains alkali ions and the confined water within the porous glassy matrix such that charges could move under the electric field (Konijnendijk, 1975). This process can be modelled by a constant phase element (CPE) in series with the capacitance of the glass-sample interface (C_G). The CPE response is significant to the overall low-frequency response (Smith & Polygalov, 2019) while the dispersion process occurs at the intermediate frequencies of the TVIS measurement range. Therefore, the overlapping of CPE response with the principal peak from TVIS is considered too small to have any impact on the overall impedance response of the TVIS vial and its contents. Consequently, CPE element is included in parallel with the glass-sample

capacitance (C_G) of the simplified model, $C_G - (R_s = C_s)$. The improved model, $(C_G = CPE) - (R_s = C_s)$, is defined as "enhanced model". The comparison between two models, with and without CPE element, is demonstrated in **Figure 35** by using water spectrum.

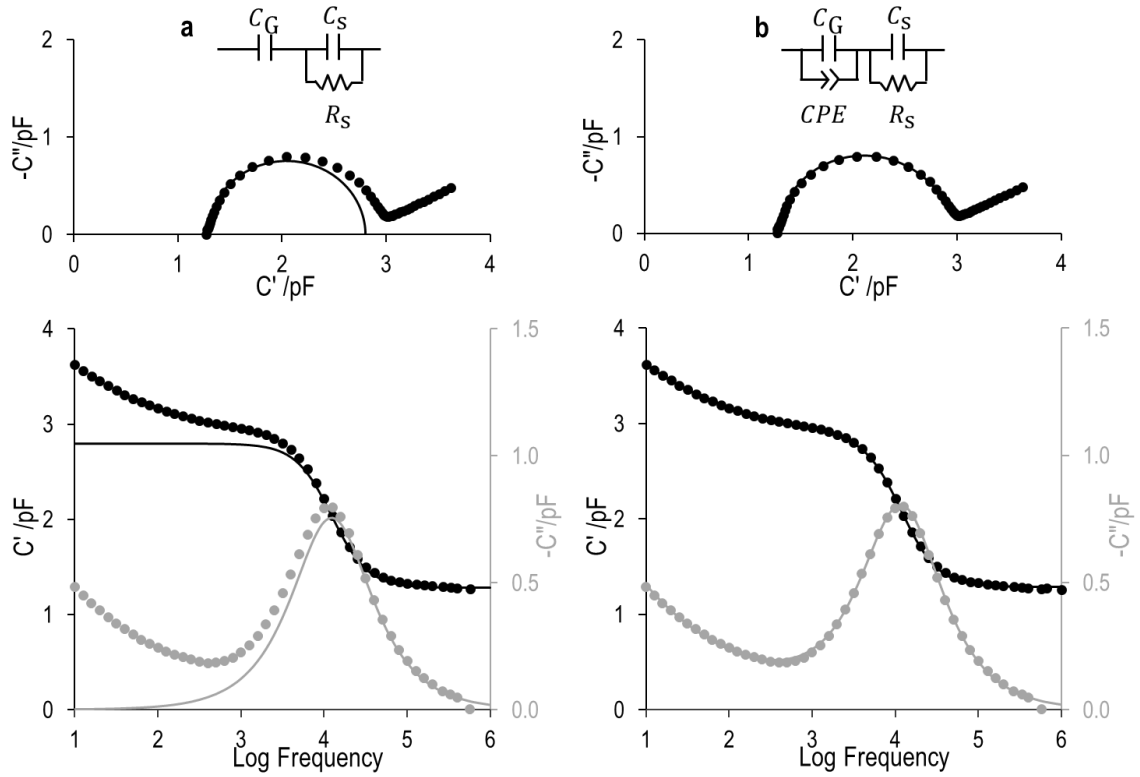

Figure 35 The TVIS response of ultrapure water equivalent to fill factor 0.7 (3.4 g) filled in the TVIS measurement vial with 19 x 10 mm electrodes at a distance of 3 mm from the vial's base is fitted to: (a) simplified model, $C_G - (R_s = C_s)$; and (b) enhanced model having CPE element to account for the physical mechanism occurring within a porous borosilicate glass matrix, $(C_G = CPE) - (R_s = C_s)$. By inclusion of CPE element, the fit results match perfectly with the data.

5.3.6. Applications of Through-vial impedance spectroscopy

TVIS applications for freeze-drying are based on TVIS responses, dielectric loss in particular, to the process variables (e.g. temperature) and related parameters (e.g. vial heat transfer coefficient) during various stages of freeze-drying. Understanding these TVIS responses and how they relate to process parameters might help to cope with their application to monitoring freeze-drying process.

TVIS parameters

Dielectric loss spectrum (imaginary-part capacitance): Peak frequency

TVIS measures the electrical characteristics of the material under test in terms of dielectric and conductive properties, including resistance. These intrinsic properties vary, with several influencing factors. One of these is frequency. Polarization mechanisms, depending on how the material reacts when it is exposed to the electric field, contribute to the frequency dependence of dielectric material. This frequency dependence can be described by regular form of Debye expression for real (dielectric storage) and imaginary (dielectric loss) part as below:

$$\varepsilon' = \frac{\varepsilon_s - \varepsilon_\infty}{1 + \omega^2\tau^2} + \varepsilon_\infty \qquad \text{Equation 51}$$

$$\varepsilon'' = \frac{(\varepsilon_s - \varepsilon_\infty)\omega\tau}{1 + \omega^2\tau^2} + \varepsilon_\infty \qquad \text{Equation 52}$$

From Equation 52, we can see that the frequency has a greater influence on dielectric loss factor (ε'') than on the real part (ε'). Again, water is a good example for this effect. The dielectric loss spectrum of pure water reaches a maximum of amplitude at ~19 GHz at 25 °C (Haynes, Lide & Bruno, 2017) due to a dipole orientation process, and this loss peak could drop to the lower frequency when it is bounded or absorbed by a material. This is because the alteration of the polarization process (i.e. change from orientation polarization to MW process) and also the relaxation time of bounded water is generally longer than that of unbounded water (Komarov, Wang & Tang, 2005). The permittivity of some common solvents can be given in terms of frequency (f, MHz) as below (Gregory et al., 1993):

$$\boldsymbol{\varepsilon}\,(water) = \frac{74.59}{1 + if/17 \times 10^9} + 5.62 \qquad \text{Equation 53}$$

$$\boldsymbol{\varepsilon}\,(methanol) = \frac{27.89}{1 + if/2.709 \times 10^9} + 5.76 \qquad \text{Equation 54}$$

$$\boldsymbol{\varepsilon}\,(ethanol) = \frac{20.84}{1 + if/0.826 \times 10^9} + 4.44 \qquad \text{Equation 55}$$

Besides frequency, temperature also affects dielectric properties. The temperature dependency of dielectric material (e.g. impure water) involves two main physical mechanisms: (1) material dielectric relaxation, and (2) ionic conduction (Komarov, Wang & Tang, 2005). According to Debye theory, especially for dipole molecule, a correlation between the relaxation time and either temperature (T) or viscosity (v) can be explained in terms of rotational Brownian movement, as in the relationship below (Komarov, Wang & Tang, 2005):

$$\tau \propto \frac{v}{T} \qquad \text{Equation 56}$$

As temperature increases, the relaxation time decreases and thereby shifts the dielectric loss peak to the higher frequency range ($f = 1/2\pi\tau$). For the latter mechanism, ion conductivity, one possible explanation is the fact that when heating up, the viscosity of solution reduces accordingly; therefore, the charge can move easily, resulting in an increase in the conductance and, in turn, a decrease in resistance. The temperature dependency of water is illustrated in **Figure 36**.

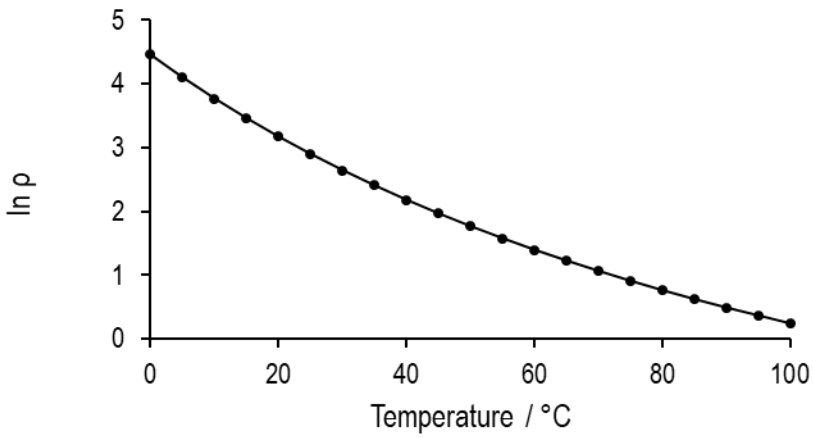

Figure 36 Experimental data of resistivity of ultrapure water from 0-100 °C (Bevilacqua, 1998)

The final influential parameter is water content. The higher the moisture content, the greater the dielectric response in both the dielectric constant and the loss factor (Nelson & Trabelsi, 2012). However, in the case of low water content, Metaxas and Meredith (1983) noted that the moisture content decreased until it reached a critical value, at which point dielectric loss

properties started to level off as a result of the bound water, whilst Pearson and Smith (1998) highlighted dielectric analysis techniques for determining the water hydration of protein.

Dielectric loss spectrum (imaginary-part capacitance): Peak amplitude

Since an analogy can be made between the TVIS measurement vial (where the dielectric material including glass wall and sample is placed in between the electrodes) and a parallel plate capacitor, an approximation of the capacitance of the TVIS vial can be calculated based on the standard formula of parallel plate capacitor as below:

$$\boldsymbol{C} = \varepsilon_o \varepsilon_r k \qquad \text{Equation 57}$$

where ε_o is the permittivity of vacuum (8.854 x 10^{-12} F·m^{-1}), ε_r is a relative permittivity of dielectric, and k is a ratio of the area of an electrode (A) to the distance between the electrodes or the thickness of dielectric material (d), $k = A/d$.

According to this equation, it would be anticipated that the electrical capacitance is directly proportional to the area of electrode making contact with the glass wall that is adjacent to the sample. Therefore, the lower the area of electrode occupied by the sample, the less the value of capacitance, as demonstrated by the calibration of the sample height in **Figure 37**.

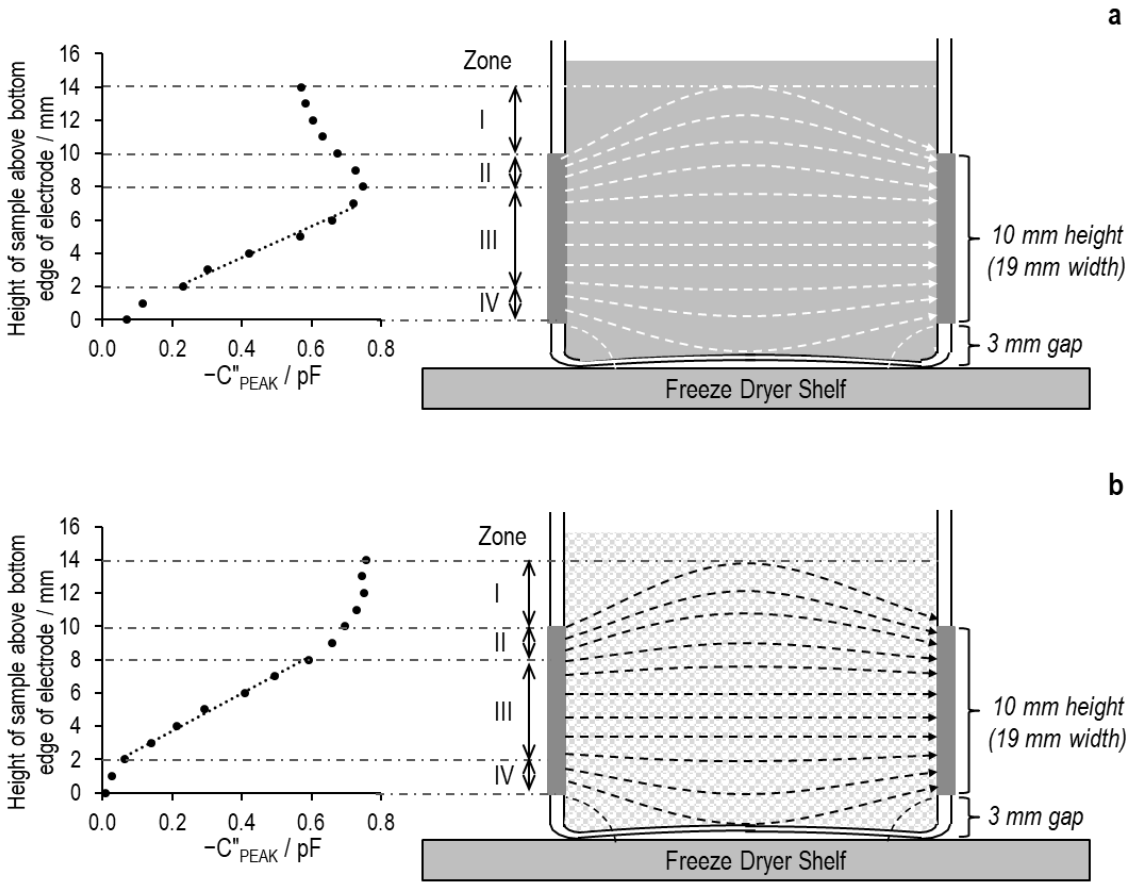

Figure 37 C''_{PEAK} dependence on the height of sample from the bottom edge of the electrode (a) ultrapure water at temperature ~ 22 °C, and (b) frozen water at −22 °C. *Zone I* is the region above the electrodes where the fringing field contributes to the overall capacitance despite the fact that the sample in this region is above the electrodes; *Zone II* is the non-linear response region when the sample is close to the top edge of the electrodes; *Zone III* is the quasi-linear response region to the sample where the electric field is uniform; *Zone IV* is the non-linear response region to the sample close to the bottom edge of the electrodes where the electric field is not constant. Note the method of C''_{PEAK} calibration for the sample height is illustrated in Appendix III and in Appendix IV for liquid and frozen sample, respectively.

Dielectric permittivity spectrum (real-part capacitance)

The real part at 10 Hz and 0.2 MHz of dielectric permittivity spectrum of TVIS containing ice recorded during re-heating shown in **Figure 38**a demonstrated that the temperature sensitivity depends on the measurement frequency. At first glance in **Figure 38**a, the real part at low frequency, C'(10 Hz), is strongly sensitive to ice temperature, whereas it is almost independent at high frequency, C'(0.2 MHz). Therefore, the real part at low frequency might be another alternative for the determination of ice nucleation while at high frequency could be applied for

the solidification end-point (Smith & Jeeraruangrattana, 2019b). Also, when comparing the real part at high frequency (0.2 MHz) between ice (**Figure 38**a) and 5% w/v sucrose solution (**Figure 38**b), the temperature dependence of the sucrose solution is stronger than that of ice. This could imply that the temperature dependence of the sucrose solution might result from the unfrozen part. Recently, Pandya et al. (2019) demonstrated the use of real part at high frequency (100 kHz) for determining the end-point of primary drying in comparison with the pressure rise test.

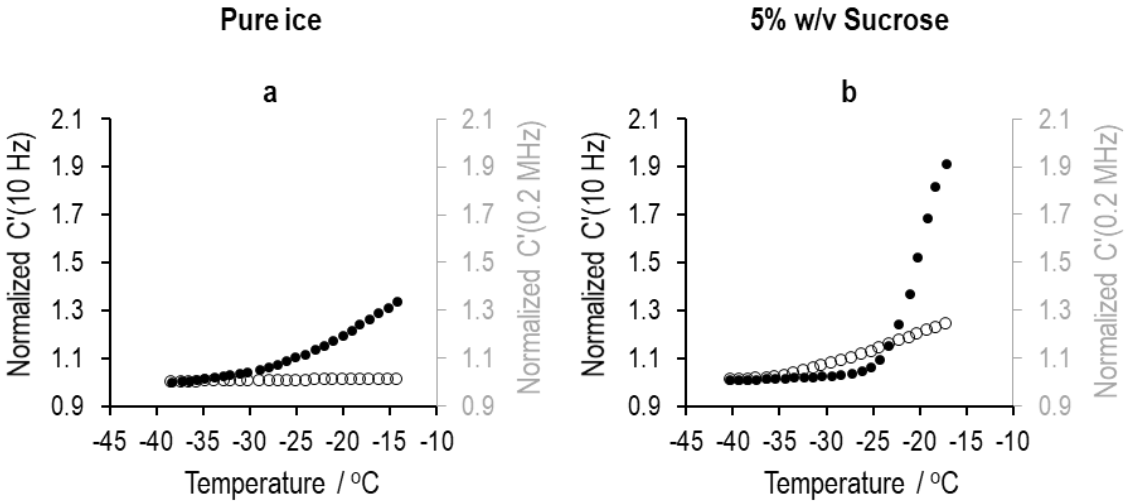

Figure 38 Demonstrating temperature dependence of real-part capacitance at 10 Hz (filled circle) and 0.2 MHz (open circle) of (a) pure ice (Smith & Jeeraruangrattana, 2019a), and (b) 5% w/v sucrose in a frozen state (data from Chapter 8). The data are recorded during the re-heating stage from −40 °C to −10 °C with 0.5 °C·min^{-1} for pure ice and from −50 °C to −10 °C with 0.2 °C·min^{-1} for the frozen 5% w/v sucrose, respectively.

The application of TVIS parameters for monitoring freeze-drying process.

The use of TVIS parameters, i.e. F_{PEAK}, C''_{PEAK}, $C'(f)$, for monitoring freeze-drying process are considered according to the freeze-drying steps.

Freezing step

Dielectric loss spectrum: The temperature dependence of dielectric properties associated with the transition of physical process from the Maxwell-Wagner (MW) process to the dielectric relaxation of ice could be used to determine liquid-solid phase transitions (i.e. nucleation). The heat release resulting from ice crystallization accompanied with the change in dielectric

mechanism causes peak frequency shifts by 1-2 decades (**Figure 39**b), leading to a spike in the peak frequency profile (Arshad, 2014; Smith & Jeeraruangrattana, 2019). Due to the temperature dependence of the dielectric loss peak, the characteristic relaxation peak moves to the lower frequency during cooling (**Figure 39**a). By plotting the temperature of the supercooled liquid (recorded from the sensor in the vial) and juxtaposing this with the TVIS vial and the peak frequency of the supercooling liquid, temperature calibration can be obtained. This calibration plot is then used for predicting ice nucleation temperature (T_n). More details of the method have been described in Smith and Jeeraruangrattana (2019).

Dielectric permittivity spectrum: In the case of high conductivity solutions, the MW process might be out of the TVIS window, as demonstrated by 0.014 mM KCl (**Figure 28**), hence it is difficult to track the dispersion process (i.e. F_{PEAK} and C''_{PEAK}) during cooling. Fortunately, the real part at low frequency, C'(10 Hz), can be used as an alternative for determining the nucleation process because this parameter is strongly temperature-dependent (**Figure 38**a). Similar to the dielectric loss spectrum, nucleation temperature can be estimated using the temperature calibration of C'(10 Hz). In addition to the real part at low frequency, the high frequency range, C'(0.2 MHz), allows us to determine the structural change during the freezing stage, such as the solidification end-point (Smith & Jeeraruangrattana, 2019).

Thermal treatment or annealing step

Dielectric loss spectrum: the dielectric loss peak moves to the higher frequencies as the temperature of ice bounded within the electrode region increases (re-heating step) as shown in **Figure 39**c. For calibration purposes, the ice temperature from the neighbouring thermocouple vial and the F_{PEAK} recorded during re-heating enables us to plot a temperature calibration; this can then be used for the prediction of the ice temperature during the primary drying step (Smith, Jeeraruangrattana & Ermolina, 2018). In the case of heating exceeding the glass transition temperature of the freeze-concentrated solution (T'_g), the viscosity of a frozen matrix dramatically decreases below 10^{12} Pa·s (Roos & Drusch, 2016b). This is followed by an increase of conductivity due to the facilitation of charges' migration through the sample; the subsequent

dielectric loss changes rapidly such that the glass transition event could be detected by a discontinuation of loss factor characteristic, or its derivative (Smith et al., 2013). Additionally, the modification of the ice structure during annealing (i.e. recrystallization process) could influence the overall dielectric properties; thus, this highlights the uses of TVIS as an in-situ tool for indicating the point where the recrystallization process is completed (Smith et al., 2014b) .

Dielectric permittivity spectrum: Since the temperature dependence of dielectric storage at high frequency is reflected in the unfrozen fraction, it is possible to determine the glass transition temperature (T_g') using the real-part parameter in the high frequency region (e.g. 0.2 MHz). This approach requires further study.

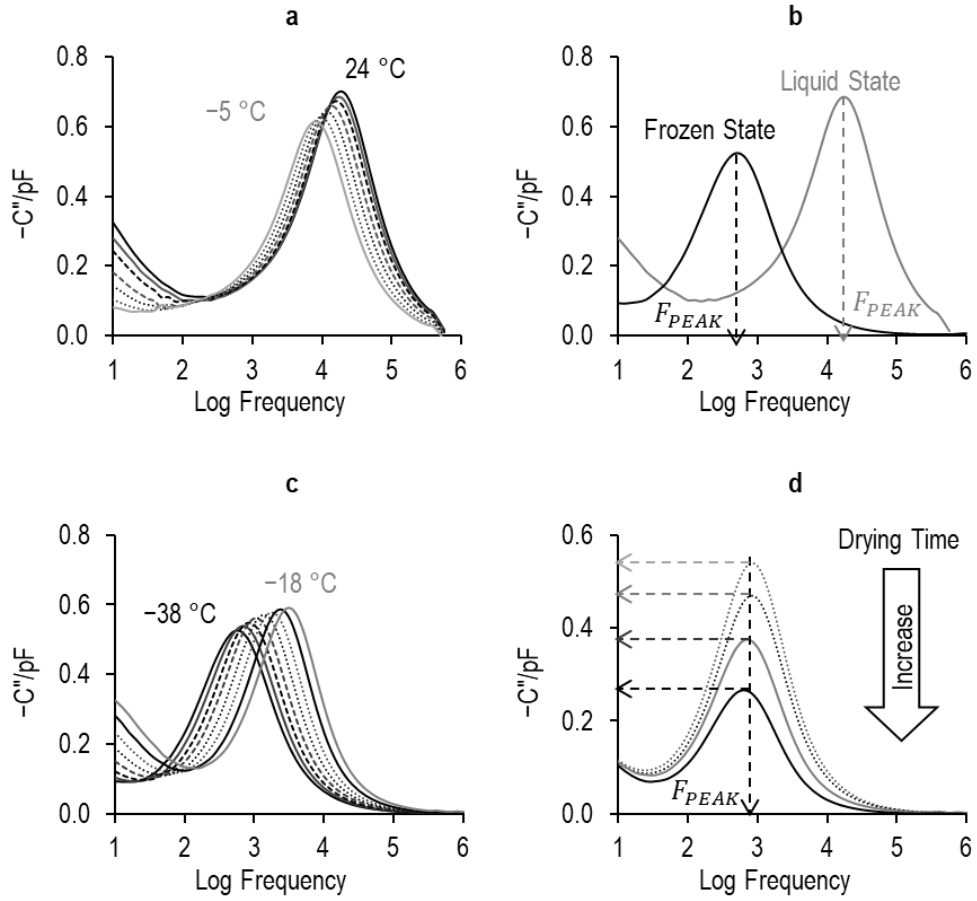

Figure 39 Basic TVIS responses of the dielectric loss spectrum (imaginary-part capacitance) of a 10 mL standard TVIS vial (electrode dimension of 19 x 10 mm at distance 3 mm from the vial's base) containing 3.5 g double-distilled water during the freeze-drying process: (a) cooling the liquid phase; (b) liquid-solid phase transition (water to ice); (c) re-heating of frozen water; and (d) primary drying.

Primary drying

Dielectric loss spectrum: the reduction of dielectric loss peak over the primary drying period (**Figure 39**d) can be used for estimating the sublimation rate according to the method described by Smith et al. (2018). Also, by applying temperature calibration from the thermal treatment stage, we can determine the ice temperature. These parameters (i.e. product temperature and sublimation rate) can be used for calculating the critical parameters - namely the vial heat transfer coefficient and the dried product resistance - required for building the design space for lyophilization.

Dielectric permittivity spectrum: Given that C'(0.1 MHz) is sensitive to the last vestiges of the ice mass and has a very low temperature coefficient, this parameter enables the determination of the primary drying end-point.

The summary of the recent TVIS approach for monitoring the freeze-drying process is shown in **Figure 40**.

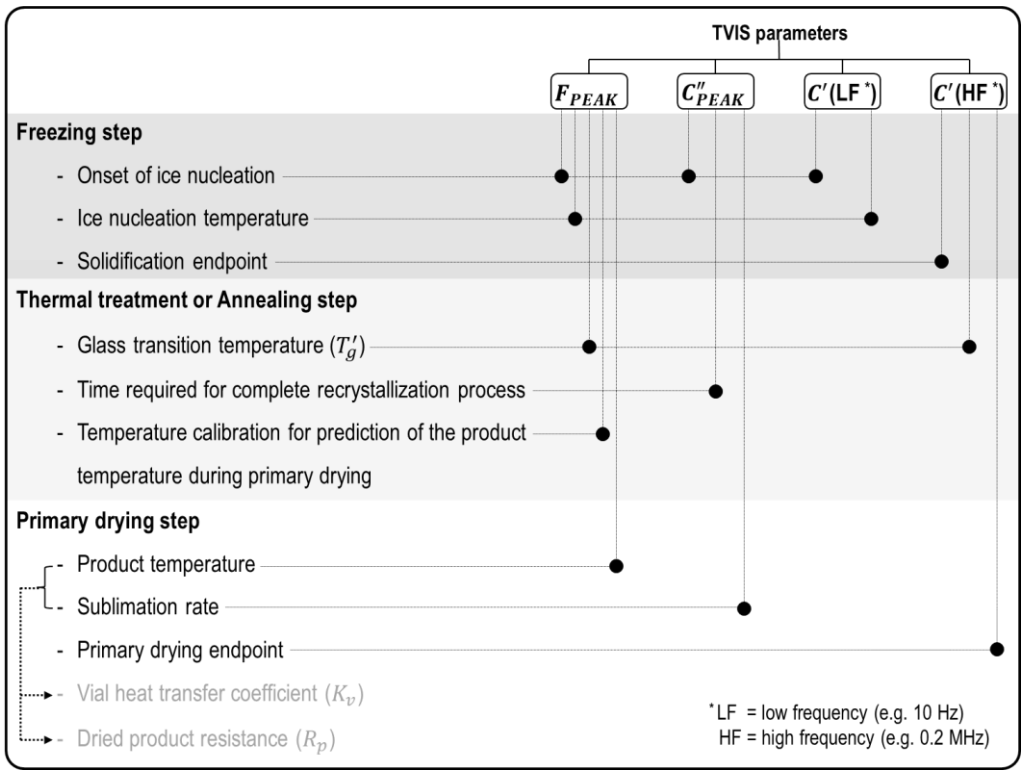

Figure 40 A schematic of the recent applications of different features of TVIS technology for monitoring the freeze-drying process.

5.3.7. Limitations of through-vial impedance spectroscopy

Through-vial impedance spectroscopy is minimally product-invasive in the sense that the electrodes are not within the vial, and do not make contact with the sample, as is the case with other single vial measurement techniques such as the thermocouple or the LyoRx system marketed by Martin Christ GmbH, Germany (Smith et al., 2017). Moreover, the thin electrode (thickness <0.1 mm) and multi-channel nature of the TVIS system may allow the shelf to be mapped for investigation in relation to various parameters (e.g. product temperature, drying rate, collapse event) across various stages of the freeze-drying process (Smith et al., 2017). In spite of this benefit, there are some limitations to this system:

(1) in a similar manner to the thermocouple, TVIS is not suitable for automatically loading systems because it requires manual manipulation;

(2) a thermocouple cannot be placed inside the TVIS vial as the metal of the hardwired thermocouple provides a conduction path to the ground and therefore the spectrum is distorted, as demonstrated in **Figure 41**. However, this perturbation is lessened once the ice has formed (opened circle symbol **Figure 41**), because the high resistance of ice can impede the current flow to the ground. Therefore, it is necessary to have the thermocouple vial juxtaposed with the TVIS vial in order to represent the product temperature in TVIS vial. Fortunately, this TVIS system is compatible with non-metallic temperature sensors such as fibre-optic and wireless sensors (TEMPRIS®), as shown in **Figure 42**. Regarding the compatibility of the TVIS system and the wireless temperature sensor, the variation of product temperature between the TVIS vial and the neighbouring vial was investigated. The temperature calibration of ultrapure water from the quartz-based temperature sensor is consistent with the calibration from the thermocouple, as demonstrated in **Figure 43**. Therefore, it is acceptable to use the temperature from the thermocouple in the nearest neighbouring vial to represent the temperature of the TVIS vial.

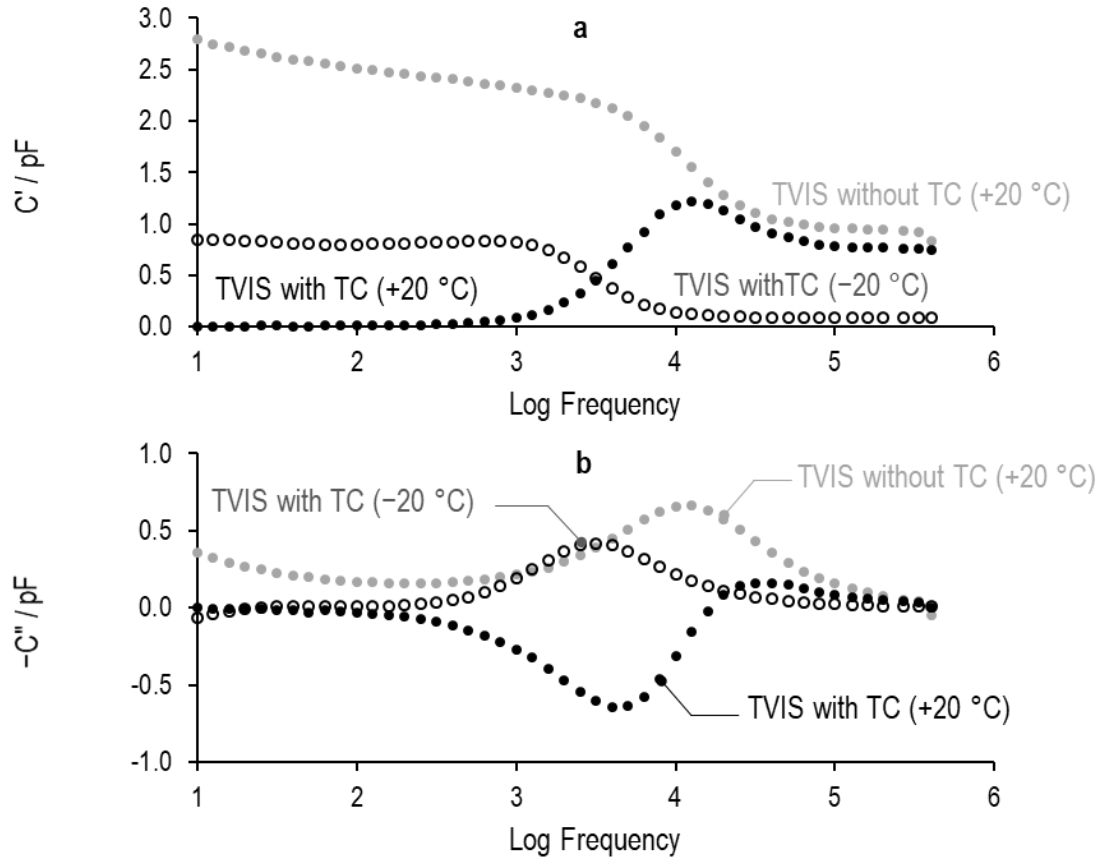

Figure 41 (a) Real and (b) imaginary-part capacitance of 3.5 g ultrapure water contained in the TVIS vial either with or without a thermocouple (TC). The influence of the thermocouple on the liquid spectra (+20 °C) is evidenced by the distortion of the spectrum of water contained in the TVIS vial with a thermocouple (filled circle); however, the thermocouple has a lower impact on the spectrum when the sample is in the frozen state at −20 °C (open circle).

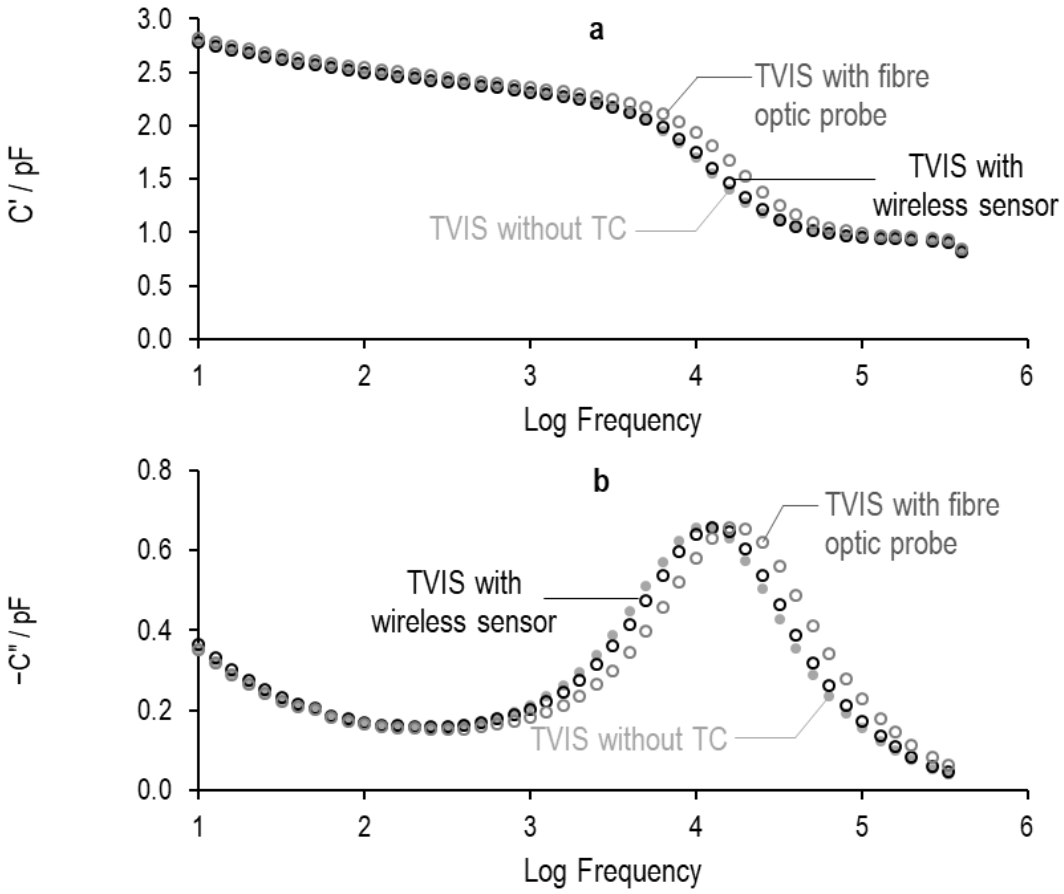

Figure 42 TVIS responses - (a) real part and (b) imaginary part - of a TVIS containing 3.2 g ultrapure water at 19 °C, showing an identical shape between the TVIS vial without thermocouple (TC) and the same vial with either a fibre-optic or wireless sensor (TEMPRIS®).

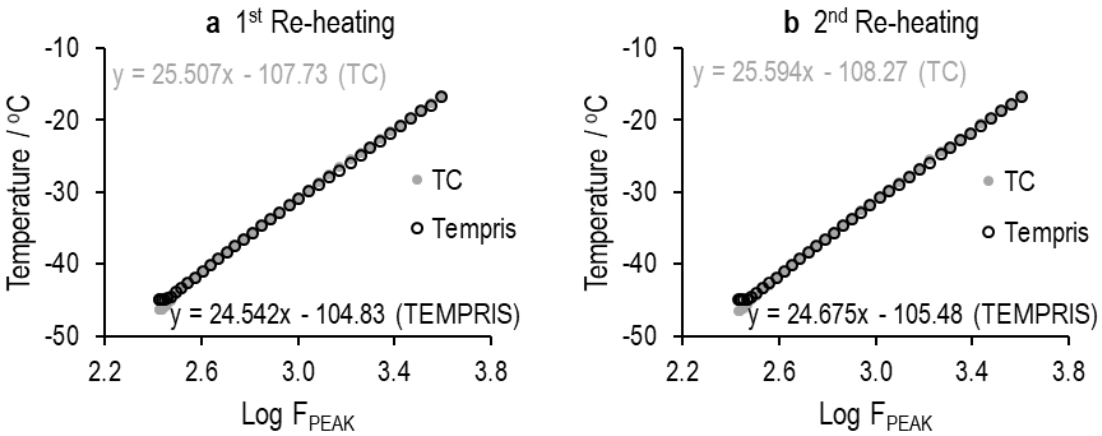

Figure 43 The temperature calibrations of two cycles of re-heating are plotted using the temperature data from (1) thermocouple (TC) in the vial close to the TVIS vial and (2) a wireless system (TEMPRIS®) within the TVIS vial. There is no significant difference in the calibration coefficient between using the product temperature in the nearest neighbouring vial and the temperature in the TVIS vial (measured by TEMPRIS®).

(3) The change in the shape of ice interface over the drying period introduces the uncertainty in TVIS measurements. Since C''_{PEAK} is directly proportional to the ice cylinder that makes contact with the side wall of the glass vial, the loss of ice contact with the glass wall can make a measurement inaccurate. The formation of a cone shape of ice can lead to overestimation of the drying rate; therefore, with this technology, the value of C''_{PEAK} for determining the sublimation rate should be selected from the time where the product temperature is constant (Smith, Jeeraruangrattana & Ermolina, 2018). Another observation obtained during primary drying is that the product temperature from TVIS ($T_{F_{PEAK}}$) diverges from the thermocouple temperature (T_{TC}), i.e. the thermocouple temperature increases whereas $T_{F_{PEAK}}$ continuously decreases. Again, this is because of the presence of air space between the ice and the glass wall, due to the change of the ice front. Smith et al. (2018) demonstrated that the glass wall impedance influenced the dielectric relaxation by increasing the peak frequency; therefore, the absence of the glass wall could shift the dielectric loss peak to the lower frequency, which is then followed by the decrease in $T_{F_{PEAK}}$.

(4) The meniscus of liquid sample in a standard TVIS vial (**Figure 44**d) can impact on the TVIS measurement, including the liquid state calibration. As can be seen in **Figure 44**, the contribution of glass wall capacitance at low frequency (< 250 Hz) is more obvious in the standard TVIS vial. This is probably because the upward curve of a liquid interface close to the surface of the glass vial provides additional glass wall capacitance. To overcome this issue, a vial with hydrophobic coating (TopLyo®) is proposed. The absence of the meniscus (**Figure 44**c) could reduce the contribution from the meniscus to the glass wall capacitance, as shown in **Figure 44**b, leading to a more reliable measurement.

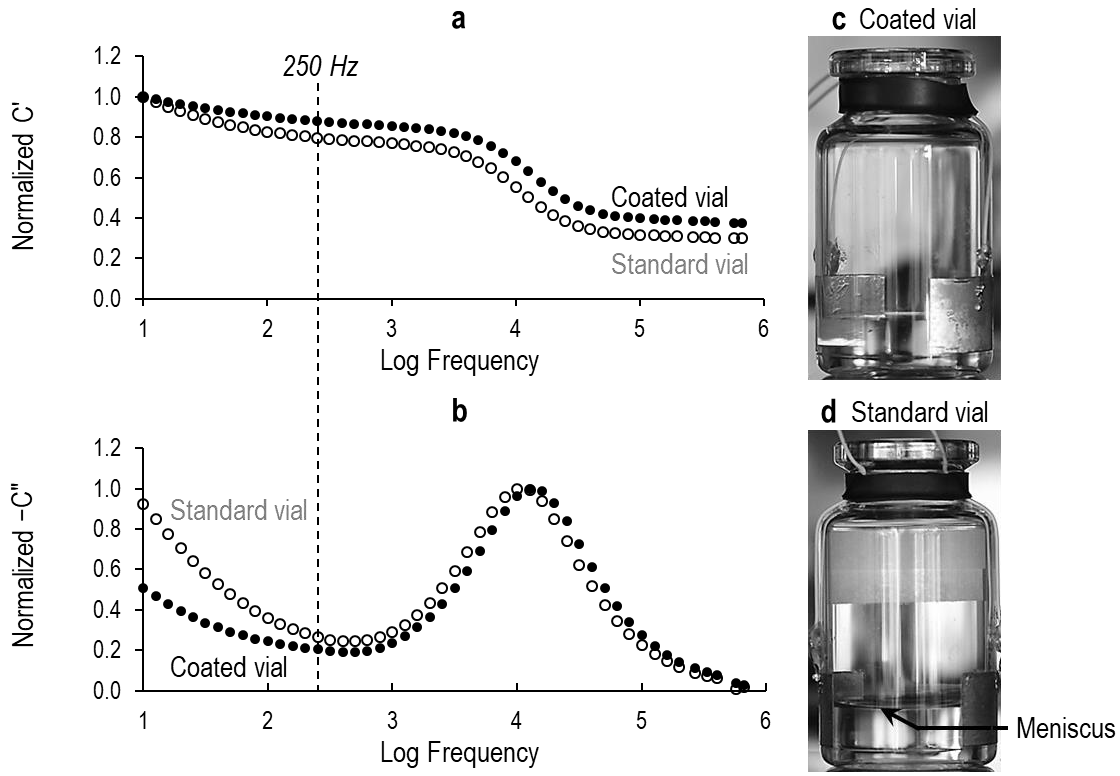

Figure 44 The capacitance spectra, (a) real and (b) imaginary part, of ultrapure water (2.5 g) contained in the TVIS vials, (c) a coated vial (TopLyo®), and (d) a standard vial. The meniscus observed in a standard vial (d) introduces additional glass wall impedance at frequencies below 250 Hz.

6. Electrode optimization for TVIS measurement vial

6.1. Objective

The purpose of this chapter is to optimize the design features of the electrode system for TVIS measurement vial in order to improve the characteristics of the impedance spectrum generated by through-vial impedance spectroscopy, and thereby the quality of the measurement. Different electrode configurations were studied in terms of (1) electrode design (i.e. whether to include guard electrode or not); (2) the electrode height; (3) the method for attaching the electrode to the glass vial; and (4) the position of electrode from the base of the vial. In order to make this assessment, the characteristics of the capacitance spectrum of water filled TVIS vial were recorded at either ambient temperature (Study I-III) or during the freeze drying cycle (Study IV-V). This research work is composed of five studies as summarized in Figure 45.

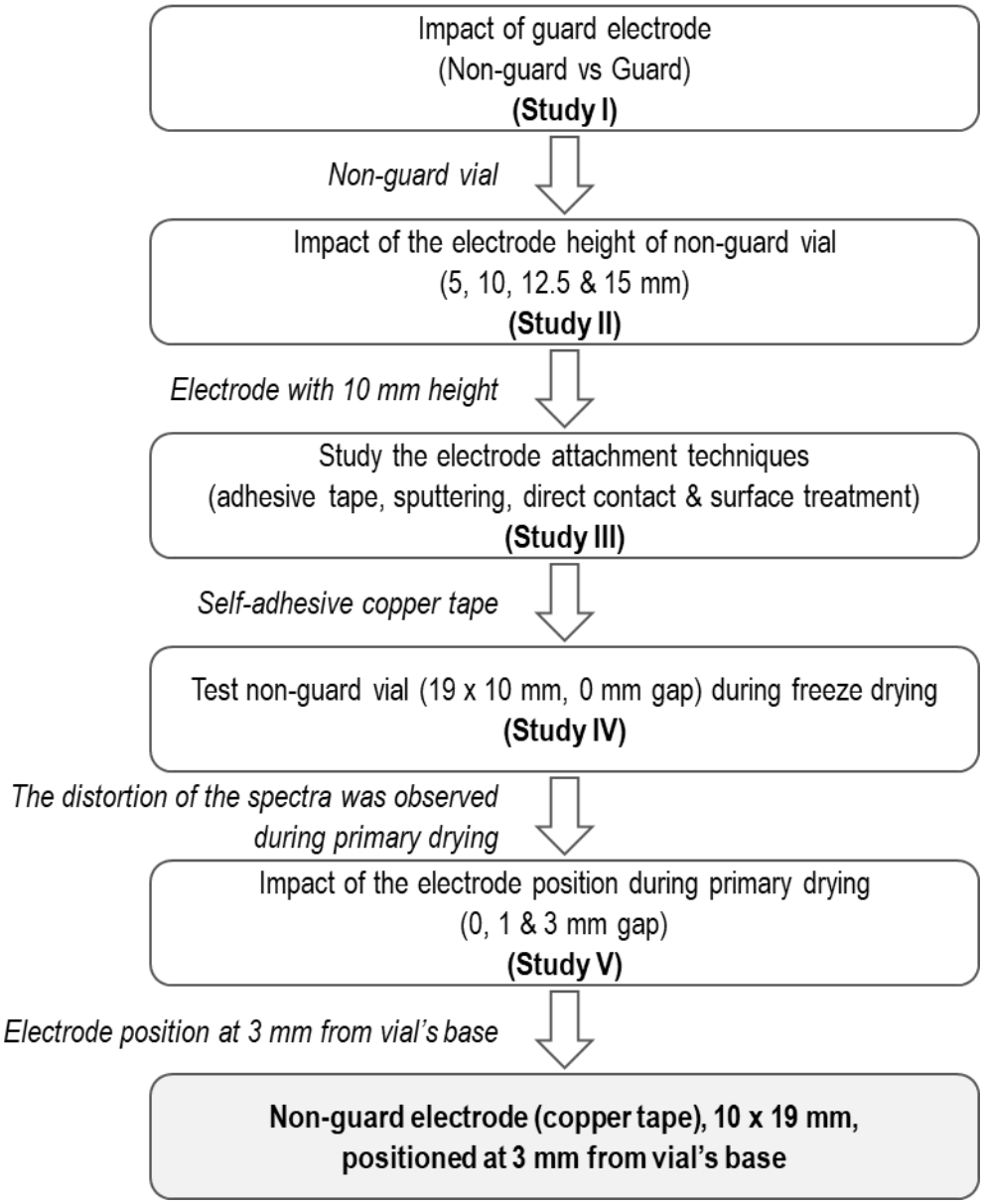

Figure 45 A summary of the experimental studies performed for optimizing TVIS measurement vial.

6.2. Materials and methods

All of the studies presented in this chapter were based on a multichannel impedance analyzer developed by De Montfort University, which hereafter is referred to as **DMU-TVIS.**

Study I

Two grams of double-distilled water was placed in two types of TVIS vials. One TVIS vial had a guard electrode (G) and the other was without guard strip (non-guard or NG), as shown in Figure 46. The electrodes for the guard vial were cut and attached to the vial by a constructor employed by GEA Pharma Systems. Both of these measurement vials had a pair of electrodes, each with dimensions of 18 x 5 mm (w x h), and were positioned just above the base of the vial to avoid the electrode from touching the conductive freeze-drying shelf. Each TVIS measurement vial was connected to the impedance analyzer (DMU-TVIS) via a junction box inside the freeze dryer (Figure 46). The electrical impedance spectra of a water-filled TVIS vial were measured over the frequency range of 1 MHz to 10 Hz at ambient temperature and then presented in Bode plot of real and imaginary capacitance spectra. The measurement data were fitted to the model for liquid water (Smith & Polygalov, 2019) using impedance analysis software (RelaxIS3, rhd instrument, Germany).

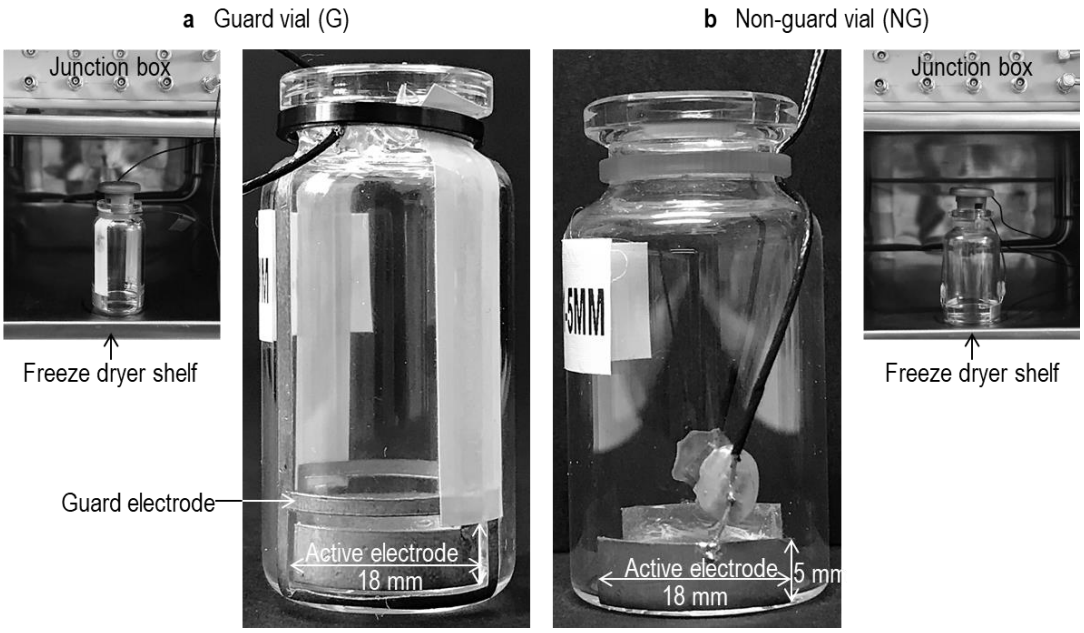

Figure 46 Photographic images of two different types of TVIS measurement vial. (a) TVIS vial with guard vial (G) with guard electrode around the active electrodes, each with dimensions of 18 x 5 mm (w x h). The guard vial with 2 g of double-distilled water placed on the freeze dryer shelf is shown on the left. (b) TVIS vial having only a pair of active electrodes (18 x 5 mm), referred to as the non-guard TVIS vial (NG). The non-guard vial with 2 g of double-distilled water placed on the freeze dryer shelf is demonstrated on the right.

Study II

Four non-guard TVIS vials were constructed from type I tubular glass vial (1096936, Schott, Hungary supplied as VC010-20C from Adelphi - HP). Each had only a single electrode pair (19 mm-wide copper adhesive tape 1181, 3M™) affixed to the outside of the vial, with a small gap between the lower edge of the electrode and the external vial's base (i.e. to avoid the curvature of the bottom heel of the vial). The height of the electrode pair varied from 5 mm to 15 mm, whereas the width of electrode was fixed at 19 mm (**Figure 47**). Aliquots of double-distilled water corresponding to the fill factors (Ø) range between 0.5 and 1.5 were added to each TVIS vial. Each TVIS measurement vial was connected to the impedance analyzer (DMU-TVIS) via a junction box inside the freeze dryer. The impedance responses within the TVIS range (10 Hz-1 MHz) at each filling height were measured at room temperature condition. Note Ø is defined as the relative height of the sample solution within the electrode region to the height of the electrode (see Appendix II for fill factor calculation) and therefore a fill factor of 1.0 is equivalent to water filled up to the upper edge of electrode (Figure 47e). Impedance analysis software, RelaxIS3 (rhd instrument, Germany) was used for fitting the spectrum to the equivalent electrical circuit model for liquid water (Smith & Polygalov, 2019).

Figure 47 Non-guard vials with an electrode height of (a) 5 mm, (b) 10 mm, (c) 12.5 mm and (d) 15 mm. (e) The non-guard TVIS vial with an electrode height of 10 mm (c) was used for demonstrating a liquid level at the fill factor of 1.

Study III

First, four standard 10 mL freeze dry vials (1096936, Schott, Hungary supplied as VC010-20C from Adelphi – HP) were used for making a number of TVIS vials. A pair of electrodes, 19 mm by 10 mm in size, was attached to the external surface of the glass vial. Each electrode in the pair was placed opposite each other and the lower edge of the electrode was located 3 mm from the external vial's base. Four different electrode-attaching techniques were investigated in this study:

Design 1: An acrylic glue of a self-adhesive electrode tape was employed to affix the electrode to the external surface of the glass vial, defined as **Typical adhesive** (Figure 48a). This is a routine approach to the electrode assembly of a TVIS measurement vial. The 19 mm-wide self-adhesive electrode tape (1181, 3M^{TM}) was shaped to have dimensions of ~12 mm height and 19 mm width. The backing of this tape was removed and then directly pressed on to the glass vial. The bottom edge of the electrode sat at the same level as the vial baseline, and then the lower and upper edge of the electrode were trimmed using the electrode trimming machine to position the electrode at 3 mm from the vial's base, and to adjust the electrode height to be 10 mm as mentioned above (see the procedure in Appendix I).

Design 2: A 30-nm film of gold was sputtered onto the external surface of the glass vial under vacuum using a rotary pumped sputter coater (Q150RS, Quorum Technologies, Sussex, UK), defined as **sputtering** (**Figure 48**b). Glass vial covered with masking tape before sputtering. The masking tape was cropped by an area of 19 mm x 10 mm on the opposite side of the glass vial, 3 mm above the external vial's base, leaving region for sputter coating gold.

Design 3: Two copper foil electrodes with dimensions of 19 x 10 mm were cut from the 19 mm-wide self-adhesive electrode tape (1181, 3M^{TM}) and were then placed in direct contact with the external surface of the glass vial by turning the backing of the tape to the

outside (without removing the backing) and carefully wrapping by a translucent adhesive tape to fasten each electrode at a height of 3 mm height from the external vial's base) and ensure no air bubble left behind. This method was named **physical direct contact** (Figure 48c).

Design 4: The outer surface of the glass vial was treated to produce a better bonding between the electrode and the glass surface with dimensions of 19 x 10 mm, 3 mm above from the external vial's base. A conductive metal was securely deposited on a modified glass vial surface. The bespoked vial with **surface treatment technique** (Figure 48d) was outsourced to Morganic Metal Solutions Ltd.

Figure 48 Various attachment techniques are conducted for making the TVIS measurement vials: (a) adhesive tape; (b) sputtering by sputter coater (Q150RS, Quorum Technologies, Sussex, UK); (c) physical direct contact; and (d) glass surface treatment.

In each test of design 1-4, 5 g of ultrapure water was introduced into these prepared vials. The filled amount of water in this study was over the electrode so as to disregard the impact from the fill height of the liquid within the electrode region and the electric fringe field. An impedance response of water contained in TVIS vial was measured by scanning spectrum from 1 MHz to 10 Hz at temperature of 23-24 °C.

Since the interaction at the glass-sample interface could have an impact on the interfacial polarization (especially the measurement of high surface tension liquid), after finishing the

screening test with the standard type I tubular glass vial (1096936, Schott, Hungary supplied as VC010-20C from Adelphi – HP), the most propitious attaching techniques were selected (i.e. only surface treatment technique was excluded) and used for preparing new TVIS measurement vials. This time the standard vials were replaced by the vial with the hydrophobic coating (TopLyo®, 1579612, Schott, Germany supplied as VCTDIN10RTLYO from Adelphi – HP).

Study IV

Aliquots of 2 g double-distilled water (corresponding to a fill factor (Ø) of 0.7) were transferred to a cluster of eighteen 10 mL type I tubing glass vial (1096936, Schott, Hungary supplied as VC010-20C from Adelphi - HP) and one TVIS measurement vial with two 19 x 10 mm copper foil electrodes (19-mm wide copper adhesive tape 1181, 3M™) attached to the outside of the vial (diametrically opposite one another), with a small separation from the external vial's base to avoid direct contact between the electrode and a freeze dryer shelf as demonstrated in **Figure 47**b. The difference between the lower edge of the electrode and the base of the vial is quite small; therefore, it could be treated as zero. Two water-filled vials close to the measurement vial had a type-T, 28 AWG, wire thermocouple (TC), and the thermocouple tips were positioned at the bottom centre of the vial. The average product temperature from those TC vials was to provide a representative temperature for the TVIS vial during the freeze-drying process.

One hundred and sixty vials were arranged on the loading tray of the freeze dryer, with the cluster of 19 water-filled vials at the centre of an array of empty vials. These vials were partially closed with 20 mm 4023/50 bromobutyl grey rubber stoppers (FDW20RTS, West Pharmaceutical Services Singapore Pte. Ltd, Singapore). Then, the full tray of 160 vials with the cluster of water-filled vials (19 vials) at the centre of an array of empty vials was then placed on a single shelf of a VirTis Advantage Plus XL benchtop freeze dryer (SP Scientific, USA). The vial arrangement is illustrated in **Figure 49**a.

The freeze dryer was equipped with a multichannel impedance analyzer (DMU-TVIS) comprising a junction box, pass-through and impedance analyzer (**Figure 49**b). The TVIS measurement vial

was connected to the DMU-TVIS impedance analyzer (located outside the freeze dryer, **Figure 49**d) via the junction box (inside the freeze dryer, **Figure 49**c) and the pass-through (installed on one of the side manifold, **Figure 49**d).

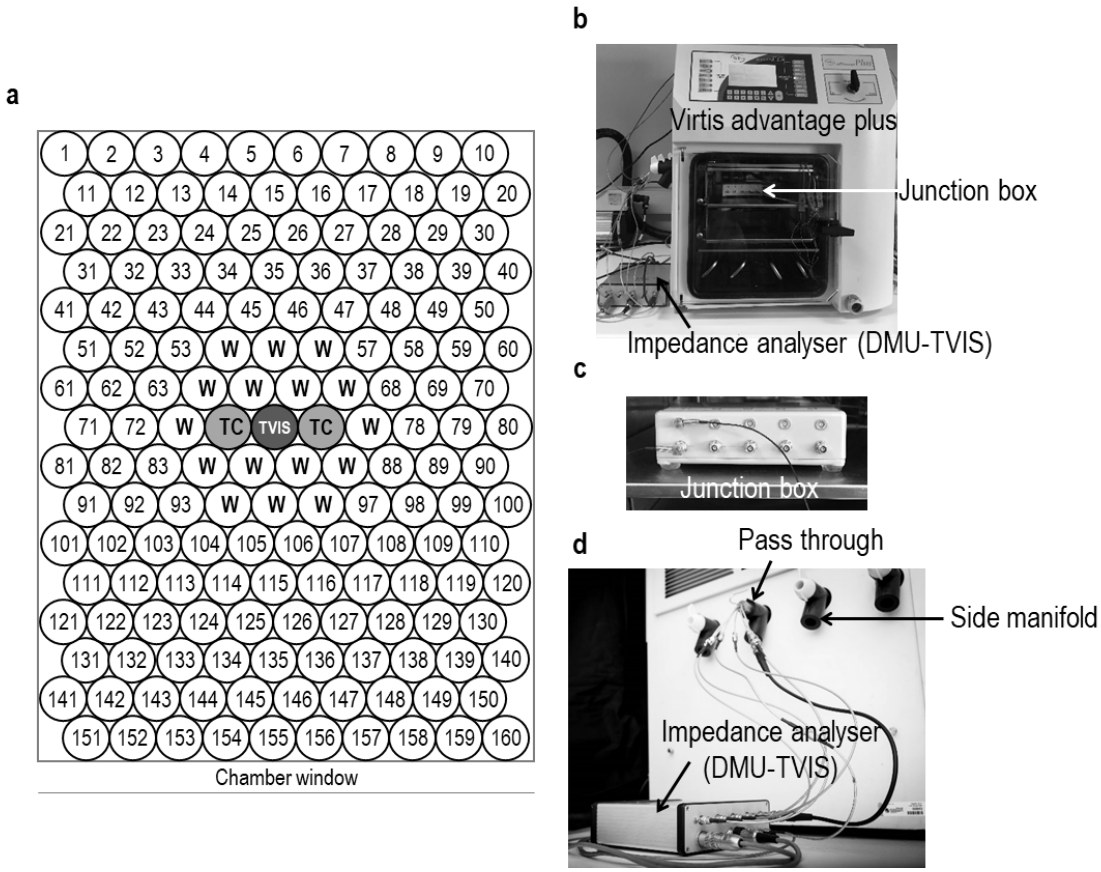

Figure 49 (a) Vial arrangement on a single shelf of the freeze dryer. The TVIS modified vial (labelled TVIS, position 75) and two thermocouple containing vials (labelled TC, position 74 & 76) were placed at the centre of the shelf. The water-filled vials are represented by "W" and those left empty are labelled with the number position in the dryer; (b) a Virtis Advantage Plus XL freeze dryer (SP Scientific, USA) equipped with DMU- TVIS system; (c) a junction box placed on the top shelf of the freeze dryer; and (d) a pass-through enabling the signal to be transmitted from the TVIS vial to the impedance spectrometer (DMU-TVIS).

A freeze-drying protocol with an annealing step (**Table 4**) was operated. The impedance spectrum was recorded across the frequency range of 1 MHz to 10 Hz, every 2 minutes throughout the freeze-drying process. The measurement time to acquire each spectrum was ~ 10 s. The measurement data was fitted to the established model (Smith & Polygalov, 2019) by using impedance analysis software (RelaxIS3, rhd instrument, Germany).

Table 4 Freeze drying protocol for study IV

Step	Temperature (°C)	Time (min)	Cumulative Time (h)	Set pressure (µbar)
Equilibrium phase	+20	10	0.17	-
Freezing temperature ramp (0.7 °C·min^{-1})	−40	90	1.67	-
Freezing temperature hold	−40	120	3.67	-
Re-heating temperature ramp (0.5 °C·min^{-1})	−10	60	4.67	-
Re-heating temperature hold	−10	120	6.67	-
Re-cooling temperature ramp (0.5 °C·min^{-1})	−40	60	7.67	-
Re-cooling temperature hold	−40	120	9.67	-
Primary drying temperature ramp (0.3 °C·min^{-1})	−20	60	10.67	400
Primary drying temperature hold	−20	1250	31.50	400

Study V

Two clear type I glass vials with a nominal capacity of 10 mL (1096936, Schott, Hungary supplied as VC010-20C from Adelphi – HP) were used for preparing a new configuration of the TVIS measurement vial. On the external glass wall of each vial a pair of 19 x 10 mm (w x h) conductive electrodes was fixed, in the parallel opposite direction. For one of the two, the lower edge of the electrodes was positioned at 1 mm from the vial baseline (TVIS1, **Figure 50**a) while for the other they were above the vial's base at 3 mm (TVIS3, **Figure 50**b). The position and size of the electrodes were adjusted using the in-house cutter (**Figure 50**c). The procedure is presented in Appendix I.

Figure 50 The TVIS measurement vial with the electrodes positioned at (a) 1 mm from base (TVIS1); and (b) 3 mm from base (TVIS3). The right image demonstrates the filling volume of double-distilled water corresponding to a fill factor 0.9 for each electrode configuration; (c) electrode trimming machine

The TVIS measurement vial with a distance of 1 mm from the vial's base (TVIS1) and one standard plain vial were filled with double-distilled water 3.2 g, whilst 3.5 g of the same water was added to the other TVIS measurement vial (with electrodes positioned at 3 mm from vial's base, TVIS3) and a plain vial. The filling weight of 3.2 and 3.5 g is equivalent to a liquid fill height

of 9 mm from the lower edge of the electrode, which corresponds to a fill factor (Ø) of 0.9. The fill factor calculation is illustrated in Appendix II. Each of two plain vials (filled with water, either 3.2 g or 3.5 g) had a thermocouple (type T, 28 AWG) inserted into the vial in order to record the product temperature during the lyo cycle. The TC vial with 3.2 g water was juxtaposed with the TVIS1 (i.e. the vial with the electrode at 1 mm from its base), and likewise the TC vial with 3.5 g of water juxtaposed with TVIS3.

An average filling weight of ~3.4 g was transferred into a cluster of fifteen plain vials. These water-filled vials (15+4=19 vials) and 141 empty vials were arranged on the loading tray as per the layout in Figure 51, and then loaded into a laboratory-scale freeze dryer, VirTis Advantage Plus XL benchtop freeze dryer (SP Scientific, USA). The freeze-drying protocol is similar to the protocol used in Study IV (**Table 5**), but the primary drying time was extended over a longer period in this experiment due to greater ice mass. The impedance spectra of the TVIS vials were taken over the frequency range of 10 Hz to 1MHz, every 2 mins throughout the entire freeze-drying process. Based on Study IV, the distortion of the spectra was observed in the primary drying process and became more obvious as sublimation proceeds. Therefore, the TVIS responses were taken at: (1) 0.2 h where the stabilized chamber pressure reached demonstration of the normal response, and (2) a time after ice sublimed more than 50%, for investigating the distortion. In this study, the time at which C''_{PEAK} reduced by 70% from its initial value was selected because we can easily detect the distorted shape and also avoid uncertainty arising from the fringing effect near the edge of the electrode. The spectrum of these time points of both Study IV (no space between the electrode and the vial's base, 0 mm) and Study V (1 mm and 3 mm) were compared with each other. An impedance analysis software (RelaxIS3, rhd instrument, Germany) was used to fit the data with the model of frozen water (Smith & Polygalov, 2019).

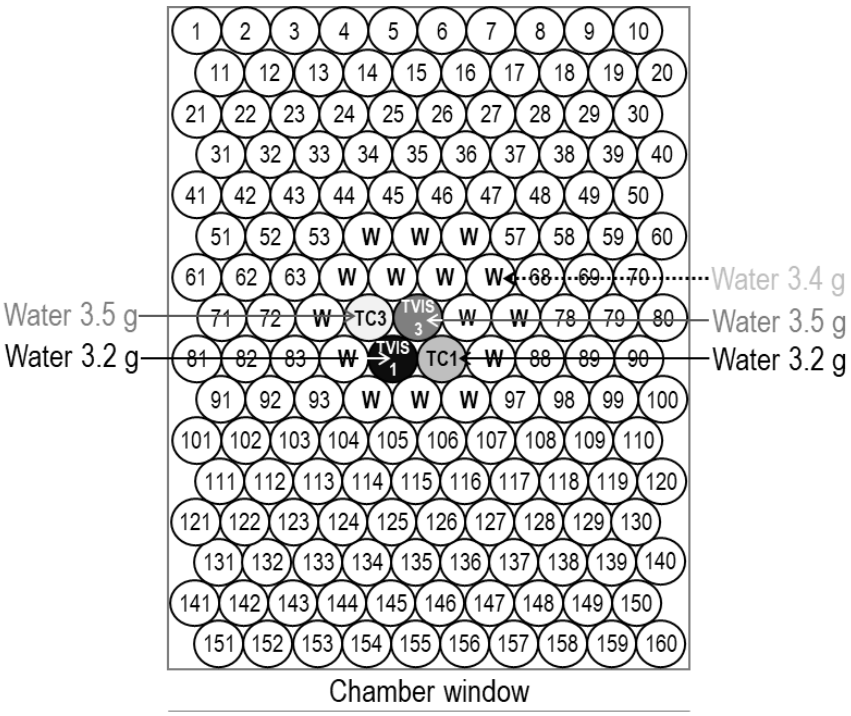

Figure 51 An arrangement of vials loaded into the freeze dryer. The TVIS vial with a distance from base of 1 mm (labelled as TVIS1, position 85) and 3 mm (labelled as TVIS3, position 75) were filled with water (3.2 g and 3.5 g, respectively). Two thermocouple-containing vials placed close to the TVIS vials are filled with water (3.2 g and 3.5 g) for representing the ice temperature in TVIS1 and TVIS3, respectively. The "W" denotes the other water-filled vials and those left empty are labelled with the position number on the freeze dry shelf. A cluster of nineteen water-filled vials is arranged at the centre of an array of the empty vials. All 160 vials are loaded into a Virtis Advantage Plus XL freeze dryer (SP Scientific, USA)

Table 5 Freeze-drying protocol for Study V

Step	Temperature (°C)	Time (min)	Cumulative Time (h)	Set pressure (µbar)
Equilibrium phase	+20	10	0.17	-
Freezing temperature ramp (0.7 °C·min^{-1})	−40	90	1.67	-
Freezing temperature hold	−40	120	3.67	-
Re-heating temperature ramp (0.5 °C·min^{-1})	−10	60	4.67	-
Re-heating temperature hold	−10	120	6.67	-
Re-cooling temperature ramp (0.5 °C·min^{-1})	−40	60	7.67	-
Re-cooling temperature hold	−40	120	9.67	-
Primary drying temperature ramp (0.3 °C·min^{-1})	−20	60	10.67	400
Primary drying temperature hold	−20	1920	43.00	400

6.3. Results and Discussion

Study I

In the early stages, this technology was based on 10 mL Type I glass vials with an electrode pair and each electrode surrounded by a guard ring defined as guard vial (Figure 46a) (Smith et al., 2013;; Smith et al, 2014a; Smith et al., 2014; Arshad et al., 2014; Smith et al., 2017). However, a measurement vial with guard configuration was complicated to make. Therefore, the non-guard electrode (NG) vial was introduced (Figure 46b).

For the purpose of Study I, the influence of the guard on the measured capacitance was studied. A capacitance spectrum of water contained in two types of measurement vials, one with a guard and the other with a single electrode pair, was measured and then compared.

Peak amplitude (C''_{PEAK}) and the magnitude of the step in the real-part capacitance ($\Delta C'$) of water measured in the guard vial was in the range of approximately 2.7 times less than non-guard one, as shown in Figure 52. For instance, C''_{PEAK} value of 0.14 pF and 0.39 pF were obtained from G and NG vial, respectively. A small difference in peak frequency (F_{PEAK}) observed in Figure 52b could be affected by: (1) size of a measurement container as demonstrated by Smith and his co-worker (2014) (i.e., the ratio of internal diameter of G to NG vial is ~ 0.98); and (2) the instrument itself (i.e. heat producing). However, the latter issue is usually observed when the measurement proceeds over a long period, and it could then be ignored in this experiment.

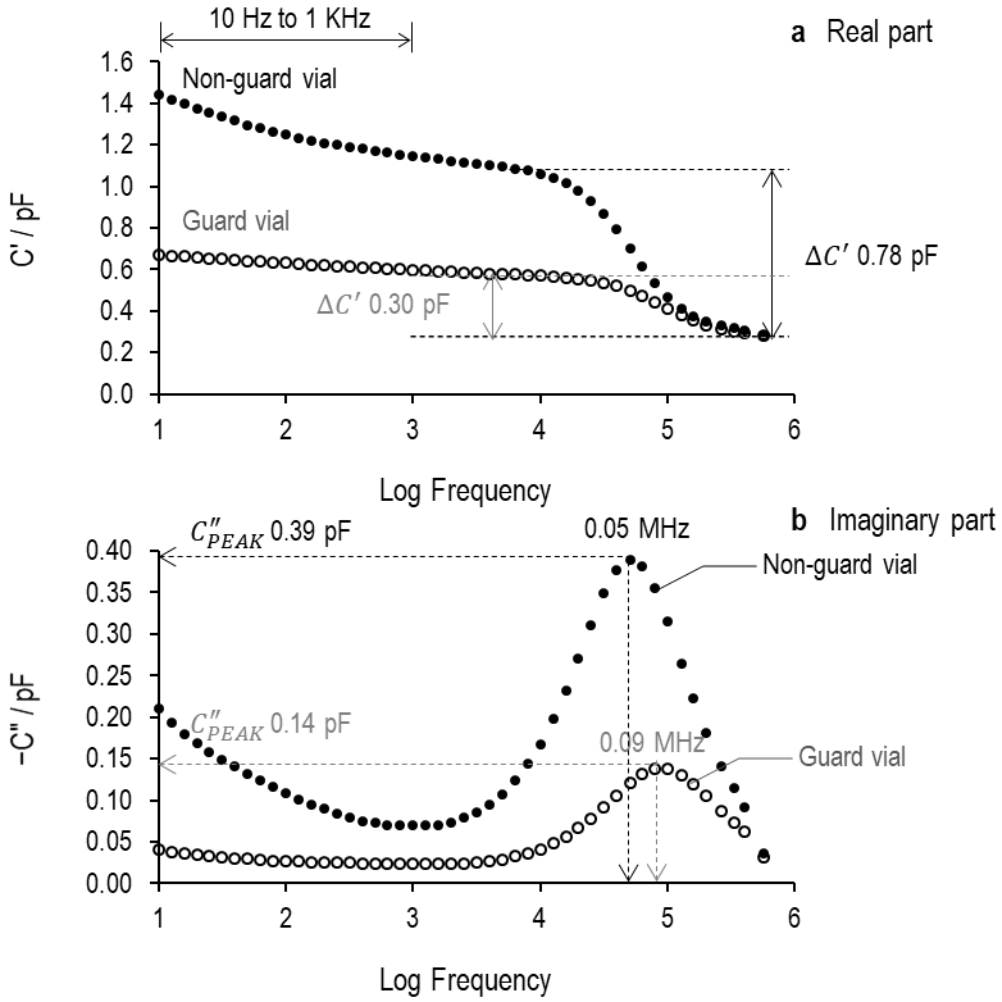

Figure 52 (a) Real and (b) imaginary-part capacitance spectra of 2 g liquid water contained in TVIS vial with a guard (open symbol) and without one (closed symbol). Both types of TVIS vials have 5 mm height for the active electrode. The measurement was conducted at ambient temperature.

The larger capacitance of the non-guard vial compared to the vial with guard might be due to the fact that the guard electrode, which is used for minimizing the fringing effect at the edge of electrode of a parallel plate capacitor, could reduce the charge accumulation on a glass surface where an active electrode was located, and consequently decrease a measured capacitance according to a direct relation between capacitance and the charge deposit on an electrode plate (Equation 58). An illustration is given in Figure 53.

$$\boldsymbol{C} = \frac{Q}{V}$$ Equation 58

where $\boldsymbol{C}$ is the complex capacitance, Q is an electric charge on electrode plate, and V is an applied voltage.

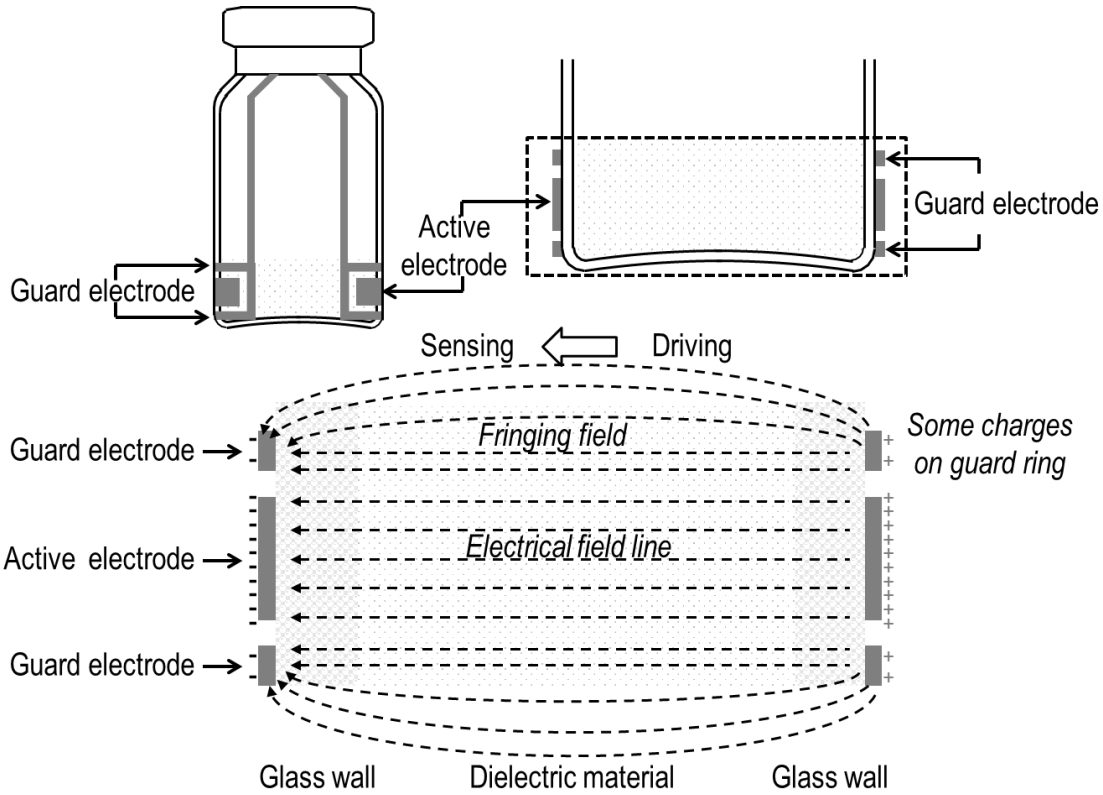

Figure 53 A schematic illustration showing the influence of the presence of a guard electrode on the electric field at the border of the active electrodes (sensing/driving electrodes). A fringing effect at the edge of the measurement electrodes can be reduced by surrounding these electrodes with a guard ring.

Any change in the amount of electric charge adsorbed on to the surface of the glass wall, close to the sensing/driving electrode, would alter the characteristic of a glass capacitor. These characteristics of the two electrode systems could be quantified by implementing an equivalent circuit model suggested by Smith and Polygalov (2019). The measurement data of a test object (i.e. water contained within the TVIS vial) was fitted to the equivalent circuit model for characterizing the properties of the material under test. The impedance response of the liquid sample filled in TVIS vial could model by circuit elements as follows: the glass capacitance (C_G);

a constant phase element (CPE); a solution capacitance (C_s); and a solution resistance (R_s). In this model, the conductive and dielectric properties of the sample were demonstrated by R_s and C_s in parallel (i.e. R_s=C_s) whereas the glass-solution interaction behaviour, including dispersion at low frequency, was represented by C_G and CPE in parallel with each other (i.e. C_G=CPE). The electric component, CPE, usually contributes to the non-ideal capacitor. Since the applied voltage drops during current flows through a test object which comprises the glass vial and liquid component, for the final model, both parallel circuit elements combine in series, i.e. (C_G=CPE)-(R_s=C_s) as illustrated in Figure 54.

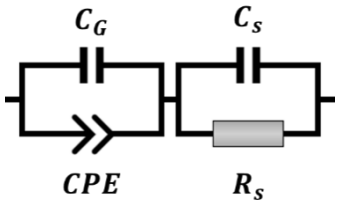

Figure 54 Equivalent circuit model for the TVIS vial containing the sample in the liquid state. C_G is a glass wall capacitance, CPE element is a low frequency contribution of glass wall, C_s and R_s are sample capacitance and resistance, respectively.

From the fitting results, the relative uncertainty (RE) of each circuit parameter for both vial types (i.e., G and NG) was within an acceptable range identified by the software (RE between 0.1% and 30%), as shown in **Figure 55**; therefore, this demonstrates that this model could define the mechanistic behaviour of water in the TVIS vial. As can be seen in the fitting results in **Table 6**, one would expect a low-frequency response C_G of the guard assembly vial to be less than the non-guard vial following Equation 58, as mentioned above. The glass wall capacitance (C_G) decreases from 1.04 pF (NG vial) to 0.52 pF (G vial). An anticipated finding is that the low-frequency dispersion behaviour is obvious in the measurement vial without a guard, owing to the fact that the feature of low-frequency response results from the protonic charges percolating through the microstructure of glass. Therefore, the less the surface charge accumulation (i.e. the existence of a guard could reduce the charge accumulated at the active electrodes), the less low-frequency dispersion behaviour as demonstrated by the more flat response in the frequency range of 10 Hz to 1 kHz in **Figure 52**. Due to the proton percolation,

an additional admittance (Y, the measure of the ease with which the current flows in the circuit or electronic device) is considered for the low-frequency dispersion that is usually modelled by CPE element (Y_{CPE}). The expression of Y_{CPE} element is given by the impedance analysis software (RelaxIS3, rhd instrument, Germany) as below:

$$Y_{CPE} = Q(i\omega)^{\alpha} \qquad \text{Equation 59}$$

where i is an imaginary number, ω is angular frequency (rad·s^{-1}), Q and α are parameters of CPE element, Q is the value of admittance and the unit of Q is F, and α is CPE exponent corresponding to the phase angle (dimensionless). If α equal 1, the CPE behaves like an ideal capacitor with the phase angle of −90° while it behaves as a resistor when α is zero.

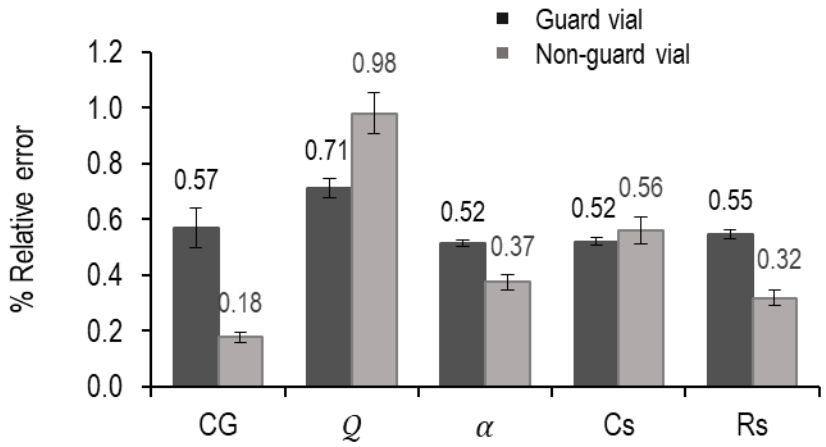

Figure 55 Percentage relative error of measurement data to fitting data from $(C_G{=}CPE)$-$(R_s{=}C_s)$ model. Note Q and α are CPE parameters.

The non-ideal response of the glass wall capacitance could be confirmed by considering the alpha parameter of constant phase element (α) that described an imperfect capacitor (i.e. α < 1). From fitting results shown in Table 6, the alpha parameter obtained from the guard vial was closer to 1 (α = 0.85) compared to the non-guard one (α = 0.70). The results demonstrated that the greater deviation from a pure capacitor was found in the non-guard vial, such that low-frequency dispersion is more noticeable (more tailing) when the guard assembly was removed.

Another CPE parameter is Q. It is observed that the Q parameter of the NG vial is higher than the G vial by a factor of ~3. It seems possible that these results are due to the percolation charge transport at the glass wall. In Equation 59, the Q parameter is directly proportional to the admittance, and is, in turn, inversely proportional to the impedance. If this parameter has a lower value then an amount of the carrier electron is low, leading to low charge accumulation and followed by a lower capacitance value (Equation 58). It might be concluded that one factor dominating process strength was the glass-sample polarization mechanism, which was impacted by the guard electrode through the modification of charge accumulation.

Table 6 The parameters from the fitting data of water contained in two types of TVIS vials (i.e. guard vial and non-guard vial) to the model, $(C_G{=}CPE)$-$(R_s{=}C_s)$, over 10 Hz to 0.5 MHz

Circuit element parameters	Fitting results	
	Guard vial	Non-guard vial
C_G	0.52E-12	1.04E-12
Q	0.30E-12	1.58E-12
α	8.52E-01	7.01E-01
C_s	5.90E-13	4.24E-13
R_s	1.45E+06	2.00E+06

Also, the influence of a low-frequency dispersion of the CPE element on the peak frequency and the peak amplitude was observed. By simulation of the CPE element only (the dotted lines in Figure 56), it was clear that this element could shift both the amplitude and the frequency of a dielectric process of the sample in the vial, i.e. Maxwell-Wagner polarization (the grey lines in Figure 56). For instance, in the case of the guard assembly vial, the CPE element could increase the peak amplitude from 0.12 pF to 0.14 pF, while the peak frequency moved from 0.1 MHz to a lower frequency (89 kHz). Although a dispersion response could affect a dielectric relaxation process (i.e., C''_{PEAK} and F_{PEAK}) in both vial types, the non-guard vial had a relatively low impact because a signal intensity of the NG vial containing water was substantially higher than the G vial.

Furthermore, the vial with a guard had a measurement uncertainty of glass wall capacitance (RE of C_G 0.57%) higher than the vial without a guard (RE of C_G 0.18%) by a factor of ~3 (**Figure 55**). This suggested that the guard vial had a greater impact on measurement uncertainty. Since the non-guard electrode vial provided an intensive signal with an acceptable uncertainty of measurement, and is also easier to manufacture, the TVIS vial with the single electrode pair design was then selected for further research.

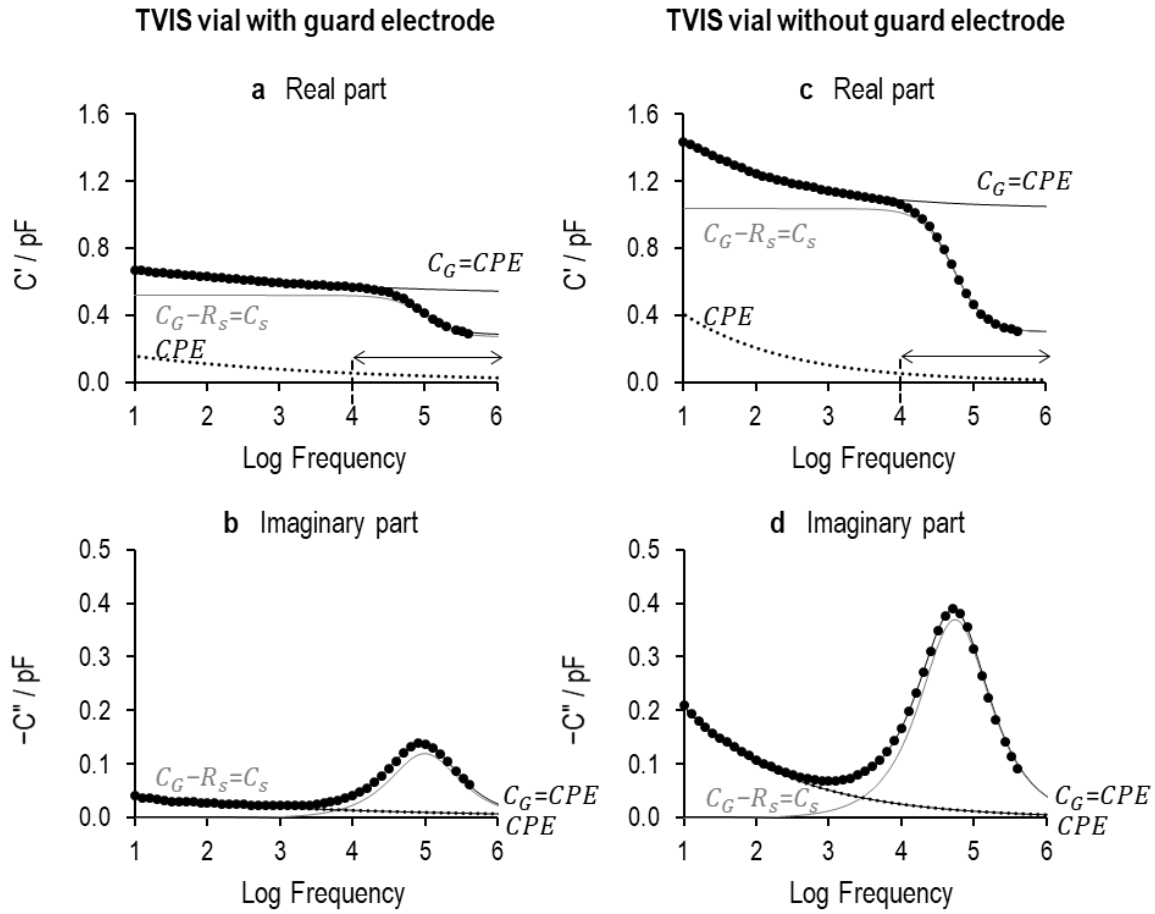

Figure 56 (a) Real and (b) imaginary part of the capacitance spectrum of water filled in the guard vial; (c) real and (d) imaginary part of the capacitance spectrum of water filled in the non-guard. The measurement is performed at room temperature. The black dots represent the measured data points whereas the simulation results of three models are represented as follows: the grey solid line is a typical model of liquid contained in the TVIS vial, C_G-(R_s=C_s); the black dot line represents a non-ideal behaviour of the capacitor at low frequency (CPE); and the black solid line is the glass wall-sample contribution element (C_G=CPE). The double-headed arrow (a and c) marks the dielectric relaxation range. The impact of CPE (low) on the peak amplitude and peak frequency is illustrated.

Study II

In the second study, four different electrode heights with three different fill factors were studied with water. The electrode heights of 5, 10, 12.5 and 15 mm and the fill factors (Ø) 0.5; 1.0 and 1.5 were compared

From **Figure 57**, at each electrode height the amplitude of an imaginary-part capacitance increased as the fill volume increased in a linear relationship when the water level was beneath the electrode. A dependency of C''_{PEAK} on sample height within the electrode region could be clarified by a parallel plate capacitor equation as follows:

$$\boldsymbol{C} = \frac{\varepsilon_o \boldsymbol{\varepsilon} A}{d} \qquad \text{Equation 60}$$

where $\boldsymbol{C}$ is the complex capacitance, ε_o is the vacuum permittivity (8.854 x 10^{-12} F·m^{-1}), $\boldsymbol{\varepsilon}$ is the complex dielectric permittivity, A is the area of an electrode plate bounded by dielectric, and d is the average distance between the electrode pair (in other words, the thickness of the dielectric material).

A gradual increase in capacitance response arose from a filling height discontinued when liquid was over the electrode. This might be because a contribution of the fringing effect to liquid in the region, which was above the electrode, could increase a sample capacitance; meanwhile, a glass capacitance was nearly constant, as shown in Figure 58. When comparing the two filling volumes (i.e., Ø = 1 and 1.4), it was clear that the glass wall capacitance had only ~2 % difference; this was a contrast with the sample capacitance, which had a percentage difference as high as ~33 %. As a result of this, an overall impedance response decrease can be seen, particularly, C''_{PEAK}.

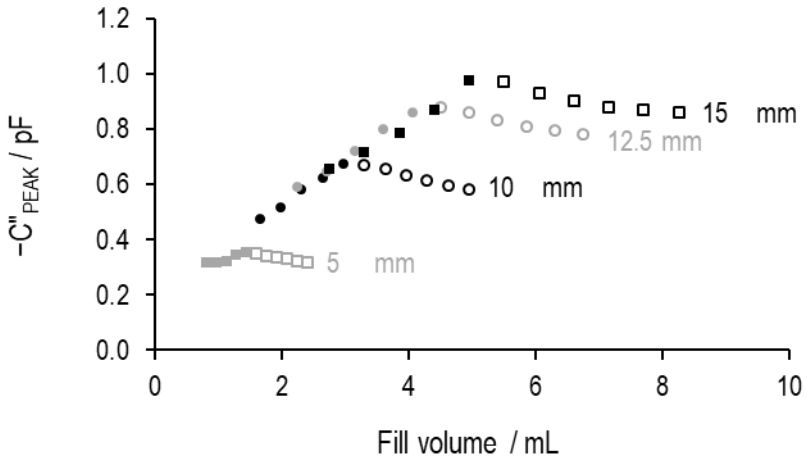

Figure 57 A non-guard measurement vial (nominal capacity 10 mL) with the following electrode geometries: 5 mm height (grey square); 10 mm height (black circle); 12.5 mm height (grey circle) and 15 mm height (black square), is used for measuring the capacitance spectra of water at different filling volumes (fill factor between 0.5 and 1.5). Peak amplitude (C''_{PEAK}) derived from data at liquid level below and above the upper edge of electrodes is represented by the closed circle and open circle symbol respectively.

The sample volume corresponding to a fill factor of 0.8 was used for further investigation in order to avoid a non-uniform electric field at the electrode edges. A fit model was performed to distinguish measurement uncertainty among electrode geometries. No noteworthy differences were found between them. A discrepancy of percentage error between electrode configurations was less than 1% in each circuit parameter (Figure 59). It would appear that the electrode having a length range from 5 mm to 15 mm could be applied for TVIS measurement. However, in general, preparation for freeze-drying typically fills one-third of a nominal vial capacity. In the case of a standard 10 mL vial (1096936, Schott, Hungary), which has a 32 mm height for nominal volume (overall height 46 mm), a 10 mm electrode seems more practical for lyophilization process and therefore this geometry was selected for the next study.

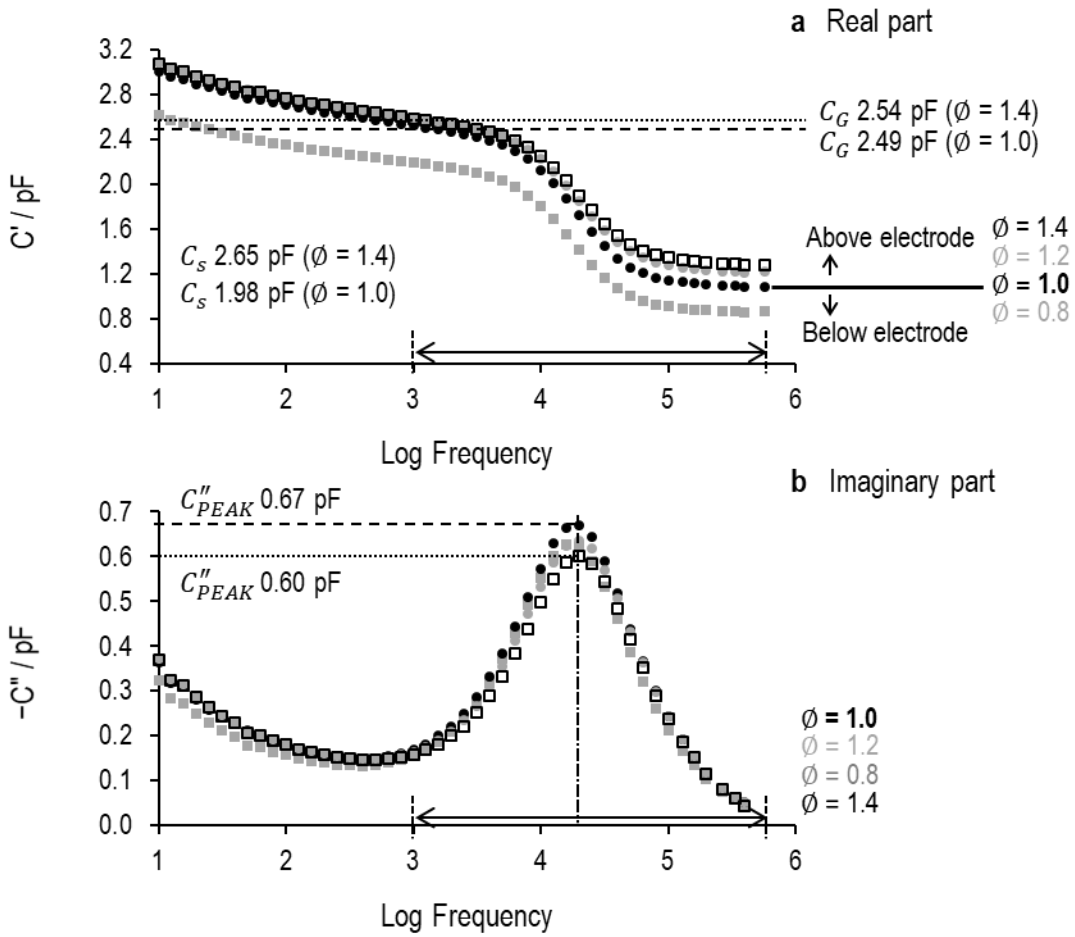

Figure 58 (a) Real and (b) imaginary-part capacitance of double-distilled water contained in a 10 mL standard vial attached with electrodes (10 mm height and 19 mm width) at four different fill factors: 0.8 (2.6 mL, grey filled square), 1.0 (3.3 mL, black filled circle), 1.2 (4.0 mL, grey filled circle) and 1.4 (4.7 mL, black open square). These were exemplified to demonstrate a decrease in the peak amplitude when the water level is above the electrode. A frequency range of 1 kHz to 0.5 MHz is selected for fitting to discard the effect of a low-frequency dispersion and high-frequency noise.

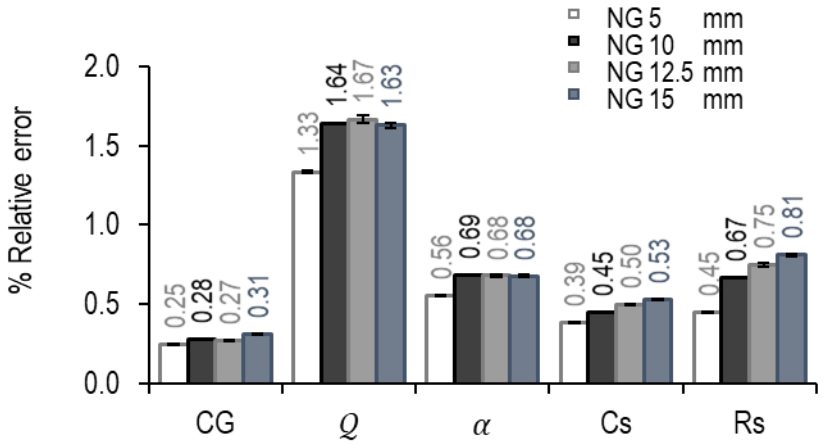

Figure 59 Percentage errors of water spectrum contained in the non-guard vial with the following electrode height: 5, 10, 12.5 and 15 mm. Relative error of water at a fill factor of 0.8 is calculated based on the basic model comprising constant phase element, $(C_G{=}CPE)$-$(R_s{=}C_s)$. The data within a frequency range of 0.5 MHz to 10 Hz have been analyzed.

Study III

Currently, the TVIS vial has used a self-adhesive copper electrode tape (3M™, 1181 with a width of 19 mm), but it is not clear whether acrylic glue used in copper foil has any influence on a measurement spectrum. In addition, the loss of adhesion, especially at the margin of electrode, usually happens when used over a long period of time. Thus, the following electrode attachment techniques have been first evaluated using a standard vial: (1) glue; (2) sputtering; (3) physical direct contact (i.e., copper foil was directly contacted to glass surface by turning adhesive inside out, and wrapped by Sellotape); and (4) surface treatment (i.e., copper was securely deposited on a modified glass vial surface), first performed in a standard vial.

From Figure 60, it was clear that surface modification (4) changed the properties of glass wall, resulting in an irregular spectrum, in the low frequency region (i.e., 0.2-3 kHz) in particular. However, it wasn't clear whether acrylic adhesive, physical direct contact or ordinary gold sputtering provided a better result (**Figure 60**). In order to verify this, a TopLyo® vial has been introduced to minimize the impact of interfacial polarization process occurring at glass-sample interface.

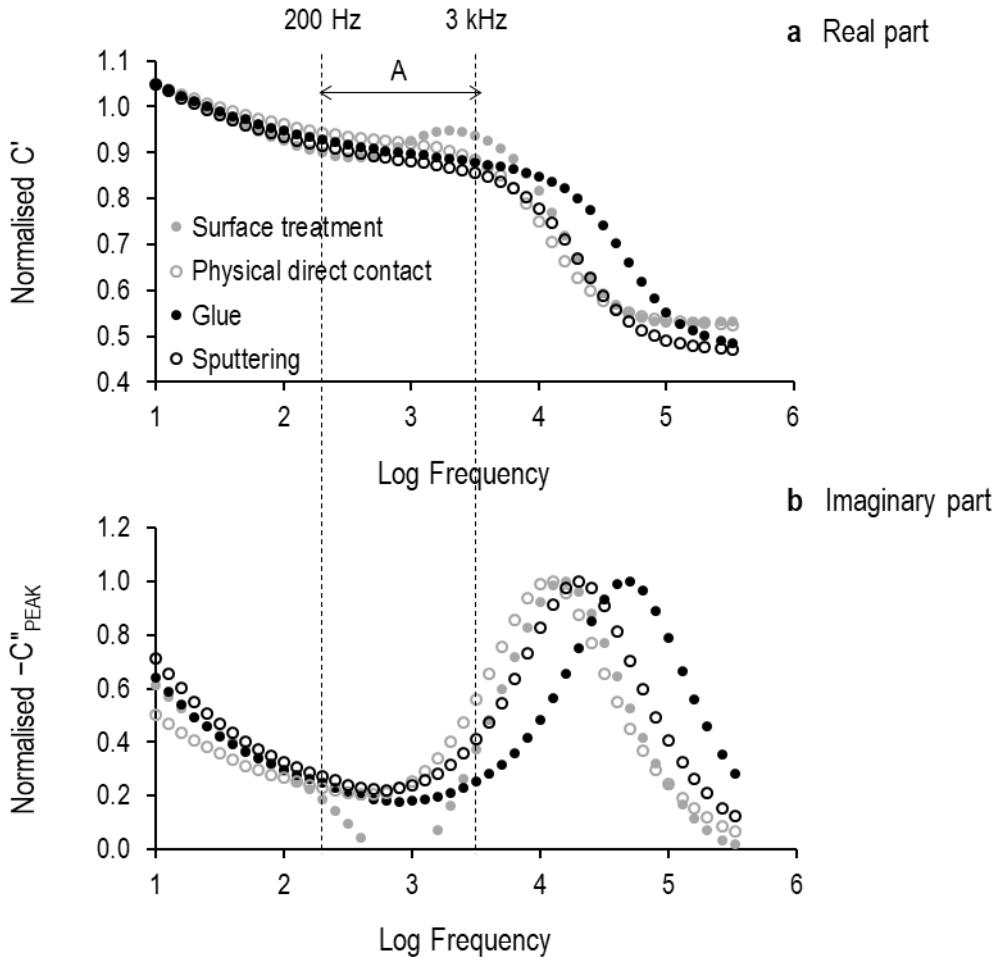

Figure 60 (a) Real and (b) imaginary-part capacitance in a normalised scale of liquid water at ambient temperature (23-24 °C). The measurement results of 5 g water filled in the TVIS vial, attached with a 19 x 10 mm electrode pair at a distance of 3 mm from the vial's base, using various attaching methods: surface treatment (grey closed symbol); physical direct contact (grey opened symbol); glue (black closed symbol); and sputtering (black open symbol). These were compared with each other.

The results in Figure 61 are somewhat surprising in that there is no significant discrimination between these three techniques (i.e. gold sputtering coating, physical direct contact and copper electrode tape). However, we found that the physical contact method has a problem with reproducibility because it is difficult to fasten rigid electrodes on to the curved surface of vial without an air gap. The results also demonstrate that the acrylic adhesive layer on the copper electrode tape does not influence the TVIS measurement such that it is acceptable to use this tape. Additionally, the TVIS vial made from the electrode tape is relatively cheap, is easier to prepare, and is more durable compared to gold sputtering: gold deposits on the glass surface

can come off more easily and require a protective coating. Therefore, the copper tape could be used as a routine method of making the TVIS measurement vial for research purposes.

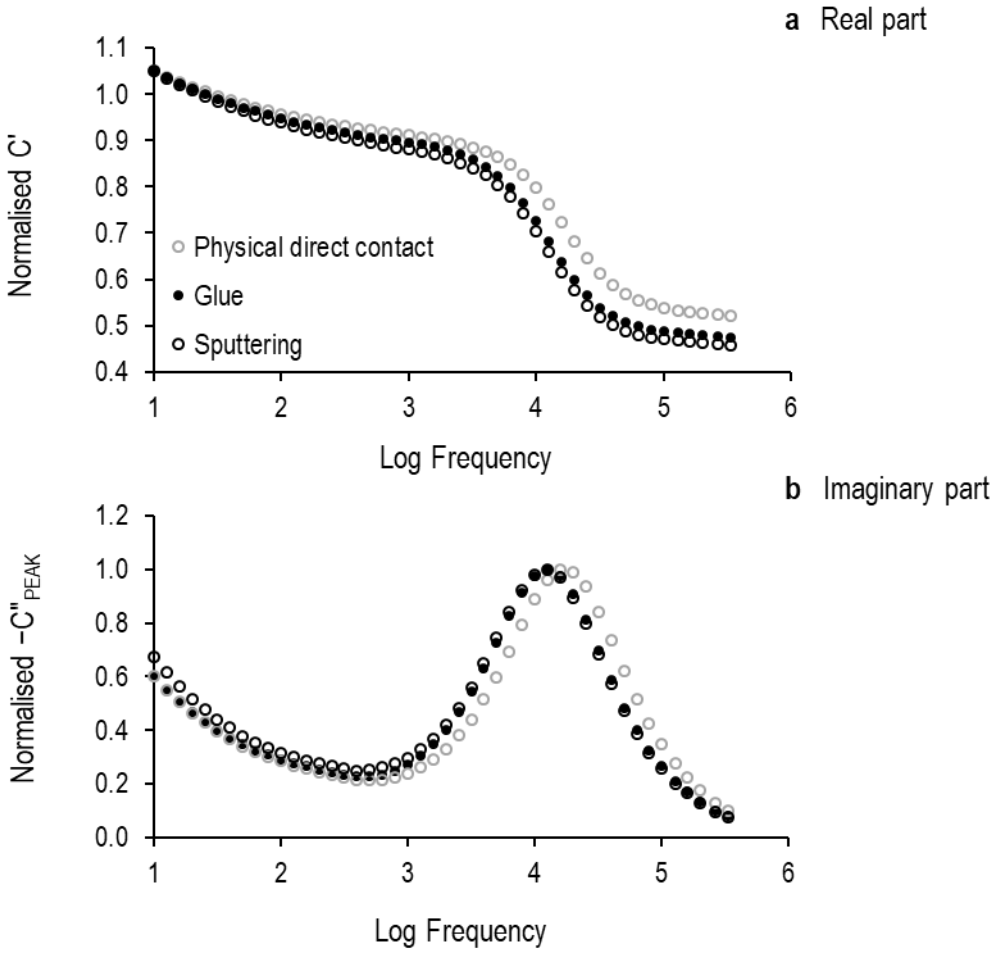

Figure 61 (a) Real and (b) imaginary-part capacitance in normalised scale of two TVIS vials, each containing 5 g of liquid water. Both vials were prepared from 10-mL type I tubular glass vials having hydrophobic coating (TopLyo®) and with an electrode pair (19 x 10 mm) attached using either physical direct contact (grey open symbol), glue (black closed symbol) or sputtering technique (black open symbol). The measurements were performed at ambient temperature (23-24 °C).

Study IV

By removing guard electrodes, a measurement vial attached with a 19 x 10 mm electrode pair was then implemented for monitoring a freeze-drying process. An application of TVIS technology using a guard assembly vial as a process analytic tool for lyophilization development has been published by Smith's group (Smith et al., 2017; Arshad, 2014). They demonstrated that TVIS

parameters derived from the capacitance spectrum that are peak amplitude (C''_{PEAK}) and peak frequency (F_{PEAK}) could be used for characterizing the lyophilization process. Hence, these main parameters would be used for studying the possibility of using the non-guard vial with electrode dimensions of 10 mm by 19 mm to characterise a freeze-drying cycle. The results from the three main steps of freeze drying cycle - freezing (**Figure 62**), annealing (**Figure 63**), and primary drying step (**Figure 64**) - shared similarities with the previous works (Arshad, 2014).

From **Figure 62**, it could be seen that a vial with thermocouple nucleates (solid line B in **Figure 62**a) before the TVIS measurement vial (dash line A in **Figure 62**b and c) because a thermocouple could initiate nucleation that followed by changing the nature of ice formation. During freezing, temperature-dependent parameters F_{PEAK} and C''_{PEAK} decreased, along with sample temperature (**Figure 62**b). Once ice formation starts (i.e. 1.13 h) (referred to as "onset of ice nucleation"), both TVIS parameters spiked in the same manner as the product temperature due to the exothermic reaction of the ice crystallization (**Figure 62**). However, this could not fully explain a rapid increase during liquid-solid phase transition to the temperature dependency of F_{PEAK} and C''_{PEAK}. So far, it is unclear what mechanism contributes this sharp increase caused by a phase transition during freezing. One possible explanation is that the interfacial polarization between ice and water surface within heterogeneous structures during ice formation was higher than complete solidification.

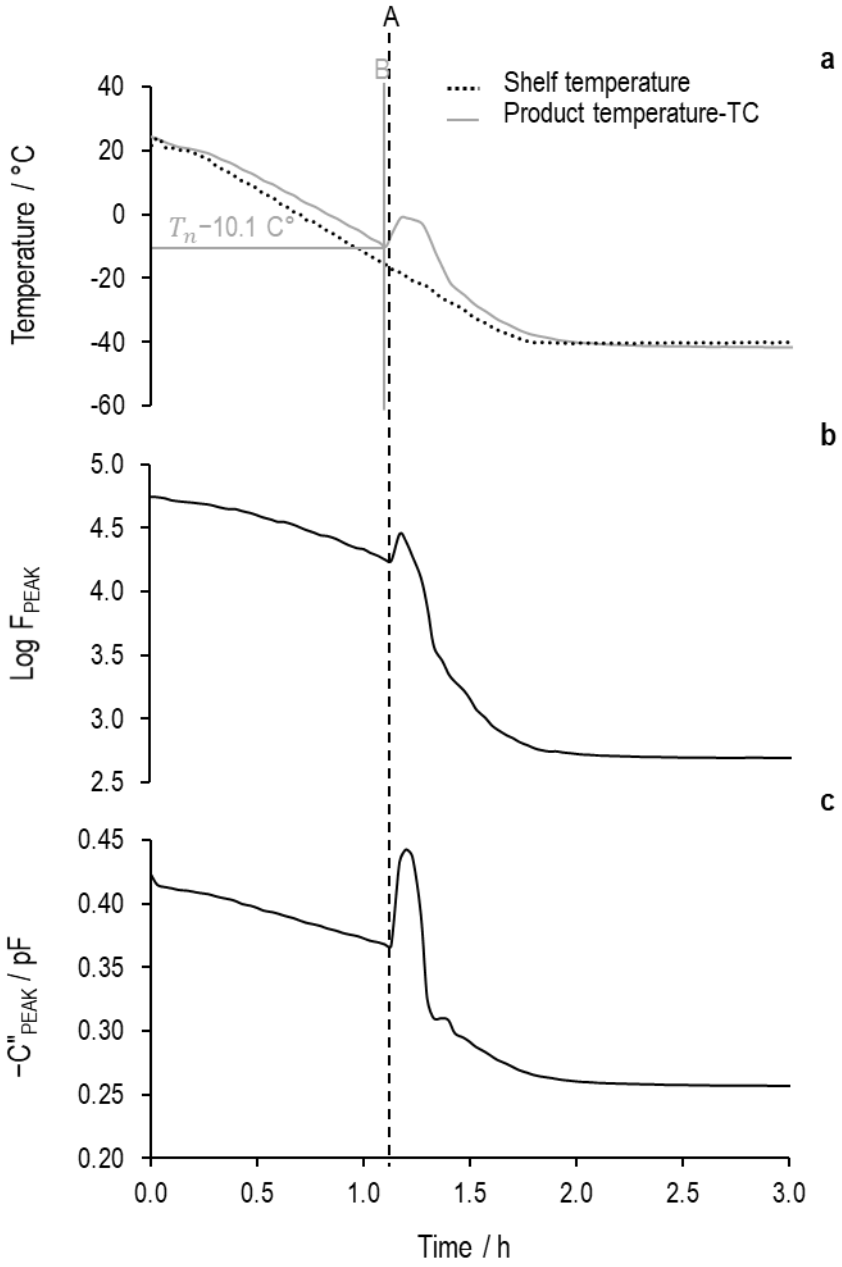

Figure 62 (a) Temperature and TVIS parameters, (b) F_{PEAK} and (c) C''_{PEAK}, of 2 g double-distilled water contained in a Type I tubular glass vial (nominal capacity 10 mL) with a pair of non-guard electrodes with dimensions of 10 x 19 mm (h x w) attached to the outside of the vial during freezing to −40 °C with 0.67 °C/min rate. The onset of ice nucleation in the TVIS vial (black dashed line A, 1.13 h) and neighbouring vial with a thermocouple (grey line B, 1.10 h) were presented. The nucleation temperature in TC vial is −10.1 °C.

Besides the freezing step, an optional thermal treatment process was investigated. The TVIS profile of F_{PEAK} and C''_{PEAK} parameters were comparable to the temperature profile from the thermocouple measurement in the neighbouring vial, as shown in **Figure 63**. A change in product

temperature during the re-heating (period C, **Figure 63**a) and re-cooling process (period E, **Figure 63**a) could be mirrored by the gradient of the F_{PEAK} (period C and E, **Figure 63**b) and C''_{PEAK} (period C and E, **Figure 63**c). A correlation between temperature and TVIS parameters was demonstrated in Figure 64, for instance, peak frequency (i.e. $Log\ F_{PEAK}$) increased ~33 %, which was around 15% higher than C''_{PEAK} when the temperature was ramped from −42 °C to −15 °C.

However, the temperature dependence of both TVIS parameters is dominated by different factors. Dielectric relaxation time of ice (τ_{ice}) increases with decreasing temperature and thereby shifts the relaxation peak of ice (Equation 61). The temperature dependence of the ice relaxation frequency is shown in Figure 64a. On the other hand, a dependency of C''_{PEAK} on temperature (Figure 64b) is influenced by the dielectric permittivity at low frequency (ε_s) and high frequency (ε_∞). The relationship between temperature and the dielectric properties of ice has been demonstrated in a report by Bittelli and co-workers (2004). As temperature increases, the static permittivity of ice (ε_s of ice) tends to increase, whereas an instantaneous permittivity of ice (ε_∞ of ice) is nearly constant. It follows that the capacitance increases. Alternately stated, a time constant of ice is responsible for the temperature dependence of F_{PEAK} and the temperature coefficient of C''_{PEAK} is contributed by the static permittivity.

$$F_{PEAK} = \frac{1}{\tau_{ice}} \qquad \text{Equation 61}$$

During 2 hours of a holding period (period D, **Figure 63**), the peak frequency of the ice relaxation stayed steady; likewise, the product temperature while C''_{PEAK} slightly declined. This indicates a structure modification inside the frozen matrix (microscale). Ice crystals become bigger and more uniform over annealing time due to the Ostwald ripening effect; therefore, the conductive path within the frozen sample is simplified (i.e. a shorter, less tortuous pathway). In other words, this process produces a more direct route through which ions flow in the microstructure of the frozen matrix. As a result, the overall pathway reduces and then decreases the capacitance value (Equation 60); therefore, the value of C''_{PEAK} in the re-freezing profile after 2 hours of annealing

is lower when compared to the re-heating data as demonstrated in **Figure 64**b. This study also further supports other research that investigates the impact of the porosity of capacitive materials on ion movement (Reale & Smith, 2018).

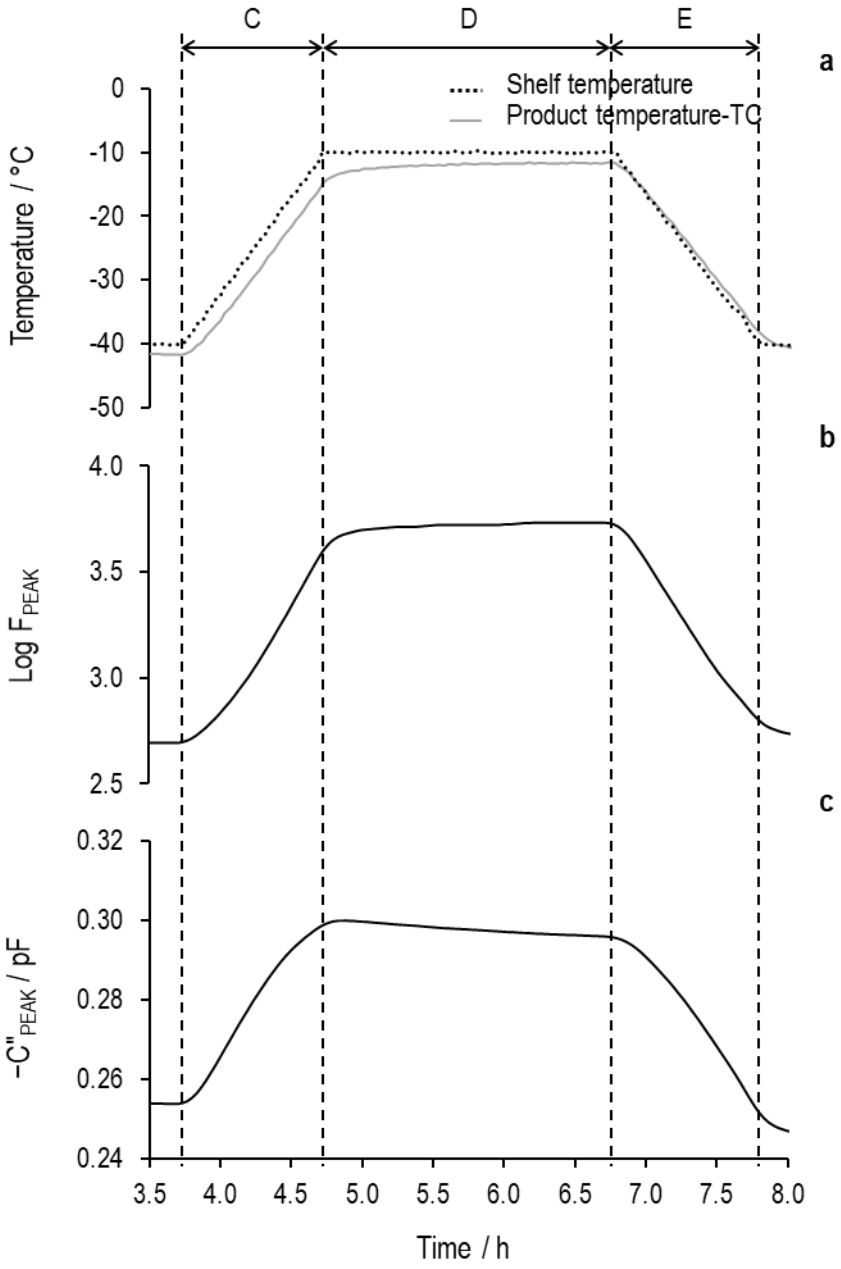

Figure 63 Time profiles of (a) temperature, (b) F_{PEAK} and (c) C''_{PEAK} parameters during annealing of 2 g frozen water contained in 10 mL glass tubing vial attached with a 10 x 19 mm (h x w) non-guard electrode pair. The various stages of annealing are as follows: re-heating (period C); holding (period D); and re-cooling (period E).

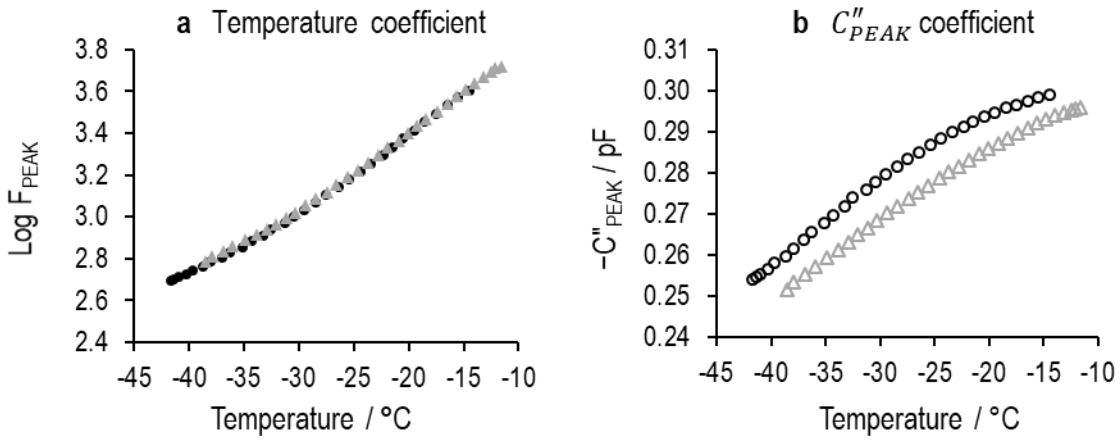

Figure 64 Temperature dependencies of (a) peak frequency (closed symbol) and (b) peak amplitude (open symbol) of frozen water contained in the non-guard vial attached with a pair of 10 x 19 mm (h x w) electrodes during re-heating (circle symbol) and re-freezing (triangular symbol)

With a regression analysis, a relationship between product temperature from a thermocouple vial and $Log\ F_{PEAK}$ from a TVIS vial, defined as temperature calibration (Figure 65), could be exploited for estimating product temperature as a non-invasive technique during primary drying in particular. Although calibration curves of the temperature ramp-up and down were identical and both plots could be applied to the prediction of ice temperature, a re-heating calibration was preferred because re-heating simulates the drying process in terms of heat supply.

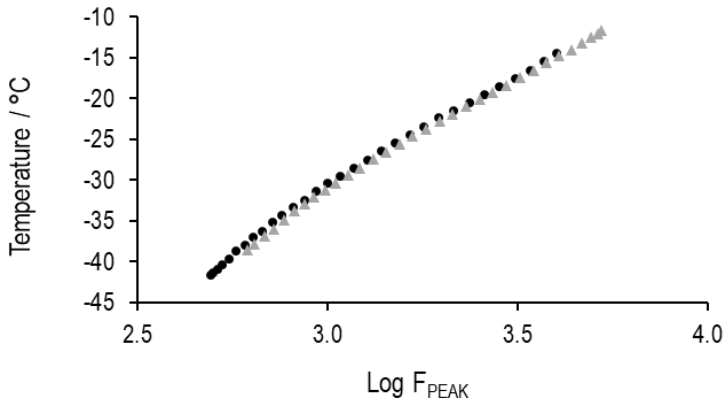

Figure 65 Temperature calibration of ice in a non-guard TVIS vial, attached with a pair of electrodes (19 x 10 mm), during the annealing process. Data from re-heating and re-freezing are represented by black circle and grey triangle, respectively.

The next section of this study was concerned with the primary drying step. Applying a vacuum at 10.83 h (dash line F in **Figure 66**) enabled a faster drying rate and thereby an accelerated cooling effect. This was followed by a sudden drop in the thermocouple temperature. A few minutes later (~6 minutes), stable chamber pressure was achieved, and therefore a steady thermocouple profile observed after the pressure stabilized for 0.8 h is likely to be due to a constant sublimation rate. However, after ~0.8 h of primary drying (at 11.63 h), a step-like increase in product temperature (TC) is evidenced (**Figure 66**b). This is probably an artefact induced by the probe of the TC losing contact with the ice and the TC sensor recording air temperature instead of ice.

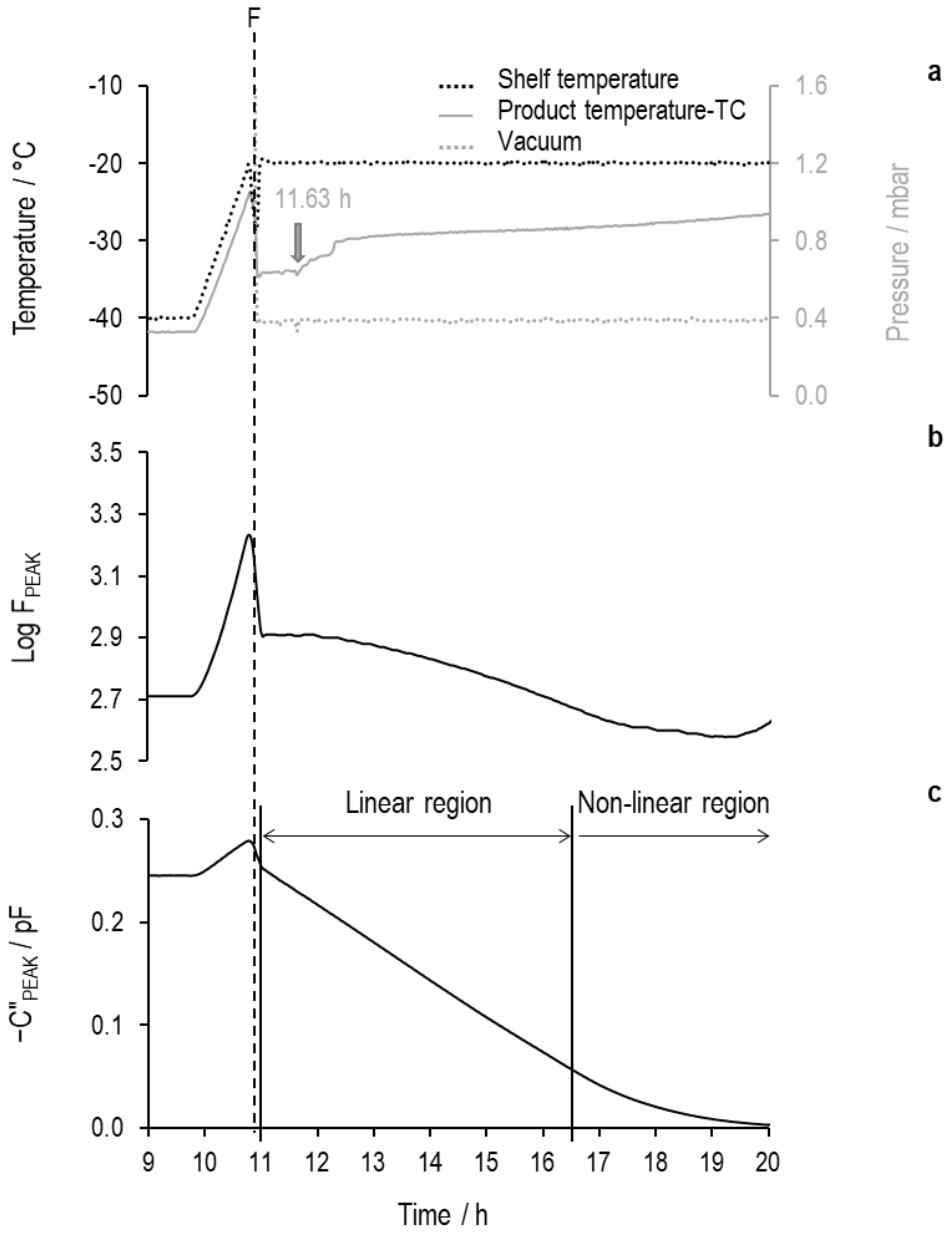

Figure 66 (a) Ice temperature and TVIS parameters, (b) F_{PEAK} and (c) C''_{PEAK}, during primary drying step. 2 g of frozen water in NG TVIS vial with 19 x 10 mm electrode pair was sublimed at −20 °C and 400 µbar (set programmed). Given that C''_{PEAK} is a function of ice mass, a gradual decrease in C''_{PEAK} after applying vacuum (F) corresponded to loss of ice mass, which could be classified into two regions according the drying profile (linear region and non-linear).

Primary drying is acknowledged as the critical step in the lyophilization process and requires a design space to achieve an acceptable product with a scalable and consistent process. To construct the control space, we need two parameters known as vial heat transfer coefficient (K_v) and the dried product resistance (R_p), which could be calculated using the sublimation rate

(dm/dt) and the product temperature either at the bottom of the vial (T_b) or at the ice interface (T_i). With the TVIS technique, the sublimation rate can be estimated from one of the TVIS parameters known as C''_{PEAK}. As matter of fact, this parameter is directly proportional to the amount of ice within the electrode boundary ($C''_{PEAK} \propto m_{RE}$) and followed by the ice height ($C''_{PEAK} \propto h_{RE}$). If we assume that the ice layer has been dried in a horizontal plane (i.e. a planar sublimation front) and also has a good contact with the inside of the glass wall, then the sublimation rate could be estimated directly from the change in the C''_{PEAK} over the drying period, referred to as surrogate sublimation rate (dC''_{PEAK}/dt). From **Figure 66**, during a stable pressure period the C''_{PEAK} decreases linearly for approximately 5.5 h (linear region) and then gradually slows down in the late stages of primary drying (non-linear region). While a reduction in sublimation rate is typically expected at this point due to increasing R_p, this circumstance could also be explained by the fact that the C''_{PEAK} has a linear relationship with ice layer height only if the ice has good contact with the glass wall of the vial (i.e. no gap between ice and glass wall). This linear region points to constant kinetics at the beginning of the primary drying step. However, as drying proceeds, the air gap between the ice and glass wall has developed, resulting in the deviation of C''_{PEAK} from the linear profile.

Nevertheless, besides the ice mass, C''_{PEAK} is also affected by temperature, as demonstrated by the temperature coefficient of both the re-heating and re-freezing step (i.e. C''_{PEAK} increase as temperature increase) in **Figure 64**b. This positive temperature dependence is a consequence of the increase in the interfacial capacitance. Hence, both the ice shape and the product temperature should be taken into account for the calculation of the drying rate in order to get the most accurate value. In this chapter, we focus on the basic response of TVIS in order to improve the measurement vial; the method of determination of sublimation rate is described in Chapter 9 and Chapter 10 later.

Another parameter required for determining K_v and R_p is product temperature. By using a temperature calibration curve (**Figure 65**), we can estimate the ice temperature during sublimation defined as $T_{F_{PEAK}}$ as shown in **Figure 67**. The time point at which primary drying

started (i.e., reducing chamber pressure by vacuum pump) was set as zero hour (time = 0 h). With a temperature difference of less than 1 °C, this highlighted a good agreement of product temperature between the thermocouple (T_{TC}) and TVIS ($T_{F_{PEAK}}$) in an early stage of primary drying stage (0.2-0.87 h). Thereafter, T_{TC} started to increase whereas $T_{F_{PEAK}}$ remained constant for half an hour. This suggests that the TVIS might be able to track product temperatures over a longer period than the TC sensor. A possible explanation is that once the ice has been sublimed, the thermocouple probe will lose contact with the ice and begin to sense the temperature of air around the TC bead instead. Conversely, the TVIS measured the average temperature of ice occupying the electrode region. Later on, however, $T_{F_{PEAK}}$ decreased continuously and significantly after 3 hours of the drying period. A decrease in $T_{F_{PEAK}}$ might be because the shape of the capacitance spectra changed after drying for 2 hours (**Figure 68**c), and is more obvious in the later phase of the drying cycle (as shown in **Figure 68**d-f).

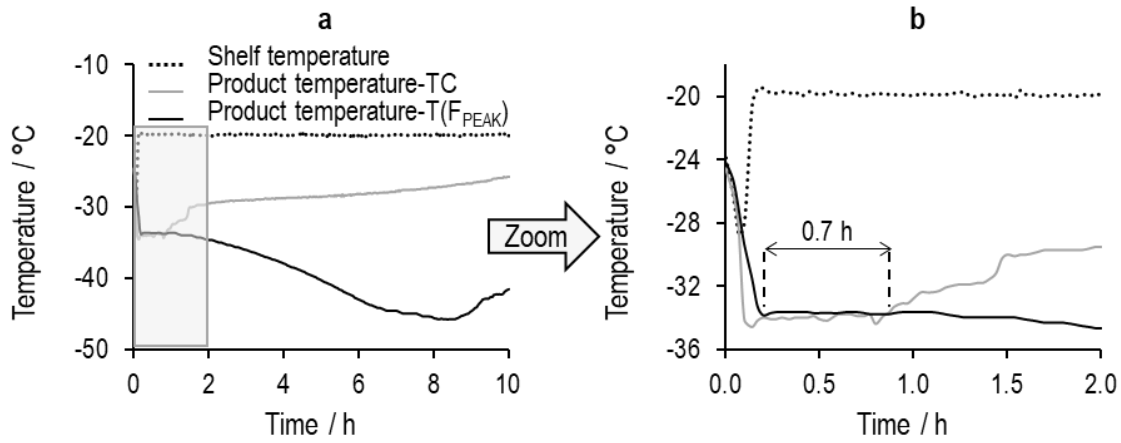

Figure 67 (a) Product temperature estimated by temperature calibration of re-heating step ($T_{F_{PEAK}}$) and measured from the thermocouple (TC) during primary drying. The point of application of vacuum is set as zero hour. (b) Close-up of the first 2 hours. $T_{F_{PEAK}}$ and T_{TC} is in agreement each other for 0.7 h period.

One possibility for the alteration of the TVIS spectrum as drying proceeds would be a leakage of current from the circuit comprising a glass and a dielectric material through a parasitic pathway. Since a large amount of conductive material (like a stainless steel shelf) can operate as the electrical grounding system, some of the measurement currents can flow through grounding if

a conductive electrode directly contacts the surface of the freeze dryer shelf. Although this unwanted incident could be prevented by using an insulator such as a high-resistivity pure ice for shielding the electrical field to ground, ice mass progressively decreases as the drying proceeds. When a certain amount of ice had been removed and the remains could not prevent current flowing through conductive metal, then the distortion of spectra would be more pronounced. Therefore, a promising way to improve the quality of the spectrum might be to increase the distance between the electrodes and the freeze dryer shelf. Based on this assumption, the adjustment of electrode distance from vial base was carried out.

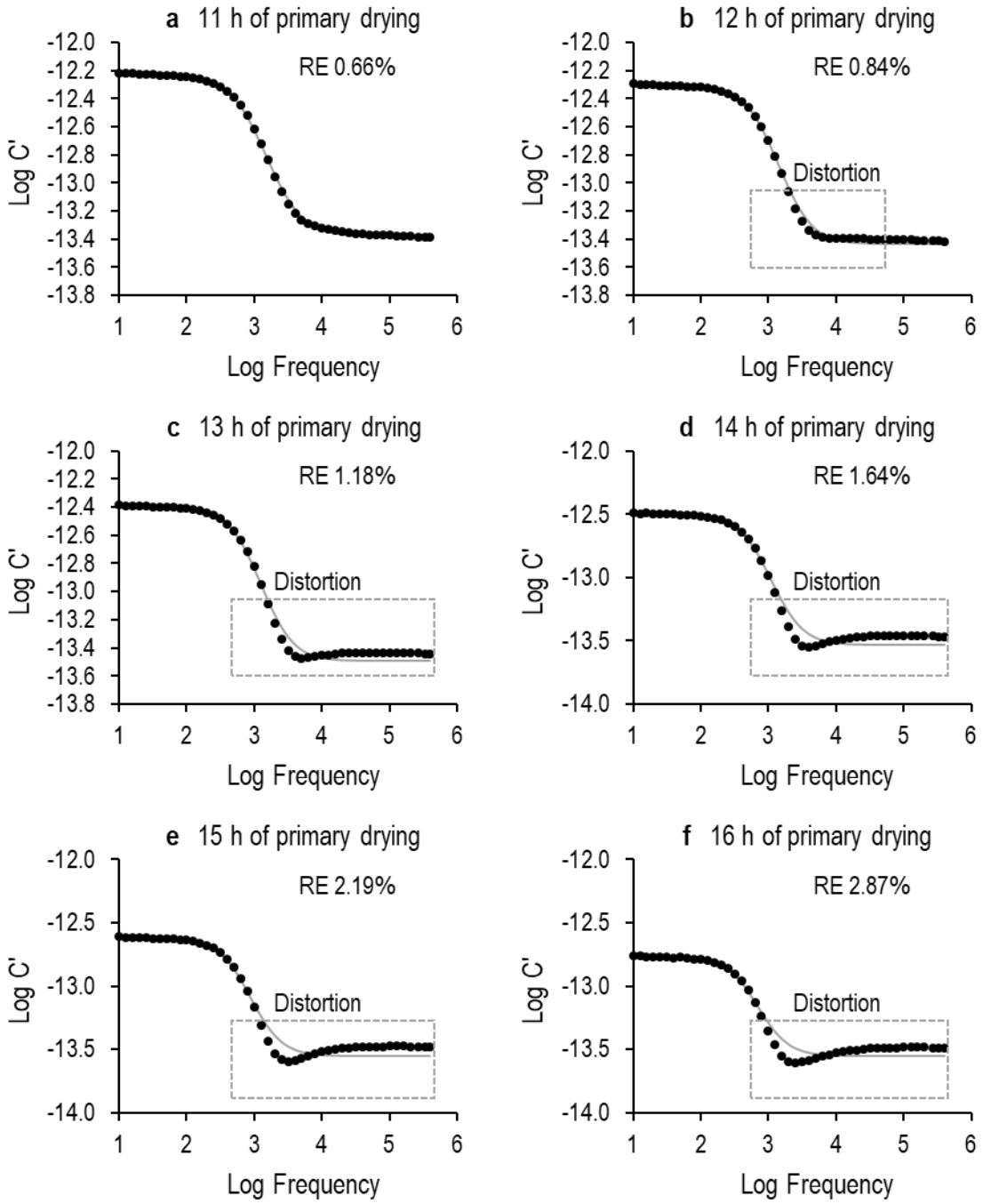

Figure 68 Real-part data (black dot) in logarithm scale and fitting results (grey solid line) to the model for dielectric relaxation of ice (i.e. capacitance in parallel with Cole-Cole element, $C{=}Co$ model) from impedance spectrum analysis software (RelaxIS3, rhd instruments, Germany) at a certain point in primary drying: (a) 11 h, (b) 12 h, (c) 13 h, (d) 14 h, (c) 15 h and (f) 16 of primary drying, before the decrease rate of C''_{PEAK} starts to slow down. The distortion was clearly observed after applying a vacuum at 10.8 h for 2 h (i.e. 13 h of primary drying. b). Percentage relative error (RE) of ice relaxation time (τ) was performed over the data between 100-0.2MHz. Note the equivalent circuit model of frozen ice has been described in Smith and Polygalov (2019).

Study V

To test our assumption, Study V was carried out. The ice spectrum (Ø = 0.7) measured from the TVIS vial with electrodes at either 0 mm (Study IV), 1 mm (Study V) or 3 mm (Study V) from the external vial's base, were investigated. For each configuration, two spectra recorded during primary drying were selected to represent a typical and a distorted spectrum. The typical spectrum was selected on the condition that the volume of ice was sufficiently high as to impede the current flow to ground (i.e. freeze dryer shelf). Here, we set the time at 0.2 h of primary drying, where the chamber pressure reached the set point. For the distorted spectrum, in order to easily detect the distortion and to avoid the uncertainty arising from the fringing effect near the edge of electrode, we selected the spectrum at which C''_{PEAK} reduced by ~70% of the initial value (i.e. vacuum applied) as demonstrated by Study IV (16 h, Figure 68f). The selected spectra are demonstrated in Figure 69.

A glance at the graph in Figure 69 reveals that the distortion is less evident when the space between the lower edge of the electrode and the vial's base increases. The smallest value of relative difference calculated from relative error (RE) between the normal spectrum and the distortion one was found in the vial with the electrode positioned 3 mm from vial's base (i.e. the value is 0.77). This finding suggests that the quality of measurement could be improved by increasing the gap between the electrodes and the external vial's bottom. Nevertheless, due to the limitation of vial size and filling volume (i.e. a small volume of liquid was filled in a small lyophilization container), the optimal separation distance between an electrode and external vial's base to reduce stray effect would be 3 mm.

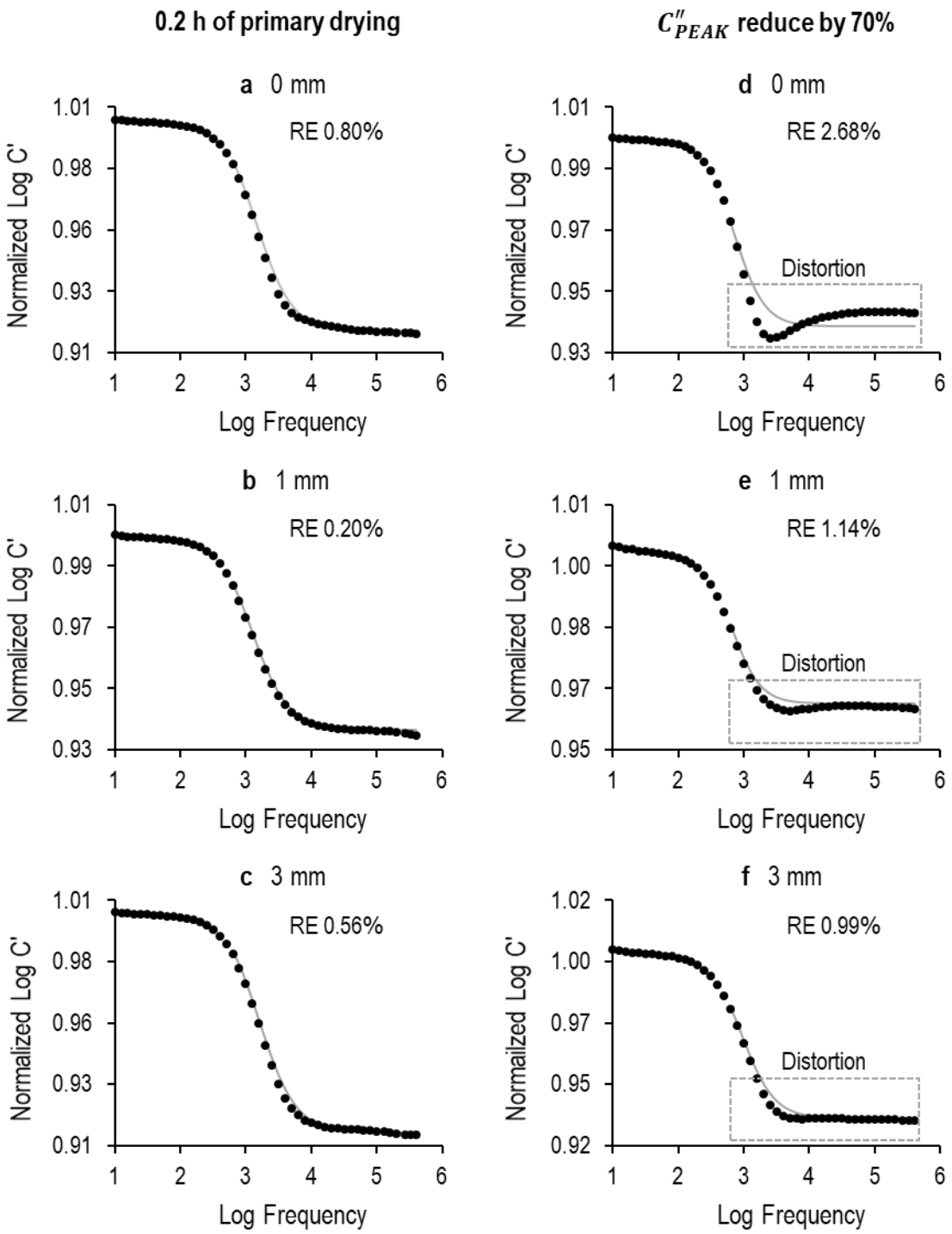

Figure 69 Real-part capacitance in logarithm scale of different electrode configurations at the selected time: (a-c) initialisation of primary drying and (d-f) when C''_{PEAK} corresponds to 30% of the initial value. The TVIS vial had different distances from the vial's base: (a and d) 0 mm; (b and e) 1 mm; and (c and f) 3 mm, were determined. The grey solid line was simulated from the fitting model, $C{=}Co$ model (Smith & Polygalov, 2019).

6.4.Summary

The quality of the TVIS signal intensity and the spectrum shape could be improved by: (1) removing the guard ring; (2) increasing the electrode area by raising the electrode height; and (3) increasing the gap between the bottom edge of the electrode and the vial's base. However, since the fill depth of a freeze-dried product is typically below 12mm, the optimal electrode height of 10 mm and the electrode positioned at 3 mm from the base of the container is suggested for a standard 10 mL vial. Also, there is no significant impact of copper adhesive on the TVIS spectrum. In summary, based on these studies, there is encouraging evidence for the use of the TVIS vial made from a 10-mL standard type I tubular glass vial (1096936, Schott, Hungary supplied as VC010-20C from Adelphi - HP), with a pair of 19 x 10 mm copper non-guard electrodes (19 mm wide copper adhesive tape 1181, 3MTM) attached and positioned at a distance of 3 mm from the vial baseline. This measurement vial will be used for general studies (chapter 7 to 9) unless otherwise modified for specific study (i.e. K_v in chapter 10).

7. Characterisation of phase transition during freezing step by TVIS

7.1. Objective

The objective of this chapter is to characterise the ice formation process in terms of ice nucleation and solidification by using the following TVIS parameters: peak amplitude (C''_{PEAK}), peak frequency (F_{PEAK}) and real part capacitance (C'), at fixed frequency of 10 Hz and 0.2 MHz. At an electrical capacitance of 5 %w/v sucrose, either 0, 0.26 or 0.55 %w/v sodium chloride, contained in a standard 10 mL TVIS vial, were measured over the frequency range of 1 MHz to 10 Hz during a freezing step in a laboratory freeze dryer. The liquid-solid phase transition is evidenced by using images from a digital camera.

7.2. Materials and Methods

7.2.1. Preparations

Sucrose (Sigma-Aldrich) and sodium chloride (Fisher Scientific International, UK) were accurately weighed and dissolved in ultra pure water (18.2 MΩ·cm) to obtain solutions at a sugar/(sugar+salt) ratio of 1.00, 0.95 and 0.90. The composition of the preparations is shown in Table 7.

Table 7 The composition of sample preparations

Sample	Sucrose / (Sucrose + NaCl) Ratio	Sucrose (%w/v)	NaCl (%w/v)
S-1	1.00	5	0
S-2	0.95	5	0.26
S-3	0.90	5	0.55

7.2.2. Vial filling and loading the freeze dryer

Aliquots of 3.6 g of each sample solution were transferred into these 10-mL standard clear type 1 tubular glass vial (1096936, Schott, Hungary supplied as VC010-20C, Adelphi-HP) and a TVIS

measurement vial. The fill weight of 3.6 g is equivalent to a solution height of 7 mm from the lower edge of the electrode, which corresponds to a fill factor (Ø) of 0.7 (where Ø is defined as the relative height of the sample solution within the electrode region to the height of the electrode), as shown in **Figure 70**. The TVIS vial was the same 10 mL type 1 tubular glass vial, but modified with a pair of copper electrodes (copper adhesive tape 1181 3M^{TM}) attached to the external surface of the tubing vial. Two electrodes, each with a height-by-width dimension of 10 × 19 mm, were diametrically opposed to each other and positioned at the height of 3 mm above the base of the vial (**Figure 70**).

Each nearest neighbour vial containing the sample solution had a T-type thermocouple wire (28 AWG) inserted through the drilled rubber stopper, to measure the temperature of each sample. The sensor tip was manually positioned at the midpoint of the sample bounded by the electrodes: equivalent to the height of the TVIS sensing node, as shown in Figure 70. The position of the thermocouple tip was manipulated and adjusted carefully by eye.

Besides the vials containing the sample solution (5 %w/v sucrose and either 0, 0.26 or 0.55 %w/v sodium chloride), another 154 vials were filled with 3.6 g of 18.2 MΩ·cm water. All 160 vials, including the 6 solution-filled vials, were arranged on the loading tray according to the layout in **Figure 71**. These were then partly closed with 20 mm 4023/50 grey bromobutyl rubber stoppers (FDW20RTS, West Pharmaceutical Services Singapore Pte. Ltd, Singapore), before being loaded into a VirTis Advantage Plus XL bench-top freeze dryer (SP Scientific, USA).

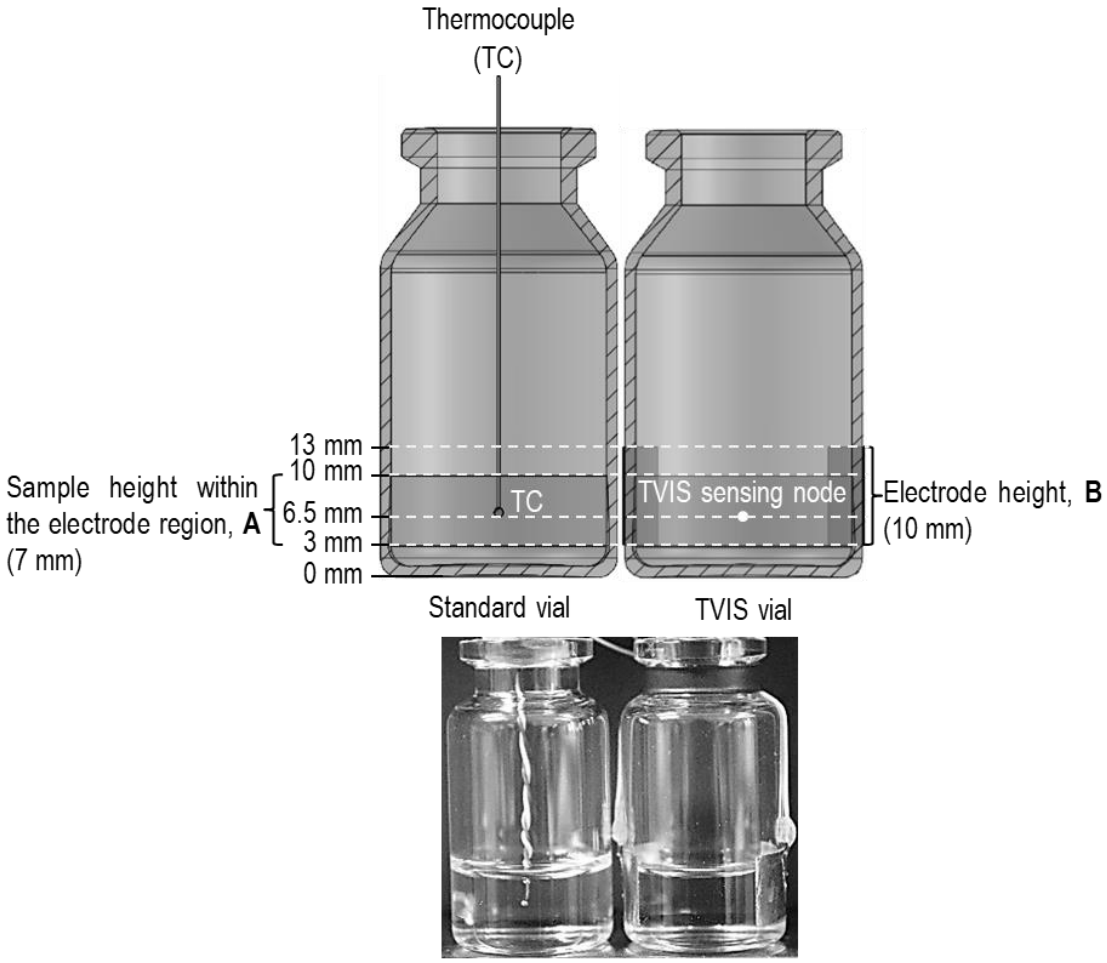

$$Fill\ factor(\emptyset) = \frac{A}{B} = \frac{(10-3)\ mm}{10\ mm} = 0.7$$

Figure 70 Schematic vertical cross-section of two vials containing 3.6 g of sucrose-salt solution. **Right:** A modified TVIS vial attached with a pair of copper electrodes (19 x 10 mm), positioned at 3mm from the vial base (~ 2 mm from the internal base of the vial). **Left:** A standard vial (10 mL nominal capacity) with a type-T thermocouple inserted in the liquid sample. The thermocouple sensor bead was positioned at a height corresponding to that of the TVIS sensing node (6.5 mm): i.e. half the 7mm sample height occupying the electrode region (7/2 = 3.5 mm) was added to the sample height below the lower edge of the electrode (3 mm). The unmodified nearest vial (left) is used to refer to the product temperature in the neighbouring TVIS vial. The fill factor (Ø) shown here is 0.7, which means that the sample height in the electrode region is 7 mm for an electrode height of 10 mm.

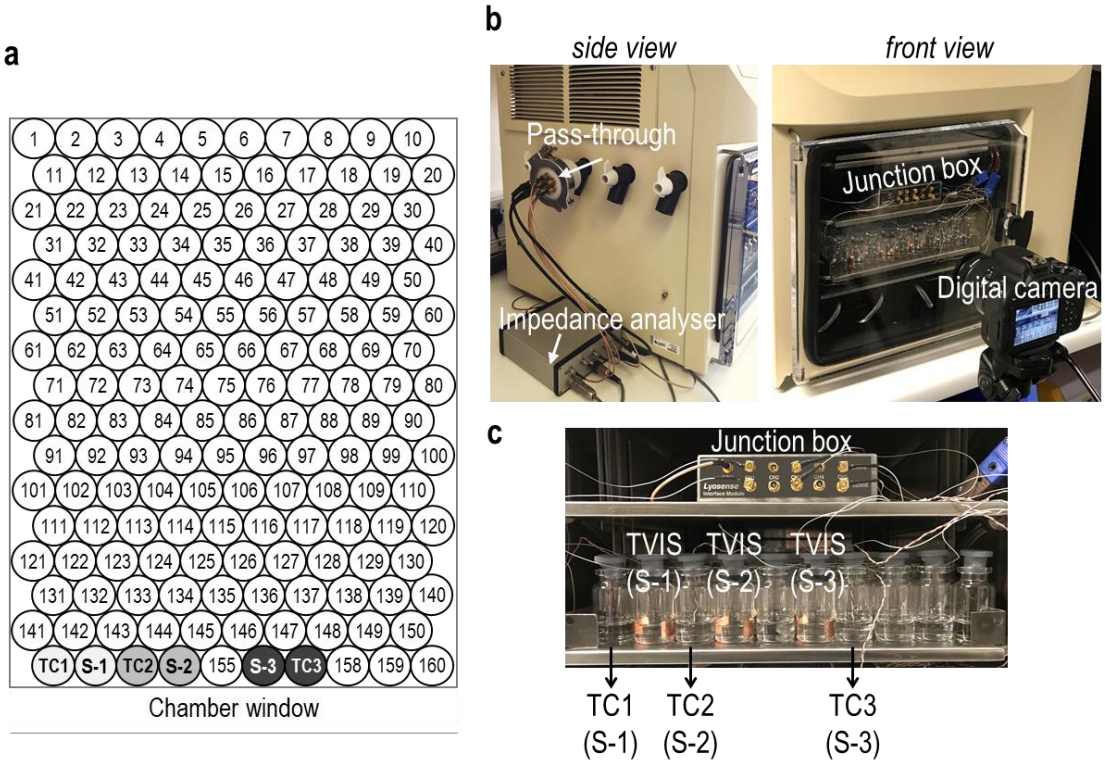

Figure 71 (a) An arrangement of vials on a shelf of the Virtis Advantage Plus XL benchtop freeze dryer. Three thermocouple-containing vials (labelled TC1, TC2 and TC3) and the TVIS vials (labelled S-1, S-2 and S-3) were placed in the first row close to the chamber window. The other vials with the numbered position on the shelf were filled with ultrapure water. (b) The Virtis Advantage Plus freeze dryer equipped with a TVIS system, comprises a five-channel TVIS junction box inside freeze dryer and an impedance analyser outside the freeze dryer. The signal from the junction box is sent and received via the pass-through installed on the manifold hose of the Virtis Advantage Plus XL freeze dryer. A digital camera was set to observe the nucleation event of the sample-filled vials. (c) The image demonstrating the position of thermocouple vials and TVIS vials containing each sample solution positioned on the freeze dryer shelf.

7.2.3. Through-vial impedance spectroscopy

A multichannel impedance analyser developed by De Montfort University was used to provide the impedance spectra of three solutions (containing 5% sucrose and either 0%, 0.26% or 0.55% sodium chloride). Each TVIS vial was connected to a bespoke 5-channel impedance analyser located outside the freeze dryer, via a junction box placed on the shelf, and an electrical pass-through (Figure 71). More detail on the TVIS measurement system is provided by Smith and Polygalov (2019). The electrical capacitance spectra of each sample were measured within the

TVIS vials over the frequency range of 10 Hz to 1 MHz, with a scan interval of 2 minutes during the freezing step in a Virtis Advantage Plus freeze dryer. Each measurement requires ~ 10 s to complete one spectrum.

7.2.4. Freezing protocol

All vials were equilibrated at the shelf temperature of 20 °C for 30 minutes before ramping to −45 °C at 0.5 °C·min^{-1}. When the shelf temperature reached −45 °C, these vials were held at −45 °C for 2 h. The process step is detailed in Table 8.

Table 8 Freezing protocol.

Step	Temperature (°C)	Time (minutes)
Equilibrium phase	+20	30
Freezing temperature ramp (0.5 °C·min^{-1})	−45	130
Freezing temperature hold	−45	120

7.2.5. Photographic images

The photos were taken by a digital camera (Canon E550D) with a time-lapse function. The timer was controlled by EOS utility software to capture a photo every 2 minutes. The photographic images were then analysed using Java-based image processing software (ImageJ, https://imagej.nih.gov/ij/download.html). These images were turned into quantifiable data in terms of vertically averaged pixel intensity along the horizontal distance of the selected region of interest (ROI). The intensity result was used to determine the solidification end point (the point at which the relative change in the intensity begins). The ROI for each sample is shown in **Figure 72**.

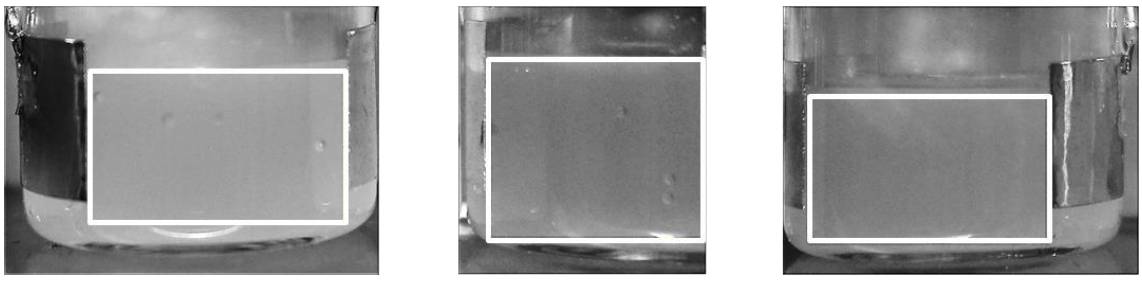

a (S-1) **b** (S-2) **c** (S-3)

Figure 72 Illustration of the region of interest (area within the rectangle) for each sample: (a) 5% w/v sucrose solution (S-1), (b) 5% w/v sucrose with 0.26% w/v NaCl (S-2), (c) 5% w/v sucrose with 0.55% w/v NaCl (S-3).

The ImageJ feature allows us to measure the thickness of the frozen mass. Images late in the freezing stage (4 h) were selected. Before making a measurement, the scale was set using a known length (called spatially calibrating); in this case, an electrode length of 10 mm was used. Then the measurement of five different positions (**Figure 73**) for each image was performed. The results of five measurements were averaged to give the estimated frozen thickness (in mm).

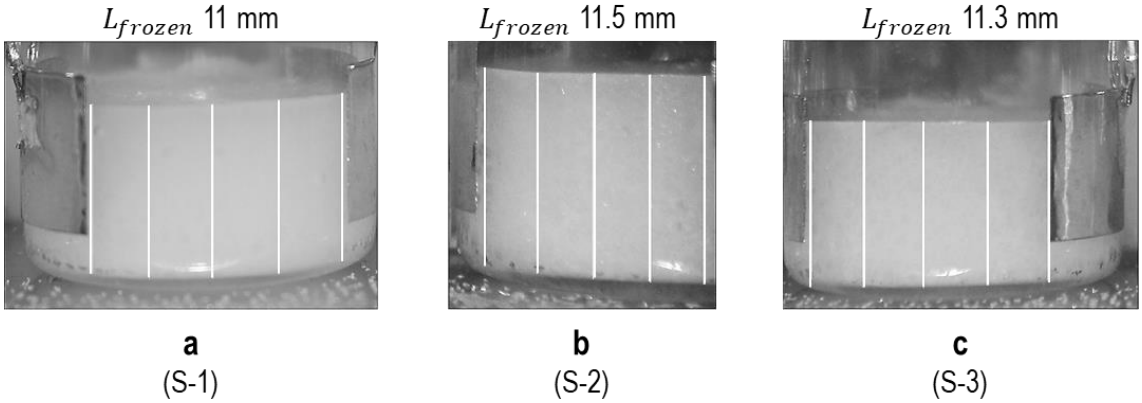

a (S-1) **b** (S-2) **c** (S-3)

Figure 73 Demonstrating five lines' selection on the image at 4 h of the freezing process: (a) 5% w/v sucrose solution (S-1), (b) 5% w/v sucrose with 0.26% w/v NaCl (S-2), (c) 5% w/v sucrose with 0.55% w/v NaCl (S-3).

7.2.6. Analysis impedance spectrum

The peak amplitude (C''_{PEAK}) and peak frequency (F_{PEAK}) of the relaxation peak of the dielectric loss spectra, recorded by TVIS during the freezing process were identified using a peak finding

algorithm created by a VBA macro in Microsoft Excel. Time slices of the real part capacitance spectra at a specific user-defined frequency (i.e. 10 Hz and 0.2 MHz) were extracted by LyoView™ software (version 18-05-18). The different aspects of the TVIS spectrum are demonstrated in Figure 74.

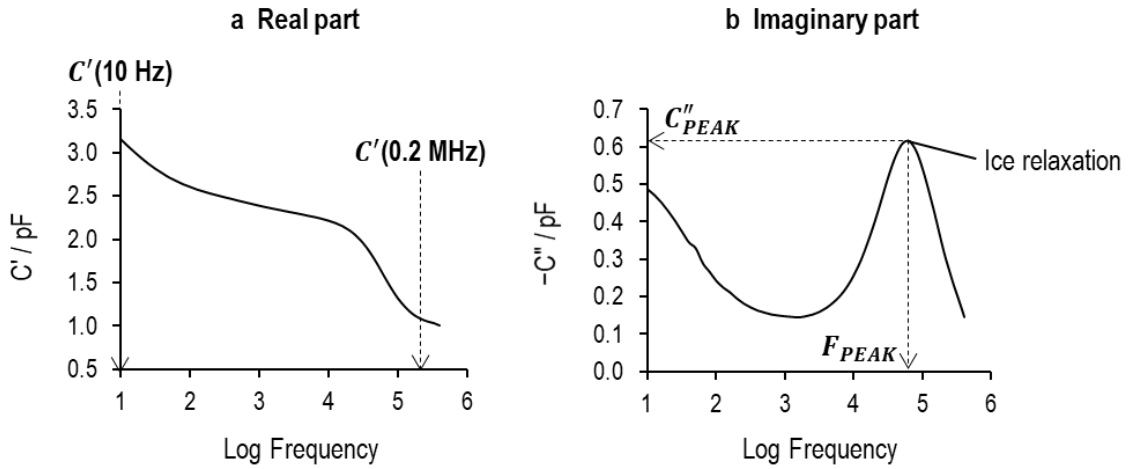

Figure 74 TVIS parameters derived from (a) real part capacitance, i.e. C'(10 Hz) and C'(0.2 MHz); (b) imaginary part capacitance, C''_{PEAK} and F_{PEAK}. This example spectrum was measured from 5% w/v sucrose solution within the TVIS vial at +20 °C before freezing.

7.3. Results and Discussion

7.3.1. TVIS parameters for characterisation of liquid-solid phase transition

The TVIS system measured the physical changes of the composite object (the TVIS vial and its contents) and displayed the relaxation process as a step in dielectric permittivity (real part capacitance) and a peak in the dielectric loss spectrum (imaginary part capacitance). In the liquid state, a step in the dielectric permittivity and a peak in the dielectric loss spectrum is apparent in pure sucrose solution (Figure 75a and b); whereas the dispersion process of the sample with higher conductivity (5% sucrose with either 0.26% or 0.55% NaCl) is positioned out of range of the instrument bandwidth of 10 Hz-1 MHz. Thus, the relaxation process could not be detected by the TVIS system, as shown in Figure 75c-f. The main polarization mechanism responsible for the relaxation process in the liquid sample is contributed through space charge polarization (also known as Maxwell-Wagner (MW) polarization), although there is a small contribution from ionic

conductivity at low frequency. This interfacial process occurs when the charge (ionic impurities, proton transfer in hydrogen bond) migrates and accumulates at the glass-sample interface.

During freezing, charge mobility is limited: resulting in an increase in electrical resistance. Therefore, the MW process shifts towards lower frequencies ($f = 1/2\pi RC$). By associating with the formation of ice, dielectric relaxation appears in place of the interfacial polarization process (**Figure 75**). In other words, the measurement window of the TVIS system (frequency range of 10 Hz to 1 MHz) captures the dielectric mechanism of ice in the frozen phase, instead of the MW relaxation of the liquid phase. This highlights the use of TVIS technology in characterising the liquid-solid phase transition (referred to as the ice nucleation) in a freeze-dry vial.

The existence of a secondary process at low frequency is clearly observed on the addition of NaCl to 5% w/v sucrose solution (Figure 75c-f). One possible explanation for the low frequency response is the suppression of sodium chloride crystallisation caused by sucrose (i.e. sugar/ (sugar + salt) ratio > 0.7) (Milton et al., 2007, Duru et al., 2015). If the added sodium chloride is in non-crystalline form at below its eutectic point, salt would form the covalent bond with water much more strongly than the ionic bonding of its molecules (NaCl); consequently, more unfreezable water remained. An increase in water and solute content (i.e. NaCl) in the unfrozen fraction could introduce molecular mobility of the cooperative α-relaxations through the presence of plasticiser (i.e. water) and the ion charge. The impact of salt concentration on the apparent α-relaxation process in dielectric relaxation profiles is demonstrated in Figure 75c-d and Figure 75e-f for 0.26% w/v and 0.55% w/v NaCl, respectively.

In terms of increasing the concentration of NaCl, the secondary relaxation is more pronounced. For the lower salt sample (0.26% w/v), the secondary process was weak in comparison; therefore, this low frequency relaxation was marked and merged into the main process from ice relaxation (Figure 75c-d). The secondary peak can shift the loss peak of ice relaxation to higher frequencies; however, the derived parameters (C''_{PEAK} and F_{PEAK}) from the main process of the capacitance spectrum could be used to track the freeze-drying process.

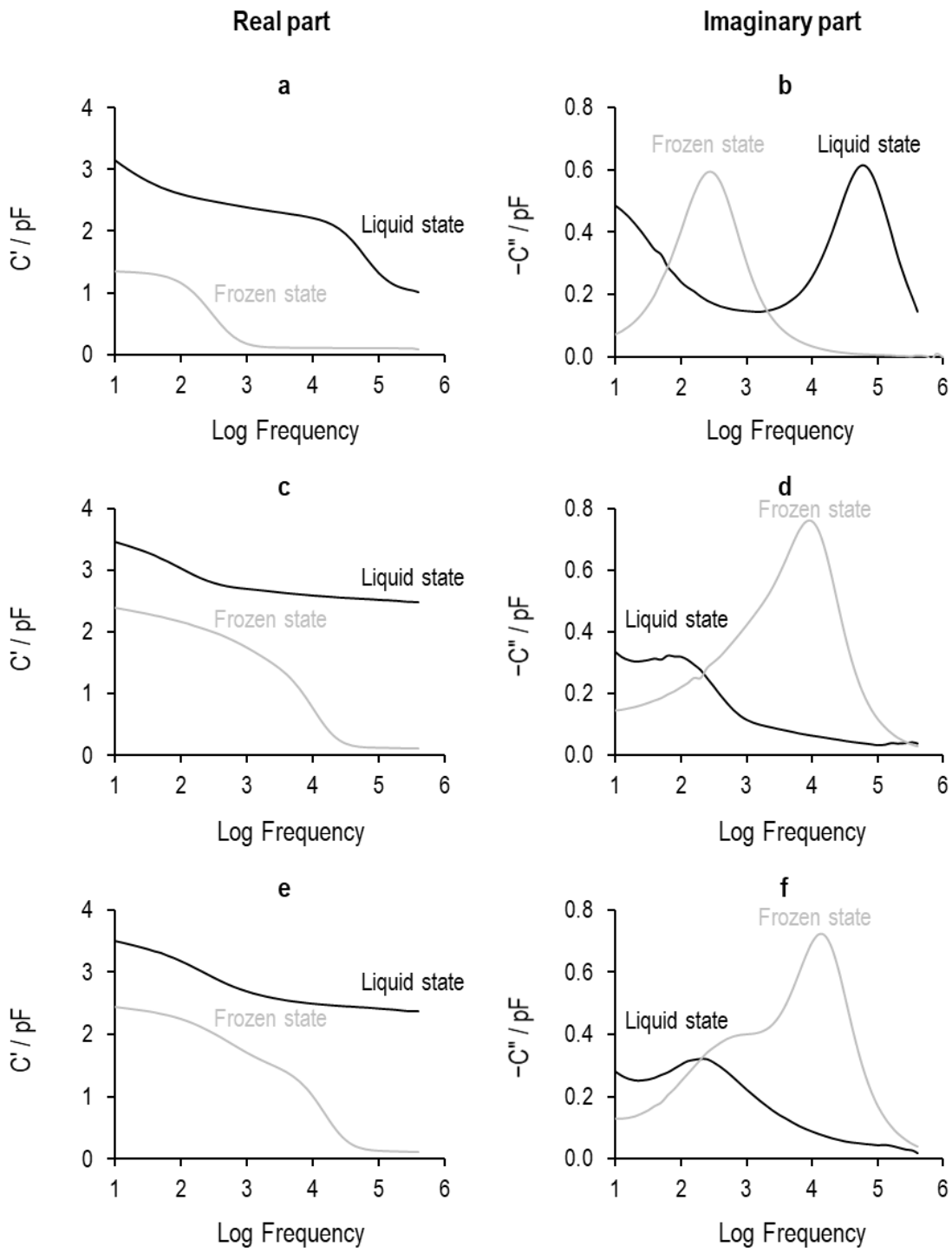

Figure 75 The TVIS response (real part and imaginary part capacitance) of 5% sucrose with different salt concentrations at +20 °C (liquid state) and −40 °C (frozen state): (a-b) 0% NaCl, (c-d) 0.26% NaCl, (e-f) 0.55% NaCl.

Previously, we have demonstrated the application of peak characteristics of phase change during the freezing of a low conductivity sample (3% w/v sucrose solution), which the MW

process could observe within the TVIS window through the freezing process (Smith et al., 2017). However, by adding the salt, the measurement window of the TVIS system could not detect the MW relaxation of the liquid phase, while the ice relaxation peak appeared after it was formed. Therefore, we could not use the peak characteristic of the dielectric loss spectrum to determine liquid-solid phase transition in this case. Here, we investigate the different features of dielectric permittivity at operating frequencies both lower and higher than the relaxation frequency of ice (i.e. C'(10 Hz) and C'(0.2 MHz)).

Temperature coefficient of real part capacitance (dielectric permittivity) depends on the measurement frequency having been demonstrated using pure ice (Figure 76b). This suggests that ice is strongly temperature-dependent at low frequency (i.e. 10 Hz); whereas there is almost no temperature dependence for the frequency above the dielectric relaxation of ice (i.e. 0.2 MHz). Thus, we can expect that the real part in a low frequency region might be sensitive to the nucleation event, as evidenced by the spike in temperature profile due to an exothermic crystallisation process during freezing. At high frequency range, the real part indicates the endpoint of ice formation process (solidification): the value of this parameter changes during ice growth and becomes more consistent after ice solidifies completely. Thus, no change in the value of C'(0.2 MHz) can be associated with the completion of ice formation.

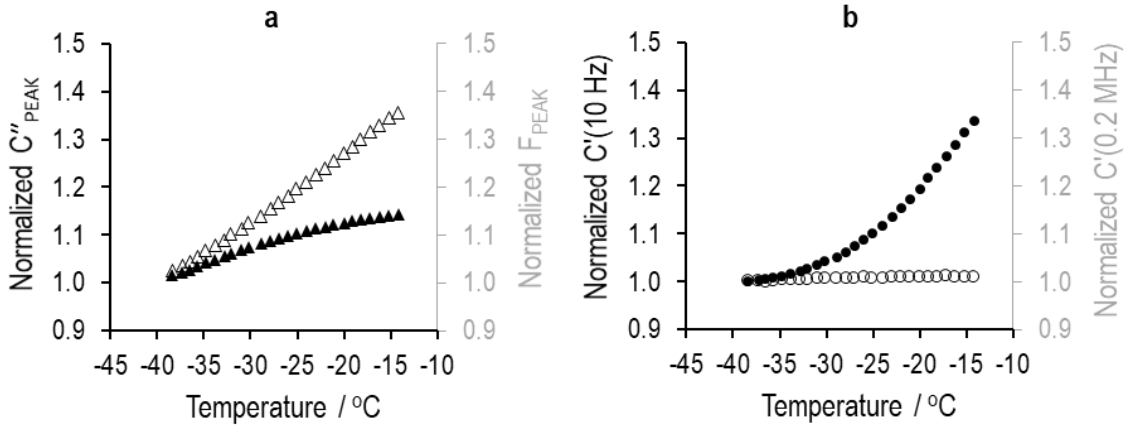

Figure 76 Temperature dependencies of (a) peak amplitude (filled triangle) and peak frequency (open triangle); (b) real part capacitance at 10 Hz (filled circle) and 0.2 MHz (open circle) for pure ice (Smith & Jeeraruangrattana, 2019). The measurement data is recorded during the re-heating stage from −40 °C to −10 °C with 0.5 °C·min-1.

Ice nucleation

During a 2-hour time period of freezing, the photographic images were recorded every 2 minutes for three solutions (**Figure 77**-**Figure 79**): providing evidence that the vial containing the thermocouple nucleated earlier than the TVIS one. As anticipated, the presence of a temperature sensor in the vial was one factor influencing the nucleation event other than the stochastic nature of the ice nucleation. The sensor probe serves as the site initiating nucleation; therefore, the TC vial tends to nucleate at the higher temperature (low degree of supercooling), followed by the frozen structure having larger ice crystals. Subsequently, the sublimation rate in the TC vial accelerates, reaching the endpoint of primary drying before the vials without TC. This issue must be accounted for when optimising the lyophilisation process.

For 5% w/v sucrose (Figure 77), the spike in the temperature profile of the TC vial at 1.90h (Figure 77a) is associated with the onset of ice formation (as confirmed by the images in Figure 77f). This dramatic rise in temperature is a result of the exothermic crystallisation process. Although this heat is removed by the supercooled solution, there is a limit for the latter to absorb the former: thereby increasing the product temperature. Inflections in the time profiles of the following TVIS parameters also coincided with the onset of ice nucleation in the TVIS vial at 1.97h (Figure 77b-e): C''_{PEAK}, F_{PEAK}, C'(10 Hz) and C'(0.2 MHz). This suggests these TVIS parameters could be used to identify the nucleation event. The discontinuity of the C''_{PEAK}, and F_{PEAK} parameters is a consequence of the positive temperature dependence of the relaxation frequency (i.e. shift to the higher frequency) and capacitance increment of the MW process, illustrated by the capacitance spectrum before and after nucleation (Figure 77g and h). However, the maximum value of the C''_{PEAK} exceeded that of the supercooled solution at 0 °C; therefore, it must have another underpinning mechanism. This is believed to have been the formation of the ice structure before solidification was completed.

At the beginning of nucleation, propagation of ice crystals coexists with a remaining liquid. An increase in the number of ice crystals can limit the mobility of charges: leading to an increase in the sample's resistance, in turn reducing its conductivity. This is followed by reducing the

sample's capacitance. However, as there is MW polarization due to residual water, a spike of the C''_{PEAK} value is likely because of the presence of liquid in the heterogeneous frozen structure. As the propagation of ice crystal proceeds, less water is contained in the frozen matrix, reducing the MW polarization effect. This leads to a drop in the C''_{PEAK} value, as shown in Figure 77c.

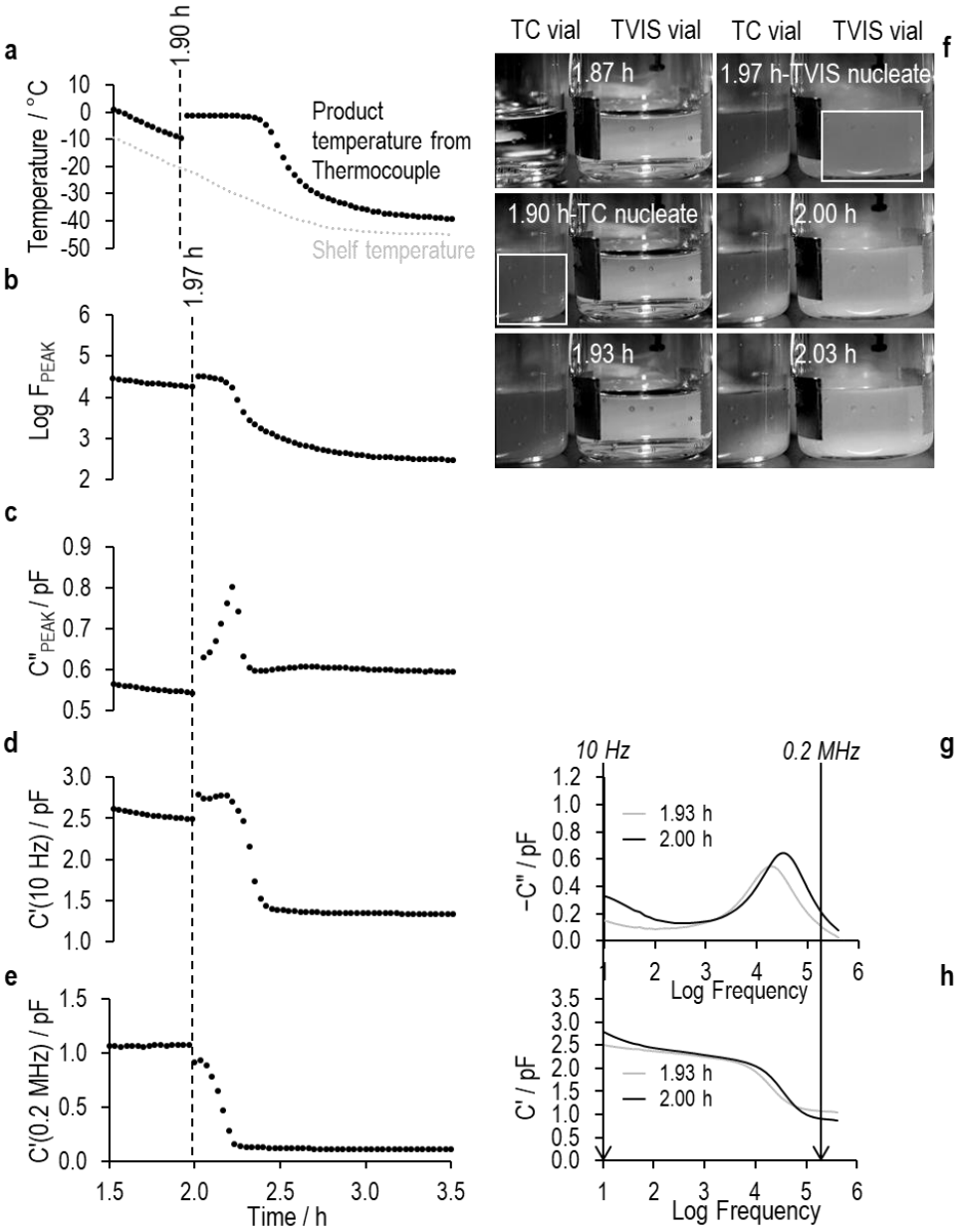

Figure 77 Experimental results for 5% w/v sucrose demonstrate the onset of nucleation. (a) is the profile of the product and shelf temperature; (b) and (c) are time profiles of the TVIS parameter C''_{PEAK} and F_{PEAK}; (d) and (e) are time profiles of real part capacitance C'(10 Hz) and C'(0.2 MHz); (f) is the images recorded using a digital camera; (g) and (h) are imaginary and real part capacitance spectra before and after nucleation in the TVIS vial. The dashed line demonstrated discontinuity in the profile due to ice nucleation.

Furthermore, it has been possible to use real part capacitance measured at a selected frequency to determine phase transition during freezing. In **Figure 77**d and e, the immediate change in the C'(10 Hz) and C'(0.2 MHz) synchronised with the onset of ice formation. This revealed an alternative way to monitor ice nucleation. A rapid increase in the real part at low frequency (i.e. 10 Hz) might be explained in terms of temperature sensitivity (**Figure 77**). As the heat released during phase change (crystallisation) can raise the product temperature, this effect might be responsible for the spike in the C'(10 Hz) profile. However, it is unclear why the ice nucleation event is reflected in the time profile of real part capacitance at high frequency range (i.e. 0.2 MHz), which is almost temperature independent (**Figure 77**). One possible explanation is that the C'(0.2 MHz) parameters are much more sensitive to frozen structure than temperature. Since the dielectric permittivity of ice is much lower than the water at the high frequency range of the TVIS window (e.g. > 0.1 MHz), the value of this parameter might be impacted by the amount of ice formed, leaving it unable to indicate the end of ice solidification. The use of TVIS technology in determining the solidification endpoint will be discussed next.

In general, when sodium chloride was added to the sucrose solution, the more ions present in the solution, the higher the conductivity. Here, the TVIS approach to characterising phase transition of a more conductive sample (5% w/v sucrose containing either 0.26% or 0.55% NaCl) was investigated (**Figure 78** and **Figure 79**).

In the case of 0.26% NaCl (Figure 78), the time profile reflected nucleation at 1.63h and 1.73h for the thermocouple (**Figure 78**a) and TVIS results (**Figure 78**d) respectively. Ice nucleation detected by the camera was delayed by approximately 2 minutes for both the TC (1.67h) and TVIS vial (1.77h) (**Figure 78**f). A small discrepancy in nucleation time between the numerical data and image can be explained by two possible causes. One is that the formation of the initial nuclei is difficult to observe by sight, while the image could only evidence secondary nucleation, normally developed after primary nuclei are formed; whereas TVIS is the more sensitive technique, which could detect any physical change in the sample, including primary nucleation. The TVIS result of 5% sucrose solution with 0.55% NaCl (**Figure 79**) could support this idea. This

shows that TVIS indicated the nucleation event faster (1.80h, **Figure 79**d) than the image (1.83h, **Figure 79**f).

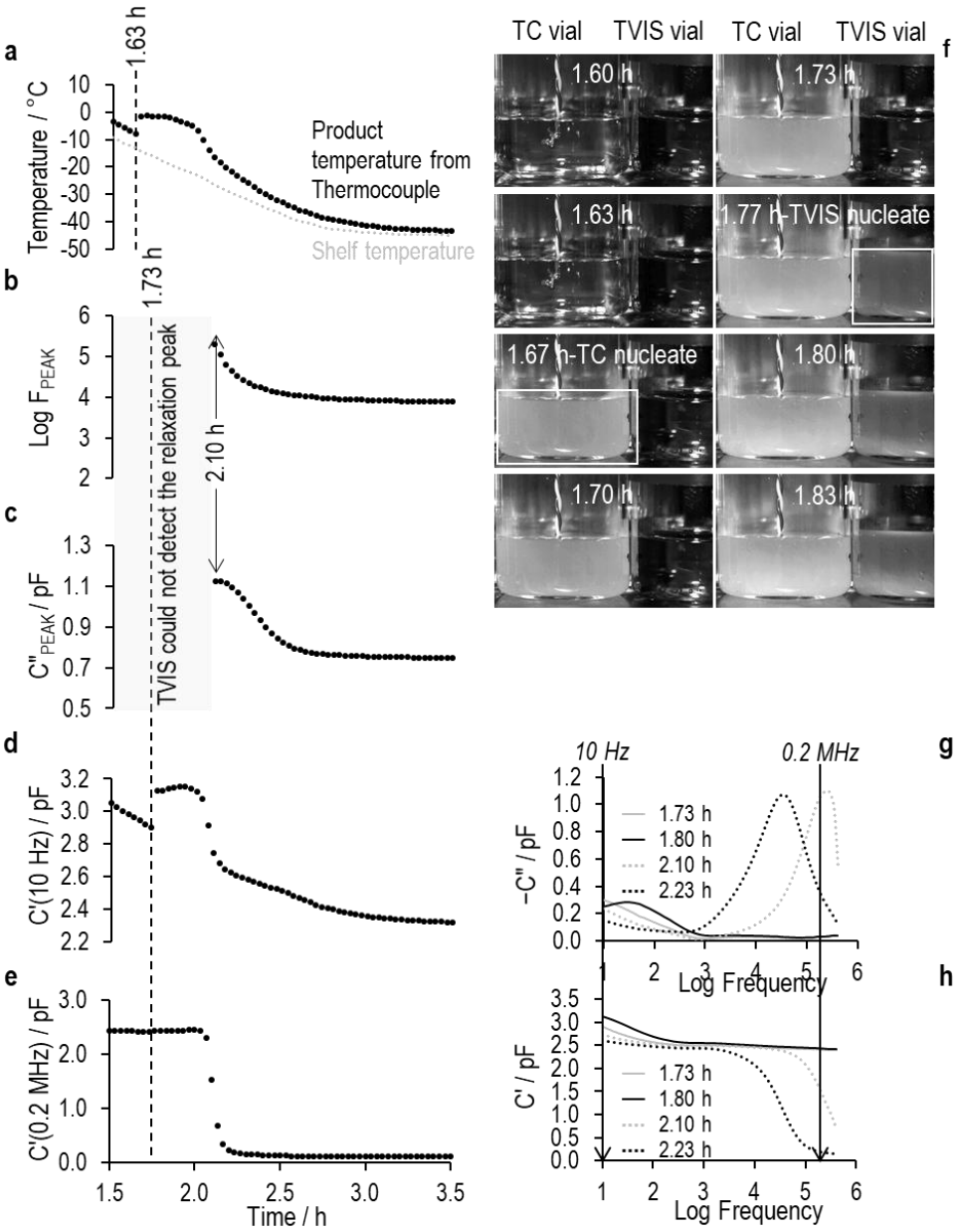

Figure 78 Experimental results for 5% w/v sucrose with 0.26% w/v NaCl demonstrate the onset of nucleation. (a) is the product profile and shelf temperature; (b) and (c) are the time profiles of the TVIS parameter C''_{PEAK} and F_{PEAK}; (d) and (e) are the time profiles of the real part capacitance C'(10 Hz) and C'(0.2 MHz); (f) is the images recorded using a digital camera; (g) and (h) are imaginary and real part capacitance spectra at the selected time points. The dashed line demonstrates discontinuity in the profile due to ice nucleation.

The second is the random error of the shooting start time (±3 s), especially when this happened a few minutes before nucleation. For example, if a camera at some point prior to nucleation started shooting before an elapsed time of 2 minutes, the photos recorded afterwards would shift to an earlier time and could not exactly match the data from the thermocouple and TVIS. In other words, the measurement data was recorded later than the photography; thus, the nucleation event indicated by both product temperature and TVIS data would be captured by the next image.

The TVIS results from a conductive sample (**Figure 78** and **Figure 79**) have also illustrated the following: (1) TVIS could not detect the relaxation process of the sample, although ice nucleation had started (as illustrated by the spectra (solid line) shown in **Figure 78**g-h and **Figure 79**g-h); (2) The relaxation peak became visible in the TVIS measurement window, as nucleation proceeded for a certain period. The dielectric relaxation process appearing at this stage was presumably the MW polarization of the frozen matrix, consisting of residual liquid water. During the ice formation process, conductivity of the frozen sample reduces in accordance with ice growth. When it drops to a value which the TVIS instrument could measure, the MW process of the heterogenous frozen sample would be obvious within the TVIS measurement range and move towards the low frequency side (as demonstrated by spectra (dot line) in **Figure 78**g-h and **Figure 79**g-h).

However, one thing to bear in mind here is that the dielectric relaxation process is a function of temperature (temperature dependence). (3) The absence of an inflection in the time profile of real part capacitance at 0.2 MHz (**Figure 78**e and **Figure 79**e) signifies that this parameter could not be exploited as the marker of nucleation onset. Before the relaxation presence in the TVIS frequency range (10 Hz to 1 MHz), the value of C'(0.2 MHz) parameter is the static permittivity (ε_s) of the combined contribution of the MW relaxation process and ionic conduction (from added NaCl). Therefore, the amount of ice does not play a predominant role in this parameter. This is illustrated by the example spectra before (solid line) and after (dotted line) the relaxation process appearing in the TVIS range (**Figure 78**g-h and **Figure 79**g-h).

This section demonstrated the use of real part capacitance at a low frequency limit to determine the onset of ice nucleation in a conductive sample. Apart from C''_{PEAK}, and F_{PEAK}, any changes in the C'(10 Hz) value, either with time or temperature, are associated with the onset of ice nucleation: an exothermic process.

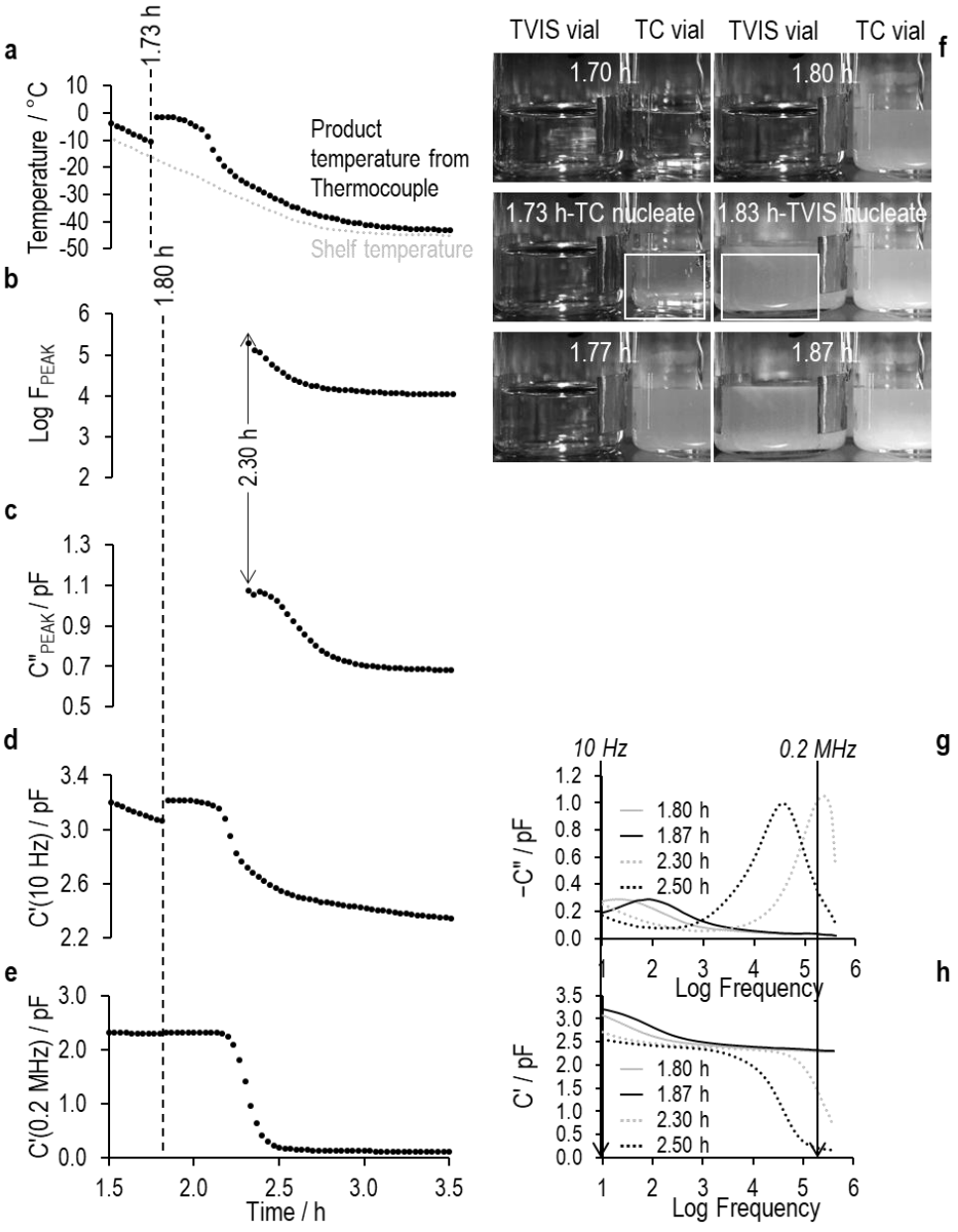

Figure 79 Experimental results for 5% w/v sucrose with 0.55% w/v NaCl demonstrate the onset of nucleation. (a) is the product profile and shelf temperature; (b) and (c) are the time profiles of the TVIS parameter C''_{PEAK} and F_{PEAK}; (d) and (e) are the time profiles of real part capacitance C'(10 Hz) and C'(0.2 MHz); (f) is the images recorded using a digital camera; (g) and (h) are imaginary and real part capacitance spectra at the selected time points. The dashed line demonstrates discontinuity in the profile due to ice nucleation.

Solidification

Once solidification is complete, the temperature of the frozen sample is gradually reduced to balance with the shelf temperature. This thermal exchange is attributed to the TVIS response. Of the TVIS parameters studied (i.e. C''_{PEAK}, F_{PEAK}, C'(10 Hz) and C'(0.2 MHz)), only real part capacitance at a high frequency limit (C'(0.2 MHz)) is less influenced by product temperature: exemplified by the TVIS data of pure ice (Figure 76). The amount of ice and unfrozen fraction, including the frozen structure, has much more an impact on the C'(0.2 MHz) value than the product temperature; any changes in the time profile of the C'(0.2 MHz) can be associated with the phase change and solidification process.

Consider the 5% w/v sucrose solution as an example. After ice nucleation at 1.97h, the value of C'(0.2 MHz) fell (Figure 80b and Figure 80c) as the ice phase increased (as evidenced by images in Figure 80d), then stabilised at the minimum of 0.11 pF (Figure 80b) after solidification was completed (confirmed by images in Figure 80d). Hence, by selecting real part capacitance at a high frequency range (e.g. 0.2 MHz), it is possible to determine the completion of ice formation. The solidification endpoint could be estimated using the lower inflection point of the C'(0.2 MHz) profile; alternatively stated, at the point where two linear fitting lines intersect, i.e. the first linear fitting line through the step data and the second linear fitting line of the plateau at the lowest value (Figure 80b).

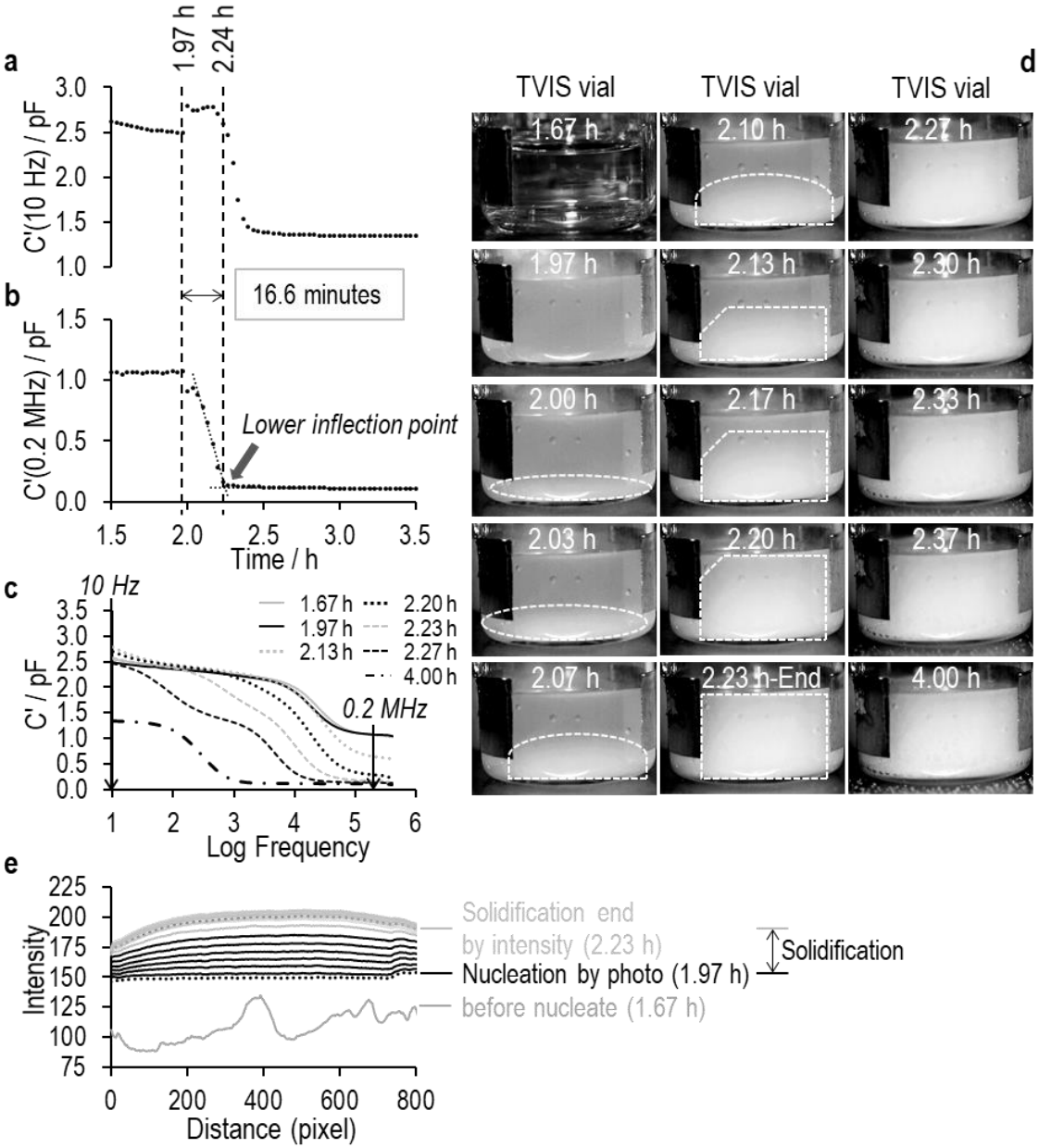

Figure 80 Experimental results for 5% w/v sucrose demonstrate the solidification endpoint. (a) and (b) are the time profiles of real part capacitance C'(10 Hz) and C'(0.2 MHz). The vertical black dashed lines demonstrate the onset of ice nucleation (1.97 h) and solidification endpoint (2.24 h) determined by TVIS; (c) is the real part capacitance spectra at the selected time points; (d) is the selected images demonstrating the solidification process. The progression of ice growth is illustrated by the white dashed line; (e) is the intensity profile of the defined area (Figure 72a) of the selected images (d). The defined area of the selected images is analysed using image processing software (ImageJ).

Although in the case of the more conductive sample, the C'(0.2 MHz) value did not drop after the ice nuclei was formed, this value fell during the development of the ice structure (**Figure 81**b and **Figure 82**b). This may be explained by the MW process of the frozen solution containing salt being out of the TVIS measurement range (10 Hz to 1 MHz). However, by increasing the ice fraction (i.e. the ice growth) and reducing the free water, sample conductivity is low enough for TVIS to result in a dielectric relaxation process within the measuring range (**Figure 81**c and **Figure 82**c). Therefore, the TVIS approach to determining the solidification endpoint of pure sucrose preparation can also be applied to a conductive sample (**Figure 81**b and **Figure 82**b).

The solidification endpoint determined by TVIS is confirmed by the photographic images in **Figure 80**d, **Figure 81**d and **Figure 82**d. As visual observation can create uncertainty in the measurement process (such as observer bias), a more accurate quantitative measurement is required. To avoid an unreliable outcome, the intensity quantification method was performed: transforming the image into numerical data in terms of pixel intensity. First, the region of interest (ROI) within the image was defined from the area of frozen mass excluding the electrode (**Figure 72**). Then, this defined area was processed by ImageJ software to obtain the intensity value. The plots of the vertical mean intensity value along the width of ROI (distance in pixel) of three samples are shown in **Figure 80**e, **Figure 81**e and **Figure 82**e. The lower the value of intensity, the more translucent it was. Pixel intensity increases (becoming opaquer) when ice is formed. The value of intensity continually increases as ice growth proceeds. Once solidification is complete, the change in intensity is not observed. In other words, the intensity of the defined area remains the same; therefore, the point where the image starts to maintain steady intensity could be used to indicate the endpoint of the solidification process (the grey dotted line in **Figure 80**e, **Figure 81**e and **Figure 82**e).

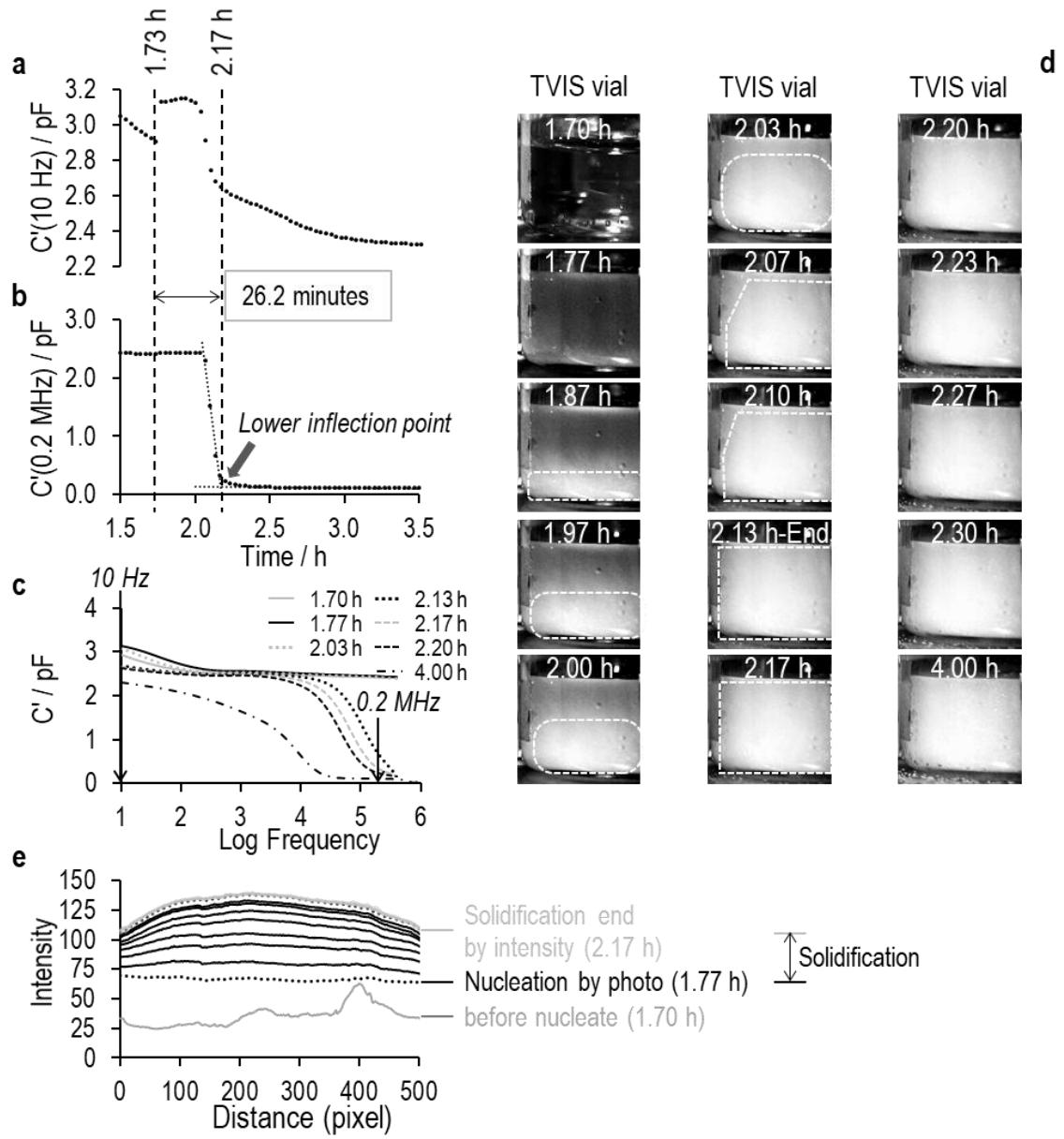

Figure 81 Experimental results for 5% w/v sucrose with 0.26% w/v NaCl demonstrate the solidification endpoint. (a) and (b) are the time profiles of real part capacitance C'(10 Hz) and C'(0.2 MHz). The vertical black dashed lines demonstrate the onset of ice nucleation (1.73 h) and solidification endpoint (2.17 h) determined by TVIS; (c) is the real part capacitance spectra at the selected time points; (d) is the selected images demonstrating the solidification process. Progression of the ice growth is illustrated by the white dashed line; (e) is the intensity profile of the defined area (Figure 72b) of the selected images (d). The defined area of the selected images is analysed using image processing software (ImageJ).

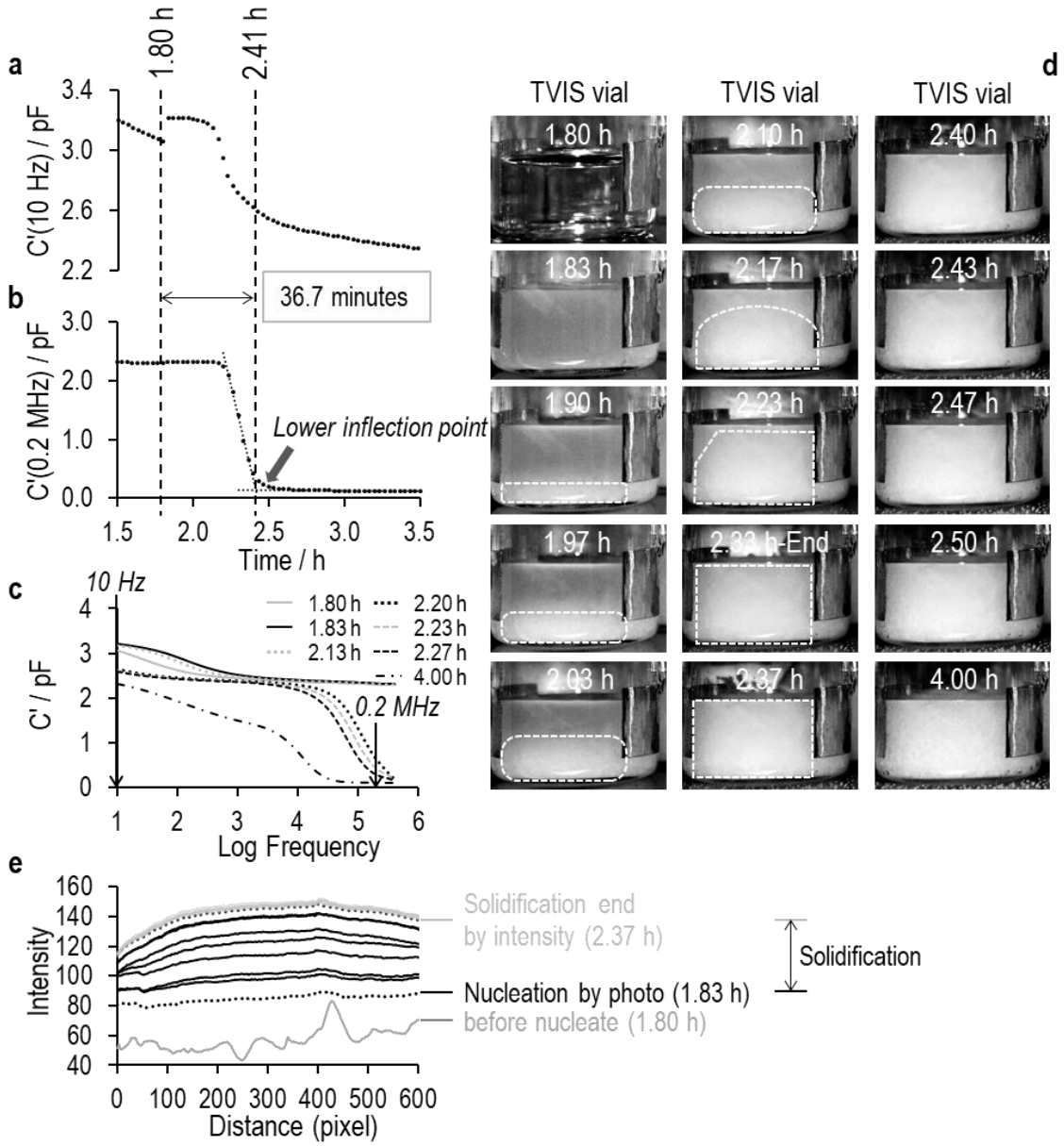

Figure 82 Experimental results for 5% w/v sucrose with 0.55% w/v NaCl demonstrate the solidification endpoint. (a) and (b) are the time profiles of real part capacitance C'(10 Hz) and C'(0.2 MHz). The vertical black dashed lines demonstrate the onset of ice nucleation (1.80 h) and solidification endpoint (2.41 h) determined by TVIS; (c) is the real part capacitance spectra at the selected time points; (d) is the selected images demonstrating the solidification process. The progression of ice growth is illustrated by the white dashed line; (e) is the intensity profile of the defined area (Figure 72c) of the selected images (d). The defined area of the selected images is analysed using image processing software (ImageJ).

Table 9 Solidification endpoint determined by different techniques: TVIS, visual inspection and an image analysis program (ImageJ)

Sample	TVIS	Visual inspection	Image analysis
S-1 (0% NaCl)	2.24 h	2.23 h	2.23 h
S-2 (0.26% NaCl)	2.17 h	2.13 h	2.17 h
S-3 (0.55% NaCl)	2.41 h	2.33 h	2.37 h

The solidification endpoint of 5% sucrose with 0, 0.26 and 0.55% NaCl, as determined by TVIS, the direct visual inspection and image analysis, is reported in Table 9. The results obtained from visual inspection and the image analysis agree with each other within 2.5 minutes; while the difference observed between TVIS and image-based techniques is less than 5 minutes. The camera is placed in front of the chamber window; thus the information obtained from the two-dimensional image is from a front view, and cannot wholly represent the solidification process of all content in the vial, especially at the centre (Burns, Stickler & Stewart, 1992). For instance, in the case of one-dimensional radial ice formation, this usually starts from the outside and moves inward; consequently, the sample near the centre of the vial might solidify more slowly than that close to the glass wall. However, the endpoint determined by TVIS is broadly accepted. The images and evidence from this study suggests the possibility of using TVIS parameters (i.e. C'(0.2 MHz)) in determining solidification endpoints.

7.3.2. Determination of ice nucleation temperature

Through a TVIS approach, we propose two scenarios of assessing nucleation temperature. First, in cases where the TVIS vial nucleates before the thermocouple is inserted, nucleation temperature can be inferred directly from thermocouple temperatures in the nearest neighbour vials. However, in general, the thermocouple vial tends to nucleate prior to the TVIS vial because of the impact of the temperature probe (Nail et al., 2017, Roy & Pikal, 1989, Pikal, Rambhatla & Ramot, 2002). This brings us to another scenario: temperature calibration is required. As expected, in this study, ice formation occurred in the vial with thermocouple before the TVIS vial (confirmed by images in Figure 77f, Figure 78f and Figure 79f). We will focus on the latter case, which applies the temperature calibration plot in determining ice nucleation temperature.

Owing to the dependency of the Maxwell-Wagner relaxation process on the product temperature (Smith & Jeeraruangrattana, 2019), it is possible to predict the product temperature of the solution (liquid state) using thermocouple temperatures (T_{TC}) in the vial next to the TVIS one against temperature-sensitive TVIS parameters such as dielectric loss spectrum (i.e. C''_{PEAK} and F_{PEAK}). The dependence of TVIS parameters, C''_{PEAK}, F_{PEAK}, C'(10 Hz) and C'(0.2 MHz) of 5% w/v sucrose solution (liquid state), is demonstrated in Figure 83. Interestingly, unlike the frozen state, the temperature coefficient of C'(10 Hz) is two times greater than that of C''_{PEAK} and F_{PEAK}; whereas the real part at the high frequency end (C'(0.2 MHz)) has almost no temperature dependence. Besides C'(10 Hz), both C''_{PEAK} and F_{PEAK} could also be used for liquid temperature calibration, even though they have less temperature dependence than C'(10 Hz).

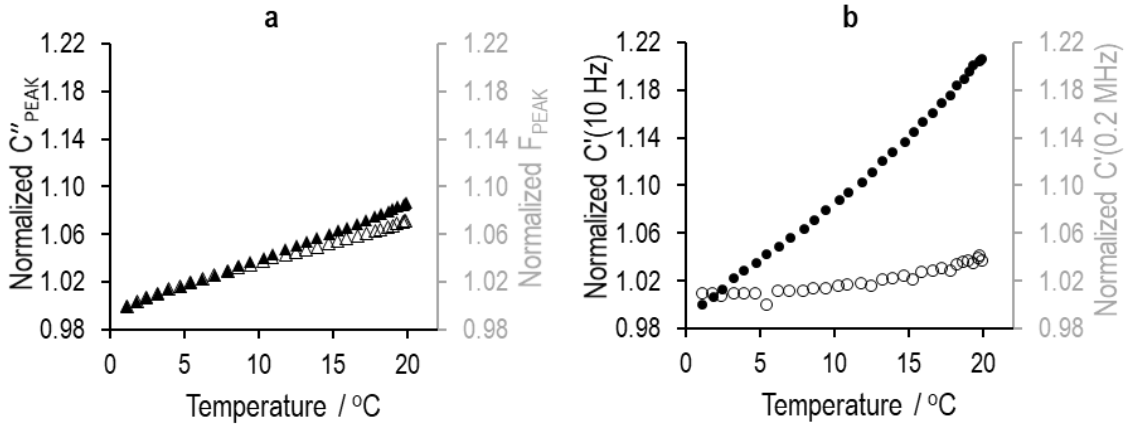

Figure 83 Temperature dependencies of (a) peak amplitude (closed triangle) and peak frequency (open triangle); and (b) real part capacitance at 10 Hz (closed circle) and 0.2 MHz (open circle) of 5% w/v sucrose solution during the liquid cooling phase.

Temperature calibration is achieved by plotting thermocouple temperatures (T_{TC}) in the vial placed adjacent to the TVIS one against the temperature-sensitive TVIS parameter: C''_{PEAK}, F_{PEAK} and C'(10 Hz), at the corresponding time point when each temperature was recorded (every 2 minutes); before fitting the data to the mathematical function. The TVIS-predicted product temperature is then extrapolated beyond calibration range by substituting the values of TVIS parameters into the x-parameter of the fitting function from the calibration curve.

In order to predict ice nucleation temperature, the calibration curve of the supercooled solution is generated. The rationale in choosing the supercooling data is that water molecules at sub-zero temperature are in a metastable state and arrange themselves differently from liquid water (Gallo & Stanley, 2017; Assegehegn et al., 2019). With the different orientation of hydrogen bonds, the dielectric properties of water and a supercooled solution are supposed to be dissimilar (Varghese et al., 2019). For our study, linear regression provides the best-fitting line for temperature calibration of C''_{PEAK} and F_{PEAK}, while the calibration plot of C'(10 Hz) fits well with a second order polynomial. The fitting coefficients for C''_{PEAK}, F_{PEAK} and C'(10 Hz) are presented in **Table 10**. By using the fitting coefficient along with the value of TVIS parameter at the onset of ice nucleation (**Figure 84**), the ice nucleation temperature is predicted.

Table 10 Temperature calibration from TVIS parameters, $Log\ F_{PEAK}$, C''_{PEAK}, and C'(10 Hz), predicting the nucleation temperature (T_n) of 5% w/v sucrose solution

Order of fitting coefficient	2	1	0
$\boldsymbol{Log\ F_{PEAK}}$		6.29E+01	-2.79E+02
$\boldsymbol{C''_{PEAK}}$		6.15E+02	-3.45E+02
$\boldsymbol{C'}$(10 Hz)	-3.74E+02	2.01E+03	-2.69E+03

From the freezing profile of product temperature (**Figure 84**a-c) and TVIS parameters (**Figure 84**d-f) of pure sucrose solution, it is clearly demonstrated that the TC vial nucleated at 1.90h, with a product temperature of −9.5 °C; followed by the TVIS vial (1.97h). The values of TVIS parameters at the onset of ice nucleation (1.97 h) are as follows: $Log\ F_{PEAK}$ 4.26 (**Figure 84**d), C''_{PEAK} 0.543 pF (**Figure 84**e) and C'(10 Hz) 2.49 pF (**Figure 84**f). Using these along with the calibration coefficient, the TVIS nucleation temperature can then be calculated. The predicted nucleation temperatures from $Log\ F_{PEAK}$, C''_{PEAK}, and C'(10 Hz) are −10.6 °C ($T_n(F_{PEAK})$), −11.0 °C ($T_n(C''_{PEAK})$) and −10.5 °C ($T_n(C'_{10\ Hz})$), respectively. These results are in good agreement (−10.7±0.2 °C). The nucleation temperature determined from $Log\ F_{PEAK}$ is more comparable to C'(10 Hz). The difference in nucleation temperatures between those two parameters is as low as 0.1 °C.

Although these TVIS parameters ($Log\ F_{PEAK}$, C''_{PEAK}, and C'(10 Hz)) can be exploited to determine ice nucleation temperature, $T_n(C''_{PEAK})$ is a less preferred approach due to the

inconsistency of C''_{PEAK} in liquid measurement. This parameter (C''_{PEAK}) is not only the function of temperature, but also depends on the height of the liquid contact with the glass vial. Liquid meniscus caused by surface tension is a simple example. For most of the liquid, the meniscus is in a concave shape. The higher the surface tension (e.g. water), the larger the surface between the sample and glass wall in contact with the electrodes; and consequently, the higher the capacitance (C), according to the standard formula for a parallel capacitor ($C = \varepsilon_o A/d$: where ε_o is the permittivity of free space, A is the area of interface between the liquid and glass adjacent to the electrode, and d is the distance between the electrodes). Although peak frequency is inversely proportional to a product of resistance (R) and capacitance (C) ($F_{PEAK} \propto 1/RC$), this parameter is dominated by resistance, which has a greater value than capacitance (Smith et al., 2017); therefore, the impact of the liquid height on F_{PEAK} could be negligible. Results so far encourage the use of $Log\ F_{PEAK}$ and C'(10 Hz) parameter in determining T_n.

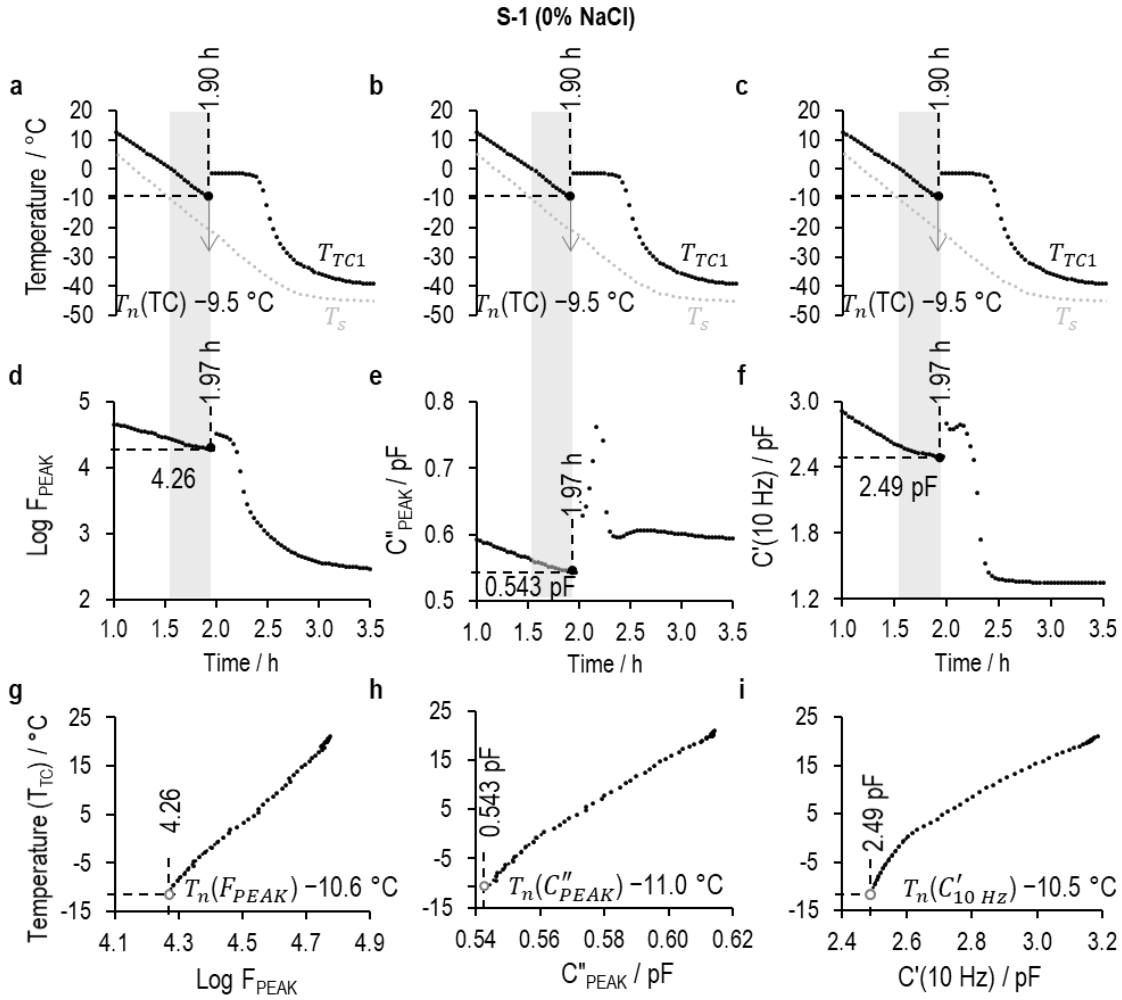

Figure 84 Determination of the ice nucleation temperatures (T_n) of 5%w/v sucrose using the following TVIS parameters: $Log\ F_{PEAK}$, C''_{PEAK}, and C'(10 Hz). (a-c) are the temperature profiles from the thermocouple in the nearest neighbour vial (T_{TC1}) and shelf temperature (T_s); (d-f) are the time profile (from 1.0 to 3.5h) of the TVIS parameters: (d) $Log\ F_{PEAK}$, (e) C''_{PEAK}, (f) C'(10 Hz); (g-i) are the calibration plots between the thermocouple temperature within the adjacent vial (T_{TC}) and the value of (g) $Log\ F_{PEAK}$, (h) C''_{PEAK} and (i) C'(10 Hz). The grey region demonstrates the data range used to create the temperature calibration curve. The nucleation temperature measured from the thermocouple (T_n(TC)) is −9.5 °C. At the onset of ice nucleation of 1.90h, the corresponding values of $Log\ F_{PEAK}$, C''_{PEAK}, and C'(10 Hz) are 4.26 pF, 0.543 pF and 2.49 pF, respectively. The nucleation temperatures of −10.6 °C, −11.0 °C and −10.5 °C are predicted from $Log\ F_{PEAK}$, C''_{PEAK}, and C'(10 Hz). Note: the nucleation temperature is extrapolated from the calibration plot of $Log\ F_{PEAK}$, C''_{PEAK}, and C'(10 Hz): denoted as $T_n(F_{PEAK})$, $T_n(C''_{PEAK})$ and $T_n(C'_{10\ Hz})$.

In practice, a parenteral product adds a tonicity agent like sodium chloride to adjust osmolarity of the preparation in order to minimise pain and irritation at the injection site; an injection preparation typically becomes more conductive than water or a pure sugar solution. The MW polarization of the conductive solution plays a role at a frequency above 1 MHz; it is difficult to detect the relaxation process by TVIS (Figure 75c-f), whereas the value of the real part at a fixed low frequency (i.e. 10 Hz) can be measured. This means that $C'(10\,\text{Hz})$ is a good option for achieving the nucleation temperature because it is a universal parameter, predicting it in both cases (i.e. the low conductive and high conductive solution). Here, we will employ $C'(10\,\text{Hz})$ to assess the nucleation temperature of 5% w/v sucrose, with 0.26% NaCl (S-2) or 0.55% NaCl solutions (S-3).

Table 11 Temperature calibration coefficient from $C'(10\text{Hz})$ parameter, predicting the nucleation temperature $T_n(C'_{10\,Hz})$

Order of fitting coefficient	2	1	0
S-2 (0.26% NaCl)	-5.26E+01	3.66E+02	-6.30E+02
S-3 (0.55% NaCl)	5.83E+01	-3.05E+02	3.74E+02

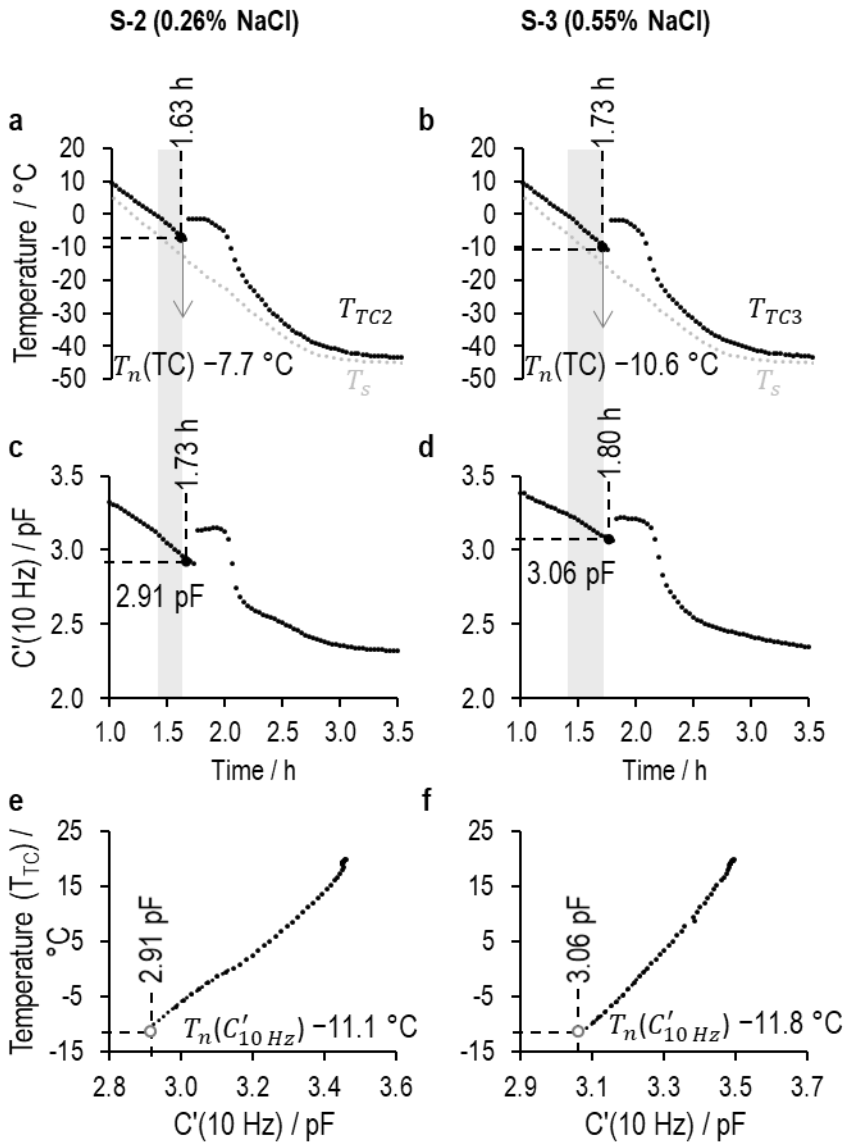

Figure 85 Determination of ice nucleation temperatures from C'(10 Hz)— $T_n(C'_{10\,Hz})$—of 5%w/v sucrose with either 0.26% (S-2) or 0.55% NaCl (S-3). (a-b) are the temperature profiles from the thermocouple in the nearest neighbour vial (T_{TC}) and shelf temperature (T_s): (a) S-2 (T_{TC2}) and (b) S-3 (T_{TC3}); (c-d) are the time profiles of the C'(10Hz) value of (c) S-2 and (d) S-3 over a 2.5 h freezing stage (from 1.0 h to 3.5 h); (e-f) are the calibration plots between the thermocouple temperature within the adjacent vial (T_{TC}) and value of C'(10Hz) for (e) S-2 and (f) S-3. The shaded region demonstrates the data range used in creating the temperature calibration of the supercooled solution. The nucleation temperatures measured from the thermocouple (T_n(TC)) are −7.7 °C and −10.6 °C for S-2 and S-3. At the onset of ice nucleation, C'(10 Hz) for S-2 and S-3 are 2.91 pF and 3.06 pF, respectively. The nucleation temperatures predicted from C'(10 Hz) are −11.1 °C and −11.8 °C.

As shown in Figure 85, the C'(10 Hz) profile of both samples demonstrated nucleation onset at 1.73h and 1.80h for S-2 (Figure 85c) and S-3 (Figure 85d), respectively. The values of C'(10 Hz) corresponding to the nucleation point in the TVIS vials are 2.91 pF (S-2, Figure 85c) and 3.06 pF (S-3, Figure 85d). Based on the freezing profile of the thermocouple temperature (T_{TC}) (Figure 85a for S-2 and Figure 85b for S-3) and the measured C'(10 Hz) (Figure 85c for S-2 and Figure 85d for S-3) at sub-zero temperatures (the shaded region in Figure 85), this allows us to construct the calibration plot of supercooled liquid. The calibration was fitted to the 2nd polynomial regression to provide best fit, as shown in Figure 85e (S-2) and Figure 85f (S-3). The fitting coefficients of the supercooled data are given in Table 11. By extrapolating the calibration curve to the C'(10 Hz) value at which ice nucleates (2.91 pF for S-2 and 3.06 pF for S-3), the nucleation temperature ($T_n(C'_{10\ Hz})$) is estimated: as shown in Figure 85e (S-2) and Figure 85f (S-3). The nucleation temperature of three samples with different NaCl concentrations are presented in Figure 86.

At first glance in **Figure 86**, the vial with the thermocouple nucleates faster at a higher temperature (low degree of supercooling) than the TVIS vial. In addition, the nucleation temperature of the TC vial T_n(TC) was random and did not show a clear trend with sodium chloride concentrations. This further supports the idea that the temperature sensor can act as the nucleation site, generating uncertainty of measurement (Pikal, Rambhatla & Ramot, 2002; Nail et al., 2017; Roy & Pikal, 1989). On the other hand, the nucleation temperature of the TVIS vial predicted from the measured C'(10 Hz) ($T_n(C'_{10\ Hz})$) was lower than that observed in the TC vial. The difference between T_n(TC) and $T_n(C'_{10\ Hz})$ for each sample is up to 3.5 °C. This highlights that the information obtained from the TC vial could not represent the entire batch. This variation should be taken into consideration during process development.

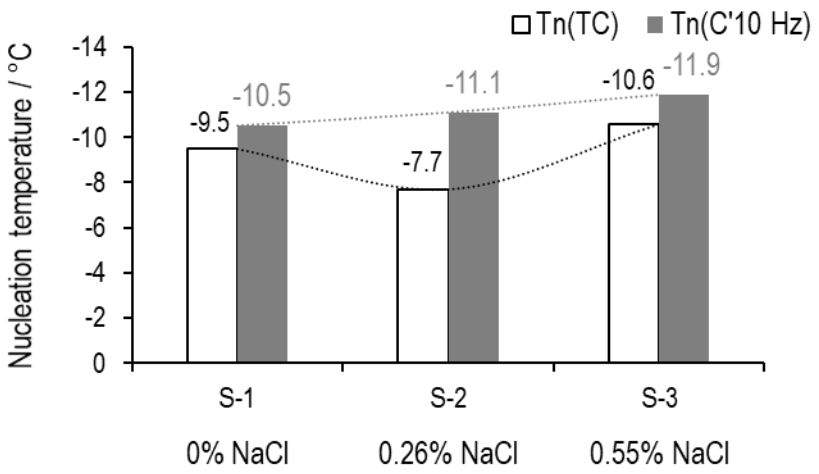

Figure 86 Nucleation temperature of 5%w/v sucrose with either 0% NaCl (S-1), 0.26% NaCl (S-2) or 0.55% NaCl (S-3). The value above the white bar and grey bay indicates the nucleation temperature from the thermocouple (T_n(TC)) and TVIS technique ($T_n(C'_{10\ Hz})$), respectively.

It is also worth noting that $T_n(C'_{10\ Hz})$ decreased when the salt concentration increased. Given that TVIS is a non-invasive technique (the electrode is attached on the outer surface of the vial), it does not alter the nature of ice formation. The nucleation temperature is directly affected by the contents: sucrose and/or NaCl. This is a known phenomenon—"freezing point depression". Wilson and Haymet (2009) reported that it fell by 7 °C as the NaCl rose from 0% to 5.8%. The addition of solute could promote the nucleation process; if it includes particulate matter, it can act as the active surface for ice nucleation. It is followed by a lower degree of supercooling. With respect to the colligative property of the solution, there is no doubt that a high level of solute content can reduce the freezing point. The linear relationship between the lowering of nucleation temperature (ΔT_n) and that of the equilibrium freezing temperature (ΔT_f), Equation 62, is observed for a heterogenous system (Wilson & Haymet, 2009; Charoenrein, Goddard & Reid, 1991)

$$\Delta T_n = k\Delta T_f \qquad \text{Equation 62}$$

where k is the experimental constant. We usually assume this constant as 2.

For example, if salt is added into water and the freezing point is reduced by 5 °C but the nucleation temperature by 10 °C, there is a higher degree of supercooling, so a smaller ice crystal is produced.

Note: the degree of supercooling is the temperature difference between the equilibrium freezing temperature (T_f) and the nucleation temperature (T_n).

An impact of the ice nucleation temperature on the ice structure (i.e. size and morphology) and a subsequent primary drying rate has been well-established (Roy & Pikal, 1989; Searles, Carpenter & Randolph, 2001; Rambhatla et al., 2004; Nakagawa et al., 2006). The lower the nucleation temperature, the higher the degree of supercooling, which can produce a small ice crystal and increase drying time. Hence, the size of the ice crystal would decrease as the salt concentration increases. In this work, if we consider NaCl concentrations only, 5% sucrose with 0.55% solution should provide the smallest ice crystal, followed by the longest processing time.

7.3.3. Impact of salts on the ice formation period

Here, we develop the method based on through-vial impedance spectroscopy, to determine the time period required to complete the ice formation process (nucleation and ice growth). This is calculated based on the time difference between the point when nucleation commences and ice completely solidifies (solidification endpoint). With a TVIS technique, a spike in time profile of C'(10 Hz) is associated with the ice nucleation event; while the end of solidification is an inflection point in the C'(0.2 MHz) profile. The determination of the ice formation period of three samples is demonstrated in Figure 80 (S-1), Figure 81 (S-2) and Figure 82 (S-3); the results are summarised in Figure 87.

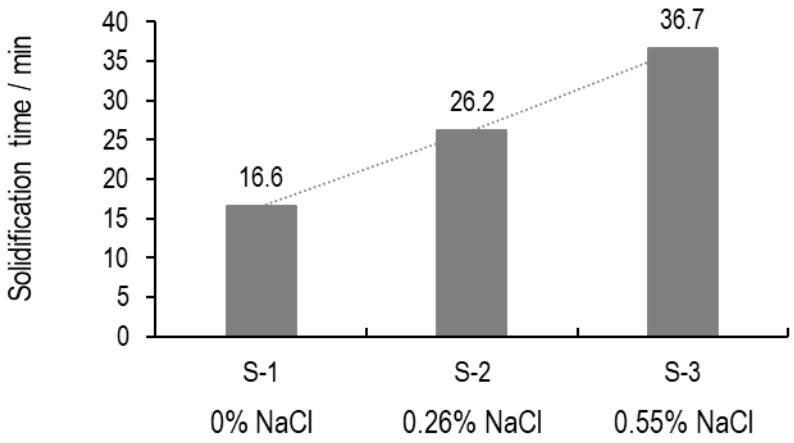

Figure 87 Time required for complete ice formation of 5% w/v sucrose solution with either 0% (S-1), 0.26% (S-2) and 0.55% NaCl (S-3). Real part capacitance at 10 Hz and 0.2 MHz is used to determine the beginning and end of the ice formation process.

In Figure 87, a twofold increase in solidification time as salt concentration increases from 0 to 0.55% is revealed. A basic understanding of ice growth is necessary to explain this result. Ice growth is a process of adding water molecules to solid-liquid interface (i.e. ice-solution), controlled by a mass transfer mechanism. Water molecules diffuse from the solution, then adhere onto the ice crystal to increase ice size; the solutes diffuse simultaneously into the surrounding bulk solution, so that the bonding interaction plays a part in ice formation. If the NaCl is dissolved in liquid water, water and ions will be formed as a particular ionic interaction. Given that an ionic bond is stronger and more difficult to break than a covalent bond (i.e. H-bond of water molecules), it follows that the water-ion interaction will restrict increases in the size of ice crystals. Ice growth is delayed by salt; solidification time increases accordingly. Another explanation is the formation of a highly concentrated layer on the outer surface of the ice due to the rejection of salt during ice growth, referred to as constitutional supercooling. The existence of this could reduce the solid-liquid equilibrium temperature at the ice surface by depressing the freezing point (i.e. more solute), increasing supercooling.

Several studies have attempted to determine the morphology of ice structure (Arsiccio et al., 2019; Grassini et al., 2016; Nakagawa et al., 2018; Rambhatla et al., 2004; Colucci, Maniaci & Fissore, 2019). The size of ice crystal could be estimated from the rate of crystalline growth (R) and

temperature gradient across the frozen zone (G), resulting in the relationship between ice crystal size (D); both factors are expressed below (Colucci, Maniaci & Fissore, 2019; Nakagawa et al., 2007):

$$D = a\mathrm{R}^{-\lambda_1}\mathrm{G}^{-\lambda_2} \qquad \text{Equation 1}$$

Where a, $-\lambda_1$ and $-\lambda_2$ are a constant value and could be obtained from the experimental data.

Here, a simplified TVIS approach to determine how fast the ice developed to the front is proposed. An average solidification rate (R_{avg}) is calculated by dividing the thickness of frozen matrix (L_{frozen}) by the solidification period:

$$R_{avg} = \frac{L_{frozen}}{t_{end} - t_{onset}} \qquad \text{Equation 63}$$

where t_{end} is the time point at which ice completes solidification and t_{onset} is the time point where nucleation is initiated. The freezing profile of C'(10 Hz) parameters is used to provide t_{onset}, while the solidification endpoint (t_{end}) is estimated from the C'(0.2 MHz) profile. Photographic images of each sample at 4h of the freezing process were processed using an image analysis program (ImageJ) to provide the thickness of the frozen mass (L_{frozen}) in five different positions (Figure 73). The value of these measurements was then averaged. All parameters used for R_{avg} calculation are listed in Table 12.

Table 12 Solidification endpoint determined by different techniques: TVIS, visual inspection and an image analysis program (ImageJ).

Sample	L_{frozen} (mm)	Solidification time ($t_{end} - t_{onset}$, min)	R_{avg} (mm·min^{-1})
S-1 (0% NaCl)	11.0	18	0.61
S-2 (0.26% NaCl)	11.5	24	0.48
S-3 (0.55% NaCl)	11.3	36	0.31

The average solidification rate at various times the amount of NaCl added into 5% w/v sucrose is reported in **Table 12**. Increasing sodium salt by 0.55% can cause an approximate decrease of 50% in the solidification rate. This means that salt could delay ice formation through water-ion

interaction and/or its accumulation on the ice surface. It comes as no surprise that ice growth rate falls as more salt is added.

7.4.Summary

Discontinuity in the time profile of TVIS parameters, (1) peak frequency (F_{PEAK}), (2) peak amplitude (C''_{PEAK}), and (3) real part capacitance at low frequency of 10 Hz (C'(10 Hz)), could indicate the onset of ice nucleation, confirmed by evidence from a digital camera. However, for the conductive sample, the real part at low frequency presented more benefit than the other two parameters. By using the temperature recorded from the nearest neighbouring vial, the nucleation temperature could be estimated from C'(10 Hz). Conversely, the real part at higher frequency (i.e. 0.2 MHz) demonstrates the possibility of determining the ice solidification endpoint (from which the freezing time can be calculated). Interestingly, solidification time increased when increasing the salt content.

8. Effect of annealing on the structure of frozen matrices

8.1. Objective

The objective of this chapter is to explore the use of TVIS parameters in characterising the physical mechanisms of frozen sucrose during the thermal treatment process. A 5% w/v sucrose solutionwas cooled to –50 °C and annealed at either –35 °C (below T_g'), –32 °C (~T_g') or –10 °C (above T_g'); three annealing cycles were run for each sample at each temperature. The cycle that heats through glass transition (i.e. –10 °C) intends determination of the glass transition within the vial. Both structural modification of frozen matrices and the glass transition event were focused on. Peak characteristics of an imaginary part capacitance spectrum (i.e. F_{PEAK}, C''_{PEAK}) were employed to study structural changes; while real part capacitance at fixed frequency (i.e. 0.2 MHz) was selected to determine the glass transition temperature.

8.2. Material and Methods

8.2.1. Preparations

A total of 5 g sucrose (Fluka) was accurately weighed and dissolved in ultrapure water (18.2 MΩ·cm) to obtain 100 mL of a stock solution containing 5% w/v sucrose.

8.2.2. Thermal analysis

Conventional differential scanning calorimetry

Standard differential scanning calorimetry (DSC) (without any modulating frequency) was used to determine the glass transition of the cryo-concentrated phase (T_g') of the 5% w/v sucrose solution at different heating rates of 5, 10, and 20 °C·min^{-1} by measuring total heat flow as a function of temperature, using a Perkin Elmer Jade DSC (USA) according to the following procedure. Approximately 10mg of 5% w/v sucrose solution was placed in a 50 µl aluminium pan (part no. BO143017) and crimped with a holed lid. The sample was cooled to −50 °C, then ramped to 30 °C. The glass transition temperature was reported at the onset, midpoint and endpoint of the thermal transition.

Modulated differential scanning calorimetry

Here, a sinusoidal temperature oscillation during the temperature ramp is applied to the traditional DSC method. This approach enables separation of responses of the heat capacity component (reversing heat flow) from the other kinetic process (non-reversing heat flow), so that the glass transition can be detected more readily.

The measurement of the glass transition (T_g') of the freeze-concentrated solution of 5% w/v sucrose solution was performed using a Q2000 modulated differential scanning calorimetry (mDSC) TA instrument (UK). An 80 µl sample was pipetted into a high volume aluminium pan (part no. 900825.902) and sealed using a sample-encapsulating press. The sample pan was cooled to −90 °C at 10 °C·min^{-1}, then ramped to 25 °C at 1.5 °C·min^{-1}, with a modulated heating rate of 0.23 °C·min^{-1} every 60s. Three regions (the onset, midpoint, and endpoint) of the thermal step in the reversing heat flow of the mDSC thermogram were analysed by Universal Analysis 2000 software (TA Instruments, New Castle, USA) and defined as the glass transition temperature of the maximally freeze-concentrated 5% w/v sucrose solution.

8.2.3. Vial filling and loading of the freeze dryer

A cluster of eighteen 10-mL standard clear Type 1 tubular glass vials (1096936, Schott, Hungary, supplied as VC010-20C, Adelphi-HP); and one through vial impedance spectroscopy (TVIS) measurement vial, were each filled with 3.2 g aliquots 5% w/v sucrose solution. The TVIS vial was manufactured from the same type of 10 mL tubing by attaching a pair of self-adhesive copper foil electrodes to the outer surface, each with height-by-width dimensions of 10 × 19 mm; they were positioned on opposite sides at a distance of 3 mm above the vial base. For the TVIS vial, a fill weight of 3.2 g is equivalent to a sample height of 9mm from the midpoint of the internal base and corresponds to a fill factor (Ø) of 0.7 (where Ø is defined as the relative height of the sample solution within the electrode region to the height of the electrode), as demonstrated in Figure 88.

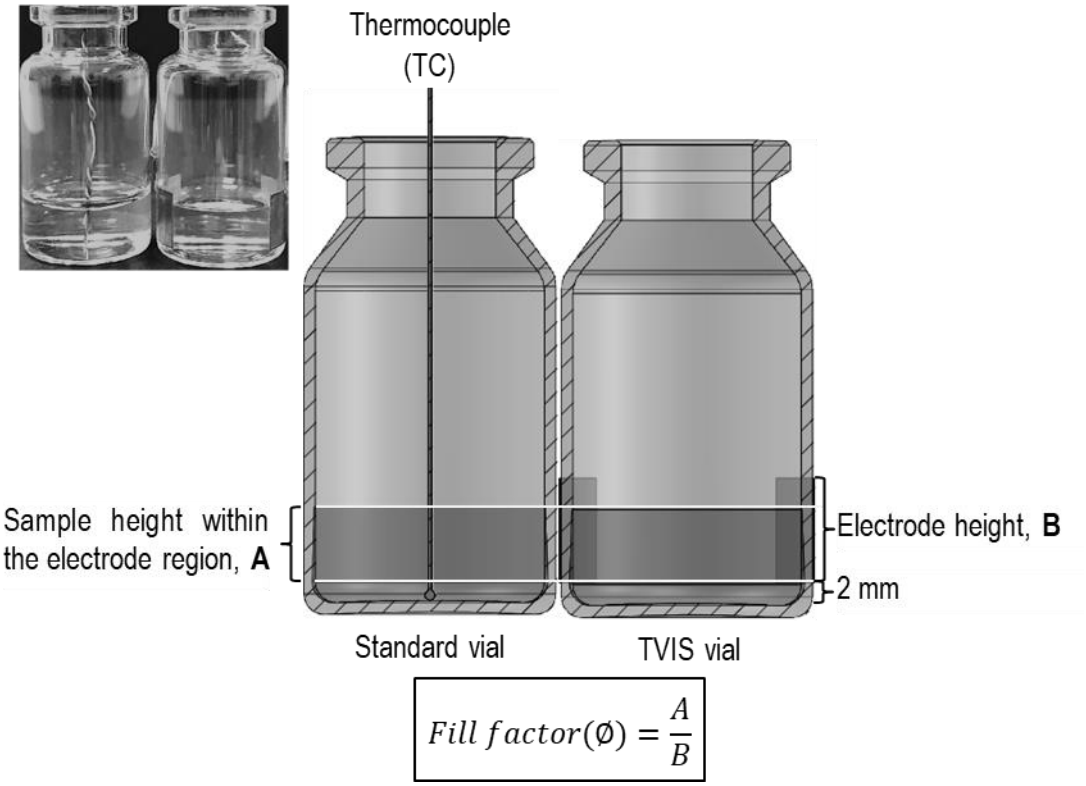

$$Fill\ factor(\emptyset) = \frac{A}{B}$$

Figure 88 Vertical cross-sections of two vials containing 3.2 g of 5% w/v sucrose solution. **Right:** Modified TVIS vial attached with a pair of copper electrodes (19 x 10 mm) positioned at 2 mm from the internal vial base. **Left:** A standard vial (10 mL nominal capacity) with a type-T thermocouple is inserted in the liquid sample, so that the thermocouple bead is positioned at the bottom centre of the vial, where it provides a surrogate product temperature for the same position in the nearest TVIS vial. The fill factor (Ø)is 0.7: which means that the sample height in the electrode region is 7 mm for an electrode height of 10 mm.

Four T-type 28 AWG thermocouples (TC) were used to measure the product temperature in three standard vials containing 5% w/v sucrose solution. In each case, the thermocouples were inserted through holes drilled into the rubber stoppers. One of the three vials had two temperature sensors, with one sensing element (TC1) placed at the bottom centre of the vial base, the other (TC2) close to the sample level (i.e. just below the sample meniscus) to assess the uniformity of product temperature in the axial direction. The other two vials had one thermocouple, each with their sensing beads (TC3 & TC4) touching the bottom centre of the vial base. Each TC vial was placed in a triangular array at three of the six positions adjacent to the TVIS vial containing 5% sucrose solution (**Figure 89**). Note that the average temperature from

the three thermocouples located at the base of the nearest neighbour vials (TC1, TC3, and TC4) was used as a surrogate for the product temperature in the TVIS vial.

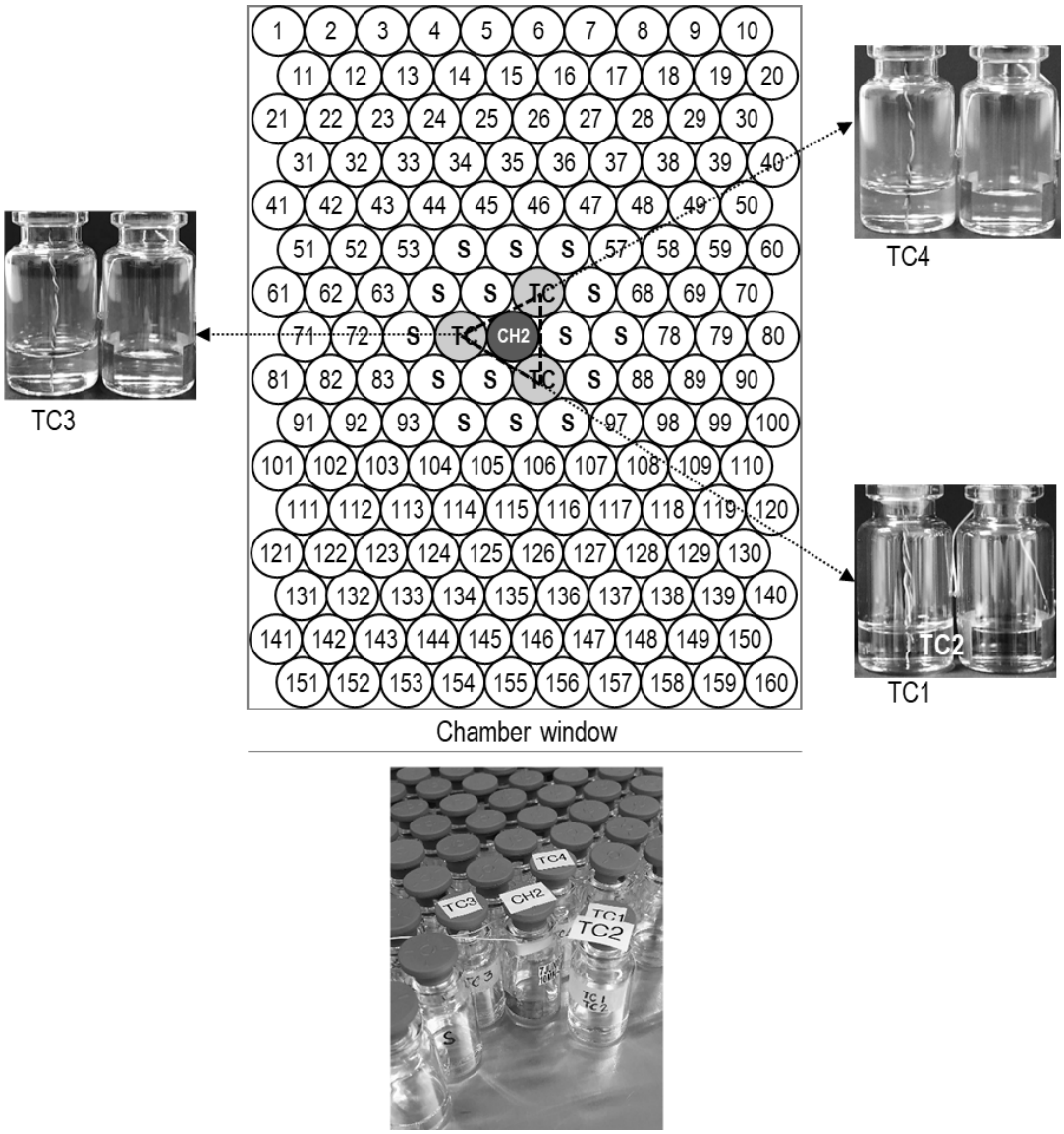

Figure 89 Arrangement of vials on a shelf of the Virtis Advantage Plus XL benchtop freeze dryer. Three thermocouple-containing vials (labelled TC) were placed in a triangle, with the TVIS measuring vial (labelled CH2) at the triangle centre. The TC vials and TVIS vial were located among the sample cluster. The sample-filled vials are represented by '**S**'; the left vials with the numbered position on the shelf were filled with ultrapure water.

Surrounding the cluster of the 19 vials containing 5% w/v sucrose solution were an additional 141 vials, each filled with 3.2g of 18.2 MΩ·cm water. All 160 vials, with the cluster of the 19 sample-filled ones at the centre, were arranged on a stainless steel tray (**Figure 89**). These were

partially closed with 20mm 4023/50 bromobutyl grey rubber stoppers (FDW20RTS, West Pharmaceutical Services Singapore Ltd., Singapore), then loaded into a Virtis Advantage Plus XL bench-top freeze dryer (SP Scientific, USA).

8.2.4. Through-vial impedance spectroscopy

A 5-channel impedance analyser (developed by De Montfort University) was used to record the impedance spectra of the TVIS vial containing the 5% w/v sucrose solution. The configuration of the system can be described as follows: the TVIS vial was connected to channel 2 of the impedance analyser (placed outside the lyophiliser), via a junction box placed on the freeze dryer shelf and an electrical pass-through attached to one of the manifold arms of the dryer (Figure 90). A more detailed description of the TVIS measurement system is provided by Smith and Polygalov (2019).

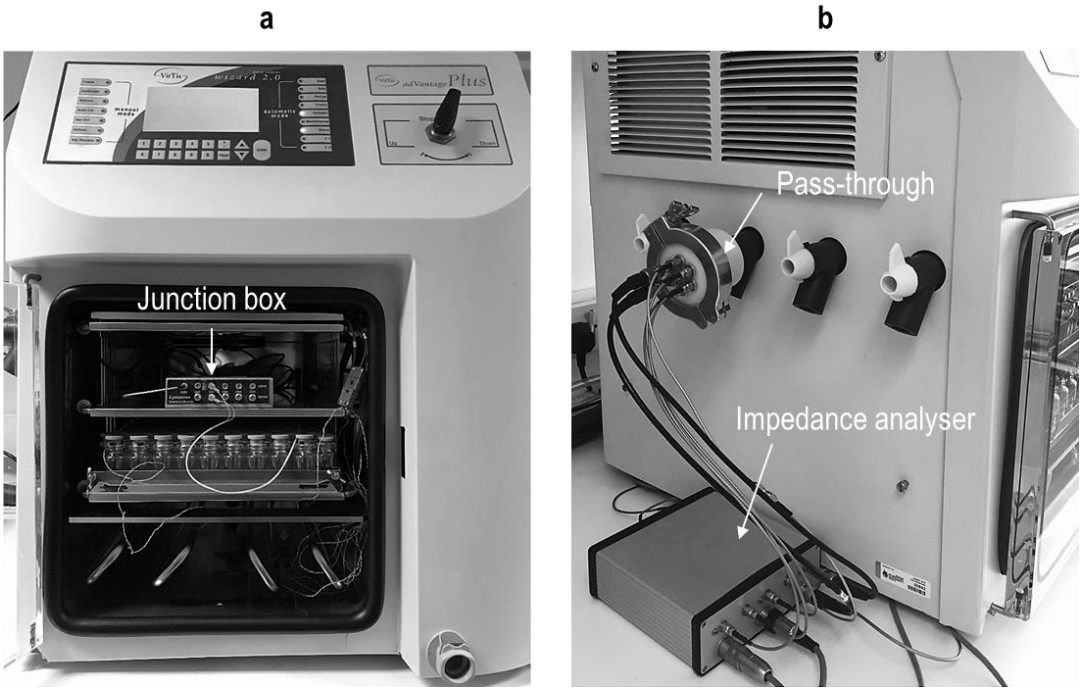

Figure 90 (a) Photograph from the front of the dryer showing the array of vials placed on the bottom shelf of the dryer and the TVIS junction box on the middle shelf. The fine white cables emerging from the right side of the vial array are connected to one channel of the 5-channel TVIS junction box. (b) Photograph of the left side of the dryer, showing the 5-channel I-to-V convertor of the impedance analyser, which sends and receives the signal to/from the junction box via the pass-through installed on the manifold hose of the Virtis Advantage Plus XL freeze dryer.

The impedance spectra of the TVIS vial were measured over the frequency range 10 Hz to 1 MHz, with a scan interval of 2 minutes (between the beginning of each spectrum) during three cycles of freeze-thawing. The acquisition time for one spectrum is ~ 10 s, so all five TVIS vials could be measured in a cycle of less than one minute.

8.2.5. Freeze-drying protocol

Three experiments with annealing temperatures of −35, −32, and −10 °C were conducted to investigate the impact of temperature on the magnitude of C''_{PEAK}: the TVIS parameter that we believe best reflects the extent to which the ice structure changes with time. In each lyophilisation cycle, the solution was cycled through the annealing stage three times.

The criteria in selecting the annealing temperature was based on the glass transition temperature of the frozen 5% w/v sucrose solution (T'_g = −34 °C), with shelf temperatures immediately below T'_g (−35 °C) and immediately above T'_g (−32 °C) selected. In addition, an annealing cycle at −10 °C was investigated to develop the TVIS method of determining the glass transition temperature. The details of the protocol are given in **Table 13**; the thermal cycle is illustrated in **Figure 91**.

Table 13 Freeze-thawing protocol

Step	Temperature (°C)	Time (minutes)
Equilibrium phase	+20	20
Freezing temperature ramp (0.5 °C /min)	−50	140
Freezing temperature hold	−50	120
1st Re-heating temperature ramp (0.2 °C /min)	−35 / −32 / −10	30 / 35 / 80
1st Re-heating temperature hold	**−35 / −32 / −10**	120
1st Re-cooling temperature ramp (0.2 °C /min)	-50	30 / 35 / 80
1st Re-cooling temperature hold	-50	120
2nd Re-heating temperature ramp (0.2 °C /min)	−35 / −32 / −10	30 / 35 / 80
2nd Re-heating temperature hold	**−35 / −32 / −10**	120
2nd Re-cooling temperature ramp (0.2 °C /min)	-50	30 / 35 / 80
2nd Re-cooling temperature hold	-50	120
3rd Re-heating temperature ramp (0.2 °C /min)	−35 / −32 / −10	30 / 35 / 80
3rd Re-heating temperature hold	**−35 / −32 / −10**	120
3rd Re-cooling temperature ramp (0.2 °C /min)	-50	30 / 35 / 80
3rd Re-cooling temperature hold	-50	120

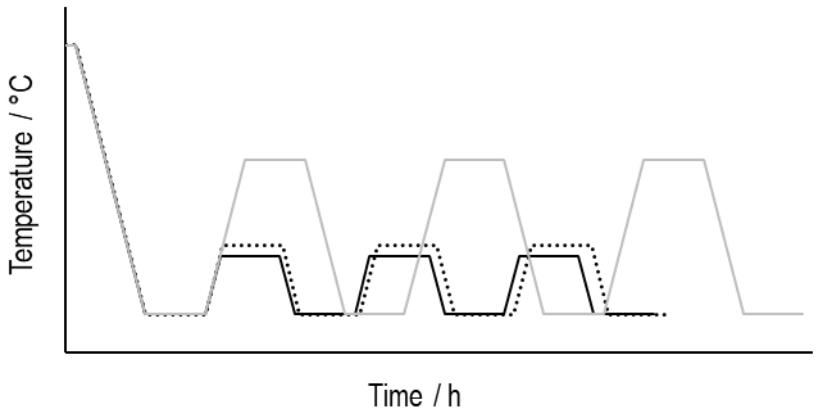

Figure 91 An illustration of the thermal cycles used in this experiment with annealing hold temperatures of −35 °C (black solid line), −32 °C (black dotted line), and −10 °C (grey solid line).

8.2.6. Impedance analysis software

LyoView™ software (version 18-05-18) was used to extract the following TVIS parameters from the measured spectra (**Figure 92**):

(1) Real part capacitance at low (i.e. 10 Hz) and high frequency (i.e. 200 kHz), denoted as C'(10 Hz) and C'(0.2 MHz), respectively (Figure 92a).

(2) Amplitude (C''_{PEAK}) and characteristic frequency (F_{PEAK}) of the dielectric loss peak associated with dielectric ice relaxation, which manifests in the imaginary part of the capacitance spectrum (Figure 92b).

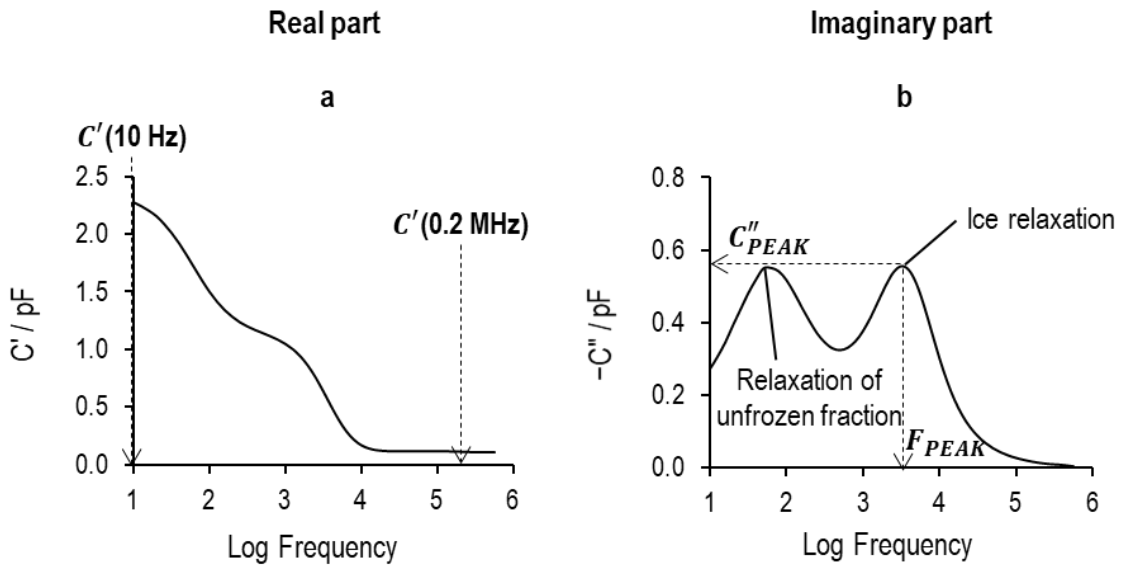

Figure 92 An example of (a) real and (b) imaginary capacitance spectrum of 5% w/v sucrose at −15.2 °C, obtained from the first re-heating stage of the annealing cycle with −10 °C as the hold temperature, demonstrating the determination of the TVIS parameters derived from the LyoView™ software: C'(10 Hz), C'(0.2 MHz), C''_{PEAK}, and F_{PEAK} (shown in bold font).

8.3. Results and Discussion

8.3.1. Determination of glass transition temperature of freeze-concentrated solution by thermal analysis

The glass transition of partially amorphous material (in our case, 5% w/v sucrose in a frozen state) can be demonstrated using the endothermic step in the heat flow of the DSC thermogram. Estimates for T'_g are taken from either the onset, midpoint, and/or endpoint of the step; however, the midpoint is invariably reported as the glass transition temperature (Gabbott, 2008). Therefore, the T'_g values of 5% w/v sucrose solution, measured using standard DSC at 5, 10, and 20 °C·min^{-1} scanning rates, were derived according to this method.

The T_g' values of the 5% w/v sucrose solution for 5, 10, and 20 °C·min^{-1} heating rates are –33.6, −34.3, and −28.3 °C, respectively (Figure 93). We can see that a faster heating rate provided higher sensitivity to the glass transition event; as a result, the glass transition temperature shifted to the higher value. The results here concord with those of previous studies (Costantino & Pikal, 2004; Her & Nail, 1994; Horn & Friess, 2018) and demonstrate the dependency of heating rates on the measured values (Her & Nail, 1994; Horn & Friess, 2018). From these observations, we might expect that the in-vial critical temperature would be lower than that determined by the thermal analysis technique, because the primary drying process operates at a slower ramp rate than DSC. In other words, the phase transition appears to happen at a temperature below the DSC value. The discrepancy between the pre-lyophilisation characterisation technique and a real lyophilisation cycle should be taken into consideration during the process design phase.

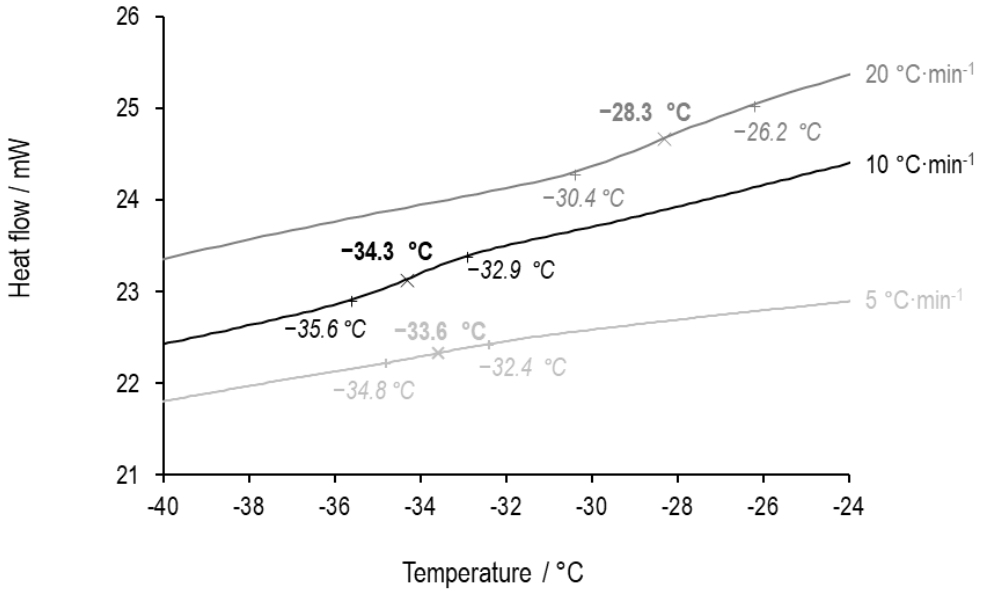

Figure 93 A DSC thermogram of frozen 5% w/v sucrose solution, showing the overlay of heat flow and midpoint T_g' values (in bold) for different scanning rates. Heating rates of 5, 10, and 20 °C·min^1 are represented by light grey, black and dark grey respectively.

The standard DSC method has one limitation. It is not sufficiently sensitive to detect weak glass transitions - thus, we sought to confirm our estimates for T_g' using the mDSC technique. The

midpoint T_g' value of −34.9 °C taken from the reversing heat flow thermogram (**Figure 94**) broadly concurs with that measured using the conventional DSC at a rate of 5 or 10 °C·min^{-1}.

Previous studies have evidenced two thermal transitions of sugar solution when determined by the conventional DSC technique (Sacha & Nail, 2009; Goff, Verespej & Jermann, 2003; Kilmartin, Reid & Samson, 2000; Roos & Karel, 1991). Although interpreted in different ways, the assumption involved the characteristics of the freeze-concentrated systems and ice content. Most of these researchers suggested that the first transition at the lower temperature is a glass transition of the maximum freeze-concentrated solution, whereas Sacha and Nail (2009) proposed the second transition at the higher temperature by comparing it with the freeze-drying microscope result as the T_g'. Our mDSC result was directly compared with Sacha and Nail (2009). They demonstrated the midpoint of the endothermic steps of the mDSC thermogram at −48 °C and −36 °C; whereas in our study, only one thermal transition at −34.9 °C could be determined, and no transition at the lower temperature was detected. This is broadly acceptable, with a value measured using a conventional DSC at a rate of 5 or 10 °C·min^{-1}.

For further TVIS assessment, the value of the onset and midpoint from the conventional DSC at a low scanning rate (5 or 10 °C·min^{-1} in **Figure 93**) and the mDSC (Figure 94) was averaged, then used as the onset of the glass transition and T_g', respectively. The onset of the transition of 5% w/v sucrose solution is −35.5°C, followed by the transition temperature: 1.2 °C warmer than the onset temperature (T_g' = −34.3 °C).

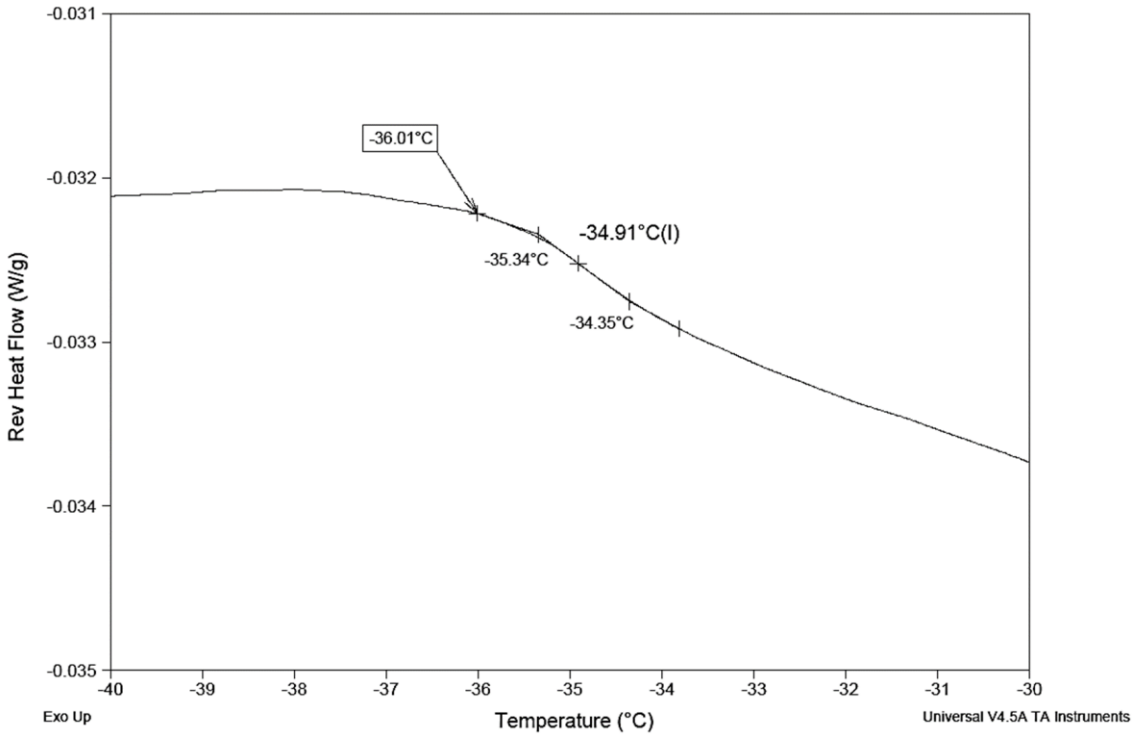

Figure 94 The glass transition temperature of 5% w/v sucrose solution of −34.9 °C is calculated from the step in the reversing heat flow of mDSC thermogram.

8.3.2. Characterisation of the structural modification of frozen matrices by the through-vial impedance spectroscopy technique

TVIS spectrum

When applying TVIS technology to the measurement of solutions in a liquid state, it is the interfacial Maxwell-Wagner (MW) polarization process that is responsible for the step in the dielectric permittivity (real part) and the peak in the dielectric loss spectrum (imaginary part). However, once the ice forms, the mechanism changes from an interfacial rlaxation process to the dielectric relaxation of ice. Both relaxation mechanisms are described by Smith and Polygalov (2019).

Previously, we demonstrated the sensitivity of the relaxation frequency (F_{PEAK}) derived from the dielectric loss spectrum to the temperature through dielectric relaxation of ice. This TVIS parameter can therefore be applied to predict the product temperature and characterise phase behaviour, such as ice formation and glass transition (Smith et al., 2017). Here, other features

of the TVIS spectrum will be explored, including (1) the real part capacitance (dielectric storage) spectrum at the low-frequency (i.e. 10 Hz) and high-frequency regions (above the ice relaxation frequency of 1 kHz, i.e. 0.2 MHz); and (2) the amplitude of relaxation peak (C''_{PEAK}) when determining structural characteristics, such as the glass transition.

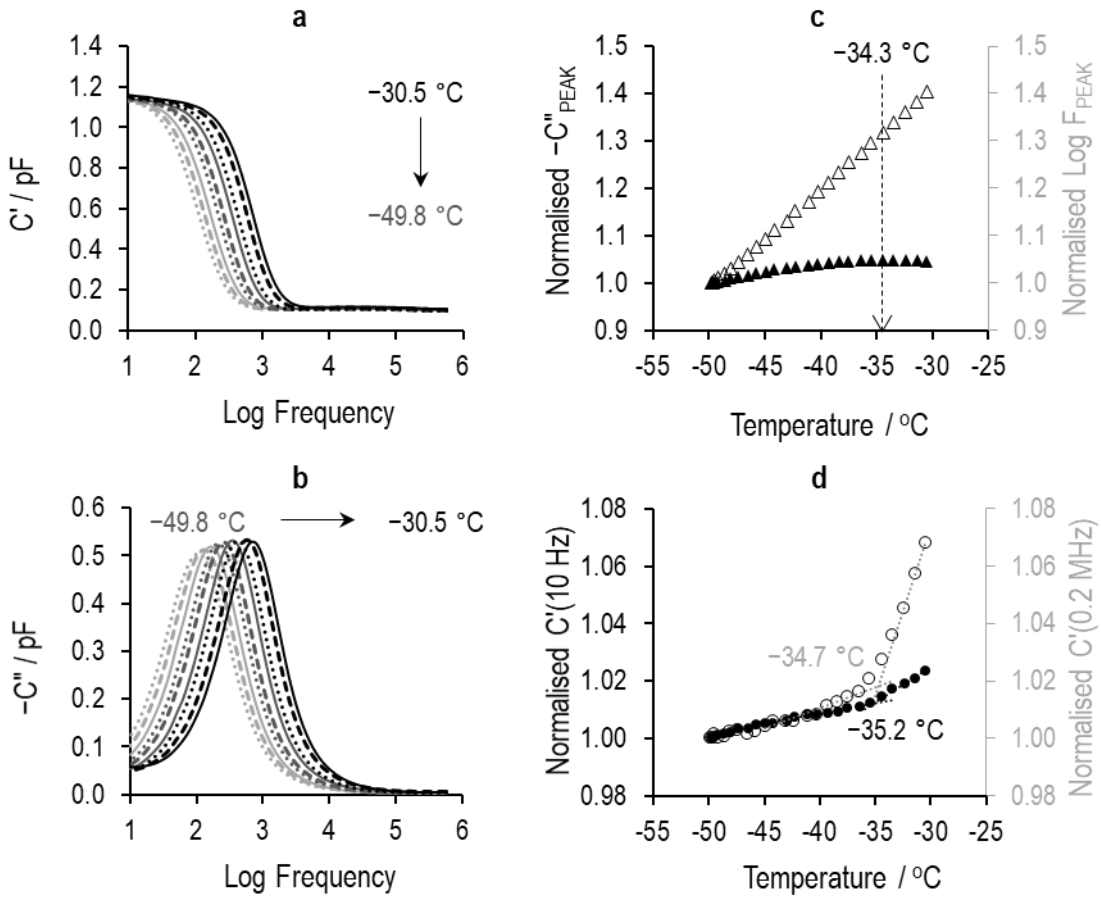

Figure 95 (a) Real and (b) imaginary part capacitance spectra of 5% w/v sucrose contained in a 10 mL TVIS vial, demonstrating the temperature dependency of the dielectric relaxation of ice at temperatures between −50 °C and −30 °C. These spectra were obtained during the first re-heating stage, from −50 °C to −10 °C, with a 0.2 °C·min^{-1} rate. The parameters from the dielectric loss peak of ice in the imaginary part (C''_{PEAK} and F_{PEAK}) and real part at the selected frequency (i.e. 10 Hz and 0.2 MHz), were extracted using LyoView™ software. (c) The normalised values of C''_{PEAK} (filled triangle) and $Log\ F_{PEAK}$ (open triangle) are demonstrated. (d) the normalised C'(10 Hz) and the normalised C'(0.2 MHz) are presented by filled and open circle, respectively. The vertical dashed line shown in (c) marks the glass transition temperature (T'_g = −34.3 °C). The transition temperature shown in (d) are −35.2°C for C'(10 Hz) and −34.7 °C for C'(0.2 MHz).

Both the real and imaginary part capacitance spectra of the TVIS vial containing 5% w/v sucrose that were recorded from the first re-heating stage of a thermal cycle are selected and illustrated in Figure 95a and Figure 95b. Various features of these spectra—i.e. C''_{PEAK}, F_{PEAK}, C'(10 Hz), and C'(0.2 MHz)—were extracted using LyoView™ software, then normalised by the value at the lowest temperature (ca.−49.8 °C) to demonstrate the temperature dependency of frozen 5% w/v sucrose contained in a TVIS vial (Figure 95c and Figure 95d). The temperature coefficient of the normalised $Log\ F_{PEAK}$ value (open triangle in Figure 95c) shows a high temperature dependency compared to the normalised C''_{PEAK} (filled triangle in Figure 95c). The positive temperature dependence of the dielectric loss peak concurs with previous reports (Smith et al., 2017; Smith, Jeeraruangrattana & Ermolina, 2018; Smith & Jeeraruangrattana, 2019). Therefore, the peak frequency responses for temperatures recorded during the re-heating of the annealing cycle can be utilised in predicting ice temperature in the primary drying stage. The method for determination of the ice temperature has recently been published (Smith, Jeeraruangrattana & Ermolina, 2018).

Turning to the magnitude of the dielectric loss peak (filled triangle in Figure 95c), the value of the C''_{PEAK} increases slightly and starts to drop as the temperature rises above the critical product temperature (T'_g = −34.3 °C). This might be explained by the expression of the C''_{PEAK} value according to Equation 64 (Smith et al., 2017).

$$C''_{PEAK} = \frac{C_G^2}{2(C_G + C_s)} \qquad \text{Equation 64}$$

By making the assumption that an intrinsic capacitance of glass at the temperature range studied is nearly constant, the C''_{PEAK} parameter is therefore inversely proportional to sample capacitance (C_s), as in the following relationship:

$$C''_{PEAK} \propto \frac{1}{C_s} \qquad \text{Equation 65}$$

For the TVIS measurement system, C_s is the capacitance of the sample within the electrode region, and can be defined by the relative permittivity (ε_r) of the sample and the cell constant occupied by the sample (k_s) according to Equation 66:

$$C_s = \varepsilon_o \varepsilon_r k_s \qquad \text{Equation 66}$$

where ε_o is the permittivity of free space (8.854 x 10^{-12} F·m^{-1}) and k_s is the geometric cell constant, which is the ratio between the area of an electrode plate (A) and the average distance between the electrode pair (d). Relative permittivity (ε_r) can also be expressed in terms of a complex number:

$$\varepsilon_r = \varepsilon_r' - \varepsilon_r'' = \varepsilon_r' - i\frac{\sigma}{\omega} \qquad \text{Equation 67}$$

where ε_r' is dielectric storage and ε_r'' is dielectric loss, which is a function of conductivity (σ) and frequency (ω).

Once the sample was ramped through the glass transition temperature, it softened and became more mobile, facilitating charge movement. It follows that an increase in electrical conductivity associated with the temperature dependence of the capacitance would result in a greater C_s value (Equation 66 and Equation 67), reducing the peak amplitude (data after the vertical dashed line marked at −34.3 °C in **Figure 95**c). We will discuss this in more detail, particularly with respect to the attributes occurring at temperatures greater than −30 °C, later.

Aside from parameters derived from a dielectric loss peak (C''_{PEAK} and F_{PEAK}), real part capacitance at the specified frequency is now considered (**Figure 95**d). The frequency of interest was selected from a low- (i.e. 10 Hz) and high-frequency range (i.e. 0.2 MHz), to investigate how capacitance changes with temperature. In **Figure 95**d, linear temperature sensitivity at a lower temperature (below −40 °C) is noticeable. The transition of the temperature coefficient appears at around −35 °C (the average value between −35.2 and −34.7°C), which broadly coincides with the onset of T_g' measured by DSC (−35.5 °C). After this inflection point, the temperature dependence of both frequencies increases gradually. However, the temperature dependence of

dielectric permittivity at high frequency, C'(0.2 MHz), is much stronger than at the lower one (i.e. 10 Hz): when it is beyond the onset of glass transition temperature of −35.5 °C. This means that the temperature dependence of real part capacitance is influenced by measurement frequency: begging the question of which frequency range is best to capture the unfrozen characteristics. One way to quantify this is to compare real part profiles at the frequency of interest of frozen water with the 5% w/v sucrose.

In pure ice, during warming, real part capacitance at 0.2 MHz has almost no temperature dependence (open dots in **Figure 96**a), whereas a positive temperature coefficient was found in the C'(10 Hz), as shown in **Figure 96**a (black dots). This suggests that the temperature effect is more significant in low-frequency capacitance. In other words, the C'(10 Hz) parameter is mainly contributed by temperature. By comparing pure ice with 5% w/v sucrose (**Figure 96**b), we reached the conclusion that the cause of temperature sensitivity of real part capacitance at a frequency well above that of ice relaxation frequency (1 kHz), such as C'(0.2 MHz), may be due to the unfreezable phase rather than ice. Thus any change in real part capacitance at the high frequency limit, either with time or temperature, can be associated with the unfrozen fraction: allowing us to characterise the structural change, such as glass transition behaviour.

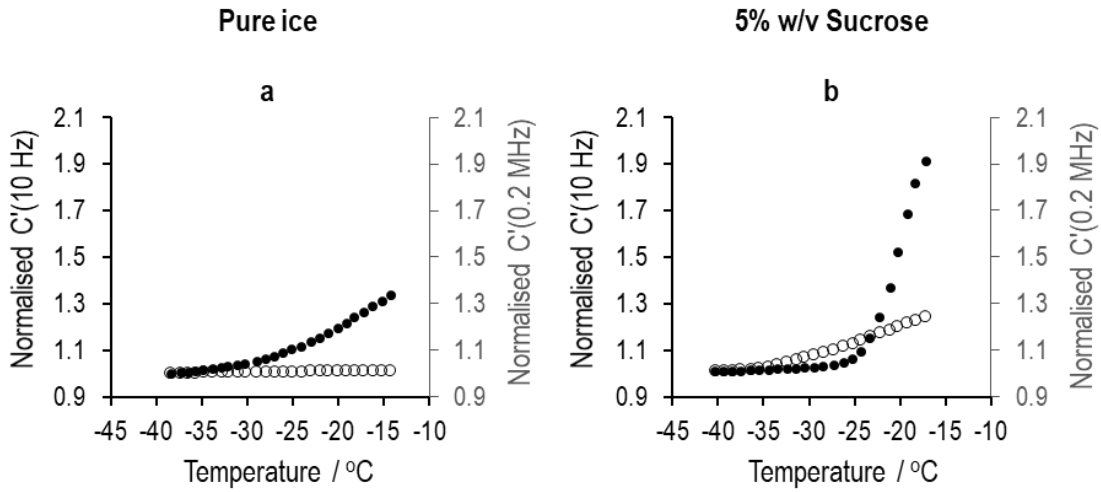

Figure 96 Temperature dependencies of real part capacitance at 10 Hz (black dots) and 0.2 MHz (open dots) of (a) pure ice (Smith & Jeeraruangrattana, 2019) and (b) 5% w/v sucrose in the frozen state. The value for real part capacitance was recorded during the re-heating stage from −40 °C to −10 °C with 0.5 °C·min^{-1} and −50 °C to −10 °C with 0.2 °C·min^{-1} for (a) pure ice and (b) the frozen 5% w/v sucrose, respectively.

Impact of annealing temperature and cycles

Three sets of annealing cycles were carried out to establish an influence on the thermal reversible behaviour of frozen sucrose. Here, TVIS was used to investigate the impact of annealing temperatures at −35 °C, −32 °C, and −10 °C. The actual product temperature during freeze thawing was typically 1-2 °C lower than the set value of the shelf temperature (**Figure 97**).

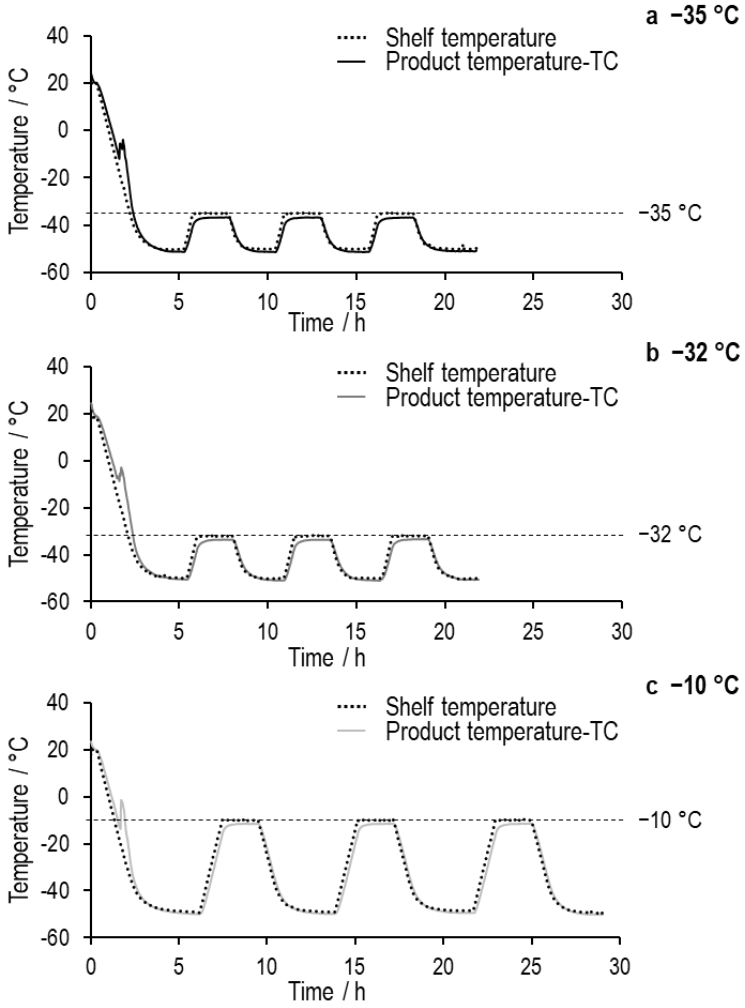

Figure 97 Freeze-thaw profiles of 5% w/v sucrose solution. The sample was initially frozen at −50 °C, and then the shelf temperature increased at the heating rate of 0.2 °C·min^{-1} until the annealing temperature of either (a) −35 °C, (b) −32 °C or (c) −10 °C was reached.

Figure 98 demonstrates the temperature difference (ΔT) between the bottom of the vial (measured from TC1) and the top part of the sample (measured from TC2). Undoubtedly, the product near the heating source (freeze dryer shelf) is warmer than the furthest part. It can be

also seen from **Figure 98** that the temperature difference between the two planar surfaces is larger when the annealing temperature falls. The average ΔT during holding period of three annealing cycles is 1.05 ± 0.1 °C, 0.39 ± 0.1 °C, and 0.07 ± 0.1 °C for the designated annealing temperatures of −35 °C, −32 °C, and −10 °C, respectively. According to Fourier's law (Equation 68), temperature difference is affected by heat flux (dq/dt) and the thermal conductivity of a material (κ) (Equation 69).

$$\frac{dq}{dt} = \kappa(\Delta T) \qquad \text{Equation 68}$$

$$\Delta T = \frac{dq}{dt} \cdot \frac{1}{\kappa} \qquad \text{Equation 69}$$

where ΔT is the temperature gradient between the region of relatively high temperature (e.g. at the bottom of the vial) and the relatively colder region (e.g. at the sample interface).

If we kept the product the same (e.g. 5% w/v sucrose in frozen state), the value of ΔT would be no different when heat was supplied to the sample at constant rate (e.g. holding at the specified shelf temperature). However, the results showed a fall in the thermal gradient. A possible explanation is that thermal conductivity was dissimilar among those three experiments. The air trapped inside the frozen mass might be one of the factors affecting this thermal parameter (Cogné et al., 2003). For instance, the thermal conductivity of air in the atmosphere is approximately 10 times less than in ice; therefore, the total thermal conductivity of frozen bulk can be reduced as air volume increases. Another factor that cannot be ruled out is the convection current as a result of differential heating. This physical phenomenon increases fluid circulation within the sample and promotes heat distribution throughout.

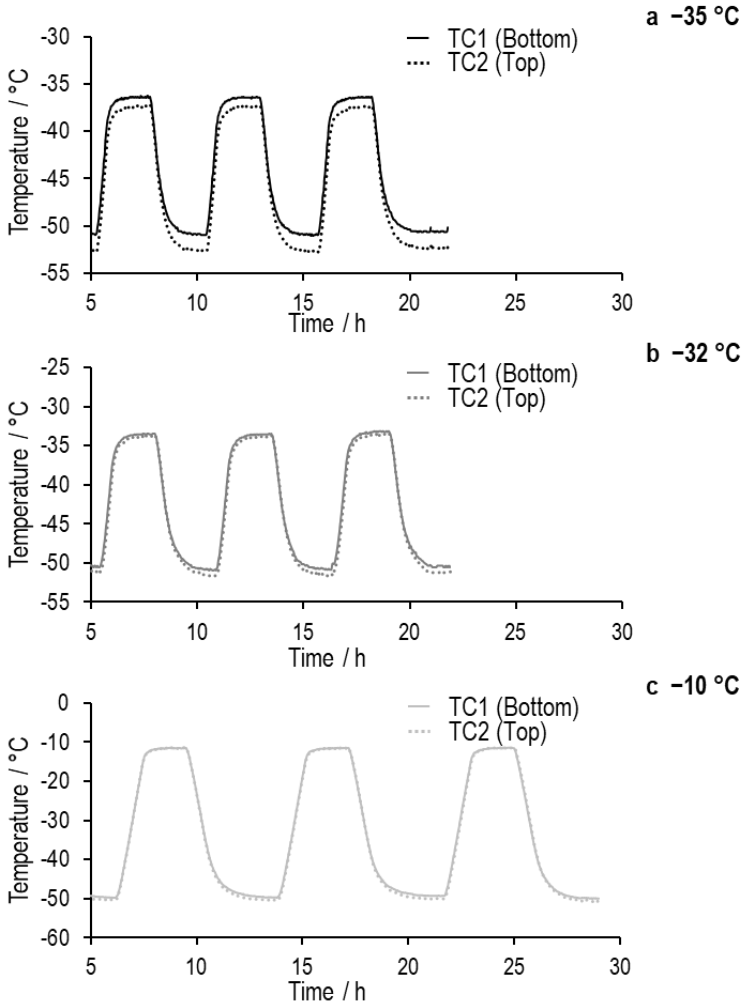

Figure 98 Temperature profiles of 5% w/v sucrose during three cycles of freeze-thaw processes: (a) −35 °C, (b) −32 °C and (c) −10 °C. Two thermocouples contained in the same vial at different positions were used to measure product temperature during the freeze-thaw processes. One temperature sensing node (TC1) was placed at the bottom centre of the vial; the other (TC2) was close to the sample level (i.e. just below the sample meniscus). The product temperatures from TC1 and TC2 are represented by a solid line and dotted line, respectively.

The impact of the annealing temperatures and cycles is demonstrated in **Figure 99**. At first glance, the higher the product temperature, the greater the value of F_{PEAK}. This temperature coefficient corresponds to a positive linear association between both $Log\ F_{PEAK}$ and average thermocouple temperatures. Although the product was annealed multiple times, an identical relationship manifests in **Figure 99**a. With the strong temperature dependence of the peak frequency, it is not surprising that we can predict the product temperature from the F_{PEAK} parameter. Thus, the average temperature from three thermocouples in the nearest neighbour

vials was plotted against the F_{PEAK} from re-heating on a logarithm scale for the corresponding times when it was recorded to provide a temperature calibration, which was then used to estimate product temperatures during the primary drying stage. Data from the re-heating stage were used to create a temperature calibration plot. Smith et al. (2018) describe a methodology for the TVIS temperature measurement.

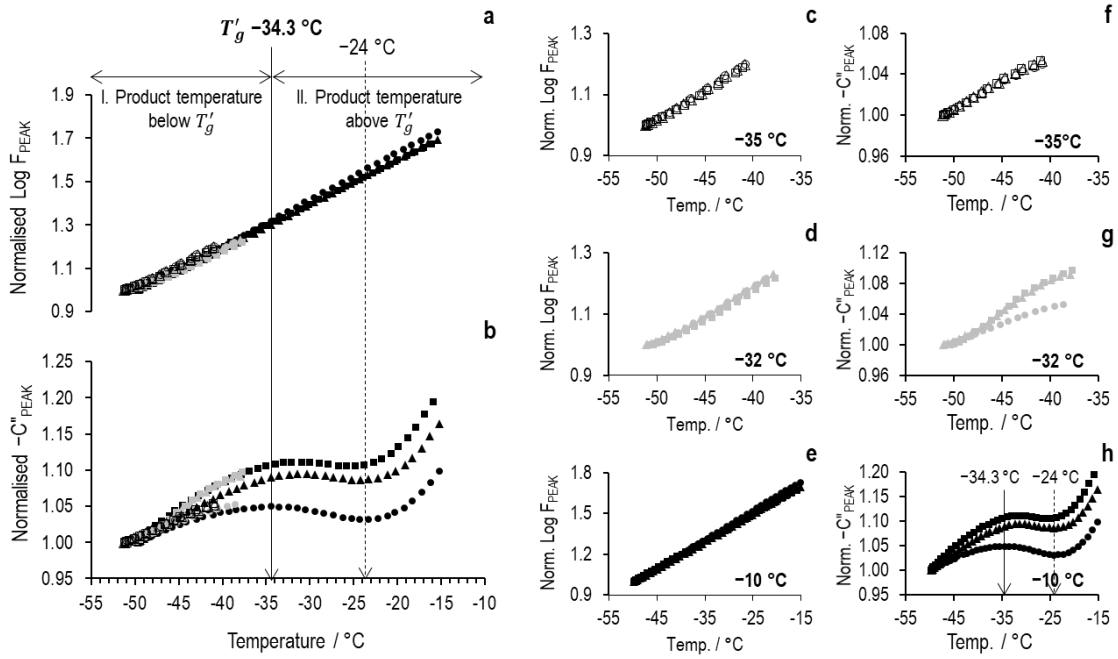

Figure 99 Temperature dependency of the normalised values of (a) $Log\ F_{PEAK}$ and (b) C''_{PEAK} parameters of the frozen 5% w/v sucrose solution from three re-heating stages of each freeze-thawing process (i.e. −35 °C, −32 °C and −10 °C). TVIS-derived parameters were plotted against the thermocouple temperature, averaged from three nearest neighbour vials. The double-headed arrow indicates the product temperature as follows: below the T'_g (region I) and above the T'_g (region II). (c)-(e) are the zoom views of (a) while (f)-(h) are the zoom views of (b) for each freeze-thawing process: −35 °C, −32 °C and −10 °C. The open symbols represent the cycle annealed below the T'_g value of −34.3 °C(i.e. −35 °C); whereas data treated at shelf temperatures of −32 °C and −10 °C (above the glass transition temperature) are presented in grey and black closed symbols, respectively. The circles, squares and triangles are the first, second and third re-heating stages, respectively.

Meanwhile, the temperature dependency of the C''_{PEAK} value is dependent on the structural characteristics under thermal conditions. Provided the product temperature is below the T'_g value, positive correlations between the magnitude of the dielectric loss peak (C''_{PEAK}) and the thermocouple temperature exist (region I in Figure 99b); but they are weaker than those

observed in the temperature coefficient of F_{PEAK} (region I in Figure 99a). The temperature dependency of dielectric relaxation of ice might well be responsible for these results (region I in Figure 99a-b). As a matter of fact, the relaxation process of ice is a function of temperature. The higher the temperature, the faster the relaxation time (τ); consequently, the dielectric loss peak shifts to a higher frequency (Equation 61).

$$F_{PEAK} = \frac{1}{\tau_{ice}} \qquad \text{Equation 61}$$

Once the product temperature is above the transition temperature of −34.3 °C (the vertical solid line marked in Figure 99b), the C''_{PEAK} parameter (black closed symbol in Figure 99b) begins to level off until a more dramatic increase commences at temperatures beyond −24 °C (the vertical dashed line marked in Figure 99b). These results are likely to relate to various factors: (1) Temperature dependence of the capacitance of the dielectric material; (2) Enhancement of the mobility of the frozen system due to reduction of viscosity by many orders; (3) Ice crystallisation during heating; (4) Change in the concentration of the freeze-concentrated solution resulting from the ice melting.

When the product temperature ranges from −34.3 °C to −24 °C, the almost levelled off pattern of C''_{PEAK} (black closed symbol in **Figure 99**b) appears to be the overall outcome of the sample capacitance (C_s) modulated by the opposite effects through the following proposed mechanisms:

(1) Peak amplitude increases as the temperature ramps up. This is probably because instantaneous capacitance at very high frequency ($C'(\infty)$) is less temperature-dependent; whereas static capacitance at a low-frequency range ($C'(0)$) tends to increase with the temperature (Figure 95a), leading to a rise in C''_{PEAK} values.

(2) Once the product temperature is across the transition region (the vertical solid line in **Figure 99**), viscosity of the glassy phase falls significantly to the minimum of 10^7 Pa·s, then promotes the degree of motion of the species, including the ion and water molecule. It follows that faster diffusion results in greater charge movement, larger

conductivity and consequently, higher sample capacitance (C_s) (see *TVIS spectrum*). Ultimately, peak amplitude decreases ($C''_{PEAK} \propto 1/C_s$).

(3) Simultaneously with the lower viscosity system, the water remaining in the unfrozen fraction is allowed to crystallise to form ice during heating (Shalaev et al., 2019) and the relative permittivity of ice is much lower than liquid water. Thus the capacitance of the frozen matrix could be lessened, increasing the C''_{PEAK} values.

A subsequent result of the overall measured capacitance, responsible for the peak magnitude (C''_{PEAK}) profile at product temperatures between −34 and −24 °C (Figure 99b), is attributed to the opposing response in the capacitance according to the above mechanisms. Both the temperature dependence of C''_{PEAK} (mechanism 1) and ice formation process known as devitrification (mechanism 3) can minimise the sample capacitance, then increase the amplitude of the dielectric loss peak; whereas the capacitance of the frozen bulk could be enhanced (i.e. decreasing C''_{PEAK}) by reducing the viscosity of the unfrozen fraction (mechanism 2).

As mentioned in Section 8.3.1, double transitions preceding the bulk ice-melting endotherm have been studied using thermal analysis (Roos & Karel, 1991; Singh & Roos, 2007; Sacha & Nail, 2009). When re-heating frozen sugar, including sucrose, transition at the higher temperature prior to the main ice-melting endotherm coincides with the onset of the small ice crystal melting (T'_m) (Levine & Slade, 1988a), so it is not easy to recognise thermal behaviours between the glass transition of the unfrozen fraction and the ice melting. Some authors have considered the onset of the ice melting, or T'_m, as T'_g (Goff, Verespej & Jermann, 2003; Levine & Slade, 1988; Sacha & Nail, 2009). Based on these studies, the T'_g value of −34.3 °C could be inferred as the onset of ice melting in our case.

When the product temperature was at least 10 °C higher than the onset of ice melting at −34.4 °C, ice crystallising during re-heating was overcome by melting; the ice formation process was prevented. Ice melting at sub-zero temperatures is evidenced by Ablett et al (1992). They used the micrograph to illustrate that the ice contained in the frozen sucrose began to melt at

−20 °C. This suggests melting of the ice crystal dominates when the product temperature is close to −20 °C, a process which also needs to be considered for peak capacitance.

As more ice melted, water coexisting within the amorphous unfrozen matrix rose; as a result, molecular mobility could be accelerated (even by a few per cent). Through this means, conductivity increased, followed by a continuous increase in capacitance, which reduced the C''_{PEAK} value. However, contrary to what we would have expected, a gradual rise in normalised C''_{PEAK} values was observed after product temperatures exceeded −24 °C (**Figure 99**b). This suggests an unidentified underlying mechanism. It might be that water from melted ice dilutes the freeze-concentrated solution (reducing the concentration of the unfrozen fraction). Due to increasing dilution, diffusion increases greatly and enables species, especially charges, to easily move through the sample before accumulating or adhering on the glass wall-sample boundary.

This distribution and deposition of ions can develop an electric double layer (EDL) and form like a capacitor, referred to as a double-layer capacitor. This double layer comprises the surface-absorbed layer (known as the compact layer) and the diffusion layer. The thickness of the diffusion layer (Debye length, L_D) is inversely proportional to the ionic strength (μ) and can be calculated according to the equation below:

$$L_D = \sqrt{\frac{\varepsilon_o \varepsilon_r k_B T}{2 \times 10^3 N_A \mathrm{e}^2 \mu}} \qquad \text{Equation 70}$$

where k_B is the Boltzmann constant (1.381×10^{-23} J·K^{-1}), T is the temperature in Kelvin, N_A is the Avogadro's constant (6.02×10^{23} mol^{-1}), e is the elementary charge of an electron (1.602×10^{-19} C) and the ionic strength (μ) in molar terms. Molar ionic strength corresponds to the concentration of all ions present in the sample and can be calculated from the molar concentration (c_i) and charge number of the ion (z_i):

$$\mu = \frac{1}{2}\sum_{i=1}^{n} c_i z_i^2 \qquad \text{Equation 71}$$

Given that the EDL has two layers, double layer capacitance (C_{dl}) can be determined mathematically based on the Stern model, which combines two layers in series. The expression of EDL capacitance is as follows:

$$\frac{1}{C_{dl}} = \frac{1}{C_c} + \frac{1}{C_d} \qquad \text{Equation 72}$$

Here, C_c and C_d are the capacitance of the compact and diffuse layer, respectively. In dilute solution, C_c >> C_d; hence, C_{dl} is dominated by C_d ($C_{dl} \cong C_d$), so that double-layer capacitance can be approximated from the capacitance of the diffusion layer according to Equation 73.

$$C_{dl} = \frac{\varepsilon_o \varepsilon_r A}{L_D} \qquad \text{Equation 73}$$

With an idea of the diffuse double layer, we can now demonstrate the influence of dilution on the double-layer capacitor. The lower concentration provides less ionic strength, resulting in a larger number of Debye length (L_D) (Equation 70 and Equation 71); in other words, the diffusion layer is thicker. The double-layer capacitance is reduced accordingly (Equation 73).

Double-layer capacitance (C_{dl}), formed at a much higher temperature than the glass transition temperature, is added in a series with basic TVIS elements (i.e. C_G and C_s); this can contribute to the overall measured capacitance. Thus a change in the C_{dl} value can influence the C''_{PEAK} value. As dilution proceeds, double-layer capacitance decreases; this is followed by a drop in total measured capacitance and increase in the C''_{PEAK} value. The continuous increase in the observed peak magnitude as the product temperature rises above −24 °C is a cumulative result of concentration dependence (dilution) and the positive temperature coefficient.

Returning to a consideration of reversible behaviour of capacitance relating to the microstructure of the frozen matrix, the three re-heating stages of each freeze-thawing protocol (**Table 13**) were investigated. When the product was initially cooled to −50 °C, there was a chance that the glassy state would be imperfect and not reach the maximally freeze-concentrated solution (Levine & Slade, 1988; Ablett, Izzard & Lillford, 1992; Sahagian & Goff;

1994, Roos, 1997). By holding the sample above the glassy-rubbery transition temperature for a certain period, it is possible to alter the microstructure of the frozen matrix via either the Ostwald ripening mechanism and/or glassy state relaxation corresponding to the viscosity of the frozen matrix. Restructuring of the frozen sample should have not occurred if annealing was conducted at a temperature below T_g' (i.e. the microstructure of the frozen mass changed insignificantly when annealed at −35 °C), resulting in consistency of the temperature coefficient profile of the three cycles, as shown in **Figure 99**f.

In the case of annealing at −32 °C (the actual product temperature had approximately the same value as T_g' of −34 °C), during the first annealing (circle symbol in Figure 99g), the increase in system mobility (glassy state relaxation) associated with ice formation can reduce the amorphous fraction of the incomplete glassy state and lead to reduction of free water; consequently, the maximally frozen concentration of the amorphous phase is finally attained. After the first cycle, the microstructure is more uniform, no more ice crystals are formed, and less free water is left in the unfrozen fraction. As a result, the second and third re-heating profiles (square and triangle symbols shown in **Figure 99**g) are in agreement, with a higher value of C''_{PEAK} compared to the first cycle (circle symbol in **Figure 99**g).

It is now understood that a microscale structure plays a role in the capacitances. In comparison with the data held at T_g', inconsistent results when the product was annealed at −10 °C are more apparent (**Figure 99**h). This can be explained in terms of the recrystallisation process (Ostwald ripening). As the frozen matrix was treated at a shelf temperature of −10 °C, some of the ice crystals were melted; the remainder matured to obtain larger ice. The microstructure of the frozen matrix depends on how the ice crystal is formed, existence of solute within the crystal, and ice growth rate. Furthermore, with a short annealing time (2 h), the optimum glassy state could not be achieved. All these factors are considered responsible for the variation in the re-heating results shown in **Figure 99**h.

Effect of annealing on the microstructure of the frozen matrix

In **Figure 100**, a clear trend of the peak frequency (**Figure 100**a) with the temperature change or ΔT (**Figure 100**c), can be seen. The $Log\ F_{PEAK}$ and temperature change gradually rise and are projected to a steady state. This pattern is relatively consistent throughout the three holding stages of each freeze-thawing cycle (i.e. −35 °C, −32 °C and −10 °C). The observed correlation between these two factors could be explained as follows: the frequency of the dielectric loss peak (F_{PEAK}) reciprocates the product of the sample resistance (R_s), the sum of glass wall capacitance (C_G) and capacitance of the sample (C_s), as defined by the expression below:

$$F_{PEAK} = \frac{1}{2\pi R_s(C_G + C_s)} \qquad \text{Equation 74}$$

However, electrical resistance has much stronger temperature dependence than electrical capacitance: the $Log\ F_{PEAK}$ is highly sensitive to the product temperature when changing the sample resistance (Smith et al., 2017; Smith, Polygalov, 2019).

The second point to note is that Figure 100b reveals marked divergence of the C''_{PEAK} profiles between the two groups of holding temperatures, above T'_g (i.e. −10 °C) and below T'_g (i.e. −35 °C and −32 °C). The temperature dependence of the peak magnitude was weak at the lower annealing temperature (open symbols and grey closed symbols shown in Figure 100b) and more pronounced when the product was annealed at −10 °C (black closed symbols shown in Figure 100b). In the first instance, the steady profile of the product annealed a few degrees below T'_g (c.a. −37 °C) could owe to limited mobility underlying the unmodified frozen structure. If the product were kept at a product temperature of −34.1 ± 0.2 °C (i.e. shelf temperature −32 °C), restructuring of frozen sucrose could be governed by devitrification associated with the plasticising effect of water (a reduction in viscosity). Spontaneous devitrification could lead to variation in the results, with C''_{PEAK} decreasing, as shown by the grey closed symbols in Figure 100b. By annealing it at the target temperature of −10 °C, we expected the frozen matrix to be simplified by Ostwald ripening as a key mechanism. Therefore, to establish the use of TVIS technology in characterising the Ostwald ripening mechanism during the holding stage of the

annealing cycle, frozen mass equilibrated at a shelf temperature of −10 °C was chosen for close investigation of recrystallisation kinetics.

At annealing temperatures well above T_g' of −10 °C, the value of C''_{PEAK} was on an upward trajectory until 1.35 h, then stabilised beyond that time (black closed symbol in Figure 100b). It may be presumed that the factors influencing the increase in C''_{PEAK} over this period (0-1.35 h) probably owed to dilution associated with and without the thermal gradient. However, as ice crystallisation is one of the increasing factors for C''_{PEAK}, this may be why ice formation is removed from consideration. By equilibrating the frozen mass at high temperatures such as −10 °C, we suppressed devitrification, so that the influence from the ice formation process could be disregarded.

Ostwald ripening is a thermodynamic process whereby the molecules on the surface of the small particles with higher energy (less stable) tend to diffuse through the bulk phase. These molecules will accumulate on the larger particles, which are more stable, to reduce the overall energy of the system. Alternatively stated in terms of the frozen product, small ice crystals are first dissolved or melted; then the larger ones are formed by accretion. More free water provided from the ice dissolution has a direct impact on the increase in C''_{PEAK} values via developing the electrical double layer as mentioned earlier.

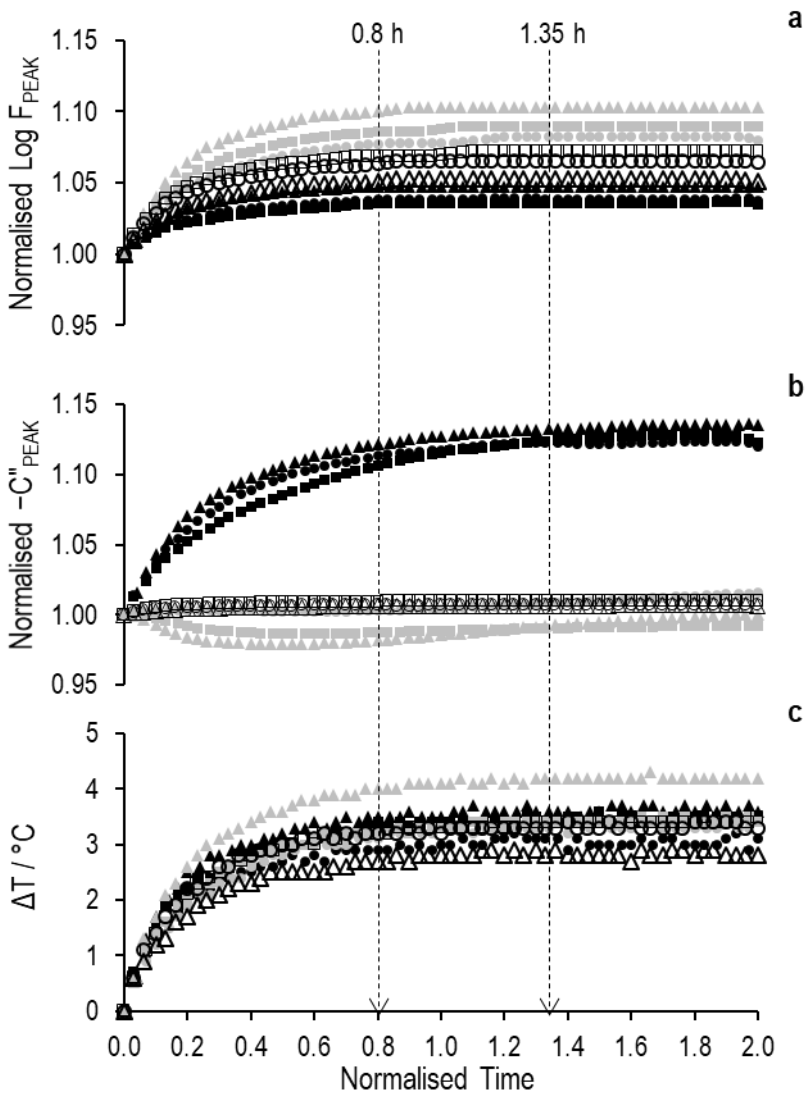

Figure 100 Effect of annealing temperature on peak frequency (F_{PEAK}) and peak magnitude (C''_{PEAK}). The frozen 5% w/v sucrose solution was annealed for 2 h (holding period) at the following shelf temperatures: −35 °C (open symbols), −32 °C (grey closed symbols), and −10 °C (black closed symbols). The circles, squares and triangles represent the first, second and third annealing cycles, respectively. The vertical dashed lines marked at 0.8 h and 1.35 h of annealing period where temperature change (ΔT) and C''_{PEAK} reach a plateau, respectively.

Moreover, temperature changes (ΔT) plateaued after 0.8 h, whereas C''_{PEAK} values continued to increase thereafter and reached a steady state at 1.35 h. For the first 0.8 h of that 2 h holding period, as a result of heat transfer into the frozen matrix (evidenced by the temperature increase), it is probable that ion diffusion accompanied by the thermal gradient engendered the main changes in the value of C''_{PEAK}. After the temperature reached equilibrium, the TVIS

parameter (C''_{PEAK}) increased by 1-2% (1.33 ± 0.40%) over the subsequent period between 0.8 h and 1.35 h. Any changes in the values of C''_{PEAK} taking place within this period (0.8-1.35 h) might have been caused by only the melting of the small ice crystal. During this period, the heat provided by the freeze dryer shelf was used to accomplish phase transition from solid into liquid: because of which, the product temperature was constant, with a slight upward profile of C''_{PEAK}. If we assume that the temperature dependency of C''_{PEAK} can be somewhat negligible, the rate of change of C''_{PEAK} could potentially be inferred from the ice-dissolving process. In addition, the time during the isothermal process at which the C''_{PEAK} enters the stable period (1.35 h) could potentially be used to indicate the approximate point where ice-melting ends and the accretion process starts.

Beyond 1.35 h, the profile of the C''_{PEAK} remained steadily constant. In fact, during the recrystallisation process, no more ice was formed, and the fraction volume increased through the ice growth process. If the bulk dielectric property of the sample depends on the composition of each component (e.g. ice, unfreezable water, sucrose, air), the net dielectric constant will fall as relative ice volume increases because the permittivity of ice is much less than liquid water. This will be followed by a reduction in sample capacitance, increasing peak amplitude. However, it is unclear why the sample annealed at −10 °C (black closed symbols in Figure 100b) reveals a stable profile of peak magnitude after 1.35 h. One possibility is that in the early stage of the ice growth process, the ice crystal size is not large enough to change the fraction volume and block the movement of charges between ice crystals. Therefore, the overall response depends on ion connectivity in the frozen sample, which could be inferred from electrical resistance (Figure 101).

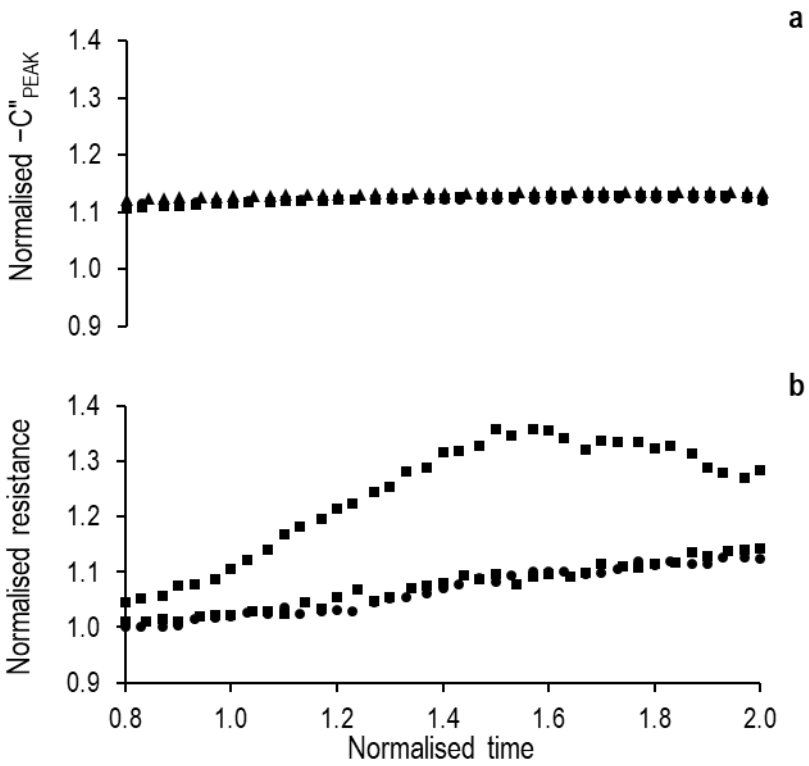

Figure 101 Time profiles of the parameters during the holding of a 5% w/v sucrose solution at −10 °C (a) Normalised C''_{PEAK} and (b) Normalised resistance. The fitting parameter resistance was determined by RelaxIS3 software (rhd instruments, Germany), using the model for a frozen solution ($C_G - [C_s = R_s = Co]$) (Smith and Polygalov 2019). Data recorded during the temperature constant (0.8 h -2.0 h) are demonstrated. The circles, squares and triangles represent the first, second and third annealing cycles, respectively.

When ice growth maximises and the microstructure of the frozen matrix is uniform so the fraction volume and conductivity maintain consistency, the C''_{PEAK} and fitting parameter resistance will not change anymore. The time point where these parameters begin to stay at an even level throughout the rest of the holding process is supposed to mark completion of the annealing process. Unfortunately, the holding period used in this study was not long enough to investigate the completion of the annealing process; it should last at least 20 h (Nakagawa et al., 2018). Further experiments that provide a full Ostwald ripening process will be required to enable more investigation.

Despite the limitations of this study, these results could support the idea that capacitance is primarily preferred for the re-crystallisation mechanism, while resistance of the unfrozen phase

is represented by connectivity within the frozen matrix. The TVIS response would help us obtain better understanding of the physical characteristics corresponding to the microstructure of the frozen matrix. In other words, the Ostwald ripening kinetics could be demonstrated by the TVIS approach.

8.3.3. Determination of glass transition temperature of freeze-concentrated solution by through-vial impedance spectroscopy technique

To establish the use of TVIS technology in determining glass transition temperature, we selected the protocol in which the frozen mass was ramped at a temperature exceeding the T_g' (ramped from −50 °C to −10 °C) for this study.

In Figure 102, it is clear that the relaxation peak frequency is strongly temperature-dependent and does not indicate any change due to physical change of the unfrozen phase; whereas the other parameters—C''_{PEAK}, C'(10 Hz), and C'(0.2 MHz)—show discontinuity within the transition region (between −35.6 and −32.9 °C). However, the inflection is more pronounced in real part capacitance at high-frequency region C'(0.2 MHz). A possible explanation is that the characteristics of the TVIS response could be marked by temperature effect. When the temperature is ramped, instantaneous capacitance at very high frequency ($C'(\infty)$) has a relatively small change compared to static capacitance in a low-frequency range ($C'(0)$). Hence, real part capacitance associated with the unfrozen fraction for the low-frequency region (i.e. C'(10 Hz)) has a temperature dependence greater than real part at the high frequency (i.e. C'(0.2 MHz)). To reduce the impact of temperature on the TVIS parameters, we will focus on real part capacitance at the high-frequency end.

Recently, the TVIS method of assessing the glass transition temperature of 10% w/v maltodextrin has been reported (Smith et al., 2014; Smith et al., 2013). The inflection in either the time-derivative or temperature profile of the peak features (C''_{PEAK} and F_{PEAK}) and fitting parameters (resistance and capacitance) were used to estimate the T_g' value. Unlike in previous

studies, the glass transition temperature of 5% w/v sucrose was determined using the inflection point in the temperature profile of the C'(0.2 MHz).

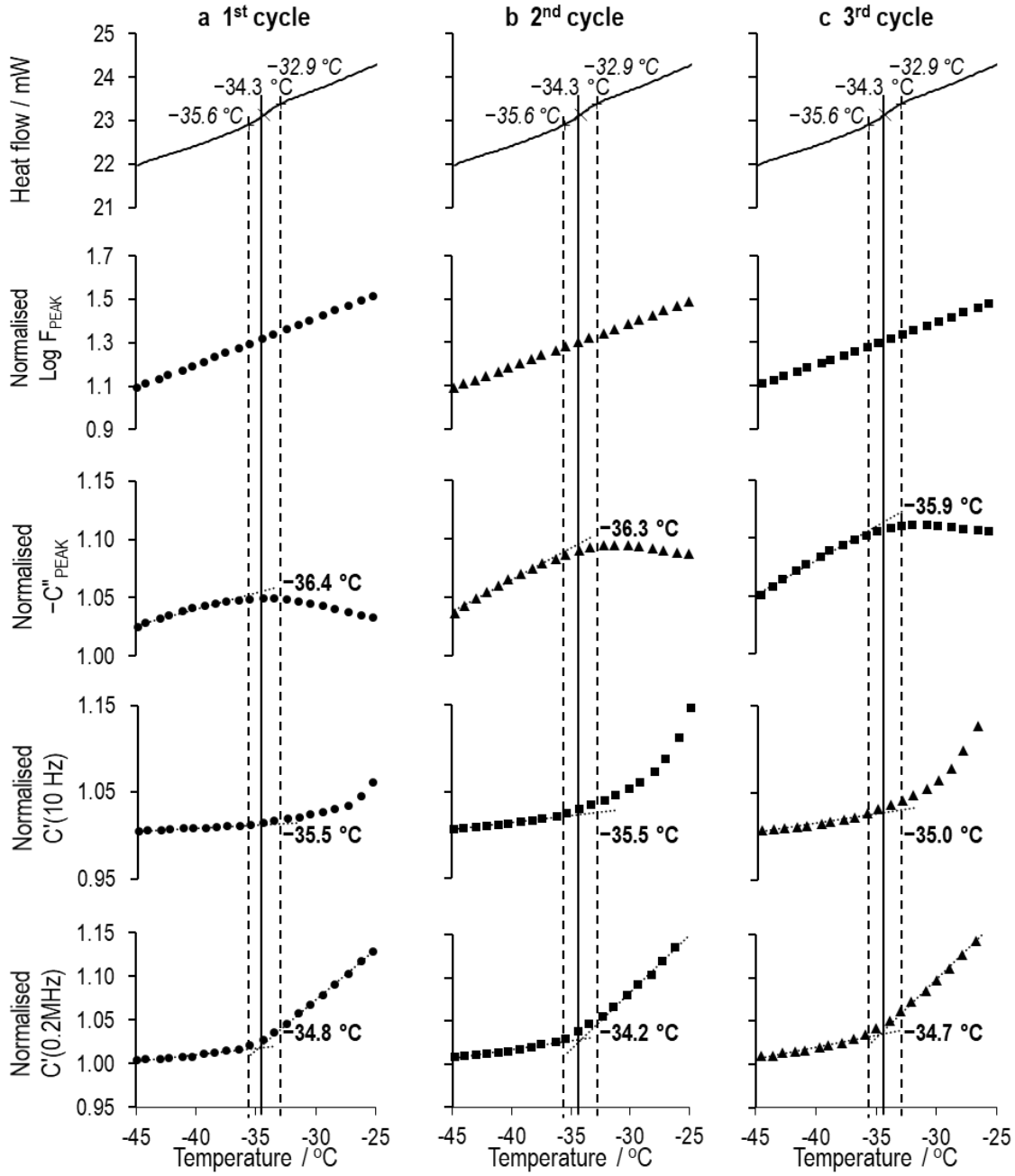

Figure 102 Normalised TVIS parameters: $Log\ F_{PEAK}$, C''_{PEAK}, C'(10 Hz), and C'(0.2 MHz), extracted from the capacitance spectrum of 5% w/v sucrose solution recorded during three reheating cycles: (a) first cycle, (b) second cycle and (c) third cycle. This figure demonstrated the normalised TVIS parameters—$Log\ F_{PEAK}$, C''_{PEAK}, C'(10 Hz), and C'(0.2 MHz)—at product temperature range from −45 °C to −25 °C. Note, each reheating step, the frozen sucrose was ramped from −50 °C to −10 °C at 0.2 °C·min^{-1}.

Given that the glass transition temperature is usually defined as that at which dramatic changes in physical characteristics (e.g. viscosity or conductivity) occur, the inflection of the C'(0.2 MHz) parameter might be evidenced by the change in resistance due to alteration of system mobility, caused by the glassy-rubbery phase transition. In other words, the temperature dependence characteristics deviate from Arrhenius behaviour. A simplified approach of determining the inflection point is to use the intersection of two fitted lines. Here, the data based on the capacitance, i.e. C'(0.2 MHz), pre- and post-the transition region (approximately −36 °C to −32 °C) were fitted to the linear function; the crossover point of these fitted lines was then calculated. From three cycles, the real part parameters—C'(0.2 MHz)—demonstrate the intersection temperature at −34.6 ± 0.3 °C (**Figure 102**).

8.4.Summary

This study demonstrates the application of through-vial impedance spectroscopy in providing an insight into the physical characteristics of frozen sucrose within the freeze-dried vial during the annealing process. Two useful observations were made: (1) The structural changes in the ice fraction was less pronounced when annealing at lower temperatures, particularly below the glass transition temperature; (2) The inflection of the temperature profile of real part capacitance at high frequency (i.e. 0.2 MHz) matched with the glass transition. These indicate the TVIS approach of providing information on the microstructure of frozen matrix and measuring the in-situ glass transition temperature.

9. TVIS approach to assessment product during primary drying

9.1. Objective

The objective of this study is to evaluate the application of through-vial impedance spectroscopy to characterise product attributes during freeze-drying process development by developing the methodology for (1) predicting ice temperature at sublimation interface; (2) determining sublimation rate; then applying these parameters to calculate dried product resistance and assess the structure-sublimation rate relationship. Electrical impedance of 5% w/v lactose solution contained in a standard TVIS vial is measured during a freeze-drying cycle which includes a temperature ramp through the collapse temperature of lactose during primary drying.

9.2. Materials and Methods

9.2.1. Preparations

D-lactose monohydrate was purchased from Sigma® Life Science (UK) and used as supplied in the preparation of a 5% w/v lactose solution in ultrapure water (18.2 MΩ·cm).

9.2.2. Differential scanning calorimetry

The glass transition (T_g') of the freeze-concentrated 5% w/v lactose solution was analysed by modulated differential scanning calorimetry (mDSC) using a Q2000 DSC, TA instrument (UK), according to the following method. A 80 µl sample of 5% w/v lactose solution was placed in a sealed aluminium pan (part number 900825.902) and cooled down to −90 °C at 10 °C·min^{-1}; then re-heated to 25 °C at 1.5 °C·min^{-1}, with modulation of 0.23 °C·min^{-1} every 60 s. Nitrogen was purged during measuring at a flow rate of 50 mL·min^{-1}. The temperature at the midpoint of the thermal transition was obtained by Universal Analysis 2000 software (TA Instruments, New Castle, USA) and used to define the glass transition temperature of the maximally concentrated solution (T_g').

9.2.3. Freeze-drying microscope

The collapse temperature (T_c) of the dry layer, resulting from the freeze-drying of the 5% w/v lactose solution, was determined using a Lyostat5 freeze-drying microscope (FDM) from Biopharma Process Systems (UK) according to the following method. A 2 µl sample of the 5% w/v lactose solution was pipetted onto a 16 mm circular quartz window located on a silver block of the FDM stage, then covered with a glass coverslip (13 mm diameter) supported by a 70 µm spacer. A small amount of silicon oil was used to improve thermal transfer from the silver block to the quartz window. The sample was cooled to −50 °C, at a rate of 10 °C·min^{-1}, and held for 2 min to ensure complete solidification, before the vacuum was applied (pressure < 0.02 mbar) to initiate sublimative drying. Once a sufficient dry layer depth had developed, the sample was heated to 20 °C, initially at a rate of 5 °C·min^{-1}, then at a slower rate of 1 °C·min^{-1} when the temperature reached −35 °C, to more accurately determine the onset of collapse temperature. Images were recorded every 5 s when the heating temperature was above −35 °C.

9.2.4. Vial filling and loading the freeze dryer

3.1 g aliquots of the 5% w/v lactose solution were transferred to a cluster of eighteen 10 mL type I tubular clear glass vials (1096936, Schott, Hungary supplied as VC010-20C from Adelphi - HP) and one TVIS measurement vial. The fill weight of 3.1 g is equivalent to a liquid fill height of 9 mm from the internal base of the vial, which corresponds to a fill factor (Ø) of 0.7: where Ø is defined as the relative height of the sample solution within the electrode region to the height of the electrode (Figure 103). The TVIS vial was the same type of tubular glass but modified by attaching a pair of copper foil electrodes to the external surface. These two electrodes, each of 10 mm height and 19 mm width, were placed diametrically opposite each other at a height of 3 mm above the exterior base of the vial.

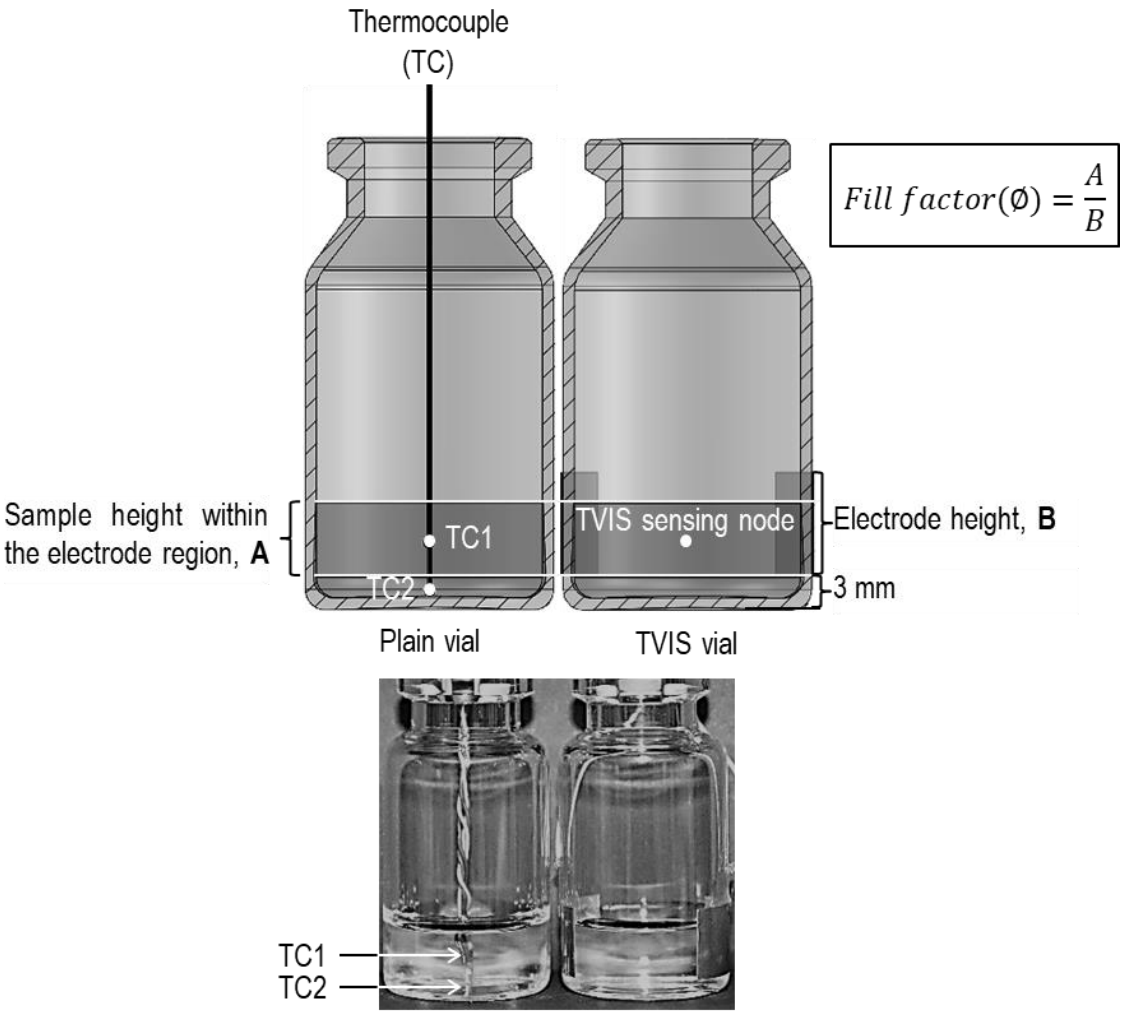

Figure 103 Vertical cross-sections of two vials containing 3.1 g of 5% w/v lactose solution. **Right***:* Modified TVIS vial attached with a pair of copper electrodes (19 x 10 mm) positioned 3 mm from the external vial base (~ 2 mm from the internal base of the vial). **Left***:* Unmodified nearest neighbour vial with two type-T thermocouples. The beads of the thermocouples were placed at the bottom centre of the vial (TC2), at the height corresponding to the middle of the sample within the electrode sensing region (TC1). The fill factor (Ø) shown here is 0.7, which means that the sample height in the electrode region is 7 mm for an electrode height of 10 mm.

TVIS measures the average product temperature at the centre-point of the volume of material bounded by the electrodes (Smith et al., 2017). In other words, at a height equivalent to half the sample height bounded by electrodes; the point we shall now call the TVIS temperature sensing node, or simply the TVIS node (Figure 103).

Two T-type thermocouples (28 AWG) were inserted into one of the vials through the rubber stopper, and the tips positioned at the two specific heights; one at the centre bottom of the vial (TC2), the other (TC1) at the equivalent height to the sensing node in the neighbouring TVIS vial (Figure 103). The positions of the TCs beads were realised through careful manipulation of the wires via a process of trial and error, with the final position determined by eye. The TC-containing vial was placed adjacent to the TVIS vial.

Assuming there is thermal equivalence between the two points in the horizontal direction of each adjacent vial, it follows that TC1 data from the annealing stage could be used to provide a calibration temperature for the TVIS vial (Section 9.3.4, *Ice temperature calibration*). This serves the purpose of providing a predictive temperature in the TVIS vial during the subsequent primary drying stage (Section 9.3.4, *Prediction of ice temperature at the TVIS node*). The second thermocouple (TC2) measures the product temperature at the base of the TC vial. Again, if we assume thermal equivalence between the two points, one at the base of the TC vial and the other at that of the TVIS vial, we can estimate the temperature at the sublimation front (T_i) using the 2-point linear extrapolation (Smith, Jeeraruangrattana & Ermolina, 2018): with the TVIS predicted temperature ($T_{F_{PEAK}}$) at the sensing node as the second point from which the extrapolation is projected.

160 vials were arranged on the loading tray of the freeze dryer, with the cluster of the 19 solution-filled vials at the centre of an array of empty vials (Figure 104), then partially closed with 20mm 4023/50 bromobutyl grey rubber stoppers (FDW20RTS, West Pharmaceutical Services Singapore Ltd, Singapore) - before being loaded into a Virtis Advantage Plus XL benchtop freeze dryer (SP Scientific, USA).

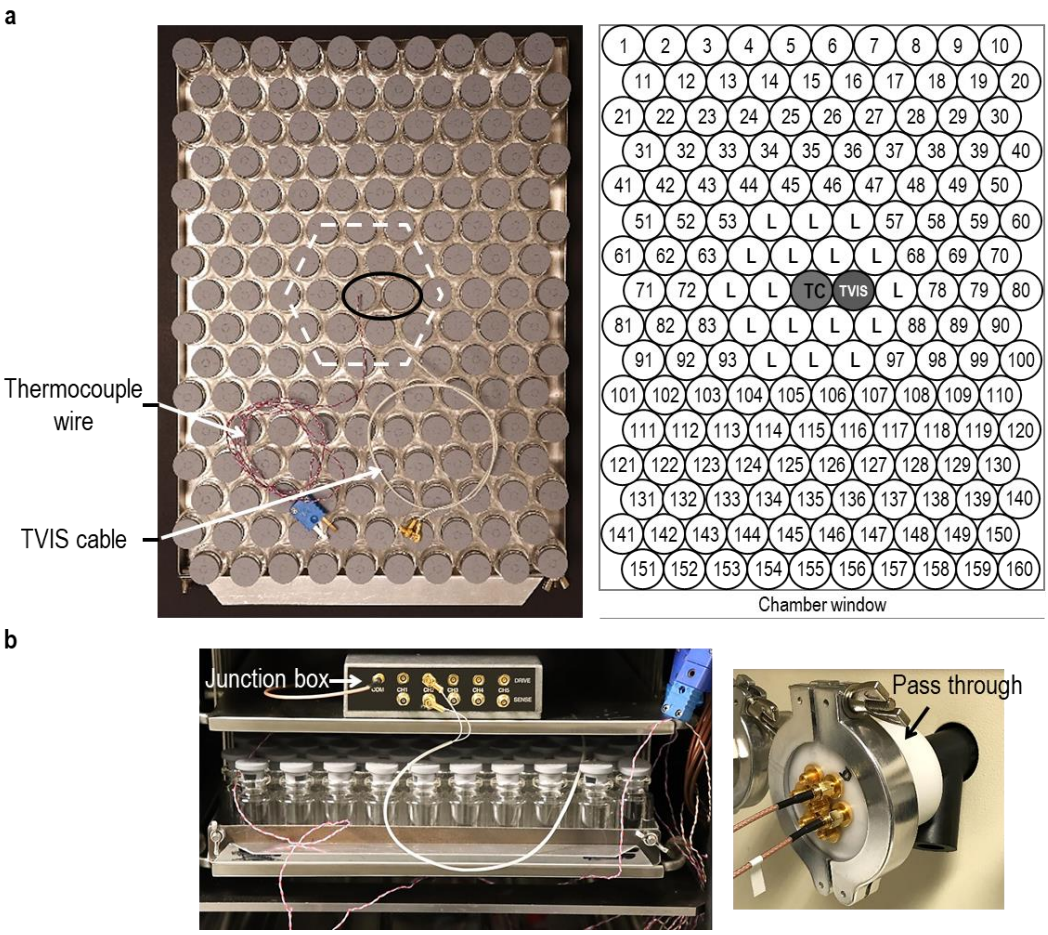

Figure 104 (a) An arrangement of vials on the shelf of the Virtis Advantage Plus XL freeze dryer. The TVIS modified vial (labelled TVIS) and the thermocouple-containing vial (labelled TC) were placed close to the centre of the shelf. The sample filled vials are represented by "L"; those left empty are labelled with the number position in the dryer. (b) Five-channels TVIS junction box (left photo) placed on freeze dryer shelf, and the pass-through (right photo) for the TVIS cabling, connected to the manifold hose on the outside of the Virtis Advantage Plus XL freeze dryer.

9.2.5. Through-vial impedance spectroscopy

The TVIS measurement vial was connected to a multichannel impedance analyser developed by De Montfort University via a junction box inside the freeze dryer (Figure 104b) and an electrical pass-through on one of the manifolds on the dryer (Figure 104b). A full description of the measurement system is given by Smith and Polygalov (2019).

Impedance spectra of the TVIS vial, over the frequency range of 10 Hz to 1 MHz, were measured throughout the entire freeze-drying process at a scan interval of 2 min. The measurement time to acquire each spectrum was ~ 10 s.

9.2.6. Freeze drying protocol

The process cycle described in **Table 14** was used to freeze dry the 5% w/v lactose solution. Three specific features were included in this cycle (see the items in bold in **Table 14**):

(1) A re-heating stage between −50 °C and −10 °C (after the freezing hold period) to calibrate the TVIS peak frequency (F_{PEAK}) against product temperature and establish the correction coefficient to compensate for impact of temperature on the TVIS parameter, C''_{PEAK}: so that product temperatures and sublimation rates may be predicted in the subsequent primary drying stage.

(2) A ramp in the shelf temperature during the primary drying step from −40 to −10 °C, in an attempt to force the product through its glass transition and thereby collapse it.

(3) A partial vacuum of ~ 290 mtorr (386.6 μbar or 0.039 kPa) during the primary drying stage was aimed to create an initial sublimation interface temperature of −30 °C (which corresponded to the glass transition measured by mDSC). Due to the freeze dryer have been operated in mtorr and imprecise relationship between the set (programmed) and actual pressure, such that a programmed value of 400 μbar (0.04 kPa) was set, in order to deliver the target chamber pressure of 290 mtorr.

Table 14 Freeze-drying protocol

Step	Temperature (°C)	Time (min)	Cumulative Time (h)	Set pressure (µbar)
Equilibrium phase	+20	10	0.17	-
Freezing temperature ramp (0.6 °C·min^{-1})	−50	120	2.17	-
Freezing temperature hold	−50	120	4.17	-
Re-heating temperature ramp (0.7 °C·min^{-1})	−10	60	5.17	-
Re-heating temperature hold	−10	120	7.17	-
Re-cooling temperature ramp (0.7 °C·min^{-1})	−50	60	8.17	-
Re-cooling temperature hold	−50	120	10.17	-
Primary drying temperature ramp (0.3 °C·min^{-1})	−40	30	10.67	-
Primary drying temperature hold	−40	30	11.17	-
Primary drying temperature hold	−40	60	12.17	**400**
Primary drying temperature ramp (0.1 °C·min^{-1})	−10	300	17.17	**400**
Primary drying temperature hold	−10	1560	43.17	**400**

In practice, the set pressure of 400 µbar (0.04 kPa) is translated to an actual chamber pressure of 291.5 ± 24.3 mtorr (378.9 ± 31.6 µbar) during the primary drying process.

9.2.7. Scanning electron microscope

The microstructure of the freeze-dried cake (following extraction from the TVIS vial) was examined by a scanning electron microscope (Carl Zeiss EVO HD, UK). A vertical cross-section of the lactose cake was mounted on an aluminium stub, using Electrodag® 1415 (Agar Scientific) coating as an adhesive; then sputtered with gold under vacuum, using Quorum Q150RS sputtering coater, to a thickness of 15 nm. Images showing the morphology of the freeze-dried cake were acquired at 25x magnification for an overview of the whole sample, and at 500x magnification for a more detailed view of the microstructure at different depths of freeze-dried cake (i.e. top, middle and bottom sections).

9.3. Results and Discussion

9.3.1. Determination of critical temperature by thermal analysis and freeze-drying microscope

An endothermic step in the reversing heat flow diagram of the mDSC thermogram was used to demonstrate glass transition behaviour of the 5% w/v lactose solution. There are several methods for assigning a temperature to the glass transition; however, the midpoint of the step is possibly the most common (Gabbott, 2008). According to this, we derived a value of T_g' = −30.2 °C for the 5% w/v lactose solution (Figure 105). This temperature agrees broadly with the midpoint T_g' values ranging from −27 and −33 °C in other works (Meister & Gieseler, 2008; Her et al., 1994; Ward & Matejtschuk, 2010).

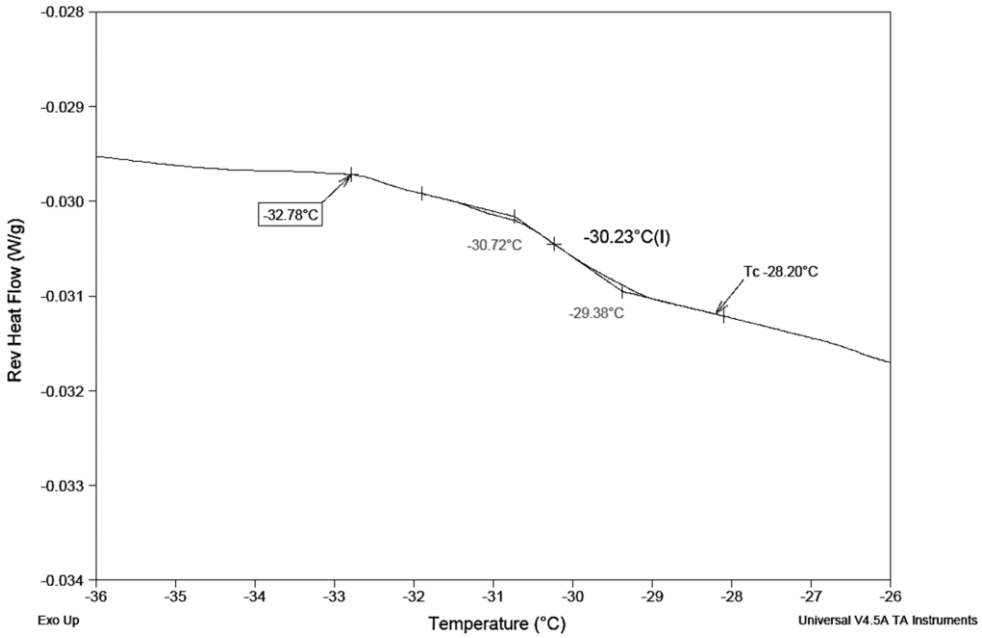

Figure 105 A mDSC thermogram of 5% w/v lactose solution. The glass transition temperature of the maximally freeze concentrated solution (T_g') of −30.2 °C is demonstrated by a step in the reversing heat flow. The arrows mark the onset of the glass transition temperature (−32.8 °C) and the collapse temperature (−28.2 °C).

The onset of the collapse of the 5% w/v lactose solution was recorded at T_c = −28.2 °C (Figure 106b), ~ 2 °C higher than our value for T_g' taken from the midpoint of the reversing heat flow thermogram. It is assumed that the higher the temperature difference between both critical

formulation parameters (i.e. T_g' and T_c), the higher the upper tolerance limit for driving the efficiency of the process while avoiding collapse.

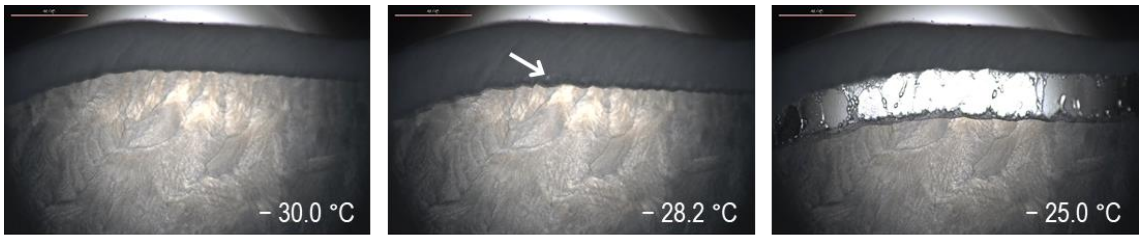

Figure 106 Freeze-drying microscope of 5% w/v lactose solution. (a) Drying at −30 °C, (b) onset of collapse at −28.2 °C, (c) complete collapse at −25 °C.

9.3.2. Process parameters

Figure 107 shows the freeze-drying profile of the standard process parameters: the shelf temperature (T_s), product temperature (T_{TC}) from the two thermocouples, and chamber pressure (P_c). Product temperature (T_{TC}) provided evidence for: (1) A nucleation temperature of −12.4 °C in the TC containing vial with an uncertainty estimate of 0.4 °C, determined from half the difference between the two temperatures recorded by TC1 and TC2 in the nearest neighbour vials; (2) thermal equilibration of the product, with the shelf reached within each 2 h hold period after (a) the freezing stage; (b) the annealing hold stage; (c) the end of the re-cooling phase of the annealing cycle. The thermocouple probe also evidenced the increase in product temperature during the shelf temperature ramp of the primary drying stage, with the slowing rate of increase in the product temperature associated with the onset of drying (due to the phenomenon of self-cooling). At 18 h, the system entered the steady state period with a constant product temperature, once the shelf temperature reached its set value of −10 °C. The onset of a step-like increase in the thermocouple temperature at 19.9 and 20.4 h (for TC1 and TC2, respectively) was probably an artefact induced by the bead of the TC detaching (i.e. losing contact) with the ice layer.

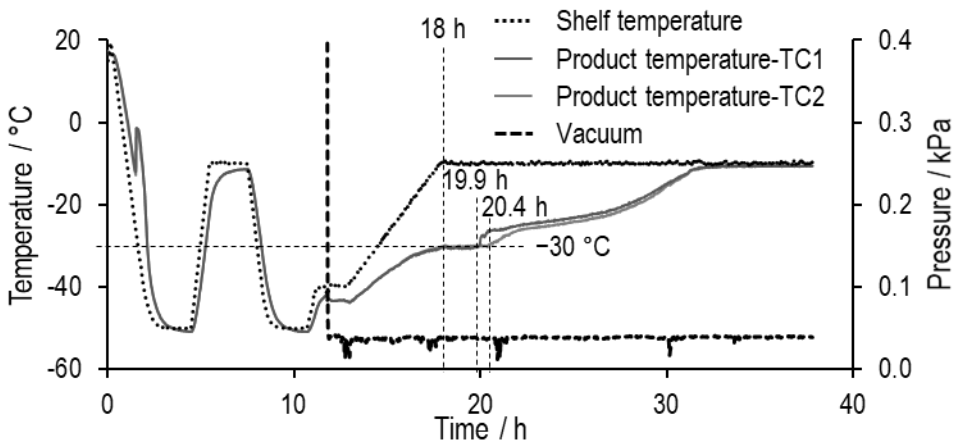

Figure 107 Freeze drying process profile of 5% w/v lactose solution.

9.3.3. TVIS results

Figure 108 shows the surface plot of the real and imaginary capacitances of the TVIS vial, filled with 3.1 g of a 5% w/v lactose solution, throughout the entire lyophilisation cycle. Each plot is made up from the multiple individual spectra acquired every 2 min throughout the cycle. The real part capacitance defines the ability of a material to store the electrical potential energy through an alignment of localized charges associated primarily with polar molecules, whereas the imaginary part capacitance defines the ability of a material to dissipate energy through either the diffusion of delocalized charges associated with ions (in the case of conductivity) or the lag between the oscillations of applied electric field and the response of the polarization processes (in the case of dielectric loss), for example.

In order to provide a clearer picture and commentary on the changes observed during the lyophilisation cycle, we have taken example spectra for each phase: then plotted these in Figure 109. Prior to ice nucleation and growth (Phase A in Figure 108), the step in real part capacitance spectra and main peak in imaginary capacitance spectra is due to the Maxwell-Wagner (interfacial) polarization of the glass wall through the solution resistance. After complete solidification of the ice mass (Phase B in Figure 108), the polarization mechanism changes and the process is associated with the dielectric relaxation of ice; the time constant of which has a temperature dependence (Johari and Whalley, 1981; Popov et al. 2017).

As the process enters primary drying (Phase C in Figure 108), the magnitude of the dielectric loss process reduces as ice starts to sublime. Smith and Polygalov (2019) gave descriptions of the mechanisms underpinning the Maxwell-Wagner process and the dielectric relaxation of ice.

Here, we note the differences between our study, Johari and Whalley (1981) and Popov et al. (2017). In their works, water is frozen and measured inside a parallel plate capacitor with direct contact between the metal electrodes and the sample; whereas in ours, we have additional impedance in series with the sample (owing to its juxtaposition of the glass wall), which shifts the characteristic frequency and amplitude of the dielectric loss peak relative to that: due to the relaxation process of ice alone. The impact of glass wall impedance on the experimentally measured relaxation process is the subject of preliminary analysis by Smith and Polygalov (2019).

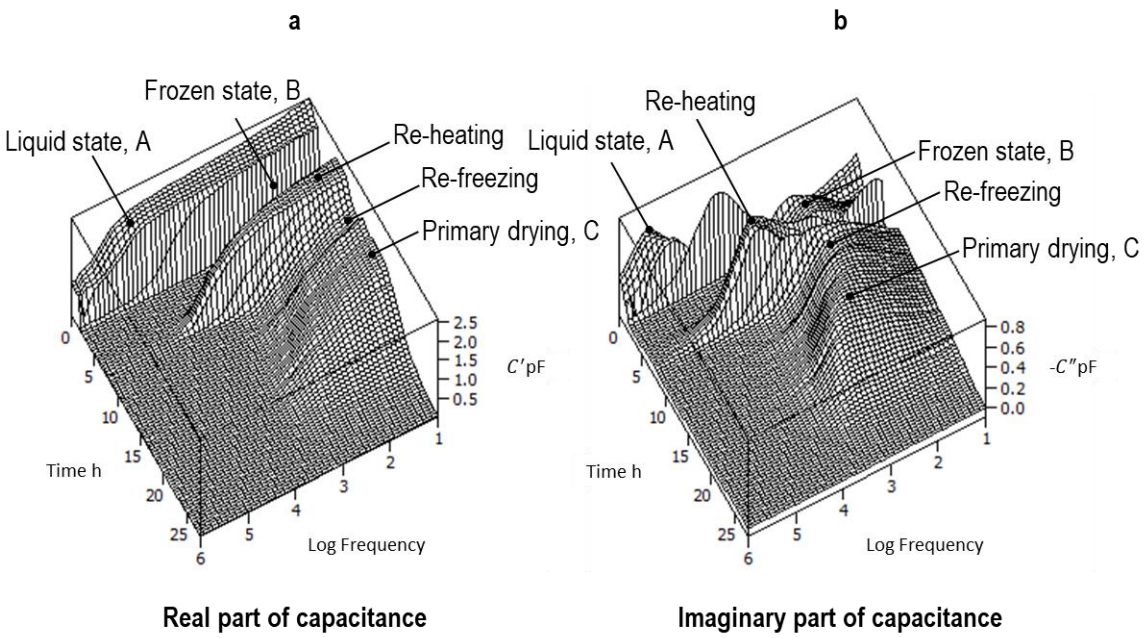

Figure 108 (a) Real and (b) imaginary capacitance spectra recorded every 2 min during the freeze-drying of the 5% w/v lactose solution.

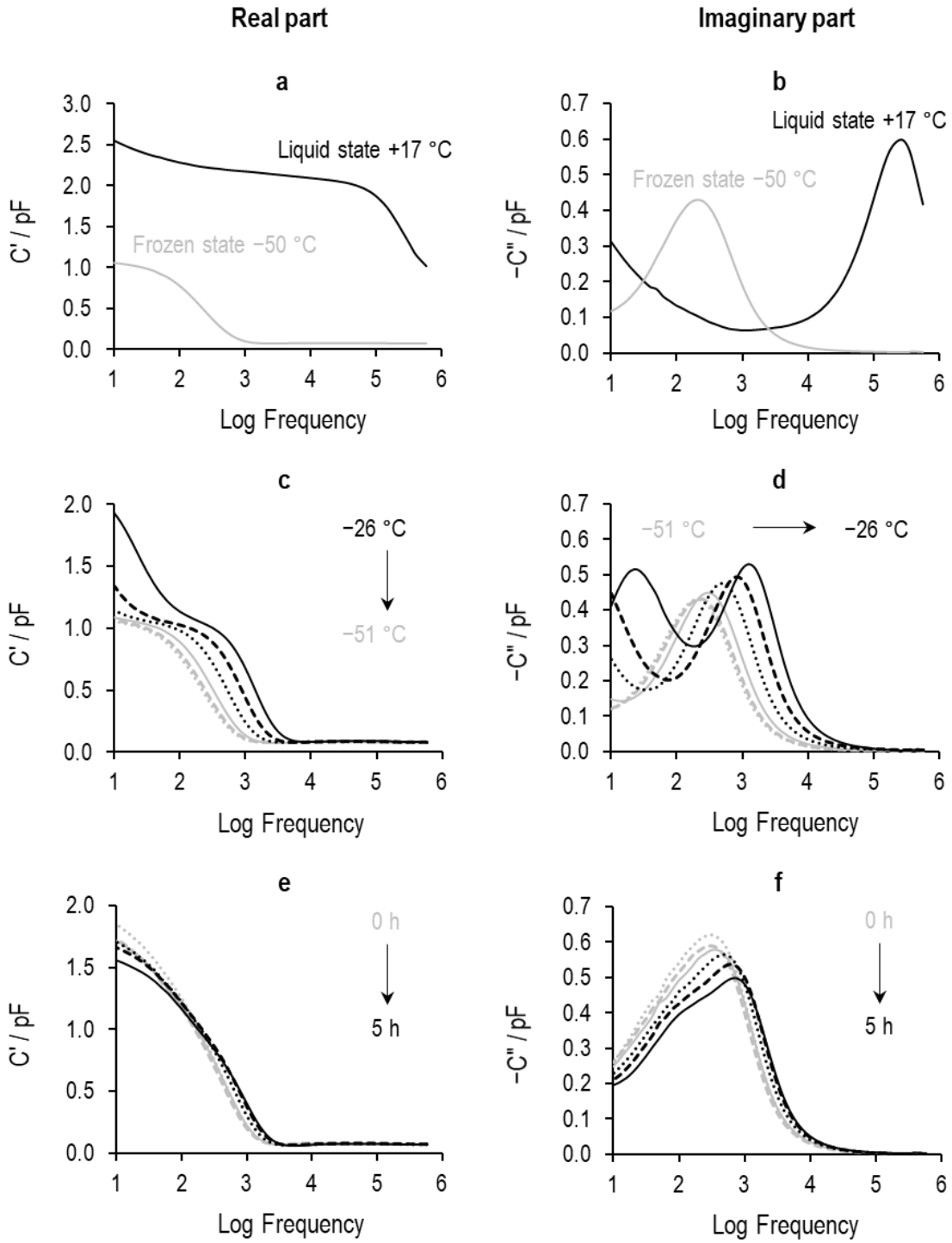

Figure 109 An example TVIS spectra of 5% w/v lactose solution during (a-b) freezing, (c-d) re-heating from −51 °C to −26 °C, (e-f) primary drying (0-5 h).

We also note that co-existence of the unfrozen fraction affects the experimentally observed spectrum by introducing a second process at lower frequencies than the main dielectric relaxation of ice. Analysis of the impact of glass wall impedance on the measured spectra is

beyond the scope of this publication. Instead, we resort to a more empirical approach based on the peak amplitude and peak frequency of the dielectric loss process associated with the dielectric relaxation of the ice fraction. Note, therefore, that peak frequency cannot be used directly to calculate the relaxation time (τ) according to the standard formula, $\tau = 1/2\pi f$, where f is frequency. Nor can we calculate the complex dielectric permittivity ($\boldsymbol{\varepsilon}$) of the ice fraction from the complex capacitance ($\mathbf{C}$) according to the standard formula, $\boldsymbol{\varepsilon} = \mathbf{C}/\varepsilon_o k_s$, where ε_o is the permittivity of free space and k_s is the cell constant of the object (in our case, the TVIS vial and its contents).

The analysis of the freezing stage of simple sugar solutions (such as lactose and sucrose) will be the subject of a further study. Instead, we focus exclusively on the annealing and primary drying stage. The peak-finding function of our LyoView™ analytical software was used to determine the amplitude (C''_{PEAK}) and characteristic frequency (F_{PEAK}) of the dielectric loss peak across the re-heating phase of the annealing and primary drying stage, from the start to the point at which C''_{PEAK} had effectively reduced to zero. An example spectrum, which highlights the determination of C''_{PEAK} and F_{PEAK} and existence of a secondary relaxation peak associated with the unfrozen fraction, is shown in Figure 110.

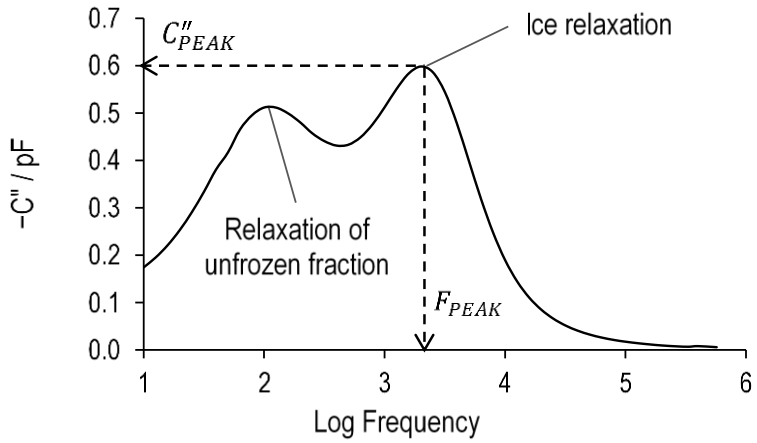

Figure 110 An example dielectric loss spectrum of the 5% w/v lactose solution at −20.3 °C (during re-heating of the frozen solution) to demonstrate the meaning of C''_{PEAK} and F_{PEAK} of the ice relaxation peak, as determined by LyoView™ software.

In our previous publication (Smith, Jeeraruangrattana & Ermolina, 2018), we demonstrated the sensitivity and subsequent application of the TVIS parameter F_{PEAK} in determining the ice interface temperature during primary drying, and sensitivity and subsequent application of the TVIS parameter C''_{PEAK} in determining the primary drying rate; from which, an estimate of the vial heat transfer coefficient could be derived. In that work, we used a dual-pair electrode system. Here, we further develop this approach and adapt it to a single pair of electrodes. Figure 111 sets out the principles of this new method.

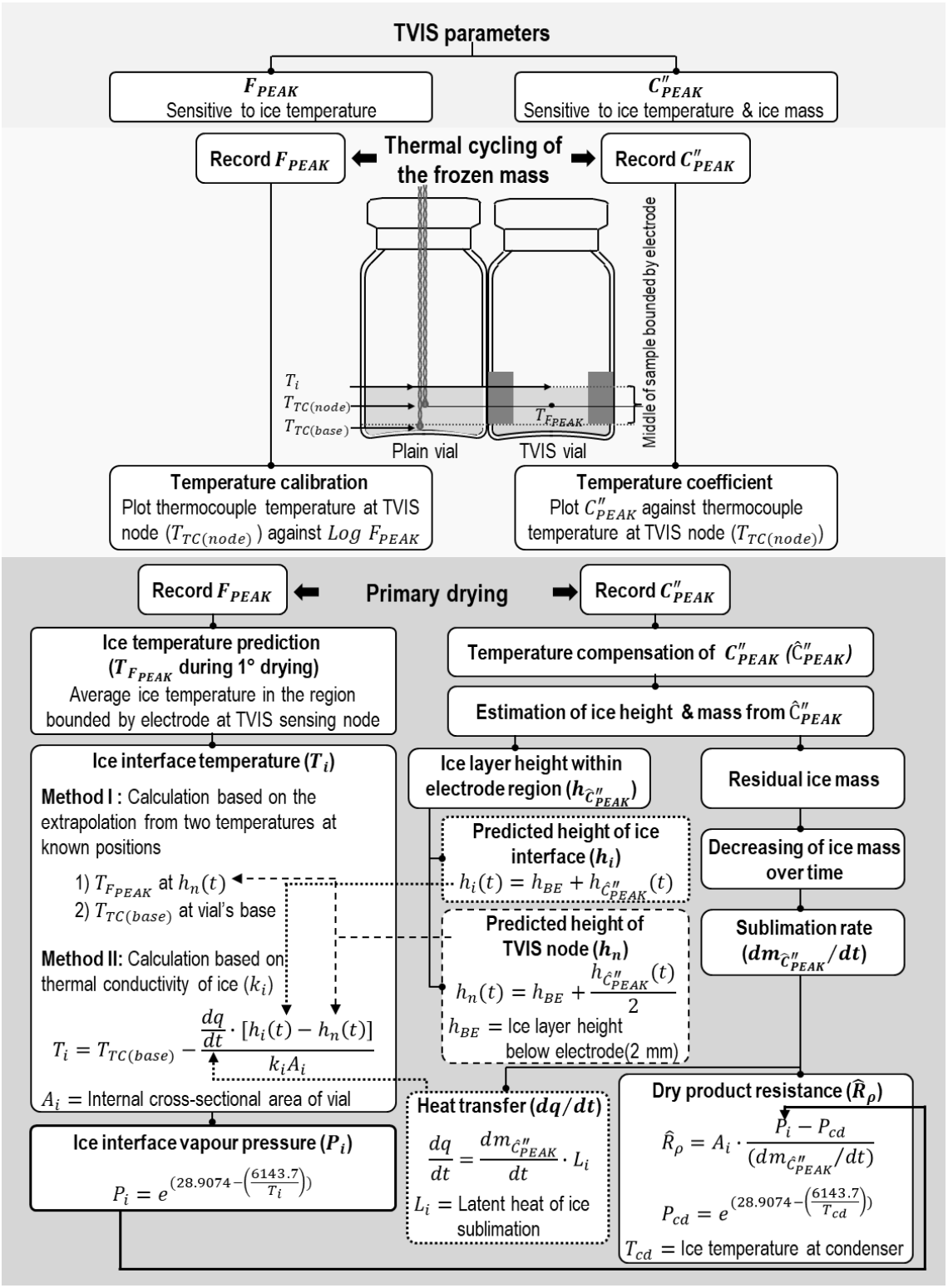

Figure 111 TVIS method for determining drying rate and ice interface temperature, from which dry layer resistance is estimated.

9.3.4. Measurement of product temperature

Ice temperature calibration

Johari and Whalley (1981) demonstrated a positive correlation between the relaxation frequency of ice and its bulk temperature. It is not surprising, therefore, to find that the peak in the imaginary capacitance spectrum shifts to higher frequencies as the temperature of the frozen matrix within the electrode region is increased (Figure 112a). A temperature calibration could be provided using TVIS data from the re-heating phase of the annealing cycle by first plotting the temperature from the thermocouple located at TVIS node (T_{TC1}) in a nearest neighbour vial against the TVIS peak frequency on a logarithm scale ($Log\ F_{PEAK}$) for the corresponding times at which the temperature was recorded, then fitting a second order polynomial function to the data (Figure 112b).

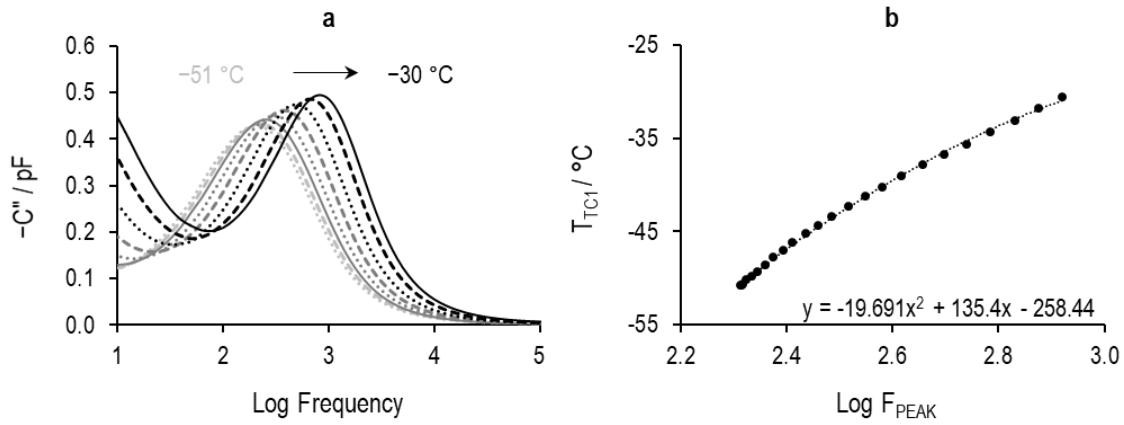

Figure 112 (a) Selected imaginary capacitance spectra of 5% w/v lactose solution in a 10 mL TVIS measurement vial with a pair of 19 x 10 mm electrodes, demonstrating temperature dependency of the dielectric loss peak during the reheating stage (temperature ramp from −51 °C to −30 °C at 0.7 °C·min^{-1}); (b) Temperature calibration used to estimate the ice temperature during primary drying is determined from the plot of the thermocouple temperature located at the TVIS node, i.e. the midpoint of the sample within the electrode region (T_{TC1}) and logarithm of the peak frequency (F_{PEAK}), recorded during the reheating period.

Prediction of ice temperature at the TVIS node

The average product temperature of the ice in the region bounded by the electrodes, during the subsequent primary drying stage, is then predicted by substituting values for $Log\ F_{PEAK}$ (from the primary drying period) into the x-parameter of the polynomial function (shown in Figure 112b). Note that the predicted temperature at the TVIS node has the symbol $T_{F_{PEAK}}$ because it is derived from the TVIS parameter F_{PEAK}. Figure 113 shows values for both the TVIS predicted temperature ($T_{F_{PEAK}}$) and thermocouple measured temperature (T_{TC1} and T_{TC2}), along with the shelf temperature (T_S).

A few initial points are worth noting on Figure 113:

(1) The temperature predicted by TVIS ($T_{F_{PEAK}}$) matched the profile from the temperature sensor (T_{TC1} and T_{TC2}) for the first 8.1 h of primary drying, with a maximum difference of 1.7 °C and 0.5 °C difference on average, throughout that period.

(2) Both $T_{F_{PEAK}}$ and thermocouple temperature ($T_{TC1}$and T_{TC2}) stabilise at a temperature of −30.6 ± 0.36 °C between 6.4 and 8.0 h (marked by the double-headed arrow), i.e. soon after the shelf temperature had entered the hold period at 6.2 h into primary drying.

(3) At 8.1 h, there is a pronounced step in the T_{TC1} profile, resulting in T_{TC1} being, on average, ~ 5 °C higher than $T_{F_{PEAK}}$ over the subsequent period between 8.2 and 12.3 h.

(4) After 10 h, both T_{TC1} and $T_{F_{PEAK}}$ increased gradually, even though the shelf temperature remained constant.

(5) The T_{TC2} profile demonstrates a similar phenomenon to the T_{TC1} profile but the step appears at the later time point (8.6 h) and is much less dramatic in terms of the rate of increase in temperature. The temperature from T_{TC2} is ~1 °C lower than that from T_{TC1} on average after 10.4 h owing to its position closer to the colder sublimation interface.

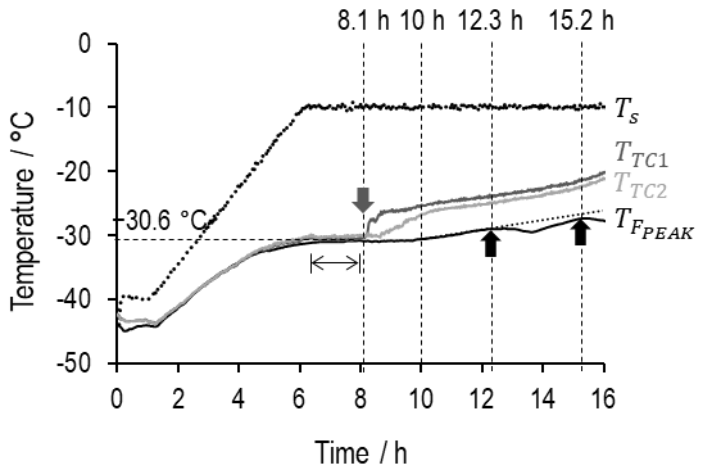

Figure 113 Temperature profiles during the primary drying stage, showing the thermocouple temperature (T_{TC}), TVIS predicted temperature ($T_{F_{PEAK}}$), and shelf temperature (T_s). The downward grey arrow points the step in the T_{TC1} profile at 8.1 h; whereas the two upward black arrows point the dips in the $T_{F_{PEAK}}$ profile at 12.3 h and 15.2 h, respectively. The dotted line extrapolated from $T_{F_{PEAK}}$ data (from the 12.3 h time point onwards) is drawn to show the expected response if it were to follow a trajectory similar to that displayed by the thermocouple temperature (T_{TC}). The double-headed arrow marks the time period where $T_{F_{PEAK}}$ and T_{TC} become stable.

As sublimation proceeds, a reduction in ice quantity could lead to the thermocouple sensor detaching from it, increasing uncertainty of the measurement of the product temperature (Hibler, Wagner & Gieseler, 2012; Scutella et al., 2017; Pikal, Roy & Shah, 1984). It is highly likely, therefore, that the step-like increase in the thermocouple temperature at 8.1 h is due to this phenomenon (see downward grey arrow in Figure 113). However, the TVIS predicted product temperature continues beyond 8.1 h along a constant trajectory, suggesting that it might be able to track the product temperature over a longer period than the TC sensor. A possible explanation for the differences in the duration of the two temperature tracking periods is that the thermocouple probe was located at the centre of the sample bounded by a sensing electrode: so once the ice had been removed to that point, the thermocouple would begin to sense the dry layer temperature rather than that of ice. In contrast, the TVIS system has the sensing electrodes outside of the vial; the temperature predicted here represents the average of that part of the product bounded by the electrodes.

Despite the systematic error of the TC sensor associated with the thermocouple profile (i.e. the step in the measured temperature), the measured temperature continues thereafter on a monotonic trajectory. In contrast, the $T_{F_{PEAK}}$ profile dips in two places: first at 12.3 h, then at 15.2 h (see upward black arrows in Figure 113). Our assumption is that dips in the trajectory of $T_{F_{PEAK}}$ are symptomatic of the change in the ice cylinder contact with the inside of the glass vial. Notwithstanding both artefacts with the TC and TVIS measurements of temperature, general profiles of both measurements beyond 10 h again follow the same trend: a gradual increase in temperature related to a slowdown in primary drying rate and associated reduction of the self-cooling of the contents. The dotted line on the $T_{F_{PEAK}}$ data beyond 12.3 h is drawn to indicate the trend if these two dips are not evident.

9.3.5. Estimate of the residual ice mass

By making an analogy between the TVIS vial (with the electrodes on the outside of a glass vial filled with a frozen solution) and a parallel plate capacitor, we can expect electrical capacitance of the TVIS vial to be a function of the interfacial area of the frozen matrix that intimately contacts the inside surface of the glass wall adjacent to the electrode. An approximation for this capacitance can be taken from the basic equation for electrical capacitance of the parallel plate capacitor (Equation 75).

$$C_s = \frac{\varepsilon_o \varepsilon_r A_s}{d_s} \qquad \text{Equation 75}$$

For the parallel plate capacitor, C_s is the capacitance of the object (i.e. the TVIS vial and its contents), ε_o is the permittivity of free space (8.854 x 10^{-12} F·m^{-1}), ε_r is the relative permittivity of the composite sample (the frozen mass in series with the glass wall of the vial), A_s is the interfacial area between the TVIS electrode and the glass wall, and d_s is the average distance between the TVIS electrode pair, including glass wall thickness.

It follows that a reduction in the interfacial area, associated with a decrease in height of the ice layer in contact with the glass wall, would result in a proportionate drop in capacitance of the

TVIS vial. In other words, capacitance of the TVIS vial is directly porportional to the amount of ice contained in it. Consequently, the rate of ice loss could be determined by the rate of change of the measured capacitance, providing an opportunity to monitor the primary drying process. Smith et al. (2017) described the basic methodology to determine the sublimation rate by using the magnitude of the dielectric loss process associated with the ice content in the vial (C''_{PEAK}).

It is thought that the linearity between the amplitude of the dielectric loss peak (i.e. C''_{PEAK}) and height of the ice cylinder is dependent on the intimacy of ice contact with the inside of the glass wall. Therefore, it is not recommended to follow this parameter throughout the entire primary drying process (for the purpose of determining the primary drying rate), due to inevitable changes in the ice-glass contact associated with a change in the shape of the ice cylinder towards the latter part of the drying process. We have suggested previously that the point at which this measurement uncertainty is realised could be predicted by a drop in the magnitude of F_{PEAK} in circumstances when the actual product temperature continues to increase during drying (Smith, Jeeraruangrattana & Ermolina, 2018). Identification of this timepoint then allows for any unreliable data to be excluded from further analysis. On this basis, we consider that the ice cylinder begins to detach from the side wall at 12.3 h (again, we refer to the first of the two upward black arrows in Figure 113). However, the combination of factors associated with ice shape, uncertainty of TVIS measurement at points near the edges of the electrode (i.e. fringing effect), and heat transfer variation means that process parameters determined from TVIS parameters, F_{PEAK} and C''_{PEAK}, are probably unreliable beyond 9 h and should be disregarded from further consideration.

Compensation of C''_{PEAK} for temperature

In our previous article documenting the use of TVIS in determining heat transfer coefficient, we demonstrated a requirement to the first compensate C''_{PEAK} for its temperature dependency before correlating the parameter with a reduction in ice mass. Figure 114a shows the correlation between peak magnitude and temperature during the temperature ramp-up of the annealing stage. The positive correlation with temperature is at first unexpected, given that static

permittivity of ice alone (i.e. without the series impedance of the glass wall) obeys the Curie-Weiss law, falling by ~ 17% from 130 at −73 °C to 108 at −33 °C (MacDowell & Vega, 2010). However, recognising that the measurement system includes an additional series impedance from the glass wall of the vial, we should also consider the impact of this capacitance on the amplitude and characteristic frequency of the relaxation peak. The impedance of this composite system (i.e. sample in series with the glass wall) is further complicated by a double layer capacitance (at the interface between the frozen solution and the glass), which also contributes to the overall measured capacitance of the TVIS vial. This double layer is a function of the protonic and ionic charge accumulation at the glass surface from thermally activated diffusion processes in the ice and unfrozen fraction. It follows that higher temperatures result in greater charge accumulation and higher interfacial capacitance; and consequently, higher overall measured capacitance. This positive temperature coefficient must be larger than the negative temperature coefficient of static permittivity of ice for the overall coefficient to be positive. It follows that C''_{PEAK} provides an indirect assessment of the microstructure of the frozen solid and suggests that reduction of ice mass is not the only factor defining the magnitude of C''_{PEAK}. It is possible, therefore, that without a correction for temperature, any change in product temperature during primary drying could manifest as either a fall in the apparent sublimation rate (if the product temperature declines during primary drying), or an increase in the apparent sublimation rate (in the case of the temperature increasing during primary drying).

In order to establish whether temperature effects are significant here, we start with the premise that we can equate the ice mass directly to C''_{PEAK} at the beginning of the primary drying stage when the amount of ice is known. The amount of ice sublimed is assumed as proportional to the reduction in C''_{PEAK} at any point in time. However, we also know that if the temperature is ramped from −51 °C to −30 °C, the impact on the initial value of C''_{PEAK} will be ~ 0.70% (per degrees Celsius) (Figure 114b). Taking the example of an initial ice mass of 2.5 g per vial, if the product temperature prior to primary drying is −40 °C but ice sublimation causes it to drop to −43 °C over a period of 15 min (0.25 h), that 3 °C reduction alone would reduce C''_{PEAK} by 2.1%.

Therefore, it would seem that 2.1% of ice mass is lost within 15 min, leading to sublimation rate uncertainty of (2.5×0.021)×(60/15)=0.21 g·h^{-1}.

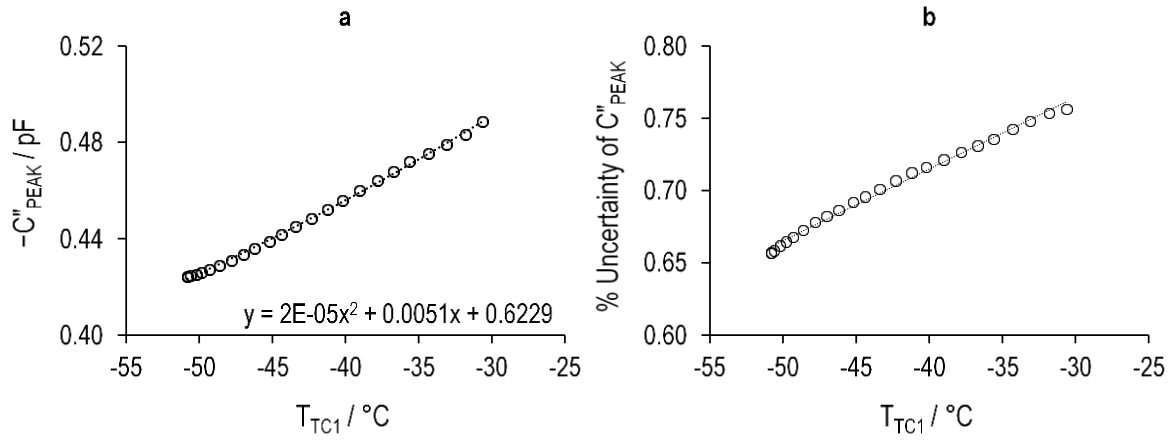

Figure 114 (a) Temperature coefficient of peak amplitude (C''_{PEAK}) during re-heating from −51 °C to −30 °C at 0.7 °C·min^{-1}. (b) The first derivative of the temperature coefficient of C''_{PEAK}, divided by the value of C''_{PEAK} at the same temperature (expressed as a percentage) is referred to as the percentage uncertainty, which on average is ~ 0.70% per °C for this particular experiment.

If the temperature dependency of C''_{PEAK} remains uncorrected, there is significant potential of introducing errors into the estimates of sublimation rate from using uncompensated values alone.

A method of compensating C''_{PEAK} for temperature was developed and reported by Smith et al. (2018). It is based on a compensation factor (ϕ) that normalises all values of C''_{PEAK} to that which would be observed if primary drying proceeded at the initial temperature (T_{ref}) (Equation 76).

$$\phi = \frac{C''_{PEAK}(T)}{C''_{PEAK}(T_{ref})} \qquad \text{Equation 76}$$

Here, $C''_{PEAK}(T)$ and $C''_{PEAK}(T_{ref})$ are the amplitudes of the relaxation process at a temperature (T) and the initial reference temperature (T_{ref}). The latter is taken as the product temperature at the beginning of primary drying, at the point when the vacuum was applied. In this work, the reference temperature (T_{ref}) was −44 °C.

The temperature dependency of C''_{PEAK} during the re-heating ramp is modelled satisfactorily by a 2nd order polynomial; therefore, the temperature compensation factor (ϕ) (Equation 76) could be expressed in terms of the polynomial coefficients, as follows:

$$\phi = \frac{aT^2 + bT + c}{aT_{ref}{}^2 + bT_{ref} + c} \qquad \text{Equation 77}$$

Values of peak amplitude at any time during primary drying ($C''_{PEAK}(t)$) were then adjusted to the C''_{PEAK} values which would be predicted if the drying were to continue at the reference temperature, i.e. the temperature at the beginning of primary drying, by dividing by ϕ to give a temperature-compensated peak amplitude ($\hat{C}''_{PEAK}$) according to Equation 78.

$$\hat{C}''_{PEAK} = \frac{C''_{PEAK}(t)}{\phi} \qquad \text{Equation 78}$$

Time profiles of the compensated and uncompensated values of C''_{PEAK} are shown in Figure 115 (solid and dotted lines respectively).

Figure 115a shows the first 9 h of primary drying over which the TVIS parameter $T_{F_{PEAK}}$ appears to provide a reliable assessment of the predicted product temperature. Figure 115b focuses on the first 3 h of that 9 h period. The purpose of this enlarged view is to demonstrate the impact of temperature on the rate of change of C''_{PEAK} with time (dC''_{PEAK}/dt); and therefore, the potential for error in determining the sublimation rate. The first point here is that, up to the point at which the shelf temperature is increased (i.e. 1.1 h into primary drying), both C''_{PEAK} and $\hat{C}''_{PEAK}$ fall at an approximately linear rate, although the C''_{PEAK} profile is not as regular as the $\hat{C}''_{PEAK}$ one. Second: the average gradient of C''_{PEAK} is ~20% greater than that of $\hat{C}''_{PEAK}$ (compare arrows A and B in Figure 115b); so the same percentage error would be expected if sublimation rate were calculated from the uncorrected values of C''_{PEAK}.

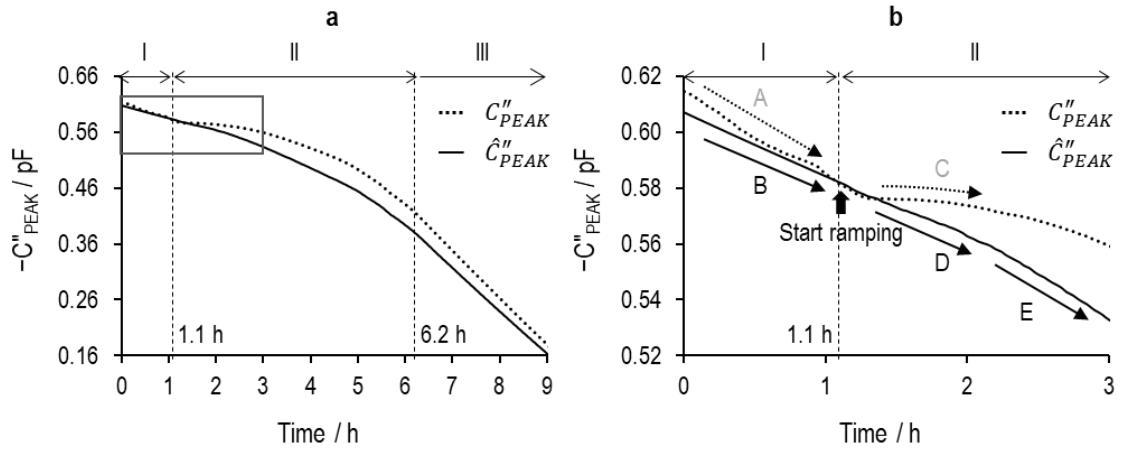

Figure 115 Primary drying profiles of peak magnitude before and after temperature correction (C''_{PEAK} and $\hat{C}''_{PEAK}$, respectively). (a) Profile for the first 9 h of primary drying; (b) Close-up of the first 3 h. The various steps of primary drying are: Period I Holding at −40 °C; Period II Ramping temperature from −40 °C to −10 °C at 0.1 °C·min^{-1}; Period III Holding at −10 °C. The standardisation temperature (T_{ref}) used to compensate the temperature dependency of C''_{PEAK} is −44 °C. Five arrows marked A, B, C, D and E run parallel to the data to demonstrate the relative differences in gradient between the uncompensated and compensated values of C''_{PEAK} both before the onset of the temperature ramp (A and B, respectively) and after the temperature ramp (C, D and E, respectively). Before ramping, the surrogate sublimation rate (from dC''_{PEAK}/dt) is higher for the uncompensated values before the temperature ramp, but reduces almost to zero immediately after it. The implication might be that the sublimation rate is slowing; whereas the compensated values continue at the same apparent sublimation rate as before the ramp. Then as the temperature continues to ramp, the apparent drying rate for the compensated values begins to increase (arrow E), as we might expect.

An average predicted product temperature ($T_{F_{PEAK}}$) of −44.3 ± 0.3 °C was recorded during the initial 0 - 1.1 h period of primary drying (Period I of Figure 115). From the decrease in $\hat{C}''_{PEAK}$ during the holding period (Period I of Figure 115)one must conclude that sublimative drying has been initiated, presumably because as a result of a combination of three factors: (i) the partial vapour pressure of water is much lower than the total pressure, and the ratio between the two pressures will be maintained during depressurization. For instance, at 20 °C and atmospheric pressure, the partial vapour pressure of water in air would be 23.3 mbar, then on depressurization reduce to 291 µbar. Then the partial water vapour would reduce proportionally to 6.7 µbar, which would be sufficient to promote sublimation (i.e. −44.3 °C has ice vapour pressure of 81 µbar); (ii) a gas diffusion gradient being created between the higher partial

pressure of water vapour at the ice surface to the lower partial pressure of water vapour at the condenser; and (iii) the vacuum pump of the freeze dryer could facilitate vapour movement by removing water vapour out of the chamber thereby further promoting drying.

The third and final point to note regarding Figure 115b is that beyond 1.1 h, when the shelf temperature and product temperature begins to ramp, there is a levelling off in the rate of change of C''_{PEAK} - whereas the temperature-compensated $\hat{C}''_{PEAK}$ shows more expected behaviour (arrow E in Figure 115b), i.e. an increase in the rate of change of $\hat{C}''_{PEAK}$. This is because the sublimation rate will have increased as a consequence of higher product temperature.

Conversion of $\hat{C}''_{PEAK}$ to ice mass

Once C''_{PEAK} values have been compensated for temperature dependence, it is possible to convert the compensated $\hat{C}''_{PEAK}$ values to ice mass by equating the initial $\hat{C}''_{PEAK}$ value to the initial ice mass in the sensing region of the electrode, at the point when the vacuum was applied.

The initial ice content in the frozen mass within the sensing region of the electrode is determined in four steps. The first of these is to estimate the quantity of solute and water in the total fill weight of solution (Equation 79 and Equation 80, respectively).

$$Solute\ (g) = \frac{Conc.solution\ (\%w/v) \times Filling\ weight.}{100\ \times Density\ of\ solution} \qquad \text{Equation 79}$$

$$Total\ water\ (g) = Filling\ weight\ - Solute\ (g) \qquad \text{Equation 80}$$

From the literature (McDonald & Turcotte, 1948), the density of the 5% w/w lactose solution was taken to be 1.0173 g·mL^{-1} at 20 °C - so the amounts of solute and water were estimated as 0.15 and 2.95 g respectively, for a sample weight of 3.1 g.

The second step is calculating the total weight of unfrozen water in the vial. By using the concentration of the amorphous solute in the unfrozen fraction (known as maximum freeze concentration, C'_g), the mass of unfreezable water can be estimated as follows:

$$Unfrozen\ water\ (g) = \frac{100 \times Solute\ (g)}{C_g'} \qquad \text{Equation 81}$$

In the case of disaccharides, C_g' is approximately equal to 80% w/w (Liesebach, Rades & Lim, 2003; Xu et al., 2017), so the unfrozen water was estimated at 0.19 g.

The third step is to estimate how much total water would convert to ice by subtracting unfreezable water (Equation 81) from the total amount of water (Equation 80), based on Equation 82.

$$m_t\ (g) = Total\ water\ (g) - Unfrozen\ water\ (g) \qquad \text{Equation 82}$$

It follows that for a fill weight of 3.1 g, the amount of ice that can be sublimed during primary drying (m_t) is 2.76 g.

The fourth step is to calculate the portion of the total amount of ice (2.76 g) that occupies the sensing region of the electrode (m_{RE}), and therefore contributes to the magnitude of $\hat{C}''_{PEAK}$. Given that 3.1 g of 5% w/v lactose solution corresponds to the total ice layer height (h_t) of 9 mm including the ice layer height within the electrode region (h_{RE}), the estimated ice mass bounded by the electrode's height of 7 mm (Ø = 0.7) would be 2.76×(7 mm/9 mm)=2.15 g. Figure 116 shows ice mass distribution between the sensing region (m_{RE}) and dead zone below the electrodes (m_{BE}), i.e. 2.15 g and 0.61 g respectively. To equate $\hat{C}''_{PEAK}$ to ice mass, we took the assumption that $\hat{C}''_{PEAK}$ is directly proportional to the amount of ice over a range of fill factors from 0 to 1; and any ice below the bottom of the electrode has a negligible contribution to $\hat{C}''_{PEAK}$.

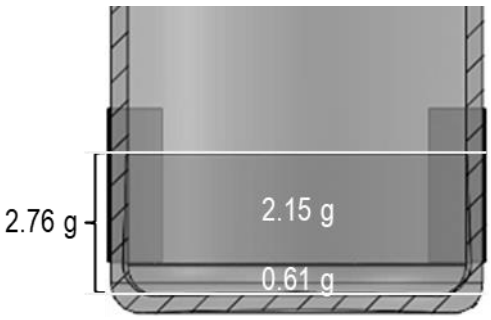

Figure 116 Illustration of ice mass in different regions at the start of primary drying. An approximate 2.15 g of the initial ice (2.76 g) occupies the electrode region.

Once the initial ice content in the sensing region of the electrodes has been determined, residual ice mass within the electrode sensing region (m_{RE}), at any time point (t) during sublimation, can be calculated using TVIS derived parameter $\hat{C}''_{PEAK}$. Thus the estimated values of $m_{RE}(t)$ can be defined as $m_{\hat{C}''_{PEAK}}(t)$ (Equation 83).

$$m_{\hat{C}''_{PEAK}}(t) = m_{RE}(0) \times \frac{\hat{C}''_{PEAK}(t)}{\hat{C}''_{PEAK}(0)} \qquad \text{Equation 83}$$

where $m_{RE}(0)$ and $\hat{C}''_{PEAK}(0)$ are the ice mass within the electrode region (2.15 g) and the compensated C''_{PEAK} (0.615 pF) at the time when the vacuum is applied (0 h of primary drying), respectively. $\hat{C}''_{PEAK}(t)$ is the compensated value of C''_{PEAK} at any time during primary drying.

Finally, the total ice mass remaining within the vial during the sublimation process is calculated by adding the ice mass in the dead zone below the electrode to TVIS estimated ice mass (Equation 84).

$$m_t(t) = m_{BE} + m_{\hat{C}''_{PEAK}}(t) \qquad \text{Equation 84}$$

Here, the amount of ice below the electrode is 0.61 g.

9.3.6. Primary drying rate determination

Any change in ice mass due to sublimation can then be converted directly into the sublimation rate ($dm_{\hat{C}''_{PEAK}}/dt$) by using the gradient of the ice mass in the time profile (Equation 85). Both

the residual ice mass (calculation from Equation 84) and the sublimation rate (calculation from Equation 85) are shown in Figure 117.

$$\frac{dm_{\hat{C}''_{PEAK}}}{dt} = -\frac{m_t\ (t_n) - m_t\ (t_{n+1})}{t_n - t_{n+1}} \qquad \text{Equation 85}$$

where t_n and t_{n+1} are consecutive measurement time for the n^{th} and $(n+1)^{th}$ data points.

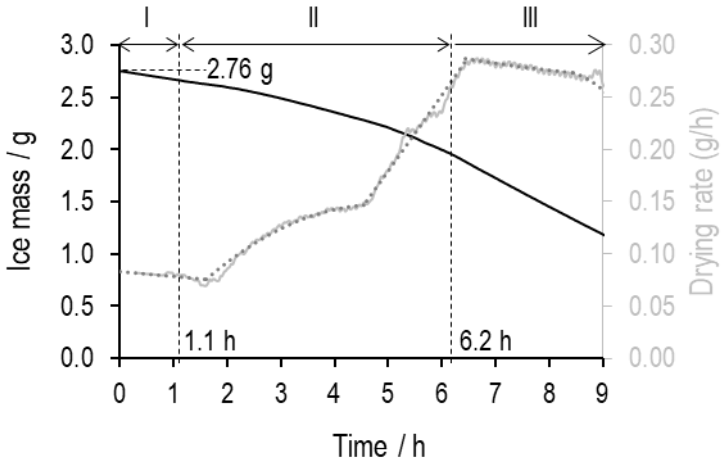

Figure 117 Ice mass contained in the vial (black solid line) and sublimation rate ($dm_{\hat{C}''_{PEAK}}/dt$) (grey solid line) over 9 h of primary drying process, estimated from the standardised C''_{PEAK} ($\hat{C}''_{PEAK}$). The different stages of primary drying are presented as periods I, II and III for the hold period at −40 °C, the re-heating stage from −40 °C to −10 °C, and the hold period at −10 °C, respectively.

Application of the linearity principle between $\hat{C}''_{PEAK}$ and ice mass over the region of fill factors of 0 to 1 only holds true if the ice cylinder reduces in height without any appreciable changes in contact with inside walls of the vial, or any changes in the ice interface's shape. Given our earlier consideration of the uncertainties in the measurement of TVIS data (Section 9.3.5), our estimates for residual ice mass are restricted to the 9 h period from the beginning of primary drying, during which time we consider that loss of contact with the glass wall is negligible.

9.3.7. Estimation of the ice height and the dry layer thickness

A simplified approach to determine the ice layer height during primary drying is to make the assumption that ice interface is flat (in other words, without a cone shape at the ice's front). Like

the determination of ice mass, the ice layer height in the region bounded by the electrode at any time of drying period ($h_{RE}\ (t)$) could also be estimated from the compensated values for peak amplitude ($\hat{C}''_{PEAK}$) by multiplying this at any time ($\hat{C}''_{PEAK}\ (t)$) by the ratio of the initial ice layer height bounded in the electrode area ($h_{RE}\ (0)$) to the initial value of $\hat{C}''_{PEAK}$ at the start of primary drying ($\hat{C}''_{PEAK}\ (0)$) (Equation 86). As the estimated ice layer height within the electrode region is calculated from temperature-compensated peak amplitude, predicted values of $h_{RE}\ (t)$ during primary drying are approximately equal to $h_{\hat{C}''_{PEAK}}(t)$. In this work, the value of the initial ice layer height in the region bounded by the electrode ($h_{RE}\ (0)$) is 7 mm.

$$h_{\hat{C}''_{PEAK}}(t) = h_{RE}\ (0) \times \frac{\hat{C}''_{PEAK}\ (t)}{\hat{C}''_{PEAK}\ (0)} \qquad \text{Equation 86}$$

As drying proceeds, development of the dry layer is synchronised with the reduction in the ice layer height in the region bounded by the electrodes. Provided the dry layer does not shrink appreciably during primary drying, its thickness (l_d) may be derived from the reduction in the ice layer height within the electrode region, according to Equation 87.

$$l_d(t) = h_{RE}\ (0) - h_{\hat{C}''_{PEAK}}(t) \qquad \text{Equation 87}$$

The dry layer arising simultaneously over 9 h as the ice layer reduces in height is shown in Figure 118.

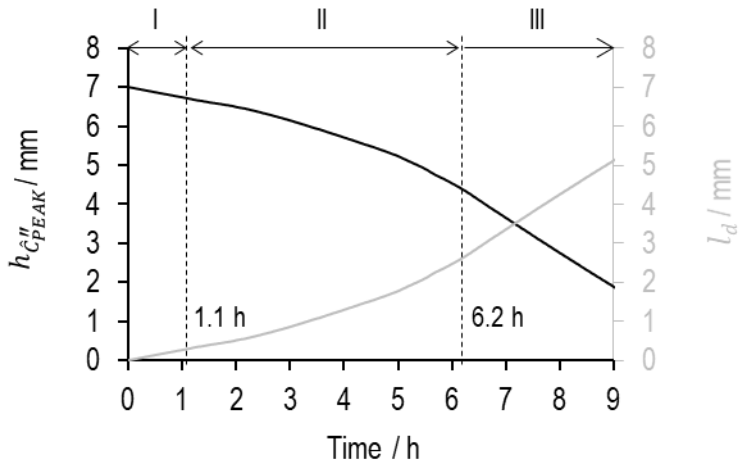

Figure 118 TVIS predicted ice height within the electrode boundary ($h_{\hat{C}''_{PEAK}}$, black solid line) and dry layer thickness (l_d, grey solid line) during the first 9 hours of primary drying of 5% w/v lactose.

9.3.8. Ice interface temperature prediction

As the sublimation rate and ice layer height in the region bounded by the electrodes is known, and we have estimates for the ice temperature at the TVIS node, the next stage is to estimate the temperature at the ice interface as a function of time during primary drying. For that, we could assume that $T_{F_{PEAK}}$ is about the same as the ice interface–temperature (T_i). However, given that (1) primary drying induces a temperature gradient in a vertical direction from the ice base (at a higher temperature) to the ice interface at (a lower temperature); and (2) $T_{F_{PEAK}}$ corresponds to the temperature at the TVIS node, it follows that $T_{F_{PEAK}}$ is likely to record a higher temperature than that prevailing at the ice interface. Two more accurate estimates for determining the ice interface temperature are therefore considered here (Figure 119).

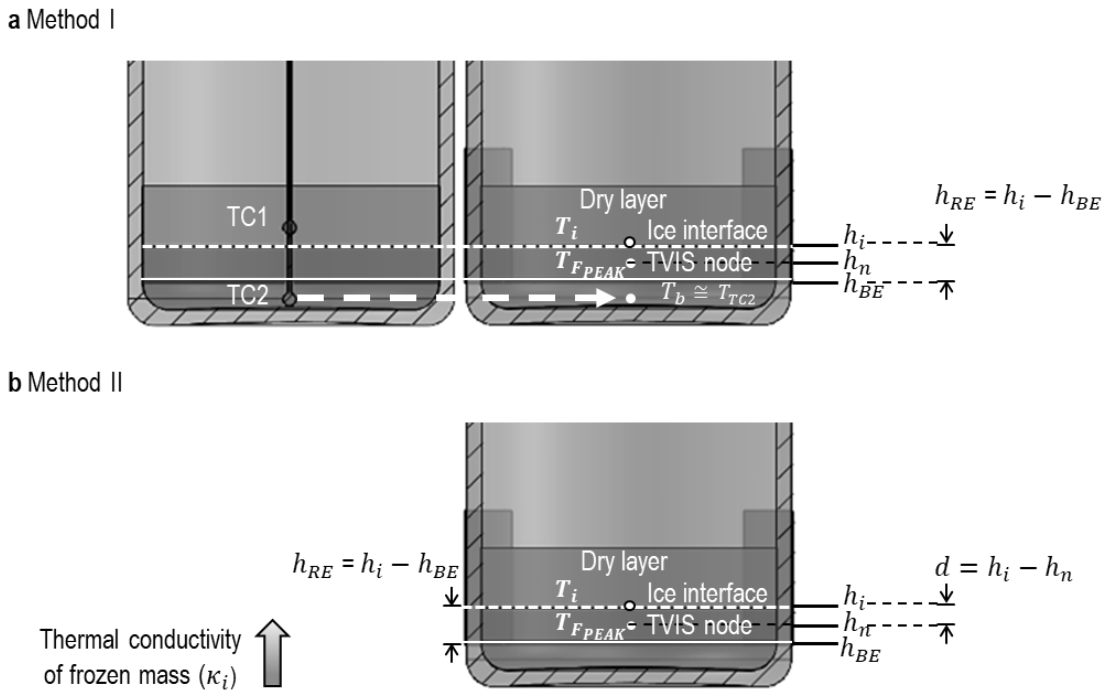

Figure 119 Illustration of the methodology predicting ice interface temperature a) Two-points extrapolation (method I), b) thermal heat transfer (method II). h_i is the position of the height of ice interface, equivalent to the sum of the ice layer height within the electrode region (h_{RE}) and the layer height below the electrode (h_{BE}); h_n is the height of the TVIS node.

Method I (Figure 119a) is based on extrapolating from two temperatures at known positions below the ice interface to the latter's position. Smith et al. (2018) use a dual electrode pair to provide an estimate of the two temperatures. In this work, with only one electrode pair, we used the product temperature at the vial base: directly inferred from the temperature measured by the thermocouple located bottom centre of the neighbouring vial (TC2) and TVIS-predicted temperature ($T_{F_{PEAK}}$) at the TVIS temperature node (h_n), positioned at half the height of the ice layer within the electrode region. The height of the TVIS node can be calculated by adding the ice layer height below the electrode region (h_{BE}) to half the ice layer height in the electrode region, ($h_{\hat{C}''_{PEAK}}(t)/2$) as below:

$$h_n(t) = h_{BE} + \frac{h_{\hat{C}''_{PEAK}}(t)}{2} \qquad \text{Equation 88}$$

The approximate height of the ice layer below the electrode (h_{BE}) is 2 mm.

Method II (Figure 119b) is based on the principles of heat transfer (dq/dt) through the frozen mass, which depends on the temperature gradient between the region of relatively high temperature at the base (T_b), and the relatively colder region at the ice interface (T_i), according to the following relationship:

$$\frac{dq}{dt} \propto (T_b - T_i) \qquad \text{Equation 89}$$

The constant of proportionality includes the cross-sectional area inside the vial (A_i), thickness of the frozen mass (d) and thermal conductivity of the frozen layer (κ_i), and leads to the expression:

$$\frac{dq}{dt} = \frac{\kappa_i A_i (T_b - T_i)}{d} \qquad \text{Equation 90}$$

Estimates for heat transfer (dq/dt) are determined from the TVIS predicted sublimation rate ($dm_{\hat{C}''_{PEAK}}/dt$), per Equation 91.

$$\frac{dq}{dt} = \frac{dm_{\hat{C}''_{PEAK}}}{dt} \cdot L_s \qquad \text{Equation 91}$$

where L_s is a latent heat of sublimation of ice (679.9 Cal·g^{-1} or 2846 .5 W·s·g^{-1} at −30 °C).

The calculation assumes that heat required to sublime the ice mass from the sublimation interface is derived solely from that supplied by the shelf and percolates in a vertical direction to the interface. This appears a reasonable assumption given that we are considering a core vial within the array of them on the freeze dryer shelf. In other words: heat flux from the upper shelf down through the stopper and the heat flux from neighbouring vials to each side of the TVIS vial are both minimal, in case of the core vials.

Returning to Equation 89, we can see that the heat transfer through the frozen mass (as a driving force for the sublimation) is a function of the temperature difference ($T_b - T_i$) between two planes. One position is at the ice interface (h_i), the sum of the ice layer height bounded by electrodes (h_{RE}) and the additional ice layer height below the electrode (h_{BE}) (Equation 92). The

other, lower position is at the base of the ice layer at a point where the thermocouple tip is positioned. However, with the TVIS application, this lower position is located at the TVIS sensing node (h_n); so the temperature difference is given by $T_{F_{PEAK}} - T_i$ (instead of $T_b - T_i$), whereas the distance (d) is that between the ice interface and the sensing node ($h_i - h_n$). By combining Equation 90 and Equation 91, and replacing $T_b - T_i$ and d with the equivalent TVIS parameters, we obtain:

$$h_i(t) = h_{BE} + h_{\hat{C}''_{PEAK}}(t) \quad \text{Equation 92}$$

$$\frac{dm_{\hat{C}''_{PEAK}}}{dt} \cdot L_s = \frac{\kappa_i A_i \left(T_{F_{PEAK}} - T_i\right)}{h_i - h_n} \quad \text{Equation 93}$$

Equation 93 is then re-arranged to provide an expression for the ice interface temperature:

$$T_i = T_{F_{PEAK}} - \frac{\frac{dm_{\hat{C}''_{PEAK}}}{dt} \cdot L_s \cdot (h_i - h_n)}{\kappa_i A_i} \quad \text{Equation 94}$$

$$T_i = T_{F_{PEAK}} - \frac{\frac{dm_{\hat{C}''_{PEAK}}}{dt} \cdot L_s \cdot \frac{h_{\hat{C}''_{PEAK}}(t)}{2}}{\kappa_i A_i} \quad \text{Equation 95}$$

Figure 120 shows predicted values for $T_{F_{PEAK}}$ along with results from the two methods of predicting the ice interface temperature (T_i). The inset plot shown in Figure 120 is a close-up of the steady state period, during which time the shelf temperature is kept constant. The difference between the predicted ice interface temperature and that at the TVIS node is around 0.5 °C; whereas the difference between the predicted T_i from the two methods is negligible.

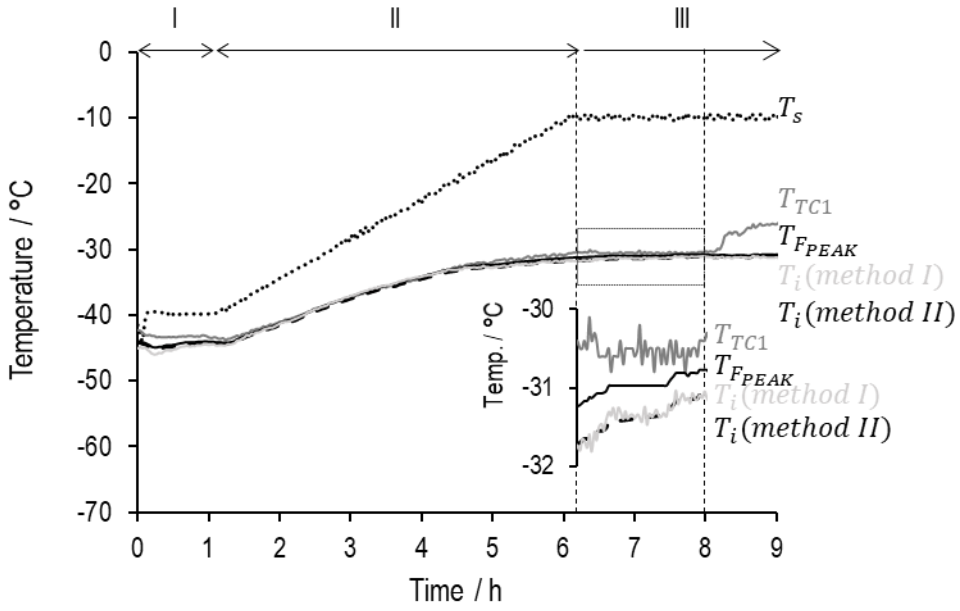

Figure 120 Comparison of ice interface temperature predicted by method I (extrapolating from two-points (Smith et al. 2018) and method II (heat transfer equation).

9.3.9. Dry product resistance determination

Dry layer resistance (R_p) of the product inside a single vial represents resistance to mass transport (i.e. water vapour flow) from the ice interface through the porous structure within the dry layer to the headspace inside the vial. It is the constant of proportionality between the driving force of vapour flow (i.e. the pressure differential across the dry layer, ΔP) and resultant vapour flow rate (i.e. the single vial sublimation rate, dm/dt). It can be presented as:

$$\Delta P = R_p \cdot \frac{dm}{dt} \qquad \text{Equation 96}$$

The significance of the single vial dry layer resistance is that for any pressure difference across the dry layer (ΔP), the higher the resistance to vapour flow (e.g. from smaller and/or more tortuous pores in the dry layer), the slower the rate of drying.

Re-arranging Equation 96 and re-writing the differential pressure across the dry layer, ΔP, as the difference between the ice interface pressure (P_i) and the headspace ice vapour pressure (P_v) gives:

$$R_p = \frac{(P_i - P_v)}{dm/dt} \qquad \text{Equation 97}$$

By considering the geometry of the dry layer in terms of its cross-sectional area and height, we can instead express dry layer resistance in terms of its resistivity (ρ_p).

$$R_p = \frac{l_d}{A_i}.\rho_p = \frac{(P_i - P_v)}{dm/dt} \qquad \text{Equation 98}$$

where l_d is dry layer thickness and A_i is the inner horizontal cross-sectional vial area (3.82 cm^2 in our case of the 10 mL tubular vial, VC010-20C supplied by Adelphi-HP).

Dry layer resistivity is an intrinsic property associated with the size, distribution, tortuosity and connectivity of the pores left behind once the ice has been sublimed and/or any cracks through or around the dry layer. In other words, anything that hinders or facilitates vapour flux from the ice interface to the headspace in the vial. Factors affecting the ρ_p range from formulation additives (Overcashier, Patapoff & Hsu, 1999; Johnson et al., 2010) to the freezing behaviour of the solution (Searles, Carpenter & Randolph, 2001; Konstantinidis et al., 2011; Rambhatla et al., 2004).

By re-arranging Equation 98 in terms of sublimation rate, it was demonstrated that the larger the internal cross-sectional area of the vial, the faster the product will dry (sublimation rate $\propto$ the area of the horizontal cross-section of the sample).

$$\frac{dm}{dt} = \frac{A_i}{l_d}.\frac{(P_i - P_v)}{\rho_p} \qquad \text{Equation 99}$$

It is common practice to normalise for any differences in cross-sectional areas, to make comparisons between products and processes: in particular, when batch-drying rates are determined using techniques such as MTM and TDLAS, where mass transport originates from many vials. This is achieved by multiplying Equation 98 by the area: whether the inner cross-section of a single vial (in the case of our TVIS measurements), or the collective inner cross-sectional area of the multiple vials in a batch (as with MTM or TDLAs measurements).

$$\hat{R}_\rho \;= l_d.\rho_p \;= A_i \frac{(P_i - P_v)}{dm/dt} \qquad \text{Equation 100}$$

where $\hat{R}_\rho$ is known as the area-normalised mass transfer resistance. It is clear from Equation 100 that $\hat{R}_\rho$ will increase as the dry layer increases in height (l_d), provided there are no structural changes in the dry layer that might affect its resistivity (ρ_p). This would hold true in cases where the ice crystal structure is uniform in the vertical direction of the vial, and where the dry layer remains stable; in other words, the dry layer is not subject to shrinkage, nor any internal collapse of the pore structure. This second condition is often (but not always) achievable if the product is dried well below its collapse temperature.

In practical terms, the application of Equation 100 to our TVIS measurements can be realised if we use $\hat{C}''_{PEAK}$ derived estimates for both the single vial sublimation rate ($dm_{\hat{C}''_{PEAK}}/dt$) (Section 9.3.6) and dry layer thickness (l_d) at time t (Section 9.3.7); and F_{PEAK} derived estimates for the ice interface temperature, T_i, (Section 9.3.8) and thus, partial pressure of ice at the sublimation front, P_i.

The only remaining parameter for consideration is partial pressure of ice inside the headspace of the vial (P_v). Often we can assume that P_v is the same as partial pressure of ice vapour inside the chamber, P_c, because there is negligible pressure drop across the vent in the stopper (known as stopper resistance, R_S). In those cases, P_c is measured by a calibrated Pirani gauge, or calculated from models used with the MTM and TDLAS techniques (Pikal, Roy & Shah, 1984; Kuu et al., 2011; Scutellà et al., 2018). However, the Virtis Advantage Plus used here does not have a water vapour pressure sensor, nor is it equipped with MTM or TDLAS, so we must predict P_c from partial vapour pressure at the sink. In other words, we need to use the temperature of the internal condenser (P_{cd}). Fortunately, the condenser is not separated from the chamber by a duct and is close to the product (installed inside the chamber under the bottom freeze drying shelf), so there will be no other pressure drop along the path between the vials and ice trap.

It follows that the two pressures required for the calculation of dry layer resistance are obtained from the respective temperatures at the ice interface and condenser. We have used the form of the Clausius–Clapeyron equation reported by Murphy and Koop (2005).

$$P_i = e^{(28.9074-\left(\frac{6143.7}{T_i}\right))} \quad \text{Equation 10}$$

$$P_{cd} = e^{(28.9074-\left(\frac{6143.7}{T_{cd}}\right))} \quad \text{Equation 101}$$

where P_i and P_{cd} are partial pressures of ice in Pascal (Pa) at the ice interface and condenser, respectively (1 Pa = 0.0075 Torr) and T_i and T_{cd} are corresponding temperatures in Kelvin (K).

By replacing the sublimation rate and P_v with the equivalent TVIS derived parameters and P_{cd} into Equation 100, the final expression for the area-normalised dry layer resistance is:

$$\hat{R}_\rho \ = l_d . \rho_p \ = A_i \frac{(P_i - P_{cd})}{dm_{\hat{C}''_{PEAK}}/dt} \quad \text{Equation 102}$$

In this experiment, $\hat{R}_\rho$ started at a value of ~ 124.4 kPa·m^2·s·kg^{-1} (2.59 Torr·cm^2·h·g^{-1}) rather than zero, presumably because of a skin on the dry product (Pikal, 1985). During the ramp phase (period II in Figure 121), shelf temperature was raised from −40 °C to −10 °C at 0.1 °C·min^{-1}. In this phase, the value of $\hat{R}p$ increased as the dry layer developed in thickness, up to 4.5 hours. At that point, the product temperature at ice interface (T_i) had reached ~−33.3 °C, and overall resistance started to fall from the maximum of 242.3 kPa·m^2·s·kg^{-1} (5.05 Torr·cm^2·h·g^{-1}) to a value of 162.7 kPa·m^2·s·kg^{-1} (3.39 Torr·cm^2·h·g^{-1}).

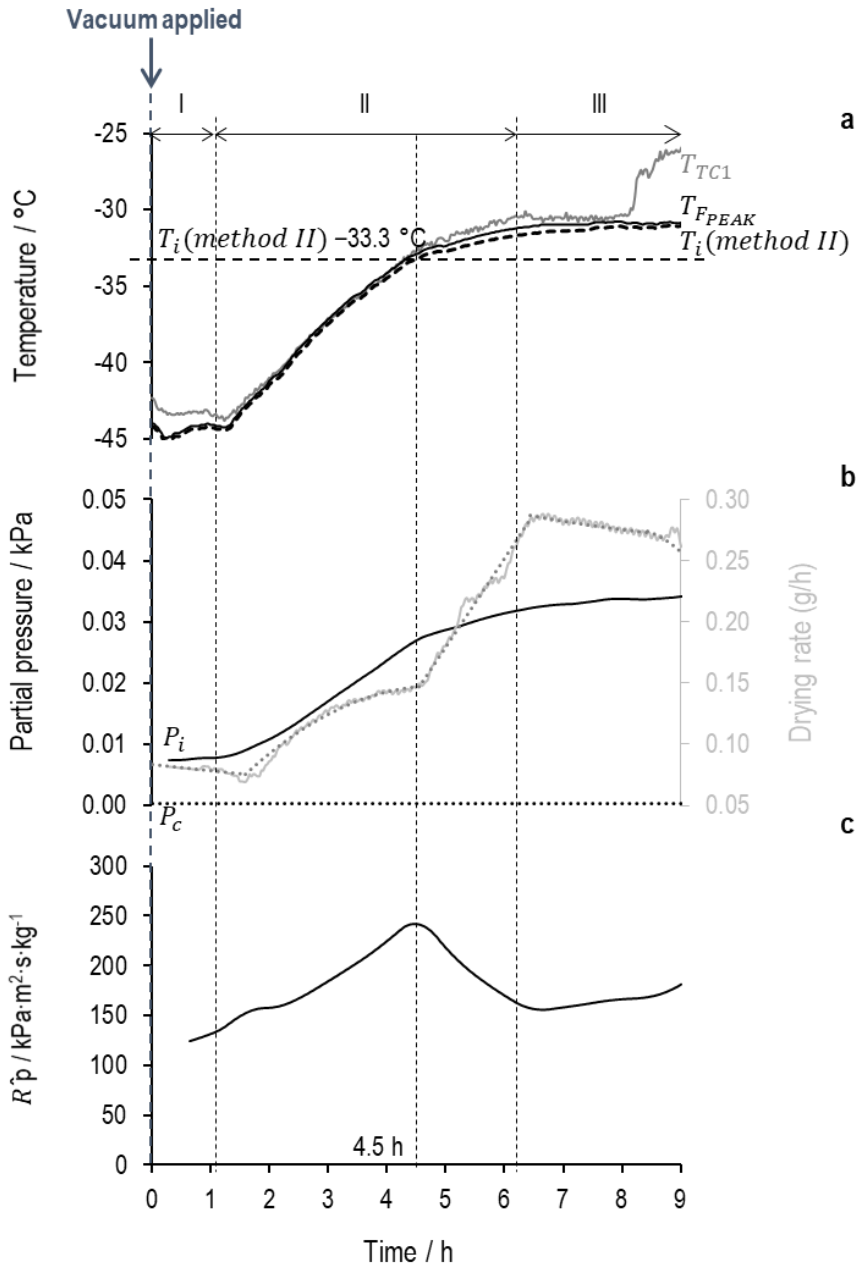

Figure 121 Results of 5% w/v lactose during the first 9 h of the primary drying stage. (a) The thermocouple temperature profile (T_{TC1}, grey solid line), TVIS predicted temperature ($T_{F_{PEAK}}$, black solid line) and calculated ice interface temperature from method II (T_i, black dashed line); (b) Ice partial pressure at the sublimation front (black solid line) and condenser (black dotted line), and sublimation rate (grey solid line) over the drying period; (c) product resistance ($\hat{R}_\rho$, black solid line). Periods I, II and III denote the first hold period of 1.1 h after applying the vacuum, the shelf temperature ramp from −40 °C to −10 °C over a period of 5.1 h, and the second hold period of primary drying, respectively. When the ice temperature at the sublimation front reaches −33.3 °C —horizontal black dashed line in (a), dry product resistance starts to decrease: which indicates the beginning of a microcollapse event.

This observation suggests that the freeze-dried cake is probably at the beginning of a collapse event; in which the sublimation rate increases as a consequence of the fusion of the pores in the dry layer, reducing its resistance. To quantify this suggestion, we plotted dry layer resistance as a function of dry layer height (Figure 122) and compared that to the SEM image taken from the cake at the end of the process (Figure 123). The larger pore size and possible cake shrinkage at the edges was seen in the dried layer at depths of greater than 1.51 mm.

Once the shelf temperature had stabilised at −10 °C (Period III in Figure 121), the product temperature predicted from TVIS parameters ($T_{F_{PEAK}}$) was almost constant at −30.9 ± 0.1 °C due to a nearly constant sublimation rate. During this hold period, $\hat{R}_\rho$ increased at a much slower rate than observed for region II.

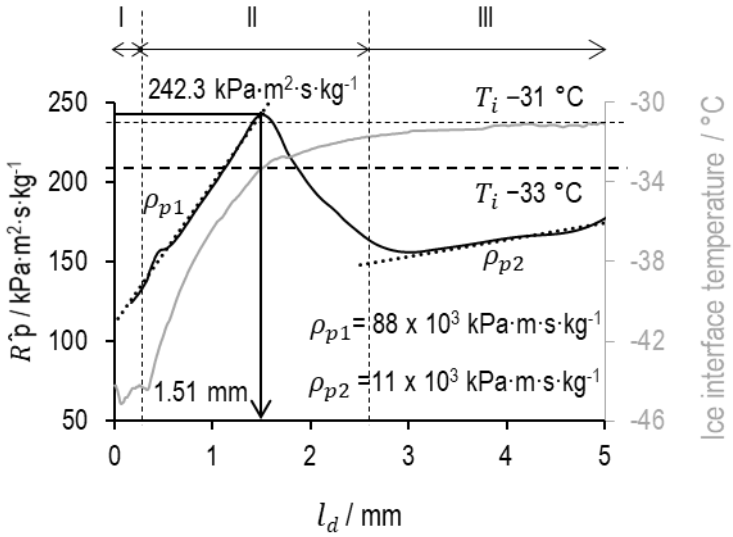

Figure 122 Dry product resistance ($\hat{R}_\rho$, black solid line) and TVIS-predicted ice interface temperature T_i (grey solid line) as a function of dry layer thickness for lactose, freeze-dried from a 5% w/v solution (over the first 8.87 h of primary drying). Period I, II and III are holding at −40 °C ($T_{F_{PEAK}}$ −44.3 ± 0.31 °C), re-heating from −40 °C to −10 °C (0.1 °C·min^{-1}), and holding at −10 °C, respectively. Product resistance starts to fall continuously after the ice interface temperature (T_i) reaches −33 °C, corresponding to the dry layer thickness of 1.51 mm.

As the dry layer increases above 3 mm (Figure 122), the magnitude of $\hat{R}_\rho$ is incomparable to that observed prior to the collapse event. However, the gradient of dotted lines ρ_{p1} and ρ_{p2} illustrate

the significant difference between dry layer resistivity of the non-collapsed and micro-collapsed product, 88 and 11 MPa·m·s·kg^{-1} respectively.

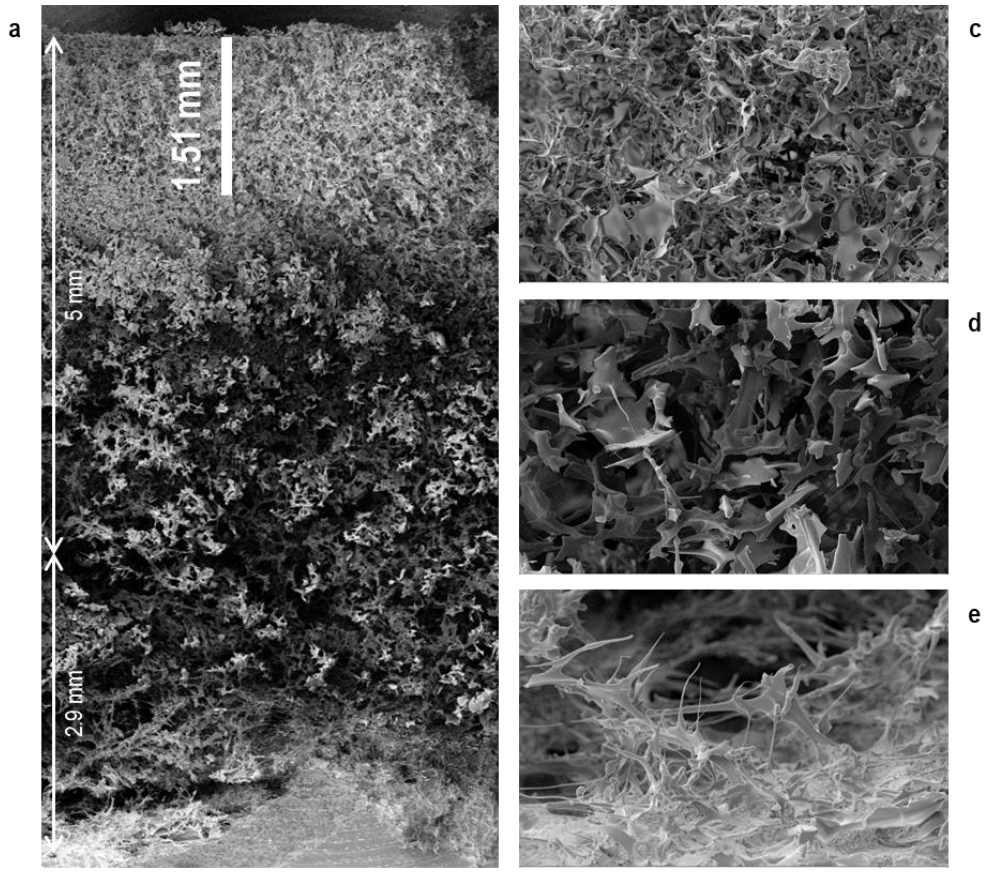

Figure 123 Scanning electron photomicrographs of a freeze-dried cake of 5% w/v lactose at the end of the cycle. (a) An overview of a vertical cross section of freeze-dried cake at a magnification of 25x; (b-d) Morphology of the dried layer at a magnification of 500x (b) top, (c) middle and (d) bottom.

9.3.10.Impact of collapse on sublimation rate

Some additional observations are now made regarding the impact of the collapse event. After 4.5 h of primary drying where the ice interface temperature was just below −33 °C, a significant increase in sublimation rate was observed (from 0.08 to 0.28 g·h^{-1}) as the ice interface temperature was increased to −30 °C and dry product resistance ($\hat{R}_\rho$) fell (4.5–6.2 h in Figure 121). Assuming that each drying rate applied was observed for the entire primary drying phase, predicted drying times at product temperatures ($T_{F_{PEAK}}$) of −44.3 ± 0.31 °C for the non-

collapsed product and −30.9 ± 0.11 °C for the micro-collapsed product would be 34 and 10 h: almost a 3.5-fold decrease (associated with the higher temperature and lower dry layer resistance). The partially collapsed status of the freeze-dried cake could not be discerned simply from its visual appearance; but only confirmed by SEM images recorded at the end of the process. Our inference is that TVIS measurements could be used as an indirect assessment of the phenonemon of micro-collapse.

9.4.Summary

This work introduces the methods for the analysis of the imaginary capacitance spectrum of a TVIS vial filled with a 5% lactose solution, to monitor the primary drying stage of the freeze-drying cycle. The two primary parameters extracted from the TVIS spectrum were the peak amplitude and frequency (F_{PEAK} and C''_{PEAK}) associated with the dielectric relaxation of ice. Both were used to develop a method to predict ice interface temperature and sublimation rate. From those process parameters, dried product resistance was then calculated. A dramatic increase in sublimation rate associated with a reduction of dried product resistance was observed at the point where ice interface temperature reaches the onset of glass transition temperature (as determined by DSC) and micro-collapse occurred (evidenced by SEM images at the end of the cycle). This suggests a prospective application of impedance measurements in driving process efficiencies by operating the dryer at the highest achievable temperature (i.e. the collapse temperature) while avoiding macro-collapse.

10. An application of dual-electrode TVIS for primary drying process monitoring

10.1. Objective

The objective of this study is to develop the application of TVIS to predict two ice interface temperatures (at the sublimation front and the bottom of a conventional glass tubing vial), while simultaneously quantifying the primary drying rate: delivering all parameters required for the estimation of the vial heat transfer coefficient. To achieve this objective, a standard 10 mL type I tubular glass vial was modified by attaching two electrode pairs on the external surface of a glass vial, referred to as the “dual electrode” system.

10.2. Materials and Methods

10.2.1.Measurement principle

In this study, a dual electrode system, comprising two pairs of copper electrodes attached to the outer surface of an Adelphi VC010-20C Type I glass tubing vial, with one large electrode pair enveloping the ice interface region and one smaller electrode pair closer to the base of the vial, was introduced. The bottom electrode (BE) has a height-by-width dimension of 5 × 19 mm and is positioned 3 mm above the base of the vial; whereas the top electrode (TE) has a height-by-dimension of 15 × 19 mm and is positioned 3 mm from the top edge of the bottom electrode (and therefore, 11 mm from the vial base) (Figure 124).

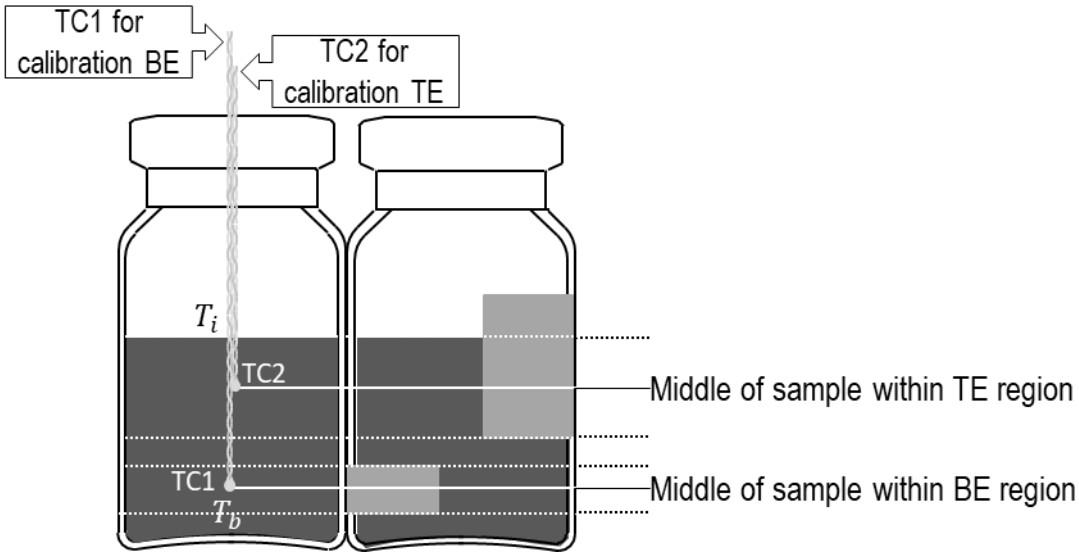

Figure 124 Method of calibrating temperature response of the TVIS system using a dual pair of electrodes. **Left**: Standard type I glass tubing vial (Adelphi VC010-20C of nominal volume 10 mL) with two type-T thermocouples placed at a height equivalent to the centre-points of the upper and lower electrodes; **Right**: a TVIS modified vial with two pairs of copper foil electrodes (only one electrode from each pair is shown here).

The TVIS measurement vial is connected via a junction box inside the freeze dryer and a bespoke pass-through (attached to the manifold) to a five-channel impedance analyser, developed by De Montfort University (Smith, Polygalov & Page, 2011). The impedance spectra from each electrode pair were measured across the frequency range of 10 Hz to 1MHz at an interval of every 2 min throughout the entire freeze-drying cycle. The time to acquire each individual spectrum was around 10 seconds. The peak frequency (F_{PEAK}) and peak amplitude (C''_{PEAK}) of the main process was determined by a simple peak finding routine, built in as a feature of our LyoView™ analytical software (Figure 125).

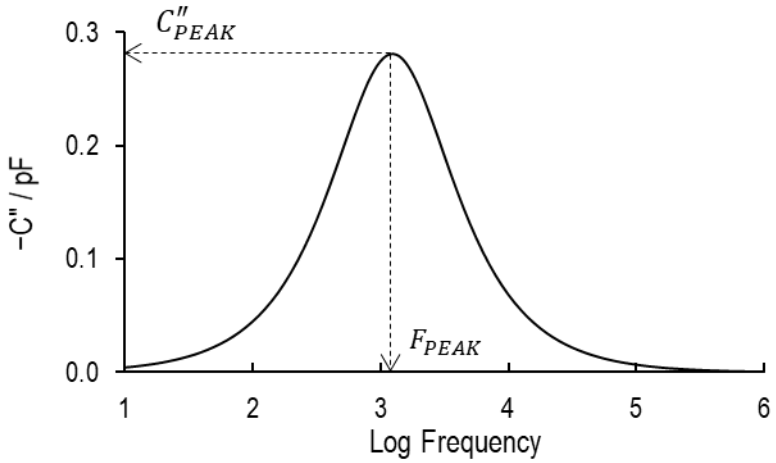

Figure 125 Example model spectrum to demonstrate determination of F_{PEAK} and C''_{PEAK} values.

We have shown in a previous article (Smith et al., 2017) that the parameter F_{PEAK} is sensitive to the average ice temperature in the region bounded by the electrodes; whereas the parameter, C''_{PEAK}, while it also has a smaller dependency on temperature, is highly sensitive to the height of the ice cylinder in the region bounded by the electrodes. We also recognise that the relationship between the magnitude of C''_{PEAK} and height of the ice layer is only linear if there is intimate contact between the ice and inside wall of the glass vial (i.e. no gaps appear during drying); and the ice dries as a cylinder without any change in the sublimation interface's shape. This might at first appear a disadvantage in terms of the technique's generalised ability to measure the sublimation rate throughout the primary drying stage.

However, in all methods for the determination of K_v, there is an expectation that the drying rate is determined from a limited period of the primary drying stage: either by gravimetric measurements of mass lost after a truncated period of drying or by some real time monitoring technique, such as TDLAS or MTM. This is to ensure that heat transfer mechanisms do not alter because of some changes in the shape of the sublimation front or the contact between the ice cylinder and vial wall. Here, we can demonstrate that it is possible to use the TVIS technique to define the period over which the ice layer maintains contact with the glass wall and derive a reliable estimate of K_v.

There are a number of stages to this new TVIS method. The **first stage** is to record F_{PEAK} values from both electrode pairs, during a slow temperature ramp of pre-frozen water, which spans the temperature range of interest for subsequent primary drying (in our case −40 to −15 °C). Given that F_{PEAK} is a function of the average ice temperature in the region bounded by a single electrode pair (Smith et al., 2017), it is possible to calibrate the two values of F_{PEAK} from each electrode pair against the two temperatures, centred at specific heights within the ice cylinder. To make the calibration, the nearest neighbour vial has two 30 AWG thermocouples positioned at heights corresponding to the centre-points of ice cylinders within each electrode pair in the TVIS vial (Figure 124).

The positioning of the thermocouples required careful manual manipulation by inserting them through a very small hole in the rubber stopper. A process of trial and error, with visual observations from multiple angles, was employed to qualify the central positioning of the thermocouple tip. The choice of the thicker 30 AWG thermocouple rather than those recommended by Nail (2017) (i.e. 36 AWG) provided some rigidity, which helped maintain the location of the probe once the positioning process was completed. Unfortunately, the insertion of a 'grounded' thermocouple within the TVIS vial results in a dramatic distortion of the spectrum to such an extent that it is rendered unusable. The calibration function, based on a second order polynomial, provides the basis for the prediction of product temperatures during the subsequent primary drying step. Predicted primary drying temperatures will be referred to as $T_{F_{PEAK}}$, given they are derived from the TVIS parameter, F_{PEAK} (see Section 10.3.1).

The **second stage** is to standardise values of C''_{PEAK} (recorded during the primary drying stage) to a reference temperature, to compensate for the small temperature dependency of this parameter (see Section 10.3.2). The standardised peak amplitude is provided by $\hat{C}''_{PEAK}$, i.e. with a circumflex over the letter C. In this experiment the temperature of −20 °C was chosen as the reference temperature.

The **third stage** is to calibrate values of C''_{PEAK} recorded at the reference temperature against known filled heights of ice occupying the internal volume of the vial bounded by the top

electrode pair; then use the calibration factor to convert the rate of change of the standardised peak amplitude ($\hat{C}''_{PEAK}$) to a drying rate (see Section 10.3.3).

The **fourth stage** is to use the methodology developed in Section 10.3.3 to determine the position of the ice interface, then extrapolate from predicted temperatures at the two known vertical positions (within the volumes bounded by the two pairs of electrodes) to the relative positions of the ice interface and ice base, to predict values for the temperatures at the sublimation front (T_i) and the base of the ice (T_b) (see Section 10.3.4).

10.2.2. Vial filling and loading the freeze dryer

8.12 g aliquots of 18 MΩ.cm water were transferred to 160 Adelphi VC010-20C type I glass tubing vials (one of which was modified for our dual electrode TVIS measurements: see Section 10.2.1). For the TVIS vial, this amount of water corresponds to a fill factor (Ø) of 0.7 for the top electrode pair (where Ø is defined as the relative height of the liquid bounded within the electrode region to the height of the top electrode). Each vial was plugged loosely with a 20 mm 4023/50 bromobutyl grey rubber stopper FDW20RTS (West Pharmaceutical Services Singapore Ltd, Singapore) and weighed to a precision of three decimal places, to determine the gross weight of each prior to commencing the freeze-drying cycle.

The vials were arranged (Figure 126) and then loaded into the drying chamber of a Virtis Advantage Plus bench-top freeze dryer. The TVIS vial was placed at the centre of the shelf, with one of the nearest neighbour vials having a pair of type T thermocouples inserted through the rubber stopper, and the sensing beads positioned at two specific heights (Figure 124).

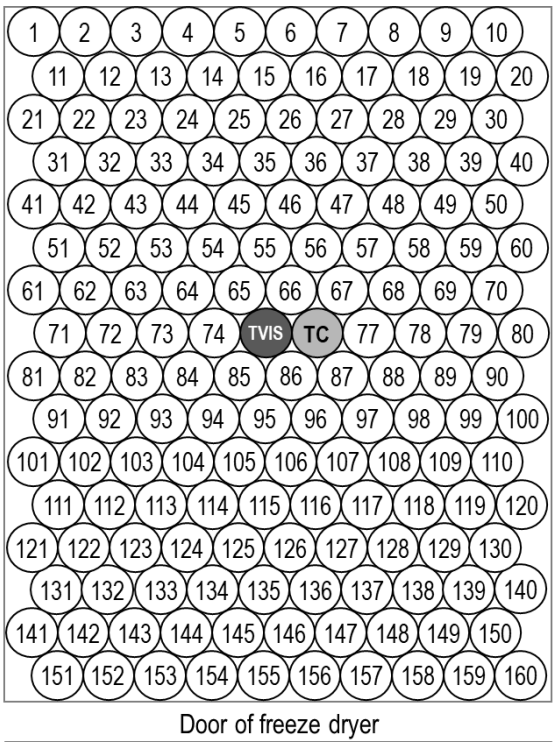

Figure 126 Arrangement of vials on the middle shelf of the Virtis Advantage Plus freeze dryer. Positions 75 and 76 are the TVIS modified vial and the thermocouple-containing vial.

10.2.3.Freeze-drying protocol

A freeze-drying protocol (Table 15) with a re-heating step (subsequent to the first freezing of ice) and an interrupted primary drying stage (quantifying the ice mass remaining in the vial) was designed with the purpose of validating the predictions of the ice interface.

Including the ramp in shelf temperature from −40 °C to 0 °C while maintaining chamber pressure at 350 µbar (~ 263 mtorr) will create an 'activation point', where the ice interface temperature approaches T_i = −30.8 °C; at which the ice interface's partial pressure exceeds the chamber pressure ($P_i \geq P_c$), causing the drying rate to increase dramatically. This may be determined from the point, during the temperature ramp, when the rate of change of C''_{PEAK} from the top electrode increases more significantly.

Table 15 Freeze drying protocol. In practice, the set pressure of 350 µbar (≈ 263 mtorr) provided an actual chamber pressure of 271 ± 7.7 mtorr (351.6 ± 10.1 µbar) during the primary drying process.

Step	Temperature (°C)	Time (min)	Cumulative Time (h)	Set pressure (µbar)
Equilibrium phase	+20	10	0.17	-
Freezing temperature ramp (0.5 °C /min)	−45	130	2.33	-
Freezing temperature hold	−45	180	5.33	-
Re-heating temperature ramp (0.5 °C /min)	−10	70	6.50	-
Re-heating temperature hold	−10	120	8.50	-
Re-cooling temperature ramp (0.5 °C /min)	−40	60	9.50	-
Re-cooling temperature hold	−40	120	11.50	-
Primary drying temperature hold	−40	30	12.00	350
Primary drying temperature ramp (0.5 °C /min)	0	80	13.33	350
Primary drying temperature hold	0	250	17.50	350

The other essential feature of the cycle was it being designed (following initial exploratory studies) to interrupt the primary drying process when only ~20% of the ice has been removed; in our case, when the ice cylinder height is reduced from 20.5 mm to 16.7 mm. This reduction can be expressed in terms of the fill factor for the top electrode receding from 0.7 to 0.45; we can expect that the C''_{PEAK} parameter will have a linear dependency on ice mass (see Section 10.3.3), provided the profile of the ice interface does not change. All vials were removed from the freeze dryer after the primary drying process was interrupted, then re-weighed. The mass of water loss during the freeze-drying run was calculated and an average drying rate determined from the difference in mass divided by time elapsed. This provides one opportunity to qualify use of the standardised peak amplitude ($\hat{C}''_{PEAK}$) when determining the mass of ice remaining within the vial.

10.3. Results and Discussion

10.3.1.Ice temperature calibration

Temperature calibration for each electrode pair is achieved by plotting the temperatures (T_{TC}) from the thermocouple-sensing probes in the nearest neighbour vial (those acquired during the temperature ramp at the slow rate of 0.5 °C·min^{-1} at heights equivalent to the centre-points within the two pairs of electrodes, against the $Log\ F_{PEAK}$ values for the corresponding timepoint when each temperature was recorded, then fitting a 2nd order polynomial function (Figure 127)). See Table 16 for the polynomial coefficients of the top and bottom electrodes.

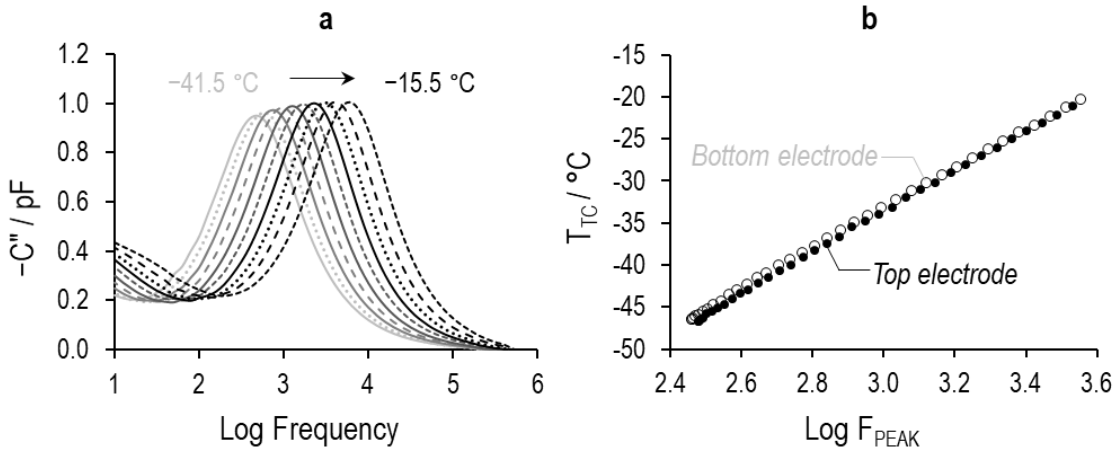

Figure 127 (a) Selection of imaginary capacitance spectra of ice from the top electrode pair of the TVIS vial, during the reheating ramp from −45 °C to −10 °C; (b) Calibration plots from the re-heating stage for the prediction of ice interface temperatures from estimates of F_{PEAK} measured during the subsequent primary drying stage.

Table 16 Calibration coefficients from the re-heating of ice: to be used for temperature prediction from measurements of F_{PEAK} during the primary drying stage.

Order of the fitting coefficient	2 (a)	1 (b)	0 (c)
Temperature coefficient-TE	-1.74	34.6	-122
Temperature coefficient-BE	-1.94	35.3	-122

10.3.2.Temperature compensate for C''_{PEAK}

The temperature dependency of C''_{PEAK} (observed during the re-heating part of the thermal cycling phase) inevitably manifests during the primary drying stage, which means that the time dependency of C''_{PEAK} during primary drying cannot be wholly attributed to loss of ice. Any change in temperature will also impact the value of C''_{PEAK}; to compensate, a standardisation factor (ϕ) is calculated, which can be used to normalise all values of C''_{PEAK} to that obtained if the temperature was fixed at some reference value. In our case, we have chosen a temperature of –20 °C as the reference value.

$$\phi = \frac{C''_{PEAK}(T)}{C''_{PEAK}(T_{ref})} \qquad \text{Equation 76}$$

Here, $C''_{PEAK}(T)$ and $C''_{PEAK}(T_{ref})$ are the peak amplitudes at temperatures T and reference temperature of −20 °C, during the re-heating ramp. Typically, the temperature dependency of C''_{PEAK}, determined during the re-heating stage, can be modelled with a 2nd order polynomial over a limited temperature range of interest (e.g. −45 to −15 °C): which means that Equation 76 may be re-written in terms of the polynomial coefficients determined in Section 10.3.1 (Equation 77).

$$\phi = \frac{aT^2 + bT + c}{aT_{ref}{}^2 + bT_{ref} + c} \qquad \text{Equation 77}$$

where T is the centre-point temperature from the top electrode ($T_{F_{PEAK}(TE)}$) at time t during the primary drying phase, and T_{ref} is the reference temperature of −20 °C. Values for the polynomial coefficients are given in Figure 128a

Values for $C''_{PEAK}(t)$ at any time (t) during the primary drying stage are then adjusted by dividing each by the calibration factor (ϕ) to give temperature-standardised values $\hat{C}''_{PEAK}(t)$. Note the use of the circumflex to indicate these are the standardised values at time *t* during the primary drying stage.

Figure 128a shows the temperature dependency of C''_{PEAK} as determined during the re-heating cycle, while Figure 128b shows the uncompensated C''_{PEAK} values and standardised C''_{PEAK} values (dashed and solid lines respectively) as a function of primary drying time. The standardised values ($\hat{C}''_{PEAK}$) are almost constant until approximately 1 h, whereas the uncompensated values (C''_{PEAK}) reflect the impact of the start of the heating ramp at 30 min.

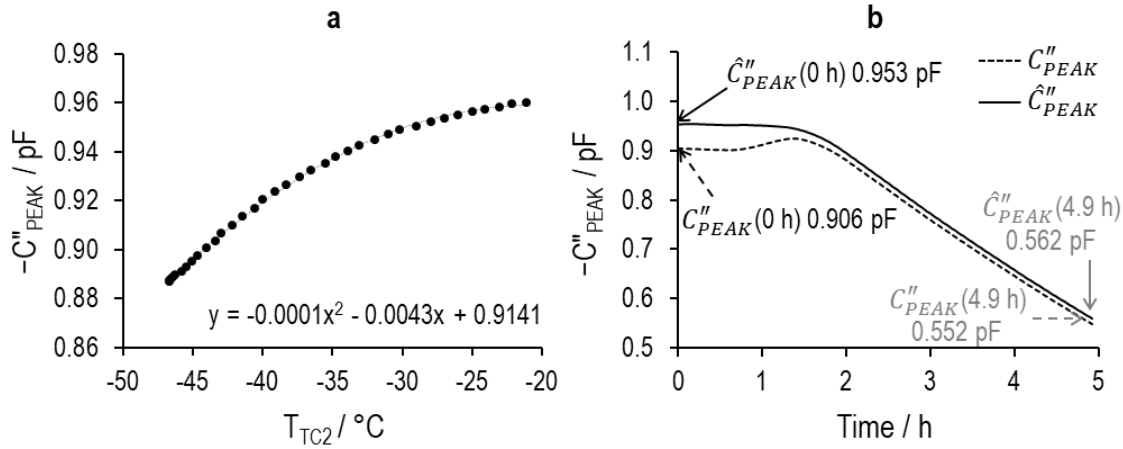

Figure 128 (a) Temperature dependency of C''_{PEAK} for the top electrode. The second-order polynomial expression for temperature coefficient of peak amplitude of top electrode is also given; (b) values for C''_{PEAK} during primary drying, before and after correction for temperature. The nomenclature of the corrected value of the peak height is $\hat{C}''_{PEAK}(t)$.

10.3.3.Primary drying rate determination

Once C''_{PEAK} has been corrected for temperature by standardising all values to a reference point, T_{ref} (in our case, T_{ref} = −20 °C), it is possible to derive a $\hat{C}''_{PEAK}(t)$-based surrogate for the sublimation rate from the difference between $\hat{C}''_{PEAK}(t)$ at two time points ($t2$ and $t1$), according to the following equation:

$$\frac{\Delta\hat{C}''_{PEAK}}{\Delta t} = \frac{\hat{C}''_{PEAK}(t2) - \hat{C}''_{PEAK}(t1)}{t2 - t1} \qquad \text{Equation 103}$$

After defining the surrogate primary drying rate (the rate of change of the standardised values of $\hat{C}''_{PEAK}(t)$ (Equation 103), it is possible to calculate an actual drying rate (in units of g/h, for example) by studying the equivalence between C''_{PEAK} and ice mass through the separate

experiment in which a range of fill heights of ice are measured at a fixed reference temperature (in our case, −20 °C).

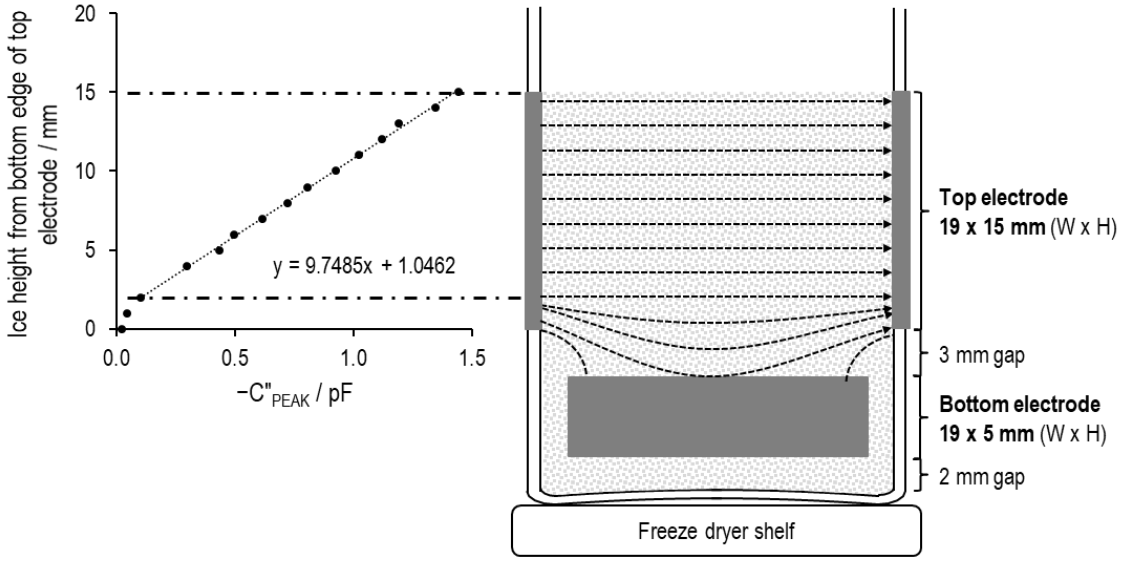

Figure 129 The dependency of C''_{PEAK} on the ice cylinder height in the region bounded by the top electrode at −20 °C. The gradient of the linear portion of the graph ($m_{h/C}$) at fill heights from the bottom edge of the top electrode greater than 2 mm is equal to 9.749 mm·pF^{-1} (0.975 cm·pF^{-1}), and provides the calibration factor to convert rates of change in C''_{PEAK} to values of the ice mass during primary drying.

The non-linear portion of the graph (Figure 129) between fill heights from zero (where the ice interface just reaches the bottom edge of the top electrode) to approximately 2 mm is the result of the non-linear field at the periphery of the lower edge of the top electrode. At fill heights greater than 2 mm, there is a linear relationship between C''_{PEAK} and fill height: so the gradient of the line ($m_{h/C}$) provides the calibration factor with which to convert the rate of change of $\hat{C}''_{PEAK}$ ($\Delta\hat{C}''_{PEAK}/\Delta t$) in the primary drying phase to that of ice cylinder height bounded within the electrode region ($\Delta h_{RE}/\Delta t$).

$$\frac{\Delta h_{RE}}{\Delta t} = m_{h/C} \cdot \frac{\Delta\hat{C}''_{PEAK}}{\Delta t} \qquad \text{Equation 104}$$

Assuming that the ice interface area remains unchanged during the truncated primary drying period, the change in ice cylinder height (h_{RE}) in the region bounded by the top electrode can

be equated to a change in mass (m_{RE}) by simply multiplying Equation 104 by the internal cross-sectional area of the vial (A_i) and density of ice (ρ_i) at the steady state temperature, when the drying rate is constant.

$$\frac{\Delta m_{RE}}{\Delta t} = \rho_i \cdot A_i \cdot \frac{\Delta h_{RE}}{\Delta t} = \rho_i \cdot A_i \cdot m_{h/C} \cdot \frac{\Delta \hat{C}''_{PEAK}}{\Delta t} \qquad \text{Equation 105}$$

It follows from Equation 105 that any change in $\hat{C}''_{PEAK}$ due to the receding ice layer can be converted directly to drying rate, provided the electrode pair is first calibrated with known heights of ice within the electrode space.

10.3.4. Prediction of ice interface and ice base temperatures

Once the calibration of $Log\ F_{PEAK}$ has been undertaken during the temperature ramp on ice (Section 10.3.1), calibration coefficients for the 2nd order polynomial fit of temperature against $Log\ F_{PEAK}$ (Table 16) can be used to predict primary drying temperatures at the centre-points of the ice cylinders in each region bounded by the top and bottom electrode, i.e. $T_{F_{PEAK}(TE)}$ and $T_{F_{PEAK}(BE)}$. However, to achieve the ice temperature at sublimation front, we first need to know the position (i.e. height) of the sublimation interface in relation to the three reference points, i.e. the two centre-points of the electrodes and interface between the bottom of the ice and base of the vial. The height of the sublimation interface can be determined from the linear relationship between $\hat{C}''_{PEAK}$ (i.e. the compensated value of C''_{PEAK} at the reference temperature of −20 °C, established in Section 10.3.3) and the height of the ice cylinder bounded by the top electrode (Equation 106), coupled to that of the bottom edge of the top electrode from the inside base of the vial (Figure 130).

$$Ice\ height = 9.7485 \times \hat{C}''_{PEAK} + 1.0462 \qquad \text{Equation 106}$$

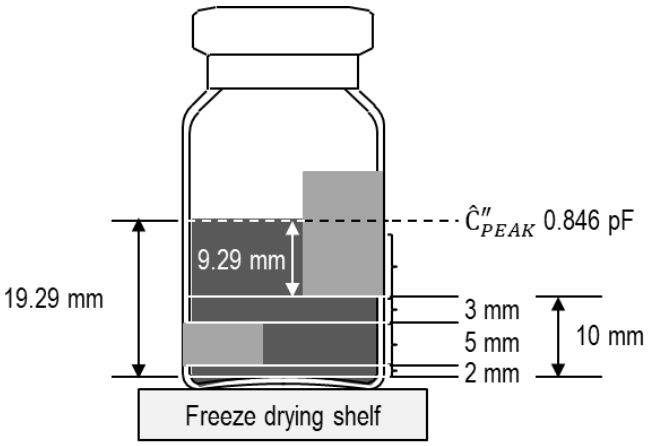

Figure 130 Illustration of the calculation of ice height at 2.4 h into the primary drying stage for an Adelphi VC010-20C type I glass tubing vial.

For example, at 2.4 h of primary drying, the temperature-compensated peak amplitude ($\hat{C}''_{PEAK}$ at T_{ref} of −20 °C) is 0.846 pF; therefore, based on Equation 106, the ice height within the top electrode region is 9.29 mm. Adding the distance between the inside base of the vial and bottom of the top electrode (10 mm) gives a sublimation front at 19.29 mm from the inside base.

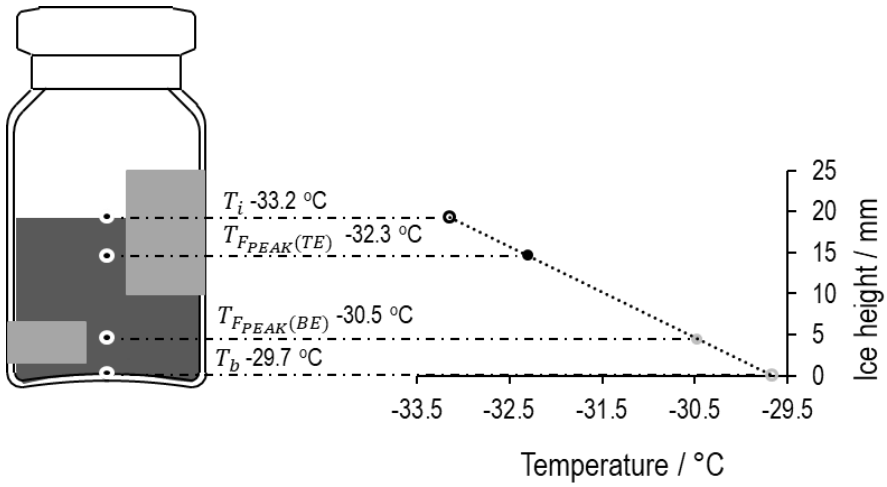

Figure 131 A 2 point-temperature determination for extrapolation to the ice interface temperatures of interest (i.e. T_i and T_b). The example shown here is from 2.4 h into primary drying (during the steady state period).

Figure 131 illustrates how this methodology is applied. In effect, we plot the two temperatures at the known positions of the centre-points of the upper and lower electrode pairs (filled circle in Figure 131), and assume that the temperature gradient up the ice layer is linear: so we can

then extrapolate to the base interface (at an ice height of zero) and sublimation front interface (at an ice height determined from Equation 106 plus the height of the lower edge of the top electrode from the inside base of the vial).

By applying this methodology across the primary stage (by using values of $\hat{C}''_{PEAK}$ corresponding to each time point), we can account for the changing position of the ice interface within the region bounded by the top electrode, and follow the ice interface temperatures at both the sublimation front and base of the ice.

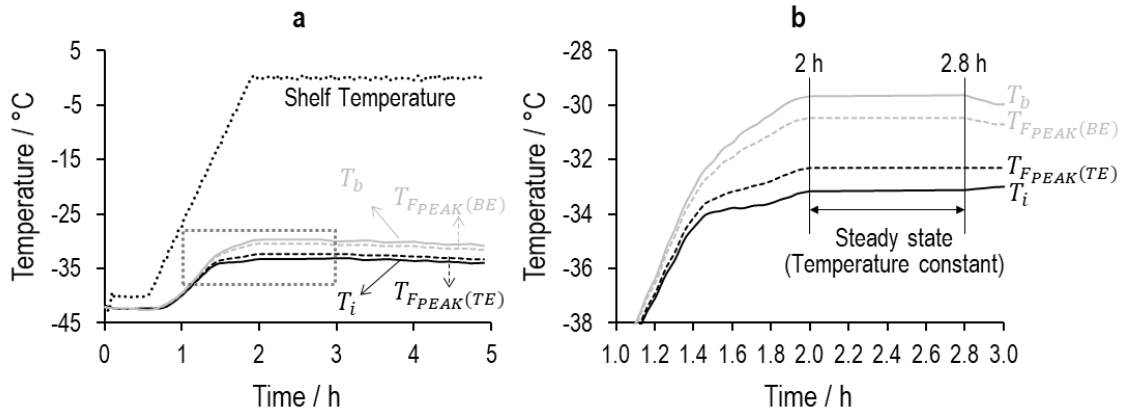

Figure 132 (a) Predicted ice interface temperatures at the sublimation front (T_i) and base of the ice (T_b), during the first 5 hours of primary drying (determined by extrapolating the TVIS predicted temperatures at the centre of the top and bottom electrode spaces); (b) A close-up view of the inset in (a).

Figure 132a shows $T_{F_{PEAK}}$ values for the top and bottom electrodes and predicted temperature values for the ice interfaces at the sublimation front and bottom of the vial (T_i and T_b, respectively). Figure 132b shows the enlarged scale to illustrate a period of steady state (between 2 and 2.8 h) when the temperature is constant (i.e. does not drift by more than 0.2 °C), so we would expect the drying rate to be constant also (see Figure 133d in Section 10.3.5).

10.3.5.Qualification of the ice interface temperature prediction

As predicted, including the ramp in shelf temperature from −40 °C to 0 °C while maintaining the chamber pressure at ~ 350 µbar (263 mtorr) causes the drying rate (evidenced by the rate of

change of $\hat{C}''_{PEAK}$ values associated with the top electrode) to increase gradually (Figure 133). In theory, a significant increase in the sublimative drying could be initiated when the ice interface temperature approaches the activation point where the partial pressure of ice will not be less than chamber pressure ($P_i \geq P_c$).

On closer inspection, the inflection in the trajectory of the predicted ice interface temperature (Figure 133c) as a result of the self-cooling mechanism that accompanies the activation of primary drying, suggests that the activation of primary drying coincides with an ice interface temperature of −34 °C. This activation process is confirmed by a more rapid rate of change in the value of $\hat{C}''_{PEAK}$, the parameter directly related to the amount of ice remaining within the region bounded by the top electrodes (Figure 133d). However, the ice vapour pressure at this point is 249.7 µbar which is lower than chamber pressure (Figure 133a). This circumstance might be caused by a surface phenomenon—"cooling effect", that can take place when the energy of the surface molecules is enough for molecules to migrate from the surface to the surrounding environment (e.g. chamber) and leads to lower surface temperatures. Therefore, the estimated value of ice pressure at the activation point is less than the expected from the programmed chamber pressure.

Moreover, the rate of change of $\hat{C}''_{PEAK}$ continues to increase as the temperature ramps further towards its set temperature of 0 °C; after which, the ice interface temperature remains stable at −33.1 °C. This value is close to temperature of −34 °C where the sublimative drying begins (Figure 133c). The heat supplied over this hold period is used for phase transition (i.e. sublimation) rather than increase in the product temperature. This result supported the assumption that the sublimation commences at this activation point.

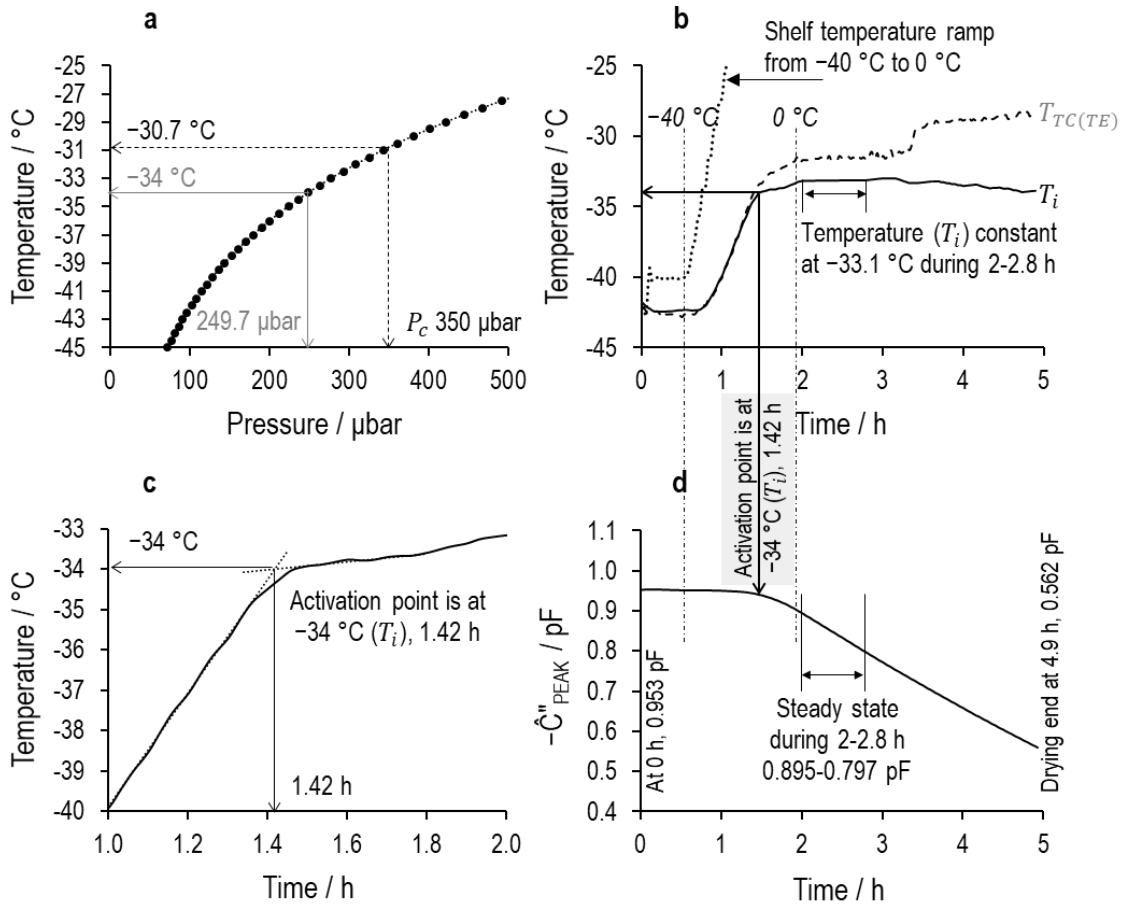

Figure 133 (a) Temperature dependency of partial pressure of ice. The grey arrow demonstrates the corresponding partial pressure of ice at the sublimation interface (~250 µbar) when drying is activated by the condition whereby the anticipated temperature of the ice interface reaches a value of −34 °C while the black arrow indicates the ice interface temperature corresponding to the set chamber pressure of 350 µbar; (b) Predicted ice interface temperature T_i (see Section 10.3.3) as a function of primary drying time. The constant temperature region between 2 and 2.8 h starts once the shelf has reached its set temperature of 0 °C. During this time, the predicted ice interface temperature is almost constant at -33.1 °C; (c) Predicted ice interface temperature T_i at the activation point when the drying rate starts to increase dramatically; (d) Temperature-standardised values of $\hat{C}''_{PEAK}$. The plot also highlights those values at the beginning and end of the steady state period in which the drying rate is constant.

10.3.6.Qualification of primary drying rate estimation

One relatively straightforward way to quantify whether TVIS may be used to determine drying rates is to compare the average drying rate estimated from the change in the temperature-standardised values of peak amplitude $\hat{C}''_{PEAK}$ with the average gravimetric drying rate determined from the loss of ice mass at the end of the interrupted primary drying period.

As before, the first step is to calculate an average surrogate drying rate ($\Delta\hat{C}''_{PEAK}/\Delta t$) by taking the difference between $\hat{C}''_{PEAK}$ recorded before the temperature is ramped (0.953 pF at 0 h of primary drying) and at the end of the interrupted primary drying cycle (0.562 pF at 4.9 h of primary drying), before dividing by the time duration of the cycle (4.9 h) to give a value for $\Delta\hat{C}''_{PEAK}/\Delta t$ of 0.0798 pF/h.

The drying rate in g/h can then be calculated by using Equation 105, reproduced here:

$$\frac{\Delta m_{RE}}{\Delta t} = \rho_i \cdot A_i \cdot m_{h/C} \cdot \frac{\Delta\hat{C}''_{PEAK}}{\Delta t} \qquad \text{Equation 105}$$

where ρ_i = 0.921 g·cm^{-3} (i.e. the density of ice at an average ice cylinder temperature of −34 °C) (Melinder, 2010), A_i = 3.80 cm^2 (calculated from the internal diameter of the Adelphi VC010-20C vial of 2.2 cm), and $m_{h/C}$ is 0.97485 cm·pF^{-1} (from Figure 129 in Section 10.3.3): giving a value for the TVIS predicted average drying rate of 0.272 g·h^{-1}. This compares favourably with an average gravimetric drying rate of 0.25 g·h^{-1} (from the loss of 1.22 g ice mass within 4.9 h). The 10% difference could be a result of the ice interface changing shape and surface area, with the height of the ice cylinder (i.e. that part in direct contact with the internal surface of the glass wall) reducing at a faster rate than the centre of the ice interface, resulting in an increase in the relative height of the ice mass that sits as an ice cone on top of the cylinder.

10.3.7. K_v determination

Understanding the heat transfer coefficient (K_v) between the heat source (i.e. the freeze-drying shelf) and vial contents is essential when seeking to predict the behaviour of large collections of vials within a batch scale freeze dryer. With this new TVIS method and its application in a small scale dryer, we have demonstrated how to use a dual electrode pair, mounted on a single vial, to estimate the temperature at the base (T_b) while capturing the sublimation rate ($\Delta m_{RE}/\Delta t$). These two parameters (T_b and $\Delta m_{RE}/\Delta t$) can then be combined to estimate K_v from Equation 107 (Pikal, Roy & Shah, 1984).

$$\frac{\Delta q}{\Delta t} = L_s \frac{\Delta m_{RE}}{\Delta t} = A_e K_v (T_s - T_b) \qquad \text{Equation 107}$$

where $\Delta q/\Delta t$ is the heating rate between the shelf and base of the ice inside the TVIS vial, $\Delta m_{RE}/\Delta t$ is the drying rate from the TVIS vial in g·h^{-1} (as determined from Equation 105, where the value for $\Delta \hat{C}''_{PEAK}/\Delta t$ is taken from the steady state period marked in Figure 133d), L_s is the latent heat of sublimation of ice—678.47 Cal·g^{-1} or 2838.72 W·s·g^{-1} at −33 °C (Hua, Liu & Zhang, 2010), A_e is the external cross-sectional area of the base of the TVIS vial (4.62 cm^2 for Adelphi VC010-20C vial), and T_s is the shelf temperature in °C. Parameters for the calculation heat transfer coefficient at 350 µbar are given in Table 17.

Table 17 Parameters for the calculation heat transfer coefficient at 350 µbar

Parameters	TVIS
TVIS drying rate during steady state, g·h^{-1}	*0.42*
Shelf temperature ($\boldsymbol{T_s}$), °C	*0.14*
Ice base temperature ($\boldsymbol{T_b}$) by TVIS, °C	*−29.7*
Heat transfer coefficient ($\boldsymbol{K_V}$) at 350 µbar	
In units of W·m^{-2}·K^{-1}	*24.0*
In units of Cal·s^{-1}·cm^{-2}·K^{-1}	*5.73 × 10^{-4}*

Steady state is defined first by the condition that the TVIS-determined product temperature, $T_{F_{PEAK}}$, for both electrodes is constant as shown in Figure 132b (in practical terms, this means that both temperatures do not drift by more than 0.2 °C); and second, by the requirement that the instantaneous rate of change in the TVIS derived sublimation rate does not change by more than ~5% from the start to the end of a steady state. In practice, the start of this coincides with that of the constant period of the shelf temperature.

The estimate we have obtained for the heat transfer coefficient at the set chamber pressure of 350 µbar (Table 17) is ~ 81%, 85% and 66% of those determined by Pikal (1985), Tchessalov (2017) and Brülls & Rasmuson (2002), respectively, for a comparable type of glass tubing vial (Figure 134). However, the dryers used in those studies were clearly different in scale to the Virtis Advantage Plus which we have used; and as dryer design and scale also impacts individual

K_v values (as does the method used for its determination). Similarly, the K_v value could also be influenced by the vial geometry (i.e. the contact area between the vial's bottom and the shelf). Therefore, it is hardly surprising that there is some disagreement between the four sets of values. That our K_v value compares favourably with that determined by Tchessalov (2017) is yet another qualification that the TVIS method developed here is a valid approach in determining a suite of critical process parameters (i.e. sublimation rate, T_i and T_b).

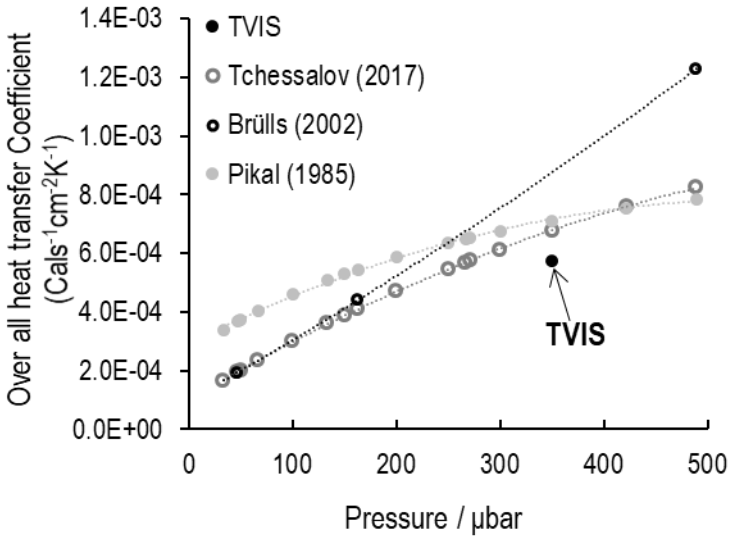

Figure 134 Comparison of the TVIS predicted estimate for the K_v value of a 10 mL glass tubing vial with previously published data for similar type of vials.

10.3.8.Limitations of TVIS system

For this application (i.e. the determination of the heat transfer coefficient), it is recognised that with the current design of the dual electrode measurement system, it is not possible to track the entire primary drying phase. Instead, we are limited to the drying conditions for the first 40% loss of the frozen mass. This percentage is a theoretical limit defined by the proportion of the total mass of ice in the vial within the linear response region of the ice, bounded by the upper electrode. Given that the linear response region is associated with fill factors between 0.13 to 0.7, or fill heights in the upper electrode region of 2 to 10.5 mm, and the lower edge of the top electrode is positioned 10 mm above the internal base of the vial, this linear response region

represents a range of ice fill heights from 12 to 20.5, measured from the internal base of the vial (i.e. a 40% change in fill height and hence, fill volume or mass).

However, the opportunity to measure as much as 40% of the ice mass lost during the sublimation process is consistent with current industrial practice for a gravimetric approach to drying rate determination: which recommends that drying is interrupted after ~ 20-25% of the ice mass is removed (Pikal, Roy & Shah, 1984; Hibler, Wagner & Gieseler, 2012; Scutella et al., 2017). The primary reason for this limit is that the shape of the ice interface and contact of the ice with the walls of the vial are highly unlikely to have changed over this period. In turn, contributions from the various heat transfer mechanisms will not have done so either, meaning drying will have occurred at a constant rate.

One limitation of TVIS technology is that the parameter $\hat{C}''_{PEAK}$ will not directly detect any change in the shape of the ice front. For example, if the external length of the ice cylinder which intimately contacts with the glass wall falls at a faster rate than the centre of the ice cylinder (Figure 135), and the ice mass develops a more substantive cone or dome shaped top surface (sublimation interface), the TVIS-determined drying rate will inevitably overestimate the true one. This scenario is more likely for those vials closer to and at the edges of each shelf which receive an additional heat source from radiation. To avoid such errors, we should limit the period over which the steady state drying period is studied. For those vials at the edge, the steady state period will be shorter than those at the core of the shelf. The key question is how to identify that part/period of the primary drying cycle over which there is minimal change in the profile of the sublimation interface.

With the TVIS approach, we can use $\hat{C}''_{PEAK}$ as a direct measure of the instantaneous drying rate, so far as the rate of drying of the ice cylinder in contact with the inside of the glass wall is concerned (see Figure 135). We can also use the evidence of a constant drying temperature ($T_{F_{PEAK}}$) and a constant drying rate (in what is predicted by TVIS) to quantify the unlikelihood of any change in the contributions from the various heat transfer mechanisms.

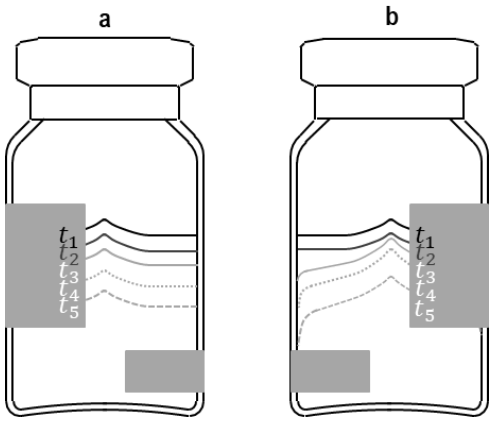

Figure 135 Two different scenarios for the shape of the sublimation interface at five equally spaced points (t_1 to t_5). (a) is the ideal scenario, whereby the shape of the sublimation interface does not change throughout the primary drying cycle; whereas (b) is the more typical pattern of changes to the sublimation shape. At the beginning of primary drying (t_1 to t_2), the shape of the ice layer does not change in either scenario; therefore, we expect C''_{PEAK} to be directly proportional to the ice mass. However, as drying proceeds (t_2 to t_5), the surface area of the sublimation interface shown in scenario (b) starts to increase and an air gap between the ice and glass wall appears. Under those circumstances, the relationship between C''_{PEAK} and ice mass will deviate from linear. Scenario (b) occurs routinely when drying ice; but the transition point between linear to non-linear will be reached sooner in the edge than the core vial.

Moreover, it appears that the time profile for F_{PEAK} might itself provide a clue on when there is a change in the curvature of the ice interface. During primary drying, we expect the drying rate to fall as contact with the side wall degrades and the rate of heat transfer slows. The rate of self-cooling is reduced accordingly, so the temperature of the ice layer starts to increase. This phenomenon is picked up by the ice temperature sensed by the thermocouple placed at the bottom of the vial. However, as the thermocouple temperature starts to increase, the value of F_{PEAK} starts to drop - so the downward trajectory of the F_{PEAK} profile has nothing to do with temperature, and must instead owe to some change in the profile of the ice interface. In fact, as noted in Section 10.3.6, the 10% discrepancy between the average gravimetric drying rate and average TVIS drying rate suggests that a change in the shape of the ice interface is possible over the time period leading up to the point of interruption.

In an initial attempt to determine the mechanism at play here, we consider how the equivalent electrical circuit model for the composite object of the glass vial and frozen contents (Figure 136) might change when the ice begins to lose contact with the inside surface of the glass wall.

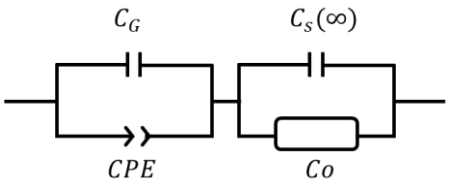

Figure 136 The equivalent circuit model for frozen water contained in the vial. The left part of the model represents the impedance of the glass wall with the instantaneous polarization of glass modelled by a capacitor (C_G); and the low frequency dispersive polarization of glass modelled by a constant phase element (CPE). The instantaneous capacitance ($C_s(\infty)$) and dielectric relaxation of ice (Co) are demonstrated on the right side of the model.

The left side of the equivalent circuit consists of the capacitance of glass (C_G) in parallel with a constant phase element (CPE) which model, respectively, the instantaneous capacitance of glass and low frequency dispersion associated with the percolation of charge through the porous matrix of fused silica glass. On the right side of the circuit, the capacitor models the high frequency (instantaneous capacitance) of ice ($C_s(\infty)$); whereas the distributed element (Co) models its dielectric relaxation.

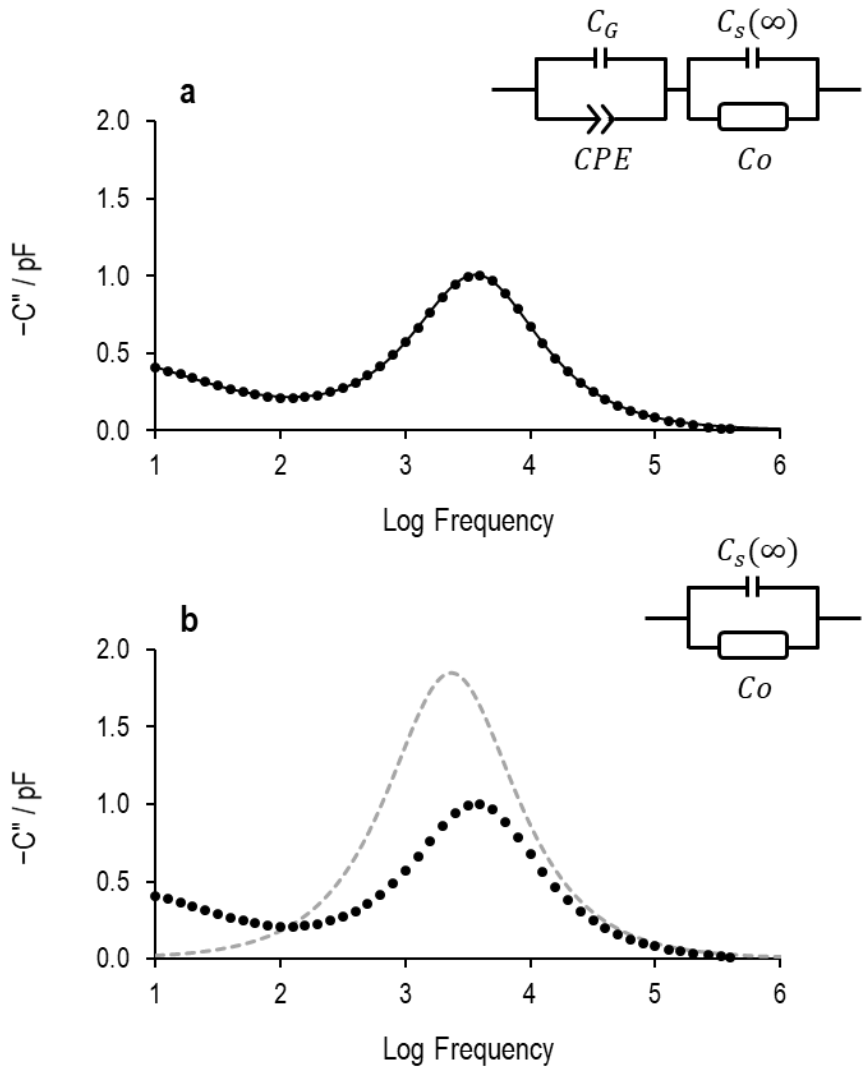

Figure 137 Equivalent circuit modelling of an example spectrum of ice. The data points are the measured values of the imaginary capacitance spectrum of ice at -20 °C during the re-heating part of the annealing stage. The black solid line in (a) demonstrates the data fitted to the complete model ($C_G = CPE - C_s(\infty) = Co$) as shown in the top right. (b) shows the simulation results (the grey dashed line) when glass wall impedance (C_G and CPE) has been removed from the completed model. RelaxIS (rhd instruments, Germany) was performed for modelling.

The data points in Figure 137 are the measured values for the TVIS imaginary capacitance spectrum for ice at -20 °C (during re-heating); the solid line shows the data fit to the model shown in the top right of each spectrum. In Figure 137a, the complete model has been fitted to the data (see Table 18 for the estimates of the fit parameters). In Figure 137b, the fitted parameters from Figure 137a have been taken, those relating to the glass wall impedance (C_G and CPE_G) removed; and a simulation of the response from the ice impedance has been

generated (see dashed line on Figure 137b). In other words, Figure 137b shows what we would expect to observe if it were possible to measure the sample without the glass wall. We could therefore anticipate that the simulated response would be similar to the dielectric relaxation of ice (Popov et al., 2017). The glass wall shifts the relaxation peak to a higher frequency than we would expect if ice were measured in the absence of the glass wall interface. It might thus be the case that an air gap between the ice and the glass wall has the opposite effect, i.e. to partly return the relaxation peak back towards that expected for ice. We presume that the decline in F_{PEAK} during primary drying at the point when the thermocouple suggests the ice temperature is either constant or increasing is in fact a sign that some macroscopic structural change has occurred within the ice mass.

Table 18 Parameters from the fitting data of the re-heating ice at −20 °C to the model for frozen water (C_G=$CPE - C_s(\infty)$=Co). RelaxIS3 (rhd instruments, Germany) was used for performing fitting.

Fitting parameters	Fitting results
C_G	6.03×10^{-12}
$CPE\text{-}Q$	6.29×10^{-11}
$CPE\text{-}\alpha$	0.386
$C_s(\infty)$	4.76×10^{-13}
$Co\text{-}C$	3.85×10^{-12}
$Co\text{-}\tau$	6.89×10^{-5}
$Co\text{-}\alpha$	0.974

Another potential issue with the application of the TVIS system for the determination of K_v relates to its use for the edge vials, thought to receive a large proportion of radiative heat transfer. Clearly, if the electrode is in the line of sight of the radiation source, it would reflect rather than absorb the heat and introduce an error in the determination of K_v. To minimise this, it would be prudent to ensure that the TVIS vial is orientated so that the intra electrode space, on the side wall, is directed towards the heat source. Given that the edge vial has one-third (33%) of the vial circumference exposed to the radiation source and the intra-vial spacing is one-quarter (25%) of the vial circumference, up to 7% of the heat radiation that would reach the vial

might be blocked by the electrode. That estimate, however, reduces by ~30% (from 7% to 5%) when we consider that the electrode does not extend to the base.

10.4. Summary

This is the first exploration of using a dual electrode TVIS system to determine the primary drying rate and critical temperatures at the ice interface and base. This study demonstrated the potential of using TVIS as a process development tool of determining heat transfer coefficient K_v at a single chamber pressure, as well as tracking the collapse potential of a frozen solution during the primary drying stage of a freeze-drying cycle.

General conclusion and future work

General conclusion

Through-vial impedance spectroscopy (TVIS), an individual vial measurement technique, has been purposed as an alternative process analytical tool, which features non-product invasiveness (no impact on ice nucleation) and a low thermal mass of electrode (with less impact on heat transfer and drying rate) when tracking the progression of the lyophilisation process. It has been developed further in the name of establishing a new approach, making it possible to determine critical parameters and build on previous research.

With this technology, a great deal of data on product behaviour and process parameters during lyophilisation can be provided by tuning its parameters. For example, the onset and endpoint of ice formation could be achieved by specifying the measurement frequency of the real part capacitance corresponding to the physical mechanism. In this case, ice nucleation onset employs the real part at low frequency (i.e. 10 Hz): which indicates the point where solidification ends. The nucleation temperature and crystallisation period could then be obtained by a simplified calculation from those parameters along with temperature from the sensor in the neighbouring vial.

Similarly, the methodologies determining ice temperature and drying rate during the primary drying stage are based on peak characteristics of the dielectric of ice, from which the critical variables (i.e. K_v and R_p) could be calculated. The further development of TVIS demonstrated here allows us to obtain better understanding of physical mechanisms underlying the in-vial product characteristics and fulfil the critical process parameters which could assist in the development of the robust freeze-drying process.

Future work

TVIS enables the continuous monitoring of the freeze-drying process without any interruption or alteration of product behaviour. Currently, TVIS research is mainly focused on freezing, annealing, and primary drying; this work has been conducted by a laboratory scale freeze dryer. Therefore, a future direction might be as follows:

(1) Establishing the appropriate model of determining the glass transition of the overlapping relaxation process. As some samples (e.g. sugar-salt solutions) could be observed in a multiple relaxation process during re-heating, one process could be shifted to another and eventually merged together during the temperature ramp. The unfitted model could help ameliorate uncertainty in the extraction fitting parameters and phase transition measurement.

(2) Exploring the opportunity of monitoring secondary drying. It is not clear whether dielectric measurement could be used with bound water (see Section 5.3.6). As a consequence, the TVIS approach of monitoring the desorption process (secondary drying) is challenged and needs further investigation.

(3) Investigating protein stability. According to Pearson and Smith (1998), dielectric analysis relates to structure and molecular properties of protein; therefore, it might be used to monitor protein stability during the lyophilisation cycle.

(4) Developing the TVIS system for a larger freeze dryer (e.g. production scale). The majority of TVIS research has been based on a small-scale freeze dryer: with a hard cable and junction box placed on the shelf and the analyser located outside the dryer. However, these parts are not compatible with the loading system and regulatory requirements. This might be resolved by developing a new system which has the electrode built into the freeze dryer. An electrode could be placed on the underside of the dryer, increasing sensitivity of the small capacitance by measuring a cluster of vials instead of a single one.

References

Abdelwahed, W., Degobert, G. & Fessi, H. 2006, "Freeze-drying of nanocapsules: impact of annealing on the drying process", *International Journal of Pharmaceutics,* vol. 324, no. 1, pp. 74-82.

Abiad, M.G., Campanella, O.H. & Carvajal, M.T. 2010, "Assessment of thermal transitions by dynamic mechanical analysis (DMA) using a novel disposable powder holder", *Pharmaceutics,* vol. 2, no. 2, pp. 78-90.

Ablett, S., Izzard, M.J. & Lillford, P.J. 1992, "Differential scanning calorimetric study of frozen sucrose and glycerol solutions", *Journal of the Chemical Society, Faraday Transactions,* vol. 88, no. 6, pp. 789-794.

Adams, G. 1991, "Freeze-drying of biological materials", *Drying Technology,* vol. 9, no. 4, pp. 891-925.

Alkeev, N., Averin, S. & von Gratowski, S. 2015, "New method for monitoring the process of freeze drying of biological materials", *AAPS Pharmscitech,* vol. 16, no. 6, pp. 1474-1479.

Andya, J.D., Maa, Y., Costantino, H.R., Nguyen, P., Dasovich, N., Sweeney, T.D., Hsu, C.C. & Shire, S.J. 1999, "The effect of formulation excipients on protein stability and aerosol performance of spray-dried powders of a recombinant humanized anti-IgE monoclonal antibody", *Pharmaceutical Research,* vol. 16, no. 3, pp. 350-358.

Arakawa, T., Prestrelski, S.J., Kenney, W.C. & Carpenter, J.F. 2001, "Factors affecting short-term and long-term stabilities of proteins", *Advanced Drug Delivery Reviews,* vol. 46, no. 1-3, pp. 307-326.

Arshad, M.S. 2014, *Application of through-vial impedance spectroscopy as a novel process analytical technology for freeze drying*. PhD thesis, De Monfort University.

Arshad, M.S., Smith, G., Polygalov, E. & Ermolina, I. 2014, "Through-vial impedance spectroscopy of critical events during the freezing stage of the lyophilization cycle: the example of the impact of sucrose on the crystallization of mannitol", *European Journal of Pharmaceutics and Biopharmaceutics,* vol. 87, no. 3, pp. 598-605.

Arsiccio, A., Sparavigna, A.C., Pisano, R. & Barresi, A.A. 2019, "Measuring and predicting pore size distribution of freeze-dried solutions", *Drying Technology,* vol. 37, no. 4, pp. 435-447.

Artemov, V.G. & Volkov, A.A. 2014, "Water and ice dielectric spectra scaling at 0 °C", *Ferroelectrics,* vol. 466, no. 1, pp. 158-165.

Assegehegn, G., Brito-de la Fuente, E., Franco, J.M. & Gallegos, C. 2019, "The importance of understanding the freezing step and its impact on freeze-drying process performance", *Journal of Pharmaceutical Sciences,* vol. 108, no. 4, pp. 1378-1395.

Awotwe−Otoo, D., Agarabi, C. & Khan, M.A. 2014, "An integrated process analytical technology (PAT) approach to monitoring the effect of supercooling on lyophilization product and process parameters of model monoclonal antibody formulations", *Journal of Pharmaceutical Sciences,* vol. 103, no. 7, pp. 2042-2052.

Baheti, A., Kumar, L. & Bansal, A.K. 2010, "Excipients used in lyophilization of small molecules", *Journal of Excipients and Food Chemicals*, vol. 1, no. 1, pp. 41-54.

Balasubramanian, S., Devi, A., Singh, K.K., Bosco, S.D. & Mohite, A.M. 2016, "Application of glass transition in food processing", *Critical Reviews in Food Science and Nutrition,* vol. 56, no. 6, pp. 919-936.

Baldan, A. 2002, "Review progress in Ostwald ripening theories and their applications to nickel-base superalloys part I: Ostwald ripening theories", *Journal of Materials Science,* vol. 37, no. 11, pp. 2171-2202.

Bandari, S., Seshasai, M. & Reddy, Y.R.C. 2013, "Optimization of lyophilization cycles for gemcitabine", *International Journal of Pharmacy and Pharmaceutical Sciences*, vol. 5, no. 2, pp. 216-221.

Bandeira, C.F., Montoro, S.R., Espindola, E.L., Botelho, E.C., Costa, M.L. & Cioffi, M.O.H. 2015, "Comparison of glass transition temperature values of composite polymer obtained by TMA and DSC", *Applied Mechanics and Materials,* vol. 719-720, pp. 91-95.

Barresi, A.A., Pisano, R., Fissore, D., Rasetto, V., Velardi, S.A., Vallan, A., Parvis, M. & Galan, M. 2009, "Monitoring of the primary drying of a lyophilization process in vials", *Chemical Engineering and Processing: Process Intensification,* vol. 48, no. 1, pp. 408-423.

Barsoukov, E. & Macdonald, J.R. (eds) 2005, *Impedance spectroscopy: theory, experiment, and applications*, 2nd edn, John Wiley & Sons, Inc., New Jersey.

Bedu-Addo, F.K. 2004, "Understanding lyophilization formulation development", *Pharmaceutical Technology,* vol. 20, pp. 10-19.

Bell, L.N., Hageman, M.J. & Bauer, J.M. 1995, "Impact of moisture on thermally induced denaturation and decomposition of lyophilized bovine somatotropin", *Biopolymers: Original Research on Biomolecules,* vol. 35, no. 2, pp. 201-209.

Bevilacqua, A.C. 1998, "Ultrapure water–the standard for resistivity measurements of ultrapure water", Semiconductor pure water and chemicals conference, 2-5 March 1998.

Bhugra, C., Shmeis, R., Krill, S.L. & Pikal, M.J. 2006, "Predictions of onset of crystallization from experimental relaxation times I-correlation of molecular mobility from temperatures above the glass transition to temperatures below the glass transition", *Pharmaceutical Research,* vol. 23, no. 10, pp. 2277-2290.

Bittelli, M., Flury, M. & Roth, K. 2004, "Use of dielectric spectroscopy to estimate ice content in frozen porous media", *Water Resources Research,* vol. 40, no. 4.

Breen, E.D., Curley, J.G., Overcashier, D.E., Hsu, C.C. & Shire, S.J. 2001, "Effect of moisture on the stability of a lyophilized humanized monoclonal antibody formulation", *Pharmaceutical Research,* vol. 18, no. 9, pp. 1345-1353.

Brülls, M. & Rasmuson, A. 2002, "Heat transfer in vial lyophilization", *International Journal of Pharmaceutics,* vol. 246, no. 1–2, pp. 1-16.

Burns, A.S., Stickler, L.A. & Stewart, W.E. 1992, "Solidification of an aqueous salt solution in a circular cylinder", *Journal of Heat Transfer,* vol. 114, no. 1, pp. 30-33.

Callister, W.D. & Rethwisch, D.G. 2013, *Materials science and engineering: an introduction,* 9th edn, John Wiley & Sons, New Jersey.

Cannon, A. & Shemeley, K. 2004, "Statistical evaluation of vial design features that influence sublimation rates during primary drying", *Pharmaceutical Research,* vol. 21, no. 3, pp. 536-542.

Carpenter, J.F., Pikal, M.J., Chang, B.S. & Randolph, T.W. 1997, "Rational design of stable lyophilized protein formulations: some practical advice", *Pharmaceutical Research,* vol. 14, no. 8, pp. 969-975.

Charoenrein, S., Goddard, M. & Reid, D.S. 1991, "Effect of solute on the nucleation and propagation of ice" in *Water relationships in foods*, eds. H. Levine & L. Slade, Springer, New York, pp. 191-198.

Cogné, C., Andrieu, J., Laurent, P., Besson, A. & Nocquet, J. 2003, "Experimental data and modelling of thermal properties of ice creams", *Journal of Food Engineering,* vol. 58, no. 4, pp. 331-341.

Colucci, D., Maniaci, R. & Fissore, D. 2019, "Monitoring of the freezing stage in a freeze-drying process using IR thermography", *International Journal of Pharmaceutics*, vol. 566, pp. 488-499.

Constantin, J.G., Schneider, M. & Corti, H.R. 2016, "Glass transition temperature of saccharide aqueous solutions estimated with the free volume/percolation model", *The Journal of Physical Chemistry B,* vol. 120, no. 22, pp. 5047-5055.

Cook, K. & Hartel, R.W. 2010, "Mechanisms of ice crystallization in ice cream production", *Comprehensive Reviews in Food Science and Food Safety,* vol. 9, no. 2, pp. 213-222.

Costantino, H.R. & Pikal, M.J. 2004, *Lyophilization of biopharmaceuticals*, American Association of Pharmaceutical Scientists, Virginia.

Crowe, L.M., Reid, D.S. & Crowe, J.H. 1996, "Is trehalose special for preserving dry biomaterials?", *Biophysical Journal,* vol. 71, no. 4, pp. 2087-2093.

DeLuca, P.P. 1977, "Freeze drying of pharmaceuticals", *Journal of Vacuum Science and Technology,* vol. 14, no. 1, pp. 620-629.

Deluca, P. & Lachman, L. 1965, "Lyophilization of pharmaceuticals: I. effect of certain physical-chemical properties", *Journal of Pharmaceutical Sciences,* vol. 54, no. 4, pp. 617-624.

Depaz, R.A., Pansare, S. & Patel, S.M. 2016, "Freeze-drying above the glass transition temperature in amorphous protein formulations while maintaining product quality and improving process efficiency", *Journal of Pharmaceutical Sciences,* vol. 105, no. 1, pp. 40-49.

Djohari, H., Martínez-Herrera, J.I. & Derby, J.J. 2009, "Transport mechanisms and densification during sintering: I. viscous flow versus vacancy diffusion", *Chemical Engineering Science*, vol. 64, no. 17, pp. 3799-3809.

DoITPoMS University of Cambridge 2004a, n.d.-last update*, The dielectric constant*. Available: https://www.doitpoms.ac.uk/tlplib/dielectrics/dielectric_constant.php [2020, 5 Feb].

DoITPoMS University of Cambridge 2004b, n.d.-last update*, Loss in dielectrics*. Available: https://www.doitpoms.ac.uk/tlplib/dielectrics/variation.php [2020, 5 Feb].

Duru, C., Swann, C., Dunleavy, U., Mulloy, B. & Matejtschuk, P. 2015, "The importance of formulation in the successful lyophilization of influenza reference materials", *Biologicals,* vol. 43, no. 2, pp. 110-116.

Esfandiary, R., Gattu, S.K., Stewart, J.M. & Patel, S.M. 2016, "Effect of freezing on lyophilization process performance and drug product cake appearance", *Journal of Pharmaceutical Sciences*, vol. 105, no. 4, pp. 1427-1433.

Evans, S.A., Morris, K.R., Mackenzie, A.P. & Lordi, N.G. 1995, "Dielectric characterization of thermodynamic first order events in model frozen systems intended for lyophilization", *PDA Journal of Pharmaceutical Science and Technology,* vol. 49, no. 1, pp. 2-8.

Fetterolf, D.M. 2010, "Lyophilization", Journal of Validation Technology, vol. 16, no. 1, pp. 18-23.

Fonseca, F., Passot, S., Cunin, O. & Marin, M. 2004, "Collapse temperature of freeze-dried lactobacillus bulgaricus suspensions and protective media", *Biotechnology Progress,* vol. 20, no. 1, pp. 229-238.

Foreman, J., Sauerbrunn, S.R. & Marcozzi, C.L. 2013, Thermal Analysis & Rheology: exploring the sensitivity of thermal analysis techniques to the glass transition, New Castle.

Franks, F. & Auffret, T. 2007, "Excipients: their role in rational formulation design", in *Freeze-drying of pharmaceuticals and biopharmaceuticals: principles and practice* The Royal Society of Chemistry, Cambridge, pp. 89-104.

Gabbott, P. 2008, "A practical introduction to differential scanning calorimetry", in *Principles and applications of thermal analysis.* Blackwell Publishing, Singapore, pp. 1-50.

Gallo, P. & Stanley, H.E. 2017, "Supercooled water reveals its secrets", *Science,* vol. 358, no. 6370, pp. 1543-1544.

Ganguly, A., Nail, S.L. & Alexeenko, A. 2013, "Experimental determination of the key heat transfer mechanisms in pharmaceutical freeze-drying", *Journal of Pharmaceutical Sciences,* vol. 102, no. 5, pp. 1610-1625.

García, I.C. 2019, "Head-to-head comparison of hydrogen peroxide and steam sterilization". Available: https://www.cphi-online.com/46/resourcefile/09/71/37/Telstar_White_Paper_Head-to-Head%20comparison%20of%20Hydrogen.pdf [2020, 3 Feb].

Gatlin, L. & Deluca, P.P. 1980, "A study of the phase transitions in frozen antibiotic solutions by differential scanning calorimetry", *PDA Journal of Pharmaceutical Science and Technology,* vol. 34, no. 5, pp. 398-408.

Gearing, J., Malik, K.P. & Matejtschuk, P. 2010, "Use of dynamic mechanical analysis (DMA) to determine critical transition temperatures in frozen biomaterials intended for lyophilization", *Cryobiology*, vol. 61, no. 1, pp. 27-32.

Geidobler, R. & Winter, G. 2013, "Controlled ice nucleation in the field of freeze-drying: fundamentals and technology review", *European Journal of Pharmaceutics and Biopharmaceutics*, vol. 85, no. 2, pp. 214-222.

German, R.M. 2010, "Thermodynamics of sintering" in *Sintering of advanced materials*, ed. Z.Z. Fang, Woodhead Publishing, Cambridge, pp. 3-32.

Gieseler, H., Kessler, W.J., Finson, M., Davis, S.J., Mulhall, P.A., Bons, V., Debo, D.J. & Pikal, M.J. 2007, "Evaluation of tunable diode laser absorption spectroscopy for in-process water vapor mass flux measurements during freeze drying", *Journal of Pharmaceutical Sciences,* vol. 96, no. 7, pp. 1776-1793.

Gieseler, H., Kramer, T. & Pikal, M.J. 2007, "Use of manometric temperature measurement (MTM) and SMART™ freeze dryer technology for development of an optimized freeze-drying cycle", *Journal of pharmaceutical sciences*, vol. 96, no. 12, pp. 3402-3418.

Goff, H.D., Verespej, E. & Jermann, D. 2003, "Glass transitions in frozen sucrose solutions are influenced by solute inclusions within ice crystals", *Thermochimica Acta,* vol. 399, no. 1-2, pp. 43-55.

Gordon, M. & Taylor, J.S. 1952, "Ideal copolymers and the second-order transitions of synthetic rubbers. I. non-crystalline copolymers", *Journal of Applied Chemistry,* vol. 2, no. 9, pp. 493-500.

Gough, S.R. 1972, "A low temperature dielectric cell and the permittivity of hexagonal ice to 2 K", *Canadian Journal of Chemistry,* vol. 50, no. 18, pp. 3046-3051.

Grassini, S., Pisano, R., Barresi, A.A., Angelini, E. & Parvis, M. 2016, "Frequency domain image analysis for the characterization of porous products", *Measurement,* vol. 94, pp. 515-522.

Greaves, R.I.N. 1954, "Theoretical aspects of drying by vacuum sublimation", in *Biological applications of freezing and drying.*, ed. R.J.C. Harris, Academic Press, New York, pp. 87-127.

Greco, K., Mujat, M., Galbally-Kinney, K.L., Hammer, D.X., Ferguson, R.D., Iftimia, N., Mulhall, P., Sharma, P., Kessler, W.J. & Pikal, M.J. 2013, "Accurate prediction of collapse temperature using optical coherence tomography-based freeze-drying microscopy", *Journal of Pharmaceutical Sciences,* vol. 102, no. 6, pp. 1773-1785.

Gregory, A.P., Clarke, R.N., Hodgetts, T.E. & Symm, G.T. 1993, *RF and microwave dielectric measurements upon layered materials using a reflectometric coaxial sensor*., Crown, Teddington.

Hagiwara, T., Hartel, R.W. & Matsukawa, S. 2006, "Relationship between recrystallization rate of ice crystals in sugar solutions and water mobility in freeze-concentrated matrix", *Food Biophysics,* vol. 1, no. 2, pp. 74-82.

Haynes, W.M., Lide, D.R. & Bruno, T.J. 2017, *CRC handbook of chemistry and physics: a ready-reference book of chemical and physical data,* 97th edn. CRC Press, Florida.

Heller, M.C., Carpenter, J.F. & Randolph, T.W. 1999, "Protein formulation and lyophilization cycle design: prevention of damage due to freeze-concentration induced phase separation", *Biotechnology and Bioengineering,* vol. 63, no. 2, pp. 166-174.

Her, L.M., Jefferis, R.P., Gatlin, L.A., Braxton, B. & Nail, S.L. 1994, "Measurement of glass transition temperatures in freeze concentrated solutions of non-electrolytes by electrical thermal analysis", *Pharmaceutical Research,* vol. 11, no. 7, pp. 1023-1029.

Her, L.M. & Nail, S.L. 1994, "Measurement of glass transition temperatures of freeze-concentrated solutes by differential scanning calorimetry", *Pharmaceutical Research,* vol. 11, no. 1, pp. 54-59.

Herman, B.D., Sinclair, B.D., Milton, N. & Nail, S.L. 1994, "The effect of bulking agent on the solid-state stability of freeze-dried methylprednisolone sodium succinate", *Pharmaceutical Research,* vol. 11, no. 10, pp. 1467-1473.

Hibler, S., Wagner, C. & Gieseler, H. 2012, "Vial freeze-drying, part 1: new insights into heat transfer characteristics of tubing and molded vials", *Journal of Pharmaceutical Sciences,* vol. 101, no. 3, pp. 1189-1201.

Hirakura, Y., Kojima, S., Okada, A., Yokohama, S. & Yokota, S. 2004, "The improved dissolution and prevention of ampoule breakage attained by the introduction of pretreatment into the production process of the lyophilized formulation of recombinant human interleukin-11 (rhIL-11)", *International Journal of Pharmaceutics,* vol. 286, no. 1-2, pp. 53-67.

Hobbs, M.E., Jhon, M.S. & Eyring, H. 1966, "The dielectric constant of liquid water and various forms of ice according to significant structure theory", *Proceedings of the National Academy of Sciences of the United States of America,* vol. 56, no. 1, pp. 31.

Hongbo, L. 2018, "Dielectrics under electric Field", in *Electric field*, ed. M.S. Kandelousi, Intechopen, London, pp. 73-90.

Horn, J. & Friess, W. 2018, "Detection of collapse and crystallization of saccharide, protein and mannitol formulations by optical fibers in lyophilization", *Frontiers in Chemistry,* vol. 6, pp. 4.

Hottot, A., Vessot, S. & Andrieu, J. 2004, "A direct characterization method of the ice morphology. Relationship between mean crystals size and primary drying times of freeze-drying processes", *Drying Technology,* vol. 22, no. 8, pp. 2009-2021.

Hottot, A., Vessot, S. & Andrieu, J. 2005, "Determination of mass and heat transfer parameters during freeze-drying cycles of pharmaceutical products", *PDA Journal of Pharmaceutical Science and Technology,* vol. 59, no. 2, pp. 138-153.

Hua, T.C., Liu, B.L. & Zhang, H. 2010, "Fundamentals of freeze drying" in *Freeze-drying of pharmaceutical and food products*, Woodhead Publishing, Cambridge, UK, pp. 18-67.

Jennings, T.A. 2008, *Lyophilization: introduction and basic principles,* Informa Healthcare, New York, USA.

Jiang, G., Akers, M., Jain, M., Guo, J., Distler, A., Swift, R., Wadhwa, M.S., Jameel, F., Patro, S. & Freund, E. 2007, "Mechanistic studies of glass vial breakage for frozen formulations. I. Vial breakage caused by crystallizable excipient mannitol", *PDA Journal of Pharmaceutical Science and Technology,* vol. 61, no. 6, pp. 441-451.

Johari, G.P. & Jone, S.J. 1976, "Dielectric properties of polycrystalline D_2O ice Ih (hexagonal)", *Proceedings of the Royal Society. A, Mathematical, physical, and engineering sciences,* vol. 349, no. 1659, pp. 467-495.

Johari, G.P. & Whalley, E. 1981, "The dielectric properties of ice Ih in the range 272–133 K", *The Journal of Chemical Physics,* vol. 75, no. 3, pp. 1333-1340.

Johnson, R.E., Oldroyd, M.E., Ahmed, S.S., Gieseler, H. & Lewis, L.M. 2010, "Use of manometric temperature measurements (MTM) to characterize the freeze-drying behavior of amorphous protein formulations", *Journal of Pharmaceutical Sciences,* vol. 99, no. 6, pp. 2863-2873.

Kasper, J.C. & Friess, W. 2011, "The freezing step in lyophilization: physico-chemical fundamentals, freezing methods and consequences on process performance and quality attributes of biopharmaceuticals", *European Journal of Pharmaceutics and Biopharmaceutics,* vol. 78, no. 2, pp. 248-263.

Kasper, J.C., Wiggenhorn, M., Resch, M. & Friess, W. 2013, "Implementation and evaluation of an optical fiber system as novel process monitoring tool during lyophilization", *European Journal of Pharmaceutics and Biopharmaceutics,* vol. 83, no. 3, pp. 449-459.

Kilmartin, P.A., Reid, D.S. & Samson, I. 2000, "The measurement of the glass transition temperature of sucrose and maltose solutions with added NaCl", *Journal of the Science of Food and Agriculture,* vol. 80, no. 15, pp. 2196-2202.

Kochs, M., Körber, C.H., Heschel, I. & Nunner, B. 1993, "The influence of the freezing process on vapour transport during sublimation in vacuum-freeze-drying of macroscopic samples", *International Journal of Heat and Mass Transfer,* vol. 36, no. 7, pp. 1727-1738.

Kochs, M., Körber, C., Nunner, B. & Heschel, I. 1991, "The influence of the freezing process on vapour transport during sublimation in vacuum-freeze-drying", *International Journal of Heat and Mass Transfer,* vol. 34, no. 9, pp. 2395-2408.

Komarov, V., Wang, S. & Tang, J. 2005, "Permittivity and measurements" in *Encyclopedia of RF and microwave engineering*, ed. K. Chang, John Wiley & Sons, New Jersey, pp. 3693-3711.

Konijnendijk, W.L. 1975, "Electrical conduction of borosilicate glasses", in *The structure of borosilicate glasses.* Eindhoven University of Technology, Eindhoven, pp. 182-195.

Konstantinidis, A.K., Kuu, W.Y., Otten, L., Nail, S.L. & Sever, R.R. 2011, "Controlled nucleation in freeze-drying: Effects on pore size in the dried product layer, mass transfer resistance, and primary drying rate", *Journal of Pharmaceutical Sciences,* vol. 100, no. 8, pp. 3453-3470.

Koontz, E. 2019, "Thermal analysis of glass" in *Springer handbook of glass*, eds. J.D. Musgraves, J.J. Hu & L. Calvez, Springer Nature, USA, pp. 853-878.

Korey, D.J. & Schwartz, J.B. 1989, "Effects of excipients on the crystallization of pharmaceutical compounds during lyophilization", *PDA Journal of Pharmaceutical Science and Technology,* vol. 43, no. 2, pp. 80-83.

Kuu, W.Y., Doty, M.J., Rebbeck, C.L., Hurst, W.S. & Cho, Y.K. 2013, "Gap-freezing approach for shortening the lyophilization cycle time of pharmaceutical formulations—demonstration of the concept", *Journal of Pharmaceutical Sciences,* vol. 102, no. 8, pp. 2572-2588.

Kuu, W.Y., Hardwick, L.M. & Akers, M.J. 2006, "Rapid determination of dry layer mass transfer resistance for various pharmaceutical formulations during primary drying using product temperature profiles", *International Journal of Pharmaceutics,* vol. 313, no. 1–2, pp. 99-113.

Kuu, W.Y., Nail, S.L. & Sacha, G. 2009, "Rapid determination of vial heat transfer parameters using tunable diode laser absorption spectroscopy (TDLAS) in response to step-changes in pressure set-point during freeze-drying", *Journal of Pharmaceutical Sciences*, vol. 98, no. 3, pp. 1136-1154.

Kuu, W.Y., O'Bryan, K.R., Hardwick, L.M. & Paul, T.W. 2011, "Product mass transfer resistance directly determined during freeze-drying cycle runs using tunable diode laser absorption spectroscopy (TDLAS) and pore diffusion model", *Pharmaceutical Development and Technology,* vol. 16, no. 4, pp. 343-357.

Laaksonen, T.J. & Roos, Y. 2000, "Thermal, dynamic-mechanical, and dielectric analysis of phase and state transitions of frozen wheat doughs", *Journal of Cereal Science,* vol. 32, no. 3, pp. 281-292.

Lesker.com. 1996 n.d.-last update*, Pressure measurement technical notes*. Available: https://www.lesker.com/newweb/gauges/gauges_technicalnotes_1.cfm [2020, 2/2/].

Levine, H. & Slade, L. 1988a, "Principles of “cryostabilization” technology from structure/property relationships of carbohydrate/water systems—a review", *Cryo-letters,* vol. 9, no. 1, pp. 21-63.

Levine, H. & Slade, L. 1988, "Water as a plasticizer: physico-chemical aspects of low-moisture polymeric systems" in *Water science reviews: water dynamics*, ed. F. Franks, Cambridge University Press Cambridge, Cambridge, pp. 79-185.

Li, S., Patapoff, T.W., Overcashier, D., Hsu, C., Nguyen, T.H. & Borchardt, R.T. 1996, "Effects of reducing sugars on the chemical stability of human relaxin in the lyophilized state", *Journal of Pharmaceutical Sciences,* vol. 85, no. 8, pp. 873-877.

Li, X. & Nail, S. 2006, "Nuclear magnetic resonance imaging of freeze-drying", *Journal of Pharmaceutical Sciences,* vol. 95, no. 11, pp. 2516-2525.

Liesebach, J., Rades, T. & Lim, M. 2003, "A new method for the determination of the unfrozen matrix concentration and the maximal freeze-concentration", *Thermochimica Acta,* vol. 401, no. 2, pp. 159-168.

Liu, J. 2006, "Physical characterization of pharmaceutical formulations in frozen and freeze-dried solid states: techniques and applications in freeze-drying development", *Pharmaceutical Development and Technology,* vol. 11, no. 1, pp. 3-28.

Lu, X. & Pikal, M.J. 2004, "Freeze-drying of mannitol-trehalose-sodium chloride-based formulations: the impact of annealing on dry layer resistance to mass transfer and cake structure", *Pharmaceutical Development and Technology,* vol. 9, no. 1, pp. 85-95.

Lueckel, B., Bodmer, D., Helk, B. & Leuenberger, H. 1998, "Formulations of sugars with amino acids or mannitol–influence of concentration ratio on the properties of the freeze-concentrate and the lyophilizate", *Pharmaceutical Development and Technology,* vol. 3, no. 3, pp. 325-336.

Lueckel, B., Helk, B., Bodmer, D. & Leuenberger, H. 1998, "Effects of formulation and process variables on the aggregation of freeze-dried interleukin-6 (IL-6) after lyophilization and on storage", *Pharmaceutical Development and Technology,* vol. 3, no. 3, pp. 337-346.

MacDowell, L.G. & Vega, C. 2010, "Dielectric constant of ice ih and ice v: a computer simulation study", *The Journal of Physical Chemistry B,* vol. 114, no. 18, pp. 6089-6098.

Mayeresse, Y., de Cupere, V., Veillon, R. & Brendle, J. 2009, "Considerations for transferring a bulk freeze-drying process from a glass container to a tray", *Pharmaceutical Engineering,* vol. 29, pp. 1-8.

Mazzobre, M.F., Longinotti, M.P., Corti, H.R. & Buera, M.P. 2001, "Effect of salts on the properties of aqueous sugar systems, in relation to biomaterial stabilization. 1. water sorption behavior and ice crystallization/melting", *Cryobiology,* vol. 43, no. 3, pp. 199-210.

McDonald, E.J. & Turcotte, A.L. 1948, "Density and refractive indices of lactose solutions", *Journal of Research of the National Bureau of Standards,* vol. 41, pp. 63-68.

Meister, E. & Gieseler, H. 2008, "A significant comparison between collapse and glass transition temperatures", *European Pharmaceutical Review*, vol. 13, no. 5, pp. 73-79.

Meister, E. & Gieseler, H. 2009, "Freeze-dry microscopy of protein/sugar mixtures: Drying behavior, interpretation of collapse temperatures and a comparison to corresponding glass transition data", *Journal of Pharmaceutical Sciences,* vol. 98, no. 9, pp. 3072-3087.

Melinder, Å. 2010, "Properties and other aspects of aqueous solutions used for single phase and ice slurry applications", *International Journal of Refrigeration,* vol. 33, no. 8, pp. 1506-1512.

Metaxas, A.C. & Meredith, R.J. 1983, "Theoretical aspects of volumetric heating", in *Industrial microwave heating.* IET, London, pp. 70-103.

Milton, N., Pikal, M.J., Roy, M.L. & Nail, S.L. 1997, "Evaluation of manometric temperature measurement as a method of monitoring product temperature during lyophilization", *PDA Journal of Pharmaceutical Science and Technology,* vol. 51, no. 1, pp. 7-16.

Milton, N., Gopalrathnam, G., Craig, G.D., Mishra, D.S., Roy, M.L. & Yu, L. 2007, "Vial breakage during freeze-drying: crystallization of sodium chloride in sodium chloride-sucrose frozen aqueous solutions", *Journal of Pharmaceutical Sciences,* vol. 96, no. 7, pp. 1848-1853.

Mitchell, B.S. 2004, "Electrical, magnetic, and optical properties of materials", in *An introduction to materials engineering and science for chemical and materials engineers.* John Wiley & Sons, New Jersey, pp. 537-680.

Morris, K.R., Evans, S.A., Mackenzie, A.P., Scheule, D. & Lordi, N.G. 1994, "Prediction of lyophile collapse temperature by dielectric analysis", *PDA Journal of Pharmaceutical Science and Technology,* vol. 48, no. 6, pp. 318-329.

Mujat, M., Greco, K., Galbally-Kinney, K.L., Hammer, D.X., Ferguson, R.D., Iftimia, N., Mulhall, P., Sharma, P., Pikal, M.J. & Kessler, W.J. 2012, "Optical coherence tomography-based freeze-drying microscopy", *Biomedical Optics Express,* vol. 3, no. 1, pp. 55-63.

Murgatroyd, K. 1997, "Freeze dryer instrumentation and control", in *Good pharmaceutical freeze-drying practice*, ed. P. Cameron, Interpharm Press Inc., Illinois, pp. 125-154.

Murphy, D.M. & Koop, T. 2005, "Review of the vapour pressures of ice and supercooled water for atmospheric applications", *Quarterly Journal of the Royal Meteorological Society,* vol. 131, no. 608, pp. 1539-1565.

Nail, S.L. 1980, "The effect of chamber pressure on heat transfer in the freeze drying of parenteral solutions", *PDA Journal of Pharmaceutical Science and Technology,* vol. 34, no. 5, pp. 358-368.

Nail, S.L. & Gatlin, L.A. 2016, "Freeze-drying: principles and practice" in *Pharmaceutical dosage forms-Parenteral medications* CRC Press, London, pp. 367-396.

Nail, S.L., Tchessalov, S., Shalaev, E., Ganguly, A., Renzi, E., Dimarco, F., Wegiel, L., Ferris, S., Kessler, W. & Pikal, M. 2017, "Recommended best practices for process monitoring instrumentation in pharmaceutical freeze drying—2017", *AAPS PharmSciTech,* vol. 18, no. 7, pp. 2373-2393.

Nakagawa, K., Hottot, A., Vessot, S. & Andrieu, J. 2006, "Influence of controlled nucleation by ultrasounds on ice morphology of frozen formulations for pharmaceutical proteins freeze-drying", *Chemical Engineering and Processing: Process Intensification,* vol. 45, no. 9, pp. 783-791.

Nakagawa, K., Hottot, A., Vessot, S. & Andrieu, J. 2007, "Modeling of freezing step during freeze-drying of drugs in vials", *AIChE Journal,* vol. 53, no. 5, pp. 1362-1372.

Nakagawa, K., Tamiya, S., Do, G., Kono, S. & Ochiai, T. 2018, "Observation of glassy state relaxation during annealing of frozen sugar solutions by X-ray computed tomography", *European Journal of Pharmaceutics and Biopharmaceutics,* vol. 127, pp. 279-287.

Nakagawa, K., Tamiya, S., Sakamoto, S., Do, G. & Kono, S. 2018, "Observation of microstructure formation during freeze-drying of dextrin solution by in-situ X-ray computed tomography", *Frontiers in Chemistry,* vol. 6, pp. 418.

Nelson, S.O. & Trabelsi, S. 2012, "Factors influencing the dielectric properties of agricultural and food products", *Journal of Microwave Power and Electromagnetic Energy,* vol. 46, no. 2, pp. 93-107.

Nickelson, L. 2019, "Fields and materials", in *Electromagnetic theory and plasmonics for engineers.* Springer, Singapore, pp. 97-194.

Oetjen, G.W. & Haseley, P. 2018, "Foundations and process engineering", in *Freeze-drying*, 3rd edn, Wiley-VCH, Germany, pp. 1-176.

Osborn, G. & Hansen, S. 2002, "Calibration of lyophilization pressure gauges", *Pharmaceutical Technology North America,* vol. 26, no. 6, pp. 72.

Overcashier, D.E., Patapoff, T.W. & Hsu, C.C. 1999, "Lyophilization of protein formulations in vials: investigation of the relationship between resistance to vapor flow during primary drying and small-scale product collapse", *Journal of Pharmaceutical Sciences,* vol. 88, no. 7, pp. 688-695.

Pandya, B., Matejtschuk, P., Jeeraruangrattana, Y. & Smith, G. 2019, "Multiplexing through vial impedance spectroscopy (TVIS) with comparative pressure measurement for the determination of the primary drying endpoint of immunoglobulin (IgG)", *ISLFD 2019-9th*

international symposium on lyophilization of pharmaceuticals. Ghent, Belgium, 2-6 September.

Pansare, S.K. & Patel, S.M. 2016, "Practical considerations for determination of glass transition temperature of a maximally freeze concentrated solution", *AAPS PharmSciTech,* vol. 17, no. 4, pp. 805-819.

Passot, S. 2007, "Effect of product temperature during primary drying on the long-term stability of lyophilized proteins", *Pharmaceutical Development and Technology,* vol. 12, no. 6, pp. 543-553.

Patel, S.M., Doen, T. & Pikal, M.J. 2010, "Determination of end point of primary drying in freeze-drying process control", *AAPS PharmSciTech,* vol. 11, no. 1, pp. 73-84.

Patel, S.M. & Pikal, M. 2009, "Process analytical technologies (PAT) in freeze-drying of parenteral products", *Pharmaceutical Development and Technology,* vol. 14, no. 6, pp. 567-587.

Patel, S.M., Lobo, B. & Shah, A. 2013, , *Practical considerations for freeze-drying process design, development and scale-Up*. Available: https://www.americanpharmaceuticalreview.com/Featured-Articles/148761-Practical-Considerations-for-Freeze-Drying-Process-Design-Development-and-Scale-Up/.[2020, 2/2/].

Pearson, D.S. & Smith, G. 1998, "Dielectric analysis as a tool for investigating the lyophilization of proteins", *Pharmaceutical Science & Technology Today,* vol. 1, no. 3, pp. 108-117.

Petrenko, V.F. & Whitworth, R.W. 2002, *Physics of ice,* Oxford University Press, Oxford.

Petzold, G. & Aguilera, J.M. 2009, "Ice morphology: fundamentals and technological applications in foods", *Food Biophysics,* vol. 4, no. 4, pp. 378-396.

Pikal, M.J. 1985, "Use of laboratory data in freeze drying process design: heat and mass transfer coefficients and the computer simulation of freeze drying", *PDA Journal of Pharmaceutical Science and Technology,* vol. 39, no. 3, pp. 115-139.

Pikal, M.J. 1994, "Freeze-drying of proteins: process, formulation, and stability", in *Formulation and delivery of proteins and peptides.* ACS Publications, Washington, pp. 120-133.

Pikal, M.J., Rambhatla, S. & Ramot, R. 2002, "The impact of the freezing stage in lyophilization: effects of the ice nucleation temperature on process design and product quality", *American Pharmaceutical Review,* vol. 5, pp. 48-53.

Pikal, M.J., Roy, M.L. & Shah, S. 1984, "Mass and heat transfer in vial freeze-drying of pharmaceuticals: role of the vial", *Journal of Pharmaceutical Sciences,* vol. 73, no. 9, pp. 1224-1237.

Pikal, M.J. & Shah, S. 1990, "The collapse temperature in freeze drying: dependence on measurement methodology and rate of water removal from the glassy phase", *International Journal of Pharmaceutics,* vol. 62, no. 2, pp. 165-186.

Pikal, M.J. & Shah, S. 1997, "Intravial distribution of moisture during the secondary drying stage of freeze drying", *PDA Journal of Pharmaceutical Science and Technology,* vol. 51, no. 1, pp. 17-24.

Pikal, M.J., Shah, S., Roy, M.L. & Putman, R. 1990, "The secondary drying stage of freeze drying: drying kinetics as a function of temperature and chamber pressure", *International Journal of Pharmaceutics,* vol. 60, no. 3, pp. 203-207.

Pikal, M.J., Shah, S., Senior, D. & Lang, J.E. 1983, "Physical chemistry of freeze-drying: measurement of sublimation rates for frozen aqueous solutions by a microbalance technique", *Journal of Pharmaceutical Sciences,* vol. 72, no. 6, pp. 635-650.

Pisano, R., Barresi, A.A., Capozzi, L.C., Novajra, G., Oddone, I. & Vitale-Brovarone, C. 2017, "Characterization of the mass transfer of lyophilized products based on X-ray micro-computed tomography images", *Drying Technology,* vol. 35, no. 8, pp. 933-938.

Popov, I., Lunev, I., Khamzin, A., Greenbaum, A., Gusev, Y. & Feldman, Y. 2017, "The low-temperature dynamic crossover in the dielectric relaxation of ice I h", *Physical Chemistry Chemical Physics,* vol. 19, no. 42, pp. 28610-28620.

Popov, I., Puzenko, A., Khamzin, A. & Feldman, Y. 2015, "The dynamic crossover in dielectric relaxation behavior of ice I h", *Physical Chemistry Chemical Physics,* vol. 17, no. 2, pp. 1489-1497.

Pržić, D.S., Ružić, N.L. & Petrović, S.D. 2004, "Lyophilization: the process and industrial use", *Hemijska industrija,* vol. 58, no. 12, pp. 552-562.

Raju, G.G. 2017, *Dielectrics in electric fields,* 2nd edn, CRC Press, Florida.

Rambhatla, S. & Pikal, M.J. 2003, "Heat and mass transfer scale-up issues during freeze-drying, I: atypical radiation and the edge vial effect", *AAPS PharmSciTech,* vol. 4, no. 2, pp. 22-31.

Rambhatla, S., Ramot, R., Bhugra, C. & Pikal, M.J. 2004, "Heat and mass transfer scale-up issues during freeze drying: II. control and characterization of the degree of supercooling", *AAPS PharmSciTech,* vol. 5, no. 4, pp. 54-62.

Rambhatla, S., Tchessalov, S. & Pikal, M.J. 2006, "Heat and mass transfer scale-up issues during freeze-drying, III: control and characterization of dryer differences via operational qualification tests", *AAPS PharmSciTech,* vol. 7, no. 2, pp. E61-E70.

Reale, E.R. & Smith, K.C. 2018, "Capacitive performance and tortuosity of activated carbon electrodes with macroscopic pores", *Journal of the Electrochemical Society,* vol. 165, no. 9, pp. A1685-A1693.

Rey, L. 2010, "Glimpses into the realm of freeze-drying: classical issues and new ventures", in *Freeze-drying/lyophilization of pharmaceutical and biological products.*, eds. L. Rey & J.C. May, 3rd edn, Informa Healthcare, UK, pp. 1-28.

Rey, L.R. 1960, "Study of the freezing and drying of tissues at very low temperatures", in *Recent research in freezing and drying*, eds. A.S. Parkes & U.S. Audrey. Blackwell, Oxford, pp. 40-62.

Rey, L.R. 1960, "Thermal analysis of eutectics in freezing solutions", *Annals of the New York Academy of Sciences,* vol. 85, no. 1, pp. 510-534.

Riley, F. 1988, A snowball's chance, *New Scientist*, 14 January, pp. 45-48.

Roos, Y.H. 1997, "Frozen state transitions in relation to freeze drying", *Journal of Thermal Analysis,* vol. 48, no. 3, pp. 535-544.

Roos, Y. H. 2007, "Phase transitions and transformations in food systems", in *Handbook of food engineering*, eds. D.R. Heldman & D.B. Lund, 2nd edn, CRC press, pp. 287-352.

Roos, Y.H. 2010, "Glass transition temperature and its relevance in food processing", *Annual Review of Food Science and Technology,* vol. 1, pp. 469-496.

Roos, Y.H. & Drusch, S. 2016a, "Methodology", in *Phase transitions in foods*, 2nd edn, Academic Press, San Diego, pp. 49-77.

Roos, Y.H. & Drusch, S. 2016b, "Prediction of the physical state", in *Phase Transitions in Foods*, 2nd edn, Academic Press, San Diego, pp. 173-214.

Roos, Y.H. & Karel, M. 1991, "Phase transitions of amorphous sucrose and frozen sucrose solutions", *Journal of Food Science,* vol. 56, no. 1, pp. 266-267.

Rossi, S., Buera, M.P., Moreno, S. & Chirife, J. 1997, "Stabilization of the restriction enzyme EcoRI dried with trehalose and other selected glass-forming solutes", *Biotechnology Progress,* vol. 13, no. 5, pp. 609-616.

Roy, M.L. & Pikal, M.J. 1989, "Process control in freeze drying: determination of the end point of sublimation drying by an electronic moisture sensor", *PDA Journal of Pharmaceutical Science and Technology,* vol. 43, no. 2, pp. 60-66.

Sacha, G.A. & Nail, S.L. 2009, "Thermal analysis of frozen solutions: multiple glass transitions in amorphous systems", *Journal of Pharmaceutical Sciences,* vol. 98, no. 9, pp. 3397-3405.

Sahagian, M.E. & Goff, H.D. 1994, "Effect of freezing rate on the thermal, mechanical and physical aging properties of the glassy state in frozen sucrose solutions", *Thermochimica Acta*, vol. 246, no. 2, pp. 271-283.

Saldivar-Guerra, E. & Vivaldo-Lima, E. 2013, *Handbook of polymer synthesis, characterization, and processing,* John Wiley & Sons Incorporated, Somerset.

Sasaki, K., Kita, R., Shinyashiki, N. & Yagihara, S. 2016, "Dielectric relaxation time of ice-Ih with different preparation", *The Journal of Physical Chemistry B,* vol. 120, no. 16, pp. 3950-3953.

Schersch, K., Betz, O., Garidel, P., Muehlau, S., Bassarab, S. & Winter, G. 2010, "Systematic investigation of the effect of lyophilizate collapse on pharmaceutically relevant proteins I: stability after freeze-drying", *Journal of Pharmaceutical Sciences*, vol. 99, no. 5, pp. 2256-2278.

Schneid, S. & Gieseler, H. 2008a, "Evaluation of a new wireless temperature remote interrogation system (TEMPRIS) to measure product temperature during freeze drying", *AAPS PharmSciTech,* vol. 9, no. 3, pp. 729-739.

Schneid, S. & Gieseler, H. 2008b, "Effect of concentration, vial size and fill depth on product resistance of sucrose solutions during freeze drying", *6th World Meeting on Pharmaceutics, Biopharmaceutics and Pharmaceutical Technology, Barcelona, Spain, April 7 – 10.*

Schneid, S.C., Johnson, R.E., Lewis, M.L., Stärtzel, P. & Gieseler, H. 2015, "Application of process analytical technology for monitoring freeze-drying of an amorphous protein formulation: Use of complementary tools for real-time product temperature measurements and endpoint detection", *Journal of Pharmaceutical Sciences,* vol. 104, no. 5, pp. 1741-1749.

Scutella, B., Passot, S., Bourles, E., Fonseca, F. & Trelea, I.C. 2017, "How vial geometry variability influences heat transfer and product temperature during freeze-drying", *Journal of Pharmaceutical Sciences,* vol. 106, no. 3, pp. 770-778.

Scutella, B., Trelea, I.C., Bourlès, E., Fonseca, F. & Passot, S. 2018, "Determination of the dried product resistance variability and its influence on the product temperature in pharmaceutical freeze-drying", *European Journal of Pharmaceutics and Biopharmaceutics,* vol. 128, pp. 379-388.

Searles, J.A. 2010, "Freezing and annealing phenomena in lyophilization", in *Freeze-drying/lyophilization of pharmaceutical and biological products.*, eds. L. Rey & J.C. May. Informa Healthcare, London, UK, pp. 52-81.

Searles, J.A., Carpenter, J.F. & Randolph, T.W. 2001a, "Annealing to optimize the primary drying rate, reduce freezing-induced drying rate heterogeneity, and determine Tg in pharmaceutical lyophilization", *Journal of Pharmaceutical Sciences,* vol. 90, no. 7, pp. 872-887.

Searles, J.A., Carpenter, J.F. & Randolph, T.W. 2001b, "The ice nucleation temperature determines the primary drying rate of lyophilization for samples frozen on a temperature-controlled shelf", *Journal of Pharmaceutical Sciences,* vol. 90, no. 7, pp. 860-871.

Seligmann, E.B. & Farber, J.F. 1971, "Freeze drying and residual moisture", *Cryobiology*, vol. 8, no. 2, pp. 138-144.

Shalaev, E. & Franks, F. 1996, "Changes in the physical state of model mixtures during freezing and drying: impact on product quality", *Cryobiology,* vol. 33, no. 1, pp. 14-26.

Shalaev, E. & Franks, F. 2002, "Solid-liquid state diagrams in pharmaceutical lyophilisation: crystallisation of solutes" in *Amorphous food and pharmaceutical systems*, ed. H. Levine, Royal Society of Chemistry, Cambridge, pp. 200-215.

Shalaev, E., Soper, A., Zeitler, J.A., Ohtake, S., Roberts, C.J., Pikal, M.J., Wu, K. & Boldyreva, E. 2019, "Freezing of aqueous solutions and chemical stability of amorphous pharmaceuticals: water clusters hypothesis", *Journal of Pharmaceutical Sciences*, vol. 108, no. 1, pp. 36-49.

Singh, K.J. & Roos, Y.H. 2007, "Frozen state transitions in freeze-concentrated lactose-protein-cornstarch systems", *International Journal of Food Properties,* vol. 10, no. 3, pp. 577-587.

Smith, G., Arshad, M.S., Polygalov, E. & Ermolina, I. 2013, "An application for impedance spectroscopy in the characterisation of the glass transition during the lyophilization cycle: the example of a 10% w/v maltodextrin solution", *European Journal of Pharmaceutics and Biopharmaceutics,* vol. 85, no. 3, Part B, pp. 1130-1140.

Smith, G., Arshad, M.S., Nazari, K., Polygalov, E., Ermolina, I., Taylor, J. & Page, T. 2014, "Through-vial impedance spectroscopy: a new in-line process analytical technology for freeze drying", *Pharmaceutical Technology,* vol. 38, no. 4.

Smith, G., Arshad, M.S., Polygalov, E. & Ermolina, I. 2014a, "Factors affecting the use of impedance spectroscopy in the characterisation of the freezing stage of the lyophilisation process: the impact of liquid fill height in relation to electrode geometry", *AAPS PharmSciTech,* vol. 15, no. 2, pp. 261-269.

Smith, G., Arshad, M.S., Polygalov, E. & Ermolina, I. 2014b, "Through-vial impedance spectroscopy of the mechanisms of annealing in the freeze-drying of maltodextrin: the impact of annealing hold time and temperature on the primary drying rate", *Journal of Pharmaceutical Sciences,* vol. 103, no. 6, pp. 1799-1810.

Smith, G., Arshad, M.S., Polygalov, E., Ermolina, I., McCoy, T.R. & Matejtschuk, P. 2017, "Process understanding in freeze-drying cycle development: applications for through-vial impedance spectroscopy (TVIS) in mini-pilot studies", *Journal of Pharmaceutical Innovation,* vol. 12, no. 1, pp. 26-40.

Smith, G., Duffy, A.P., Shen, J. & Olliff, C.J. 1995, "Dielectric relaxation spectroscopy and some applications in the pharmaceutical sciences", *Journal of Pharmaceutical Sciences*, vol. 84, no. 9, pp. 1029-1044.

Smith, G. & Jeeraruangrattana, Y. 2019a, "Electrical impedance methods for developing a lyophilization cycle", *ISLFD 2019-9th international symposium on lyophilization of pharmaceuticals, Ghent, Belgium, 2-6 September.*

Smith, G. & Jeeraruangrattana, Y. 2019b, "Through-vial impedance spectroscopy (TVIS): a new method for determining the ice nucleation temperature and the solidification end point" in *Freeze drying of pharmaceutical products*, eds. D. Fissore, R. Pisano & A. Barresi, 1st edn,.CRC Press, Florida, pp. 77-98.

Smith, G., Jeeraruangrattana, Y. & Ermolina, I. 2018, "The application of dual-electrode through vial impedance spectroscopy for the determination of ice interface temperatures, primary drying rate and vial heat transfer coefficient in lyophilization process development", *European Journal of Pharmaceutics and Biopharmaceutics,* vol. 130, pp. 224-235.

Smith, G. & Polygalov, E. 2019, "Through vial impedance spectroscopy (TVIS): a novel approach to process understanding for freeze-drying cycle development", in *Lyophilization of pharmaceuticals and biologicals: new technologies and approaches*, eds. K.R. Ward & P. Matejtschuk. Humana Press, New York, pp. 241-290.

Smith, G., Polygalov, E., Arshad, M.S., Page, T., Taylor, J. & Ermolina, I. 2013, "An impedance-based process analytical technology for monitoring the lyophilisation process", *International Journal of Pharmaceutics,* vol. 449, no. 1, pp. 72-83.

Smith, G., Polygalov, E. & Page, T. 2011, *Electrical monitoring of a lyophilization process*, GB2480299(A) edn, Great Britain.

Suherman, P.M. 2001, *A novel dielectric technique for monitoring the lyophilisation of globular proteins*. PhD thesis, De Monfort University.

Suherman, P.M., Taylor, P.M. & Smith, G. 2002, "Development of a remote electrode system for monitoring the water content of materials inside a glass vial", *Pharmaceutical Research,* vol. 19, no. 3, pp. 337-344.

Tang, X.C., Nail, S.L. & Pikal, M.J. 2006a, "Evaluation of manometric temperature measurement (MTM), a process analytical technology tool in freeze drying, part III: heat and mass transfer measurement", *AAPS PharmSciTech,* vol. 7, no. 4, pp. E105-E111.

Tang, X.C., Nail, S.L. & Pikal, M.J. 2006b, "Evaluation of manometric temperature measurement, a process analytical technology tool for freeze-drying, part I: product temperature measurement", *AAPS PharmSciTech,* vol. 7, no. 1, pp. E95-E103.

Tang, X.C., Nail, S.L. & Pikal, M.J. 2006c, "Evaluation of manometric temperature measurement, a process analytical technology tool for freeze-drying, part II: measurement of dry-layer resistance", *AAPS PharmSciTech,* vol. 7, no. 4, pp. E77-E84.

Tang, X.C., Nail, S.L. & Pikal, M.J. 2005, "Freeze-drying process design by manometric temperature measurement: design of a smart freeze-dryer", *Pharmaceutical Research,* vol. 22, no. 4, pp. 685-700.

Tang, X.C. & Pikal, M.J. 2004, "Design of freeze-drying processes for pharmaceuticals: practical advice", *Pharmaceutical Research,* vol. 21, no. 2, pp. 191-200.

Tchessalov, S. 2017, "Application of modeling to lyophilization process design and scale up: Process validation approaches". *The 8th International Conference of ISL-FD, 24-28 April*.

Thomas, L.C. 2005, *Modulated DSC: characterization of pharmaceutical materials*, TA Instruments, USA.

Tsotsas, E. & Mujumdar, A.S. (eds) 2011, *Modern drying technology, volume 3: product quality and formulation*, Wiley-VCH, Weinheim.

University of Washington 2018, n.d.-last update, *Impedance basics.* Available: https://www.cei.washington.edu/wordpress/wp-content/uploads/2018/05/EIS-and-NLEIS-Wiki.pdf [2020, 7/2/].

US Food and Drug Administration 2014, 11/11/-last update, Guide to inspections of lyophilization of parenterals. Available: https://www.fda.gov/inspections-compliance-enforcement-and-criminal-investigations/inspection-guides/lyophilization-parenteral-793 [2020, 1/2/].

Varghese, S., Kannam, S.K., Hansen, J.S. & Plasseril Sathian, S. 2019, "Effect of hydrogen bonds on the dielectric properties of interfacial water", *Langmuir,* vol. 35, pp. 8159-8166.

Wallaur, J. 2013, *RelaxIS 3 impedance spectrum analysis: user's manual*, Rhd instruments GmbH, Marburg.

Wang, B. & Pikal, M.J. 2012, "Stabilization of lyophilized pharmaceuticals by process optimization: challenges and opportunities", *American Pharmaceutical Review,* vol. 15, no. 6.

Wang, W. 2000, "Lyophilization and development of solid protein pharmaceuticals", *International Journal of Pharmaceutics,* vol. 203, no. 1–2, pp. 1-60.

Ward, K.R. & Matejtschuk, P. 2019, "Characterization of formulations for freeze-drying", in *Lyophilization of pharmaceuticals and biologicals: new technologies and approaches*, eds. K.R. Ward & P. Matejtschuk, 1st edn, Humana Press, New York, pp. 1-32.

Ward, K.R. & Matejtschuk, P. 2010, "The use of microscopy, thermal analysis, and impedance measurements to establish critical formulation parameters for freeze-drying cycle development", in *Freeze drying/lyophilization of pharmaceutical and biological products*, eds. L. Rey & J.C. May, 3rd edn, Informa Healthcare, London, pp. 111-135.

Wilson, P.W. & Haymet, A. 2009, "Effect of solutes on the heterogeneous nucleation temperature of supercooled water: an experimental determination", *Physical Chemistry Chemical Physics,* vol. 11, no. 15, pp. 2679-2682.

Xu, M., Chen, G., Zhang, C. & Zhang, S. 2017, "Study on the unfrozen water quantity of maximally freeze-concentrated solutions for multicomponent lyoprotectants", *Journal of Pharmaceutical Sciences,* vol. 106, no. 1, pp. 83-91.

Zaritzky, N. 2016, "Physical–chemical principles in freezing", in *Handbook of frozen food processing and packaging*, ed. D. Sun. CRC Press, Florida, pp. 3-38.

Publications

Journal articles

Smith, G., **Jeeraruangrattana, Y.** & Ermolina, I. 2018, "The application of dual-electrode through vial impedance spectroscopy for the determination of ice interface temperatures, primary drying rate and vial heat transfer coefficient in lyophilization process development", *European Journal of Pharmaceutics and Biopharmaceutics,* vol. 130, pp. 224-235.

Smith, G. & **Jeeraruangrattana, Y.** 2019, "Through-vial impedance spectroscopy (TVIS): A new method for determining the ice Nucleation temperature and the solidification end point", in *Freeze drying of pharmaceutical products*, eds. D. Fissore, R. Pisano & A. Barresi, 1st edn, CRC Press, Florida, United States, pp. 77-98.

Jeeraruangrattana, Y., Smith G., Polygalov E. & Ermolina, I. 2020, "Determination of ice interface temperature, sublimation rate and the dried product resistance, and its application in the assessment of microcollapse using through-vial impedance spectroscopy", *European Journal of Pharmaceutics and Biopharmaceutics,* vol. 152, pp. 144-163.

Poster presentations

Jeeraruangrattana, Y., Pandya, B., Ermolina, I. & Smith, G. 2016, The application of through vial impedance spectroscopy (TVIS) for optimisation freeze-drying. The International PharmTech Conference 2016, Leicester, UK, 4 November 2016.

Jeeraruangrattana, Y., Pandya, B., Vhokiwa, H., Shah, S. & Smith, G. 2016, The application of through vial impedance spectroscopy (TVIS) for optimisation freeze-drying. 5th Quality by Design Symposium, Leicester, UK, 29 March 2017.

Jeeraruangrattana, Y., Polygalov E., Ermolina, I. & Smith, G. 2017, "Prediction of the collapse of freeze-dried lactose solution using through-vial impedance spectroscopy (TVIS). 8th APS International PharmSci Conference, Hertfordshire, UK, 5-7 September 2017.

Jeeraruangrattana, Y., Polygalov E., Ermolina, I. & Smith, G. 2018, Application of impedance based technology to investigate the collapse of freeze-dried sugar-salt solutions. Freeze drying of pharmaceuticals and biologicals, Garmisch-Partenkirchen, Germany, 18-21 September 2018.

Jeeraruangrattana, Y., Polygalov E., Ermolina, I. & Smith, G. 2019, Through-Vial Impedance Spectroscopy (TVIS): A new approach to characterising phase transition of sugar-salt solutions. ISLFD 2019: 9th International Symposium on Lyophilization of Pharmaceuticals. Ghent, Belgium, 2-6 September 2019.

Pandya, B., Matejtschuk, P., **Jeeraruangrattana, Y.** & Smith, G. 2019, Multiplexing through vial impedance spectroscopy (TVIS) with comparative pressure measurement for the determination of the primary drying endpoint of immunoglobulin (IgG)". ISLFD 2019: 9th International Symposium on Lyophilization of Pharmaceuticals, Ghent, Belgium, 2-6 September 2019.

A Novel Process Analytical Technology (TVIS) for the Prediction of Micro-Collapse during a Freeze-Drying Process

Yowwares Jeeraruangrattana, Bhaskar Pandya, Harriet Vhokiwa, Shrinath Shah, Geoff Smith

Pharmaceutical Technologies, School of Pharmacy, De Montfort University, Leicester LE1 9BH

INTRODCTION During the primary drying stage of a freeze-drying cycle, an increase in product temperature above the glass transition temperature of the freeze concentrated solution, Tg', may cause the collapse of a freeze-dried cake (at a temperature known as the collapse temperature, Tc) with the possible rejection of the entire production batch. Consequently, the product is usually dried at a low temperature but at the expense of a more prolonged drying time. To achieve a cost-efficient cycle, with acceptable product quality, then the process should be designed with due consideration to this critical temperature.

QbD and the DESIGN SPACE

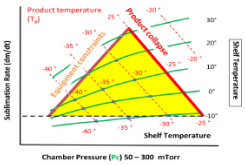

THE AIM is to evaluate the application of through vial impedance spectroscopy (TVIS) system for the prediction of micro-collapse during a freeze-drying cycle.

TVIS – Overview The TVIS system comprises a bespoke multichannel high precision impedance analyser which was connected to a TVIS measurement vial, which is a standard 10 mL.

freeze drying vial that has been modified with copper electrodes (19 x 10 mm) attached to the outside of the glass wall, thus making the measurement non-product invasive.

TVIS – Theory Two parameters, C''_{PEAK} and F_{PEAK} of the imaginary capacitance spectra of the TVIS vial (Fig.2) are considered to be invaluable in the assessment of a range of critical process parameters.

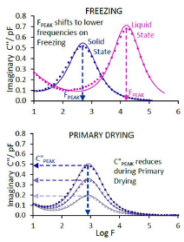

Fig.2 Imaginary capacitance spectra of the TVIS vial which demonstrates the principle changes in the dielectric loss peak during the freezing and drying stages of the cycle

F_{PEAK} may be used to predict the product temperature and for determining phase behaviour (ice formation, eutectic formation and glass transition events) *in situ*, whereas C''_{PEAK} can be used to determine the amount of ice remaining during the primary drying phase from which one can then predict both drying rate and end point (Smith et al. 2013).

HYPOTHESIS By combining an assessment of the drying rate with the predicted product temperature it might be possible to first witness the micro-collapse event while at the same time confirming the accuracy of the temperature prediction.

METHOD The electrical impedance of a 5%w/v lactose solution contained within modified glass freeze-drying vial was measured over the frequency range of 10 Hz to 1 MHz during an entire freeze-drying process. A critical feature of the drying cycle is the inclusion of a ramp in the shelf temperature during primary drying that will force the product through its collapse event.

RESULTS & DISCUSSION The correlation between Log F_{PEAK} from the TVIS vial and the thermocouple temperature in a neighbouring vial (Fig.?) provides an opportunity to calibrate the TVIS response to give a predictive temperature known as T-FPEAK.

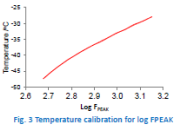

Fig. 3 Temperature calibration for log FPEAK

The premise for the prediction of the collapse event is the assumption that the calibration for the product temperature in the TVIS vial (as determined during the re-heating phase of the annealing stage) holds true during the primary drying stage, when the height of the ice layer in contact with the glass wall decreases progressively due to sublimation.

At 5.5 h into primary drying there is a significant increase in the rate of change of C''_{PEAK} which corresponds to an increase in drying rate as shown in Fig. 4a. This suggests there is a microscopic change in cake structure, due to micro-collapse, which results in an increase the pore size distribution in the freeze-dried matrix thereby decreasing the product resistance and consequently improving vapour flux. This suggestion is confirmed by cake morphology images of the middle layer by SEM as shown in Fig. 4(b). The predicted temperature at this point in time is equal to the collapse temperature (– 32 °C).

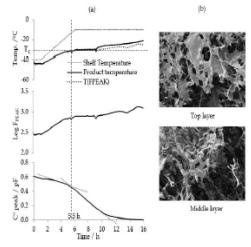

Fig. 3 (a) The temperature and TVIS parameter profile of 5%w/v lactose solution during the primary drying stage (b) SEM of top and middle layer of lactose cake at the end of the cycle

CONCLUSION A significant decrease in C"PEAK at the point of micro-collapse (as confirmed by SEM) highlights the potential for using TVIS for monitoring microscopic changes in the product resistance to vapour flow associated with the phenomenon of micro-collapse. This study also demonstrated a good correlation between TVIS data (Log FPEAK) and temperature of the frozen solution during the annealing stage of the cycle. By using a temperature calibration from the annealing stage it was possible to predict the onset of collapse

This study demonstrates the potential for TVIS to be used as a process control tool that would allow the cycle to be driven at the highest achievable temperature whilst avoiding collapse

G. Smith, E. Polygalov, M.S. Arshad, T. Page, J. Taylor, I. Ermolina, An impedance-based process analytical technology for monitoring the lyophilisation process, Int. J. Pharm. 449 (1–2) (2013) 72–83

Supervisor : Prof. G Smith

The Application of Through Vial Impedance Spectroscopy (TVIS) for Optimization Freeze-Drying Process

Yowwares Jeeraruangrattana and Bhaskar Pandya
Leicester School of Pharmacy, Faculty of Health and Life Sciences, De Montfort University
Supervisors: Professor Geoff Smith and Dr Irina Ermolina

"Non-invasive, real time lyophilisation process monitoring would increase process understanding and accelerate development of stabilized biopharmaceutical formulations at room temperature."

TVIS Technology

In-line monitoring system for the freeze drying process consisting of:
- Freeze-drying vial with external electrodes
- Pass through for cabling
- External Impedance spectrometer.

TVIS Advantage

1. Non-invasive, real time full cycle lyophilisation monitoring including :
   - Cooling rate, Freezing and Annealing
   - Primary and Secondary Drying end point
2. Optimization of the primary drying process by:
   - Heat Transfer Coefficient (K_V) Determination
   - Dried Product Resistance (R_P) Determination
3. Can be applied in standard freeze dryers
4. Integrated, bench top, single vial, TVIS enabled analytical freeze dryer

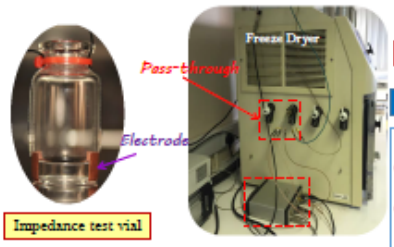

Figure 1. TVIS Technology

TVIS Technology Principle

Process analytical technology based on impedance spectroscopy
- Electrical impedance determines the ability of materials to conduct electricity under an applied voltage .
- Impedance is a function of dielectric and conductive properties and therefore the physical state of vial and its contents.
- Principal parameter effecting measured impedance is resistance/conductivity of sample within the vial.
- Changes in electrical parameters mirror the condition of the sample throughout the lyophilisation process.
- The capacitance spectrum is related to *the resistance/ conductivity and capacitance of the vial contents*
- Data viewing software (LyoView ™) identifies the peak frequency (F_{PEAK}) and the peak amplitude (C''_{PEAK}) in the imaginary part of the capacitance spectrum
- F_{PEAK} can be used to monitor phase behaviour (ice formation, glass transitions) and product temperature
- C''_{PEAK} can be used to monitor the amount of ice remaining during primary drying, from which the drying rate and the end point may be determined.

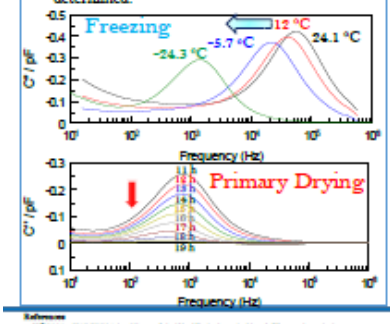

TVIS APPLICATIONS

Heat Transfer Coefficient (K_V) Determination

- The product temperature ($T_{PRODUCT}$) derived by ***TVIS*** is one of the parameters needed for K_V determination
- Sublimation rate or drying rate (dm/dt) is estimated by ***TVIS***

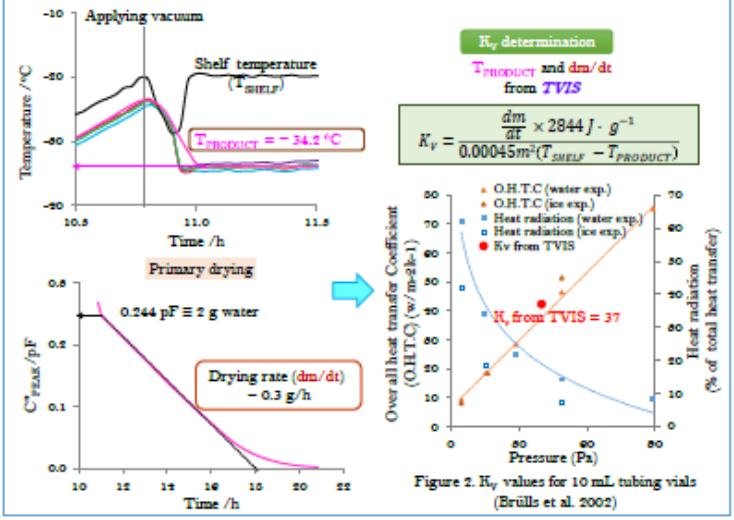

Figure 2. K_V values for 10 mL tubing vials (Brülls et al. 2002)

Dried Product Resistance (R_P) Determination

- C''_{PEAK} from ***TVIS*** is proportional to the amount of ice, therefore it is estimated for drying rate (dm/dt)
- Partial pressure of ice (P_{ICE}) and condenser ($P_{CONDENSER}$) calculated from temperature of ice (T_{ICE}) and condenser ($T_{CONDENSER}$) by using Clausius- Clapeyron derived equation

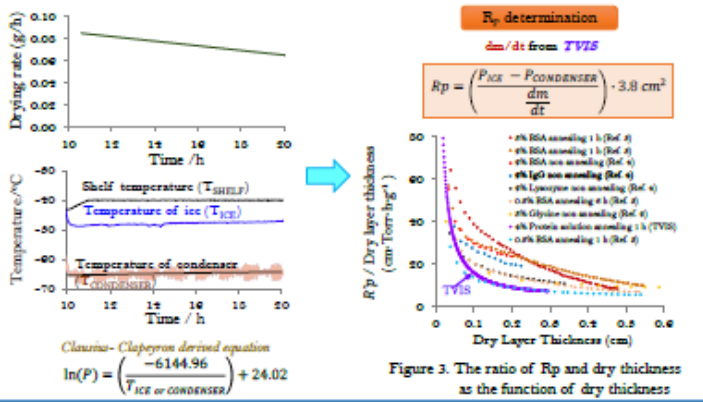

Figure 3. The ratio of Rp and dry thickness as the function of dry thickness

References

Prediction of the Collapse of Freeze-Dried Lactose Solution using Through Vial Impedance Spectroscopy (TVIS)

Yowwares Jeeraruangrattana, Eugene Polygalov, Irina Ermolina , Geoff Smith

Pharmaceutical Technologies Group, Leicester School of Pharmacy, De Montfort University, UK

Introduction

- Collapse is referred as the loss of the pore structure of freeze-dried cake whereas **"Micro-collapse"** is an intact cake with increasing pore in dried layer and can promote drying.

- **Dry product resistance (R_P)** is one of critical variables having a great impact on primary drying process.
- R_P is defined as the resistance to mass flow of water vapour from the product through the pores structure in the dried layer and can be expressed by:

$$\frac{dm}{dt} = A_p \frac{\Delta P}{R_P}$$

where $\frac{dm}{dt}$ is the drying rate (g/h/vial), A_p is the internal cross-sectional area of the vial, ΔP is the pressure difference between pressure of ice at sublimation interface and chamber pressure and R_P is the area normalized resistance of the dried product.

- An increase in product temperature during primary drying stage above the **Collapse Temperature (To)** may cause the collapse of a freeze-dried cake with the possible rejection of the entire production batch
- Collapse temperature could be determined by
  - A freeze-drying microscope (FDM)
  - An optical coherence tomography based freeze drying microscopy (OCT-FDM), Mujat (2012)
- However, these current techniques have some limitations
  - FDM → Off-line measurement, Not always provide the information of micro-collapse, Varshney (2015)
  - OCT-FDM → Single vial technique
- **Through vial impedance spectroscopy (TVIS)**,a novel non-invasive techniques has been shown previously to be sensitive to the collapse event itself, through dramatic changes in the electrical capacitance of a solution filled in freeze-drying vial, Smith (2014).

Aim

- To evaluate the application of TVIS system for the prediction of micro-collapse during a freeze-drying cycle.

Materials and Methods

- The electrical impedance of a 5%w/v lactose solution contained within modified glass freeze-drying vial (TVIS vial, Fig.1A) was measured over the frequency range of 10 Hz to 1 MHz by using TVIS system during a freeze-drying process.
- A full load of vials with TVIS vial at the center (Fig.1B) was then placed on a single shelf of a Virtis Advantage Plus benchtop Freeze-dryer.
- A freeze drying protocol with an annealing step is performed to dry the solution. A critical feature of the drying cycle is the inclusion of a ramp in the shelf temperature during primary drying that will force the product through its collapse event.
- Scanning electron microscopy (SEM) images of the freeze-dried cake were acquired at a 500x magnification.

Fig. 1. (A) TVIS vial (left) and a neighboring vial with thermocouple (right), (B) The cluster of vials with TVIS vial at center

Results and Discussions

- The correlation between $\text{Log}F_{PEAK}$ from TVIS vial and the thermocouple temperature in a neighboring vial of the re-heating part of annealing step (Fig.2A) provides a predictive product temperature at primary drying process defined as T-FPEAK (Fig.2B).
- The decrease in C^*_{PEAK} parameter corresponding to the amount of ice bounded within electrode region can be used to estimate drying rate. However, this parameter also depends on temperature. As the temperature is increased, C^*_{PEAK} value increases (Fig.2C). Therefore, the temperature compensation for this parameter defined as normalized C^*_{PEAK} ($\hat{C}^*_{PEAK}$) is required (Fig.2D) by using the **temperature correction factor (ϕ)** which is calculated from the re-heating phase of the annealing stage and C^*_{PEAK} at starting temperature of primary drying as the reference value.
- C^*_{PEAK} can be normalized by the following equation:

$$\hat{C}^*_{PEAK} = \frac{C^*_{PEAK}(T_t)}{\phi}$$

where $C^*_{PEAK}(T_t)$ is C^*_{PEAK} at time (t) and temperature (T) during primary drying and ϕ is the temperature correction factor from C^*_{PEAK} calibration of re-heating step

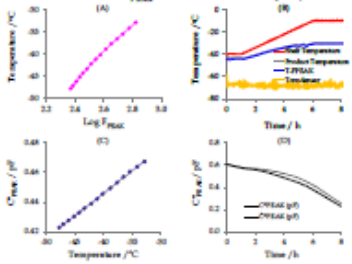

Fig. 2. The temperature and TVIS parameters profile of 5%w/v lactose solution during the primary drying stage. (A) Temperature calibration from re-heating step, (B) a predictive temperature during primary drying, (C) C^*_{PEAK} calibration from re-heating step and (D) Temperature-compensated C^*_{PEAK} ($\hat{C}^*_{PEAK}$)

- At 4.8 hour into primary drying there is a significant increase in the rate of change of $\hat{C}^*_{PEAK}$ which corresponds to an dramatic increase in drying rate as shown in Fig.3B. This suggests there is a microscopic change in cake structure, due to micro-collapse, which results in an increase the pore size distribution in the freeze-dried matrix thereby decreasing the product resistance (Fig.3C) and consequently improving vapour flux. The predicted temperature at this point in time is equal to the collapse temperature of – 32 °C (Fig.3A).
- This suggestion is confirmed by cake morphology images by SEM as shown in Fig.3E. At dried layer thickness of 0.27 cm corresponding to 4.8 hour of primary drying Fig.3D, a micro-collapse layer has developed which can be demonstrated by SEM as larger pores in middle layer.

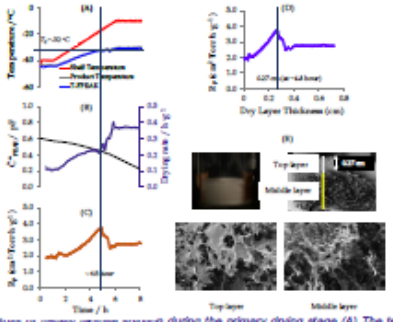

Fig. 3. Results of drying lactose solution during the primary drying stage (A) The temperature (T-FPEAK) profile, (B) $\hat{C}^*_{PEAK}$ parameters and drying rate over drying period, (C) Product resistance (Rp) as a function of drying time, (D) Product resistance (Rp) as a function of dry layer thickness and (E) SEM of top and middle layer of lactose cake at the end of the cycle.

Conclusions

- A significant decrease in $\hat{C}^*_{PEAK}$ at the point of micro-collapse (as confirmed by SEM) highlights the potential for using TVIS for monitoring microscopic changes within cake during primary drying step.
- This study demonstrates a prospective use of TVIS as a process control tool that would allow the cycle to be driven at the highest achievable temperature whilst avoiding collapse.

References

Mujat, M., Greco, K., Galbally-Kinney, K.L., Hammer, D.X., Ferguson, R.D., Iftimia, N., Mulhall, P., Sharma, P., Pikal, M.J., Kessler, W.J., 2012. Optical coherence tomography-based freeze-drying microscopy. Biomed. Opt. Express, 3, 55-63.

Smith, G., Arshad, M.S., Nazari, K., Polygalov, E., Ermolina, I., Taylor, J., Page, T., 2014. Through-Vial Impedance Spectroscopy: A New In-Line Process Analytical Technology for Freeze Drying. Pharm Technol, 38.

Varshney, D., Singh, M., 2015. Lyophilized Biologics and Vaccines: Modality-Based Approaches., Springer, New York.

Acknowledgements

GEA Pharma Systems and AstraZeneca (2008-12) and co-funded by Innovate UK (formerly the Technology Strategy Board).

Through Vial Impedance Spectroscopy

Application of Impedance Based Technology to Investigate the Collapse of Freeze-dried Sugar-salt Solutions

Yowwares Jeeraruangrattana, Irina Ermolina, Eugene Polygalov, Geoff Smith

Pharmaceutical Technologies Group, Leicester School of Pharmacy, De Montfort University, UK

dmu.ac.uk DE MONTFORT UNIVERSITY LEICESTER

INTRODUCTION

During primary drying, an increase in product temperature above the glass transition temperature of a freeze-concentrated solution (T'_g) may provide a more efficient freeze drying process. However, it is essential to control the product temperature below its collapse temperature (T_c) to avoid a loss of cake structure leading to a decrease in sublimation rate. Moreover, a collapsed cake typically has a high moisture content which may then impact product quality in terms of the appearance and stability critical quality attributes.

Recently, an impedance based technique known as **Through Vial Impedance Spectroscopy (TVIS)** has been shown to be sensitive to the collapse event through the changes in the electrical capacitance of the sample filled in TVIS vial (Smith, et al. 2014). In this study, the impact of microcollapse on the primary drying process of sugar-salts preparations is observed using TVIS technology.

AIMS

To evaluate the applicability of TVIS system for the impact of collapse on the sublimation rate during a freeze-drying cycle

MATERIALS AND METHODS

Instrument / Sensor	Measurement / Process
TVIS	Electrical capacitance of TVIS vial containing sample measured every 2 min during freeze drying process
Thermocouple	Thermocouple temperature in nearest neighbour vial provides predictive temperature of TVIS vial (calibration)
VirTis Advantage Plus Freeze-dryer (lab scale)	Freeze drying with a reheating (temperature calibration) step and ramping during primary to to force the product through collapse
Differential scanning calorimetry (DSC)	Critical product temperature (T'_g)
Digital camera	Photographic image for observation of visual collapse event

Sample preparations

Sample	Sucrose (%)	NaCl (%)
S-1	5.00	0.00
S-2	5.00	0.26
S-3	5.00	0.55

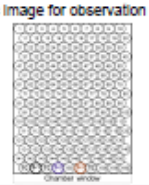

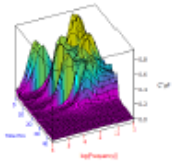

RESULTS AND DISCUSSION

- The correlation between $Log\ F_{PEAK}$ and temperature of neighboring TC containing vial, during re-heating step (Fig.1a-c), predicts the in-vial temperature ($T_{P(PEAK)}$) during primary drying (Fig.1d-f)
- Predicted temperature from the TVIS measurement system ($T_{P(PEAK)}$) before the temperature was ramped (23.3-23.6 hour) were -36, -37 and -38 °C respectively for the solutions of 5% sucrose with 0%, 0.26% and 0.55% NaCl (Fig.1d-f). However, only pure sucrose had a product temperature lower than its respective T'_g (-34 °C from DSC) as shown in Fig.1d
- Higher surrogate drying rates (i.e. the rate of change in the C'_{PEAK} value which is proportional to the amount of ice) of 0.06 and 0.09 pF/h were found in sample with 0.26 and 0.55% NaCl (Fig.1h-i) as compared with the formulation without NaCl (0.04 pF/h) in Fig.1g .
- This finding suggests an alteration in microstructure that was not seen in the photographic evidence, which could promote mass flux due to an increase in pore size (microcollapse) (Milton, et al. 1997).

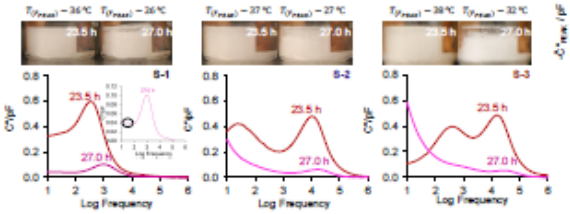

Fig.2 Image and imaginary capacitance of three sugar-salt solutions demonstrating the progression of collapse over drying period; without the loss of macroscopic structure at 23.6 hour and macro-collapse at 27.0 hour

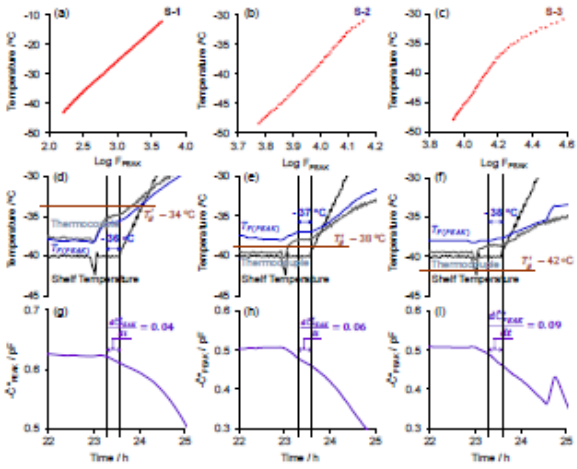

Fig.1 TVIS parameters of three sugar-salt solutions during freeze drying; (a-c) temperature calibration from re-heating step, (d-f) a predicted temperature during primary drying, (g-i) surrogate drying rate calculated from temperature-compensated C'_{PEAK} ($\tilde{C}'_{PEAK}$)

- Later in the cycle when the temperature was ramped (after 26 hour), a significant change in a capacitance spectrum, at low frequency range in particular, appeared to relate to the loss in macroscopic structure or macro-collapse as confirmed by the photographic images (Fig.2)

CONCLUSIONS

TVIS is a promising tool that would allow to the design the efficient process whilst avoiding collapse.

REFERENCES

Smith, G., Arshad, M.S., Nazari, K., Polygalov, E., Ermolina, I., Taylor, J., Page, T., 2014. Through-vial impedance spectroscopy: a new in-line process analytical technology for freeze drying. Pharm Technol, 38.

Milton, N., Pikal, M.J., Roy, M.L., Nail, S.L., 1997. Evaluation of manometric temperature measurement as a method of monitoring product temperature during lyophilization. PDA J Pharm Sci Technol, 51, 7-16

TVIS Through Vial Impedance Spectroscopy

Through-Vial Impedance Spectroscopy (TVIS): A New Approach to Characterizing Phase Transition of Sugar-Salt Solutions

Yowwares Jeeraruangrattana, Eugene Polygalov, Irina Ermolina, Geoff Smith
DMU LyoGroup, School of Pharmacy, De Montfort University, UK
ISL-FD's 9th International Conference, 2-6 September 2019, Ghent University, Belgium

DE MONTFORT UNIVERSITY LEICESTER

INTRODUCTION

The development of a robust freeze-drying product and processes necessitates an understanding of the in-vial characteristics during processing especially freezing stage. The majority of techniques up to date for determining ice nucleation are restricted to the off-line instrument. Through-vial impedance spectroscopy (TVIS) is a relatively new technique which could explore the different facets of the in-situ material behaviour under freezing process (i.e. ice nucleation to solidification end points); however, the TVIS applications for the determination ice nucleation process have been recently restricted to the low-conductivity solutions such as pure water [1].

AIM

In this study, other features of TVIS system were explored to develop a new approach for determining nucleation process of conductive samples.

EQUIPMENT

Instrument / Sensor	Measurement / Process
TVIS	Electrical capacitance of TVIS vial containing sample measured every 2 min during freezing
Thermocouple	Thermocouple temperature in the nearest neighbour vial provides predictive temperature of TVIS vial (calibration)
VirTis Advantage Plus Freeze-dryer	Freezing from +20 to −45 °C at 0.5 °C·min^{-1}
Digital camera	Photographic image for observation of ice nucleation event

MATERIALS & METHODS

Sample	Sucrose (%)	NaCl (%)
S-1	5.00	0.00
S-2	5.00	0.26
S-3	5.00	0.55

1. In-vial measurement

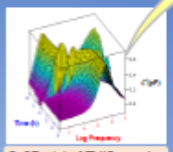

2. 3D-plot of TVIS spectra

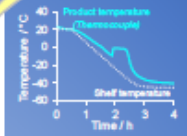

3. Freezing sample

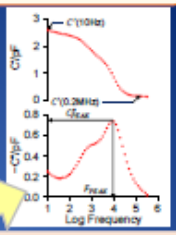

5. Identifying TVIS parameters using LyoView software

4. Monitoring nucleation event

RESULTS & DISCUSSIONS

- Inflections in the time profiles of TVIS parameters [C'_{PEAK}, F_{PEAK} and C'(10Hz)] corresponded with the onset of ice nucleation of 5% sucrose (as confirmed by images) as demonstrated in Fig 1b – 1e.
- However, samples having the higher conductivity (5% sucrose with either 0.26% or 0.55% NaCl), the relaxation process before frozen could not be detected by TVIS system (Fig 1l – 1j and Fig 1p – 1q, for 0.26% and 0.55% NaCl respectively). This could be exemplified by the spectrum of liquid state of sugar-salts solution (Fig 1n & Fig 1u) and pure sugar (Fig 1g). Hence, only real part capacitance at 10 Hz was used to indicate the onset of ice formation in a high conductive solution (Fig 1k & 1r).

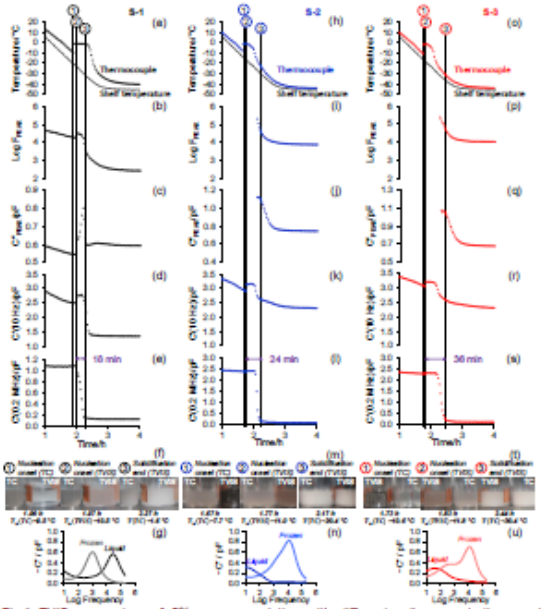

Fig.1 TVIS parameters of 5% sucrose solution with different salt concentrations and images during freezing; (a-g) 0% NaCl, (h-n) 0.26% NaCl, (o-u) 0.55% NaCl

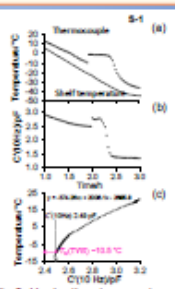

Fig.2 Nucleation temperature of 6% sucrose predicted by TVIS C'(10Hz) [T_n(TVIS)]

- TVIS vial generally nucleate later than TC vial due to the impact of thermocouple probe. In this case, the nucleation temperature can be predicted by fitting a curve to the plot of temperature from neighboring vial (TC vial) against TVIS parameter [i.e. C'(10Hz)] as demonstrated in Fig 2c, which are −10.5, −11.0 and −11.8 °C respectively for the solutions of 5% sucrose with 0, 0.26 and 0.55% NaCl (Fig 3).

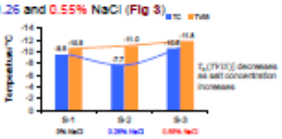

Fig.3 Nucleation temperature of sugar-salt solutions predicted by TVIS parameter $C'(10Hz)$

- At 200 kHz or 0.2MHz (which is well above the ice relaxation frequency of 1 kHz), the capacitance of ice has almost no temperature dependence and so any changes in C'(0.2MHz) either with time or temperature, can be associated with the completion of ice formation on freezing (Fig 4b). Here, the end point of solidification for 5% sucrose with 0, 0.26 and 0.55% NaCl were 2.27, 2.17 and 2.43 h, respectively.
- By using the time different between nucleation point (Fig 4a) and solidification end point (Fig 4b), ice forming duration was obtained. The results were reported in Fig 6, and also demonstrated a twofold increase in the solidification time as salt concentration increases from 0 to 0.55 %.

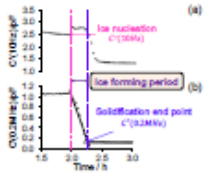

Fig.4 Determination of nucleation period of 6% sucrose by TVIS

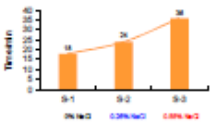

Fig.6 Time required for complete solidification of sugar-salt solutions estimated by real part capacitance at 10Hz and 0.2MHz by TVIS

CONCLUSION

TVIS creates new opportunities to detect phase change during freezing process including the nucleation onset and the solidification end point.

REFERENCE

[1] G. Smith, E. Polygalov, M.S. Arshad, T. Page, J. Taylor, I. Ermolina, An impedance-based process analytical technology for monitoring the lyophilisation process, Int. J. Pharm. 449 (2013) 72-83.

TVIS Through Vial Impedance Spectroscopy

@LyoGroupDMU

DMU LyoGroup

Multiplexing Through Vial Impedance Spectroscopy (TVIS) with Comparative Pressure Measurement for the Determination of the Primary Drying Endpoint of Immunoglobulin (IgG)

ISL-FD's 9th International Symposium on Lyophilization of Pharmaceuticals, September 2-6, 2019, Ghent, Belgium

Bhaskar Pandya[a], Paul Matejtschuk[b], Yowwares Jeeraruangrattana[a], Geoff Smith[a], Irina Ermolina[a]
[a]Leicester School of Pharmacy, De Montfort University, Leicester, United Kingdom
[b]National Institute of Biological Standards and Control (NIBSC), Potters Bar, United Kingdom

Introduction

- Attaining a long-term stability by freeze-drying can be attractive as it can **eliminate the need for cold chain storage** of biopharmaceutical products (e.g. proteins).
- A precise determination of the point of **complete ice removal** during primary drying has been one of the strategies for avoiding product collapse or eutectic melt [1].
- Common batch techniques include the **comparative pressure measurement**: the Pirani gauge (more sensitive to the water vapour) with a capacitance manometer (CM) (controls the absolute pressure of the chamber). The point at which the Pirani pressure approaches that of CM is taken as the endpoint for the whole batch [2].
- Single vial techniques (e.g. thermocouples, resistance temperature detectors, etc) involve inserting an **invasive probe** into the product to measure the product temperature, which when equals the shelf temperature, is generally taken as the endpoint for the batch; but it is known that **probe containing vials dry faster** than the vials without the invasive probes and front row **edge vials** receive an additional heat contribution via **heat radiation** from the Plexiglass door [3].
- Through Vial Impedance Spectroscopy (TVIS) **senses the amount of ice in the vial in real time** by measuring the dielectric properties of the frozen solid by employing a pair of copper electrodes attached externally to a single vial (i.e. **non-product invasive**) [4].
- Previously, the time-line of the imaginary part capacitance at 1 kHz, C''(1kHz), has been used to determine the primary drying endpoint for a simple sucrose solution [4].

Aim and Objectives

The aim of this study is to develop an impedance-based methodology to determine the primary drying endpoint with the following objectives:

- to use the time-line of the C'(100kHz) parameter for determining the primary drying endpoint of ice in a complex protein formulation located at the edge and the core
- to compare the endpoint from TVIS with the endpoint given by the comparative pressure measurement

Materials and Methods

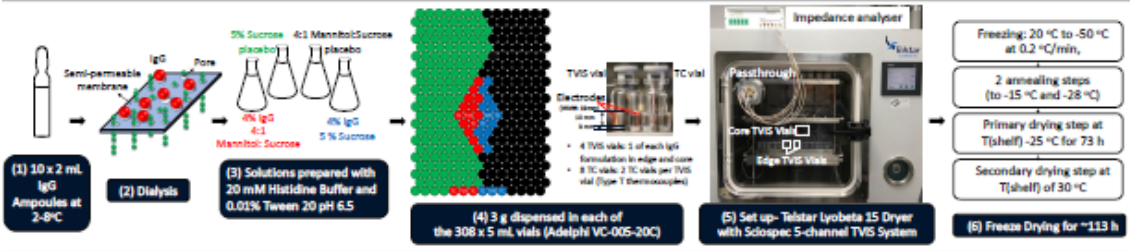

Results and Discussion

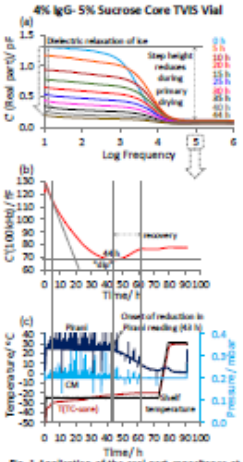

Fig. 1 Application of the real part capacitance at 100 kHz, i.e. C'(100kHz): TVIS is most sensitive to the height of the ice cylinder in intimate contact with the glass wall in the region bounded by the electrodes. When the ice mass retracts from the glass wall, the characteristic "dip" and recovery in C'(100kHz) are subsequently used to track the point of complete ice removal in a single vial.

- The dielectric relaxation of ice was characterized by a step in the real part around 10 kHz (Fig.1a) where,

$$Step\ Height \cong C'(10Hz) - C'(100kHz)$$

- The step height is proportional to the height of the sublimation front which manifests as an ice cylinder when it is in intimate contact with the glass wall bounded by the electrodes.
- For the IgG-sucrose formulation in the core vial, the step height had decreased by 85% by ~44 h, yet the Pirani vapour pressure was still approaching the CM value (Fig.1c).
- The time-line of C'(100kHz) was then used to track sublimation and understand the changes in the shape of the sublimation interface (Fig.1b).
- First 5 h: C'(100kHz) decreased linearly with time; suggests the sublimation front was drying in a horizontal plane.
- 5 to 44 h: the rate of decrease in C'(100kHz) exhibited a non-linear behavior; suggests the shape of the sublimation front had changed over this period.
- At 44 h: a characteristic dip in the time-line was observed; corresponds to the point when the ice mass had retracted from the glass wall.
- After 44 h: C'(100kHz) started to recover as it was still sensitive to the remaining ice mass.
- In Fig.2(b to e), the inflection in time-line of d(C'100kHz)/dt after the completion of the C'(100kHz) recovery was used as an endpoint indicator for all TVIS vials.
- **Endpoint Summary:** Sucrose-IgG edge vial (Fig.2b) dried 11 h earlier than the onset of the reduction in the Pirani vapour pressure (43 h). In addition, the TVIS endpoint for both core TVIS vials (Fig.2d&e) occurred at 62 h and yet the Pirani was still active until 73 h. This may be due to one or both of two factors: (i) other core vials were still drying (most probable) and/or (ii) the Pirani continued to sense water vapour in the dryer even when all the ice had sublimed (least probable).

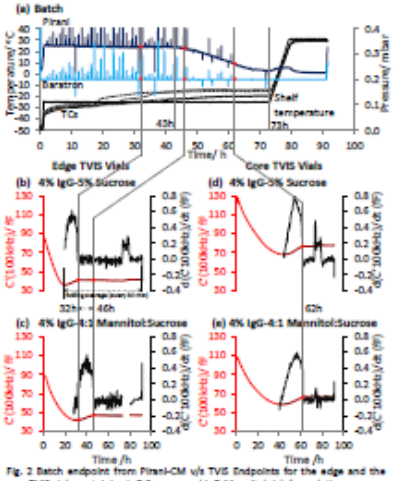

Fig. 2 Batch endpoint from Pirani-CM v/s TVIS Endpoints for the edge and the core TVIS vials containing IgG-Sucrose and IgG-Mannitol rich formulations

TVIS Vial Location	4% IgG with 5% Sucrose	4% IgG with 4:1 Mannitol:Sucrose IgG
Front Edge	32 h	46 h
Core	62 h	62 h

Conclusion

- Core vials may take almost twice as long to dry than edge vials and/or not all core vials dry at the same time.
- TVIS used in conjunction with batch sensors can enhance one's understanding of the hot and cold spots on the shelf.

References

[1] S.M. Patel, T. Doen, M.J. Pikal, Determination of End Point of Primary Drying in Freeze-Drying Process Control, Aaps Pharmscitech 11 (2010) 73-84.
[2] S.L. Nail, W. Johnson, Methodology for in-process determination of residual water in freeze-dried products, Dev. Biol. Stand. 74 (1992) 137.
[3] S. Nail, S. Tchessalov, E. Shalaev, A. Ganguly, E. Renzi, F. Dimarco, L. Weglel, S. Ferris, W. Kessler, M. Pikal, G. Sacha, A. Alexeenko, T.N. Thompson, C. Reiter, J. Searles, P. Colteux, Recommended Best Practices for Process Monitoring Instrumentation in Pharmaceutical Freeze Drying—2017, Aaps Pharmscitech 18 (2017) 2379-2393.
[4] G. Smith, E. Polygalov, M.S. Arshad, T. Page, J. Taylor, I. Ermolina, An impedance-based process analytical technology for monitoring the lyophilisation process, Int. J. Pharm. 449 (2013) 72-83.

Acknowledgements

This study was undertaken as part of the Innovate UK AtlasBio Project. Special thanks to Dr Paul Matejtschuk and team at NIBSC.

Appendix I

Standard operating procedure for assembling a copper foil electrode and wiring of a TVIS measurement vial

Components and equipment

The following components and equipment are required for wiring the measurement vial:

Components	Illustrations
Glass vial	
Ethanol & cleaning cloth	  Cleaning cloth
Copper electrode tape	
Scalpel	

Ruler	
Electrode trimmer	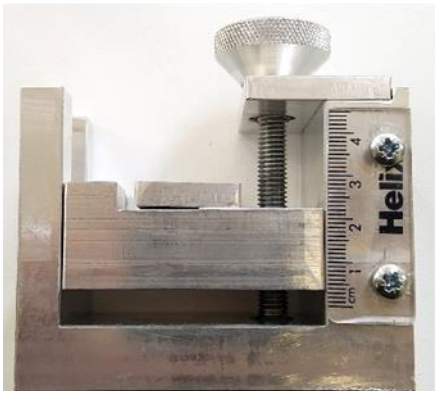 *Side view*  *Front view*
Holding clamp	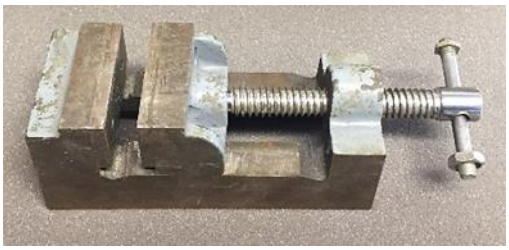
Heat glue rod	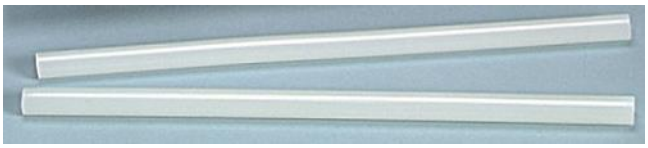
Cutter	
Tweezer	

Soldering wire (solder)	
Cable	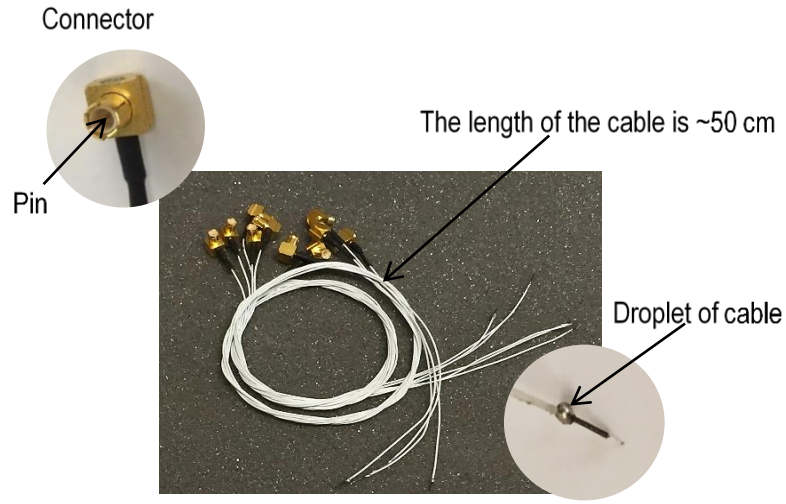
Digital soldering station	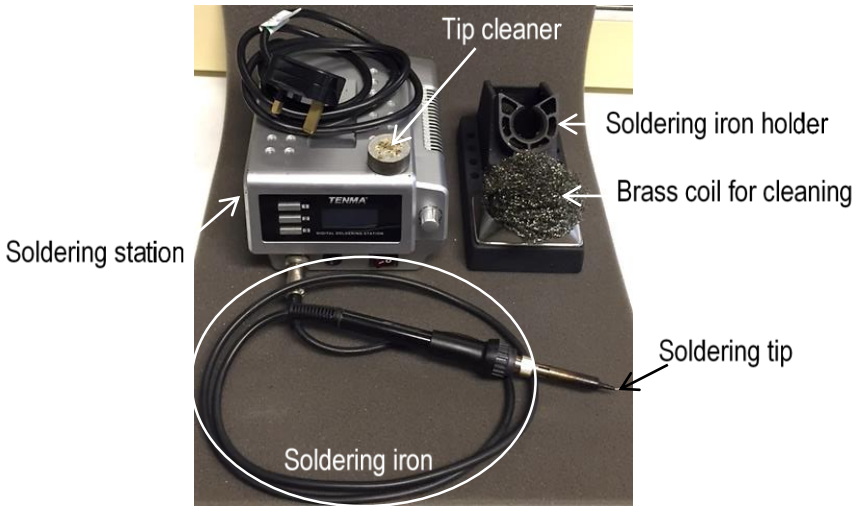

Blow torch	
Heat shrink tubing	
Digital multimeter	

Procedure

There are four main steps in wiring the measurement vial for the TVIS system:

1. Electrode attachment
2. Wiring the cable
3. Check for an integrity
4. Check a measurement signal

1. Electrode attachment

1.1 Clean the external surface of the glass vial with ethanol and cleaning cloth (Figure 1). The vial must be well-cleaned (free from dust and contamination, including fingerprints).

Figure 1 Cleaning the external surface of the vial

1.2 Draw lines for two identical size of electrodes on copper electrode tape (Figure 2). The electrode size should be oversized in height with 19 mm width. The bottom and top parts of this electrode will be removed to arrive the target electrode height at the target separation from the base. For instance, if the user requires the electrode to be of 10 mm height and located 1 mm above the base of the vial, the electrode height should be at least 12 mm (Figure 2).

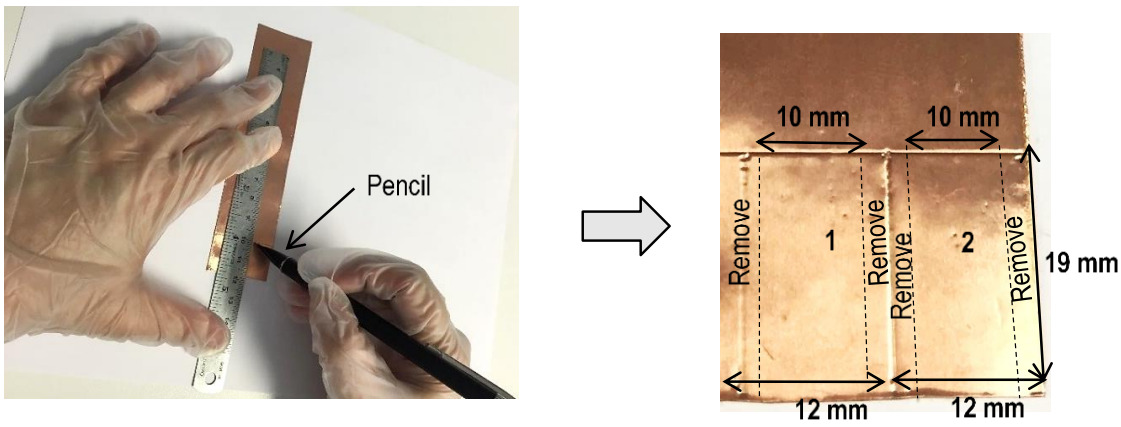

Figure 2 Preparation of copper electrodes

1.3 With a scalpel, cut the copper electrode tape obtained from step 1.2 according to a line drawn into the oversized strip, as shown in Figure 3.

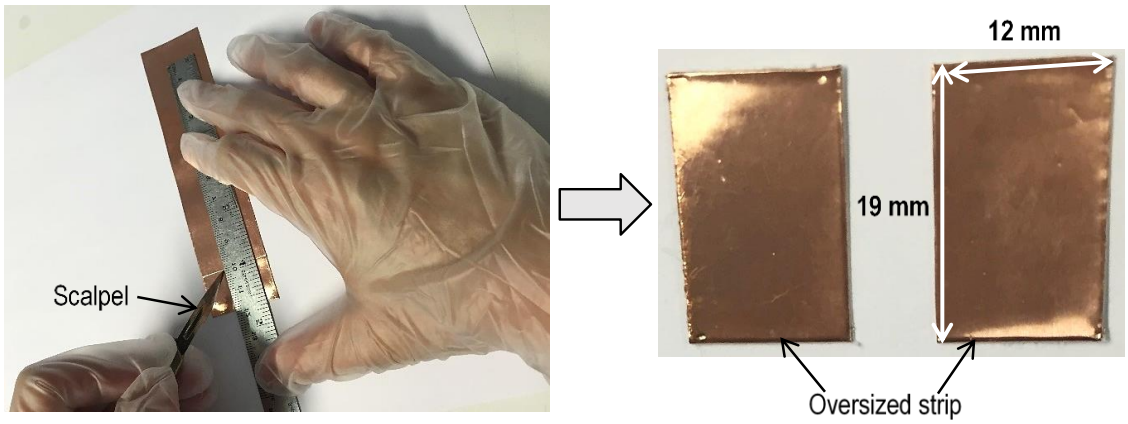

Figure 3 The oversized electrode strips

1.4 Mark two points opposite each other on the vial to indicate the electrode position by using an elastic band marker (Figure 4).

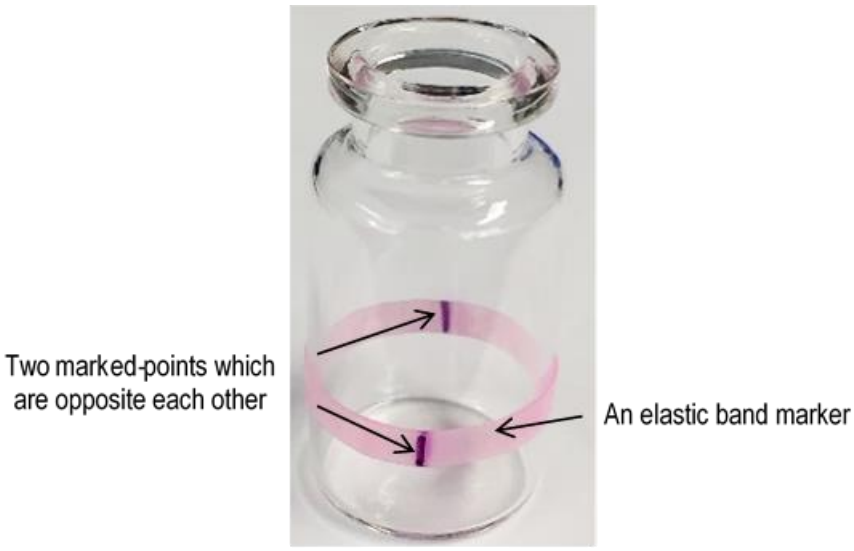

Figure 4 Mark electrode positions on the vial

1.5 Remove the liner of copper electrode strip from step 1.3 and attach this electrode at the marked position on the vial (Figure 5). Then once the electrode is attached, press it and the vial tightly together.

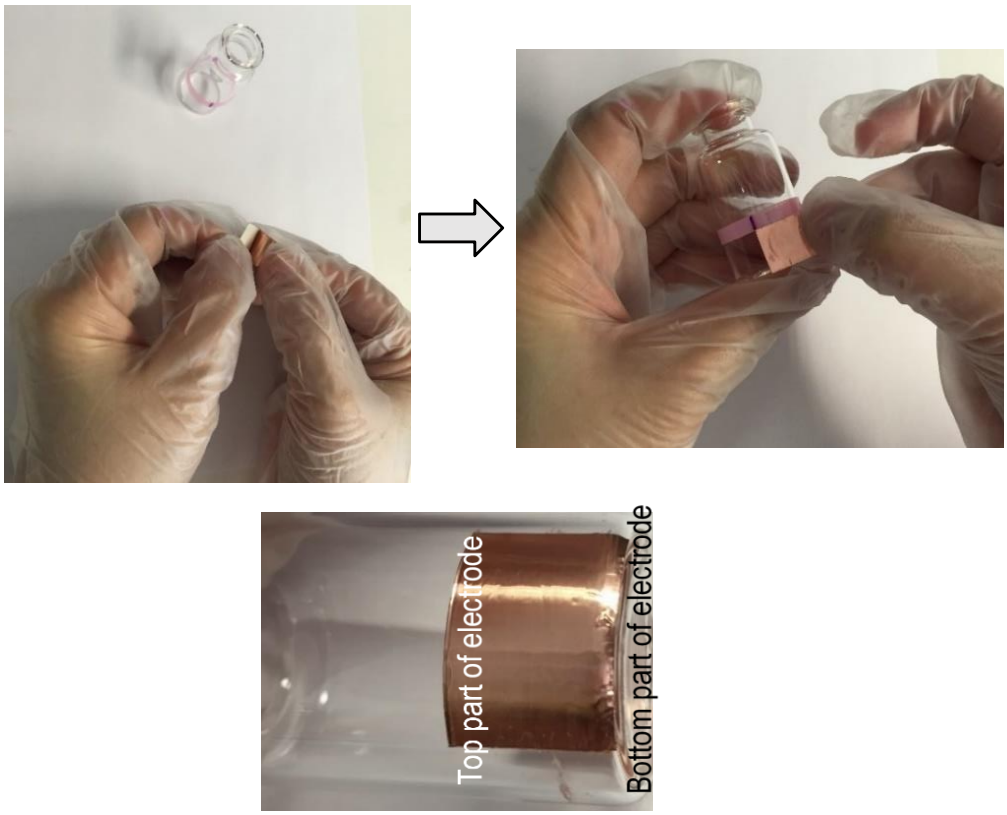

Figure 5 Copper electrodes attached on the vial

1.6 Set the scale of an electrode trimming machine at the electrode position from the vial's base (e.g. 1 mm) and then remove the bottom part of the copper electrode attached to the vial to get the target position above the base by using the electrode trimmer (Figure 6).

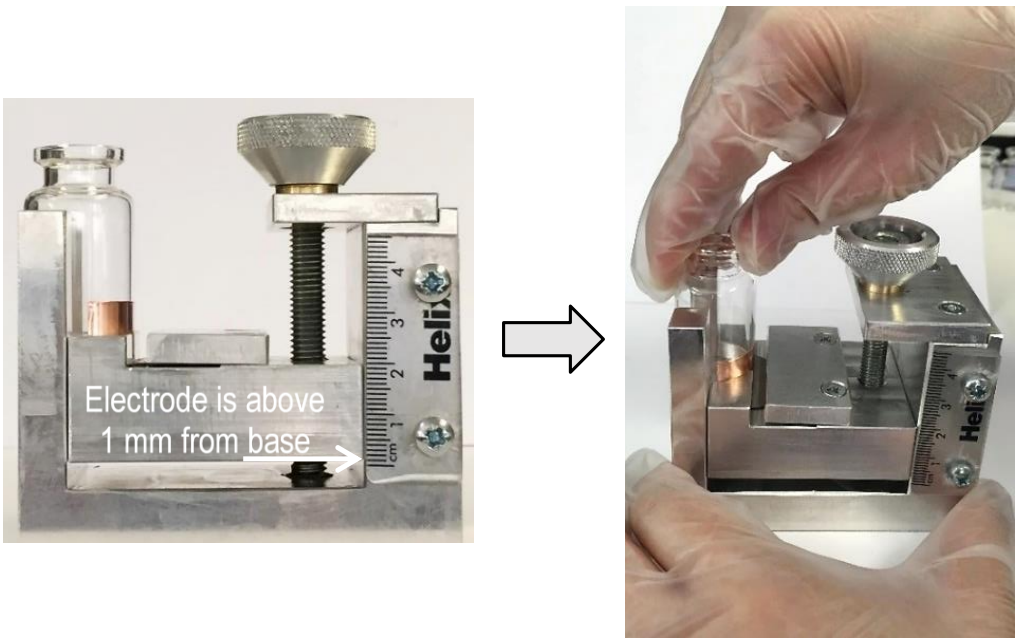

Figure 6 Trimming the bottom part of copper electrodes attached to the vial

1.7 Set the scale of an electrode trimming machine for the position of the top edge of electrode from the vial's base. For example, if the user requires the electrode height of 10 mm and the electrode positioned at 1 mm from the base, the scale of the electrode trimmer has to be set at 11 mm (10 + 1 mm) and then remove the top part of copper electrode attached to the vial to get the target electrode height by using the trimmer (Figure 7).

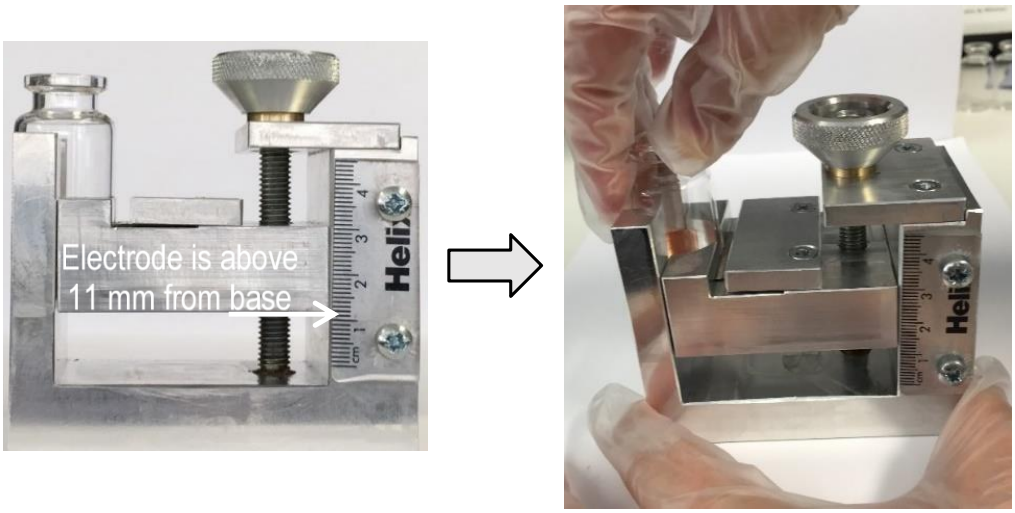

Figure 7 Trimming the top part of copper electrodes attached to the vial

1.8 After trimming the bottom and top parts of the electrode, a vial with 10 mm electrode height and separated from the base by 1 mm is obtained (Figure 8).

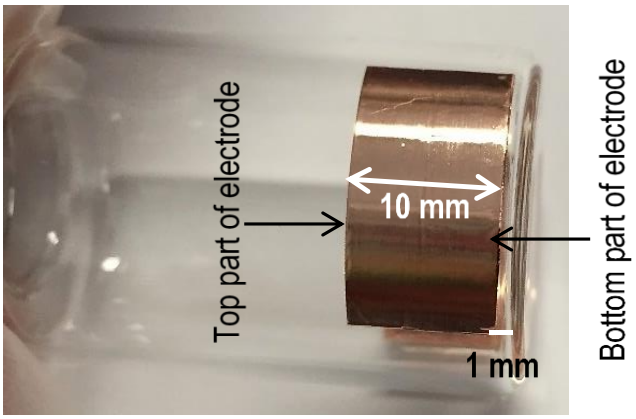

Figure 8 The vial with 10 mm electrode height and 1 mm above base

2. Wiring the cables

2.1 Hold the vial with the copper electrode from step 1.8 by using the holding clamp as shown in Figure 9. Do not tighten the holding clamp too strong, because it could break the vial.

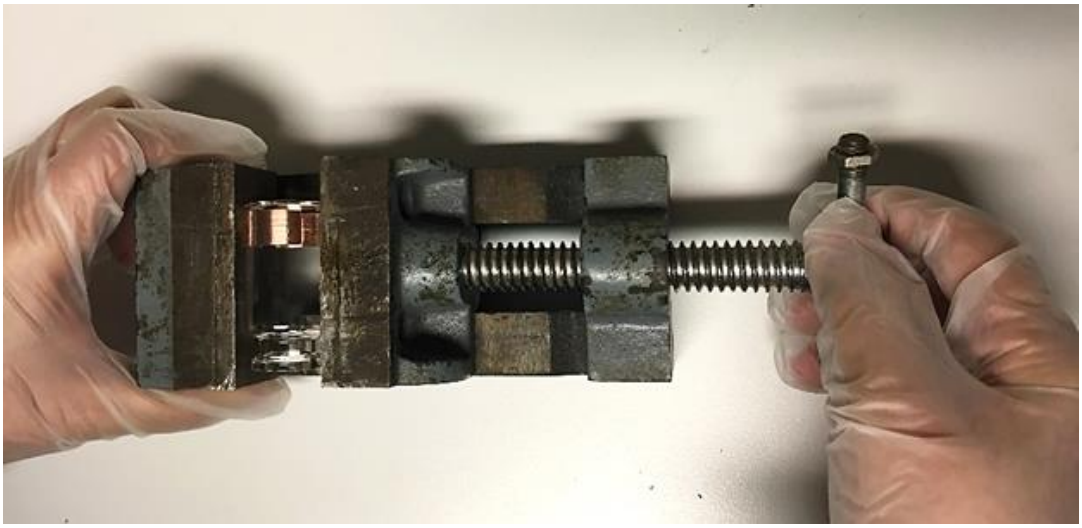

Figure 9 The vial is held by the holding clamp

2.2 Turn the soldering station “ON” (Figure 10) and allow the soldering iron to reach the set-up temperature. 290 °C is usually used.

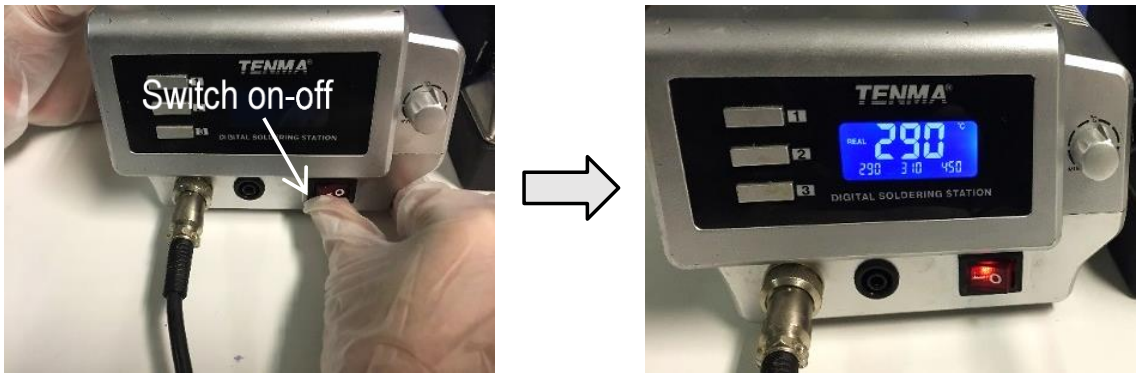

Figure 10 Turn on the soldering station and setting up temperature

2.3 Prepare the heat glue by cutting the heat glue rod approximately 2 mm thick, then halve it (Figure 11).

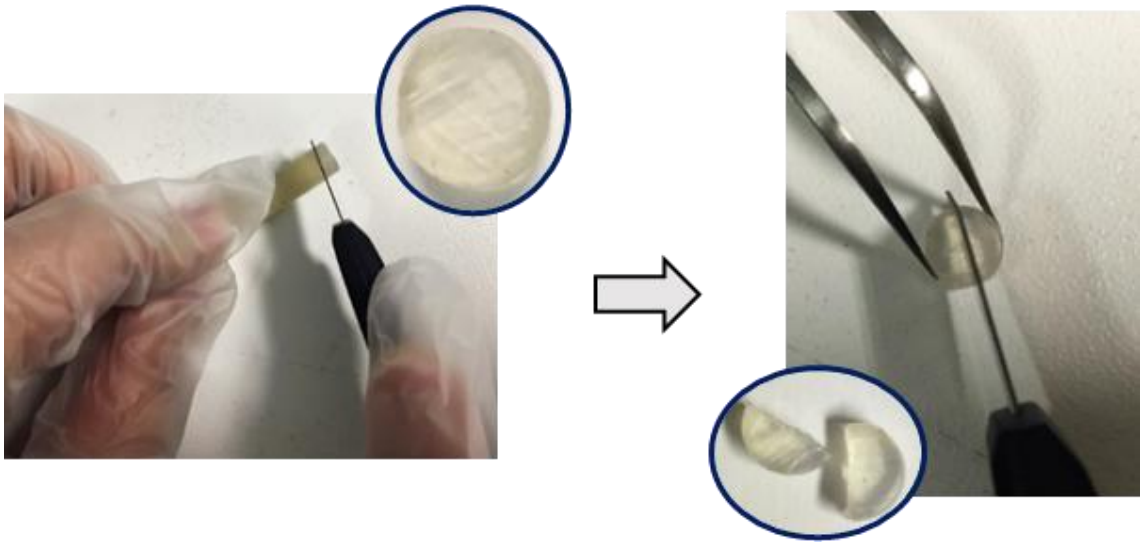

Figure 11 Preparation of the heat glue

2.4 Clean the hot soldering tip with either the brass coil or a tip cleaner (Figure 12).

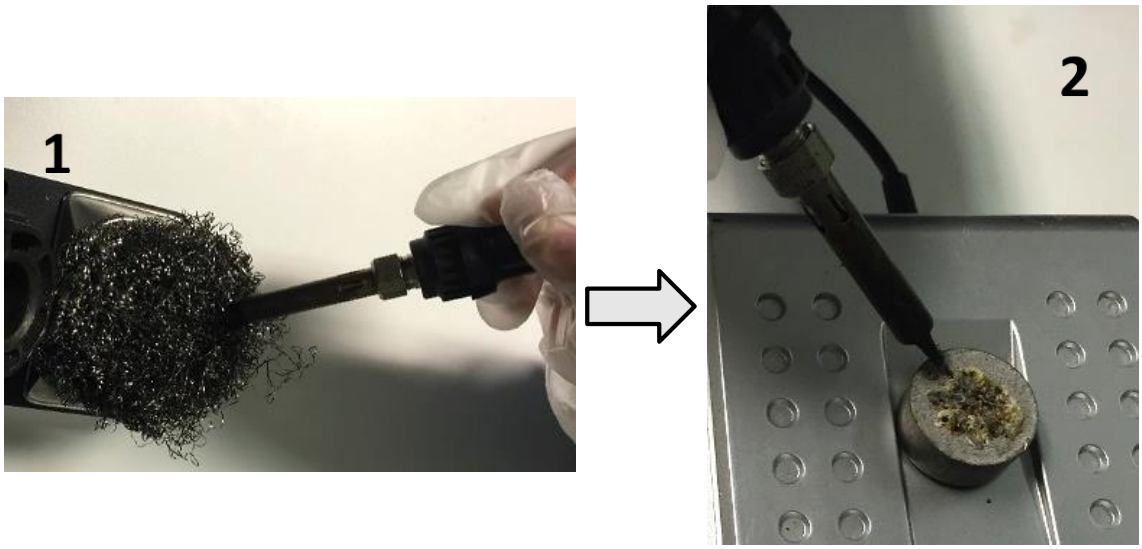

Figure 12 Cleaning the soldering tip

2.5 Place the soldering wire at the mid-point of the top part of the electrode, melt or solder it with a soldering iron, then leave it to cool down (for approximately 1 minute) as shown in Figure 13. Clean the soldering iron according to step 2.4 after use.

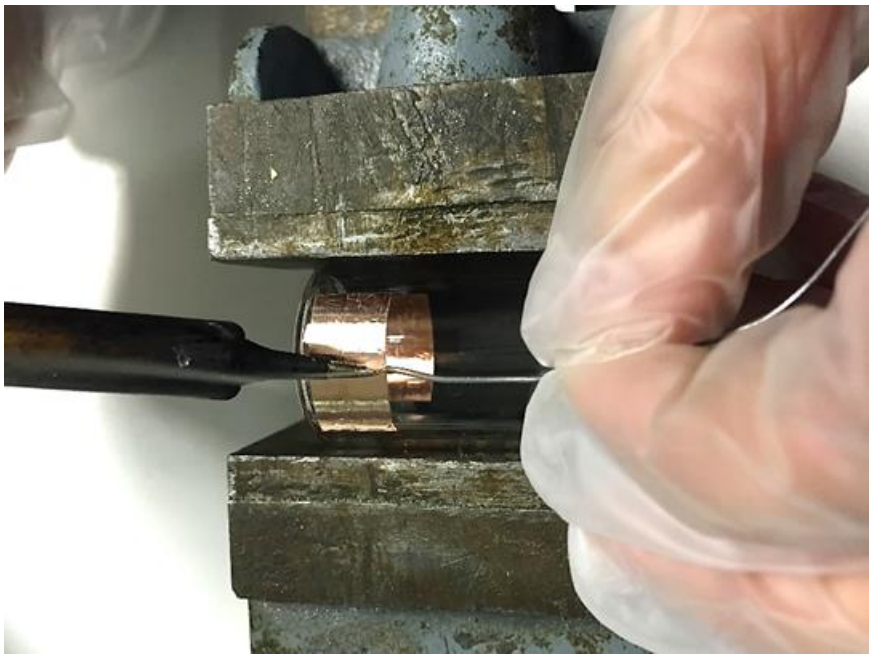

Figure 13 Tin soldering

2.6 Clean the gluing area on the external surface of the glass vial with ethanol and a cleaning cloth (Figure 14) to remove any flux left.

Figure 14 Cleaning the gluing area

2.7 Place a half piece of glue from step 2.3 in the gluing area, melt it (Figure 15), and clean the soldering iron according to step 2.4.

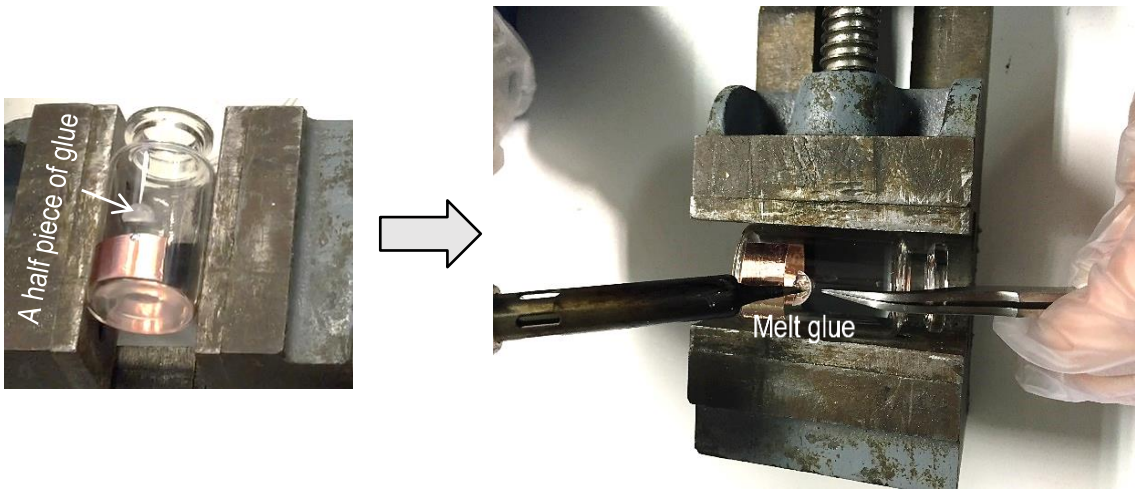

Figure 15 Melting the glue

2.8 Place the cable and touch the soldering iron onto the joint made in step 2.5 (Figure 16).

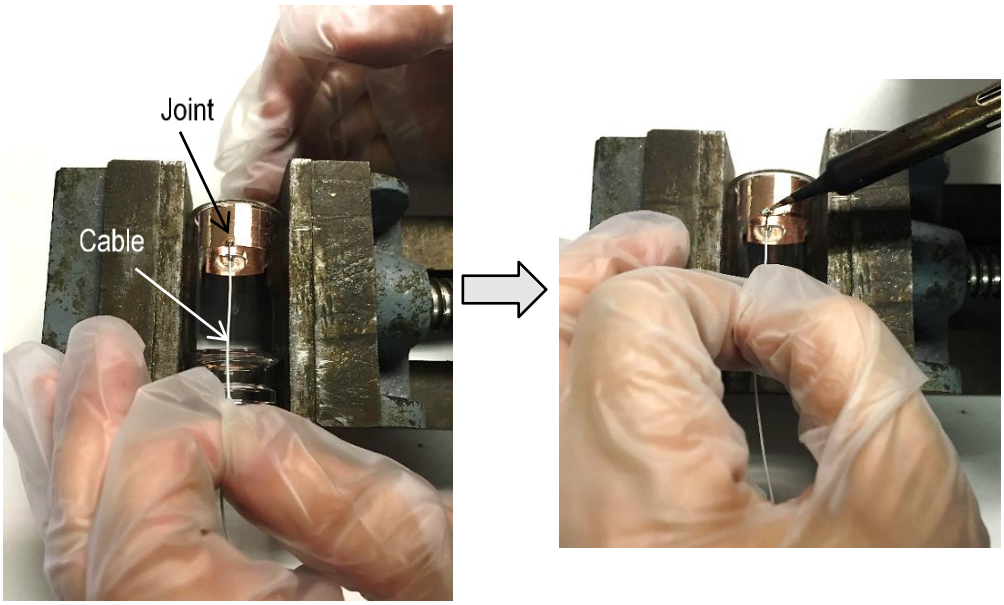

Figure 16 Soldering cable

2.9 Straighten the cable along the vial and hold it carefully (Figure 17).

Figure 17 Straighten and hold the cable

2.10 Touch the soldering tip on the droplet part of cable, press into the melted glue (Figure 18) and wait for the glue to dry or become more solid for a few minutes. Clean the soldering iron according to step 2.4.

Figure 18 Attach the cable to the vial with melted glue

2.11 Place the soldering wire at the joint, solder it with the iron. The soldering wire should be spread on the copper electrode and not form a ball to improve the contact between the conductive wire and electrode. Inappropriate connection causes failure in impedance measurement in disturbance, quality of signal and irregular spectrum. Leave it to cool down for approximately 1 minute, as shown in Figure 19. Clean the iron again (step 2.4) after soldering.

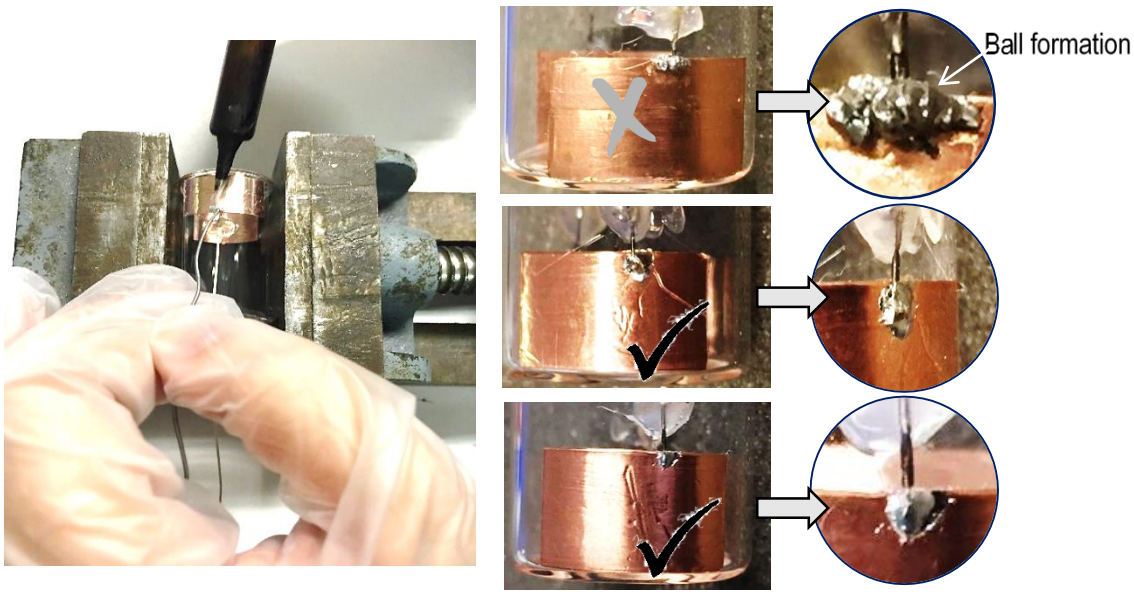

Figure 19 Tin soldering

2.12 Turn over another attached electrode, then repeat steps 2.4 to 2.11.

2.13 Turn the soldering station off, as shown in Figure 20.

Figure 20 Turn off the soldering station

2.14 Cut the heat shrink tubing to 5mm height, then put it on the vial (Figure 21).

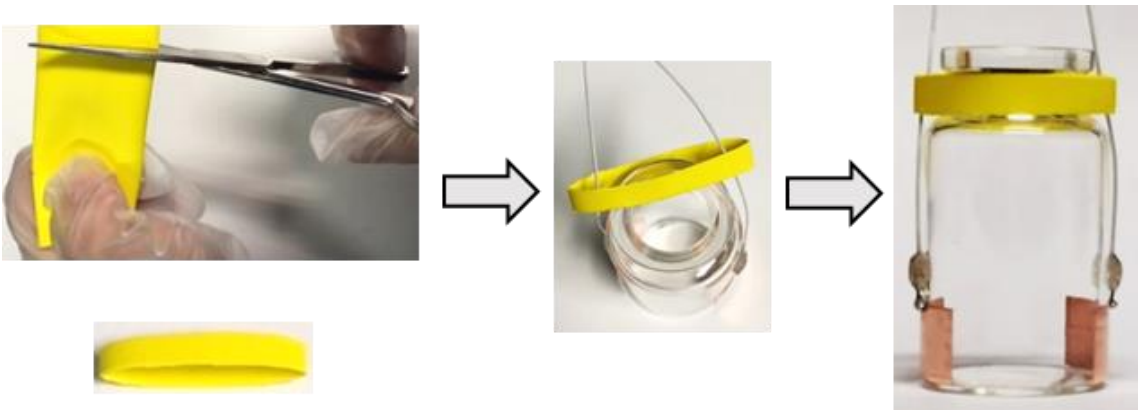

Figure 21 The vial with heat shrink tubing

2.15 Shape the heat shrink tubing with a blow torch to fix the cable, as shown in Figure 22.

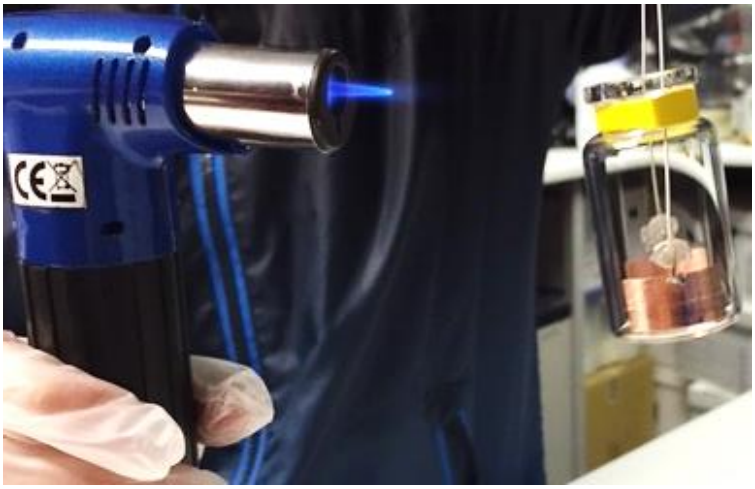

Figure 22 Shape the heat shrink tubing

3. Check integrity of wiring cable

3.1 Turn the dial of a digital multimeter to Ω (resistance, or ohms) then check it before use by touching the two probes together (Figure 23). It must beep.

Figure 23 Check a digital multimeter

3.2 Next, place one probe of the digital multimeter at the outside of the connector and another probe at the electrode attached to the vial, as shown in Figure 24. The digital multimeter must display zero on its screen.

Figure 24 Check for a short circuit of wiring cable

3.3 Then place one probe of the digital multimeter at the connector pin and another probe at the electrode attached on the vial, as shown in Figure 22. The digital multimeter must beep if the integrity of the wiring connection is okay.

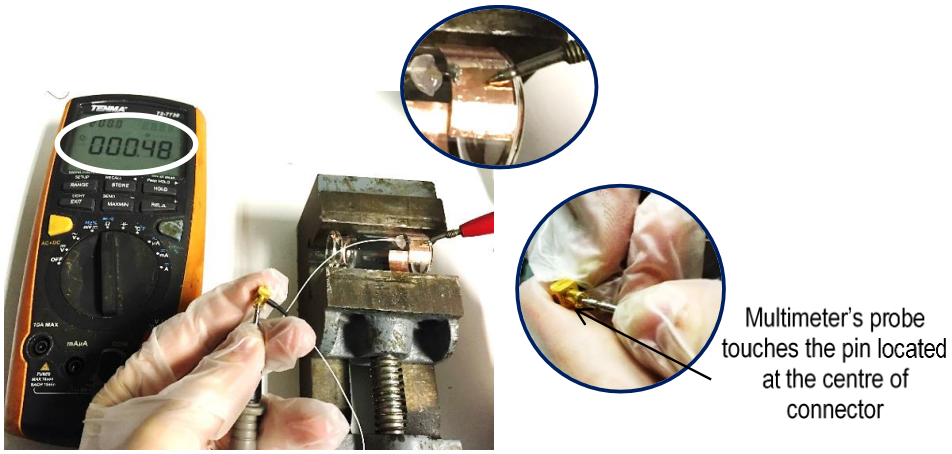

Figure 25 Check for a short circuit of wiring cable

4. Check measurement signal

4.1 Measurement the empty vial

4.1.1 Place the empty vial on the freeze dryer shelf, then connect two wires of the measurement vial to the junction box. One wire is connected to "STIMULATE"; another to "SENSE" in the junction box (Figure 26).

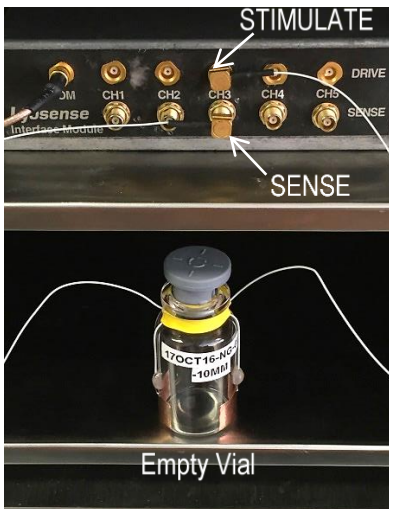

Figure 26 The empty vial connected to the junction box

4.1.2 Measure the empty vial with the TVIS system. The following data acquisition should be observed (Figure 27).

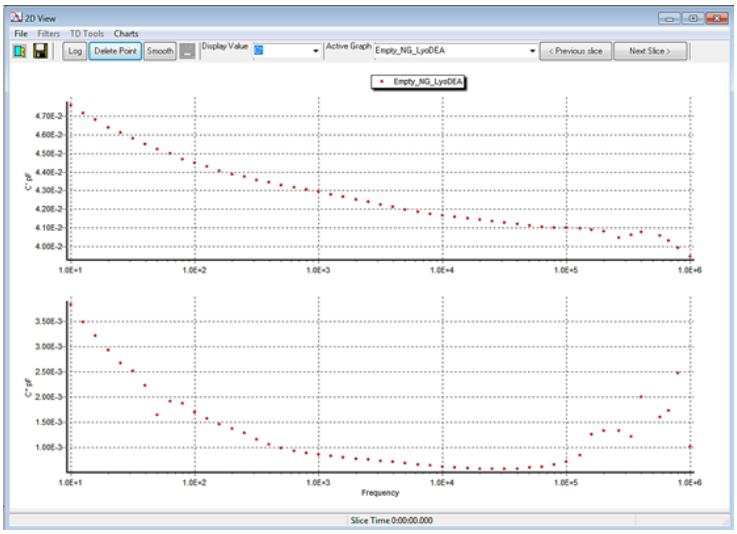

Figure 27 Data acquisition of empty vial

4.2 Measure the vial filled with 5 mL water.

4.2.1 Place the 5 mL water-filled vial on the freeze dryer shelf, then connect two wires of the measurement vial to the junction box. One wire is connected to “STIMULATE”; another to “SENSE” in the junction box (Figure 28).

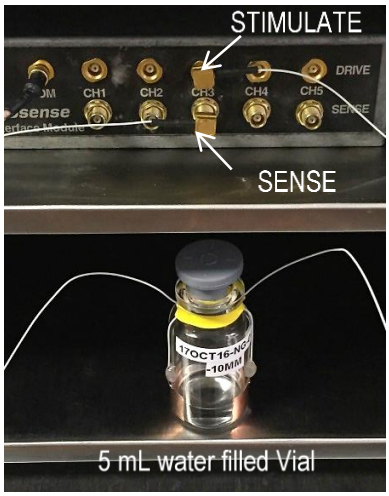

Figure 28 Prepared TVIS vial containing 5 mL water connected to the junction box

4.2.2 Measure the water-filled vial with the TVIS system. The following data acquisition should be observed (Figure 29).

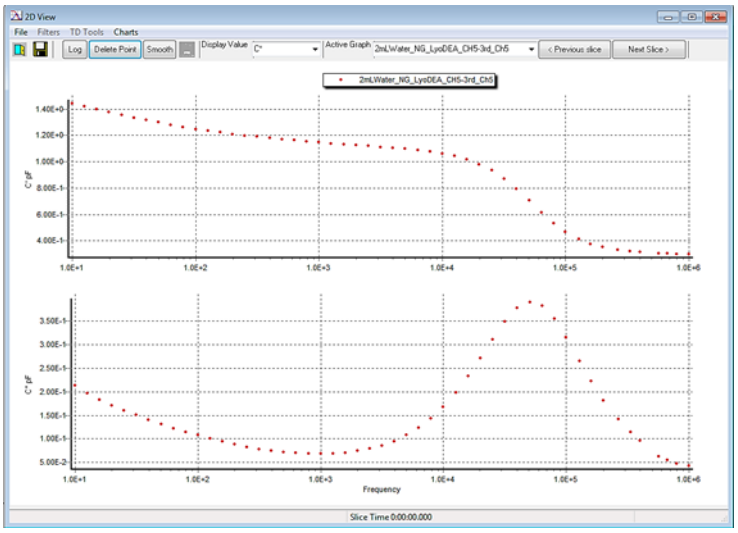

Figure 29. Data acquisition of vial filled with 5 mL water

Appendix II

Fill factor calculation

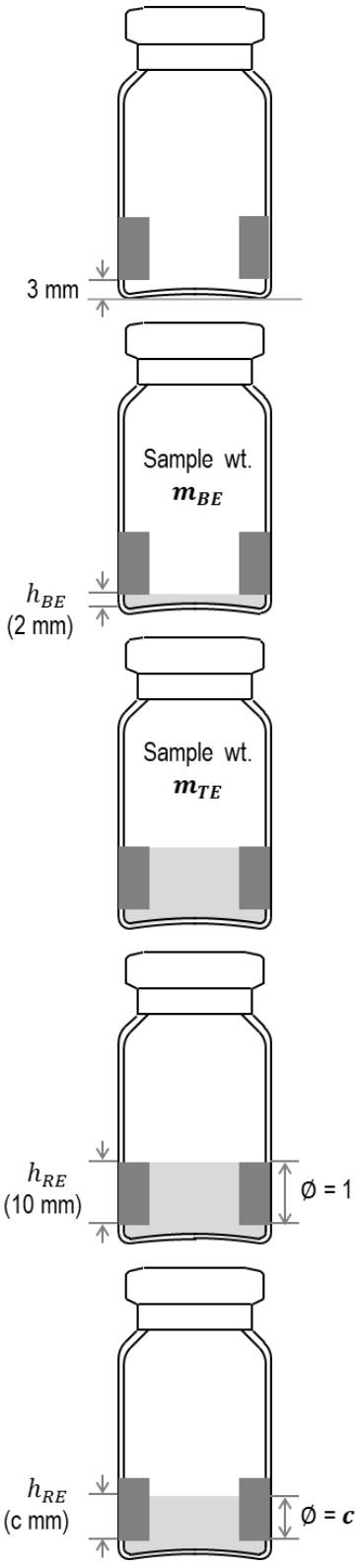

Tare an empty TVIS vial

Note: The height of the lower edge of electrode above the external base of the vial is 3 mm

Add the solution until the volume reaches the lower edge of the electrode and then record the weight of the solution ($\boldsymbol{m_{BE}}$)

Note: The height of sample below the lower edge of electrode from the internal base of the vial (h_{BE}) is 2 mm

Add more of the same solution until the volume reaches the upper edge of electrode and then record the weight of the solution ($\boldsymbol{m_{TE}}$)

Calculate the weight of the solution in the region bounded by the electrode for a fill factor (Ø) of 1:

$$Ø\ (1) = \boldsymbol{m_{TE}} - \boldsymbol{m_{BE}}$$

Note: The height of the solution bounded by the electrodes is defined as h_{RE}. For fill factor of 1, the value of h_{RE} is 10 mm

Once the individual vial is calibrated for fill factor of 1, then calculate the weight of the solution in the region bounded by electrode for any fill factor of $\boldsymbol{c}$:

$$Ø\ (\boldsymbol{c}) = [(\boldsymbol{m_{TE}} - \boldsymbol{m_{BE}}) \times \boldsymbol{c}] + \boldsymbol{m_{BE}}$$

Note: For electrode height of 10 mm, the value of h_{RE} is c mm for any fill factor of c

Appendix III

Calibration of C''_{PEAK} for liquid height

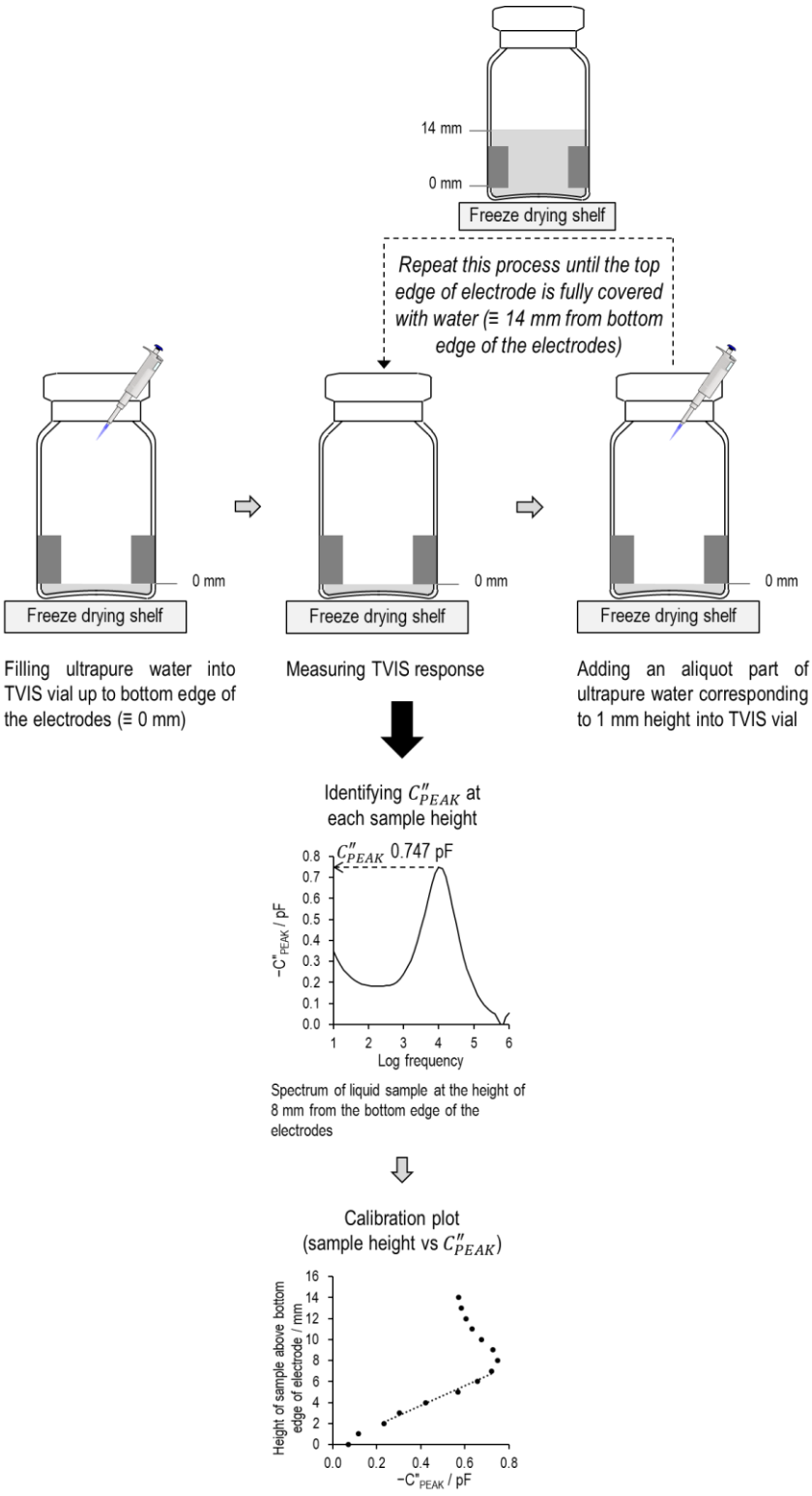

Appendix IV

Calibration of C''_{PEAK} for ice height